MMS 2018

PROCEEDINGS

THE FIRST INTERNATIONAL CONFERENCE

ON MATERIAL, MACHINES AND METHODS
FOR SUSTAINABLE DEVELOPMENT

Research Development in Industrial Material, Machining and Methods towards Sustainability

Da Nang, Vietnam
May 18 - 19, 2018

Vol 2



BACH KHOA PUBLISHING HOUSE

MMMS 2018

PROCEEDINGS

THE FIRST INTERNATIONAL CONFERENCE
ON MATERIAL, MACHINES AND METHODS FOR SUSTAINABLE DEVELOPMENT

Research Development in Industrial Material, Machining and Methods towards Sustainability

Da Nang, Vietnam
May 18 - 19, 2018

Vol 2

BACH KHOA PUBLISHING HOUSE

Edited by:
Banh Tien Long, Hyungsun Kim, Kozo Ishizaki, Nguyen Duc Toan, Nguyen Thi Hong Minh

Proceedings
of
The First International Conference
on Material, Machines and Methods for Sustainable Development

MMMS2018

Danang, Vietnam 18-19 May, 2018

Organized by:

Vietnam Association for Science Editing (VASE)

In cooperation with:

Hanoi University of Science and Technology, Hanoi, Vietnam

University of Da Nang (UDN)

Kyungpook National University (KNU-Korea)

Nagaoka University of Technology, Japan

Supported by:

Vietnam's National Foundation for Science
and Technology Development

Vietnam Peace Universtity

Electric Power University

Research Institute of Agriculture Machinery

Viet Nam Maritime University

Dong Thap University

Nong Lam University

Vietnamese-German University

Proceedings of the First International Conference on Material, Machines and Methods for Sustainable Development
Danang, Vietnam 18-19 May, 2018

Edited by:
Banh Tien Long
Hyungsun Kim
Kozo Ishizaki
Nguyen Duc Toan
Nguyen Thi Hong Minh

The conference organizers are especially grateful to Vietnam National Foundation for Science and Technology Development (NAFOSTED) for financial support.

All rights reserved. No part of the contents of this book may be reproduced or transmitted in any form or by any means without the written permission of the authors.

Preface

On behalf of the Organizing Committee, we are delighted to issue the proceedings which contains papers presented at the first International Conference on Material, Machines and Methods for Sustainable Development (MMMS) from 18-19 May, 2018 in Danang, Vietnam. The MMMS2018 continues enabling researchers from all over the world to share their research and accomplishments as well as review the research currently being conducted by their peers.

The purpose of the conference is to explore and ensure an understanding of the critical aspects which contributed to sustainable development, especially materials, machines and methods. From such understanding, the conference aims at an overall approach to assist policy makers, industries and researchers at various levels to position the local technological development towards sustainable development in the global context, to assist decision making towards a greener approach especially for material, machines and methods.

The papers published in this proceedings represent the state-of-the-art in the field of materials science and mechanical engineering. The contents of manuscripts from authors representing universities, research institutes and industrial companies demonstrate the results of very wide spectrum of research, from material design and processing, to the application material, the mechanical engineering technology in industry. The largest number of the papers answer the vital question of how to obtain the advanced properties and technologies required of final task and products by the way of the verifications and selections of the process and control parameters. Other important problems of new special materials are also covered by several researchers. A large group of papers focus on the material modeling as well as the eco-material technologies processes and mechanical manufacturing.

We would like to express our gratitude to the members of International Organizing and Academic Committees of the Conference, for their hard work and advices which were helpful in maintaining the high level of the Conference. We hope that the proceeding will become a source of valuable information in the scientific work for academics, researchers, engineers and students.

Best regards

Banh Tien Long, Hyungsun Kim, Kozo Ishizaki, Nguyen Duc Toan, Nguyen Thi Hong Minh

INTERNATIONAL ORGANISING COMMITTEE

Banh Tien Long, Vietnam Association for Science Editing, Vietnam
Bui Van Ga, Ministry of Education and Training, Vietnam
Dang Vu Minh, Vietnam Union of Science and Technology Associations, Vietnam
Dinh Van Phong, Hanoi University of Science and Technology, Vietnam
Do Huu Hao, Vietnam Federation of Mechanical Engineering Associations, Vietnam
Hoang Van Phong, Council for National Policy of Science and Technology, Vietnam
Kim Hyungsun, Council of Asian Science Edditors, Korea
Kim Kyuman, Kyungpook National University, Korea
Kim Youngsuk, Kyungpook National University, Korea
Kozo Ishizaki, Nagaoka University of Technology, Japan
Nghiem Vu Khai, Vietnam Union of Science and Technology Associations, Vietnam
Nobuhiko Azuma, Nagaoka University of Technology, Japan
Tran Quoc Khanh, Ministry of Science and Technology, Vietnam
Tran Van Nam, Da Nang University, Vietnam

INTERNATIONAL ADVISORY COMMITTEE

Chinda Charoenphonphanich, King Mongkut's Institute of Technology Ladkrabang, Thailand
Erik Bohez, Asian Institute of Technology, Thailand
Gyu Man Kim, Kyungpook National University, Korea
Heidy Visbal, Kyot University
Holger Kohl, Fraunhofer IPK Berlin, Germany
Hyungsun Kim, Inha University, Korea
Jong Kyu Ha, Seoul National University, Korea
Jung Il Jin, Korea University, Korea
Kozo Ishizaki, Nagaoka University of Technology, Japan
Makoto Nanko, Nagoya Institute of Technology
Nobumasa Sekishita, Toyohashi University of Technology, Japan
Nobutaka Ito, Chang Mai University, Thailand
Ralph J. Hexter, UC Davis, US
Ramanathan Subramaniam, National Institute of Education, Singapore
Ramesh s. Kanwar, University of Hawaii, US
Seung Han Yang, Kyungpook National University, Korea
Soo Wohn Lee, Professor, Sunmoon University
Takashi Shirai, Kyoto Institute of Technology, Japan
Tetsuro Majima, Osaka University, Japan
Wim Dewulf, Katholieke Universiteit Leuven, Belgium
Worachart Sirawaraporn, Mahidol University, Thailand
Yoshiki Mikami, Nagaoka University of Technology, Japan
Yukari Matsuo , Hosei University, Japan

LOCAL ORGANIZING COMMITTEE

Banh Tien Long, Vietnam Association for Science Editing, Vietnam
Dinh Van Chien, Vietnam Association for Science Editing, Vietnam
Nguyen Thi Hong Minh, Vietnam Association for Science Editing, Vietnam
Nguyen Duc Toan, Vietnam Association for Science Editing, Vietnam
Nguyen Huu Quang, Vietnam Association for Science Editing, Vietnam
Pham Duc An, Hanoi University of Science and Technology, Vietnam
Phan Van Hieu, Vietnam Association for Science Editing, Vietnam
Hoang Long, Vietnam Association for Science Editing, Vietnam
Dinh Van Phong, Hanoi University of Science and Technology, Vietnam
Le Anh Tuan, Hanoi University of Science and Technology, Vietnam

Nguyen Minh Hong, Ministry of Information and Telecomunication, Vietnam
Duong Thanh Binh, Journal of Vietnam Mechanical Engineering, Vietnam
Tran Trung, Hung Yen University of Technology and Education, Vietnam
Tran Van Nam, Da Nang University, Vietnam
Doan Quang Vinh, Da Nang University, Vietnam
Duong Viet Dung, Da Nang University, Vietnam
Luu Duc Binh, Da Nang University, Vietnam
Vu Trung Hung, Da Nang University, Vietnam

SCIENTIFIC COMMITTEE

Banh Tien Long, Hanoi University of Science and Technology, Vietnam
Chinda Charoenphonphanich, King Mongkut's Institute of Technology Ladkrabang, Thailand
Chu Van Dat, Military Technical Institute, Vietnam
Dao Hong Bach, Hanoi University of Science and Technology, Vietnam
Erik Bohez, Asian Institute of Technology, Thailand
Gyu Man Kim, Kyungpook National University, Korea
Jung Il Jin, Korea University, Korea
Le Anh Tuan, Hanoi University of Science and Technology, Vietnam
Le Chi Hiep, Ho Chi Minh City University of Technology, Vietnam
Le Danh Lien, Hanoi University of Science and Technology, Vietnam
Le Quang, Hanoi University of Science and Technology, Vietnam
Nobuhiko Azuma, Nagaoka University of Technology, Japan
Nobumasa Sekishita, Toyohashi University of Technology, Japan
Nghiem Trung Dung , Hanoi University of Science and Technology, Vietnam
Nguyen Dang Binh, Viet Bac University, Vietnam
Nguyen Hong Lanh, Military Technical Institute, Vietnam
Nguyen The Mich, Hanoi University of Science and Technology, Vietnam
Nguyen Thi Thu Hien, Hanoi University of Science and Technology, Vietnam
Nguyen Viet Dung, Hanoi University of Science and Technology, Vietnam
Pham Minh Tuan, Hanoi University of Science and Technology, Vietnam
Pham Thanh Huy, Hanoi University of Science and Technology, Vietnam
Pham Van Hung, Hanoi University of Science and Technology, Vietnam
Seung Han Yang, Kyungpook National University, Korea
Soo Wohn Lee, Professor, Sunmoon University
Tran Van Dich, Hanoi University of Science and Technology, Vietnam
Tran Van Nam, The University of DaNang, Vietnam
Truong Ngoc Than, Hanoi University of Science and Technology, Vietnam
Vu Duc Lap, Military Technical Institute, Vietnam
Vu Quoc Huy, Hanoi University of Science and Technology, Vietnam
Wim Dewulf, Katholieke Universiteit Leuven, Belgium
Heidy Visbal, Kyot University
Holger Kohl, Fraunhofer IPK Berlin, Germany
Hyungsun Kim, Inha University, Korea
Jong Kyu Ha, Seoul National University, Korea
Kozo Ishizaki, Nagaoka University of Technology, Japan
Makoto Nanko, Nagoya Institute of Technology
Nobutaka Ito, Chang Mai University, Thailand
Ralph J. Hexter, UC Davis, US
Ramanathan Subramaniam, National Institute of Education, Singapore
Ramesh S. Kanwar, University of Hawaii, US
Takashi Shirai, Kyoto Institute of Technology, Japan
Tetsuro Majima, Osaka University, Japan

Worachart Sirawaraporn, Mahidol University, Thailand
Yoshiki Mikami, Nagaoka University of Technology, Japan
Yukari Matsuo, Hosei University, Japan

CONTACT

Email: mmms@hust.edu.vn

Website: mmms2018.hust.edu.vn

Facebook: facebook.com/mmms2018/

Science Secretary

Assoc. Prof. Nguyen Duc Toan

Email: toan.nguyenduc@hust.edu.vn

Local organizer

Assoc. Prof. Nguyen Thi Hong Minh

Email: minh.nguyenthihong@hust.edu.vn

TABLE OF CONTENTS

CHAPTER 1. ADVANCED RESEARCH FOR SUSTAINABILITY IN ENGINEERING

1. Innovative Porous Ceramics And Their Applications 1...5

   PID 424 - Corresponding author: Kozo Ishizaki - Nagaoka Univ. of Tech.

2. Lighting For A Sustainable Future: High Power White Leds With Phosphor-In-Glass 6...14

   PID 201 - Corresponding author: Hyungsun Kim - Inha Univ.

3. Development Of High Specific Strength Alloys For Sustainable Society 15...15

   PID 115 - Corresponding author: Nack J. Kim - POSTECH

4. Effects Of Starting Materials On Preparation And Properties Of Pure Sic Ceramics Via The Htpvt Method 16...22

   PID 310 - Corresponding author: Jianfeng Yang - Xi'an Jiaotong University, China

CHAPTER 2. ADVANCED MATERIALS, MATERIAL APPLICATIONS TOWARDS SUSTAINABILITY

5. Brittleness Indicators Of High-Performance Steel-Fiber-Reinforced Concretes Under Compression With Their Size Effects 23...30

   PID 29 - Corresponding author: Duy-Liem Nguyen - Ho Chi Minh City University of Technology and Education

6. Effect Of Residual Stress In Chrome Plating Layer To Fatigue Strength Of The Axial Machine Parts 31...37

   PID 42 - Corresponding author: Thien Ngon Dang - HCM City University of Technology and Education

7. Study On Microstructure And Properties Of Cu-9Ni-6Sn Alloy Applied For Electric Measurement 38...43

   PID 43 - Corresponding author: Nam Nguyen Duong - Viet Nam Maritime University

8. Hysteresis Identification Of Bidirectional Magneto-Rheological Actuators Employing Preisach Model 44...49

   PID 51 - Corresponding author: Thanh Danh Le - Ho Chi Minh City University of technology Viet Nam

9. Full-Field Strain Measurements Of A Novel Lead-Free Solder Based On Digital Image Correlation 50...57

   PID 58 - Corresponding author: Quang Bang Tao - The University of Danang - University of Science and Technology

10. Strong And Ductile Steels For Lightweight Applications 58...58

    PID 138 - Corresponding author: Alireza Zargaran - Graduate Institute of Ferrous Technology, POSTECH

11. Designing Magnesium Alloy With High Strength And High Formability 59...59

PID 139 - Corresponding author: Thi Thanh Tram Trang - Graduate Institute of Ferrous Technology, Pohang University of Science and Technology

12. Development Of Precipitation Hardened Austenitic High Mn Steels For Automotive Applications 60...60

PID 155 - Corresponding author: Yunik Kwon - POSTECH

13. Development Of Self-Healing Materials Applied To Ebcs System For Sic Sic Composites 61...61

PID 179 - Corresponding author: Huy Vu Dinh - Nagaoka University of Technology

14. Effects Of Using Nitrile Rubber Foam And Solar Panels On Cover For Cooling Outdoor Sparking Car 62...69

PID 183 - Corresponding author: Nguyen Luong - School of Transportation Engineering, Hanoi University of Science and Technology

15. Influence Of Working Condition On Properties Of Superheater Steel Pipe (Astm Grade P11) 70...76

PID 261 - Corresponding author: Cao Son Nguyen - Hanoi University of Science and Technology

16. Hollow Zif-8 As An Efficient Photocatalytic Material For The Degradation Of Indigo Carmine 77...77

PID 265 - Corresponding author: Thanh Nhan Nguyen - Sun Moon University, Korea

17. Study For Continuous Fabrication Of The Dry Adhesive 78...78

PID 279 - Corresponding author: Sung Ho Lee - Kyungpook National University

18. Compressive Resistance Of Environmental Concrete Using Fly Ash And Fine Aggregate For Replacing Traditional Sand 79...84

PID 318 - Corresponding author: Duy-Liem Nguyen - Ho Chi Minh City University of Technology and Education

19. Mechanical Properties Of Composites With Geopolymer Matrices Reinforced By Basalt Fabric 85...88

PID 405 - Corresponding author: Iva Petríková - Technical University of Liberec

CHAPTER 3. MATERIALS MACHINING AND PROCESSING TECHNOLOGIES FOR REDUCTION OF ENVIRONMENTAL IMPACT

20. Investigation Of Springback Prediction For An Al70Xx Sheet Subjected To Press Forming Process 89...97

PID 59 - Corresponding author: Pham Quoc Tuan - Kyungpook National University

21. Effect Of Ultrasonic Vibration On Increasing Embossing Speed During Hot Glass Embossing Process 98...105

PID 66 - Corresponding author: Lanphuong Nguyen - Hanoi University of Science and Technology

22. Researching On Texture Microstructure Treatment Of Jis G4051 S45C Small Diameter Rolled Steel 106...112

PID 76 - Corresponding author: Thien Ngon Dang - HCM City University of Technology and Education

23. Adsorption Properties Of Congo Red From Aqueous Solutions On Activated Humin 113...119

PID 81 - Corresponding author: Duy Phan The - Ho Chi Minh City University of Natural Resources and Environmental

24. Study The Effect Of Chemical Treatment On Substrate Surface On The Formation Nanodots Array And Its Optical Properties 120...126

PID 90 - Corresponding author: Truong Duc Phuc - School of Mechanical Engineering, HUST

25. Synthesis And Photocatalytic Activity Of F-Doped G-C3N4 127...135

PID 103 - Corresponding author: Vien Vo - Quy Nhon University

26. Surface Modification Process By Electrical Discharge Maching With Tungsten Carbide Powder Mixing In Kerosene Fluid 136...143

PID 120 - Corresponding author: Le Van Tao - MTA

27. A Study On The Effect Of Ti Target Poisoning To Tin Coating Deposited By A Dc Magnetron Sputtering 144...149

PID 190 - Corresponding author: Cuong Pham Duc - Hanoi University of Industry

28. Asian Agriculture Growth Strategy 150...156

PID 259 - Corresponding author: Nobutaka Ito - Chiang Mai University

29. Evaporation Of Tramp Elements In Liquid Steel For Ferrous Scrap Recycling 157...157

PID 270 - Corresponding author: Youn-Bae Kang - Pohang University of Science and Technology

30. Analysis And Fabrication Of A Mechanical Quick-Stop For Research On Chip Formation In Hard Turning Process 158...165

PID 341 - Corresponding author: Dung Nguyen - Thai Nguyen University of Technology

31. Multi-objective optimization of powder mixed electrical discharge machining using titanium powder by Topsis method 166...174

PID 357 - Corresponding author: Nguyen Huu Phan - Hanoi University of Industry

32. Study On The Cutting Properties Of The Singer Layer Metal Bonded Cbn Grinding Wheel By Electroplating In Grinding Of Heat-Treated Steel Skd11 175...181

PID 406 - Corresponding author: Truong Hoanh Son - Hanoi University of Science and Technology

33. Vibration Analyses Of A Tapered Composite Thin-Wall Box Beam With Rectangular Section 182...190

PID 407 - Corresponding author: Le Thuong Hien - University of Power Electric

CHAPTER 4. SUSTAINABLE MACHINE DESIGN: MECHATRONICS, CAD/CAM/CAE, MARITIME ENGINEERING

34. Research On Modeling And Calculating Vibration Characteristic Of Car Body Assembled And Manufactured In Vietnam 191...198

PID 35 - Corresponding author: Nguyen Thanh Cong - University of Transport and Communications

35. Auto-Tuning Parameters For Motion Cueing Algorithms With Mean-Variance Mapping Optimization Method 199...206

PID 80 - Corresponding author: Duc An Pham - Hanoi University of Science and Technology

36. Modeling Energy Harvesting Devices With Non-Uniformly Polarized Piezoceramic Materials 207...213

PID 111 - Corresponding author: Arkadiy Soloviev - Department of Theoretical and Applied Mechanics, Don State Technical University, Rostov-on-Don, Russia

37. Ball For Cam Mechanism Design 214...214

PID 114 - Corresponding author: Ha Nguyen Van - Technical University of Liberec

38. New Approaches In Tool Path Optimization Of Cnc Punching Machine By Simulated Annealing 215...223

PID 126 - Corresponding author: Nguyen Thanh Tan - HCMC University of Technology and Education

39. First Experiences With Microsoft Kinect V2 For 3D Modelling Of Mechanical Parts 224...231

PID 128 - Corresponding author: Van Bien Bui - Hai Phong University

40. Designing, Manufacturing And Testing The Cycling Training System Featuring Magnetorheological Brake 232...242

PID 148 - Corresponding author: Quoc Hung Nguyen - www.vgu.edu.vn

41. Design And Optimization Of A New Hollow Circular Flexure Hinge For Precision Mechanisms 243...250

PID 161 - Corresponding author: Huy-Tuan Pham - HCMC University of Technology and Education

42. Dynamic Behavior of Tilting–Pad Journal Bearings with Variable Pivot Stiffness 251...258

PID 192 - Corresponding author: Phuoc Vinh Dang - The University of Danang - University of Science and Technology

43. Re-Designing Cam Profiles Of Internal Combustion Engine With Simulation Method 259...266

PID 220 - Corresponding author: Khoa Nguyen Xuan - Smart Powertrain Laboratory of Ulsan University, South Korea

44. Optimal Design Of A New Compliant Micropositioning Rotary Stage For Nanoindentation Tester Using Taguchi Method, Response Surface Method And Teaching Learning Based Optimization 267...274

PID 230 - Corresponding author: Thanh-Phong Dao - Ton Duc Thang University

45. Optimal Design For A New Compliant Torsion Spring Of An Assistive Device For Upper Limb Using Hybrid Approach Of Taguchi Method, Response Surface Method, And Cukoo Search Algorithm 275...282

PID 232 - Corresponding author: Thanh-Phong Dao - Ton Duc Thang University

46. Design And Analysis Of A Displacement Sensor-Integrated Compliant Micro-Gripper Based On Parallel Structure 283...290

PID 277 - Corresponding author: Thanh-Phong Dao - Ton Duc Thang University

47. Developing A High Oxidation Water Machine Using Plasma Technology For Vegetable Sterilizing 291...296

PID 354 - Corresponding author: Tran Ngoc Dam - Ho Chi Minh University of Technology and Education

48. Design Of Heat-Forming Machine Using Induction Coil For Small Scale Plastic Recycling Enterprises 297...305

PID 360 - Corresponding author: Tan Bui Duy - Vietnamese German University

CHAPTER 5. RENEWABLE ENERGY, ENERGY SAVING, LIFE CYCLE ENGINEERING

49. Experimental Investigation On Establishing The Hcci Process In A Single Cylinder Diesel Engine At Different Compression Ratios 307...313

PID 27 - Corresponding author: Tuan Le Anh - School of Transportation Engineering, Hanoi University of Science and Technology

50. Effects Of Capacitor On The Hybrid Ignition System 314...320

PID 52 - Corresponding author: Ngoc Nguyen - HCMCUTE

51. Some Results Research Of Current Turbine Working At Low Speed Flow To Apply In The Power Generator Equipment For The Independent Consumer, Fishing And Marine Transportation 321...328

PID 60 - Corresponding author: Ngo Van He - Hanoi University of Science and Technology

52. Experimental Investigation Into The Influence Of Compression Ratio On Operating Characteristics Of Single Cylinder Cng Engine With Port Injection 329...335

PID 105 - Corresponding author: Tran Dang Quoc - Hanoi University of Science and Technology

53. Improvement In Operating Performance Of A Solenoid Used For Natural Gas Injector 336...341

PID 182 - Corresponding author: Hung Nguyen Ba - University of Ulsan

54. Supporting Data Sharing In The Medical Treatment Process: A Plm Perspective 342...349

PID 187 - Corresponding author: Thanh Nghi Ngo - Ecole Centrale de Nantes

55. Dual Free-Piston Si Engine Dynamics And Piston Motion Control 350...356

PID 196 - Corresponding author: Nam Vu Dinh - University of Ulsan

56. Improving The Energy Efficiency And Reducing The Emission Of Motorcycle With Hydrogen-Rich Gas 357...363

PID 274 - Corresponding author: Jau-Huai Lu - National Chung Hsing University, Taiwan

57. Snow Utilization As Cold Heat Source - Advantages And Features 364...373

PID 404 - Corresponding author: Seiji Kamimura - Nagaoka University of Technology

58. The Influence Of Temperature, Residence Time, And Heating Rate Of The Slow Pyrolysis Process On Woody Biochar Quality 374...381

PID 417 - Corresponding author: Duc Dung Le - Hanoi University of Science and Technology

CHAPTER 6. INDUSTRIAL ENGINEERING AND NEW TECHNOLOGY TOWARDS SUSTAINABILITY

59. Surface Modified Carbonyl Iron Based Magnetorheological Elastomer And Its Magnetorheological Characteristics 383...383

PID 75 - Corresponding author: Hyoung Jin Choi - Inha University

60. Applying Particle Swarm Optimization For Solving The Production Planning Problem 384...391

PID 147 - Corresponding author: Hai Dung Dinh - Vietnamese German University

61. A Simulation Study On Improving Formability Of Sus304 Sheet Metal Deep Drawing Process 392...397

PID 153 - Corresponding author: Vu Duc Thuyen - Faculty of Mechanical Engineering, Hungyen University of Technology and Education, Hungyen, Vietnam

62. Experimental Study On Polishing Process Of Cylindrical Roller Bearings 398...404

PID 154 - Corresponding author: Nguyen Duc Nam - Industrial University of Ho Chi Minh City

63. Study Computational Simulation And Experimental Of Butt-Joint By Visual-Weld Software And Mig Welding Process 405...412

PID 160 - Corresponding author: Quoc Manh Nguyen - Education

64. Continuous Improvement Of Productivity And Quality With Lean Six Sigma: A Case Study 413...420

PID 249 - Corresponding author: Ngoc Hien Do - Ho Chi Minh City University Of Technology, Vietnam National University

65. Flexible Job Shop Scheduling With Batch And Discrete Processing Machines 421...428

PID 250 - Corresponding author: Lam Le Ngoc Quynh - Ho Chi Minh City University of Technology, Vietnam National University

66. Improving Working Postures And Increasing Productivity By Re-Design Work Station And Layout 429...435

PID 312 - Corresponding author: Quoc-Cong Tran - Ho Chi Minh City University of Technology

67. Blade Design And Numerical Testing Of A Small Wind Turbine For A Low Wind Speed Conditions 436...443

PID 347 - Corresponding author: Phan Thành Long - Danang University of Science and Technology

68. Investigation The Stiffness Characteristic Of Self-Aligning Hydrodynamic Bearing On External Cylindrical Grinding Machine Based On Numerical Simulation 444...451

PID 409 - Corresponding author: Toan Nguyen - Hanoi University of Science and Technology

69. Research On The Flattening Of The 3D Clothing Pattern Into 2D Clothing Parts 452...459

PID 418 - Corresponding author: Trung Ngo Chi - Hanoi Uninversity of Science and Technology

CHAPTER 7. DRIVING AND POWER ENGINEERING TOWARDS SUSTAINABILITY

70. Research To Evaluate The Quality Of Bus Body Frame, Assuring The Passive Safety In The Design Process 461...467

PID 48 - Corresponding author: Nguyen Thanh Cong - University of Transport and Communications

71. A Research On Locating Agv Via Rss Signals 468...474

PID 70 - Corresponding author: Minh Khoi Huynh - Ho Chi Minh City University of Technology

72. Researching And Applying The Line Balancing Methods In Optimizing Automobile Assembly Lines 475...480

PID 85 - Corresponding author: Minh Tai Le - Ho Chi Minh City University of Technology and Education

73. The Research On Position Response Of Table Transmission By Hydraulic Motor 481...488

PID 152 - Corresponding author: Hai Tran Ngoc - University of Science and Technology, The University of Da Nang, Viet Nam

74. Finite Element Analysis In Automobile Chassis Design 489...496

PID 164 - Corresponding author: Nguyen Thanh Quang - Hung Yen University of Technology and Education

75. Numerical Investigations Of Aerodynamics Characteristics Of Main Rotors In Helicopter Uav Using For Spraying Pesticide In Agriculture 497...505

PID 178 - Corresponding author: Hoang Thi Kim Dung - Hanoi University of Science and Technology

76. Experimental Research On The Effect Of Wing Structure On Aeroelasticity Phenomenon 506...512

PID 181 - Corresponding author: Hoang Thi Kim Dung - Hanoi University of Science and Technology

77. Effect Of Shapes And Turbulent Inlet Flow To Vortices On Delta Wings 513...518

PID 186 - Corresponding author: Hoang Thi Kim Dung - Hanoi University of Science and Technology

78. Optimal Selection Of Marine Propellers Based On Wageningen B-Series 519...525

PID 223 - Corresponding author: Khanh Hieu Ngo - Ho Chi Minh City University of Technology, VNU-HCM

79. An Approach To Improve On Stiffness For Aerostatics Bearing 526...531

PID 238 - Corresponding author: Thien Ngon Dang - HCM City University of Technology and Education

80. Research On Control Actuator Rehabilitation For Knee Flexion - Extension Using The Arduino Uno Controller 532...541

PID 325 - Corresponding author: Duc Dao - Pham Van Dong University

81. A Way To Enhance The Efficiency Of A Vertical Axis Wind Turbine 542...549

PID 400 - Corresponding author: Phan Quang The - Thai Nguyen University of Technology

CHAPTER 8. ADVANCED MACHINABILITY TOWARDS SUSTAINABILITY

82. Probabilistic Analysis On The Uncertainty In Natural Frequency Of Functionally Graded Material Beams 551...555

PID 33 - Corresponding author: Van Thuan Nguyen - Nha Trang University

83. Machining Based Geometric Error Estimation Method For 3-Axis Cnc Machine 556...561

PID 40 - Corresponding author: Trung Kien Hoang - Ho Chi Minh City University of Technology and Education

84. Evaluating Energy Efficiency Of Production Machine 562...569

PID 47 - Corresponding author: Thi Ai Lanh Nguyen - University of Technology and Education - The University of Danang

85. Modelling And Simulation Of Low Frequency Vibration Isolation Table 570...575

PID 50 - Corresponding author: Thanh Danh Le - Ho Chi Minh City University of Technology Viet Nam

86. Effect Of Feed Rate, Toolpath And Step Over On Geometric Accuracy Of Freeform Suface When 3 Axis Cnc Milling 576...584

PID 73 - Corresponding author: Quy Hoang Van - Hai Phong University

87. Hysteresis Investigation Of Shear-Mode Mr Damper For Front-Loaded Washing Machine 585...594

PID 150 - Corresponding author: Quoc Hung Nguyen - www.vgu.edu.vn

88. A Methodology For Generating A Variable-Pitch Rotor Of Twin-Screw Vacuum Pump 595...603

PID 151 - Corresponding author: The Van Tran - Department of Mechanical Engineering, Hung Yen University of Technology and Education

89. Experimental Researching Of Thermal - Assisted Milling With Induction On Surface Roughness Of Skd11 Steel 604...609

PID 219 - Corresponding author: Bich Mac – Dai Hoc Su Pham Ky thuat Hung Yen

90. Model Design And Numerical Simulation For Plastic Recycle Machine 610...618

PID 222 - Corresponding author: Tung Ho Thanh - Vietnamese German University

91. Fundamentals Of Computing And Designing A Rotary Feeder 619...624

PID 268 - Corresponding author: Thinh Van Huu - HCM city University of Technology and Education

CHAPTER 9. MATERIALS PROPERTIES TOWARDS SUSTAINABILITY

92. Mechanical Properties Of Ss400 Steel Plate At Elevated Temperatures 625...631

PID 25 - Corresponding author: Gia-Hai Vuong - The University of Hai Phong

93. Sulfur-Doped G-C3N4 With Enhanced Visible-Light Photocatalytic Activity 632...641

PID 104 - Corresponding author: Vien Vo - Quy Nhon University

94. Investigation Of Blended Cement Hydration In The Reactive Powder Concrete With Increasing Levels Of Silica Fume Addition 642...650

PID 109 - Corresponding author: Bach Quoc Si - University of Technology and Education - University of Danang, Danang, Vietnam

95. Quantitative Study Of Hydration Of C3S And C2S In The Reactive Powder Concrete Together With Its Strength Development 651...660

PID 110 - Corresponding author: Bach Quoc Si - University of Technology and Education - University of Danang, Danang, Vietnam

96. Study On Local Induction Hardening For Flat Surface 661...671

PID 118 - Corresponding author: Pham Son Minh - SPKT

97. Design, Manufacturing And Testing Of Magnetorheological Brake For Small Size Motorcycle 672...682

PID 149 - Corresponding author: Quoc Hung Nguyen - www.vgu.edu.vn

98. Researching On Measurement Strategies Of Fuel Tank Corrosion Using Phased Array Technology 683...690

PID 176 - Corresponding author: Thien Ngon Dang - HCM City University of Technology and Education

99. Influence Of Nitride Hard Coating On Friction And Soldering On Surface Of Aluminum High Pressure Die Casting Core 691...698

PID 340 - Corresponding author: Luu Thuy Chung - Vinh University of Technology Education

100. Applied Studies on Material of Biocomposite Biological Origin Prepared from Oxide Nano and Biogum for the Treatment of Methylene Blue 699...706

PID 344 - Corresponding author: Nguyen Vo Chau Ngan - Can Tho University

101. Removal Of Metal Ions From Plating Wastewater By Ferromagnetism Nano-Oxide (Cofe2O4) And Ferromagnetism Nano-Oh 707...712

PID 345 - Corresponding author: Nguyen Vo Chau Ngan - Can Tho University

102. Effects Of Some Parameters On Properties Of Cu-Al2O3 Composite Materials Synthesized By Internal Oxidation Process 713...717

PID 366 - Corresponding author: Thanh Ho Ky - Thai Nguyen University of Technology

103. A Comparative Investigation Of The Porous Niti Alloys Synthesized By Self-Propagating High-Temperature Synthesis And Combined Process Of Decomposition And Sintering 718...722

PID 370 - Corresponding author: Thanh Ho Ky - Thai Nguyen University of Technology

104. Effects Of Sintering And Compress On Porosity, Mechanical Properties And Conductivity Of Cu-Al2O3 Composite Materials Fabricated By Mechano-Chemical Method 723...727

PID 382 - Corresponding author: Thanh Ho Ky - Thai Nguyen University of Technology

CHAPTER 10. SCIENCE AND TECHNOLOGY DEVELOPMENTS TOWARDS SUSTAINABILITY

105. A Multiple Objective Model For Vehicle Routing Problem With Time Windows: A Case Study 729...736

PID 44 - Corresponding author: Ai Ho - Can Tho University

106. Producing Of Carbon Fibers From Commercial Viscose Fibers 737...743

PID 45 - Corresponding author: Thai Hung Le - HUST

107. The Influence Of Alumina Filler On Mechanical, Thermal And Electrical Properties Of Bulk Moulding Compounds (Bmcs) Composite 744...748

PID 46 - Corresponding author: Thai Hung Le - HUST

108. Study On Reasonable Ratios Of Straight Vegetable Oil And Diesel Oil As An Alternative Fuel For Marine Diesel Engine Application In Vietnam 749...755

PID 49 - Corresponding author: The Nam Tran – Vietnam Maritime University

109. Biocompatibility Of Ultrafine Grained Pure Titanium Fabricated By Equal Chanel Angular Pressing 756...762

PID 54 - Corresponding author: Van Hai Dinh - Ha Noi University of Science and Technology

110. Transient Numerical Simulation For Solid-Liquid Flow In A Centrifugal Pump Using Dense Discrete Phase Model-Ddpm 763...769

PID 55 - Corresponding author: Hoang Bui - Hanoi university of mining and geology

111. Effect Of Geometric Parameters On The Performance Of H-Type Darrieus Turbine 770...776

PID 56 - Corresponding author: Nguyen Tuan - Institute for hydro power and renewable

112. Analyzing Rotor Profile'S Effects To Performance Of Roots Vacuum Pump Applied The Cfd Method 777...784

PID 57 - Corresponding author: Nguyen Tung - Ha Noi University of Mining and Geologys

113. The Effect Of Turbocharging On The Performance And Pollutant Emission Level Of The Diesel Engine 785...792

PID 62 - Corresponding author: Cuong Duong Quoc - Military Technical Academy

114. Finite Element Modeling Method Of Centrifugally Rotary Processing 793...799

PID 92 - Corresponding author: Arkadiy Soloviev - Department of Theoretical and Applied Mechanics, Don State Technical University, Rostov-on-Don, Russia

115. Determining The Optimal Parameters Of Chip Shrinkage Coefficient And Cutting Force In High-Speed Machining For Aluminum Alloy A6061 800...806

PID 98 - Corresponding author: Hoa Pham - Utehy

116. Preparation Of High Porous Aerogel Nanocomposites As Electrode Materials Supercapacitors 807...807

PID 123 - Corresponding author: Van Hoa Nguyen - Nha Trang University

117. Design Of A Novel Adaptive Prescribed Controller For Mr Suspension 808...815

PID 124 - Corresponding author: Phu Do Xuan - Vietnamese-German University

118. Design Of A Novel Magnetorheological Damper For Exoskeleton Suspension 816...821

PID 125 - Corresponding author: Phu Do Xuan - Vietnamese-German University

119. A New Novel Magnetic Damper Using Flexible Gap For Knee Exoskeleton Suspension 822...828

PID 127 - Corresponding author: Phu Do Xuan - Vietnamese-German University

120. Preparatio Of Chitosan Chloride Salt In Solid State Using Hydrogen Chloride Gas 829...829

PID 130 - Corresponding author: Van Hoa Nguyen - Nha Trang University

121. Preparation Of Nanochitosan Using Chitosan Extracted From Squid Pens And Its Antibacterial Property 830...830

PID 131 - Corresponding author: Van Hoa Nguyen - Nha Trang University

122. Predictive Surface Roughness Of Workpiece In Cylindrial Grinding 831...837

PID 132 - Corresponding author: Do Duc Trung - Ha Noi University of Industry

123. A Machine Vision Based Automatic Optical Inspection System For Detecting Defects On Electronic Boards 838...845

PID 134 - Corresponding author: Huan Le - EIU

124. Effects Of Different Drying Techniques On Drying Characteristics And Quality Of Dried Moringa Oleifera Leaves 846...852

PID 136 - Corresponding author: Anh Duc Le - Nong Lam University, HCM City

125. Rhythmic Behavior Analysis For Vision Inspection Using Perception Neuron And Unity 853...859

PID 143 - Corresponding author: Thanh Vo Nhu - University of Science and Technology, the University of Danang, VietNam

126. Study Of The Possibility Of Syngas Making From The Industrial Scale Continuous Downdraft Coffee Husk Gasifier 860...869

PID 171 - Corresponding author: Nguyen Dinh Tung - Vietnam Research Institute Agricultural Machinery

127. Experimental Investigation And Optimization Of Machine Parameters In High Speed Cutting Of Titanium Alloys 870...880

PID 175 - Corresponding author: Nguyen Duc Nam - Industrial University of Ho Chi Minh City

128. Microstructure Of Fes Layer Developed On Die Steels By Sulfonitridation 881...881

PID 185 - Corresponding author: Truong To Quoc - Nagaoka University of Technology

129. Synthesis Of Mo-Modified Tio2 With Enhanced Photocatalytic Activity 882...889

PID 202 - Corresponding author: Lan Nguyen Thi – Quy Nhon University

130. A Technical Solution Providing Fuel Mixed For High Power Engines Using Only Biogas 890...897

PID 212 - Corresponding author: Phong-Thanh Tran - Tien Giang University

131. Investigation Of Btex Adsorption On Carbon Nanotubes Cartridges From Air Samples 898...905

PID 235 - Corresponding author: Huu Quynh Anh Le - University of Natural Resources and Environment

132. Investigation And Optimization Of Power Based Smart Home Module Integrated With Automatic Solar Tracking System And Mppt Technique 906...912

PID 254 - Corresponding author: Thai-Viet Dang - Hanoi University of Science and Technology

133. Iron (Iii)-Based Metal-Organic Frameworks As Potential Visible Light – Driven Catalysts For The Removal Of Nox: A Solution For Urban Air Purification 913...914

PID 263 - Corresponding author: Hoang Phuc Nguyen - SunMoon University, Asan, Chungnam, Korea

134. Fabrication Of Sn Doped Blue And Black Tio2 For Nox Removal 915...916

PID 264 - Corresponding author: Adriana Martinez Oviedo - Sun moon university

135. Investigation Of Geometric Properties Of Melt-Electrospun Microfibers For Precision Deposition 917...917

PID 266 - Corresponding author: Tung Nguyen Nhat - Kyungpook National University

136. Caculating Cutting Force In Grinding 918...923

PID 269 - Corresponding author: Do Duc Trung - Ha Noi University of Industry

137. Investigation Of Particles Separation Efficiency Of A Dielectrophoresis Microfluidic Device 924...925

PID 273 - Corresponding author: Kyung Won Kim - Kyungpook National University

138. The Micro-Holes Array In Thin Ag-Film As A Chemosensor And Biosensor 926...931

PID 276 - Corresponding author: Nguyen Thi Huyen Trang - Lebedev Physical Institute, Moscow Institute of Physics and Technology, Ha Tinh University

139. Effect Of Ethylene Vinyl Axetate (Eva) On The Mechanical Properties Of Low-Density Polyethylene Eva Blends 932...939

PID 283 - Corresponding author: Nga Pham Thi Hong - HCMC University of Technology and Education

140. Utilization Of Functionalized Graphene In Based-Epoxy Paint Coatings For Anti- Corrosive Protection Of Steel Surfaces 940...947

PID 314 - Corresponding author: Phan Thi Thuy Hang - The University of Danang – University of Science and Technology, Vietnam

141. Fabrication Of Glucose Oxygen Biofuel Cell Controlling Limiting Factors In Microfluidic Channel 948...948

PID 339 - Corresponding author: Haroon Khan - Kyungpook National University

142. Effect Of Angle Of Attack Of The Buoyant Shell On The Aerodynamic Performance Of The Airborne Wind Turbine In Shell Configuration 949...949

PID 349 - Corresponding author: Arslan Saleem - Kyungpook National University

143. Shaft Torsional Vibration Reduction Using Tuned-Mass-Damper (Tmd) 950...957

PID 351 - Corresponding author: Chinh Nguyen Duy - Faculty of Mechanical Engineering, Hung Yen University of Technology and Education

144. Determination Of Optimal Parameters For Reducing The Vibration To An Inverted Pendulum Type Structure With The Tuned Mass Damper Using The Maximum Method Of Equivalent Resistance 958...965

PID 352 - Corresponding author: Chinh Nguyen Duy - Faculty of Mechanical Engineering, Hung Yen University of Technology and Education

145. Determination Of The Expedient Motion Trajectory Of The Bucket On The Side Dump Bucket Wheel Loader Mvc E500-1 During The Digging And Filling Material. 966...972

PID 353 - Corresponding author: Ta Van Huy - Military technical institute

146. Controlled Synthesis Of Tio2 Graphene Photocatalysts By Hydrothermal Method 973...981

PID 375 - Corresponding author: Le Thi Thanh Lieu - Quy Nhon University

147. Optimizating Spray Parameters Of High Velocity Oxy Fuel (Hvof) For Cr3C2 - Nicr Coating 982...989

PID 376 - Corresponding author: Phu Thanh - Hung Yen University of Technology and Education

148. Investigation Of The Effects Of Technological Parameters On Surface Roughness In Extrusion Bars Of Aluminum Alloy 990...995

PID 383 - Corresponding author: Nguyen Trong Mai - Hanoi University of Industry

149. A Reseach On Manufacturing Technology Body Shell Of Anti-Tank Rocket 996...1003

PID 385 - Corresponding author: Khanh Bui Khac - Hungyen University of Technology and Education

150. Research On Relative Wear And Roughness Follow The Current Density In Edm Die Sinking 1004...1007

PID 401 - Corresponding author: Quang Huy Tran - Namdinh university of technology education

151. The Influence Of Part Geometry On Changes Of The Dynamic Geometric Parameters Of Cutting Tools And Cutting Conditions When Contour Turning On Cnc Lathes 1008...1014

PID 403 - Corresponding author: Nguyen Chi Cong - Cong ty TNHH MTV Hoa chat 21

152. Biological Hydroxyapatite Nanomaterial Extracted From Fish Bones 1015...1015

PID 411 - Corresponding author: Van Hoa Nguyen - Nha Trang University

153. Researching On Bearing Ability Of Canopy Of 2Ansha Powered Roof Support By Finite Element Method 1016...1019

PID 413 - Corresponding author: Chan Phuong Nguyen - Institute of Energy and Mining Mechanical Engineering

154. Prediction Of Combustion Behavior In A Boiler Fired By Mixture Of Vietnamese Anthracite And Coal Gas Using Cfd 1020...1025

PID 414 - Corresponding author: My Tran Gia - Hanoi University of Science and Technology

155. A Study On The Recovery Of Precious Metals From Gold Mine Tailing 1026...1026

PID 423 - Corresponding author: Jei Pil Wang - Pukyong National University

156. Improving the efficiency of Dye sensitized solar cells by using Cr-doped TiO2 material 1027...1027

PID 262 - Corresponding author: Huy Hao Nguyen - Sun Moon University

157. Dissimilar metals joining between AA5083 and high strength steel sheets 1028...1028

PID 275 - Corresponding author: Kwangjin Lee - Korea Institute of Industrial Technology

Chapter 8.
Advanced machinability towards sustainability

Probabilistic analysis on the uncertainty in natural frequency of functionally graded material beams

Van Thuan NGUYEN [1, a *] and Duy Liem NGUYEN[2,b]

[1]Nha Trang University, Nha Trang City, Vietnam

[2]Ho Chi Minh City University of Technology and Education, Ho Chi Minh City, Vietnam

[a]thuannv@ntu.edu.vn, [b]liemnd@hcmute.edu.vn

*Corresponding author. Tel: (+84) 1693007896; E-mail: thuannv@ntu.edu.vn

Abstract

This paper applies the stochastic finite element method (SFEM) to perform the natural frequency analysis of functionally graded material (FGM). It is assumed that the elastic modulus and width of the FGM beam vary along the thickness and width directions following exponential functions. The stochastic eigenvalue problem is solved independently by first-order perturbation and Monte Carlo simulation (MCS) method through changing elastic modulus as spatial randomness. The results show that the first-order perturbation method based SFEM produces a very close value to MCS method.

Keywords: Functionally graded materials, First-order perturbation technique, Beam, Spectral representation.

Introduction

Functionally graded material (FGM) have attracted extensive attention in engineering fields such as aerospace, micromechanics and nuclear power, since the concept of FGM was initially proposed by Japanese scientists in 1984 [1]. In fact, the manufacturing and fabrication process of FGM are extremely complex. The stochastic analysis is a useful analysis tool to predict accurately the response of structures with random material properties. In this direction, Kitipornchai *et al.* deals with the random free vibration of functionally graded laminates in a number of independent input variables [2]. In the stochastic analysis of FGM structures, the first-order perturbation technique has been extensively used [3, 4]. Jagtap *et al.* investigated the stochastic finite element nonlinear free vibration analysis of FGM plate with material uncertainties [5]. Shegokar *et al.* investigated the stochastic finite element nonlinear free vibration analysis of FGM beam with the random material properties [6]. The effect of respective random parameters on the response variability of natural frequency and the effect of correlation between the two random parameters as well are discussed in [7]. However, the researches work using the perturbation method for free vibration of FGM beams are still limited. The focus of the present study is to perform the natural frequency analysis of FGM beam by using the perturbation based stochastic finite element method. During stochastic analysis of Monte Carlo simulation, the natural frequencies of FGM beam are obtained from the random processes generation technique of spectral representation [9]. The results obtained from these two methods are compared.

Model of FGM beam

Let us consider a functionally graded with length *L*, width *b* and thickness *h* as shown in Fig. 1.

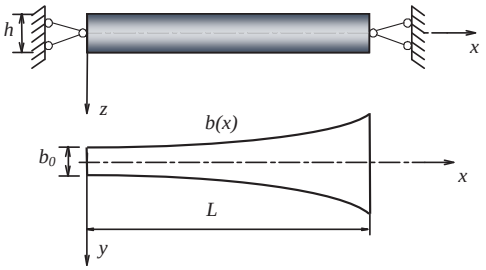


Fig. 1. Model of FGM beams

The material parameter of Young's modulus *E*, mass density ρ and the width of the FGM beams vary with exponential function as follows:

$$E(z) = E_0 e^{\beta|z|};\ \rho(z) = \rho_0 e^{\nu|z|};\ b(x) = b_0 e^{\delta x}. \quad (1)$$

E_0 and ρ_0 denote Young's modulus and mass density at the mid-plane (z=0) of the beam.

Stochastic finite element analysis

In this study, only the Young's modulus of elasticity is considered to be random. The equation for free vibration problem is:

$$[K(r) - \omega^2 M(r)]d(r) = 0. \quad (2)$$

From Eq. (2), we can derive the following relation for the *ith* eigenvalue. Introducing Eq. (3) into the expression of Taylor expansion on the eigen value λ we can get the first two moments as follows for the $k-th$ eigenvalue.

$$\mu_\lambda = \lambda_{ok};\quad \lambda_{i,j} = X_i^T \left[K_{,j} - \lambda_i M_{,j} \right] X_i. \quad (3)$$

$$Var_\lambda = \sum_{i=1}^{NR}\sum_{j=1}^{NR} \lambda_{k,i}\lambda_{k,j} R_{ij}. \quad (4)$$

The coefficient of variation (COV) is a ratio of the standard deviation of eigenvalue λ to the absolute of the mean eigenvalue as:

$$COV = \frac{\sqrt{Var(\lambda)}}{|\lambda|}. \quad (5)$$

Example analysis

The thickness, length and width of the example FGM beam are h=2m, L=20m, and b_0=2m, respectively. The material properties are E_0=70.0 GPa and ρ_0=2780.0kg/m^3. The number of samples used is 10,000 for all the cases.

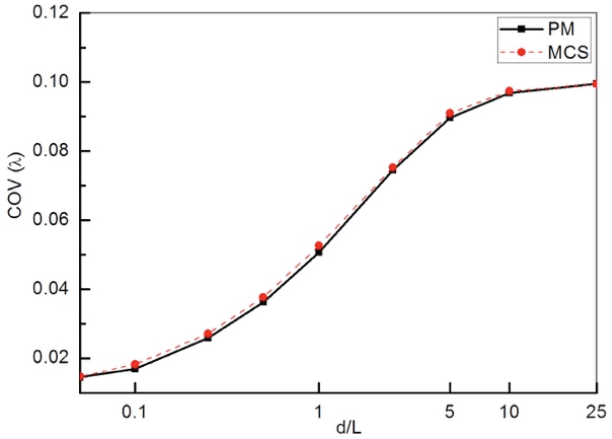


Fig. 2. COV of natural frequency as a function of the correlation distance for different standard deviation of stochastic process.

The effect of the ratio correlation distance (*d)* and length beam (*L)* of the stochastic field on the variability of the natural frequency is shown in Fig. 2, where the results of the proposed formulation are compared with those of the MCS for the same cases SFEM. The results designated by a dotted line denote the corresponding results of the MCS for a standard deviation of the stochastic filed 0.1. As seen in Fig. 2, the response variability of natural frequency is converging to certain values as the correlation distance tends to infinity in both analyses schemes. In this study, the converging value is obtained approximately to be 100% in perturbation method and slightly over 100% in Monte Carlo simulation of the assumed standard deviation of the stochastic field. We observe that the increasing rate of the correlation distances is accelerated with an increase in the coefficient of variation of the stochastic field and also there appears good agreement between the proposed scheme and the MCS.

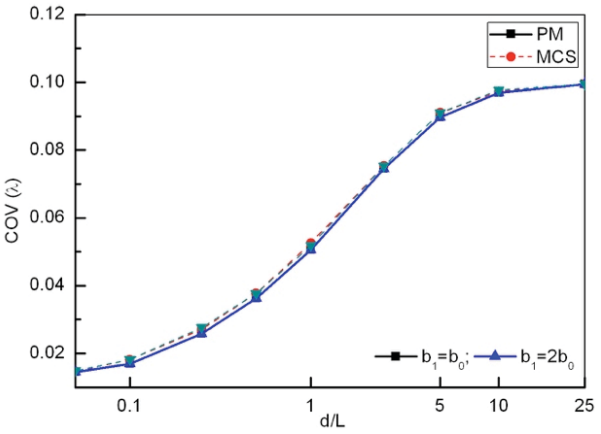


Fig. 3. COV of natural frequency as a function of the correlation distance d for different width ratio.

The effect of non-uniformity parameter of the FGM beam on the response variability according to perturbation based stochastic finite element and Monte Carlo methods is shown in Fig. 3. The number of elements used in the finite element mesh is 20 elements. The non-uniform parameter is investigated for two cases of 1.0 and 2.0. As seen in Fig. 3, the response variability is virtually not affected by the parameter in both analysis methods. This mean that the non-uniformity parameter only affects the deterministic stiffness of the structure (Hien *et al*. 2014).

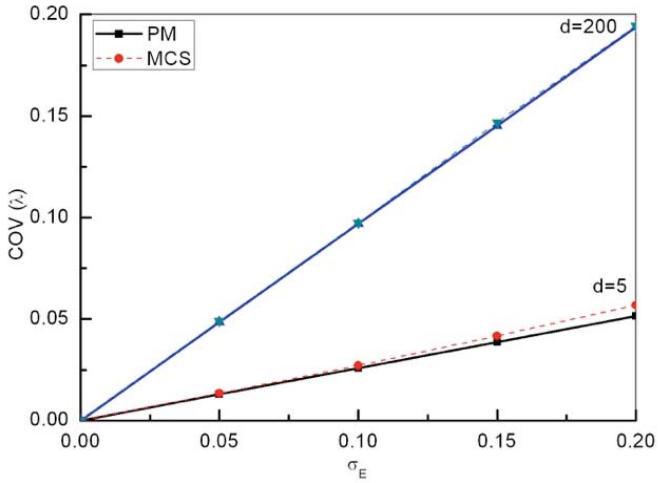


Fig. 4. COV of natural frequency as a function of the standard deviation of stochastic process.

The additional response variability of natural frequency obtained by the proposed scheme is shown in Fig. 4 for various values of the two cases of the correlation distances (5 and 200). The results of Monte Carlo and perturbation method are discussed in four cases of the standard deviation of stochastic process 0.05, 0.1, 0.15 and 0.2. As seen in Fig. 4, the response variability shows nonlinear in MCS and slight nonlinear in perturbation method results as the small correlation distance value.

Conclusion

The perturbation based stochastic finite element method and Monte Carlo simulation for natural frequency of FGM beam with random Young's modulus are performed. For all the cases, the results determined by the first order perturbation method are adopted to check the Monto Carlo simulation that shows a good comparison. The ratio of width of FGM beam does not affect the response COV in the given beam.

References

[1] M. Koizumi, FGM activities in Japan, Composites Part B: Engineering, Vol. 25 (1997) 1-4.
[2] S. Kitiponchai, J. Yang, K.M. Liew, Random vibration of the functionally graded laminates in thermal environments, Comput. Methods Appl. Mech. Eng. 195 (2006) 707–714.
[3] A. Shaker, W. Abdelrahman, M. Tawfik, E. Sadek, Stochastic finite element analysis of the free vibration of functionally graded material plates, Comput. Mech. 41 (2008) 707–714.
[4] A. Lal, B.N. Singh, Stochastic nonlinear free vibration response of laminates composite plates resting on elastic foundation in thermal environments, Computational mechanics. Vol. 44, pp.15-29 (2009).
[5] K.R. Jagtap, A. Lal, B.N. Singh, Stochastic nonlinear free vibration analysis of elastically supported functionally graded materials plate with system randomness in thermal environment Composite structures, 93 (2011) 3185–3199.
[6] N.L. Shegokar, A. Lal, AStochastic finite element nonlinear free vibration analysis of piezoelectric functionally graded materials beam subjected to thermo-piezoelectric loadings with material uncertainties, Meccanica 49 (2014) 1039–1068.
[7] T.D. Hien, N.V. Thuan, C.N. Hyuk, Eigen analysis of functionally graded beams with variable cross-section resting on elastic supports and elastic foundation, Structural Engineering and Mechanics, Vol. 52, No. 5 (2014).

[8] N.V. Thuan, C.N. Hyuk, Investigation into the effect of random material properties on the variability of natural frequency of functionally graded beam, KSCE Journal of Civil Engineering, Volume 21, 4 (2017) 1264–1272.
[9] M. Shinozuka, G. Deidatis, Simulation of stochastic processes by spectral representation, Applied Mechanics Reviewers, Vol. 44, No 1 (1991).

Machining based geometric error estimation method for 3-axis CNC machine

HOANG Trung Kien[1,a *] and TA Nguyen Minh Duc [1,b]

[1]Faculty of Mechanical Engineering, HCMC University of Technology and Education, No.1 Vo Van Ngan, Thu Duc, Ho Chi Minh City, Vietnam

[a] kienhtr@hcmute.edu.vn, [b] minhduc@hcmute.edu.vn

Keywords: Geometric error; Machining; 3-axis machine tool.

Abstract. Computer numerical control (CNC) machine tool plays an extremely significant role in any manufacturing industry due to its automation and high accuracy. Keeping the CNC machine tool at its highest performance to meet the demand of high accuracy machining is always significant. To maintain the accuracy of a machine tool over the time, it is important to measure and compensate the geometric error, one of the main error source of machine tool, especially when the machine get old. There are totally 21 geometrical errors in a 3-axis machine tool including three translational errors and three rotational errors for each axis and three perpendicular error (Squareness) within three axes of the machine. This paper presents an economical and simple method for measuring the geometric error of a 3-axis CNC machine tool based on the machining of actual samples. Three samples for each axis will be machined following a design cutting path. The samples will then be measured using a coordinate measuring machine (CMM). The collect data will be used for estimating the geometric errors. The volumetric errors will be then computed and verified through machining of 3D geometries.

Introduction

Geometric error of a machine tool is caused by the geometrical deviation when the machine components are manufactured and assembled. According to the ISO 230-1, a linear axis consists of six geometrical errors including three translational deviations: positioning deviation, horizontal straightness, vertical straightness and three rotatory deviations: roll, pitch, yaw. Therefore, in a 3-axis machine tool, including the three Squareness within the axes, there will be twenty-one geometrical error components.

Many researches had been carried out to measure and estimate the geometric error in multi-axis machine tool and different methods had been proposed [1-5]. Laser interferometer is one of the most accurate method and devices to measure the geometric error of machine tool. However, laser interferometer is very expensive and is not suitable for small and medium scale factory. In addition, the operation of a laser interferometer system required skillful technicians which can causes extra training fee and payment. Another commercial measurement device for geometric error is the Ball-bar system. The cost of the ball-bar system is quite reasonable for its measuring capability, however, the system has a limited measure range and cannot measure all the error components.

Beside the listed methods above, there is another method that can measure the geometric error indirectly. This method is a standard method that estimates the error through measuring the dimension of the machined samples. This method, thus, requires only common dimension measurement devices instead of specific measurement devices for measuring geometric error. Moreover, the measurement instruction is simple that can be performed easily in the QC department in the factory. Therefore, it can be used widely in the manufacturing industry.

This paper presents this indirect measurement method for estimating the geometric error of a 3-axis machine tool and proposed a suitable measuring procedure for a large range of manufacturing scale. The compensation method will also be presented in this paper as a part of the machine tool accuracy maintenance.

Geometric error

Geometric deviation in a linear axis. Figure 1 shows the geometric error components of a linear axis (X-axis). The geometrical error components are then the deviation between the ideal and real position in and around each direction. E_{XX} is the positioning error and E_{YX} and E_{ZX} are respectively the vertical and horizontal straightness. The angular deviation includes roll (E_{AX}), pitch (E_{CX}) and yaw (E_{BX}) errors.

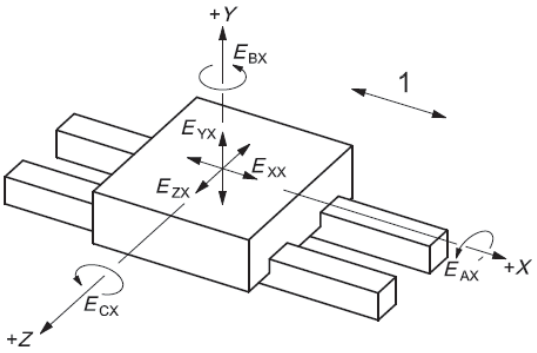


Fig. 1 Geometric error of a linear axis [ISO 230-1]

Squareness. In a multi-axis machine tool, the angular deviation within axes is defined as the Squareness. Therefore in a 3-axis machine tool, there will be totally three Squareness errors.

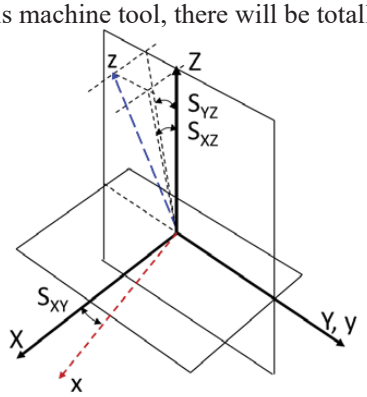


Fig. 2 Squareness

Geometric error model

Homogeneous transformation matrix. Homogeneous transformation matrix (HTM) is a 4 by 4 matrix that can find the relative coordinate of a point in the reference coordinate system (RCS) based on the coordinate of a local coordinate system (LCS) and the relationship between two CSs [6]. An HTM is presented in Eq. 1. The direction transformation is represented by the first three columns with scale factors that are all equal to zero. The position of the LCS's origin with respect to the RCS is represented by the last column with the scale factors Ps.

$$ {}^{R}T_{n} = \begin{bmatrix} O_{ix} & O_{iy} & O_{iz} & P_x \\ O_{jx} & O_{jy} & O_{jz} & P_y \\ O_{kx} & O_{ky} & O_{kz} & P_z \\ 0 & 0 & 0 & P_s \end{bmatrix} \qquad \text{Eq. (1)} $$

The equivalent coordinates of a point in a coordinate frame n, with respect to the RCS, can be expressed as:

$$\begin{bmatrix} X_R \\ Y_R \\ Z_R \\ 1 \end{bmatrix} = {}^{R}T_n \begin{bmatrix} X_n \\ Y_n \\ Z_n \\ 1 \end{bmatrix} \quad \text{Eq. (2)}$$

Thus, in case of ideal linear motion carriages, the coordinate transformation of a point from the X-LCS (X-axis) to the RCS (Fig.3) using HTM is:

$${}^{R}T_X = {}^{R}T_Y \cdot {}^{Y}T_X = \begin{bmatrix} 1 & 0 & 0 & x \\ 0 & 1 & 0 & y \\ 0 & 0 & 1 & 0 \\ 0 & 0 & 0 & 1 \end{bmatrix} \quad \text{Eq. (3)}$$

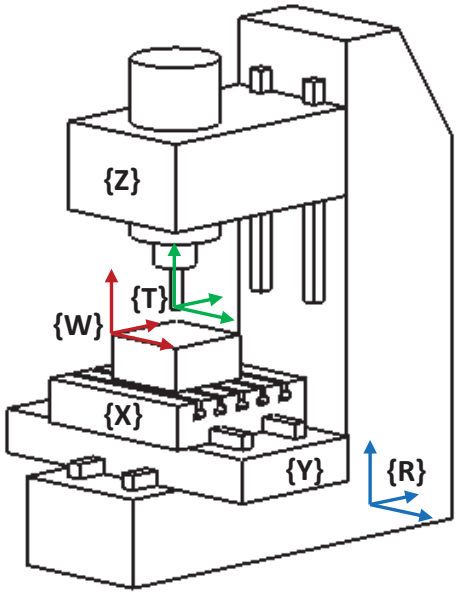


Fig. 3 Vertical 3-axis CNC machine configuration

In practical, however, there are three rotational errors and three positional errors in each movement. In addition, there are Squareness between three pair of perpendicular axes. These geometric errors are presented in the transformation matrix as:

$${}^{Y}T_X = \begin{bmatrix} 1 & -E_{CX} & E_{BX} & x+E_{XX} \\ E_{CX} & 1 & -E_{AX} & x\,S_{XY}+E_{YX} \\ -E_{BX} & E_{AX} & 1 & E_{ZX} \\ 0 & 0 & 0 & 1 \end{bmatrix} \quad \text{Eq. (4)}$$

$${}^{R}T_Y = \begin{bmatrix} 1 & -E_{CY} & E_{BY} & E_{XY} \\ E_{CY} & 1 & -E_{AY} & y+E_{YY} \\ -E_{BY} & E_{AY} & 1 & E_{ZY} \\ 0 & 0 & 0 & 1 \end{bmatrix} \quad \text{Eq. (5)}$$

$${}^{R}T_Z = \begin{bmatrix} 1 & -E_{CZ} & E_{BZ} & z\,S_{XZ}+E_{XZ} \\ E_{CZ} & 1 & -E_{AZ} & z\,S_{YZ}+E_{YZ} \\ -E_{BZ} & E_{AZ} & 1 & z+E_{ZZ} \\ 0 & 0 & 0 & 1 \end{bmatrix} \quad \text{Eq. (6)}$$

Geometric error modeling. Assume that when machining happens, the tool tip cut the workpiece at point P. The coordinates of P in tool frame is {0,0,0} since the origin of the tool CS is at the tool tip. On the other hand, the coordinate of P in work frame (${}^{W}P$) is $\{x_w,y_w,z_w\}$. ${}^{W}P$ can be found by measuring the dimension of the workpiece after machining.

In RCS, the coordinates of P are expressed as:

$$^{R}P = {}^{R}T_{Z}.\ {}^{Z}T_{T}.\ {}^{T}P = {}^{R}T_{Y}.\ {}^{Y}T_{X}.\ {}^{X}T_{W}.\ {}^{W}P \qquad \text{Eq. (7)}$$

With:

$$^{Z}T_{T} = \begin{bmatrix} 1 & 0 & 0 & T_X \\ 0 & 1 & 0 & T_Y \\ 0 & 0 & 1 & T_Z \\ 0 & 0 & 0 & 1 \end{bmatrix} \qquad \text{Eq. (8)}$$

is the offset of the tool with respect to Z-axis.

And:

$$^{X}T_{W} = \begin{bmatrix} 1 & 0 & 0 & W_X \\ 0 & 1 & 0 & W_Y \\ 0 & 0 & 1 & W_Z \\ 0 & 0 & 0 & 1 \end{bmatrix} \qquad \text{Eq. (9)}$$

is the offset of the work with respect to X-axis.

Substitute Eq. (4-6) and Eq. (8-9) into Eq. 7 and ignore the high order term, the error model is found as:

$$E_{XX}+E_{XY}-E_{XZ}+(W_Z+z_W)E_{BX}-(W_Y+y_W)E_{CX}+(W_Z+z_W)E_{BY} -(W_Y+y_W)E_{CY}-(T_Z+Z_T)E_{BZ}+(T_Y+y_T)E_{CZ}-z\,S_{XZ}=T_X+x_T-x-W_X-x_W \qquad \text{Eq. (10)}$$

$$E_{YX}+E_{YY}-E_{YZ}-(W_Z+z_W)E_{AX}+(W_X+x_W)E_{CX}-(W_Z+z_W)E_{AY}+(x+W_X+x_W)E_{CY} +(T_Z+z_T)E_{AZ}-(T_X+x_T)E_{CZ}+x\,S_{YX}-z\,S_{YZ}=T_Y+y_T-y-W_Y-y_W \qquad \text{Eq. (11)}$$

$$E_{ZX}+E_{ZY}-E_{ZZ}+(W_Y+y_W)E_{AX}-(W_X+x_W)E_{BX}+(W_Y+y_W)E_{AY} -(x+W_X+x_W)E_{BY}-(T_Y+y_T)E_{AZ}+(T_X+x_T)E_{BZ}=z+T_Z+z_T-W_Z-z_W \qquad \text{Eq. (12)}$$

Measurement method

Target object. Target object is a workpiece which is machined followed a designed cutting path. The designed dimension of the targeted object will be measured on a CMM after machining. The geometric error, then, will be estimated based on Eq. (10-12). To estimate all 21 geometric errors, these errors must be separated.

Geometric error separation method

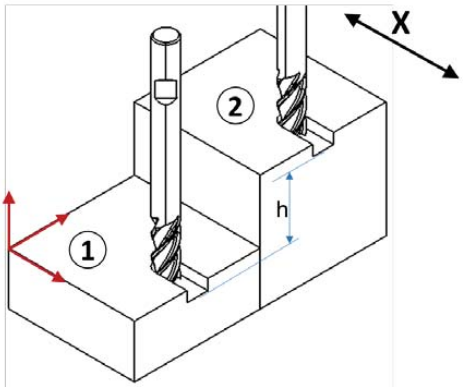


Fig. 4 Machined sample (target object) for measurement

Error separation for X-axis. To separate the positioning error, workpieces with different heights will be used (Fig. 4). These workpieces will be machined with the same amount of X and Y displacements that form a horizontal stair slot. In X-direction, the influenced parameters are reduced and remain only $\mathbf{E_{XX}}$ and $\mathbf{E_{BX}}$. The difference of the height will separate the angular error from the positioning error.

In case of the vertical straightness, the influenced parameters are $\mathbf{E_{ZX}}$, $\mathbf{E_{BX}}$ and $\mathbf{E_{AX}}$. Since $\mathbf{E_{BX}}$ has been separated, $\mathbf{E_{ZX}}$ and $\mathbf{E_{AX}}$ can be distinguished using Eq. (12). The remained errors $\mathbf{E_{CX}}$ and $\mathbf{E_{YX}}$ can be then easily estimated using Eq. (10) and Eq. (11), respectively.

At position (1), Eq. (10), (11) and (12) are shorten as:

$$E_{XX}+(W_{Z1}+z_{W1})E_{BX}-(W_{y1}+y_{W1})E_{CX}=T_X+x_T-x-W_{X1}-x_{W1} \quad \text{Eq. (13)}$$

$$E_{YX}-(W_{Z1}+z_{W1})E_{AX}+(W_{X1}+x_{W1})E_{CX}+xS_{YX}=T_Y+y_T-y-W_{Y1}-Y_{W1} \quad \text{Eq. (14)}$$

$$E_{ZX}+(W_{Y1}+y_{W1})E_{AX}-(W_{X1}+x_{W1})E_{BX}=z+T_Z+z_T-W_{Z1}-z_{W1} \quad \text{Eq. (15)}$$

At position (2):

$$E_{XX}+(W_{Z2}+z_{W2})E_{BX}-(W_{Y2}+y_{W2})E_{CX}=T_X+x_T-x-W_{X2}-x_{W2} \quad \text{Eq. (16)}$$

$$E_{YX}-(W_{Z2}+z_{W2})E_{AX}+(W_{X2}+x_{W2})E_{CX}+xS_{YX}=T_Y+y_T-y-W_{Y2}-Y_{W2} \quad \text{Eq. (17)}$$

$$E_{ZX}+(W_{Y2}+y_{W2})E_{AX}-(W_{X2}+x_{W2})E_{BX}=z+T_Z+z_T-W_{Z2}-z_{W2} \quad \text{Eq. (18)}$$

In matrix form these above six equation are rewritten as:

$$A\boldsymbol{E}=B \quad \text{Eq. (19)}$$

Where:

$$A=\begin{bmatrix} 1 & 0 & 0 & 0 & W_{Z1}+z_{W1} & -(W_{y1}+y_{W1}) \\ 0 & 1 & 0 & -(W_{Z1}+z_{W1}) & 0 & W_{X1}+x_{W1} \\ 0 & 0 & 1 & W_{Y1}+y_{W1} & -(W_{X1}+x_{W1}) & 0 \\ 1 & 0 & 0 & 0 & W_{Z2}+z_{W2} & -(W_{Y2}+y_{W2}) \\ 0 & 1 & 0 & -(W_{Z2}+z_{W2}) & 0 & W_{X2}+x_{W2} \\ 0 & 0 & 1 & W_{Y2}+y_{W2} & -(W_{X2}+x_{W2}) & 0 \end{bmatrix}$$

$$\boldsymbol{E}=\begin{bmatrix} E_{XX} \\ E_{YX} \\ E_{ZX} \\ E_{AX} \\ E_{BX} \\ E_{CX} \end{bmatrix}$$

$$B=\begin{bmatrix} T_X+x_T-x-W_{X1}-x_{W1} \\ T_Y+y_T-y-W_{Y1}-Y_{W1} \\ z+T_Z+z_T-W_{Z1}-z_{W1} \\ T_X+x_T-x-W_{X2}-x_{W2} \\ T_Y+y_T-y-W_{Y2}-Y_{W2} \\ z+T_Z+z_T-W_{Z2}-z_{W2} \end{bmatrix}$$

From Eq. (19), the geometric error of X-axis can be easily found using Eq. (20):

$$\boldsymbol{E}=(A^TA)^{-1}A^TB \quad (20)$$

The separation method is conducted in similar way for Y-axis. The Squareness S_{XY} can also be estimated based on Eq. (11) and Eq. (12) with both X- and Y-axis movements.

Error separation for Z-axis. For Z-axis, a vertical stair-step target object will be used. Since for Z axis, the tool position is fixed, the error separation method is different compared to X and Y-axis. To separate angular errors, two different points on vertical direction will be measured for one position (Fig. 5).

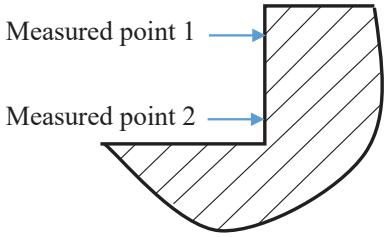


Fig. 5 Z-axis measured positions for angular error separation

Summary

This research proposed a useful method to estimate the geometric error of a 3-axis machine tool which can be utilized in an error prediction model to compensate and improve the machining accuracy. The machining-based measurement method is cost effective compared to many other measurement systems and is suitable for a vast scale of machine tools.

References

[1]. J.H. Lee and S.H. Yang, Measurement of geometric errors in a miniaturized machine tool using capacitance sensors, Journal of Materials Processing Technology. 164–165, (2005) 1402-1409.

[2]. R Ramesh, M.A Mannan, A.N Poo, Error compensation in machine tools — a review: Part I: geometric, cutting-force induced and fixture-dependent errors, International Journal of Machine Tools and Manufacture. 40 (2000) 1235-1256.

[3]. S. Sartori, G.X. Zhang, Geometric Error Measurement and Compensation of Machines, CIRP Annals - Manufacturing Technology. 44 (1995) 599-609.

[4]. A.C. Okafor, Yalcin M. Ertekin, Derivation of machine tool error models and error compensation procedure for three axes vertical machining center using rigid body kinematics, International Journal of Machine Tools and Manufacture. 40 (2000) 1199-1213.

[5]. Mahbubur Rahman, Jouko Heikkala, Kauko Lappalainen, Modeling, measurement and error compensation of multi-axis machine tools. Part I: theory, International Journal of Machine Tools and Manufacture. 40 (2000) 1535-1546.

[6]. H. Slocum, Precision machine design, Chapter 2, Society of Manufacturing, 1992.

Evaluating energy efficiency of production machine

Nguyen Thi Ai Lanh[1, a *], Tran Le Nhat Hoang[1,b], Paris Henri[2,c] and Mathieu Museau[2,d]

[1]University of Technology and Education, The University of Da Nang, 48 Cao Thang, Da Nang, Vietnam

[2]G-SCOP laboratory, 46 Félix Viallet, 38031, Grenoble, France

[a]ntalanh@ute.udn.vn, [b]tlnhoang@ute.udn.vn, [c]henri.paris@univ-grenoble-alpes.fr, [d] matthieu.museau@g-scop.fr

Keywords: energy efficiency; energy consumption; production machine; energy efficiency indicator; potential energy gain

Abstract. Industry is one of the most important energy consumption sectors. In the world, industry sector accounts for almost a third of energy consumption (28.3%, in 2012) [1]. According to the U.S. Department of Commerce: "Sustainable manufacturing is the creation of manufactured products through economically-sound processes that minimize negative environmental impacts while conserving energy and natural resources". Nowadays, due to different environmental issues: the deficit of energy resources, the growing concern of the carbon emission, the environment impact… the awareness of energy consumption takes its important in manufacturing industries. In a manufacturing system, production machine is one of the basis energy consumed devices. In order to achieve the long-term goal "sustainable manufacturing", it is necessary then to take into account the energy efficiency of production machine [2]. In fact, increasing energy efficiency of production machine allows to reduce not only energy costs but also the overall environmental impact. Energy efficiency evaluation of production machine is therefore one of the prerequisites for energy saving in manufacturing [3]. In order to support designers during the design phase of the next production machine generation, in this paper, the principal objective is to propose a method to evaluate energy efficiency of a production machine.

Introduction

Manufacturing industry is one of the main energy consumers and the largest emitter of CO2 emissions due to its large share of final energy consumption (33%) [4]. Raising energy efficiency is therefore now considered like one of the most important challenges to achieve a cleaner and more efficient manufacturing. In fact, according to Mc Kinsey&Company, "energy efficiency represents around 40 percent of the greenhouse gas reduction potential that can be realized at a cost of less than EUR 60 per metric ton of carbon dioxide equivalent" [5]. Moreover, raising energy efficiency is an essential pillar of sustainable business strategies. It holds a great benefit for industrial companies.

This paper aims at proposing an energy efficiency evaluation method for a production machine. In the first section, a literature review on energy consumption of a production machine is analyzed. Then the method allowing to evaluating energy efficiency proposed in the paper will be introduced. An energy efficiency indicator will be proposed in the second part of this paper. This indicator allows to analyze and to evaluate the actual energy using of production machine and its organs. In fact, in the manufacturing phase, the energy consumed by a production machine is not entirely used for the manufacture of the final product. It always exists an important part of energy that is lost in the production process. The energy efficiency indicator proposed is a support to quantify the percentage of actual energy consumption of production machine and its organs participating in adding value to the final product. In the next section of this paper, a potential energy gain will be proposed. This potential energy gain allows to identify how much energy of production machine and its organs can be potentially saved. From that, the energy saving opportunities of production machine are identified. An application will be presented at the end of this paper to show that the energy efficiency evaluation method proposed can provide fundamental support

for evaluating energy efficiency and reducing total energy consumption of production machine in the future.

Literature review

It has been proven in different researches that energy consumed by a production machine during its production phase is significantly greater than the theoretical energy required to produce the desired product [6,7,8]. In case of a hydraulic press using to bend a 1,5mm thick and 170mm wide steel plate (St-37) over an angle of 170° in a 12mm die [6], the part of energy relating directly to the manufacture of the final product is energy needed to create the punch movement. This part of energy is small (just 35%) compared to the total energy consumption. There is until 65% of energy consumed without directly relating to the manufacture of the final product. Fig. 1 illustrates the distribution of the energy consumed by a hydraulic press according to the different production modes: tool positioning (1), preparation on PC control station (2), positioning of the workpiece manufacture (3-4), lowering of the punch (5a), raising of the punch (5b), transport and measurement of the finished product (6-8) and the pause time of the operator (9).

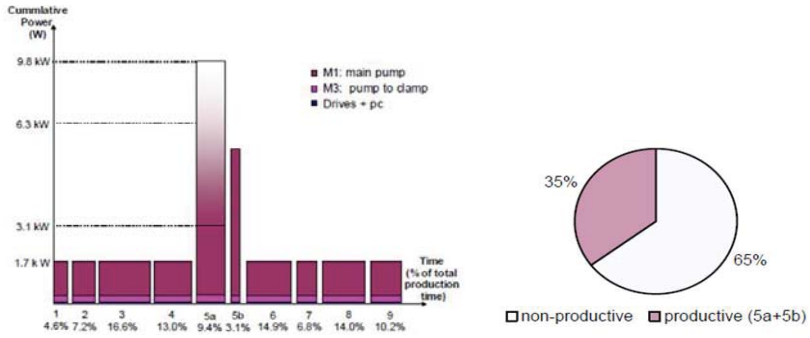


Fig. 1: Energy consumption of a hydraulic press [6]

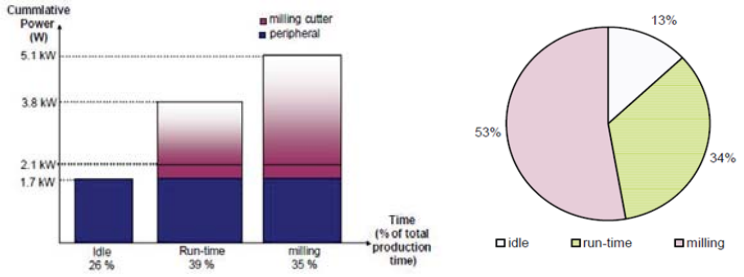


Fig. 2**:** Energy consumption of a 5-axis machining center [6]

Fig. **2** [6] illustrates energy consumption of a 5-axis machining center for milling operations during one year (2000 hours) according to its different use modes: power-up (idle mode), fast motion of the axes without producing chip (run time mode) and machining (milling mode). The authors showed that for 65% of the total time the machining center is non-productive (idle time and run time) with 47% of the energy consumed. The share of energy consumed not related directly to the manufacture of the final product remains important.

In case of a machine tool from a large Toyota production machining center [7], some parts of the machine tool consume energy as soon as the machine is turned on event if the machine does not produce

chip like hydraulic system, lubrification system…. The share of energy related to the manufacture of the product, it means the energy consumed by the machine when the machine produces chip, is small compared to the total energy consumption (14,8% in Fig. 3).

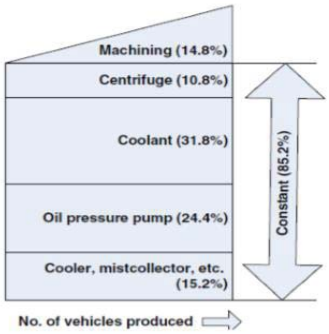


Fig. 3: Energy consumption decomposition of a machine tool [7]

From these above observations, there is a significant part of the energy consumed by the production machine without adding value to the final product. This allows to conclude that it is possible and necessary to carry out actions to reduce the energy consumption of the production machine. To reduce energy consumption of production machine, evaluating energy consumption hold an important pillar. This step allows to have a visualization of energy consumption in term of adding value energy and lost energy part. From that, the authors identify the energy saving opportunities of production machine and propose different scenarios to increase its total energy efficiency in the future. In the following section of this paper, an energy efficiency evaluation method is proposed.

Energy efficiency evaluation method

Valued energy:

Manufacturing process are different steps through which raw materials are transformed into a desired product. It allows to create the *product evolution* by using a production machine. The *product evolution* term is the transformation of the product from a state A to a desired state B. For example, in the case of machining, the product evolution corresponds to changes in the shape or product characteristics versus input material.

A production machine consists of different organs. The total energy consumption of the production machine is therefore the sum of the energy consumed by its various organs. The energy consumed by the production machine does not entirely participate in creating *"value added"* to the product. The *"value added"* term used here corresponds to the product evolution after its passage on the production machine.

Production machine consumes resources and input energy to achieve product evolution and also generates waste. In the same way, energy consumed by a production machine in the manufacturing phase is not entirely used for the manufacture of the desired product. In reality, energy consumed by a production machine is actually much higher than that necessary to achieve only the product evolution. There is always an important part of lost energy (Fig. 4).

An ideal production machine is a machine where its energy consumption moves towards an "ideal target" which is defined as the part of energy just needed to achieve the product evolution. To achieve an ideal production machine in term of energy consumption, the objective is to reduce this lost energy to reach the ideal target.

It is therefore necessary to evaluate the energy consumption of production machine and its organs to identify which part of energy is used to create "value added" to the desired product and how much energy is lost.

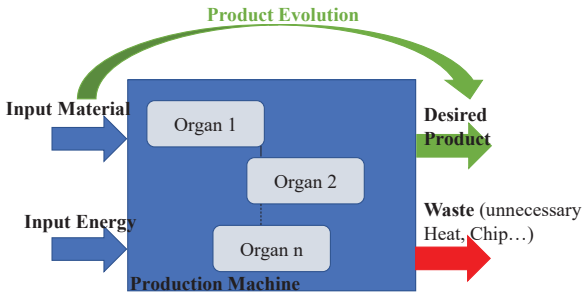


Fig. 4: Input and Output Source of a production machine

By looking at energy consumption of production machine from the product evolution point of view, energy consumed by a production machine can be devised into two parts different: *valued energy* and *lost energy part*.

Valued energy is defined as the part of energy strictly necessary to perform the essential actions, in the production phase, which is not eliminated to create value added to the desired product. In the paper, this energy is called *"valued energy"* E_valued.

Valued energy is calculated by using manufacturing process knowledge and production machine knowledge. In the paper, it supposes that the initial manufacturing process is unchanged. So, the authors get all the information from the knowledge of the manufacturing process like: the cutting time, volume of material removed… in case of a machining center. Moreover, the authors get all the information related to production machine itself. These information depend on the specific character of each production machine.

All organs that do not add value added to the final product have a value of *valued energy* E_valued equal to zero.

In the case of a machine tool which executes a lot of cutting tool change during its production phase (a cutting tool change after each cutting operation), the essential actions in the production phase to create only the evolution product are: the change of the cutting tool, the material removal and the lubrication of the cutting process. Therefore, the valued energy E_valued in this case is the sum of:

- The part of energy necessaire to execute a material removal: this value of energy is calculated by using knowledge of the manufacturing process: the volume of material removed V and the specific energy consumption SEC:

$$E_1 = SEC * V. \quad \text{(Eq. 1)}$$

Or, this part of energy can be also calculated by using manufacturing parameters like: cutting time t_c, cutting force F_c, cutting speed V_c, feed force F_a, feed rate V_a:

$$E_1 = (F_c * V_c + F_a * V_a)t_c. \quad \text{(Eq. 2)}$$

- The part of energy necessaire to make a cutting tool change: this value of energy corresponds to the part of energy consumed by the hydraulic system that is necessary to achieve the loosening of the cutting tool and maintain it until the next cutting tool arrives. By knowing the knowledge of machine tool model using, it is easy to get all information: the loosening time t_{lo}, the loosening power P_{lo} for cutting tool change. The value of energy needed to make a cutting tool change is calculated:

$$E_2 = P_{lo} * t_{lo}. \quad \text{(Eq. 3)}$$

- The part of energy needed to evacuate the heat that generate at the contact Piece-Tool during the chip production phase to ensure the good process operation of machine tool. This value of energy corresponds to the part of energy consumed by the lubrification system just in the cutting time when the machine tool produces the chip. Based on the knowledge of the manufacturing process: cutting time t_c

and the knowledge of machine tool itself: pump system power P_p, the value of energy needed to ensure the good process operation of machine tool is given by:

$$E_3 = P_p * t_c. \quad \text{(Eq. 4)}$$

Energy efficiency indicator:

Efficiency energy is a ratio between the obtained result and the used resources [9]. In this paper, the term "energy efficiency" is used here to determine whether the energy consumed by an organ of production machine really serves to create value added to the desired product.

In order to evaluate the energy efficiency of each organ of the production machine, an energy efficiency indicator is proposed. It is defined as a ratio between the part of valued energy E_valued and the total consumed energy of each organ i:

$$I_i = E\_valued_i / E\_consumed_i. \quad \text{(Eq. 5)}$$

$E\_consumed_i$ is the real energy consumption of each organ of production machine. This value can be measured directly on the production machine by using an energy measuring device. Indicator I shows the percentage of energy consumption of an organ that is used to add value added to the desired product. For example, if the indicator value of an organ i is equal to 0.6, it means that 60% of the energy consumed by this organ is used to create value added to desired product.

According to (Eq. 5, the value of indicators is between 0 and 1. The more the value of the indicator I_i is close to 0, the lower the energy efficiency of organ i is. The more it is close to 1, the higher energy efficiency of this organ i is.

From the point of view of improving energy efficiency, the organs having a low indicator I_i must be redesigned to tend towards an indicator close to 1.

The potential energy gain:

In a context of improving energy efficiency, "energy hot spots" of a production machine is defined as the organs that have a low energy efficiency indicator value and that contribute mainly to the total energy consumption of production machine. To identify them, a potential energy gain is proposed. Taking into account the energy efficiency indicator I_i and the energy contribution of each organ to the total energy consumption of the production machine A_i, the potential energy gain is calculated as follows:

$$G_i = (1 - I_i)A_i. \quad \text{(Eq. 6)}$$

With:

$$A_i = E\_consumed_i / E\_consumed\_total. \quad \text{(Eq. 7)}$$

$E\_consumed_i$: total energy consumption of organ i

E_consumed_total: total energy consumption of the production machine

The potential energy gain allows to identify the percentage of energy to be theoretically saved for each organ. It is obvious that the higher the potential energy gain of an organ is, the greater the possibility of energy saving is. For a production machine, the energy saving opportunities are defined like organs that have high potential energy gain value.

At the end of this energy efficiency evaluation, a complete consumption cartography of production machine is achieved. This cartography allows designers to identify the organs of production machine to be analyzed and redesigned to improve total energy efficiency by based on the potential energy gain of each organ.

Application

This application is aim at illustrating how the energy efficiency indicator and potential energy gain can be used during the energy efficiency evaluation step of a production machine.

The production machine studied is a 4-axis machine tool center. The cutting parameters chosen are given in the Table 1.

Table 1: Cutting parameters

Parameters	Value	Parameters	Value
Average cutting power/operation (P_c)	4.2 kW	Number of operation	10
Average cutting time/operation (t_c)	7.2 seconds	Loosening time (t_{lo})	3.5 seconds
Number of tool change (N)	10	Cutting speed (v_c)	1507 m/min
Total time of the machining cycle (t_{cyc})	280 seconds	Feed rate (v_a)	2250 mm/min

The study started with measuring actual energy consumption of each organ of machine tool. The energy measurement result is given in the Table 2. The actual total energy consumption of machine tool is the sum of energy consumed by all organ and equals to 1215Wh.

Table 2: The actual energy consumption of different organs of the machine tool

Organs (i)	Energy value E_i	Organs (i)	Energy value E_i
Spindle (1)	190 (Wh)	Electrical cabinet (5)	50 (Wh)
Axis (2)	60 (Wh)	Refrigeration system (6)	260 (Wh)
Hydraulic group (3)	40 (Wh)	Compressed air (7)	225 (Wh)
Lubrification center (4)	350 (Wh)	Chip conveyor (8)	40 (Wh)

As explained previously in the paper, for a machine tool, the valued energy E_valued is related to the following actions: material removal (I), changes of cutting tools (II) and evacuating the heat that is generated at the contact Piece-Tool during the production of the chip (III).

The value of E_valued of machine tool is therefore: E_valued =E_I + E_{II} + E_{III}.

Calculation of E_I to carry out a material removal: the energy to execute a material removal is given by:

$$E_I = (P_c + P_a)t_c = 84.04Wh. \quad \text{(Eq. 8)}$$

Calculation of E_{II} to carry out cutting tools changes: The hydraulic system is used to manipulate cutting tool changes and the workpiece. By looking at the actual operation of this machine tool, the hydraulic system activates all the time once the machine tool is started, but it only creates value added when the cutting tool is changed. The valued energy E_{II} is therefore the part of energy consumed by hydraulic system to achieve the loosening of cutting tool and to maintain it until the next cutting tool arrival. To simplify the calculation, in this application, it is assumed that the hydraulic system only participates in cutting tool changes and the actual power consumption of the hydraulic system is equal to the cutting tool loosening power. So, the valued energy E_{II} is calculated by:

$$E_{II} = \frac{E_3 * N * t_{lo}}{t_{cyc}} = \frac{40*10*3.5}{280} = 5\ Wh. \quad \text{(Eq. 9)}$$

Calculation of E_{III} to evacuate the heat that generate at the contact Piece-Tool during the production of the chip: By looking at the actual operation of this machine tool, the lubrification center, which is used to evacuate the heat that generate at the contact Piece-Tool in the cutting process, activates all the time, but it only creates value added to the final production when the machine produces chips. The value of E_{III} is therefore:

$$E_{III} = \frac{E_4 \times t_c}{t_{cyc}} = \frac{350 \times 7.2 \times 10}{280} = 90\ Wh. \quad \text{(Eq. 10)}$$

Then, the total value of value adding energy of machine tool is:

$$E\_valued = E_I + E_{II} + E_{III} = 90\ Wh. \quad \text{(Eq. 11)}$$

So, the potential energy gain of machine is:

$$G_{machine} = 1 - \frac{E\_valued}{E\_consumed\_total} = 1 - \frac{179.04}{1215} = 85.3\%. \quad \text{(Eq. 12)}$$

It is obvious that the potential energy gain of this machine tool is very high, so it is interesting to analyze it in more detail. For this, the energy gain of each element i (i=1..8) is calculated by using equation (Eq. 6 in order to diagnose the organs needed to be redesigned to improve total energy efficiency of machine tool:

- *For the spindle system:*

$$G_1 = (1 - I_1)A_1 = \left(1 - \frac{84}{305}\right) * \frac{305}{1215} = 18.2\%. \quad \text{(Eq. 13)}$$

- *For the axis system:*

$$G_2 = (1 - I_2)A_2 = \left(1 - \frac{0.04}{60}\right) * \frac{60}{1215} = 4.9\%. \quad \text{(Eq. 14)}$$

- *For the hydraulic system:*

$$G_3 = (1 - I_3)A_3 = \left(1 - \frac{5}{40}\right) * \frac{40}{1215} = 2.9\%. \quad \text{(Eq. 15)}$$

- *For the lubrification center:*

$$G_4 = (1 - I_4)A_4 = \left(1 - \frac{90}{350}\right) * \frac{350}{1215} = 21.4\%. \quad \text{(Eq. 16)}$$

- *For the refrigeration system, the electrical cabinet, the compressed air system and the chip conveyor*:

In fact, for an ideal machine tool, the refrigeration system, the electrical cabinet, the compressed air system and the chip conveyor are not theoretically related to add value added to the final product (e.g: remove material, ensure the good process operation of machine tool and change the cutting tool). It means that these organs are not theoretically necessary so that the valued energy of these organs equal to zero. The potential energy gain of these organs is calculated as below:

$$G_5 = A_5 = \frac{50}{1215} = 4.1\%. \quad \text{(Eq. 17)}$$

$$G_6 = A_6 = \frac{260}{1215} = 21.4\%. \quad \text{(Eq. 18)}$$

$$G_7 = A_7 = \frac{225}{1215} = 9.05\%. \quad \text{(Eq. 19)}$$

$$G_8 = A_8 = \frac{40}{1215} = 3.3\%. \quad \text{(Eq. 20)}$$

After having the potential energy gain of all organ, a consumption cartography of machine tool with the potential energy gains of its different organs is given by Fig. 5.

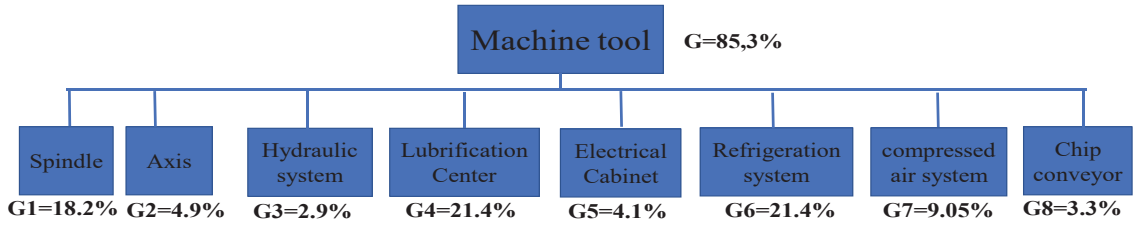


Fig. 5: Consumption cartography of machine tool

From this consumption cartography of machine tool achieved, the potential energy gain of the machine is very high (up to 85,3%). It means that the energy consumed by the machine tool is actually much higher than that necessary to achieve only the product evolution in theory. The part of lost energy remains very important. This part of lost energy can be explained by the part of energy consumed when the working table movement without cutting, the hydraulic unit system is always active even if it is not necessary… Moreover, the value of potential energy gain of: the spindle system, lubrification system, refrigeration system is so high (up to 61%/ total 85,3%). So that, these organs are defined as the "energy hot spots" of this machine tool. They are considered as energy saving opportunities of this machine tool.

In redesign context for energy efficiency for the next machine tool generation, designers can propose various solutions that allow to reduce energy consumption of these organs like: activate the hydraulic system just when it is necessary (just during the cutting tool change) or accumulate energy in order to have enough energy for each change of cutting tools...; choosing an alternative spindle technology that can be used without refrigeration system, or optimizing refrigeration system in term of energy consumption… in order to reduce total energy consumption of this machine tool.

Conclusion:

In this paper, an energy efficiency evaluation method is presented. It is one of the important phases in reducing energy consumption of production machine. This method allows to have a clear vision about the actual energy efficiency and gain potential energy of production machine and its components. In this method, an energy efficiency indicator is proposed to determine the energy efficiency of production machine and its organs. Moreover, a potential energy gain is also proposed to determine the energy saving opportunities of existing production machine. This step of energy efficiency evaluation allows to get the consumption cartography of production machine. From that, in the future, the authors can propose different re-design actions and scenarios to increasing energy efficiency of production machine and its component in order to reduce the total energy consumption of existing production machine. This step is being studied and developed.

References

[1] IEA (2014). Key word energy statistics 2014. Information on: http://www.cdcclimat.com/IMG/pdf/14-10_reperes_2015_eng_part_2.pdf

[2] T.A.L. Nguyen, M. Museau, H. Paris, Méthodologie de (re)conception de l'outil de production pour minimiser sa consommation d'énergie, 21ème Congrès Français de Mécanique CFM 2013, Bordeaux, France (2013).

[3] T.A.L. Nguyen, M. Museau, H. Paris, Evaluating energy consumption of production system, Proceeding of the 3rd international conference on sustainable life in manufacturing, Istanbul, Turkey (2012), 115-119.

[4] International Energy Agency (IEA): Worldwide Trends in Energy Use and Efficiency, Key Insights from IEA Indicator Analysis. Information on: http://www.iea.org.

[5] Information on https://www.mckinsey.com/business-functions/sustainability-and-resource-productivity/our-insights/pathways-to-a-low-carbon-economy.

[6] T. Devoldere, W. Dewulf, W. Deprez, B. Willems, J. R. Duflou, "Improvement potential for energy consumption in discrete part production machines". Advances in Life Cycle Engineering for Sustainable Manufacturing Businesses, Springer. (2007) 311-16.

[7] T. Gutowski, C. Murphy, D. Allen, D. Bauer, B. Bras, T. Piwonka, P. Sheng, J. Sutherland, D. Thurston, E. Wolff, "Environmentally Benign Manufacturing: Observations from Japan, Europe and the United States". Journal of Cleaner Production 13 (1), (2005) 1-17.

[8] J. B. Dahmus, T. G. Gutowski, "An environmental analysis of machining". ASME 2004 International mechanical engineering congress and exposition, American Society of Mechanical Engineers (2004), 643-52.

[9] ISO 9000: 2005 Energy management systems — Fundamentals and vocabulary

MODELING AND SIMULATION OF LOW FREQUENCY VIBRATION ISOLATION TABLE

T.D. LE[1, a *] and N.Y.P. VO [2,b]

[1] Ho Chi Minh City University of Technology, Vietnam
[2] Ho Chi Minh City University of Technology and Education, Vietnam

[a] le_thanh_danh@hotmail.com, [b] yenphuongctm@gmail.com

Keywords: Vibration isolation table, low frequency, Quasi-zero stiffness

Abstract.
This paper will propose and investigate a low frequency vibration isolation table (LFVIT). Here, a negative stiffness mechanism is introduced to correct the dynamic stiffness of the system. In addition, the isolated load is supported by another mechanism having positive stiffness. Due to the opposite of the positive and negative stiffness mechanisms, the designed system attains the low dynamic stiffness but still remains the load bearing ability. The correlation between configurative parameters and the stiffness of the proposed isolator is taken into account. Then, simulation of the isolation effectiveness of the LFVIS is performed via using Matlab/Simulink software. This simulation shows the isolation effectiveness of the LFVIS when the dynamic stiffness of the system is changed. Finally, some conclusions are also given.

1. Introduction

The conventional passive vibration isolator [1,2], which is widely used for controlling unwanted vibration, consists of a linear stiffness spring, K, in parallel to and a damper, C. Vibration attenuation is obtained for input frequencies greater than $\sqrt{2}$ times the natural frequency of the isolation system. For input frequencies below $\sqrt{2}$ times the natural frequencies, and especially those close to the natural frequency, the vibration level of the isolated equipment is actually increased, as compared with that of the base. In order to extend the isolation region toward the ultra-low excitation frequencies, the stiffness of spring K is mostly employed to reduce the natural frequency of the system, especially from 0.5 to 5Hz, in which the vibration is harmful and dangerous to humans, and has been investigated by many researches [3]. This idea indicates that the stiffness of the system is decreased. However, the reduction in stiffness leads to a large static deformation and a low bearing capacity. So, this isolator only offers a good effect with high excitation frequencies. Many papers and reports have given solutions to reduce the resonance frequency, such as using a highly deformed elastica structure working as a nonlinear spring to support a static load [4-7] or another structure that is also based on the elastica model with extreme geometric nonlinearity [8]. The purpose of elastica structures is to reduce the resonance frequency. However, these structures easily lose stability and their low load bearing capacity when the stiffness of the elastic elements is very low. In additional, an alternative structure is also studied to improve the isolation vibration for low excitation frequency regions [9]. For this reason, this paper proposes a mode of a low frequency vibration isolation table (LFVIT). The main goal of which is to obtain efficient attenuation of the vibration at low frequency regions but to ensures at a given load bearing capacity. This paper is organized as following: LFVIT is described in section 2. Next, the dynamic stiffness of the system is analyzed in section 3. The simulation results are presented in section 4. Finally, some conclusions are drawn in section 5.

2. Description of LFVIS

The physical model of the low frequency vibration isolation table is designed as shown in Fig. 1. In this structure, the table 4 is supported by a mechanism with the positive stiffness which includes an air spring 6, one pair of roller 3 and the wedge 2. In addition, another mechanism consisting of a semicircular cam, one pair of roller 7 and an air spring 8, which offers a negative stiffness in vertical direction, is introduced to correct the dynamics stiffness of the isolation table. During operation, the rollers 3 and 7 always roll and without slide on the surface of the wedge 2 and cam, respectively. The free vibration of the system will be died away in time by using the positive damping 5.

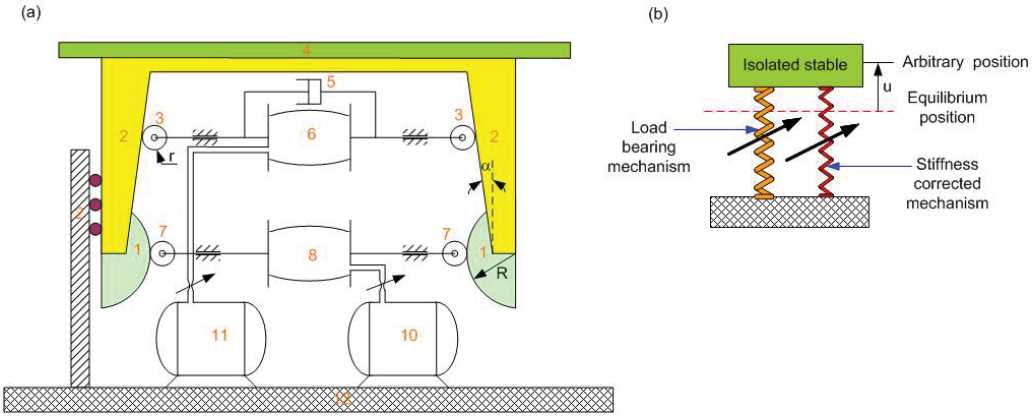


Fig 1. (a): Schematic diagram of vibration isolation table. (b): Model simplification model

3. Dynamic stiffness

Figure 2 presents a sketch of an air spring with auxiliary chamber. When the gas flows from the tank into the air spring, this causes a displacement of piston an announce x compared with the initial position (drawn by dot line), the continuous equation for volume of cylinder and the auxiliary chamber is expressed by:

$$G_{in} = \frac{dm}{dt} = \dot{\rho}V_s + \rho\dot{V}_s$$
$$G_{out} = \frac{dm}{dt} = \dot{\rho}V_c + \rho\dot{V}_c \quad (1)$$

where: G_{in} and G_{out} are mass low rate into cylinder and going out from the chamber, ρ is density of the air, V_s and V_c are volumes of spring and chamber, respectively.

Considering all processes are adiabatic n, the pressure-time derivative are obtained as:

$$\dot{P}_s = \frac{nRT_o}{V_s}\left(\frac{P_s}{P_{so}}\right)^{\frac{n-1}{n}} G_{in} - \frac{nP_s}{V_s}\dot{V}_s$$
$$\dot{P}_c = \frac{nRT_o}{V_c}\left(\frac{P_c}{P_{co}}\right)^{\frac{n-1}{n}} G_{out} \quad (2)$$

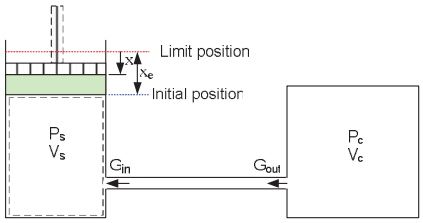


Fig.2: model of air spring with auxiliary chamber

Ignoring all pressure drops and G_{in}=-G_{out}, the equation 3 is rewritten as below:

$$\dot{P}_s = \frac{nP_sA}{Ah - Ax + V_c\left(\frac{P_c}{P_o}\right)^{\frac{n-1}{n}}}\dot{x} \tag{3}$$

where P_s and P_o are the absolute pressure of the air spring at the time t and intial time t_o, A is spring effective area and h is the height of spring.

The geometric relationship between the horizontal displacement x of the air spring and vertical one y of the table is given in Eq. 4.

$$\begin{aligned} x_1 &= y\tan\alpha \\ x_2 &= \sqrt{b^2-(H_o-y)^2} - \sqrt{b^2-H_o^2} \end{aligned} \tag{4}$$

By letting: $\hat{F}_s = \frac{F_s}{A_2P_{o2}}$; $\hat{A}=\frac{A_1}{A_2}$; $\mu=\frac{P_{o1}}{P_{o2}}$; $\hat{P}_{ap} = \frac{P_{ap}}{P_{o2}}$; $\hat{u}=\frac{u}{b}$

The vertical resultant forces acting on the table are expressed in dimensionless form as bellow:

$$\hat{F}_s = \hat{A}\left(\left(\frac{m_1}{m_2+2A_1b\hat{u}\tan\alpha}\right)^n\mu - \hat{P}_{ap}\right)\tan\alpha + \left(\left(\frac{m_3}{m_4-2A_2b\sqrt{1-\hat{u}^2}}\right)^n - \hat{P}_{ap}\right)\frac{\hat{u}}{\sqrt{1-\hat{u}^2}} \tag{5}$$

with: $m_1 = A_1h_1 + V_{c1}$; $m_2 = A_1h_1 - 2A_1H_o\tan\alpha + V_{c1}$; $m_3 = A_2h_2$; $m_4 = A_2h_2 + 2A_2\sqrt{b^2-H_o^2}$; H_o is the static deformation of the isolation table and P_{ap} is the absolute ambient pressure

The non-dimension dynamic stiffness is obtained by taking derivation of Eq. 5 versus the dimensionless position ($\hat{K} = d\hat{F}_s / d\hat{u}$). The dynamic stiffness of the isolated table is depicted as a function of dimensionless displacement as shown in Fig. 3. It can be seen that, the dynamic stiffness of the system offers the minimum value at the equilibrium position (u=0) and increases when the position of the isolated object is moved away from equilibrium one. Besides, the stiffness curve depends on the pressure ratio μ, if this value is chosen unsuitably, the stiffness of isolated table will be negative. It means that the table can not bear the load. Namely, around equilibrium position, the isolated table will achieve negative stiffness for μ<2.1 and positive stiffness with μ>2.1. Especially, if μ=2.1 this table will have quasi-zero stiffness at the equilibrium position and the stiffness value is increased according to increase of the pressure ratio.

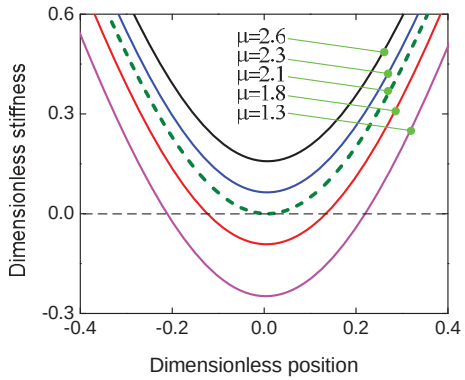


Fig. 3: Dynamic stiffness curve for various values of the pressure ratio

4. Numerical simulation

In order to investigate the isolation effectiveness of the LFVIS, the dynamic response simulation of the isolated table will be performed in this section via Matlab/Simulink software. The physical parameters used for simulation are listed in table 1. The simulation will present the dynamic response of the system with the corrected mechanism and which of system without the corrected mechanism. Here, the excited source is sinusoidal with amplitude 10mm and frequency 1Hz

Table1. Simulation parameters

Physical parameter	Values
The radius of semicircular cam R	60 mm
The radius of rollers r	20 mm
The angle of wedge α	37^0
Initial pressure of air spring 2 P_{o2}	2 bar
Pressure ratio μ	2.1 and 2.6
Damping ratio ζ	0.3
Effective area of air spring 1 A_1	0.0079 m^2
Effective area of air spring 2 A_2	$^{0.23}$ m^2

Case 1: The LFVIS without corrected mechanism. In other words, the air spring 8 and pair of roller 7 is not appeared in the isolated table model. The displacement response versus time of the table is presented in Fig. 4a and the the phase orbit of the isolated table are plotted in Fig. 4b which is a two–dimensional plot of displacement and velocity of the isolated object. It reveals that the isolation table model regardless the corrected mechanism cannot isolate the vibration source having frequency 4rad/s and amplitude 10mm.

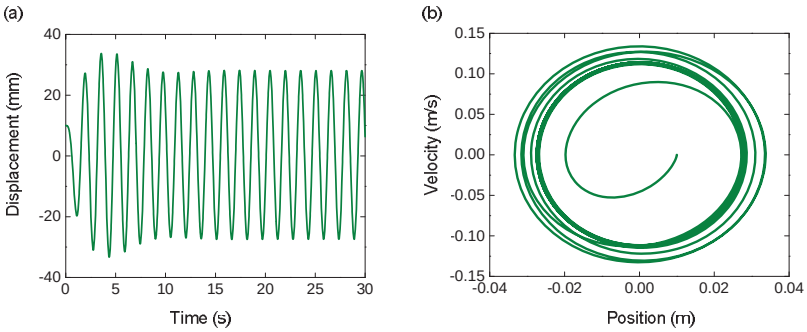


Fig. 4. (a) Displacement response of the isolation table. (b) Phase trajectory

Case 2: The LFVIS with corrected mechanism

Here, two values of stiffness at the equilibrium position are considered to evaluate the isolation effectiveness. Case 1: the pressure ratio μ=2.1, for which the dimensionless dynamic stiffness at equilibrium position is quasi-zero as shown in Fig. 3. Case 2: the μ=2.6 for this value, the dimensionless stiffness is equal to 0.15. From Fig. 3 it can be seen that with two cases, the dynamic stiffness of the isolated table around the equilibrium position is smaller than one.

Figure 5 presents dynamic response of the isolated table. It can be seen that both of two cases, the vibration level of the table is reduced compared with the excitation. As shown in Fig. 5a, when μ=2.1, the amplitude of the table at the steady state is nearly equal to 1.5 mm and this amplitude value is equal to 3 mm when the pressure ratio μ of isolated table obtains the value of 2.6 as plotted in Fig. 5b.

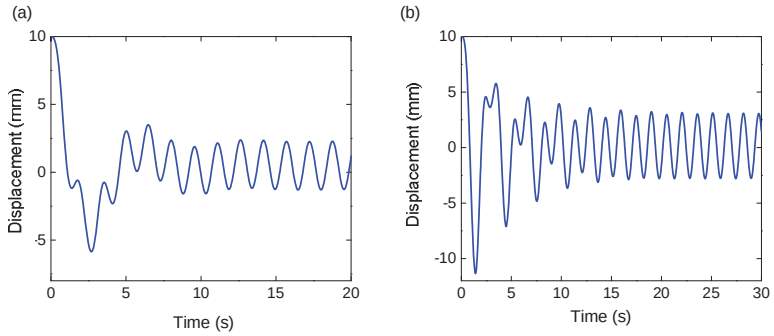


Fig. 5: Time history of displacement response

In addition, the phase orbits of the isolated table are also plotted in Fig. 6. This figure confirmed that the isolation effectiveness of the table having quasi-zero stiffness is better than that of the one with the dimensionless stiffness value being 0.15 at the equilibrium position. Indeed, when μ=2.1, the phase trajectory of LFVIT is shrunk remarkably compared with that of isolated table having the pressure ratio μ=2.1.

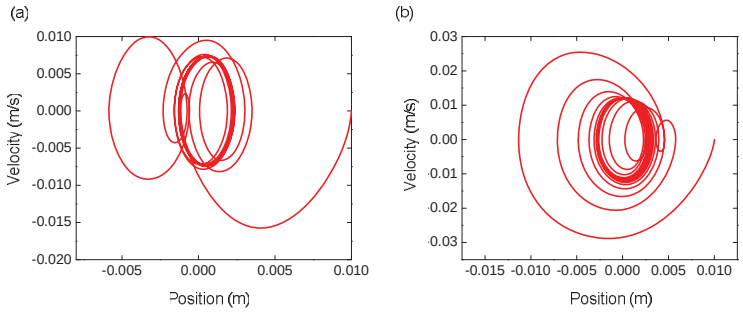


Fig. 6: Phase orbit of the isolated table under excitation amplitude 10mm

5. Conclusions

A model of the low frequency vibration isolation table has been introduced. The restoring force and dynamic stiffness of the LFVIS was analyzed. In this work, the influence of the pressure ratio on the dynamic stiffness curve was investigated. Then, isolation effectiveness and effects of the dynamic stiffness at the static equilibrium position on dynamic response of the system has been assessed via numerical simulation. Besides, a comparison of the isolation performance between the model with the stiffness corrected mechanism and model without stiffness corrected mechanism was realized. The simulation results shown that the innovative table model can offer a good effectiveness of isolation for the low excitation frequencies. Especially, this result indicates that the LFVIS having quasi-zero stiffness at the static equilibrium position is easier for preventing the kinetic energy from the base to the isolated object.

Acknowledgements

This research is funded by Vietnam National Foundation for Science and Technology Development (NAFOSTED) under grant number 107.04-2016.35

References

[1]. Douglas Thorby, Structural dynamic and vibration in practice, *Elsevier Ltd*, 2008.

[2]. S. Graham Kelly, Fundamentals of mechanical vibrations, *McCraw-Hill*, 2002.

[3] G.S. Paddan, M.J. Griffin, Evaluation of whole-body vibration in vehicle, *Journal of Sound and Vibration* 253 (1) (2002) 195 - 213.

[4] L.N Virgin, R.B. Davis, Vibration isolation using buckled struts, *Journal of sound and vibration* 260 (5) (203) 965 - 973.

[5] E.J. Chnin, K.T. Lee, J. Winterflood, L. Ju, D.G. Blair, Low frequency vertical geometric anti-spring vibration isolators, *Physics letters A* 336 (2-3) (2005) 97 - 105.

[6] J. Winterflood, T.A. Barber, D.G. Blair, Mathematical nanlysis of Euler spring vibration isolator, *Physics letters A* 300 (2-3) (2002) 131 - 139.

[7] R.H. Plaut, H. M. Favor, A.E. Jeffers, L.N. Virgin, Vibration isolation using buckled or pre-bent columns-part 1: Two-dimentsional motion of horizontal rigid bar, *Journal of Sound and Vibration* 310 (1-2) (2008) 409 – 420.

[8] L.N. Virgin, S.T. Santillan, R.H. Plaut, Vibration isolation using extreme geometric nonlinearity, *Journal of Sound and Vibration* 315 (3) (2008) 721 - 731.

[10] T.D. LE and P.T. NGUYEN, Dynamic simulation of seat suspension system with virtual prototyping technology, *Journal of Advanced Mechanical Design, Systems, and Manufacturing*, 11(5) (2017) 1-11

Effect of feed rate, toolpath and step over on geometric accuracy of freeform suface when 3 axis CNC milling

Bùi Ngọc Tuyên[1,a], Hoàng Văn Quý[2,b*]

[1]Hanoi University of Science and Technology, Ha Noi, Viet Nam
[2]Hai Phong University, Hai Phong, Viet nam

[a] Tuyen.buingoc@hust.edu.vn, [b] Hoangquyctm@gmail.com

Abstract

The use of freeform (sculptured) surfaces in the product design process is accelerating at an exponential rate driven by functional as well as esthetics demands. CAD/CAM software is a must in their design are relatively well-covered, issues still remain when it comes to the actual manufacture of freeform surfaces. The major issues are related to the chosen feed rate, toolpaths and step over that would assure the required surface quality, the minimization of the total machining time, etc. This research presents an experimental study to define the effects of machining's parameters (including: feed rate; toolpath and step over) for CNC 3-axis ball end milling process. The result shows a model for cutting is formulated and incorporated into the parameters of machining that is compatible with all CAD/CAM systems. This result can be used to choose parameters of optimum including federate, toolpath and step over when machining of other freeform surfaces.

Keywords: Freeform surface; tool-path; ball-end milling

1. Introduction

The machining is one of the most important manufacturing processes in the industry today. This is usually defined as the process of removing material from a workpiece or part in the form of chips. A mechanical part could be machined using different techniques without major differences in the final results. However, the efficiency is not the same for all techniques. In other words, to obtain the same part, there is a machining technique most appropriate that gives the best quality for the lower machining time and energy consumption. The choice of the technique depends on the goal to be achieved and, for machining, is related to the part material and its geometry, as well as, machines and tools available. According to the machining goal and the choice of cutting tool, there are different combinations of parameters, like feed rate, spindle speed, axial or radial depth of cut to obtain different results in terms of quality of machined surface and tool wear [1, 2]. Each parameter's techniques in machining process combination will result in a different surface shape and roughness. However, for many different parameters to control with several levels for each one is very difficult to define the best combination that provides the accuracy surface shape and lower surface roughness. The most important features in the manufacturing industry is to predict the surface quality, tool life and the manufacture costs for a particular combination of machining parameters.

The Taguchi approach is based in statistical analysis of tests that can economically satisfy the product or process for a defined optimal design. One advantage of this method is that multiple factors are considered at once, including noise factors. Taguchi method when combined with other statistical tools, like analysis of variance (ANOVA) transforms into a powerful tool for optimization of the machining parameters. [3–5]. To define the most controllable parameters, such as: feed rate, step over and toolpath. The main goal is rise of accuracy the surface shape, this study authors used three levels for each factor through the use of Taguchi L9 (3^3) array. In this paper the authors analysis the influence of each machining parameters in the surface shape on CNC 3-axis use ball end milling operation. The main goal is the determination of the optimal combination of milling parameters to obtain the accuracy surface shape value.

2. Cutter path strategies

Milling of free surfaces feature in machining parts may be accomplished by employing different cutter path strategies. In general, three of them, which are one direction, back and forth, and spiral cutter path strategies, are often utilized in CAM software. One direction is a cutter path strategy where the cutter moves in parallel lines across the surface to be machined. At the end of the line cutter moves up and comes back, it then scans the area with a fixed step over values (see Figure 1 (b)). In back and forth milling, the cutter draws a zigzag cuter path by moving back and forth across the workpiece in the X–Y plane (Figure 1 (a)). In this strategy, in order to reduce machining time, the machining direction suggested to be chosen along the long side of the surface. In the milling strategy since the cutter makes zigzag movements, up and down milling are occurred. Spiral milling is a strategy where the cutter may start at the center of the surface and then proceeds spirally outwards. The cutter recurs to the starting point in each cycle and then cuts outwards to the next outer cycle. As shown in Figure 1(c), the cutter then proceeds towards the periphery of the surface until the entire workpiece surface is machined.

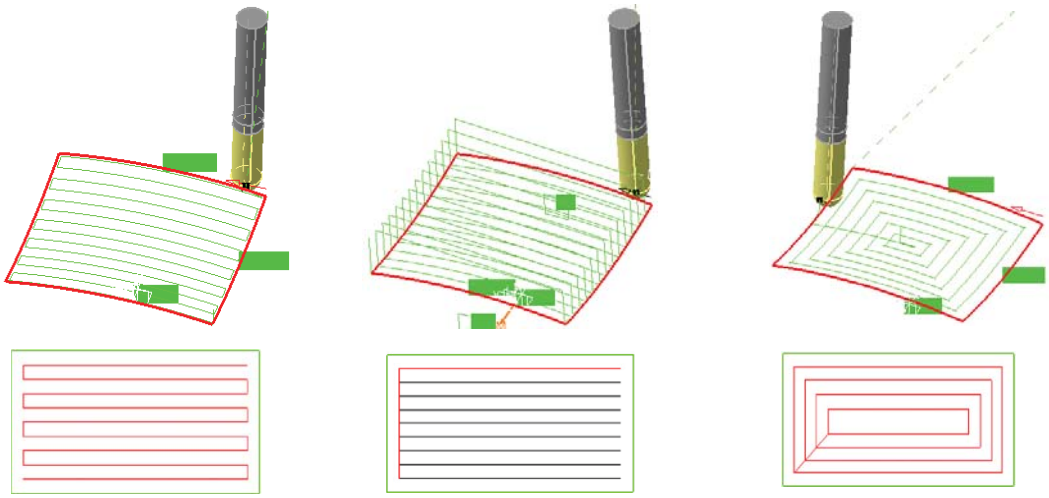


Figure 1. Cutter path strategies in surfaces milling: a) Back and forth; b) One direction; and c) Spiral

In order to obtain desired surface shaped, cutting parameters values should be determined before the machining processes put in action. Some of those data could be taken from machinist handbooks or by conducting experiments. Identifying optimum conditions for a specific operation by experiments is very costly in terms of time and materials to be used. In recent years, a more efficient method Taguchi parameter design has been used for experimental studies in different machining fields [6, 7].

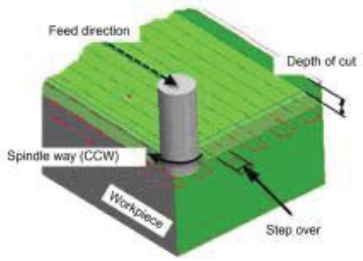


Figure 2. Cutting Parameters

3. Taguchi Method

Taguchi has emphasized that introducing quality concepts at the design stage is moving valuable than through inspection after manufacture [8]. Therefore, Taguchi method aims to optimize processes in order to minimize quality loss with one of the objective functions of "the-nominal-the-best", "the-larger-the-better", or "the-smaller-the-better" depending on the experimental objective. Taguchi classifies the stages in the design process as system design, parameter design and tolerance design. In the first stage, the overall form of the system is identified, in the second stage attribute values are specified, and in the final stage allowable ranges of deviations are defined. Among them parameters design is important to achieve at a robust design. The variation in design parameters is described as noise. The philosophy of robust design suggests lessening the noise factor so far as possible by selecting design parameters that minimize the sensitivity of the design to noise [9].Two important tools used in parameters design are Signal to Noise (S/N) ratios and orthogonal arrays.

3.1. Signal to nose ratio

S/N (η, dB) is defined as the ratio of the wanted signal to unwanted random noise and, in general, it represents quality characteristics for the observed data. Maximization of S/N is desired for parameters of the design. In design there are often many interacting design parameters. So, an exploration of the effects of the combinations of parameters is a necessity. It will, however, not be realistic if there are many numbers of parameters. Because the total number of experiments involved is n_p, where p is the number of design parameters to be examined and n is the number of values to be used for each parameter. [9]

The S/N = -10log$_{10}$ (MSD) was selected for this study, since the objective is to improve the surface shaping, by measuring the points on freeform surface.

Where MSD = mean squared deviation from the target value of the quality characteristic.

Consistent with its application in engineering and science, the value of S/N is intended to be the large, hence the value of MSD should be small. Thus, the mean squared deviation (MSD) is defined differently for each of the three quality characteristics considered, smaller, nominal or larger.

For small is better:

$$MSD = \frac{y_1^2 + y_2^2 + y_3^2 + \cdots + y_n^2}{n} \quad (1)$$

For nominal is the better:

$$MSD = \frac{((y_1 - m)^2 + (y_2 - m)^2 + \cdots + (y_n - m)^2)}{n} \quad (2)$$

For bigger is better

$$MSD = \frac{(1/y_1^2 + 1/y_2^2 + \cdots + 1/y_n^2)}{n} \quad (3)$$

Where $y_1, y_2 \ldots y_n$ result of experiments, observations or quality characteristics such as length, weight, surface finish…

m Target value of results

n Number of repetitions (y_i)

3.2. Design of experiments

The high amount of experiments to be conducted can be lessened by using Taguchi's orthogonal arrays. In fact, they are tables where the design parameters are located at columns as factors and the combinations of parameters values are placed at the rows as levels. The levels of each factor are equally presented in the trails. Once the trails based on the rows are carried out, the deviations are investigated. ANOVA tables are compiled to determine the relative importance of the factors in the experiment and to estimate error variance by calculating various statistical values [10]. Orthogonal arrays help facilitate studying many design parameters concurrently and can be employed to estimate the effects of each factor independently.



Figure 4. CNC Milling Machine, symbol Manford MCB-850

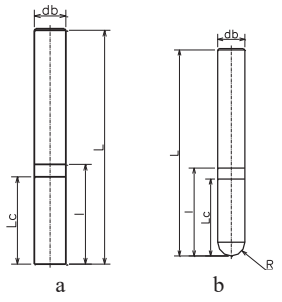


Figure 4. Cutting Tools a) End mill b) Ball end Mill

Experiment Conditions

Machine: The test is carried out on CNC milling machine MANFORD MCB850 (working space, X, Y, Z movements being 1000 x 500 x 400 (mm); variable spindle speeds, max 8000r.p.m; main spindle power, 10 kW; and feed rate max 4000 mm/min); Tool Magazine: 16; The machine shown in Figure 4.

Cutting Tool: Carbide insert PCT 600 (under ISO standard) made in Taiwan. Main parameters of cutting tool are shown in Table 1; the insert is installed on the standard CNC tool's body of Sandvik.

Table 1. Parameters of Cutting tools

No.	Properties	Symbol	End mill (mm)	Ball End mill (mm)
1	Nominal Diameter	D	12	10
2	Corner Radius	R_c	x	5
3	Overall Length	L	75	75
4	Cutting length	L_c	30	28
5	Length	l	34	32
6	Body diameter	d_b	12	10
7	Noncutting diameter	D_{nc}	0	0

Coordinate Measuring Machine

The coordinate measuring machine decided are Accretech, Model SVA NEX 9106 to measuring z-coordinate of point on freeform surface of nine parts. Specification of measuring machine shown in Table 2.

Table 2. Specifications of Measuring Machine		
Name	Parameters	
Measuring range	x-axis (mm)	850
	y-axis (mm)	1000
	z-axis (mm)	600
Measuring length scale	Linear scale	
Minimum display value	0.01	
Table	Usable with (X) (mm)	1000
	Usable depth (Y) (mm)	1810
	Height from floor (mm)	725
Workpiece	Max. Height (mm)	770
	Max. Weight (kg)	1000



Figure 5. Coordinate Measuring Machine Accretech

Model's experiments

The model for experiments was designed have saddle surface (a kind of surface useful in mold's manufacture) [11, 12]. The saddle surface shown in Figure 7 was designed with points array (matrix points 5 x 4).

4. Design for experiments

To evaluate which cutting parameters affect the surface shape in freeform surface milling a number of experiments have been conducted for each of cutter path strategies. Feed rate (F), step over (S), and toolpath (T) (see Figure 2) were determined as controllable cutting parameters to be used in the experiments and each parameter having three levels of values (see Table 3). Selecting of cutting input parameter ranges depends on variety of conditions such as cutter, workpiece material, cutting strategy, coolant, etc. However, here cutting velocity and feed rate values are mostly dependent on manufacturers. The ranges are determined by the cutter producers when taking mainly cutter and workpiece materials into consideration. So, the values with low and high level of these parameters have been taken from firm's catalogue. The amount of depth of cut is determined based on a typical finishing operation for which roughing operation let to leave about 0.2–0.5 mm material on the surface. The selected tools are end mill with diameter 12 mm for rough machining and ball – end mill with diameter 8 mm for finish machining.

The first step for design of the experiments is to identify the quality characteristics and to select the process parameters. In this machining processes, three parameters include feed rate (F), step over (S) and Toolpath (T) were used to evaluate the geometric accuracy of the freeform surface. There are other parameters that could also be controlled, like insert cutting speed, depth of cut, radius or others geometrical parameter of tool. However, these parameters are more restricted and are associated to the properties of tools, which is not the goal of this study. The quality characteristic of machined

surface is one of the most important properties in the machining processes. So, the objective of this study determined the levels of influence of the three milling parameters on the geometric accuracy of freeform surface when 3 axis CNC milling.

After defining the process parameters and the quality characteristic that will be controlled, it is necessary to designate the number of levels of process parameters. The three levels of the cutting parameters selected for this study are shown in Table 3.

Table 3. Parameter for Experimental and their levels

Factors	Levels		
	1	2	3
Feed rate (mm/min)	400	600	800
Step Over (mm)	1	1.5	2
Toolpath Style	Back and forth	One direction	Spiral

Before machining and measurements, the coordinate machining and measure machine was calibrated by only entering the reference value described in the precision specimen. The mean points array of surface values obtained from the experiments were listed in Table 4. The experimental tests were performed through a machining operation of freeform surface milling a saddle surface. The initial dimensions of workpiece were length x wide x high = 70 x 65 x 30 mm. Tool was selection in this study with specification shown in Figure 4 and Table 1. This material of tool and workpiece was chosen because is freeform surface in machining process not variable by force and temperature that is can be variable shaping surface in machining process.

5. Experiments details and results

The nine parts corresponding to the number of experiments shown in Figure 8 and results of measure z-coordinate corresponding to the parts are shown in Table 4 (column 1 to 9). Column 0 shown z-coordinate corresponding model was designed on CATIA V5R20 to export CNC code for experimental from No. 1 to No. 9.

The designed points matrix (5 x 4) of the freeform surface (Figure 7) that are shown in column 0 (Table 4) corresponding to the point's matrix shown of the nine parts that are shown in column 1 to 9 (Table 4). The average values of error for surface shape corresponding to the number of experiments are shown in column Delta (Table 5)

Table 4. Experimental result for points z-coordinate of surfaces

No.	0	1	2	3	4	5	6	7	8	9
1	26.620	26.731	26.224	26.214	26.178	26.174	26.066	26.276	26.655	26.377
2	27.226	27.975	27.822	27.922	28.009	27.223	26.389	26.839	26.806	26.019
3	27.762	27.806	28.324	28.463	28.517	27.732	27.105	27.789	27.336	27.474
4	27.226	27.074	27.938	27.988	28.170	27.417	26.570	27.001	26.678	26.912
5	25.620	26.895	26.477	26.288	26.629	25.697	25.251	25.569	25.308	25.456
6	24.863	25.802	24.882	25.013	25.161	24.137	24.668	23.995	24.566	24.373
7	26.476	26.374	26.539	26.456	26.966	26.738	26.186	26.173	26.957	26.900
8	27.013	26.830	27.046	27.048	27.285	26.677	26.779	26.791	26.329	26.414
9	26.476	26.197	26.755	26.678	26.868	26.326	26.308	25.770	25.659	25.916
10	24.863	24.943	25.284	24.887	25.295	24.629	25.971	24.398	25.191	25.142
11	25.243	25.142	25.806	25.210	25.546	25.516	25.319	25.951	25.487	26.761
12	26.243	26.884	26.423	26.715	27.211	26.499	26.728	26.637	26.919	26.048

13	27.389	27.012	26.961	27.405	27.574	27.184	27.411	27.110	27.194	27.479
14	26.853	26.248	26.691	26.094	26.124	26.848	27.007	26.340	26.564	26.599
15	25.243	25.007	25.269	25.212	25.725	25.895	25.597	25.690	25.303	25.039
16	26.760	26.888	26.358	26.589	26.968	26.913	26.490	26.536	26.434	26.020
17	28.358	28.086	28.126	28.253	28.540	27.858	28.106	27.992	27.865	28.263
18	28.890	28.681	28.590	28.650	28.961	28.554	28.664	28.445	28.133	28.509
19	28.358	28.062	28.098	28.215	28.593	28.111	28.290	28.692	28.547	28.046
20	26.760	26.617	26.933	26.554	26.232	26.328	26.217	26.651	26.965	26.408

5.1. Analysis of the signal – to – noise ratio

The orthogonal array chosen was the L9 (3^3) has 9 rows corresponding to the number of experiments (3 factors with 3 levels each). The array has 8 of freedom and it can cover five design parameters are shown in Table 5. The experiments were conducted with three cutter path strategies according to the sequence given in Table 5.

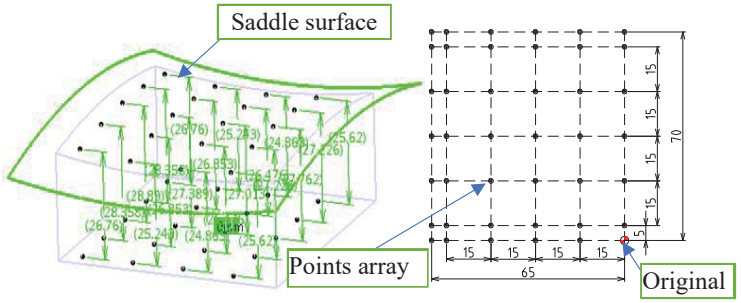


Figure 7. Model of experimental and points to measuring

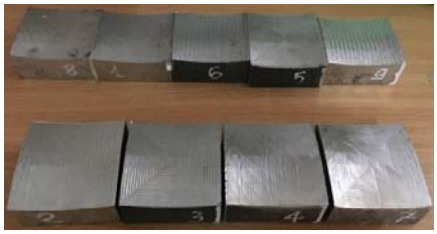


Figure 7. Model of experimental

Table 5. Experimental layout using L9 (3^3) orthogonal array

Exp. No.	End milling machining parameters			Delta	MSD	S/N ratios
	Feed rate (F)	Step over (S)	Tool path (T)			
1	1	1	1	0.0506	0.2230	13.0339
2	1	2	2	0.1152	0.1646	15.6714
3	1	3	3	0.0806	0.1597	15.9339
4	2	1	2	0.3155	0.3137	10.0697
5	2	2	3	- 0.0893	0.1135	18.9001
6	2	3	1	- 0.1560	0.2158	13.3190
7	3	1	3	- 0.1799	0.1817	14.8129
8	3	2	1	- 0.1673	0.1981	14.0623
9	3	3	2	- 0.2044	0.3137	10.0697

The mean S/N ratio for each cutting parameter at levels 1, 2 and 3 can be computed by averaging the S/N ratios for correspondent experiments. The mean of S/N ratio for each level of cutting parameters presented in Table 5, common is defined as the mean S/N ratio response table for the MSD surface shape. In the Figure 8 is shown the S/N ratio response graph for surface shape. One gets a high S/N ratio for smaller variance of surface shape around the desired value. Nevertheless, the relative importance among the milling parameters for the surface shape still required to be identified so optimal combinations of the milling parameter levels can be determine more accurately using an ANOVA analysis.

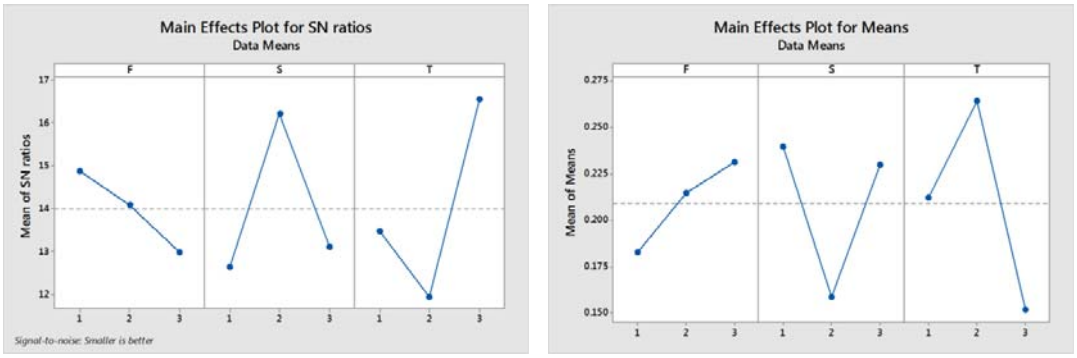


Figure 8. Main effect plots for SN ratios of main

5.2. Analysis of Variance

The goal of the analysis of variance is to determine which design parameters affect meaningfully the surface shape. This goal is achieved by splitting the variability of the S/N ratios that is measured by the sum of the squared deviations from the total mean S/N ratio, in the contributions of each cutting parameters and the error.

The F-Ratio test is statistic tool to verify which design parameters affect significantly in the quality characteristic. This is defined as the ratio of the mean squared deviations to the mean squared error. Generally, when show a value greater than four, it means the variation of the design or cutting parameter has an important effect in the quality characteristic.

The analysis of the F-Ratio values reveals that the toolpath and the step over of cut are the most significant cutting parameters. The toolpath with almost 52%, followed by the step over and then feed rate, respectively, with 31.883% and 10.057% contribution. The optimal cutting parameters for the best surface shape are the toolpath at level 2, the step over at level 1 and, finally, the fee rate at level 3

Table 6. Anova results for surface shape

Source	Degree of freedom	Sum of squares	Mean Squares	**F-ratio**	**Contribution (%)**
A: F	2	0.003676	0.001838	1.64	10.057%
B: S	2	0.011654	0.005827	5.20	31.883%
C: T	2	0.018980	0.009490	8.46	51.925%
Error	2	0.002243	0.001121		6.135%
Total	8	0.036553			100

6. Conclusion

The surface shape in milling process with different cutter path strategies was measured along with orthogonal array in experiments. The conclusions drawn from the results are as follows: According to the results obtained, the most influential effects within the range of specified cutting conditions are feed rate level three, step over level one and one direction cutter path strategies. Confirmation experiments at optimal conditions were carried out. The outcomes for one direction cutter path strategy are the best result. The result of back and forth cutter strategy is better than the result of spiral cutter path strategy. From the ANOVA analysis, we could identify the most the

parameter which mostly influents on the accuracy of surface is the toolpath with a contribution of approximate 52%.

7. References

[1] B. A. Khidhir and B. Mohamed, "Analyzing the effect of cutting parameters on surface roughness and tool wear when machining nickel based hastelloy - 276," *IOP Conf. Ser. Mater. Sci. Eng.*, vol. 17, no. 1, 2011.

[2] W. Grzesik, "Influence of tool wear on surface roughness in hard turning using differently shaped ceramic tools," *Wear*, vol. 265, no. 3–4, pp. 327–335, 2008.

[3] M. Yasir, T. L. Ginta, B. Ariwahjoedi, A. U. Alkali, and M. Danish, "Effect of cutting speed and feed rate on surface roughness of AISI 316l SS using end-milling," *ARPN J. Eng. Appl. Sci.*, vol. 11, no. 4, pp. 2496–2500, 2016.

[4] M. A. İnce and İ. Asiltürk, "Effects of Cutting Tool Parameters on Surface Roughness," *Int. Ref. J. Eng. Sci. ISSN*, vol. 4, no. 8, pp. 2319–183, 2015.

[5] A. Gök, K. Gök, M. B. Bilgin, and M. A. Alkan, "Effects of cutting parameters and tool-path strategies on tool acceleration in ball-end milling," *Mater. Tehnol.*, vol. 51, no. 6, pp. 957–965, 2017.

[6] B. J. L. Yang and J. C. Chen, "A Systematic Approach for Identifying Optimum Surface Roughness Performance in End-Milling Operations A Systematic Approach for Identifying Optimum Surface Roughness Performance in End-Milling Operations," *J. Ind. Technol.*, vol. 17, no. 2, pp. 1–8, 2001.

[7] J. S. Kwak, "Application of Taguchi and response surface methodologies for geometric error in surface grinding process," *Int. J. Mach. Tools Manuf.*, vol. 45, no. 3, pp. 327–334, 2005.

[8] R. Ranjit, *A Primer on the Taguchi Method*. Van Nostrand Reinhold, 1990.

[9] J. Ribeiro, H. Lopes, L. Queijo, and D. Figueiredo, "Optimization of cutting parameters to minimize the surface roughness in the end milling process using the Taguchi method," *Period. Polytech. Mech. Eng.*, vol. 61, no. 1, pp. 30–35, 2017.

[10] H. Rushing, A. Karl, and J. Wisnowski, "Design and Analysis of Experiments," in *Design and Analysis of Experiments by Douglas Montgomery: A Supplement for Using JMP*, Copyright © 2013, SAS Institute Inc., Cary, North Carolina, USA, 2013, pp. 101–128.

[11] S. P. Radzevich, *Geometry Kinematic Geometry Machining*. Taylor & Francis Groups, LLC, 2008.

[12] D. F. Rogers, *An introduction to NURBS: with historical perspective*. 2001.

HYSTERESIS INVESTIGATION OF SHEAR-MODE MR DAMPER FOR FRONT-LOADED WASHING MACHINE

Duy Quoc Bui[1,2,a], Tri Bao Diep[1,2,b], Hiep Dai Le[3,c], Vuong Long Hoang[2,d] and Hung Quoc Nguyen[2,*]

[1]HCMC University of Technology anh Education, Ho Chi Minh, Việt Nam

[2]Industrial University of Ho Chi Minh City, Ho Chi Minh, Viet Nam

[3]Faculty of Engineering, Vietnamese-German University, Binh Duong, Viet Nam

[a]1500102@student.hcmute.edu.vn, buiquocduy@iuh.edu.vn, [b]1500103@student.hcmute.edu.vn, diepbaotri@iuh.edu.vn, [c]ledaihiep1999@gmail.com, [d]hoanglongvuong@iuh.edu.vn,

* Corresponding author. Tel: (+84)938485812; E-mail: nguyenquochung@iuh.edu.vn

Keywords: Front-loaded washing machine; MR damper; semi-active suspension system; vibration control, hysteresis model

Abstract. In this research, a shear-mode MR damper that can replace conventional passive damper of a front-loaded washing machine is designed, manufactured and an experiment based model is employed to characterize hysteresis behavior of the damper. Firstly, an optimized MR damper for front loaded washing machine is manufactured and an experimental system is set up for testing hysteresis behaviour of the damper. The experimental test is then conducted and presented. From experiential results, hysteresis of the damper is investigated and a suitable hysteresis model is proposed for the damper. The proposed hysteresis model of damper is then evaluated through experimental results.

Introduction

It is well-known that a washing machine is one of helpful equipment in human life as it releases people from hard washing works for more free time. Recently, in order to satisfy the high demands of customers, the laundry capacity and the spin speed are increased, while the machine weight and cost are reduced. With these, the vibration of washing machine becomes a more challenging issue that should be under consideration. The vibration of washing machine is transferred from the washing drum to the frame and then to the floor causing acoustic noises, uncomfortable feeling for human and gradual decrease of the machine life-span.

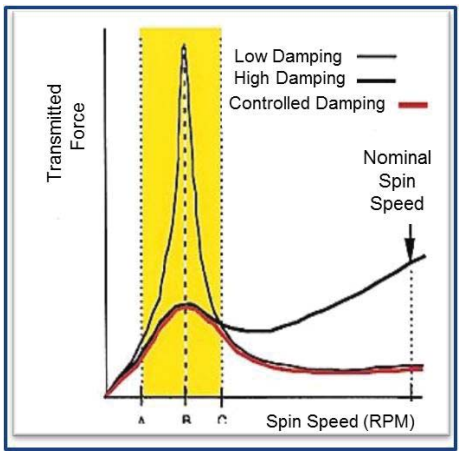


Figure 1. Control of washing machine vibration featuring semi-active suspension system

In order to effectively attenuate the vibration of washing machine at low resonance frequency whereas the one at high excitation frequency is well isolated, a semi-active suspension system with controllable damping coefficient should be employed, as shown in Figure 1. Among new tools applied in the suppression of washing machine vibration, magneto-rheological (MR) damper is one of the most promising candidates due to its possibilities of rapid response, easy control and reverse. However, the main obstacle in control of MR damper is the nonlinear hysteresis in force-displacement and force-velocity response. For that, in this paper, a shear-mode MR damper is designed, manufactured and a suitable hysteresis model is proposed for the damper.

Various models have been developed to descibe the hysteresis behavior of MR damper. According to the properties expressed, these models can be classified as quasi-static models and dynamic models. There are several researches on the quasi-static models such as Phillips 1969 [1], Kamath et al. 1996 [2], Wereley and Pang 1998 [3], , Lee and Wereley 2000 [4], Lee et al. 2002 [5], Hong et al. 2008 [6]. The quasi-static models are beneficial to the design of MR damper and can well represent the force-displacement behavior, nevertheless they are not sufficient to capture the nonlinear force-velocity behavior of MR damper under dynamic loading. In order to overcome this drawback, the dynamic models have been investigated.

Non-parametric dynamic models are explored based on soft-computing approaches and depict the hysteresis phenomenon through data analysis and working principle of device, for example, polynomial model (Choi et al. 2001 [7], Ma et al. 2002 [8], Kim et al. [9]), neural network model (Chang and Roschke 1998 [10], Wang and Liao 2005 [11]), fuzzy model (Schurter and Roschke 2000 [12], Kim and Roschke 2006 [13]). These models are robust, flexible and capable of effectively representing the hysteresis behavior. However, they are quite complicated and may not obviously maintain physical meaning in the appearing parameters.

Contrary to the above models, parametric dynamic models are more desirable due to physical meaning of their parameters. Yet, these models require initial assumptions and appropriate constraints so that the approach could be converged. Different kinds of parametric dynamic models for MR damper have been proposed and validated, consisting of Bingham model (Stanway et al. 1987 [14]), viscoelastic-plastic model (Gamota and Filisko 1991 [15]), bivicous model (Wereley et al. 1998 [16]), LuGre model (Jimenez and Alvarez 2002 [17])... Among the most general parametric models, the Bouc-Wen model has been widely applied for its simplicity and ability to express a large class of hysteretic behavior. This model was initially formulated by Bouc 1971 [18] as an analytical description of a smooth hysteretic model and later generalized by Wen 1976 [19]. However, one of the major issues when applying the Bouc-Wen model is the prediction of its essential parameters. Spencer et al. 1997 [20] and Yao et al. 2002 [21] have employed several optimization tools such as trial and error or sequential quadratic programming (SQP) to identify these parameters, but some remarkable differences between the simulations and experimental data have ocurred. Furthermore, the parameters can only descibe the hysteresis phenomenon of MR damper under limited conditions. To surmount this shortcoming, Dominguez et al. 2004-2006 [22, 23] and Aurelio et al. [24] developed a method to estimate the parameters of Bouc-Wen model using individual effect analysis over the hysteresis curve. Moreover, they proposed current-amplitude-frequency dependent Bouc-Wen models which are applicable for changed excitation conditions. Nevertheless, these models are built on characterization tests with a general MR damper model RD-1005-3 manufactured by Lord Corporation.

The main contribution of this research is to present an optimal design of shear-mode MR damper for front-loaded washing machine and an experiment based model which can characterize hysteresis behavior of the damper. Firstly, an optimized MR damper for front loaded washing machine is manufactured and an experimental system is set up for testing hysteresis behaviour of the damper. The experimental test is then conducted and presented. From experiential results, hysteresis of the damper is investigated and a suitable hysteresis model is proposed for the damper. The proposed hysteresis model of damper is then evaluated through experimental results.

MR damper for front-loaded washing machine

Figure 2 shows the configuration of proposed shear-mode MR damper. In this configuration, two coils are wounded directly on the coil grooves of the housing. The section of the thin wall between the coil grooves and the MR gap is designed to have a small area so that the magnetic flux going through it promptly reaches to saturation and hence is forced to go across the MR gap. In response to the magnetic field, the MR fluid solidifies and resists the relative movement between the shaft and the housing producing the damping force.

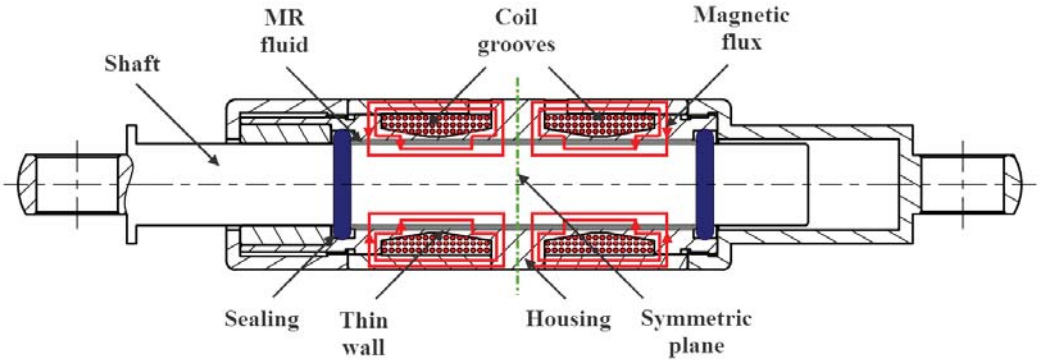


Figure 2. Schematic configuration of proposed shear-mode MR damper

In this work, the commercial front-loaded washing machine, Samsung WF8690NGW, was considered as a prototype. Optimal design of the proposed shear-mode MR damper is performed based on quasi-static model of the MR damper and dynamic equation of the washing machine. The detailed procedure can be found in the previous study [25]. The optimization of the MR damper design for the washing machine can be expressed as follows: Find optimal values of significant geometric dimensions of the proposed MR damper that minimize the off-state force F_{s0}, subjected to the maximum damping force F_{sd} is greater than 80N, the length of MR duct L_d is smaller than 80mm, the outer radius of the damper R is smaller than 19mm, and the height of coil grooves h_c is greater than 4.65mm. In order to obtain the optimal solution, a FEA code integrated with first order method and golden section algorithm of ANSYS optimization tool is employed.

From commercial aspects, the C45 steel and the copper wire gauge 28 (0.33mm-diameter) are employed for magnetic components of the MR damper. The MR fluid gap size is set from 0.5mm to 1mm based on the consideration of manufacturing, amount of MR fluid and size of o-rings. Furthermore, the applied current is limited by 1A in order to reduce the consumption power and the heating of the coils. The optimal solutions of the proposed MR damper are summarized in Table 1 and the magnetic flux distribution of the optimized damper is shown in Figure 3. It is observed from the figure that the magnetic flux density in the shaft and the housing reach to saturation and so does the damping force as the applied current is above 1A.

Table 1. Optimal parameters of the proposed shear-mode MR damper

Parameters			
Off-state force F_{s0} (N)	13.4	Coil width w_{c0} (mm)	2.62
Max damping force F_{sd} (N)	80.02	Axial chamfer ch_1 (mm)	9.77
MR duct length L_d (mm)	61.24	Shaft radius R_s (mm)	8.25
Outer radius R (mm)	17.96	MR duct gap t_g (mm)	0.8
Coil groove height h_c (mm)	5.11	Thin wall t_i (mm)	0.8
Coil height h_{c0} (mm)	2.53	Sliding housing t_0 (mm)	3
Radial chamfer ch (mm)	2.58	Coil to centerline t_{fi} (mm)	4.23

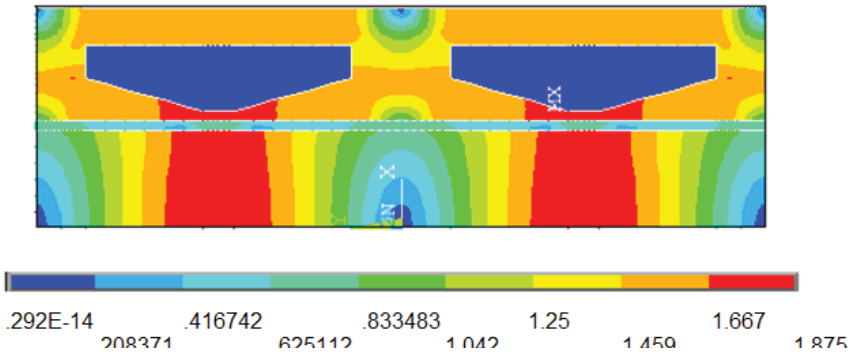


Figure 3. Magnetic flux density of the proposed optimized MR damper

Experimental setup

In order to test hysteresis behavior of the MR damper, a prototype of the optimized MR damper is manufactured, and an experimental system is set up. Figure 4 shows the experimental setup to test performance of the prototype MR damper. As shown in the figure, a crank-slider mechanism is used to convert the rotary motion of the motor to the reciprocal motion of the damper shaft. The motor with a gearbox is employed to rotate the crank shaft at a constant angular speed of 10π rad/s. The instantaneous velocity and displacements are measured by a LVDT sensor while the damping force of the MR damper is measured by a force sensor. The output signal from the force sensor is then sent to the computer via the A/D converter for assessment. During the experiment, different current excitations of 0-1A are applied to the coils of the MR damper via a current power supply. The crank radius (the distance from the center of the eccentric cam to the pin of the transmission rod) is set by 20mm so that the mechanism could provide the required maximum stroke of the MR damper, 40mm.

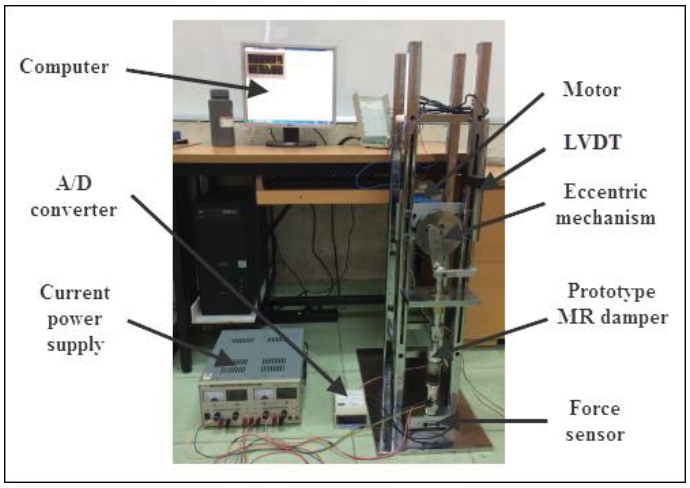


Figure 4. Experimental setup to test hysteresis behavior of the optimized MR damper

Experiment based hysteresis model

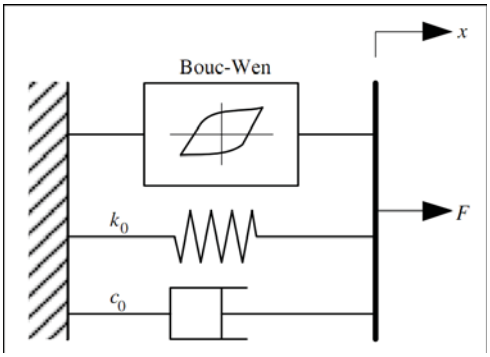


Figure 5. Schematic illustration of the Bouc-Wen model

The Bouc-Wen model represented in Figure 5 is one of the most widely applied models due to its simplicity and ability to express a large class of hysteretic behavior. The damping force in this model can be stated as

$$F\left(x(\tau),\dot{x}(\tau),0\le\tau\le t;t\right)=c_0\dot{x}+k_0x+\alpha z \tag{1}$$

where z is an evolutionary variable determined by

$$\dot{z}=-\gamma\left|\dot{x}\right|\left|z\right|^{(n-1)}z-\beta\dot{x}\left|z\right|^{n}+A\dot{x} \tag{2}$$

The shape of hysteresis curve is basically defined by the seven characteristic parameters c_0, k_0, α, β, γ, n and A. However, as mentioned above, they are only valid for specific conditions and hence should be redetermined when the excitation conditions vary. This is one of the main drawbacks of the traditional Bouc-Wen model. In equation (1), the first and second terms are, respectively, the viscous and spring forces while the last term describe the evolutionary force. Figure 6 expresses a typical hysteresis curve and its decomposition in proportion to Bouc–Wen components.

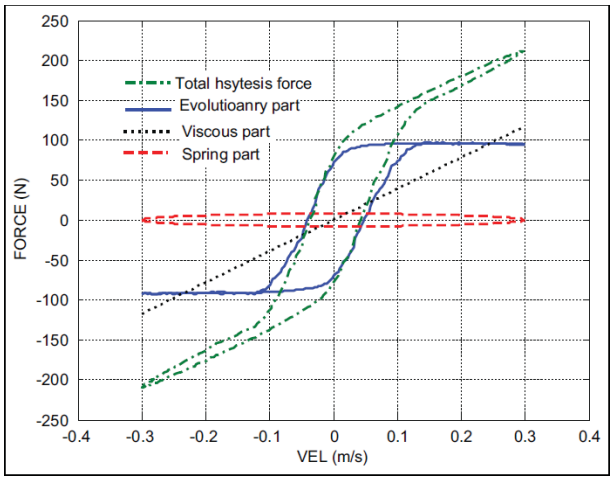


Figure 6. Typical hysteresis loop and its corresponding Bouc–Wen components [24]

In this research, the seven characteristic parameters are estimated using individual effect analysis over the hysteresis curve [22, 24]. This method is very efficient because it does not require any optimization technique to obtain the necessary parameters. According to Figure 6, it is observed that a typical hysteresis curve is composed of three components in corresponding to viscous (dot straight

line), spring (dash ellipse) and evolutionary behavior (continuous curve) of the Bouc-Wen model. The parameters can be determined by [22, 24]

$$\beta = 0$$

$$n = 2 \ [20]$$

$$c_0 = \frac{F_{ku} + F_{kl} - F_{iu} - F_{il}}{2\left(\dot{x}_k - \dot{x}_i\right)} \tag{3}$$

$$k_0 = \frac{\dot{x}_{\max}\left(F_{iu} - F_{il}\right)}{2\sqrt{\dot{x}_{\max}^2 x^2 - x^2 \dot{x}_k^2}} \tag{4}$$

$$\alpha = F_{z\max} = F_{\max} - c_0 \dot{x}_{\max} \tag{5}$$

$$A = \gamma = \frac{1}{v_{z0}} \alpha \tanh z_{v0} \tag{6}$$

in which F is experiment based force, $\dot{x}$ is velocity, k and i represent the different points in the vicinity, the indices u and l represent the upper and lower parts of the hysteresis curve, $\dot{x}_{\max}$ is the maximum velocity, x is the amplitude of the displacement, F_{zmax} is the maximum evolutionary force, F_{max} is the maximum total hysteresis force, v_{z0} is the velocity at evolutionary variable of 0 and z_{v0} is the evolutionary variable at velocity of 0.

Based on the method explained above, the characteristic parameters are automatically specified and the hysteresis curve can be plotted using a MATLAB code. The comparison between the results obtained from the Bouc-Wen model and the experimental data for different current excitations is illustrated in Figure 7. It can be realized that there is a good correlation between the simulation results and the experimental data.

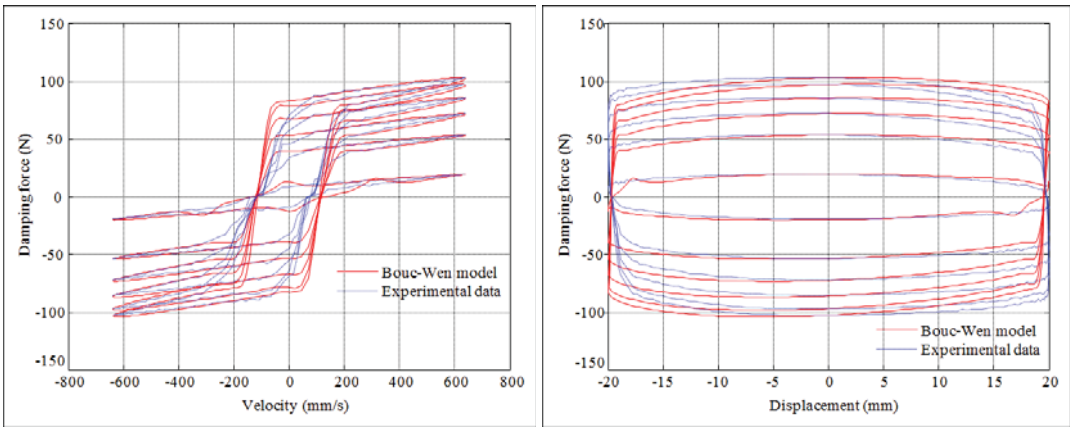


Figure 7. Comparison between the results obtained from the Bouc-Wen model and the experimental data for current excitations of 0, 0.2, 0.4, 0.6, 0.8 and 1A (from inside to outside)

The variation trend of the estimated parameters with regard to current excitation is demonstrated in Figure 8. It is observed that the estimated characteristic parameters c_0, k_0, α, γ and λ tend to follow root squared functions with respect to the currents.

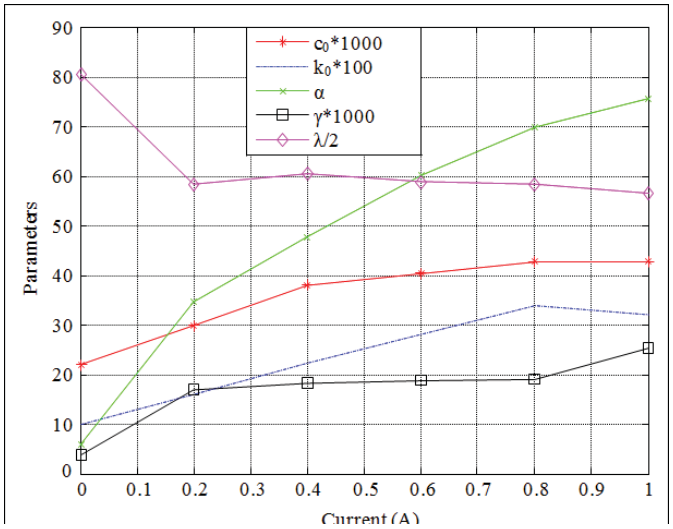


Figure 8. Characteristic parameters obtained from experimental data

In this research, a modified Bouc-Wen model incorporated the current excitation as a variable is proposed for the hysteresis investigation of the MR damper. The damping force in equation (1) can be rebuilt as follows

$$F\left(x(\tau),\dot{x}(\tau),I,0\le\tau\le t;t\right)=c_0(I)\dot{x}+k_0(I)x+\alpha(I)z \tag{7}$$

where z is an evolutionary shape variable determined by

$$\dot{z}(I)=-\gamma(I)\left|\dot{x}\right|\left|z\right|z+\gamma\dot{x} \tag{8}$$

and the characteristic parameters c_0, k_0, α, γ and λ are proposed by the relations to current as follows

$$c_0(I)=c_1+c_2\sqrt{I} \tag{9}$$

$$k_0(I)=k_1+k_2\sqrt{I} \tag{10}$$

$$\alpha(I)=\alpha_1+\alpha_2\sqrt{I} \tag{11}$$

$$\gamma(I)=\gamma_1+\gamma_2\sqrt{I} \tag{12}$$

$$\lambda(I)=\lambda_1-\lambda_2\sqrt{I} \tag{13}$$

in which ten constant parameters c_1, c_2, k_1, k_2, α_1, α_2, γ_1, γ_2, λ_1 and λ_2 should be estimated for a good match between the hysteresis loop and the experimental data. The results are shown in Table 2.

Table 2. Final values of the characteristic parameters using the least-squares approach.

Characteristic parameters			
c_1 (N.s.mm^{-1})	0.0218	c_2 (N.s.mm^{-1}A$^{-0.5}$)	0.0226
k_1 (N.mm^{-1})	0.0806	k_2 (N.mm^{-1}.A$^{-0.5}$)	0.2492
α_1 (N)	4.4943	α_2 (N.A$^{-0.5}$)	71.2425
γ_1 (rad^2.s.mm^{-1})	0.0039	γ_2 (rad^2.s.mm^{-1}.A$^{-0.5}$)	0.0202
λ_1 (s)	156.7348	λ_2 (s.A$^{-0.5}$)	47.6095

Figure 9 describes the simulated hysteresis curves using the proposed model in comparison with the experiment results for various current excitations. It can be seen from the figure that a good agreement is obtained between the proposed model and the experimental data with error of about 10%. However, there are some disappointed positions existing at the region of force reverse. This may come from the simplicity of the proposed model and the least-squares approach to determine the characteristic parameters. Optimization techniques may result in better estimation of the parameters and reduction of error.

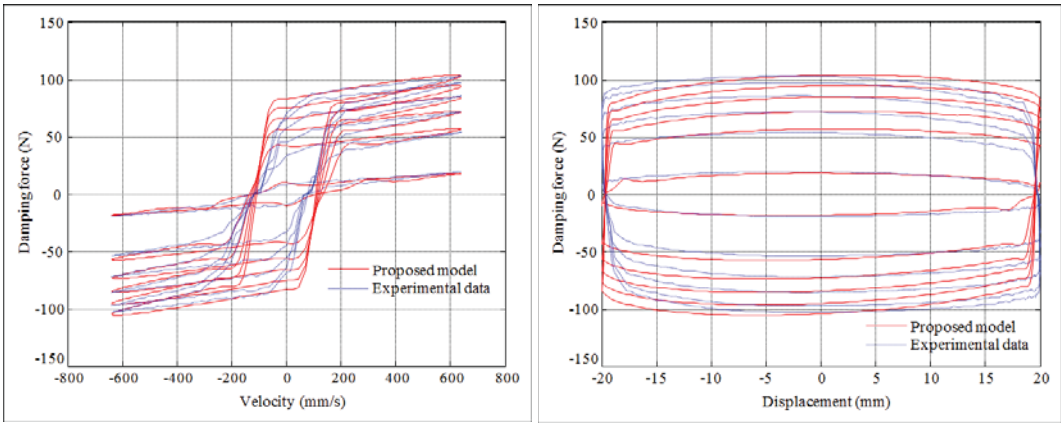


Figure 9. Comparison between the results obtained from the proposed model and the experimental data for current excitations of 0, 0.2, 0.4, 0.6, 0.8 and 1A (from inside to outside)

Conclusions

This paper focused on the design of a shear-mode MR damper for front-loaded washing machine and the proposal of an experiment based model to characterize hysteresis behavior of the damper. Firstly, an optimized MR damper for front loaded washing machine was manufactured and an experimental system was set up for testing hysteresis behaviour of the damper. The experimental test was then conducted and presented. From experiential results, hysteresis of the damper was investigated and a suitable hysteresis model was proposed for the damper. The model was based on the Bouc-Wen model and incorporated the current excitation as a variable. The characteristic parameters of the model was estimated using individual effect analysis over the hysteresis curve. The proposed hysteresis model of damper was then evaluated through experimental results. It was observed that a good agreement was obtained between the proposed model and the experimental data with error of about 10%. It is finally remarked that as the second phase of this research, the MR dampers will be employed in appropriate positions of washing machine and an appropriate controller based on the proposed hysteresis model will be applied for the dampers.

Acknowledgements

This work was supported by the Vietnam National Foundation for Science and Technology Development (NAFOSTED) under grant no. 107.01-2016.32 and partially funded by Industrial University of Ho Chi Minh City.

References

[1] R. W. Phillips, Engineering applications of fluids with a variable yield stress, PhD Thesis University of California, Berkeley, California, 1969.

[2] G. M. Kamath and N. M. Wereley, A nonlinear viscoelastic-plastic model for electrorheological fluids, Smart Mater. Struct. 6 (1996) 351–9.

[3] N. M. Wereley and L. Pang, Nondimensional analysis of semi-active electrorheological and magnetorheological dampers using approximate parallel plate models, Smart Mater. Struct. 7 (1998) 732–43.

[4] D. Y. Lee and N. M. Wereley, Analysis of electro- and magneto-rheological flow mode dampers using Herschel–Bulkley model, Proc. SPIE Smart Structure and Materials Conf. (Newport Beach, CA) vol 3989 (Bellingham, WA: SPIE Optical Engineering Press) (2000) pp 244–52.

[5] D. Y. Lee, Y. T. Choi and N. M. Wereley, Performance analysis of ER/MR impact damper systems using Herschel–Bulkley model, J. Intell. Mater. Syst. Struct. 13 (2002) 525–31.

[6] S. R. Hong, S. John , Wereley N. M., Choi Y. T. and Choi S. B., A unifying perspective on the quasi-steady analysis of magnetorheological dampers, J. Intell. Mater. Syst. Struct. 19 (2008) 959–76.

[7] S. B. Choi, S. K. Lee and Y. P. Park, A hysteresis model for the field-dependent damping force of a magnetorheological damper, J. Sound Vib. 245 (2001) 375–83.

[8] X. Q. Ma, Wang E. R., Rakheja S., et al., Modeling hysteretic characteristics of MR-fluid damper and model validation, Proceedings of the 41st IEEE Conference on Decision and Control 1 (2002) 1675–1680.

[9] Kim K. J., Lee C. W. and Koo J. H., Design and modeling of semi-active squeeze film dampers using magneto-rheological fluids, Smart Mater. Struct. 17 (2008) 035006

[10] Chang C. C. and Roshke P., Neural network modeling of a magnetorheological damper, J. Intell. Mater. Syst. Struct. 9 (1998) 755–64.

[11] Wang D. H. and Liao W. H., Modeling and control of magnetorheological fluid dampers using neural networks, Smart Mater. Struct. 14 (2005) 111–26.

[12] Schurter K. C. and Roschke P. N., Fuzzy modelling of a magnetorheological damper using ANFIS, Proceedings of the 9th IEEE International Conference on Fuzzy Systems 1 (2000) 122–127.

[13] Kim H. S. and Roschke P. N., Fuzzy control of base-isolation system using multi-objective genetic algorithm, Comput.-Aided Civil Infrastruct. Eng. 21 (2006) 436–49.

[14] Stanway R., Sproston J. L. and Stivens N. G., Non-linear modeling of an electrorheological vibration damper, Journal of Electrostatics 20 (1987) 167–184.

[15] Gamota D. R. and Filisko F. E., Dynamic mechanical studies of electrorheological materials: moderate frequencies, Journal of Rheology 35(3) (1991) 399–425.

[16] Wereley N. M., Pang L. G. and Kamath M., Idealized hys teresis modeling of electrorheological and magnetorheological dampers, Journal of Intelligent Material Systems and Structures 9 (1998) 642–649.

[17] Jimenez R. and Alvarez L., Real time identification of structures with magnetorheological dampers, Proc. 41st IEEE (Las Vegas, Nevada, USA) (2002) pp 1017–22.

[18] Bouc R., Modele mathematique d'hysteresis, Acustica 24 (1971) 16–25.

[19] Wen Y. K., Method of random vibration of hysteretic systems, Journal of Engineering Mechanics: ASCE 102(EM2) (1976) 249–263.

[20] Spencer B. F., Dyke S. J. Jr., Sain M. K., et al., Phenomenological model of a magnetorheological damper, Journal of Engineering Mechanics: ASCE 123 (1997) 230–238.

[21] Yao G. Z., Yap F. F., Chen G., et al., MR-damper and its application for semi-active control of vehicle suspension system, Mechatronics 12 (2002) 963–973.

[22] Dominguez A., Sedaghati R. and Stiharu I., Modeling the hysteresis phenomenon of magnetorheological dampers, Journal of Smart Materials and Structures 13 (2004) 1351–1361.

[23] Dominguez A., Sedaghati R. and Stiharu I., A new dynamic hysteresis model for magnetorheological dampers, Journal of Smart Materials and Structures 15 (2006) 1179–1189.

[24] Aurelio D. G., Ion S. and Ramin S., Practical hysteresis model for magnetorheological dampers, Journal of Intelligent Material Systems and Structures 0(0) (2013) 1–13.

[25] D. Q. Bui, V. L. Hoang, H. D. Le, H. Q. Nguyen, Design and evaluation of a shear-mode MR damper for front-loaded washing machines, Proceedings of the International Conference on Advances in Computational Mechanics (2017)

A methodology for generating a variable-pitch rotor of twin-screw vacuum pump

Van-The Tran[1, a *]

[1]Department of Mechanical Engineering, Hung Yen University of Technology and Education, 39A Rd., Hung Yen City, Vietnam

[a]vanct4.hut@gmail.com

*Corresponding author. Tel: (+84) 904162701

Keywords: Screw rotors; turning process; variable pitch tooth; twin-screw vacuum pump.

Abstract. The twin-screw vacuum pump is widely used in low and medium-low vacuum applications. Its core element consists of a pair of rotors rotating in opposite direction on parallel axes. Screw rotors with uniform pitch are usually finished by the form grinding method, but the rotors with variable pitch are not. In this paper, a novel manufacturing process for generating the tooth profile of the screw rotor with variable pitch by CNC lathe turning is proposed. The initial position of turning tool and normal profile error of the manufactured screw rotors are derived and verified numerically. Numerical examples are presented to validate the proposed method. The simulation results reveal that the proposed CNC turning process is feasible and flexible.

Introduction

The advantage of variable pitch twin-screw vacuum pump is high energy efficiency due to high volumetric compression ratio when transporting gas from inlet to outlet. The screw rotor with uniform pitch and square-threaded shape can be milled by at least three finger-shape tools or two form grinding wheels. However, the screw rotor with variable pitch can't be manufactured by the same way. Therefore, in this study, a novel turning process for generating a variable-pitch twin-screw vacuum pump by CNC lathes is proposed. Wherein the workpiece is rotated around to it's axis while a single point cutting tool is moved parallel to the axis of rotation. Both standard and non-standard screw threads can be turned by a CNC lathe by using an appropriate cutting tool. Thus the rotor with uniform pitch or variable pitch can be manufactured by turning process.

The square-thread rotor [1] is often used for the tooth profile of vacuum pump rotor. Its wrap angle is more than $360°$, its screw is single-threaded with uniform pitch or variable pitch, and the left-hand and right-hand rotors have the same tooth profile. The most mathematical models of profile for rotors or gears with conjugated surface are derived by the enveloping theory [2]. A vacuum pump with a variable pitch will perform more efficiently than one with a uniform pitch. In 2004, Becher [3] proposed an asymmetric transverse profile of the rotor with variable pitch. This rotor has the compression ratio of 1.0~10.0 achieved by wrap angle of 2π. The variation of lead is divided into three sections and the first and second sections are mirror symmetry. North [4] suggested a screw rotor with the variable pitch and conical shape. The root diameter of rotor increases whereas the pitch of the rotor threads decreases in a direction from inlet to outlet of the pump. Yan et al. [5] studied various variable pitch lead screws and derived the generalized mathematical expressions of the pencil grinding wheel profiles. These expressions strong influence on the applications in designing various automatic machines with variable pitch lead screws. Han et al. [6] deduced and analyzed three parameterized mathematic models on variable pitch, depth, and groove width screw. These models not only provide a theoretical foundation for machining control system about this type of heterotypic screw, but also offer a feasible method for designing variable pitch screw. Yan et al. [7] developed a surface geometry and machine tool settings for a double-threaded variable pitch lead screw with four cylindrical meshing elements. And a 4-axis machining center with a rotary milling head attachment is adopted for manufacturing the screw profile. Lee et

al. [8] presented a method for generating the tooth profile of a helical rotor on five-axis machine.

This study proposes a novel method to manufacture the tooth profile of screw rotors with variable pitch. According to the simulation results, the tooth profile error of the proposed rotor with the variable pitch and uniform pitch is reached the required precision and the proposed CNC turning process is feasible and flexible.

Mathematical model for turning screw rotor

In this section, a manufacturing process for the variable-pitch screw rotor by CNC lathe is proposed. The initial position and trajectory of turning tools and the mathematical model for calculating the profile error of the manufactured screw rotor are derived and verified numerically.

Mathematical model for tooth profiles of the screw rotors

The tooth profile of the rotors of twin-screw vacuum pump on the transversal section are composed of an extended epicycloid curve AB, a dedendum circle BC, an extended epicycloid curve CD , a circular arc DE, and an arc enveloped curve EF, as shown in Fig. 1. The extended epicycloid curve is used to design the tooth profile of rotors due to it can provide excellent sealing. However, the extended epicycloid curve is basically an undercutting curve and a concave shape. The manufacturing tooth profile included the extended epicycloid curve is difficult.

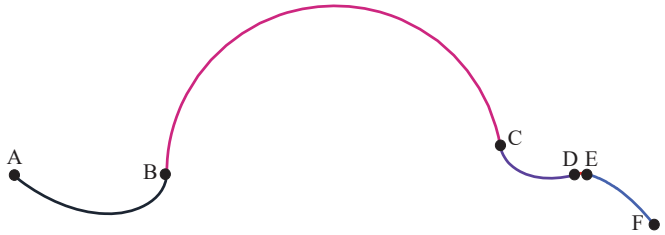


Fig. 1. Transversal section of the screw rotor.

In general, the tooth profile of twin-screw vacuum pump is usually presented on the transversal section of the rotors. A 2D coordinate system for a pair of the mating rotors with their relative motion is shown in Fig. 2. The coordinate systems, $S_1(x_1, y_1)$, $S_2(x_2, y_2)$, and $S_f(x_f, y_f)$, are rigidly connected to the rotational axes of the rotors 1, 2 and frame, respectively.

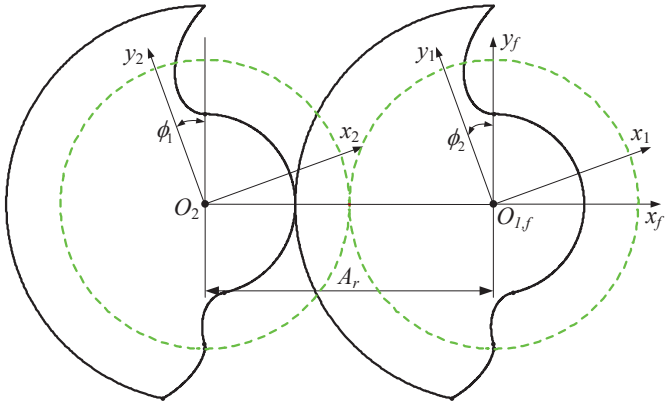


Fig. 2. Coordinate systems with relative motion between two rotors.

The parameters ϕ_1 and ϕ_2 are the rotation angles of the rotors 1, 2, respectively. The parameter A_r is the center distance between axes of the rotors 1, 2. The tooth profiles of rotors can be obtained by using the mathematical equation or discrete data points. If the tooth profile of rotor 1 is given and mating rotors are conjugated, the tooth profile of rotor 2 can be calculated by applying the envelope

theory. However, if the tooth profile of the rotor is not conjugated, the tooth profile of the two rotors should be given.

Assume the positional vector of the rotor, $\mathbf{r}_2(u_2)$, presented in the coordinate system S_2 is given, since the mating rotors rotate in a opposite direction with a constant ratio, so $\phi_1 = i\phi_2$. The positional vector of the rotor in transversal section $\mathbf{r}_1$ is the locus of $\mathbf{r}_2$ in coordinate system S_1 can be expressed as

$$\mathbf{r}_j(u_j) = [x_j(u_j) \;\; y_j(u_j) \;\; 0 \;\; 1]^T, (j = 1,\; 2). \tag{1}$$

where u_j are the geometric parameters.

The coordinate transformation matrix from S_2 to S_1 is represented as follows

$$\mathbf{r}_1 = \mathbf{M}_{12} \cdot \mathbf{r}_2 . \tag{2}$$

The unit normal vector can be presented as follows:

$$\mathbf{n}_1 = \mathbf{k} \times \frac{\partial_{u_2}(\mathbf{r}_1)}{\sqrt{\partial_{u_2}\mathbf{r}_1 . \partial_{u_2}(\mathbf{r}_1)}} . \tag{3}$$

Based on the theory of planar gearing, equation of meshing between two matting rotors can be presented as

$$f_1(u_2, \phi_2) = \mathbf{n}_1 \cdot \partial_{\phi 2}\mathbf{r}_1 = 0 \;\; . \tag{4}$$

Mathematical model for turning screw rotor by the lathe machine

The turning process for generating tooth profile of the rotor needs two simultaneously motions: one is the cutter moved horizontally along the rotational axis and other one is the rotor rotated about its rotational axis. Although the transversal profiles of the rotors with uniform pitch and variable pitch are the same, their axial profiles are different. The variation of the rotor's axial profile is much effect to the turning process of the rotors. The axial profile of the rotor with uniform pitch is shown in Fig. 3 (a), and the axial profile of the rotor with variable pitch is shown in Fig. 3 (b). Obviously, tooth cavity of the uniform pitch rotor has not changed. And tooth cavity of variable pitch rotor has decreased along with the variation of pitch from inlet to outlet.

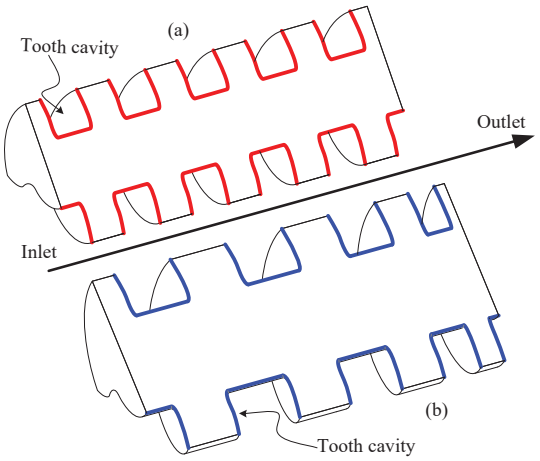


Fig. 3. Axial sections of rotors with: (a) uniform pitch and (b) variable pitch.

As shown in Fig. 4, v_{zi} is the horizontal velocity of the turning tool and it is related to the pitch and the rotational speed of the screw rotor. $z_{1,3}$ is the rotational axis of the screw rotor, θ_3 is the wrap angle of the screw rotor. Coordinate systems $S_1(x_1, y_1)$ and $S_3(x_3, y_3)$ are rigidly connected to the transversal and axial sections of the rotors, respectively. The blade of insert is aligned to one of the points of the axial profile at every instance. Because there are many axial sections corresponded to the variation of rotational axis, the insert is arranged along with the axial profile based on the height of *y*-direction and has not changed in the axial section of the rotor. Therefore, the horizontal velocity, v_{zi}, is depended on the pitch of the rotor.

The axial tooth profile of the rotor can be derived from the Eq. (2) and shown in the Eq. (5)

$$\mathbf{r}_3 = \mathbf{M}_{31}.\mathbf{r}_1. \tag{5}$$

where $\mathbf{M}_{31}$ is the coordinate transformation. w is dependent on the pitch of the rotor (called the positional curve). It is defined as $w = p\theta_3$ if the pitch of the rotor is uniform, and w is a curve if the pitch of the rotor is variable.

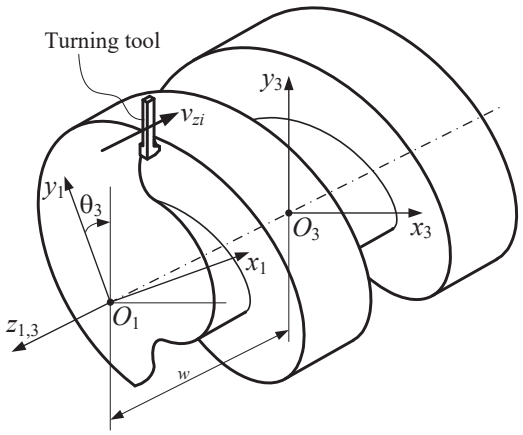


Fig. 4. Coordinate system of the screw rotor and the turning tool.

Setting of the turning inserts

Figure 5 show a turning process for cutting workpiece. The workpiece is fixed by the chuck that rotates by a set angular velocity ω. The turning process is applied to the workpiece to create an object about an axis of rotation.

In the turning process, the insert of tool performs two feed directions: a radial feed direction (f_R) and an axial feed direction (f_Z), as shown in Fig. 5. Normally, the feed radial direction (f_R) is set before performing the axial feed direction (f_Z). The radial feed direction is usually fixed until the next cutting process. The height of the radial feed direction, f_R, is divided into $R_1 \sim R_N$ and $R_1 \sim R_N$ are used to determine the position of the center of the inserts in radial direction f_R during every cutting. Thus, turning the screw rotor by the CNC lathe can be achieved if the position of the center of the insert is arranged according to the axial profile of the screw rotor in every cutting process. The variation of axial feeding v_{zi} in manufacturing the screw rotor can be achieved by using the G34 of G-code or reading the variation of axial feeding directly via M-code to call sub-program.

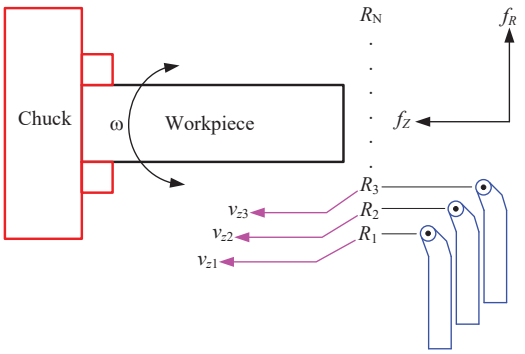


Fig. 5. The turning process for cutting workpiece.

Examining the figure on the bottom of Fig. 6, the wrap angle θ_3 can be divided into many tiny angle values, a plane can be corresponded to a tiny angle value and many planes can be gotten. These planes are denoted as $Plane_i$ $(i=1...n)$. Imagining these planes perform the screw motion along the groove of the rotor with the positional curve w_1 and w_2 by a tiny angle value, every single time.

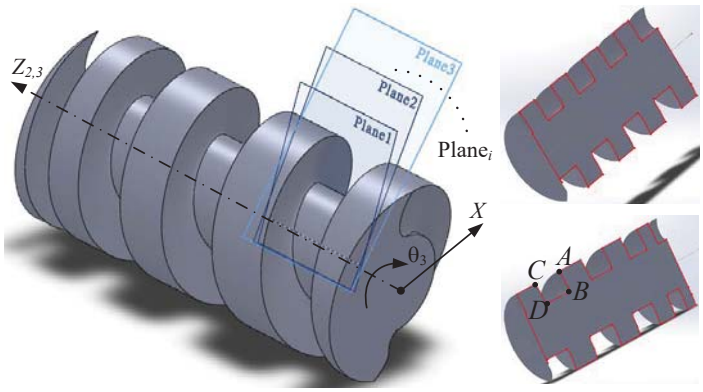


Fig. 6. Axial tooth profile of the screw rotor.

The axial section of the rotor can be calculated by using the Eq. (5) and expressed in the form of discrete points. To simplify the question, the position vector of axial tooth profile $\mathbf{r}_3$ can be rewritten as shown in Eq. (6).

$$\mathbf{r}_4 = \{-w_j, r_4\} = \{-w_j, \sqrt{x_3^{\,2} + y_3^{\,2}}\}. \tag{6}$$

where $j=1,2$. If the range of wrap angle θ_3 is between 0 and 4π, then $w_j = w_1$. If the range of wrap angle θ_3 is more than 4π, then $w_j = w_2$. The cubic-spline is used to fit the discrete points of $\mathbf{r}_4$. Therefore, the axial tooth profile $\mathbf{r}_4$ on the axial section can be rewritten as the vector $\mathbf{r}_5$ and shown as Eq. (7) and its normal vector is expressed as Eq. (8). The arc length is expressed as t_{arc} and the k presents k_{th} axial sections, and the i presents i_{th} Cubic-spline sections of the axial tooth profiles.

$$\mathbf{r}_5^{k,i}(t_{arc}) = \{x_5^{k,i}(t_{arc}), y_5^{k,i}(t_{arc})\} \quad \begin{cases} (k=1...501) \\ (i=1...n) \end{cases}. \tag{7}$$

$$\mathbf{n}_5^{k,i}(t_{arc}) = \{x_{n5}^{k,i}(t_{arc}), y_{n5}^{k,i}(t_{arc})\} = \mathbf{k} \times \frac{\partial_{t_{arc}} \mathbf{r}_5^{k,i}(t_{arc})}{\partial_{t_{arc}} \mathbf{r}_5^{k,i}(t_{arc}) \cdot \partial_{t_{arc}} \mathbf{r}_5^{k,i}(t_{arc})}. \quad (8)$$

Calculation of the normal error

The manufactured profile of the screw rotor by turning with the circular inserts can be assumed that fitting the tooth profile by many sequential circles. Therefore, the error between the manufactured profile and the original profile can be calculated by finding out the intersection point between the circle and other circles. As shown in Fig. 7, the axial tooth profile, k, is drawn in the red line.

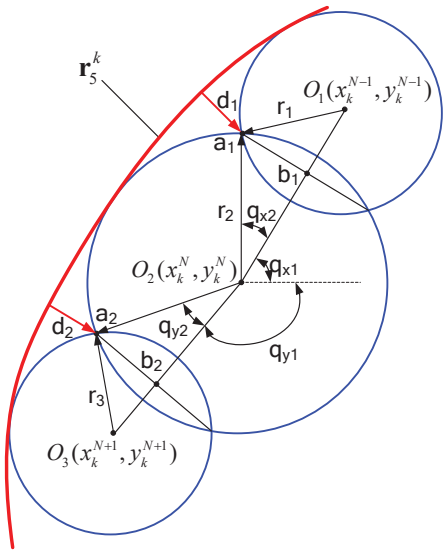


Fig. 7. Calculating the normal profile errors of the manufactured tooth profile.

The normal profile error of N cutting can be calculated by the central coordinates and the radius of the insert of the $N-1$, N, and $N+1$ cutting. The circles $N-1$ and $N+1$ are intersected with N at the points a_1 and a_2, respectively, and the line of centers are intersected with the common chord at the points b_1 and b_2, respectively. The maximum errors δ_1 and δ_2 between the circle N and the axial tooth profile are calculated at the points a_h through the normal vectors of the i_{th} section of the k_{th} axial tooth profile. The normal error δ_m $(m = 1,2)$ of the manufactured axial profile in every axial section can be obtained as

$$\begin{cases} (x_5^{k,i}(t_{arc}) + \delta_m x_{n5}^{k,i}(t_{arc})) - ax_h \\ (y_5^{k,i}(t_{arc}) + \delta_m y_{n5}^{k,i}(t_{arc})) - ay_h \end{cases} \quad (24)$$

Numerical examples

Example 1

In this example, the normal profile errors of rotor with variable pitch have compared with that of the rotor with uniform pitch to verify the effects of proposed method. The allowable error of the rotor should be smaller than $0.02mm$. In order to conduct the arrangement of the inserts of the tool in turning, three kinds of radii were chosen for the inserts, the radii are $2.5mm$, $0.4mm$, and $0.2mm$ respectively. The spindle speed is 300 *rpm*. The basic given parameters are listed in Table 1.

Table 1. Basic parameters of screw rotor.

Basic parameters of screw rotor	**Value**
Wrap angle (deg.)	1800
Lead of rotor with uniform pitch (mm)	78.5
Maximum lead of the rotor with variable pitch (mm)	104
Minimum lead of the rotor with variable pitch (mm)	36
Helix angle (deg.)	78.02
Thread number of rotor	1
Revolution number of thread	4
Spindle speed (rpm)	300
Length of rotor (mm)	314
Diameter of rotor (mm)	120
Allowable error of rotor (mm)	0.02
Radii of insert (mm)	2.5, 0.4,0.2

The total times of cutting process for rotor with uniform pitch are 136. The profile of rotor can be finished about 3 minutes. The normal profile errors of rotors are shown in Fig. 8. It shows that normal profile errors of rotor with variable pitch equals $0.0045mm$ (Fig. 8(a)) much smaller than that of the rotor with uniform pitch equals $0.02mm$ (Fig. 8(b)). Therefore, the proposed CNC turning process is feasible.

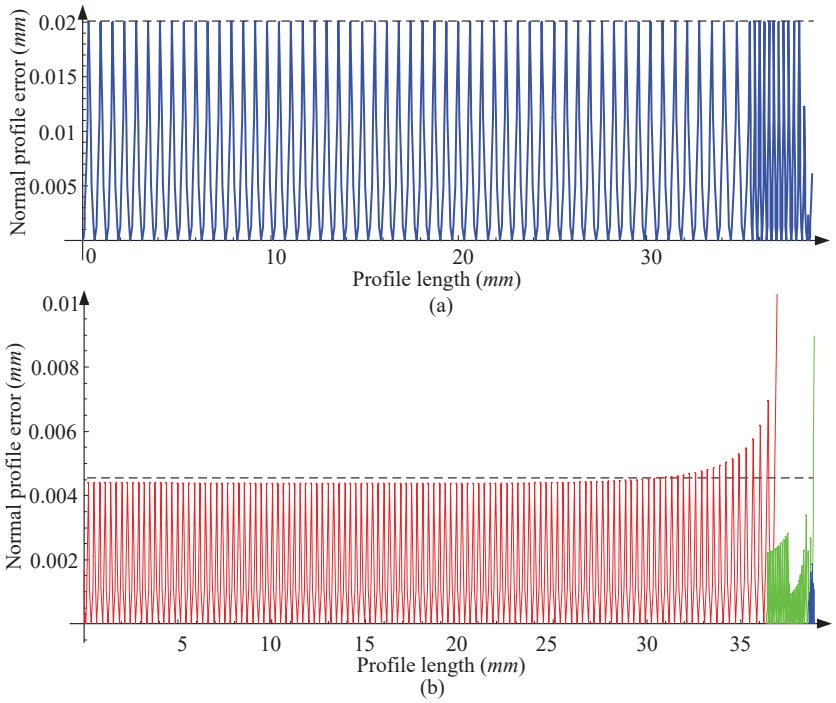


Fig. 8. Normal profile errors of rotors with: (a) uniform pitch and (b) variable pitch.

Example 2

The acceleration of a cutting tool rapidly changes lead to premature tool wear and result in uneven cuts. Jerk is considered for the variation of acceleration when the excitation of vibrations is a concern. The jerk curve of each insert is obtained by calculating the third derivative of the time-position curve with respect to time. As shown in Fig. 8, horizontal axis demonstrates the time and vertical axis demonstrates the jerk of insert in turning process. By observing the jerk curve, the maximum value occurs for normal variable pitch at 0.4 *s*, as shown in Fig. 9(a). Because the jerk is abruptly, the variable pitch curve should be modified. And the jerk curve for the modified variable pitch curve is shown in Fig. 9(b). It represents that jerk curve is much smooth and the turning tool used to manufacture the profile of screw rotor is steady. Further, it is feasible to manufacture the screw rotor with variable pitch by CNC lathe.

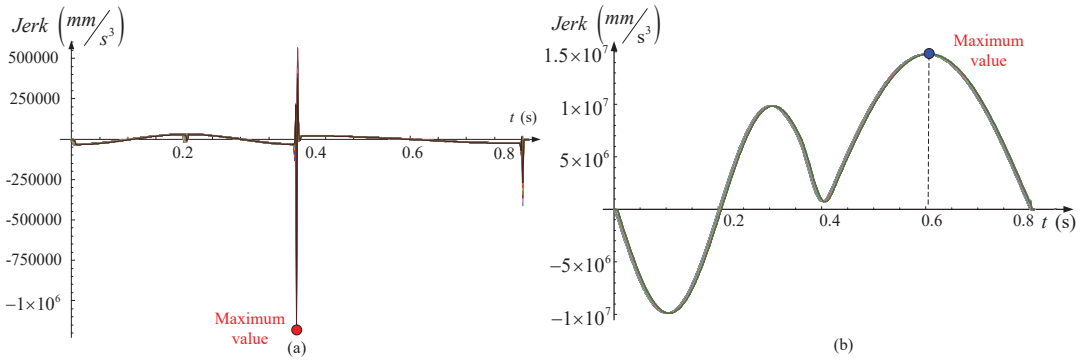


Fig. 9. The jerk curve for each insert of the tool in turning process.

Summary

In this paper, a feasible and simple mathematical method is proposed for manufacturing the screw rotor with variable pitch and uniform pitch on CNC lathe. According to the numerical examples, some following conclusions can be drawn:

1. A mathematical model of the normal profile errors is constructed for screw rotor on CNC lathe turning machine. And the normal profile errors of rotor with variable pitch are much smaller than that of the rotor with uniform pitch.
2. The jerk curve of each insert is presented to consider the excitation of vibrations and it is modified to improve the result by a new variable-pitch curve. And the new jerk curve is much smooth by using new variable-pitch curve.

The proposed CNC turning process is feasible and flexible. However, further experiments are required to check the tool life and machining accuracy.

Acknowledgements

This research was supported by Center for Research and Applications in Science and Technology, Hung Yen University of Technology and Education, under grant number UTEHY.T018.P1718.04.

References

[1] O. Ozawa, Gas exhaust system and pump cleaning system for a semiconductor manufacturing, Kashiyama Industry Co., Ltd., Tokyo, US Patent No. 5,443,644 (1995).
[2] F.L. Litvin, A. Fuentes, Gear Geometry and Applied Theory (2nd ed.), Cambridge University Press, Cambridge, 2004.

[3] U.F. Becher, Twin Screw Rotors and Displacement Machines Containing the Same, U. S. Patent No. 6,702,558,B2 (2004).
[4] M.H. North, Vacuum Pump, U. S. Patent No. 6,672,855,B2 (2004).
[5] H.S. Yan, H.Y. Cheng, The Generation of Variable Pitch Lead Screws by Profiles of Pencil Grinding Wheels, International Journal of Mathematical and Computer Modeling. 25(3) (1997) 91-101.
[6] M. Han, S. Li, L.T. Deng, Study on the Computer Numerical Control Process of Variable Pitch, Groove Depth and Groove Width Screw, Advanced Materials Research. 201-203 (2011) 85-88.
[7] H.S. Yan, J.Y. Liu, Geometric Design and Machining of Variable Pitch Lead Screws with Cylindrical Meshing Elements, ASME Transactions, Journal of Mechanical Design. 115(3) (1993) 490-495.
[8] J.N. Lee, C.B. Huang, T.C. Chen, Tool path generation method for four-axis NC machining of helical rotor, Journal of Achievements in Materials and Manufacturing Engineering. 31(2) (2008) 510-517.

Experimental researching of thermal - assisted milling with induction on surface roughness of SKD11 steel

Mac Thi – Bich[1,2,a,*], Pham Thi – Hoa[2,b], Banh Tien – Long[1,c], Nguyen Duc – Toan[1,d]

[1]School of Mechanical Engineering, Hanoi University of Science and Technology, No. 1A, Dai Co Viet, Hai Ba Trung, Hanoi, Vietnam

[2]Department of Mechanical Engineering, Hung Yen University of Technology and Education, Dan Tien, Khoai Chau, Hung Yen, Vietnam

[a]bich.utehy@gmail.com

[b]hoapt2108@gmail.com

[c]long.banhtien@hust.edu.vn

[d]ductoancae@gmail.com

Keywords: Thermal - assisted milling (TAM), surface roughness, induction heating, SKD11 steel

Abstract. This paper presents experimental studied results about surface roughness during end milling SKD11 steel under room temperature and work-piece preheated condition. Conventional samples were first performed. The samples which are same technical parameters were then performed at elevated temperatures to evaluate effective of heating process on the surface roughness. Orthogonal array Taguchi method was used to experimental design. The results showed that the surface quality of product was significantly improved under thermal - assisted milling. The surface roughness model during machining at room and elevated temperatures were evaluated and showed a good agreement with result of experiments.

Introduction

Nowadays, continuous development of science with new material which are difficult – to – cut by conventional machining. The thermal – assisted machining was a new machining method was studied from the early of 20th century . It is not only supporting for cutting, but also increasing producted machining. Beside it improves quality of surface and reduces cost of product. In TAM, soften material and decreased hardness are the reasons machining process is easier [1].

There are various preheating technologies are applied in manufacturing industry as LAM (laze – assisted machining), PEM (plasma-enhanced machining), electrical resistance, induction heating… The studies [2-5] research on different preheating methods. However, every preheating technology has advantage, disadvantage and coincides with some of machining method. Induction heating is effective and cheap preheating method. It is the right choice for machining with magnetic alloys and metals [6].

Researching on surface roughness is important. Because, the surface roughness is directly effecting to quality of product. Beside it shows rigidity of the technology system, level vibration of cutting process. Amin et al. [3] studied effects of work-piece preheating on surface roughness, chatter and tool performance during end milling of hardened steel D2. The research concluded that thermal - assisted machining of the material leads to values of surface roughness well below 0.4µm. Therefore the grinding and polishing process can be avoided when machining at higher cutting speeds.

Harpreet et al. [7] analysis of surface roughness and material removal rate in dry and thermal – assisted machining of EN8 steel. The study showed that, TAM is alternative pathway to improve tool life, reducing strength and hardness of work-piece material, reducing cutting force and

decreasing surface roughness. The reason is material is softer under elevated temperature helping cutting process is easier and material removal rates increase significantly.

This paper studied the effect of technological parameters on the surface roughness during the conventional and thermal – assisted milling SKD11 steel. The work-pieces are heated by induction current in TAM. The samples when machining at room temperature and elevated one are built by Taguchi method. Mathematical model of the surface roughness depend on control parameters were constructed by Nonlinear – Regresstion tool in Minitab 17 software showed good results in comparing with data of experiment.

Experiment condition

Material.

In this research, SKD11 steel is used for the work-piece material. This is the material is widely applied in mold manufacturing industry. Table 1 shows the chemical composition of SKD11 steel.

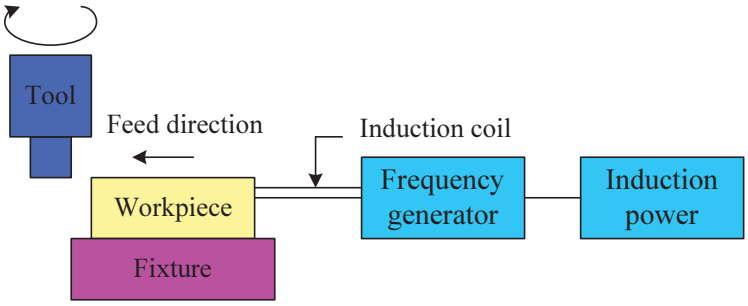
Table 1. Chemical compositions of SKD11 tool steel (%) [8]

C	Cr	Mo	Si	Mn	Ni	V
1,4 – 1,6	11 – 13	0,7 – 1,2	≤ 0,6	≤ 0,6	-	0,15 – 0,3

Experimental equipment.

This part presents the experimental set-up for thermal – assisted end milling of SKD11 steel as shown in Figure 1. Experiments are conducted on MC500 milling machine without lubricant or cooling. Carbide insert cutting tool APKT 1604PDR – GM of PRAMET, Czech Republic is used with diameter of 40 mm. Induction temperature is created from 84kHz of high frequency power made by magnetic induction heating equipments which are induction power and frequency generator.

The surface roughness is measured by Mitutoyo SV - C3200 equipment in combination with Formtracepak software. The X-axis and Z-axis controllers are equipped with linear encoders (ABS type on the Z axis) with high accuracy. Measurement speed of the equipment is from 0.02 mm/s to 5 mm/s. The transducer is perpendicular to the workpiece.



a)



b)

Fig.1. Experiment setup thermal – assisted milling a) and MC500 CNC machine vertical milling b)

Control parameters and their level

Table 2. Parameters with levels

No.	Control parameter	Symbol	Unit	Level 1	Level 2	Level 3
1	Cutting speed	Vc	m/min	190	235	280
2	Feed rate	f	mm/min	230	305	380
3	Cutting depth	t	mm	0.5	1.0	1.5
4	Temperature	T	^{o}C	200	300	400

This study used Taguchi method to design experiment. Four parameters that were chosen to analyze because of their effect on the surface roughness namely cutting speed (V_c), feed rate (f), cutting depth (t) and work-piece temperature at processing time (T). Table 2 shows the control parameters and their levels. In order to the heating process does not affect the mechanical properties of the material, this research choose the studied area of temperature as from 200°C to 400°C.

Studied result in conventional machining

The experiments at room temperature are first performed to elevated the effecting of control parameters on the surface roughness. Table 3 shows nine samples are designed by Taguchi method and corresponding results.

Table 3. Experimental result in during machining at room temperature

Exp. No.	Cutting speed (m/min)	Feed rate (mm/min)	Cutting depth (mm)	Ra (μm)
1	190	230	0.5	0.177
2	190	305	1	0.208
3	190	380	1.5	0.221
4	235	230	1	0.161
5	235	305	1.5	0.184
6	235	380	0.5	0.157
7	280	230	1.5	0.148
8	280	305	0.5	0.128
9	280	380	1	0.165

The mathematical model of the surface roughness depends on control parameters in conventional machining SKD11 tool steel (Ra_R) is determined as the equation 1:

$$Ra_R = a \cdot V_c^{\,b} \cdot f^c \cdot t^d \quad (1)$$

Where the coefficients a, b, c, d are determined by experiment. The Nonlinear Regression tool in Minitab software is used to specify these coefcients. The result of the surface roughness's equation is specified as the equation 2:

$$Ra_R = 4.9758 \cdot V_c^{-0.806915} \cdot f^{0.181702} \cdot t^{0.15646} \quad (2)$$

To determine the accuracy of equation 2 and comparing with experiment data, error percents of the roughness values between experimental and numerical one which are specified from formula (2) are based on formula 3. The analysis results are presented in Table 4 and Figure 2.

$$\Delta Ra(\%) = \frac{|Ra_{EQ} - Ra_{EX}|}{Ra_{EX}} \times 100\% \quad (3)$$

Where Ra_{EX} and Ra_{EQ} are the experimental surface roughness value and numerical one, respectively

Table 4. Analysis result the accuracy of the surface roughness model during conventional machining

Exp. No.	1	2	3	4	5
ΔRa_R(%)	1.8	2.1	2.3	1.2	0.7
Exp. No.	6	7	8	9	
ΔRa_R(%)	2.2	1.8	4.5	5.9	

Figure 2 is compared graph between experimental surface roughness and numerical one which is calculated by equation 2. The result of the surface roughness model which are analyzed in Table 4 and Figure 2 showed a good agreement with experimental data with 5.9% of maximum error percent.

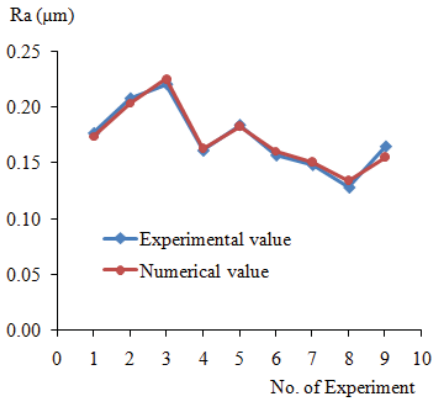
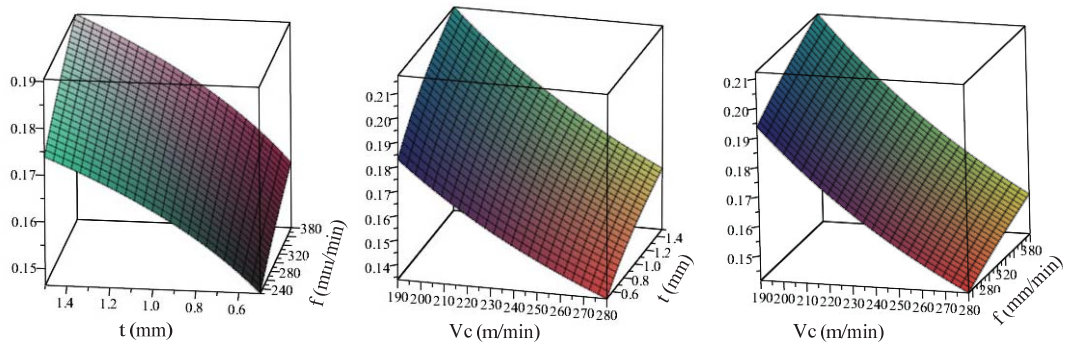


Fig. 2. Comparing the experimental and numerical surface roughness values during conventional machining

From equation 2, the graphs of the surface roughness depend on the technological parameters are built by Maple software tool as shown in Figure 3. Figure 3.a, 3.b and 3.c are corresponding graphs of the surface roughness with fixed the cutting speed, with fixed the feed rate and with fixed cutting depth. Figure 3 shows decreased the surface roughness when decreased the feed rate and the cutting depth or increased the cutting speed.



a) b) c)

Fig. 3. Relationship between Ra_R and technological parameters
a) with fixed V_c, b) with fixed f, with fixed t

Studied result in thermal - assisted machining

The experiments at elevated temperature are then performed to analyze the effect of technological parameters and heating process on the surface roughness. With four control parameters are V_c, f, t and T (elevated temperature). By using Taguchi method, orthogonal array L9 are designed and result of the surface roughness as shown in Table 5.

Table 5. Orthogonal array L9 and corresponding result of the surface roughness

Exp. No.	Cutting speed (m/min)	Feed rate (mm/min)	Cutting depth (mm)	Temperature (^oC)	Ra (µm)
1	190	230	0.5	200	0.128
2	190	305	1	300	0.137
3	190	380	1.5	400	0.159
4	235	230	1	400	0.091
5	235	305	1.5	200	0.176
6	235	380	0.5	300	0.126
7	280	230	1.5	300	0.109
8	280	305	0.5	400	0.090
9	280	380	1	200	0.162

The mathematical model of the surface roughness during machining SKD11 steel at elevated temperatures (Ra_T) is described as equation 4 as follow:

$$Ra_T = e \cdot V_c^{\ f} \cdot f^g \cdot t^h \cdot T^i \quad (4)$$

Where e, f, g, h, i are the coefficients are found by experiments. By using Nonlinear Regression tool in Minitab software, these coefficients are determined by 1.10015, - 0.512293, 0.610263, 0.229099, - 0.498074 respectively. Thereby, equation 4 is rewritten into equation 5 as follow:

$$Ra_T = 1.10015 \cdot V_c^{-0.512293} \cdot f^{0.610263} \cdot t^{0.229099} \cdot T^{-0.498074} \quad (5)$$

The accuracy of equation 5 is evaluated and analyzed by Table 6 and Figure 4. Table 6 shows error percent of the surface roughness value of each sample which is determined by mathematical model and comparing with experiment. In which, the error percents are calculated by equation 3. In combination of analysis the Table 6 and Figure 4, equation 5 has high accuracy with 4.4% of maximum error percent. The graphs which is built by experimental data is closed with one which is built by numerical data from equation 5.

Table 6. Analysis accuracy result of the surface roughness model during Thermal - assisted machining

Exp. No.	1	2	3	4	5
ΔRa_T(%)	1.6	4.4	1.8	2.6	1.7
Exp. No.	6	7	8	9	
ΔRa_T(%)	0.5	0.1	3.1	1.7	

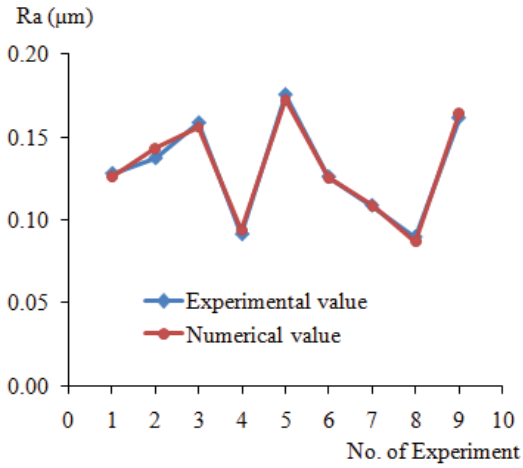


Fig. 4. Comparing the experimental and numerical surface roughness values during thermal - assisted machining

Effect of thermal – assisted machining on the surface roughness

Figure 5 is a graph presents the results of the surface roughness in machining at room and elevated temperatures with the same technological parameters. It shows that the surface roughness is increased during Thermal – assisted machining in comparing with conventional machining. From equation 5, using Maple software tool, the graphs show relationship between the surface roughness with technological parameters at various elevated temperatures are built as shown in Figure 6. Figure 6.a, 6.b, 6.c are corresponding graphs of the surface roughness with fixed the cutting speed, with fixed the feed rate and with fixed cutting depth at various elevated temperatures. In which, The graphs are labeled 1, 2, 3 in order of roughness graph at 200°C, 300°C and 400°C. Figure 6 shows that in thermal – assisted machining, the surface roughness value is proportional to the cutting speed and cutting depth value but inversely proportional to the cutting speed value. Besides, the heating temperature is more elevated, the surface roughness is more decreased.

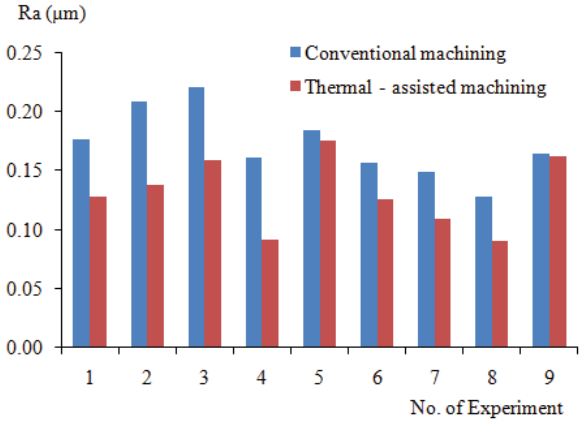
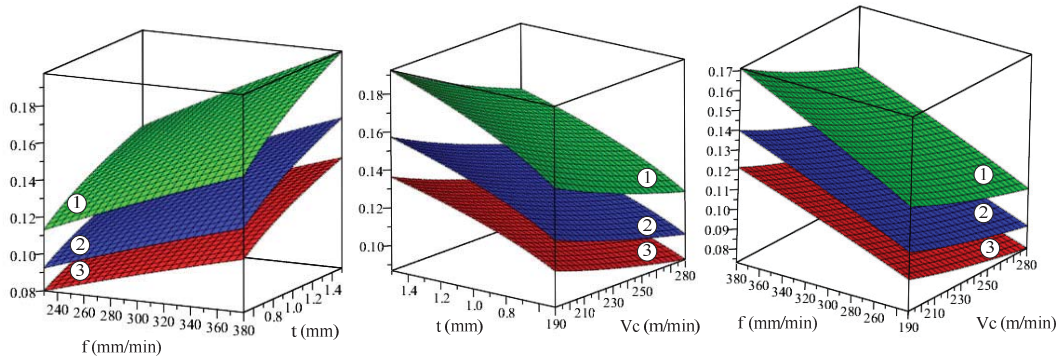


Fig. 5. The surface roughness in conventional and thermal – assisted machining



a) b) c)

Fig. 6. Relationship between Ra_T and technological parameters
(The graphs are labeled 1, 2, 3 in order of roughness graph at 200°C, 300°C and 400°C)
a) with fixed V_c, b) with fixed f, with fixed t

Conclusion

This paper presents an experimental research on the surface roughness during conventional and thermal – assisted machining SKD11 steel. Results of research show some conclusions as follow:

1. The mathematical models of the surface roughness depend on technological parameters when machining SKD11 steel at room temperature and elevated temperatures are described and show a good agreement with experimental data
2. The surface roughness value decrease in thermal – assisted machining when comparing with conventional machining at same technological parameters.
3. Within the control parameters range, the heating temperature is more elevated, the surface roughness is more decreased

References

[1] C. Brecher, M. Emonts, C. Rosen, and J. Hermani, "Laser-assisted Milling of Advanced Materials," vol. 12, pp. 599–606, 2011.
[2] G. Germain, P. Dal Santo, and J. L. Lebrun, "Comprehension of chip formation in laser assisted machining," *Int. J. Mach. Tools Manuf.*, vol. 51, no. 3, pp. 230–238, 2011.
[3] A. K. M. N. Amin, S. Binti, M. Binti, and M. A. Lajis, "Effects of workpiece preheating on surface roughness , chatter and tool performance during end milling of hardened steel D2," vol. 1, pp. 466–470, 2007.
[4] Z. Y. Wang, K. P. Rajurkar, J. Fan, S. Lei, Y. C. Shin, and G. Petrescu, "Hybrid machining of Inconel 718," vol. 43, pp. 1391–1396, 2003.
[5] L. Ozler * ; A.Inan; C. Ozel, "Theoretical and experimental determination of tool life in hot machining of austenitic manganese steel," *Int. J. Mach. Tools Manuf.*, vol. 41, pp. 163–172, 2001.
[6] A. K. M. Nurul Amin and T. L. Ginta, *Heat-Assisted Machining*, vol. 11. Elsevier, 2014.
[7] E. M. G. Singh Harpreet, Er.Sandeep Sharma, "Analysis of surface roughness and material removal rate in dry and thermal assisted machining of EN8 steel," *Int. J. Eng. Sci. Res. Technol.*, vol. 4, no. 11, pp. 577–583, 2015.
[8] C. Wang, Y. Xie, L. Zheng, Z. Qin, D. Tang, and Y. Song, "International Journal of Machine Tools & Manufacture Research on the Chip Formation Mechanism during the high-speed milling of hardened steel," *Int. J. Mach. Tools Manuf.*, vol. 79, pp. 31–48, 2014.

Model Design and Numerical Simulation for Plastic Recycle Machine

Ngo Anh Phuong[1, a *], Ho Thanh Tung[1, b] and Phan Tan Huy[1, c]
Thomas Guidat[2, d], Thanh T. Tran[2, e] and Do Huynh Minh Hieu[3, f]

[1]Graduate Student, Global Production Engineering & Management Program, Vietnamese-German University, Binh Duong, Vietnam

[2]Lecturer, Global Production Engineering & Management Program, Vietnamese-German University, Binh Duong, Vietnam

[3]GPEM lab supervisor, Vietnamese-German University, Binh Duong, Vietnam

[a*]Phuong.ngoanh@outlook.com.vn, [b]gpem2016_tung.ht@student.vgu.edu.vn, [c] gpem2016_huy.pt@student.vgu.edu.vn, [d]thomas.guidat@vgu.edu.vn, [e]thanh.tt@vgu.edu.vn, [f]hieu.dhm@vgu.edu.vn

Keywords: heating, forming, recycled plastic, Finite element method, extrusion

Abstract. One of the biggest environmental challenges of Vietnam is plastic wastes without recycling such as bottle, cans, plastic bag. The Vietnamese government have recognized these problems and called the reforming campaign to develop the sustainable technology to re-producing the wasted plastic. Thus, this research aims to contribute to deal with the issue by designing a plastic recycling machine. To satisfy domestic market of over 120 units at the first time, this research attempted to make a small machine at a low cost, but its throughput still reaches about 8kg plastic/hour and it can run within 16 consecutive hours a day. Hence, most of components is expected to be supplied by local vendors. As the result, the product price as well as maintenance cost is anticipated to be reduced. With the aim to produce the automated machine can incorporate continuous raw materials flow and at the same time move melted plastic in screw conveyor as defined by the regulation of the Programmable Logic Controllers (PLC) with timer to detect a velocity of melted plastic which come out from a nozzle of the screw conveyor and go to a mold. The hydraulic pressure, then, applies force to compressing and forming products. There are potential risks that can happen in fact, to deal with them. That is a reason Computer aid engineering and Finite element method modeling were conducted to make sure the force pressed in mold sufficiently and controlled the thickness of production as customer requirements.

1. Introduction

Vietnam has witnessed a dramatic growth in economy and industry, but it is facing many environmental challenges. One of the biggest challenges is solid waste such as bottles, cans and so on. This research aims to contribute to deal with the issue through producing a machine called Heat-Forming Machines for Plastic Recycling. Insite of the fact that there are various types of heat forming machines for plastic in wide range of price in the market, but they are designed to process a huge amount of recycled plastic roughly more than a ton. As the consequence, they are quite heavy and not portable. It is undoubted that they require a high of investment, so small organizations cannot afford it. One more concern that should be considered is that they are difficult for maintenance, because most of producers are based on foreign countries. Consequently, spare parts for the machines as well as technical supports as soon as need are prohibitive. To satisfy the demand of market for small heat forming machines for recycled machines, a research initiated by the evergreen labs based on Danang in cooperation with Global Production Engineering and Management program (GPEM), Vietnamese German University (VGU) with the purpose of creating feasible concepts and prototypes of the machine for mass production in the future. Firstly, the price of machine must be reasonable, approximately 1200 US dollar per machine. This is the most critical requirement that prospective

customers need, because, the local organizations do not have a high budge in order to afford to pay an expensive machine. Secondly, the machine can operate in 16 consecutive hours a day and release an output of 5 kilograms per hour. These requirements are really challenging, there are a tradeoff between the price of product and its productivity. Thirdly, prospective customers also have a requirement of outcome product of the machine. It is likely to be sheets of plastic with its specific dimensions that width x length is 300 x 300 millimeters and its thickness might vary in range of between 5 and 9 millimeters. Fourthly, as mentioned previously, it is beneficial as long as the machine is portable or easy to assemble/disassemble. Hence, the weight of machine should be around from 100 to 150 kilograms. It could reduce the transportation cost as well as installation cost. Fifthly, the raw materials that the machine can process are polypropylene (PE), polyethylene, polystyrene, and other types of thermal plastic. These are most common plastic used for producing consumer products that may become rubbish. Sixthly, the lifespan of product is expected to be lasted in 5 years. Other requirements that should be taken into account are that the machine must use a residential voltage (V) – 220V, and its components are supplied by local vendors.

After clarifying customer's need, several concepts were created based on a principle of product research and development [1,2]. The finite element method (FEM) was applied for the final concept for solving problems of engineering and mathematical physics. Section 2 will show how the research worked based on the systematic product development and numerical simulation results by using the Abaqus software are demonstrated in Section 3. Meanwhile, the results of the first prototype are represented in section 4. Finally, conclusions and discussion are made for a further clarity of the machine design.

2. Approach

From the perspective of customers, they want to have products with a reasonable price at high performance, while from the view of the cooperators, they expect to maximize the profit and sales. Therefore, the product development process is essential to make products satisfying the most of customer's needs. This research followed the systematic product research and development [1] as follow:

- Planning
- Concept development
- System level design
- Detail design
- Testing and refinement
- Production Ramp-up

2.1. Planning

Initially, a team composing of 6 members attempted to make a plan for the product development. The research was going to the third phase of the project with producing several prototypes to be assessed before the final prototype will go to a mass production as Fig. 1. Thus, it is very important to have a good planning in any project with the aim of avoiding potential risks which may influence the critical path of the project. The research and development of concepts was projected to take about 480 hours of effort of the research team.

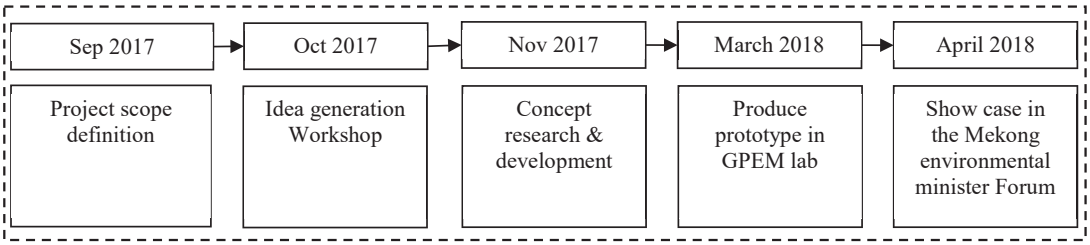


Fig. 1. Heat forming machine for recycled plastic milestones

2.2. Conceptual development and system-level design

First of all, customer's needs were gathered and analyzed to get whose insights to further steps of the development process. In total, there are 27 needs from the customers that were divided into two group, demand group marked "D" in column "D/W" and wishes group marked "W" in the column as Table 1. In which, demand are mandatory requirements that were taken into consideration in the next step, while wishes are additional requirements.

Table 1. List of customer's needs

No	D/W	Heading	Requirement	Value	Unit	Tolerance	Source	Test method	Responsibility
1	D	Assembly	Standard spare parts						Huy
2	W	Assembly	Easy maintenance						Huy
3	D	Costing	Total cost equal or lower than	<=1200	$		Customer	Activity base costing	Phuong
4	D	Costing	Fully localization of parts					Activity base costing	Tung
5	D	Costing	Mantenance cost after 5 years do not exceed 25% of total cost of a	<=300	$		Customer	Accounting	Phuong
6	D	Durability	5 years life time	5	years	6 months		Simulation	Duc
7	D	Energy consumtion	Saving energy (Main motor)	0.15	kWh	+-5Wh	Team	Measuring	Phuong
8	D	Energy consumtion	Saving energy (Hydraulic pump)	0.25	kWh	+-10Wh	Team	Measuring	Tung
9	D	Energy consumtion	Saving energy (Heating)	1	kWh	+-50Wh	Team	Measuring	Phuong
10	D	Ergonomics	Portable	4 or 6	wheels		Team	Simulation	Duc
11	D	Ergonomics	Control system				Team	Simulation	Phuc
12	W	Geometry and dimension	Length x Width x Height	1200 x 1000 x	mm	+- 5mm	Duc	Geometric measurement and	Duc
13	D	Geometry and dimension	Lower than 100kg	<100	kg	5kg	Customer	Weighting	Tung
15	D	Performance	16 consecutive hour operation/day	16	hours	30 minutes	Customer	Measuring	Thong
16	D	Performance	Process at least 5kg of raw materials/hour	5	kg/hour	0	Customer		Thong
17	D	Performance	Output: a sheet with dimension Length x Height	300 x 300	mm		Customer		Huy
18	D	Performance	Output: thickness of a product	7	mm	+-2	Customer		Huy
19	D	Performance	Materials: PP, PE, PS or PC				Customer		Huy
20	W	Performance	Distant controlling via Apps on smartphone				Phuc		Phuc
21	D	Performance	Operation under 220V electricity				Customer		Duc
22	D	Performance	Product without gas prosity and blow hole				Customer		Duc
23	D	Safety	Insulation resistance	>=1000	kΩ			Electrical safety	Thong
24	D	Safety	Circuit breaker						Thong
25	D	Safety	Overheating circuit breaker						Thong
26	W	Safety	Water proof	IP1			Team		Huy
27	~~W~~	~~Safety~~	~~Dust resistance~~	~~IP6~~			~~Team~~		~~Thong~~

Afterwards, the customer's needs must be converted to product's specifications through Quality Functional Deployment (QFD). This tool aims to match the most appropriate and necessary specifications to customer's requirements. After the QFD was carried out, the important specifications were listed down as Table 2. The shortlist of important customer's requirements shows specific specifications and their expected values in Table 2. It is not compulsory to satisfy all requirement in the first concept, because it is very hard for the machine run smoothly at risk. A continuous improvement process will be applied to make a future generation of the machine better. Thus, customer's requirements are not only crucial for the current product development, it also reflect to the vision of the future product.

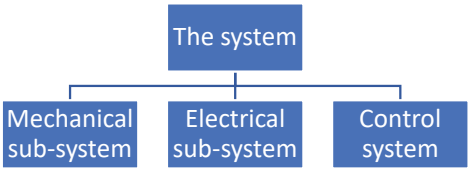


Fig. 2. Structure of the concept

Thanks to the result of applying QFD method, the research team has enough insights from customers to come up with ideas for producing some prototypes. In the stage, the prospective products were broken down into 3 levels for an orientation of concepts generation.

State of the art were carried out for sub-systems and control system with the aim of finding out relevant research. As the result, many solutions were created for components of the system. A component individually could not compose a system, so group of relevant components were made up to generate several solutions as Fig. 3. The research had decided to choose the best fit solutions to the customer's requirements through applying the Pugh matrix method.

Table 2. Refining of customer's requirements

No.	Specification	Value	Unit
1	Machine dimension: Length x Width x Height	200 x 1000 x 1000	mm
2	Standard spare parts		
3	Disassemble mechanics	Easy	Rank
4	Number of wheels	4	Wheels
5	Number of operation	16	hour
6	Life cycle time	5	year
7	Total cost	1200	USD
8	Motor energy consumption	250	Wh
9	Hydraulic pump energy consumption	150	Wh
10	Heating energy consumption	1300	Wh
11	Weight of machine	100	kg
12	Program logic controller intelligence	Fully	Auto grade
13	Localization of parts rate	100%	%
14	Ratio of Mantenance cost/total cost after 5 year	25%	%
15	Insulation resistance	1000	Ohm
16	Circuit breaker voltage	>240 or <180	Volatge
17	Overheating circuit breaker temperature	250	oC
18	Capacity/hour	5	kg/hour
19	Output product dimension	30x30	cm
20	Tolerance of output thickness	5-9	mm
21	Heating temperature range	110-250	oC
22	Dust resistance	IP1	IP
23	Input voltage	220	Voltage

The Morphological Matrix was implemented to identify the most feasible solution and the 1st and 2nd design concepts were disqualified because if our group use this design, the force needed to extrude plastic will be extremely high because the nozzle size is significantly small. The research team, then, started to change the design to the final concept which is the solution 3, to increase the nozzle size and use less power than the previous concept. We believe that the final concept will be

fulfill the requirement of customer with affordable price, high efficiency, low maintenance cost and human power.

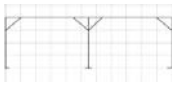
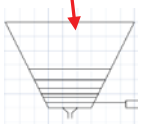
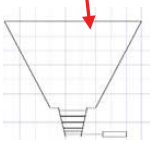
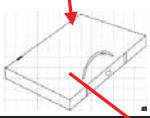
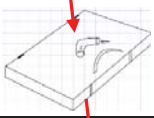
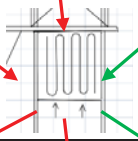
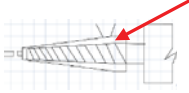
Morphological Matrix		Solution		
		1	2	3 (final solution)
A	Rotating base			
B	Hopper			
C	Molding			
D	Mold Heating			
E	Pressure			
F	Mold moving system			
G	Controlling System			

Fig. 3. Pugh matrix of the product development of process

2.3. Detail design

In this phase, the 3D model was created for the final concept with the purpose of giving a first look to the real machine. From the point of view of engineers, they can analyze and predict potential risks. Consequently, they can give corrective or preventive actions before the design come to the production. After, the most critical parts were tested based Finite element method. This method is powerful to give a deep view as well as parameter which is likely to a real situation. However, it is time-consuming. It took about 2 hours to run a set of parameters, but many sets were put into the model to find out the optimal one.

2.4. Testing and Refinement, and Production Ramp-up

These last phases are conducting in cooperation between GPEM and Evergreen Labs to delivery the machines to Vietnam market in timely manner.

3. Conceptual Design of Plastic Recycle Machine

3.1. 3D-Modelling

All things considered, two feasible solutions were put in the short-list, namely the first solution and the third one as Fig. 4 and Fig. 5, respectively:

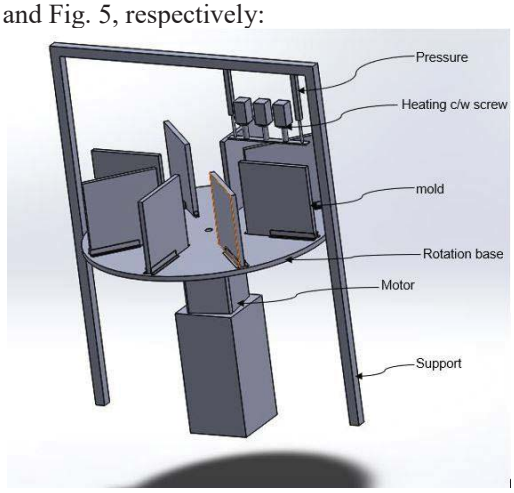


Fig. 4. The first concept of product

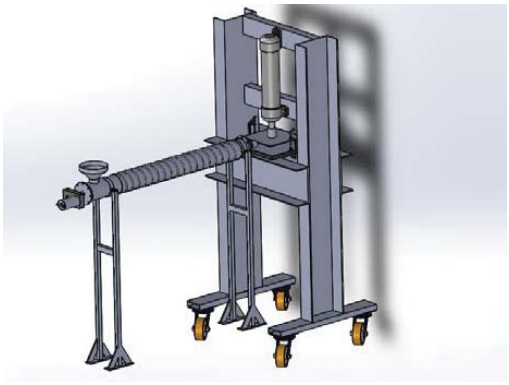


Fig. 5. The third concept of product

After deeply consideration, the design concept of the first concept had a concern that the force needed to extrude plastic will be extremely high because the nozzle size is significantly small. The third concept had a different approach in nozzle from the other concepts, so the force provided to the nozzle is not high. This is reason why the third concept was chosen. After that, the final concept is developed its 3D model and its concrete technical drawings which as well as carried out Computer Aided Engineering with a special software and include the calculation of its throughput and energy consumption. For the goals of a concise paper, machine element designs are not presented here.

3.2. Computer-Aided Engineering

This Finite element method phase is facilitated by Abaqus software [2]. This problem demonstrates the following aspects of a forming analysis in Abaqus/Explicit in extreme deformation. The aim of simulation is to find out a minimum pressure from cylinder subjects to the mold in 0.11 second with 0,2m/s of velocity. Die dimensions are 300 x 300 mm wide by 30 mm deep. The work-

piece is formed by means of a uniform pressure due to the flat punch. Axisymmetric three-dimensional model for forming. The punch and die are harder than the plastic work-piece as the Fig. 6 and Fig. 7.

3.2.1. Initial testing with Abaqus

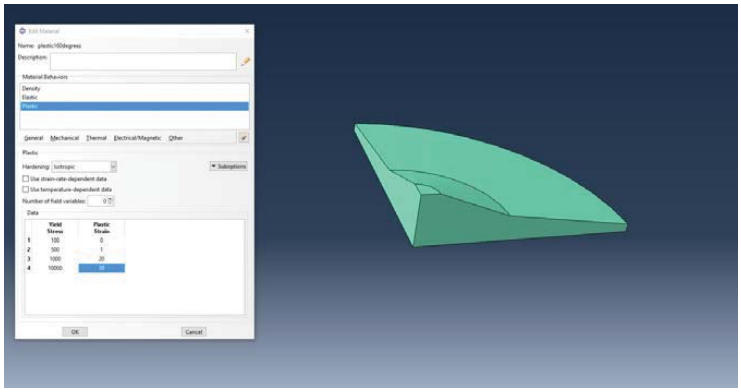


Fig. 6. A quarter part of melted plastic in the mold

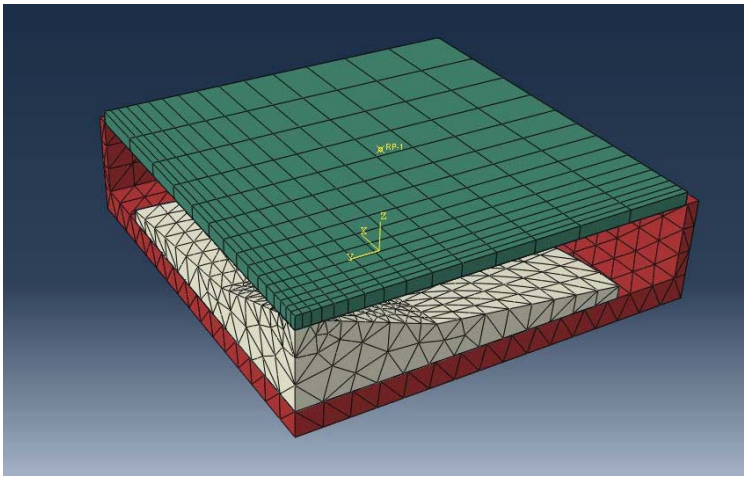


Fig. 7. FEM of Mold and melted plastic in mold

3.2.2. Further testing with FEM modeling in Abaqus

- Materials

The Fig. 6 and Fig. 7 illustrate that the A36 steel punch and die in this model are composed of an elastic behavior. The blank is modeled as an elastic-plastic material. The viscoelastic properties have a strong dependence on the temperature for many polymers. Therefore, an assumption is used in the future research for more accurate findings.

- Boundary conditions and loading

The forming process is simulated through the enforcement of displacement boundary conditions. The die is constrained to a fixed location. The punch is displaced downward a distance of 22 mm to make a satisfied product thickness of 8 mm.

- Interactions

Contact interactions must be enforced between the plate and all installation tool components; the deformation of the plate depends on contact loads delivered through the displacement of the tool.

- Analysis types

Both analysis cases are conducted using explicit dynamic procedures. Results after the punch moving 22 mm.

- Results for analysis

The 3D model simulation was carried out in the special software that could predict the potential risks in the fact as Fig. 8. Tis numerical simulation will be used for selecting the materials and structures of the mold for the machine.

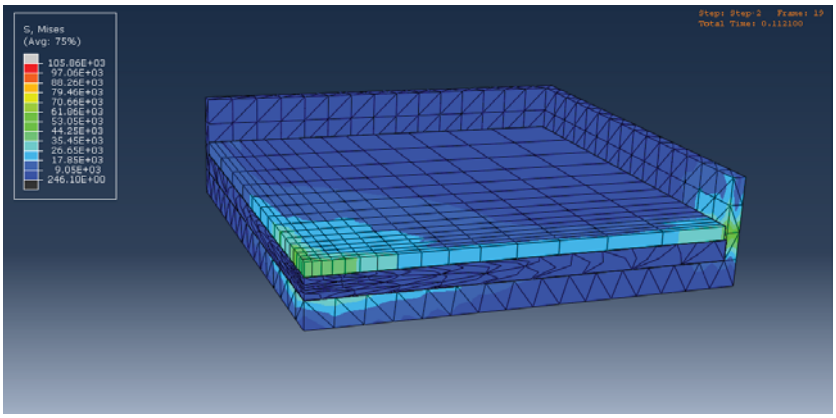


Fig. 8. The result of simulation on Stressing - V. Mises

3.3. Output specification estimation

The thermal energy required for the feed is calculated as below

$$Qd = Vt.C.(Tr - Ti).\rho \quad (1)$$

Where:

- Qd: is the thermal energy required to achieve desired temperature
- $Tr - Ti$: (220-25) is the initial temperature of the material
- ρ: is the specific weight of the material ($\rho = 0{,}85g/cm3$)
- C: is the heat capacity characteristic ($C = 1{,}48KJ/Kg$)
- V: is the volume of material that being heated

According to the design, the lead screw has:

- Diameter (d): 6 cm
- Length (L): 50 cm

Since material only fill 50% of the volume,

$Vm = V/2$

with $V = \pi d2L/4$ (The volume of the lead screw)

Insert these data into the equation (1), we got the thermal energy required, besides that, the efficiency of the heater is around 85% and heat loss to the outside environment, we got the power of the heater is 1400W. With the calculated amount of material inside the screw, the weight of it is obtained, multiply the weight with contact area and friction coefficient of plastic-steel (0.3 for static 0.28 for dynamic), the power to push the screw is acquired.

3.4. Costing

In the research, the expenditure on mass production is also considered for manufacturing. However, the capacity was still vague. Therefore, cost-volume analysis was being conducted as following:

Table 3. Cost for Manufacturing

Function	Value	Remark
Fixed cost	24000	Annually: Setup cost, facility, energy consumption…
Varaiable cost	996,98	

The value in the table support to the functions below:

$$TC = 24000 + 996{,}98p \quad (2)$$

Where the parameter TC is the total production cost by product with

- TR = 1200.p
- TR: Total revenue
- p: sales

The cross-point of these function is the break-even-point that is a reference for the volume in which the mass production must exceed.

4. Results

With a great effort, the first prototype of machine was produced as the design as Fig. 9a. Due to some fails in making components of the machine, the prototype cost reached at 1500 US dollar, but it is promising to be reduced in next prototypes and final products. As stated, the machine used recycled plastics as its input of raw materials as Fig. 9b and it can be easily found in Vietnam. Several trial runs were conducted in the first prototype. Overall, the machine released plastic plates at acceptable quality as Fig. 9c.

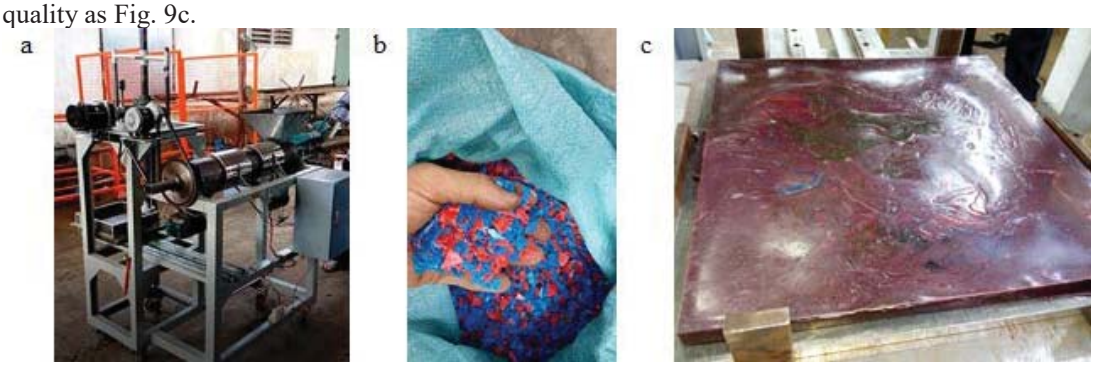


Fig. 9. (a) the first prototype; (b) raw materials; (c) a final product of the machine

5. Conclusion and Discussion

In the paper, conceptual analysis and design of a plastic recycle machine with a simple structure and a low cost is presented. From the customer requirements of specified parameters and capability of the machine. Using the QFD method, a morphological matrix is constructed to implement to identify the most feasible solutions for the 1st and 2nd design concepts. Based on conceptual design, a 3D-modelling analysis and design of the machine is provided for clarity. Also, results of the numerical simulation by using the Abaqus software is made for selecting the materials and structure of the mold.

References

[1] Ulrich KT, Eppinger SD (2012) Product design and development. 5th ed. McGraw-Hill/Irwin, New York.

[2] Akinfresoye Waleola Ayo, OJ Olukunle and DJ Adelabu, Development of a Waste Plastic Shredding Machine, International Journal, Vol 7, No. 2, 2017.

[3] Dassault systems. Abaqus student edition - complete solution for realistic simulation. https://academy.3ds.com/en/software/abaqus-student-edition.

Fundamentals of computing and designing a rotary feeder

Van Huu Thinh

Ho Chi Minh City University of Technology and Education, Vietnam

thinhvh@hcmute.edu.vn

Keywords: rotary feeder, PP-R Tee 90^0, parts per minute, inclined rotating disc, revolving bowl.

Abstract

This paper presents the fundamentals of computing and designing a rotary feeder for feeding plastic moulded Tee 90^0. This feeder is composed of an inclined rotating disc and revolving bowl.The function of this feeder is to supply automatically the PP-R Tee 90^0 for coding by laser.The aims of the research is to calculate, and design this feeder.The paper focus on evaluating capacity, torque of driving motors, main parameters of the feeder. The computing results are used in designing, and complete design is used for manufacturing a rotary feeder with its capacity up to 200 parts per minute.

1. Introduction

On the world, the rotary feeder has been in existence for a long time, and was manufactured by several suppliers. Vibratory Feeder Inc. is a leading centrifugal feeder manufacturer. This supplier focus on centrifugal feeder for scrap metal, nuts and bolts, electrical terminals [1]. SSH Automation supplies parts feeding systems, for examples vibratory, centrifugal, linear feeder, and other peripherals for industrial applications[2]. So far, there are many patents of the centrifugal feeder. One of them is United States Patent invented by R. Scott Corbin, patent number 7,472,782 B2, date of patent January, 6, 2009 [3]. In recent years, the authors of scientific paper "Centrifugal Orienting Feeder" [4] present the methods and technology for orienting parts in feeding systems. The authors introduced typical orienting system and modern orienting systems. However, no scientific document presents the fundamentals of computing and designing the centrifugal feeder. Therefore, the paper focus on evaluating capacity, torque of driving motors, main parameters of the feeder. The computing results are used in designing, and complete design is used for manufacturing a rotary feeder with its capacity up to 200 parts per minute. The feeded part as shown in Fig.1 is PP-R Tee 90°, which would be manufactured in accordance with DIN standard 8077-8078 [5]. The main parameters of this Tee are length 60mm, diameter Ø25mm, mass 43 gram.

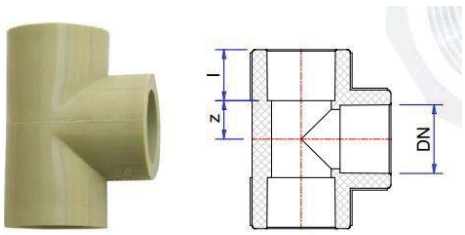


Fig.1: PP-R Tee 90°

2. Principle of operation

The parts are supplied from elevator on the inclined rotating disc. When inclined disc rotates, due to the centrifufal force it carries the parts to the highest position, and moves to the rim of the revolving bowl. The rotating bowl makes the parts to move along a single lane. Some mechanical qualifiers are mounted to the inner wall of the bowl for orienting and qualifying the parts. Improperly oriented parts are ejected from the rim to the disc for recirculation. Properly oriented parts continue

to move along the lane and out of the feeder. In the next stage of the feeding system, from the feeder the properly oriented parts are transferred by conveyor for coding by laser.

3. Equipment description

The rotary feeder is made up of inclined rotating disc and revolving bowl. Bowl drive consists of gear-motor, timing belt drive, and the bowl. The bowl has a spherical inner surface. This allows the disc to rotate in an inclined orientation and maintains a small gap with the bowl around its perimeter. The rotating bowl includes bowl, static hub, and driven pulley of timing belt drive. The driven pulley is bolted on the static hub. The bowl is bolted on the static hub which rotates over the shaft of base plate. The base plate is bolted on the frame. Diagram of bowl drive is shown in Fig. 2.

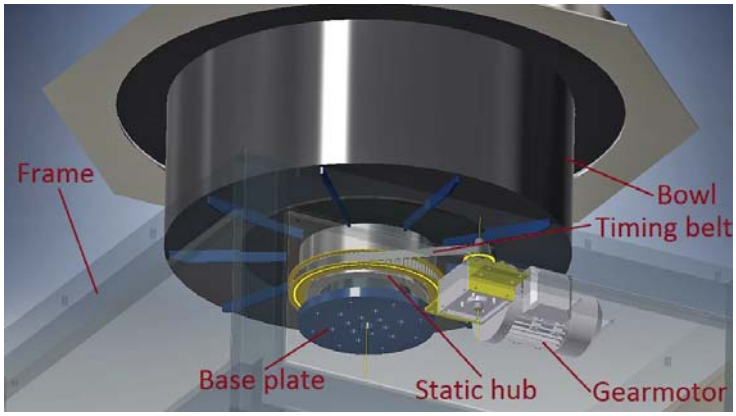


Fig. 2: Diagram of bowl drive [6]

Disc drive consists of gear-motor and rotating disc. The rotating disc is mounted directly to the output shaft of gear motor. The gear-motor is bolted on the base with inclined upper surface. The base is bolted on disc hub. The disc hub is fixed to the base plate above. The inclined degree of the rotating disc depends on the inclined upper surface of the base. In this case, the rational inclined is 30^0. Diagram of disc drive is shown in Fig. 3.

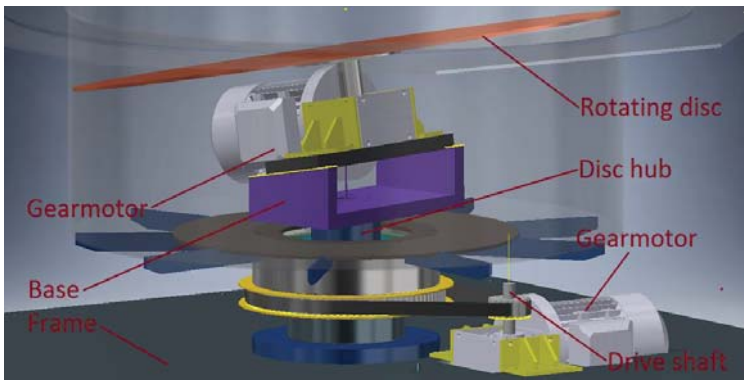


Fig. 3: Diagram of disc drive [6]

Comparing to the rotary feeder manufactured by the other suppliers, the design of this feeder has several advantages. The inclined degree of rotating disc shaft is due to the inclined upper surface of the base. This makes convenience in manufacturing. Using timing belt driver operates more silent than chain driver. The structure of disc drive is simple and small dimension.

4. Fundamentls of calculation

4.1 Capacity (Feed rate) of the feeder:

Capacity Q of the feeder is measured in parts per minute. Q is the amount of properly oriented parts moved out of the feeder.

The velocity of the part: $v = \frac{\pi D_b n_b}{1000}$

The amount of parts is supplied by rotating bowl: $\frac{\pi D_b n_b}{1000L}$. However, this contains properly oriented parts and improperly oriented ones.So, we have to take into account of the percentage of parts that will be in the properly oriented. In this case, the capacity of the feeder is determined by the formula:

$$Q = \frac{H\pi D_b n_b}{1000L} \quad (1)$$

Where:

L: the part longest dimension (mm)

Q: The capacity of the feeder (PPM)

D_b : bowl rim diameter (mm)

n_b : bowl rotating speed (rpm)

H: the percentage of parts that will be in the desired orientation.

From (1) with determined bowl rotating speed n_b, we can determine the bowl rim diameter, disc diameter and other dimensions of the feeder.

***4.2* Gearmotor output torque:**

Gearmotor output torque of disc drive or bowl drive is determined according to the formula:

$$T = (I + W_p \frac{D^2}{4})A + T_f \quad (2)$$

Where:

I: total rotational inertia of disc or bowl(kg.mm^2)

W_p : mass of the parts carried by disc or bowl (kg).

D: disc or bowl diameter (mm)

A: required disc or bowl acceleration after complete stop.

$A = \frac{\pi n}{30t}$ (rad/s^2)

n: gearmotor output speed (rpm)

t: time to accelerate (≤2sec)

T_f= frictional torque in the bearings (N.mm)

From (2) we can calculate the torque and power of electric motor for driving disc or bowl.

5. Calculation for designing the feeder

5.1 Calculation for disc drive:

With the capacity 200PPM, we determine the bowl rotating speed n_b =120 rpm, and the disc rotating speed n_d =130 rpm. From (1), where: L = 60 mm, H = 40%, n_b =120 rpm, we have D_b = 796

mm. With the gap between the bowl and the disc is 5mm, and according to the standard dimensions we choose disc and bowl diameter: D_d = 795mm, D_b = 805mm.

From (1), let us note that bigger bowl diameter leads to higher capacity, but the feeder has large dimention. Faster the part speed the result is higher capacity, but the speed shall not exceed maximum speed to prevent damages. Thus, it is important to choose the bowl diameter and the part speed that are rational.

Gearmotor output torque of disc drive is determined from formula (2), where:

+ W_p= 30 mg = 12.9 N: mass of the parts carried by disc

+ n: gearmotor output speed (rpm)

+ D_d = 795 mm: disc diameter.

The rotating disc is made of Bakelite with its mass m_d = 3.5kg, we have total rotational inertia of disc: I=1.1kg.mm^2.

$$T_f = 0{,}01T_d.$$

$$T_d = 41177 \text{ Nmm}.$$

After calculating, the power on the motor shaft is:

$$P_d = 0.29 \text{ kW}$$

Table 1: Parameters of motor for disc drive [6]

Motor model	Power [kW]	Speed [RPM]	Mass [kg]
SITI FC712-4	0.37	1370	3.2

5.2 Calculation for bowl drive:

Similar to that, Gear-motor output torque of bowl drive is determined from formula (2). After calculating, the power on the motor shaft is:

$$P_d = 0.19 \text{ kW}$$

For convenience, the selected motor is shown as table 1 above.

Designing timing belt drive and design procedures are based on [7]:

Module is determined to the formula:

$$m = 35\sqrt[3]{\frac{P_1}{n_1}} = 2.77mm$$

According to the timing belt standard, we choose m = 3mm.

After calculation, the parameters of timing belt drive are:

Number of teeth of driving pulley: $Z_1 = 20$.

Number of teeth of driven pulley: $Z_2 = 96$

Diameter of driving pulley: d_1= 59.876 mm.

Diameter of driven pulley: d_2=290.301 mm.

With of belt: b = 25 mm

Number of teeth of timing belt: `Z = 136.

The designing result is shown in Fig 4. Its technical parameters:

- Overall dimensions: 3200x1500x1400 (mm)
- Capacity : 200 PPM (respective to Ø25mm)
- Parts feeding range: PP-R Tee 90^0 Ø20, Ø25, Ø32, Ø40, Ø50 mm.

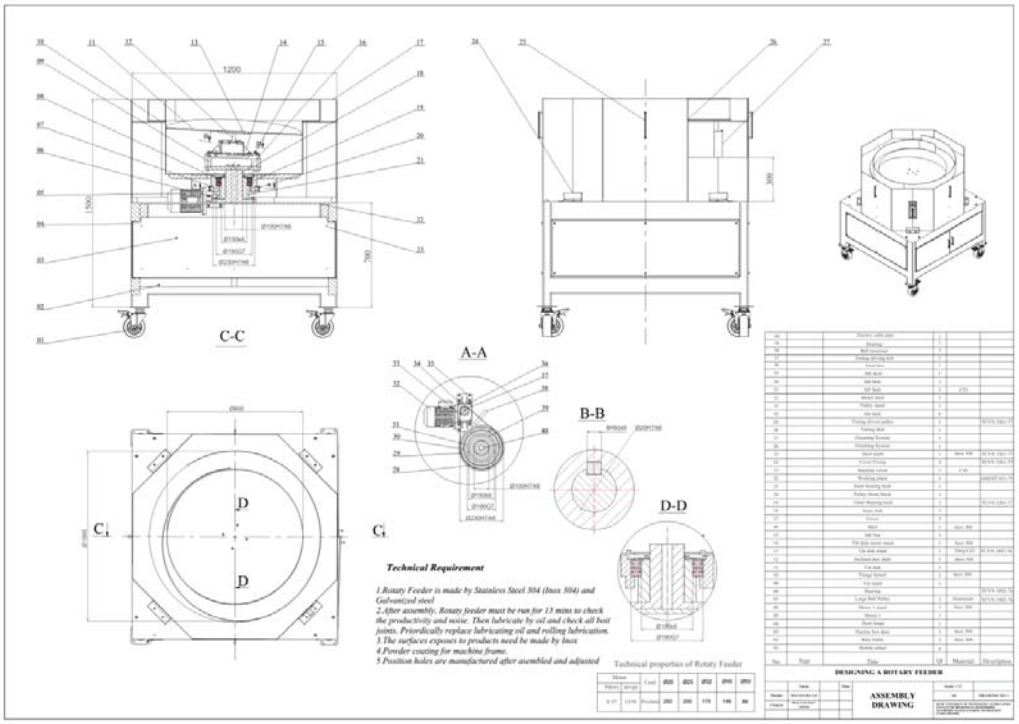


Fig. 4: Assembly drawing

With the bowl rotating speed n_b =120 rpm, and the disc rotating speed n_d =130 rpm, its capacity respective to parts feeding range is shown in table 2.

Table 2: Capacity of the rotary feeder

Tee 90^0	Ø20	Ø25	Ø32	Ø40	Ø50
Capacity [ppm]	250	200	175	146	86

In practice, each gear-motor is separately controlled by the inverter Yaskawa V1000 in order to adjust their rotating speed respective to Tee 90^0 types. From designing results, we manufactured the rotary feeder as shown in Fig 5. Manufactured rotary feeder is capable of:

- Performing at very low noise levels.
- Feeding parts reliable and efficient.
- Improving the work environment for the operator.
- Being economic because it is designed and manufactured in Vietnam.

Especially, the rotary feeder was transferred to Tien Phong Plastic Joint stock Company (TIFOPLAST), Haiphong City, Vietnam. The company confirmed that the feeder is reliable and efficient.



Fig. 5: Manufactured rotary feeder

6. Conclusions

This work leads to the following conclusions:

- Researching and proposing rational structure for the rotary feeder
- Constructing the fundamentals calculation on the rotary feeder.
- Designing and manufacturing a finished machine transferred to the company, and confirmed that it is reliable and efficient.

Acknowledgements: The author would like to thank engineers Nguyen Ba Tai, Le Thanh Đat for their contribution. This research is supported by Ho Chi Minh City University of Technology and Education, Vietnam.

References

[1] Vibratory Feeder Inc.
[2] SSH Automation PTE LTD, Parts Feeding Systems- Products Catalogue.
[3] United States patent-Patent No 74727 82 B2-2009.
[4] Venkata Phani Babu. V, N. Mahesh Babu, P. Naveen Reddy, R. Sreevardhan Reddy, R. L. krishna Sagar, Cetrifugal Orienting Feeder, International Journal& Magazine of Engineering, Technology, Management and Research, Vol No 3(2016), Issue No 5(May), pp. 236-245.
[5] Tien Phong Plastic Joint Stock Company (TIFOPLAST), Catalogue.
[6] Nguyen Ba Tai, Le Thanh Đat, Capstone Project, HCMUTE,2017.
[7] Van Huu Thinh, Nguyen Minh Ky, Designing Project on Machine Design,Vietnam National University-HCMC Publishing House 2016, pp. 43-107.

Chapter 9.
Materials properties towards sustainability

Mechanical Properties of SS400 Steel Plate at Elevated Temperatures

Vuong Gia Hai[1,a] , Nguyen Thi Hong Minh[2,b] and Nguyen Duc Toan[3,c]

[1]Hai Phong University, Hai Phong, Viet Nam

[2]Hanoi University of Science and Technology, Ha Noi, Viet Nam

[3]Hanoi University of Science and Technology, Ha Noi, Viet Nam

[a]vuonghai84@gmail.com, [b]minh.nguyenthihong@hust.edu.vn, [c]toan.nguyenduc@hust.edu.vn

Keywords: Mechanical properties; strength; elevated temperature; structural steel

Abstract.

This paper presents the experimental test results on mechanical properties of steel plate grade SS400 at elevated temperatures. The steel is often used as structural steel due to its weldability and machinability. The steel plates were heated by a high frequency heating system to reach specific temperatures before being tested on a tensile testing machine. Five different temperature conditions were used, namely room temperature, 100^0C, 300^0C, 500^0C and 600^0C. The data of mechanical properties measured for SS400 steel plates at various temperature conditions were recorded and analysed. The research showed that when the temperature is increased, the force in tensile test is decreased while the strain is increased. The observation and the data were then used to setup the stress – strain – temperature relation for formability study of SS400 steel plates. The same method can be used to establish the mechanical properties at elevated temperatures.

1. Introduction

The behaviour of the mechanical properties of different steel grades at elevated temperatures needs to be well known to understand the behaviour of steel and composite structures at fire. Quite commonly simplified material models are used to estimate the structural fire resistance of steel structures. In more advanced methods, for example in finite element or finite strip analyses, it is important to use accurate material data to obtain reliable results. To study thoroughly the behavior of certain steel structure at elevated temperatures, one should use the material data of the steel obtained by testing. The tests have to be carried out so that the results can be used to evaluate the behaviour of the structure, i.e. the temperature rate should be about the same as that used in the modelling assumptions. [5]

Extensive experimental research has been carried out since 1994 in the Laboratory of Steel Structures at Helsinki University of Technology in order to investigate the mechanical properties of several structural steels at elevated temperatures by using mainly the transient state tensile test method. The basic material research programme is still going on, but the main test results so far were published in 2001 in the Laboratory of Steel Structures' publication series [1]. The publication is freely available from the laboratory's website: http://www.hut.fi/Units/Civil/ Steel/Publications/jsarj.html. Some of the test results were also presented in the previous 'Structures in Fire' –workshop in Copenhagen [2].

The test results have recently been used in some research projects studying the behaviour of cold-formed steel members in fire [3, 4]. The results seem to work quite well with the structural analyses carried out within these projects.

In this paper the steady state test results of structural steel grades SS400 are presented with a short description of the testing facilities.

2. Experimental study

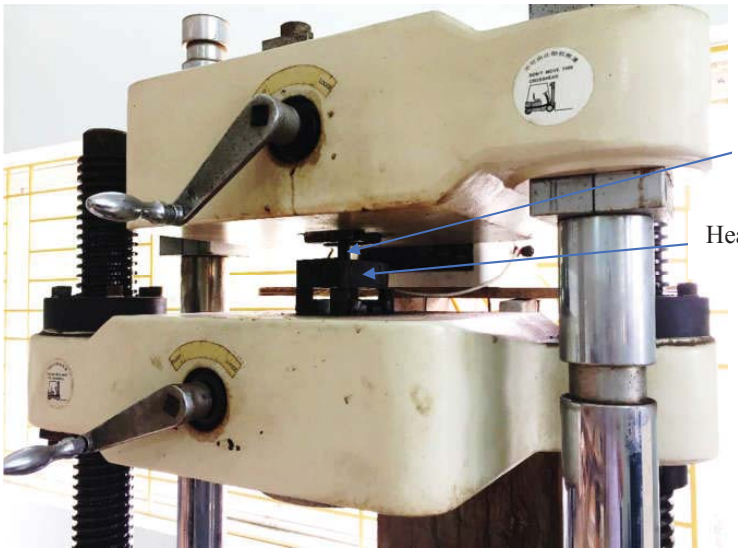
2.1. Test device

The tensile testing machine used in the tests is **Hung Ta H-200kN**. The testing machine was calibrated before testing. The installation of the specimen and the testing device used in this study are

shown in Fig. 1. The heating device of an experimental study is a high frequency furnace with a maximum temperature of 700^0C was used.



a) System Tensile testing



b) Setup tensile test

Fig. 1 Testing device

In this study, the preheating temperature was determined before via the relationship between the temperature and the time baking (Fig. 2). The study measured the variation in temperature and time of the heater through 08 specimens and showed the results as shown in Fig. 3. Through the chart shows that when heating the 8 specimens reach then the heat levels: 100^0C, 200^0C, 300^0C, 400^0C, 500^0C, 600^0C, then 8 specimens have maximum different thermal are 13 seconds at 600^0C.



Fig. 2 Heating device

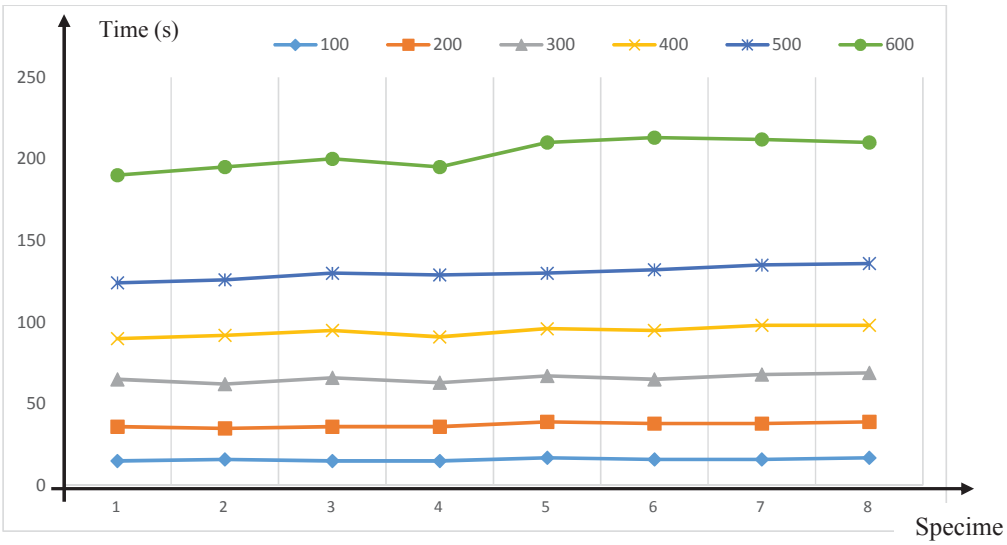


Fig. 3 Relationship between the heat and the time baking

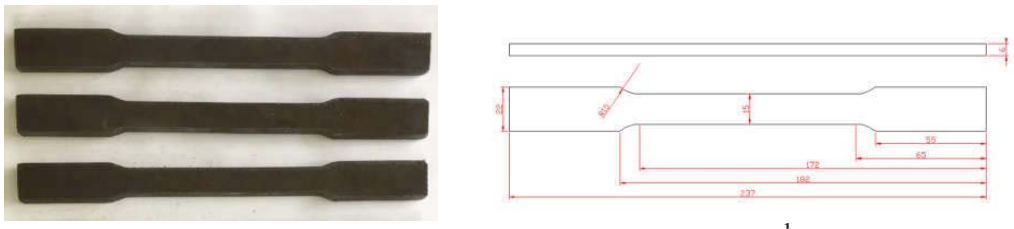
2.2. Test material and specimen

All test specimens were cut from the same SS400 steel sheet ordered for this experimental study with a nominal thickness of 6 mm. SS400 is weldable normalized steel for steel constructions, with mid yield strength and toughness, produced in compliance with JISG 3101 [7]. The chemical composition of the tested high strength steel SS400 was shown in Table 1.

Table 1 Chemical composition and mechanical properties of JISG 3101 – SS400 material

C	Si	Mn	P	S	Cr	Yield stress (N/mm2)	Tensile Strength (N/mm2)
0.19 -0.21	0.05-0.17	0.4 – 0.6	0.04	0.05	≤0.3	215 - 245	400 - 550

The shapes and dimensions of the specimens were prepared in accordance with TCVN 197-1:2014 (ISO 6892-1:2009) [8]. As shown in Fig. 4.



a b

Fig. 4 Tensile test coupon and dimensions. (a) Test coupons and (b) Dimensions.

2.3 Test method

To assess the mechanical properties of steels, the commonly used method is to conduct tensile tests either in steady state or transient state. Comparing to transient state test method, the steady state test method is used more commonly in research as it is easier to perform and provides the stress–strain curves directly. However, the transient state test method is considered to be more realistic in simulating the performance of steel components in a natural fire. And, the steady state test method was conducted in this experimental study.

2.4 Test procedure

Tensile tests at elevated temperatures were carried out in the tensile testing machine Hung Ta H-200kN, as show in Fig 1. In steady state test, the specimen was heated up to a specified temperature then loaded until it failed. And the preselected temperatures were: room temperature (32^0C), 100^0C, 300^0C, 500^0C and 600^0C. After reaching the preselected temperature then tensile load was applied to the specimen until failure. In order to compare the elevated temperature effect on mechanical properties of SS400, tensile tests were conducted at ambient temperature as well.

3. Experimental results

3.1. Yield strength

In this study attempted to tensile test steel plate grade SS400 at five different temperature conditions. At different temperatures the yield strength of the material are different (Table 2).

Table 2 Yield stress of steel plate grade SS400 at five different temperature conditions

Temperature (^{0}C)	32	100	300	500	600
Yield stress (N/mm^2)	244	235	162	58	44

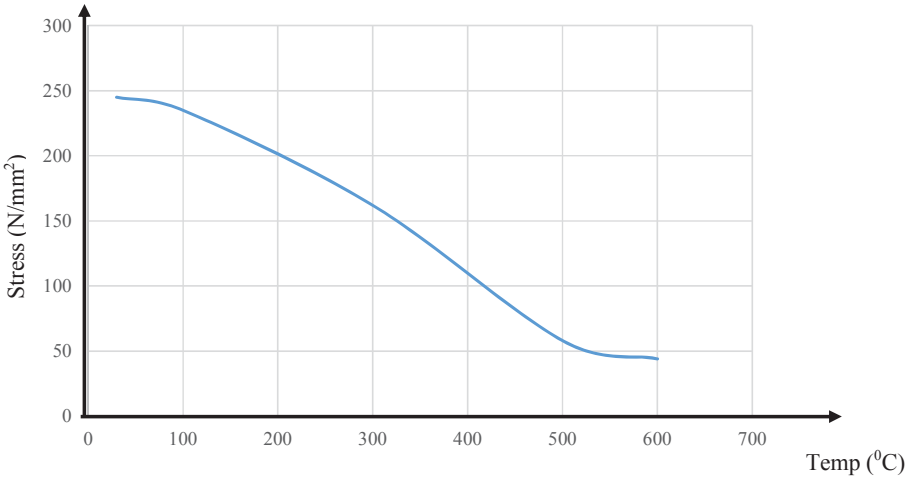


Fig. 5 Comparison of yield stress at five different temperatures

The chart in Fig. 5 show that, when the temperatures are increasing then yield stress are reduction. This shows that at the temperature higher, the better to the shape of SS400 steel plate.

3.2 Tensile strength

The tensile strength reduction factors were calculated based on the ratio of ultimate strength at a particular elevated temperature (600^0C) to that at room temperature (32^0C), show in Table 3.

Table 3 Tensile stress of steel plate grade SS400 at five different temperature conditions

Temperature (^{0}C)	32	100	300	500	600
Tensile stress (N/mm2)	425	391	355	149	97

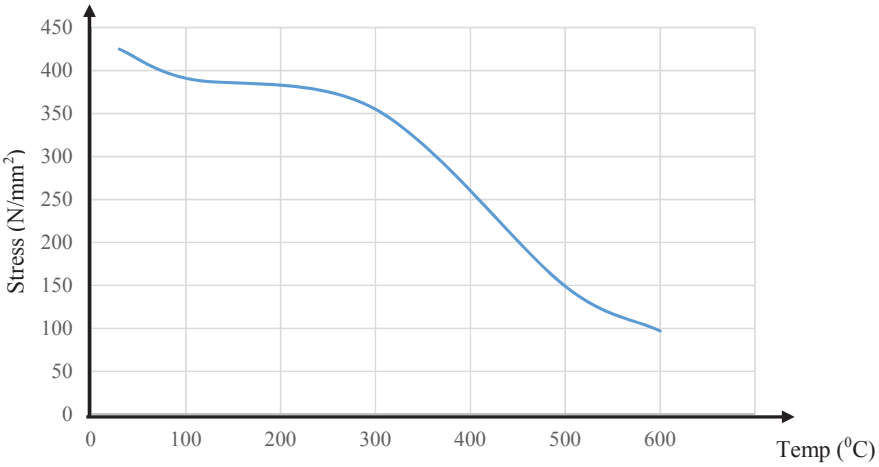


Fig. 6 Comparison of tensile stress at five different temperatures

From the Fig.6 we can see that the tensile strength reduction from room temperature to 600^0C. It is the most reduction from 250^0C to 600^0C.

3.3 Ductility and tensile failure modes

Ductility of steel is defined based on the deformation that steel can undergo before fracture. The stress–strain curves at different temperatures obtained from this steady state test were plotted in Fig. 7. The effect of temperature on the ductility of steel plate SS400 was studied by comparing the displacement values at fracture

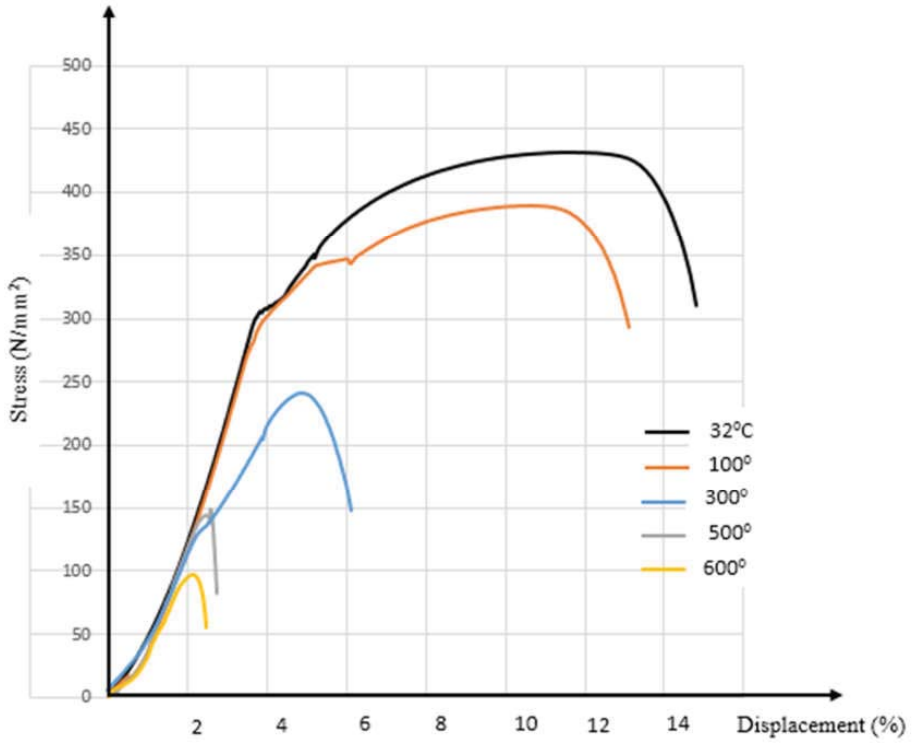


Fig. 7 Stress–Displacement curves of SS400 at elevated temperatures

The effect of temperature on the ductility of steel plate SS400 was studied by comparing the displacement values at fracture. The ductility reduces when temperature increases.

Summary

This paper presents a detailed experimental study on the mechanical properties of plate steel SS400 at elevated temperatures. Tensile tests were conducted on SS400 specimens with thickness of 6.3 mm at elevated temperatures ranged from room temperature (32^0C) to 600^0C. The elevated-temperature yield and tensile strengths and typical failure modes of SS400 were obtained. In this study showed the deterioration of mechanical properties of steel plate SS400 was dependent on elevated temperatures.

This paper also highlights the necessity of more researches on mechanical properties at elevated temperatures for all steel structural grades used in construction or ship building.

References

[1] J Outinen, O Kaitila, P Mäkeläinen. High-Temperature Testing of Structural Steel and Modelling of Structures at Fire Temperatures. Laboratory of Steel Structures Publications: TKK-TER-23, Finland, 2001.

[2] J Outinen, O Kaitila, P Mäkeläinen. A study for the development of the design of steel structures in fire conditions. 1st International Workshop of Structures in Fire, Copenhagen, Denmark, 2000.

[3] Feng M, Wang YC, Davies JM. Behaviour of cold-formed thin-walled steel short columns under uniform high temperatures. Proceedings of the International Seminar on Steel Structures in Fire, Tongji University: China, 2001; 300–312.

[4] Kaitila O. Imperfection sensitivity analysis of lipped channel columns at high temperatures. Journal of Constructional Steel Research 2002; 58:333–351.

[5] EN1993-1-2 European Committee for Standardisation (CEN), Eurocode 3: Design of Steel Structures, Part 1.2: Structural Fire Design. CEN: Brussels, 1993.

[6] SFS-EN 10002. Metallic Materials. Tensile Testing. Parts 1–5.

[7] STEEL PLATE, JFE Steel Corporation.

[8] TCVN 197: 2002, Vật liệu kim loại – Thử kéo Phần 1-2.

SULFUR-DOPED g-C_3N_4 WITH ENHANCED VISIBLE-LIGHT PHOTOCATALYTIC ACTIVITY

An Tran Doan[1,a*], Phuc Nguyen Van[1,b], Tri Nguyen Ngoc[1,c], Phu Huynh Thi[1,d], Hung Nguyen Phi[1,2,e], Huong Nguyen Thi Thanh[1,f], Dien Vo Thanh[1,g], Vien Vo[1,3,h]

[1]Department of Chemistry, Quy Nhon University
[3] Institute of Pedagogical and Educational Science, Quy Nhơn University, Binh Dinh, Vietnam
[3] Applied research Institute for science and technology, Quy Nhon University,
170 An Duong Vuong, Quy Nhon city, Vietnam
[a]trandoanan@moet.edu.vn
[b]nguyennguyenphucnguyen@gmail.com
[c]nguyenngoctri@qnu.edu.vn
[d]huynhthiphusphk37@gmail.com
[e]nguyenphihung@qnu.edu.vn
[f]huongnguyenkt15@gmail.com
[g]vthdien@gmail.com
[h]vovien@qnu.edu.vn

Keywords: Sulfur-doped graphitic carbon nitride, photocatalyst, urea, thiourea, Rhodamine B

Abstract

The S-doped g-C_3N_4 materials were prepared by heating mixtures of urea and thiourea with various weight ratios at 550 ºC, and denoted as x:y SCN, where x:y is weight ratios of urea to thiourea. The obtained samples were characterized by X-ray diffraction, diffuse reflectance ultraviolet-visible spectroscopy, X-ray photoelectron spectroscopy, thermogravimetric differential thermal analysis, scanning electron microscopy and infrared spectra. The results showed that all the x:y SCN materials exhibit the presence of doping S in the structure of g-C_3N_4 and higher capability in the photodegradation of Rhodamin B in aqueous solution under visible light condition than pure g-C_3N_4. Among the SCN samples, 75:25 SCN performed the highest photocatalytic activity, which is believed the presence of the largest amount of doping S in the matrix of g-C_3N_4, leading to reduction of their bandgap. The reduction of bandgap for S-doped g-C_3N_4 materials compared to pure g-C_3N_4 was proved by theoretical calculation.

Introduction

Nowadays humans consume much fossil energy to meet insatiable demands for more high-quality products and high-efficiency transportation, leading to the increasing problem of energy shortage and environmental deterioration. It is generally considered that a prospective strategy is to utilize solar resources effectively and efficiently. Semiconductor-based photocatalysts provide promising approaches in water splitting and pollutant degradation directly using solar energy and have gained considerable attention from research experts in materials science and chemistry.

The development of nanotechnology in the creation of new materials with high applicability has brought many outstanding achievements in various fields. Among the new materials, the semiconductors made of photocatalysts are widely studied in the field of environmental treatment and generation of clean energy resources, such as hydrogen from the water-splitting [1,2]. A number of semiconductors have been used as the effective photocatalysts such as ZnO, TiO_2, WO_3, CdS, Zn_2TiO_2 and tungstate salts [3,4]. Despite that, due to the large band gap, they only absorb ultraviolet light which is accounted for only about 5% of the total volume of the sunlight photon. To use sunlight more efficiently, many investigations have been done to improve catalytic ability of materials.

Recently, an organic polymer semiconductor material, carbon nitride with graphite-liked structure (g-C_3N_4), has attracted much attention for application in photocatalytic water splitting and degradation of organic pollutants under visible light [5,6]. This material has some advantages such as band gap of 2.7 eV, production ability in large scale, non-toxicity, and durability. However, the photocatalytic efficiency of pure g-C_3N_4 is poor because of its large band gap, which restricts the ultilization of solar energy ($\lambda < 460$ nm). Besides, the pure g-C_3N_4 exhibits high-rate recombination of the photogenerated electron-hole pairs [7]. In order to solve these drawbacks, several strategies have been applied to modify g-C_3N_4 such as preparation of g-C_3N_4 in mesostructure [8] and combining g-C_3N_4 with other materials by doping or grafting [9-16]. The obtained materials showed an improvement in photocatalytic performance. For the purpose of synthesizing the sulfur-doped g-C_3N_4, some different methods were reported, from different material sources and different temperatures [14-17]. However, the number of published works on S doping are restricted.

In this paper, we report a facile synthesis by heating mixtures of urea and thiourea with various weight ratios at 550 ºC. The obtained samples show higher photocatalytic activity than the bare g-C_3N_4 in degradation of Rhodamine B under visible light.

Experimental

Chemicals

Urea $(NH_2)_2CO$, Thiourea $(NH_2)_2CS$ and Rhodamine B were purchased from Guangdong Chemicals Inc., Ltd. (China). All the chemicals were of reagent grade (99% purity) and used without further purification.

Synthesis

The S-doped g-C_3N_4 materials were prepared via the following process. 10 g mixtures of urea and thiourea with various weight ratios of 25:75, 50:50, 75:25, 85:15, and 95:5, were well ground in an agate mortar. The 5 mixtures were transferred into different alumina crucibles, sealed with aluminum foil and calcined at 550 ºC for 1 hour under air medium. The obtained samples were naturally cooled to room temperature. Finally, the as-prepared samples were well ground and rinsed with 0.1 M nitric acid solution and distilled water until neutral pH. The collected samples were dried in 80 ºC for 12 hours, and denoted as x:ySCN, where x:y is weight ratios of the urea and thiourea. For comparison, pure g-C_3N_4 was prepared by the same procedure for S-doped g-C_3N_4 materials except absence of thioure, and the as-prepared sample was referred as CN.

Characterization

Powder X-ray diffraction (XRD) patterns of the samples were recorded by a D8 Advance X-ray diffractometer with Cu Kα radiation ($\lambda = 1.540$ Å) at 30 kV and 0.01 A. Infrared spectra (IR) were measured by IRPrestige-21 (Shimadzu). X-ray photoelectron spectroscopy (XPS) was obtained by ESCALab spectrometer (Thermo VG, U.K.). The scan electron microscopy (SEM) images were recorded on Nova Nano SEM 450. UV-Vis diffuse reflectance spectroscopy (UV-Vis-DRS) was carried out on Cary 5000 (Varian, Australia). The thermogravimetric-differential scanning calorimetry analysis was conducted on the SETRAM LABSYS TG system under air flow with the heating rate of 10 ºC/min.

Photocatalytic activity

In order to evaluate the photocatalytic activity, RhB was selected as an organic pollutant. In a typical experiment, 0.12g of the as-prepared materials was dispersed into 120 mL of 30 mg/L aqueous solution of RhB. This dispersion was kept in dark for 2 h in continuously stirred condition. After that, the solutions were irradiated under a visible light source from a tungsten wire lamp (220V – 100W) with a UV cut-off filter. The degradation of RhB was monitored by taking the suspension at the time intervals of 1h. Each of the suspension was centrifuged to separate the

catalyst from the RhB solution. Subsequently, the degradation efficiency was calculated as a function of irradiation time and absorbance change at a wavelength of 553 nm in UV-vis spectrophotometer (Jenway 6800).

DFT Calculations

The optimized structures of g - C_3N_4 and S-doped g-C_3N_4 (SCN) with 224 atoms in unit cell are performed using VASP program. The DFT method and PBE functional is chosen for all calculations for optimization and density of state (DOS). The lattice parameters are used in all calculations taken from the primitive unit cell of g- C_3N_4: a = 13.31 Å; b = 23.74 Å; c = 7.92 Å. The cutoff energy for all calculations is set up at 450 eV. Relax geometry is calculated with Gama grid of 2 x 1 x 3 k-points and density of state (DOS) is further performed with 4 x 2 x 6 higher k-points. The initial structures of S-doped g-C_3N_4 are created by replacing N atom at the sites in the g - C_3N_4 structure by S atom.

Results and discussion

Characterization of catalysts

In order to reveal phase structure of the samples, XRD patterns were recorded. Fig. 1 shows that, at the heating temperature of 550 ºC, all the obtained sulfur-doped g-C_3N_4 products include two peaks at 27.4º (d = 0.325 nm) which is assigned to the interplanar stacking unit (002) of the aromatic systems, and the peak at around 13.4º corresponding to d-spacing of 0.658 nm of (100) plane [17-19]. All of these results are associated with an innerplane structural packing motif (the hole-to-hole distance of the nitride pores).

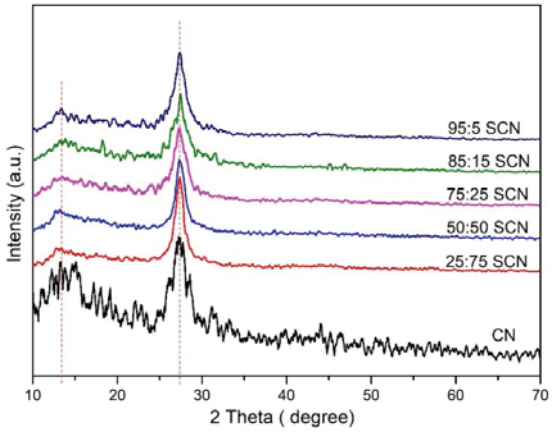


Fig.1. XRD patterns of CN and x:ySCN materials.

Formation of g-C_3N_4 phase is also confirmed by FT-IR spectra (Fig. 2) which are identical for all samples. Specifically, the vibrational modes at 810.3 and 887.9 cm^{-1} are corresponding to the breathing mode of triazine units in condensed CN heterocycles and deformation of N – H, respectively [19-21]. The absorption bands in the range 1242 –1638.5 cm^{-1} are typical for g-C_3N_4 and corresponding to the stretching vibration modes of heptazine heterocyclic ring (C_6N_7) units [19-21]. The band with a variable intensity at 2359 cm^{-1} is attributed to CO_2 physically adsorbed from the atmosphere. The broaden shoulder absorption bands at 3169 cm^{-1} are corresponding to the N-H stretching mode. The absence of bands assigned to the vibrations of S-containing groups could be related to a small amount of S atoms while the position of C–S vibrational modes in 1200–1050 cm^{-1} region could be ascribed to the slight shoulder at 1079 cm^{-1} [20, 21].

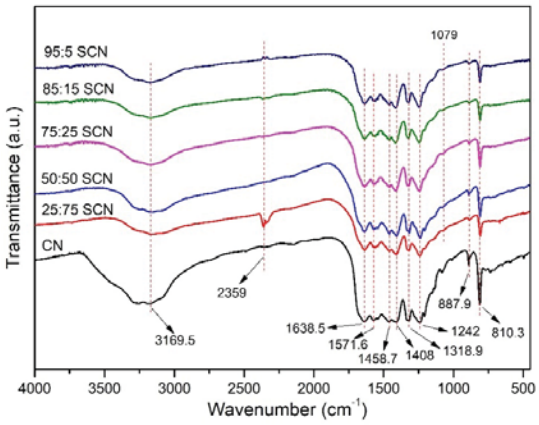


Fig. 2. FTIR spectra of CN and x:ySCN samples.

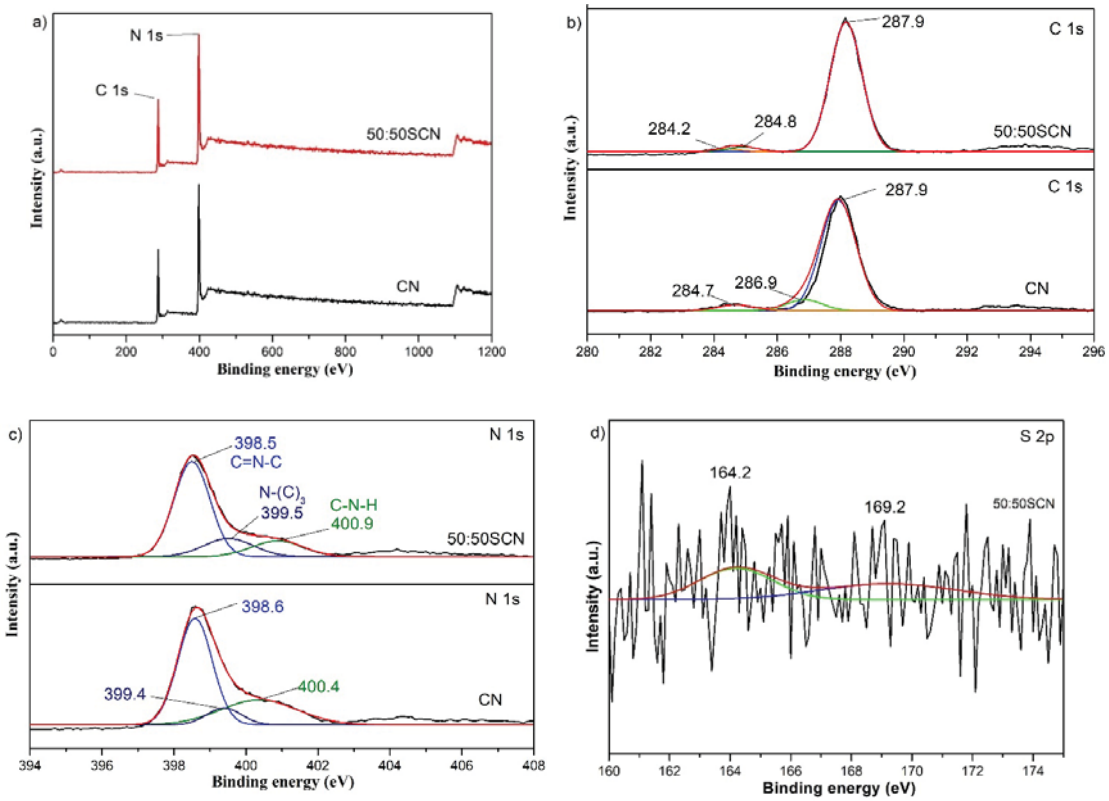


Fig. 3. (a) XPS survey spectrum of CN and 50:50SCN samples and (b) expanded high-resolution XPS spectrum for the C 1s, (c) N 1s, and (d) S 2p regions.

The chemical state of C, N, S and O elements in the obtained S-doped g-C_3N_4 was characterized by XPS (Fig. 3). The high-resolution C 1s XPS spectra of the samples are presented in Figure 3b. Comparing to the bare g-C_3N_4 sample, three peaks are found for the 50:50SCN sample at binding energies of 284.2, 284.8, and 287.9 eV. The main peak at the binding energy of 287.9 eV is assigned to the sp^2 - bonded carbon of N=C−N in g-C_3N_4, whereas the peak at 284.2 eV is ascribed to the C−C coordination due to carbon impurities [19, 20]. The characteristic peak centered at 284.8

eV is related to the C−S bond, which reveals that the S atom is indeed covalently bound to the CN framework. Figure 3c shows the expanded high-resolution N 1s XPS spectra of the samples, which could be splited into three peaks. The highest intensity peak at 398.5 eV is assigned to the sp^2 - bonded nitrogen of the C=N−C group. The peaks at 399.5 and 400.9 eV are attributed to the tertiary nitrogen of N-$(C)_3$ and the amino functional groups with hydrogen (C−N−H), respectively. For S 2p XPS spectrum (Figure 3d), the S 2p peak centered at 164.2 eV can be assigned to the S-C chemical bonds formed in g-C_3N_4 by substituting the lattice N atoms with the S atoms. Thus it can be concluded that a part of nitrogen is substituted with sulfur [19, 20].

SEM images (Fig. 4) show a difference in morphology of the S-doped g–C_3N_4 and non-doped samples. The CN sample consists of relatively large nanoflakes with size from few to dozens of microns (Figure 4a). The S-doped samples possesses smaller lamella-liked structure (from a few to several microns), with many slots and high porosity (Figure 4b-f). This difference may come from the presence of thiourea in the reaction mixtures for preparation of S-doped g–C_3N_4 samples.

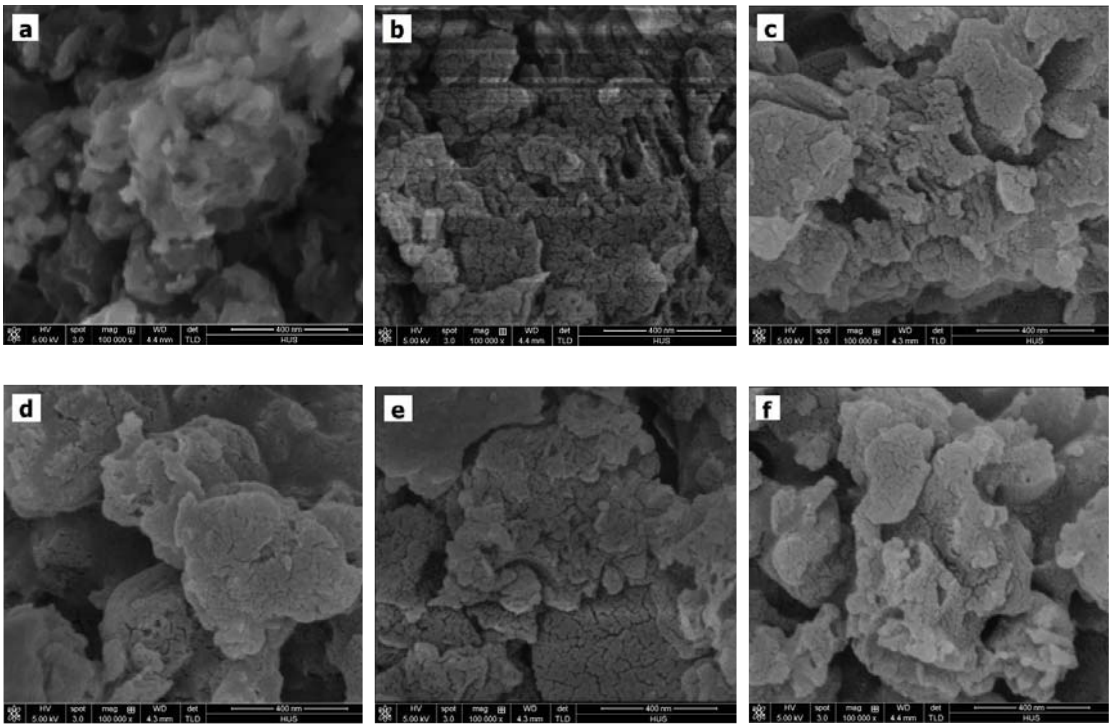


Fig. 4. SEM images of CN-550 (a), 25:75SCN (b), 50:50SCN (c), 75:25SCN (d), 85:15SCN (e) and 95:5SCN (f).

Optical properties of the as-prepared samples were investigated by UV-Vis-DRS and the results were shown in Figure 5. The absorption band of all the S-doped samples is stronger and shifts to the longer wavelength region with increasing weight of thiourea in the reaction mixtures. Table 1 shows that the adsorption edge performs a red shift to lower band gap energy in the region of 2.68 - 2.7 eV for the S-doped g-C_3N_4 samples compared to CN. The absorption intensity is enhanced in the visible region after the S-doping [20]. The absorption peaks around 300–400 nm are assigned to π–π* transitions in the conjugated ring systems, including heterocyclic aromatics. The features near 500 nm are due to n–π* transitions involving lone pairs on the edge N atoms of the triazine rings and the intensity increases for the S-doped g-C_3N_4 materials compared with the non-doped sample. These results reveal that the S doping g-C_3N_4 materials could significantly

promote the optical absorption performance and enhance the utilized efficiency of solar light, which subsequently results in its promotion of the photocatalytic activity.

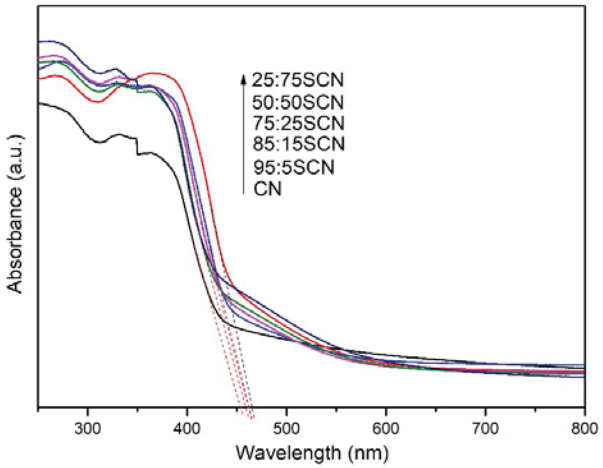


Fig. 5. UV-Vis DRS spectra of CN and x:y SCN samples

Table 1. Estimated band gap of obtained samples via equation of $E_g = 1239.9/\lambda_g$

No.	Sample	Absorption Band Edge λ_g (nm)	E_g (eV)
1	25:75SCN	463.5	2.68
2	50:50SCN	462	2.68
3	75:25SCN	461.9	2.68
4	85:15SCN	458.9	2.70
5	95:5SCN	458.8	2.70
6	CN	456	2.72

The thermal stability of the materials was examined by thermogravimetric analysis of a representative sample, 75:25SCN. As shown in Fig. 6, it can be observed that the thermogram of g-C_3N_4 exhibited a sharp weight loss in the range of 531 to 627 ^oC. The 75:25SCN material displayed a similar weight loss pattern as CN, which may be due to complete degradation of the materials.

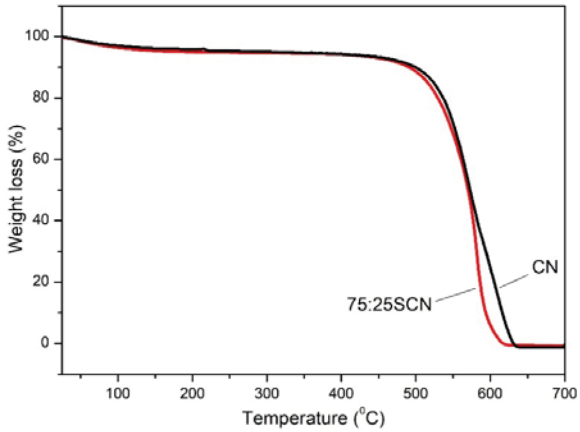


Fig. 6. TGA curves of CN and 75:25SCN.

Photocatalytic test

The photocatalytic activity of the samples was determined by the degradation of RhB in water under visible light. Fig. 7 showed the variation of RhB concentration (C/C_o) with irradiation time on the catalysts. It was reported that RhB can be easily adsorbed on many materials and therefore, a long time is required to reach adsorption equilibrium [22]. Therefore, an investigation on adsorption-desorption equilibrium of RhB on the materials was conducted. As shown in Fig. 7, all the sulfur-doped samples exhibit a higher decomposition efficiency than CN. Among the doped

samples, 75:25SCN executes the highest conversion of 84.25 % while the 85:15SCN closely follows by the efficiency of 71.61 % after 7-hour irradiation with visible light. The kinetic survey was also carried out via Langmuir-Hinshelwood model shown in Fig. 8, presenting the linear relationship of $\ln(C_o/C)$ versus irradiation time. This indicates that the photodegradation of RhB fits well with the pseudo-first-order kinetic model according to the equation: $\ln(C_o/C) = k.t$, where C is the equilibrium concentration of RhB (mg/L), C_o is the initial concentration of RhB before irradiation (mg/L), t (h) is the reaction time and k (h^{-1}) is the reaction rate constant. The kinetic results confirm that 75:25SCN exhibits the highest photo-reactivity with a reaction rate constant of 0.232986 h^{-1}.

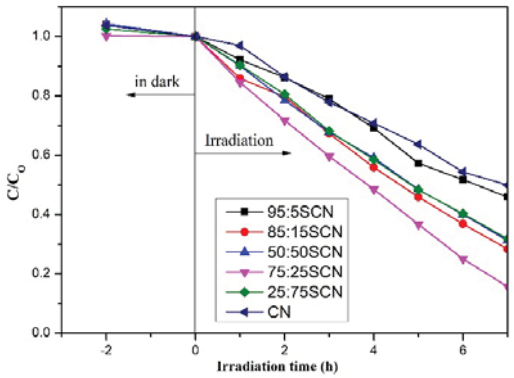


Fig. 7. Photodegradation efficiency by time for the as-prepared samples

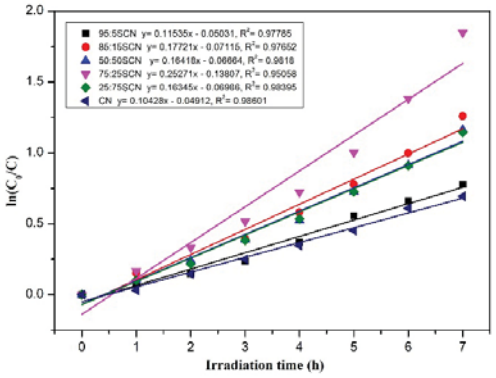


Fig. 8. Kinetic survey of the samples via Langmuir-Hinshelwood model

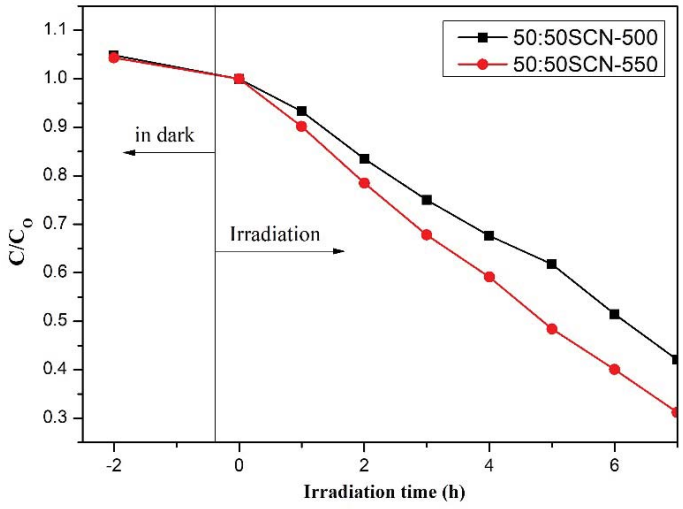
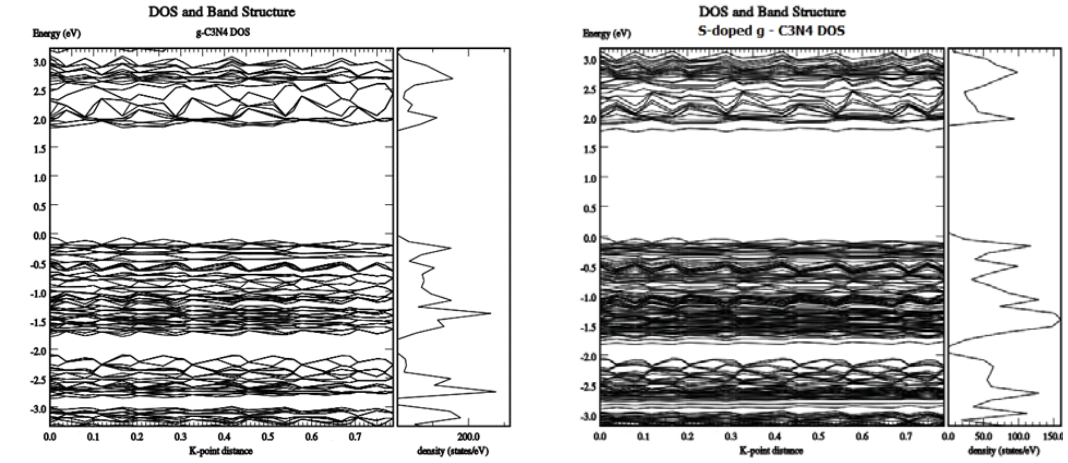


Fig. 9. Photodegradation efficiency by time of 50:50SCN-500 and 50:50SCN-550 samples

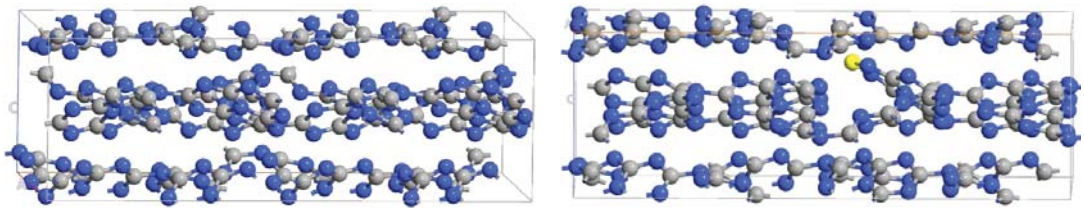
In order to obtain more information about the effect of synthesis condition on the performance of S-doped samples, another sample, 50:50SCN was synthesized in the same way but different temperature, 500 ^oC, and denoted as 50:50SCN-500. The 50:50SCN-500 sample was tested by photo-decomposition efficiency to compare with the 50:50SCN-550 sample. Fig. 9 shows that at lower preparation temperature, the S-doped g-C_3N_4 exhibits much lower photo-reactivity, which could be assigned to imperfect structural frameworks of g-C_3N_4 system.

Theoretical results

As shown in Fig. 10, the DOS of g-C_3N_4 and S-doped g-C_3N_4 is slightly different. The band gap energy values of g-C_3N_4 and S-doped g-C_3N_4 are 1.89 eV and 1.78 eV, respectively. As a result, the replacement of N atom by S atoms increase orbital quantity involving in bonds in material, leading to that the conduction band edge decreases more strongly than that of valence band edge in the S-doped g-C_3N_4 band structure as compared with the original g-C_3N_4 material. Thus, the band gap energy in S-doped g-C_3N_4 is smaller than that of g-C_3N_4. These results well agree with our experimental values mentioned above. Therefore, the replacement of N by S atom in g-C_3N_4 material may improve photocatalytic activity compared with pure g-C_3N_4 material.



g-C_3N_4, band gap: 1.89 eV S-doped g-C_3N_4, band gap: 1.78 eV



g- C_3N_4 S-doped g-C_3N_4

Fig. 10. The DOS of g-C_3N_4 and S-doped g-C_3N_4

Conclusion

The sulfur-doped g-C_3N_4 materials were synthesized via a facile calcination treatment of mixture containing urea and thiourea. The structure of the samples was defined via XRD, IR and XPS spectra, which demonstrated that the S-C chemical bonds formed in g-C_3N_4 by substituting lattice N atoms with S atoms. All the S-doped samples perform the higher photo-degradation of RhB compared to undoped material (CN) under visible light irradiation. Among them, 75:25SCN exhibited the highest reaction rate constant of 0.232986 h^{-1}. The enhancement of photocatalytic performance of doped g-C_3N_4 could be explained by the effect of reducing band gap value which was confirmed by UV-Vis DRS spectra and supported by information from DFT calculation.

Acknowledgements: This work was supported by The World Academy of Sciences (Grant 16-496 RG/CHE/AS_G – FR3240293298).

References

[1] R. Abe, Recent progress on photocatalytic and photoelectrochemical water splitting under visible light irradiation, Journal of Photochemistry and Photobiology C: Photochemistry Reviews, (2010), 11, 179-209.

[2] J. Zhang, Y. Wu, M. Xing, S. A. K. Leghari, S. Sajjad, Development of modified N doped TiO_2 photocatalyst with metals, nonmetals and metal oxides, Energy Environ. Sci. (2010), 3, 715-726.

[3] R. M. Mohamed, D. L. McKinney, W. M. Sigmund, Enhanced nanocatalysts, Materials Science and Engineering R 73, 1-13, (2012).

[4] A. Lei, B. Qu, W. Zhou, Y. Wang, Q. Zhang, B. Zou, Facile synthesis and enhanced photocatalytic activity of hierarchical porous ZnO microspheres, Materials Letters 66, 72-75, (2012).

[5] X. Wang, K. Maeda, X. Chen, K. Takanabe, K. Domen. Y. Hou, X. Fu, M. Antonietti, Polymer Semiconductors for Artificial Photosynthesis: Hydrogen Evolution by Mesoporous Graphitic Carbon Nitride with Visible Light, J. Am. Chem. Soc, 131, 1680-1681, (2009).

[6] Y. Wang, X. Wang, M. Antonietti, Polymeric Graphitic Carbon Nitride as a Heterogeneous Organocatalyst: From Photochemistry to Multipurpose Catalysis to Sustainable Chemistry, Angew. Chem. Int. Ed, 51, 68-89, (2012).

[7] S. C. Yan, Z. S. Li, Z. G. Zou, Photodegradation Performance of g-C_3N_4 Fabricated by Directly Heating Melamine, Langmuir, 25, 10397-10401, (2009).

[8] F. Su, S. C. Mathew, G. Lipner, X. Fu, M. Antonietti, S. Blechert, X. Wang, mpg-C_3N_4-Catalyzed Selective Oxidation of Alcohols Using O_2 and Visible Light, J. Am. Chem. Soc, 132, 16299-16301, (2010).

[9] Y. Wang, J. Zhang, X. Wang, M. Antonietti, and H. Li, Boron- and Fluorine-Containing Mesoporous Carbon Nitride Polymers: Metal-Free Catalysts for Cyclohexane Oxidation, Angew. Chem. Int. Ed., 49, 3356-3359, (2010).

[10] Y. Li, S. Wu, L. Huang, J. Wang, H. Xu, H. Li, Synthesis of carbon-doped g-C_3N_4 composites with enhanced visible-light photocatalytic activity, Materials Letters 137, 281-284 (2014).

[11] J. Li, B. Shen, Z. Hong, B. Lin, B. Gao, Y. Chen, A facile approach to synthesize novel oxygen-doped g-C_3N_4 with superior visible-light photoreactivity, Chem. Commun, 48, 12017-12019, (2012).

[12] L. Zhang, X. Chen, J. G. Y. Jiang, T. H. X. Mu, Facile, Synthesis of phosphorus doped graphitic carbon nitride polymers with enhanced visible-light photocatalytic activity, Materials Research Bulletin 48, 3485-3491 (2013).

[13] Y. Zhang, T. Mori, J. Ye and M. Antonietti, Phosphorus-Doped Carbon Nitride Solid: Enhanced Electrical Conductivity and Photocurrent Generation, J. Am. Chem. Soc. 132, 6294-6295 (2010).

[14] J. Hong, X. Xia, Y. Wang and R. Xu, Mesoporous carbon nitride with in situ sulfur doping for enhanced photocatalytic hydrogen evolution from water under visible light, J. Mater. Chem, 22, 15006-15012 (2012).

[15] J. Zhang, J. Sun, K. Maeda, K. Domen, P. Liu, M. Antonietti, X. Fu and X. Wang, Sulfur-mediated synthesis of carbon nitride: Band-gap engineering and improved functions for photocatalysis, Energy Environ. Sci., 4, 675-678 (2011).

[16] X. Wang, K. Maeda, X. Chen, K. Takanabe, K. Domen, Y. Hou, X. Fu, M. Antonietti, J. Am. Chem. Soc, 131, 1680, (2009).

[17] K. Wang, Q. Li, B. Liu, B. Cheng, W. Ho, J. Yu, Sulfur-doped g-C_3N_4 with enhanced photocatalytic CO_2-reduction Performance, Applied Catalysis B: Environmental, 176, 44-52, (2015).

[18] I. Papailias, T. Giannakopoulou, N. Todorova, D. Demotikali, T. Vaimakisc, C. Trapalis, Effect of processing temperature on structure and photocatalytic properties of g-C_3N_4, Applied Surface Science 358, 278-286, (2015).

[19] Milad Jourshabani, Zahra Shariatinia, and Alireza Badiei, Controllable Synthesis of Mesoporous Sulfur-Doped Carbon Nitride Materials for Enhanced Visible Light Photocatalytic, **2017**, Degradation, Langmuir 2017, 33, 7062−7078

[20] Ran You, Hailong Dou, Lu Chen, Shaohui Zheng and Yongping Zhang, Graphitic carbon nitride with S and O codoping for enhanced visible light photocatalytic performance, **2017**, RSC Adv.,7,15842–15850

[21] Nataliya D. Shcherban, Svitlana M. Filonenko, Mykhailo L. Ovcharov, Andriy M. Mishura, Mykola A. Skoryk, Atte Aho, and Dmitry Yu. Murzin, Simple method for preparing of sulfur–doped graphitic

carbon nitride with superior activity in CO2 photoreduction, **2016**, Chemystry Select, 1, 4987 – 4983.

[22] S. Dharmambal, N. Mani, D. Kannan, Adsorption of Rhodamine–B Dye from the aqueous Solution by using Tectonagrandis Bark Powder, **2015**, Asian Journal of Research in Chemistry, Volume 8, Issue 5, 0974-4169.

Investigation of blended cement hydration in the Reactive Powder Concrete with increasing levels of silica fume addition

BACH Quoc Si[1, a]

[1]University of Technology and Education - University of Danang, Danang, Vietnam

[a]bachquocsi@gmail.com

Keywords: Blended cements; Hydration; Pozzolanic reaction; Silica Fume, Heat of Hydration.

Abstract. Hydration is a chemical reaction in which the major compounds in cement form chemical bonds with water molecules and become hydration products. By the process of hydration Portland cement mixed with sand, gravel and water produces the synthetic rock we call concrete. The Therefore, the concrete properties always accompanies with the hydration degree of cement. This paper presents some experimental test results on how silica fume affects the cement hydration in cement pastes of the Reactive Powder Concrete as increasing levels of silica fume addition with the content from 0% to 30% of cement mass. The hydration process of cement/silica fume paste was followed from the estimation of heat of hydration, rate of heat evolution, of binder pastes obtained by isothermal calorimetry (TAM-Air). In addition, the portlandite content, the hydration degree of pure cement, reaction degree of binder paste as well as reaction degree of silica fume were investigated. The quantitative assessment on these characteristics are due to the simulation of the hydration of Portland cement pastes containing silica fume.

Introduction

As we know it, the concrete is construction material that used as most widely. In the properties of concrete, compressive strength is the most important characteristic. The Reactive Powder Concrete (RPC) is designed towards using fine aggregate such as sand and increases the density. This basic principles for the development of RPC have been explained in 1990's by French company Bouygues. Conventional RPC is composed of cement and ultra-fine powders such as Crushed Quartz (CQ) and Silica Fume (SF) for the purpose of enhancing the density. On the other hand, the addition in the concrete by the active puzzolans such SF as aims to improve the performance of concrete as well as contributing to reduce environmental pollution. With the good formulas designed for RPC aims to the best packing density, RPC can achieve over 150 MPa in compressive strength for the samples without fiber reinforced. Therefore, RPC is also classified as Ultra High Performance Concrete (UHPC).

After *Thomas. M [8]*, there is greater than 85% of amorphous SiO_2 in silica fume, which may cause secondary reactions with $Ca(OH)_2$ (portlandite) produced in cement hydration for for more formating calcium silicate hydrate gel (C-S-H). This makes the concrete significantly increase performance. In this paper, the hydration process of Ordinary Portland Cement (OPC) in the RPC with increasing levels of silica fume addition with the content from 0% to 30% of cement mass was investigated. Hydration of OPC pastes containing seven levels of SF addition was investigated using isothermal calorimetry (TAM-Air). The measurement results such as heat evolution characteristics, rate of hydration heat evolution of cement and silica fume mixture were analyzed. Based on these experimental results, a hydration kinetic model for Portland cement containing the silica fume was established and verified. This simulation program allows to identify microstructure development in binder paste as well as the hydration degree of pure cement, reaction degree of binder paste and reaction degree of silica fume. These results are used to evaluate the blended cement hydration in the RPC with increasing levels of silica fume addition.

Materials

For producing concrete, the materials used are: the SF; the Quartz crushed (QB) with a maximum nominal size of 0.41 mm; the fine sand (SB) and the OPC type CEM I 52.5N. The clinker were chosen of OPC Type I (according to the ASTM classification) and their chemical compositions, physical properties, Bogue's composition are given in the *Table 1*. The characteristics of the concrete mixtures containing different amounts of SF are given in the *Table 2*.

Table 1. *Chemical composition and physical properties of cementitious materials*

Chemical composition ratio by weight, (%)			**Mineral composition ratio by weight:** $r(t_0)_{i/c}^{mass}$ **, (%)**		
Item	**OPC**	**SF**	**Item**	**OPC**	**SF**
SiO_2	21.86	93	C_3S	62.501	-
Al_2O_3	5.31	0.59	C_2S	15.522	-
Fe_2O_3	3.43	-	C_3A	8.268	-
CaO	66.34	1	C_4AF	10.437	-
MgO	0.96	-	$C\bar{S}H_2$	1.300	-
Cl	0.02	1	**Physical properties**		
SO_3	0.30	2	**Item**	**OPC**	**SF**
K_2O	0.28	-	Density: ρ_c, (g/cm^3)	3.18	2.24
Na_2O	0.10	0.1	Blaine fineness: m^2/kg	372	17500
LOI	0.09	2			

Table 2. *Mixture proportions of concrete containing different amounts of silica fume*

Mix No.	**Mix components**						
	Unit	**Cement**	**Sand**	**Silica fume**	**Crushed quartz**	**Superplasticiser**	**Water**
B0	Mass to cement ratio, [-]	0.16	1.10	0.00	0.05	1.18	0.16
	Mass of 1 m^3, (kg/m^3)	1083.00	1191.30	0.00	54.15	19.49	173.29
B1	Mass to cement ratio, [-]	1.00	1.10	0.05	0.05	0.018	0.16
	Mass of 1 m^3, (kg/m^3)	1057.3	1163.00	52.86	52.86	19.03	169.17
B2	Mass to cement ratio, [-]	1.00	1.10	0.10	0.05	0.018	0.16
	Mass of 1 m^3, (kg/m^3)	1032.70	1136.00	103.27	51.63	18.59	165.24
B3	Mass to cement ratio, [-]	1.00	1.10	0.15	0.05	0.018	0.16
	Mass of 1 m^3, (kg/m^3)	1009.30	1110.20	151.40	50.46	18.16	161.49
B4	Mass to cement ratio, [-]	1.00	1.10	0.20	0.05	0.018	0.16
	Mass of 1 m^3, (kg/m^3)	986.90	1085.60	197.38	49.34	17.76	157.91
B5	Mass to cement ratio, [-]	1.00	1.10	0.25	0.05	0.018	0.16
	Mass of 1 m^3, (kg/m^3)	965.50	1062.0	241.38	48.27	17.37	154.48
B6	Mass to cement ratio, [-]	1.00	1.10	0.30	0.05	0.018	0.16
	Mass of 1 m^3, (kg/m^3)	945.00	1039.5	283.50	47.25	17.01	151.20

Methods

Isothermal calorimetry. All mixture concrete were tested on heat flux emitted from chemical reaction process by isothermal calorimeter (TAM Air) as shown in *Figure 1*. In order to control the test condition, the isothermal calorimeter was placed in a temperature control chamber at $20^0 C$ and RH 75%. The isothermal calorimeter contains eight separate channels, each hold a single specimen during a test and the heat of hydration in the first 7 days was recorded by the computer. The chemical reactions in binder paste containing the SF are the exothermic processes, the value of heat release from binder paste during the reaction process ($Q(t)_L^{Test}$) is calculated as show in *Eq. 1*, and the reaction degree of binder paste by testing is calculated in *Eq. 2*. In the *Eq. 2*, the Q_L^{com} is the total heat generated when the binder paste completely reaction and calculated according to the *Eq. 3*.

$$Q(t)_L^{Test} = \int_0^t q(t)_L^{Test}.dt \quad (1) \qquad \xi(t)_{Binder}^{Test} = \frac{Q(t)_L^{Test}}{Q_L^{com}} \quad (2)$$

$$Q_L^{com} = P_c . \sum r(t_0)_{i/c}^{mass} . Q_i^{com} + P_{SF} . \sum r(t_0)_{S/SF}^{mass} . Q_S^{com} \quad (3)$$

where the $q(t)_L^{Test}$ is rate of heat development at the instant (t); P_c is the percentage by mass of cement in dry binder (cement-silica fume); the P_{SF} is the percentage by mass of silica fume in dry binder; the $r(t_0)_{i/c}^{mass}$ is the mineral composition ratio by weight of each phase "i" in cement; the $r(t_0)_{S/SF}^{mass}$ is the silic composition ratio by weight in silica fume; the Q_i^{com} is the maximum heat liberated when a mass unit of the phase "i" has hydrated completely; the Q_S^{com} the maximum heat liberated when a mass unit of the silica fume completely solubilized by pozzolanic reaction; the phase "i" is the clinker phase (i = C_3S, C_2S, C_3A, C_4AF) and the phase "S" is the silica dioxide (S = SiO_2 of silica fume). The values of Q_i^{com} and Q_S^{com} are referenced in *[2, 3, 4, 5, 6]*.

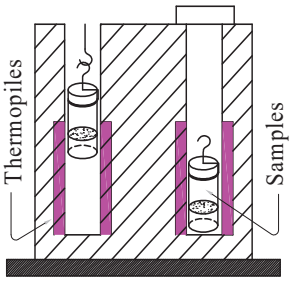


Figure 1. *Schematic of measuring on heat flux emitted by the Isothermal Calorimeter*

Hydration kinetic model for portland cement containing the silica fume

Mechanism of the hydration of cement containing the silica fume. The four main components of cement minerals include: C_3S, C_2S, C_3A, C_4AF. These mineral composition are hydrated when interacted with water. These chemical reactions of the mineral components are shown by simple chemical *equations* as describes for each compound with coexisting $C\bar{S}H_2$ (gypsum) in OPC at ordinary temperature following from *Eq. (4) to Eq. (9)*.

$$C_3S + 5.3H \rightarrow C_{1.7}SH_4 + 1.3CH \quad (4)$$

$$C_2S + 4.3H \rightarrow C_{1.7}SH_4 + 0.3CH \quad (5)$$

$$C_3A + 3C\bar{S}H_2 + 26H \rightarrow C_6A\bar{S}_3H_{32} \quad (6)$$

$$C_3A + 0.5C_6A\bar{S}_3H_{32} + 2H \rightarrow 1.5C_4A\bar{S}H_{12} \quad (7)$$

$$C_3A + CH + 12H \rightarrow C_4AH_{13} \quad (8)$$

$$C_4AF + 2CH + 10H \rightarrow C_3AH_6 + C_3FH_6 \quad (9)$$

$$S + 1.7CH + 2.3H \rightarrow C_{1.7}SH_4 \quad (10)$$

For a pozzolanic reaction, the chemical reaction between S (silica fume) and *CH* described through the *Eq. 10*. The chemical reactions from *Eq. 4* to *Eq.10* have been described according to references in *[2, 3, 4, 5, 6]*. According *[2, 3, 4, 5, 6]*, these chemical reactions are occurring in a certain order is described as shown in *Fig. 2*.

Model of the reaction degree of blended cement systems. As we know, the degree of hydration of cement is defined as the fraction of Portland clinker that has already fully reacted with water relative to the final reacted cement. In the other hand, the reaction degree of blended cement systems is defined as the fraction of dry binder that has already fully reacted with water relative to the complete reacted blended cement systems. With these definitions, the model of the hydration degree of pure cement and the model of the reaction degree of blended cement systems are presented in *Eq. 11* and *Eq. 12*, respectively. The reaction degree of pozzolan is calculated as follows *Eq. 13*.

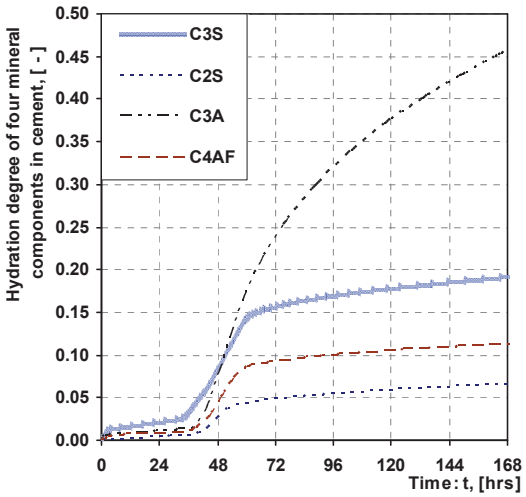


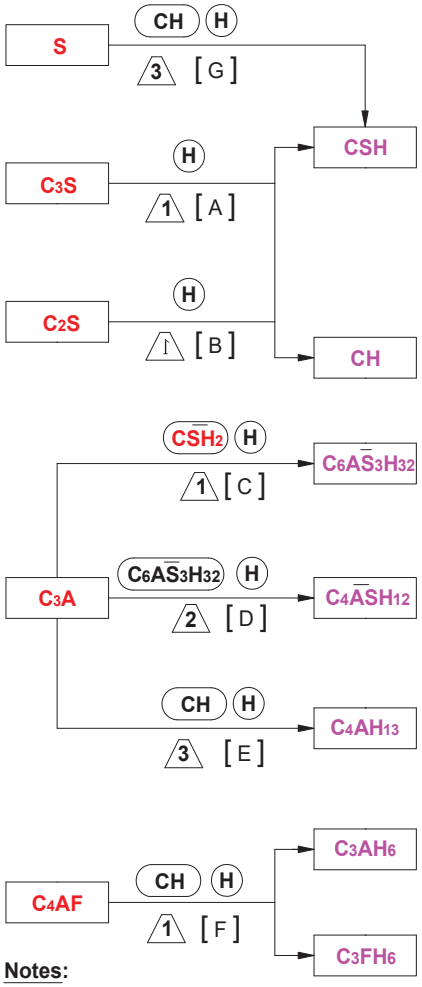
Figure 3. *The model of the hydration degree of four main components minerals.*

$$\xi(t)_c^{Model} = \frac{\sum_i [r(t_0)_{i/C}^{mass} . \xi(t)_i^{Model}]}{\sum_i [r(t_0)_{i/c}^{mass}]} \quad (11)$$

$$\xi(t)_{binder}^{Model} = P_c . \xi(t)_c^{Model} + P_{SF} . \xi(t)_s^{Model} \quad (12)$$

$$\xi(t)_s^{Model} = \frac{M(t)_s}{M(t_0)_s} \quad (13)$$

where: $\xi(t)_c^{Model}$ is the hydration degree of cement paste; $\xi(t)_{binder}^{Model}$ is the reaction degree of binder paste; $\xi(t)_s^{Model}$ is the reaction degree of Silica Fume; the $M(t)_s$ is the mass of SiO_2 (in silica fume) dissolved by the *Eq. (10)* at the instant t (this value is calculated according reaction mechanism as



Notes:

[A] ... [G] : The chemical equations

1 : Priority order of the reactions (*)

C3S : Mineral composition of cement

C6AS3H32 : The products of hydration

C6AS3H32 : Participating in the reaction

H : The water

→ : Orientation of chemical reactions

(*) : It is meaning that the chemical reactions will occur in order of the priority (at first 1, then 2, then 3), if at a certain moment there are several different oriented of chemical reactions in the possibility.

Figure 2. *Chemical reaction mechanism in a binder systems C-SF.*

described in *Fig. 2*; the $M(t_0)_s$ is the initial mass of SiO_2 in dry binder (Cement- Silica Fume); $\xi(t)_i^{Model}$ is the hydration degree of the phase i of four main components minerals in cement (C_3S, C_2S, C_3A, C_4AF). The $\xi(t)_i^{Model}$ is reference in *[7]* and *Fig. 3* is a typical for B0.

Model of the evolution of phase volume fractions in binder paste of RPC. The model of the evolution of phase volumes in binder paste (un-hydrated cement and hydrated) are calculated basing on the evolution of the hydration degree of each mineral phase in cement. These formulas are shown in from *Eq. 14 to Eq. 22*.

$$V(t)_{Hy\_i,s}^{Model} = \xi(t)_{i,s}^{Model}.V(t_0)_{i,s} \quad (14)$$

$$V(t)_{Unhy\_i,s}^{Model} = [1-\xi(t)_{i,s}^{Model}].V(t_0)_{i,s} \quad (15)$$

$$V(t)_{\mathrm{Pr}o\_hy\_j}^{\overleftrightarrow{e}} = r_{i,s/j\_\mathrm{stoichiometry}}^{\overleftrightarrow{c}} . (M_{i,s}^{molar} / M_j^{molar}).(\rho_{i,s} / \rho_j).V(t_0)_{i,s}.\xi(t)_i^{Model} \quad (16)$$

$$V(t)_{Hy}^{Model} = \sum V(t)_{Hy\_i,s}^{Model} \quad (17)$$

$$V(t)_{Un\_hy}^{Model} = V(t_0)_{Dry\_binder} - V(t)_{Hy}^{Model} \quad (18)$$

$$V(t)_{\mathrm{Pr}o\_hy}^{Model} = \sum V(t)_{\mathrm{Pr}o\_hy\_j}^{\overleftrightarrow{e}} \quad (19)$$

$$V(t)_{E\_gel}^{Model} = V(t)_{Pore\_gel}^{Model} = 0.28.V(t)_{CSH}^{Model} \quad (20)$$

$$V_{E\_cap}^{Model} = V_{Pore\_cap}^{Model} = V(t_0)_E - V(t)_{E\_gel}^{Model} - V(t)_{E\_non\_\mathrm{evaporable}}^{Model} \quad (21)$$

$$V(t)_{Hy\_pore}^{Model} = V(t_0)_{Binder} - V(t)_{Unhy}^{Model} - V(t)_{\mathrm{Pr}o\_hy}^{Model} - V(t)_{Pore\_cap}^{Model} - V(t)_{Pore\_gel}^{Model} \quad (22)$$

where: $V(t)_{Hy\_i,s}^{Model}$ is the volume of hydrated of phase i of clinker at t (or S of SF); $V(t)_{Unhy\_i,s}^{Model}$ is the volume of un-hydrated of phase "i" (or S) of clinker at time t; $\sum V(t)_{\mathrm{Pr}o\_hy\_j}^{\overleftrightarrow{e}}$ is the volume of hydration products of phase j at t by the equation of chemical reaction e (e = (4), (5), (6), (7), (8), (9), (10); $V(t)_{Hy}^{Model}$ is the total volume of four major phases hydrated of dry-binder at t; $V(t)_{Un\_hy}^{Model}$ is the total volume of un-hydrated dry-binder at time t; $V(t)_{\mathrm{Pr}o\_hy}^{Model}$ is the total volume of the solid products of hydration in binder paste at time t; $V(t_0)_{i,s}$ is the initial volume of minerals constituent "i" (or S); $r_{i,s/j\_\mathrm{stoichiometry}}^{\overleftrightarrow{c}}$ is the stoichiometry ratio between phase "j" and phase "i" in the reaction at the equation "e" ("j" is the phases of products of hydration: C-S-H, CH, ...); $M_{i,s,j}^{molar}$ is the molar weight of each phase "i", "S" and "j"; $\rho_{i,S,j}$ is the density of each phase "i" , "S" and "j"; $V(t_0)_{Dry\_binder}$ is the initial dry-binder volume; $V(t)_{E\_gel}^{Model}$ is the volume of gel water at time t; $V(t)_{Pore\_gel}^{Model}$ is the volume of gel pore at time t; $V(t)_{E\_cap}^{Model}$ is the volume of capillary water at time t; $V(t)_{E\_non\_\mathrm{evaporable}}^{Model}$ is the volume of non-evaporable water at time t; $V(t)_{Pore\_cap}^{Model}$ is the volume of capillary pores at time t; $V(t)_{Hy\_pore}^{Model}$ is the volume of hydration pore at time t. In the *Equation 20*, the value of 0.28 is referenced in *[4]*.

The volume fraction of each phase (Φ_{Phase}^{Model}) in binder paste (un-hydrated cement, products of hydration, insoluble silica fume, water in gel pore, water in capillary pore) is defined as the volume of a constituent (V_{Phase}) divided by the volume of all constituents of the binder paste ($\sum V_{Phase}$), and the sum of all volume fractions of binder paste is equal to 1. This definition is shown in *Eq. 23* and *Eq. 24*.

$$\Phi_{Phase}^{Model} = \frac{V_{Phase}}{\sum V_{Phase}} \quad (23) \qquad \sum V_{Phase} = 1 \quad (24)$$

Calculated model for the CH content in binder paste. The CH content (W_{CH}) is evaluated as shown in *Eq. 25*. In the *Eq. 25*, $M(t)_{CH}$ is the weight of CH in binder paste at time t; $M(t_0)_{Binder}$ is the weight of initial binder paste.

$$W(t)_{CH} = \frac{M(t)_{CH}}{M(t_0)_{Binder}} \quad (25)$$

Results and Discussions

Evaluation of hydration kinetic model for Portland cement containing the silica fume.

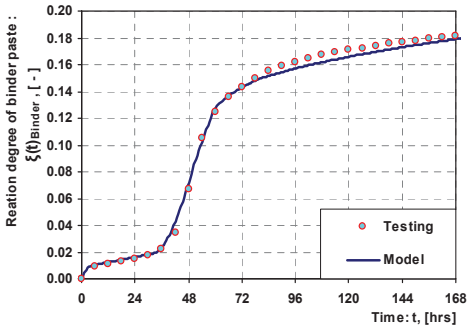


Figure 4. *Comparison between measuring and calculating results on the reaction degree of binder paste for sample No. B1.*

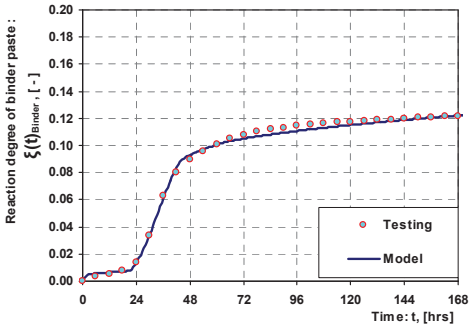


Figure 5. *Comparison between measuring and calculating results on the reaction degree of binder paste for sample No. B4.*

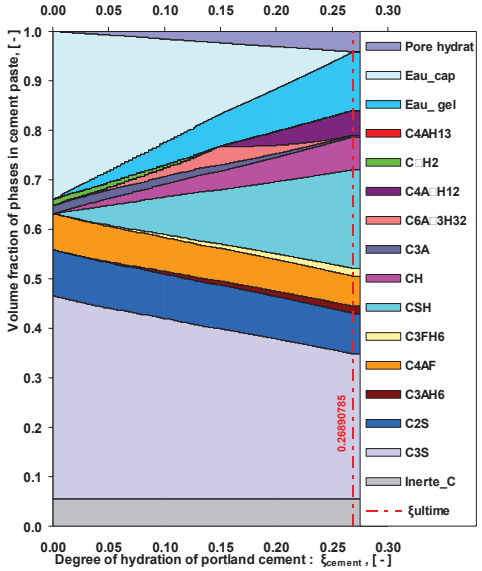


Figure 6. *The evolution of the volume fractions of the different component phases of a binder paste as function of the hydration degree of pure cement for sample No. B1.*

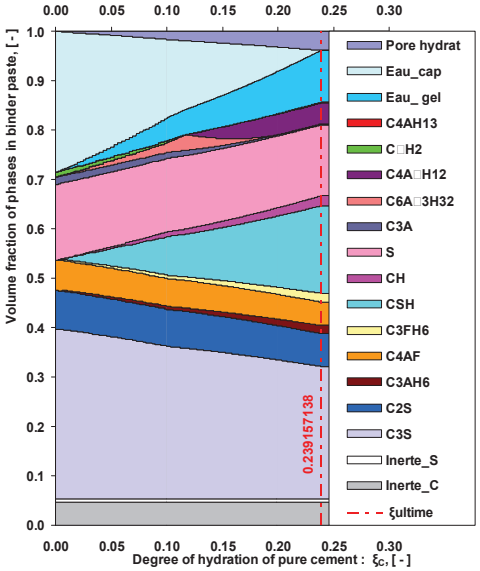


Figure 7. *The evolution of the volume fractions of the different component phases of a binder paste as function of the hydration degree of pure cement for sample No. B4.*

From the results of the reaction degree of binder paste by testing calculated in *Equation (2)* and the reaction degree of binder paste model as described above in *Equation (5),* we perform a comparison and shown on the same axis for all concrete samples from B1 to B6 as we see two typical results in *Fig. 4* for sample *No B1*. and in *Fig. 5* for sample *No B4*.

We can clearly find that good agreement between predicted value and experimental value. This allows us to believe in the hydration kinetic model for Portland cement containing the silica fume as mentioned above. In addition, we can see the model of the evolution of the phases in binder paste of RPC according to the *equations* from Eq. *14 to Eq. 22* is shown in *Fig. 6* and *Fig. 7* for sample No B1 and for sample *No B4*, respectively. From *Fig. 4* and *Fig. 5*, we find that the increase SF content in binder paste always associated with a decrease on the reaction degree of binder paste. And in a similar way, we find that the increase SF content in binder paste always associated with a decrease on the CH content in binder paste as shown in *Fig. 6* and *Fig. 7*. With the definition the CH content in binder paste as *Eq. 25,* the quantitative assessment on CH content in binder paste with different silica fume contents were shown in *Fig. 8* and *Fig. 9*. When the $SF/C = 0.05$, the CH content decreases by 50% compared to the mixture without SF, and when the SF/C ratio increases to 0.3, the CH content decreases to in the range of 60-80% compared to the mixture without SF for the age of 2-28 days. This explains why silica fume increases resistance to Sulphate Attack in RPC.

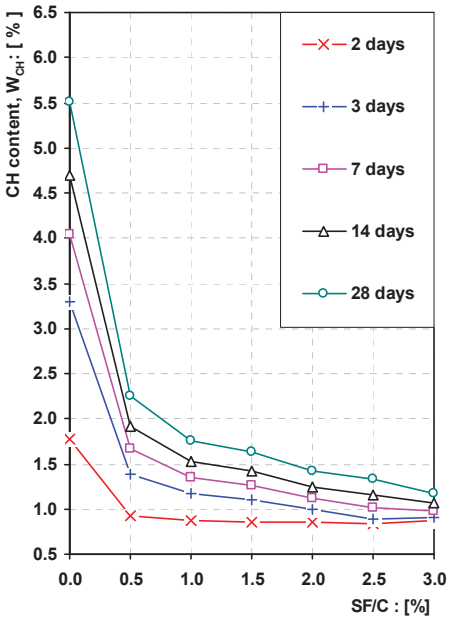


***Figure** 8. The CH content in binder paste with different silica fume contents.*

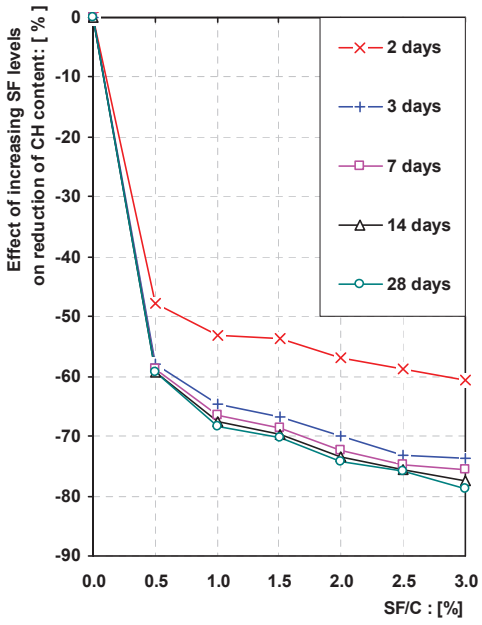


***Figure 9.** Effect of increasing SF levels on reduction of CH content.*

To determine the effect of silica fume contents on the rate of cement hydration and reactivity of silica fume, an isothermal calorimeter was used to monitor the heat generated in the cement pastes with six levels of silica fume as cement replacement in comparison with that of the control Portland cement paste. *Fig. 10* gives indication on the rate of heat evolution as a function of time for the control cement paste and the paste with six levels of silica fume as cement replacement during the first 168 h at the temperatures of $20^0 C$, respectively. From the figures, it can be observed that the rate of reactions decreased with the increasing silica fume contents, whereas the duration of the induction period (first 48 h) increased with the with the increasing silica fume contents. The main peaks in the silica fume pastes after the induction period occurred earlier and the intensity of these peaks were lower than those of the corresponding Portland cement paste.

From the same data, cumulative heat developed in the control Portland cement paste and the pastes with six levels of silica fume as cement replacement at the temperatures of $20^0 C$ was plotted and shown in *Fig. 11*. For the cement pastes with and without silica fume, the cumulative heat evolved in the first 48 h increased with an increase in silica fume contents. The extent of heat evolution in the silica fume pastes was generally smaller than in the control Portland cement paste at after first 48 h.

Based on the *Eq. 12,* the reaction degree of binder paste was determined and shown in *Fig. 12* which we find that it is completely congruent with *Fig. 11*. In a similar way, based on the *Eq. 13* was calculated and shown in *Fig. 13*. In *Fig. 13,* we realize that the reaction degree of silica fume always decrease with time when silica fume content increases.

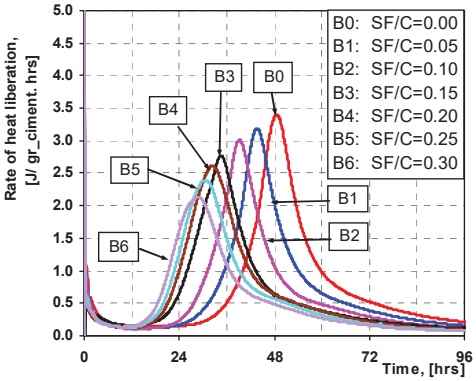


Figure 10. *The measuring results of the rate of heat evolution.*

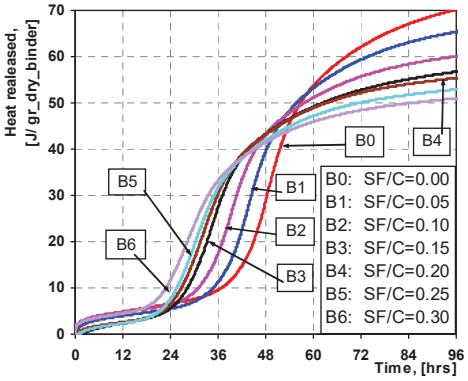


Figure 11. *The measuring results of the heat liberated.*

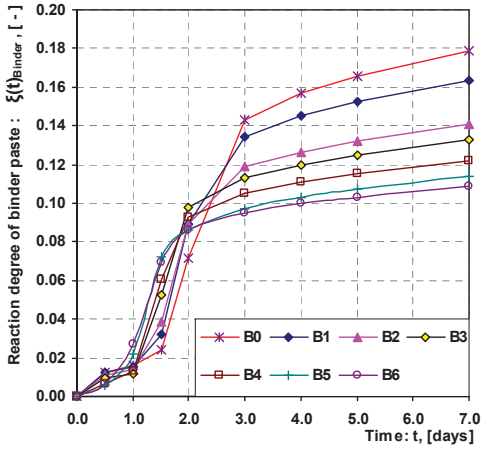


Figure 12. *Reaction degree of binder paste as function of time.*

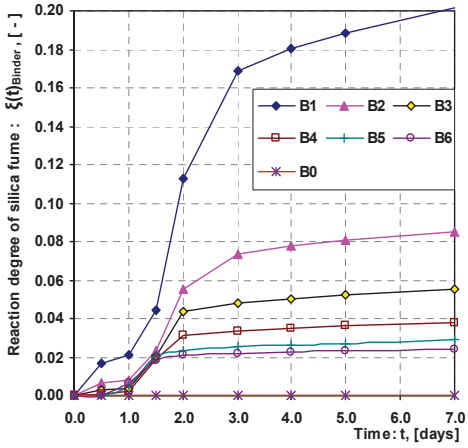


Figure 13. *Reaction degree of silica fume as function of time.*

Conclusions

The paper has briefly presents a kinetic hydration model of Cement-Silica Fume blends and a numerical procedure to evaluate the phases development of binder pastes containing Silica Fume. Using the hydration model of the four major minerals in cement (C_3S, C_2S, C_3A, C_4AF), the reaction degrees of cement, the reaction degree of binder paste, the reaction degree of silica fume has been calculated and analyzed.

Also in this article, the evolution volume model of the different component phases of a binder paste was built. And based on this model, the portlandite (CH) content has been quantified and evaluated along with the increase in SF content. In addition, The measuring results of the rate of heat evolution, of the heat liberated by isothermal calorimeter (TAM Air) on all concrete samples were recorded and comment. These measuring results were also used for verifying the kinetic hydration model through measurement results of the reaction degree of binder paste.

Acknowledgements

This research is funded by Funds for Science and Technology Development of the University of Danang under grant number B2016-DNA-30-TT. The author gratefully acknowledge for this financial support.

References

[1] EN 196-1:2005, Methods of testing cement (Part 1): Determination of strength. British Standards Institute/The European Committee for Standardisation. Chiswick, London, 2005

[2] H.F.W. Taylor, Cement Chemistry, Thomas Telford, London, (1997).

[3] I. Soroka, Portland Cement Paste and Concrete, Macmillan, London, 1979.

[4] K. Maekawa, T. Ishida, T. Kishi, Multi-scale Modeling of Structural Concrete. Taylor & Francis, London, (2009).

[5] P.C. Hewlett, Lea's Chemistry of Cement and Concrete, 4th edition, Elsevier, 2013.

[6] R.H. Bogue, Chemistry of Portland Cement, Van Nostrand Reinhold, New York. 1955.

[7] Q.S. Bach, Développement, caractérisation et modélisation des Bétons de Poudres Réactives à impact environnemental réduit. Thèse de Doctorat, Université de Nantes, France. 2014.

[8] Thomas. M, Supplementary Cementing Materials in Concrete, CRC Press, New York, 2013.

Quantitative study of hydration of C3S and C2S in the Reactive Powder Concrete together with its strength development

BACH Quoc Si[1, a]

[1]University of Technology and Education - University of Danang, Danang, Vietnam

[a]bachquocsi@gmail.com

Keywords: Blended cement; Reactive Powder Concrete; Compressive strength; C-S-H gel; C3S; C2S.

Abstract. The compressive strength development always go along with the microstructure development in concrete through the process of cement hydration. In the hydrated products of cement, calcium silicate hydrate (C-S-H) forms a network of nano-particles so C-S-H gel is the main compound giving compressive strength of concrete. As we know that C-S-H gel produced by the reactions with water of two main minerals in cement such as Tricalcium Silicate (C_3S) and Dicalcium Silicate (C_2S). In addition, the increase of C-S-H content in concrete due to the pozzolanic reaction of the pozzolan with calcium hydroxide (CH). With the aim of this research is quantitative study of hydration of C_3S and C_2S in the Reactive Powder Concrete (RPC) together with its compressive strength development, three concrete formulas were estimated in this study which made from three different types of cement ownership different mineral compositions content were tested on compressive strength and on heat flux emitted from hydration process by isothermal calorimetry. The purpose of measuring heat flux emitted from chemical reaction process in concrete is to verify the hydration kinetic model for Portland cement containing the silica fume. Basing on this simulation program, the amount of C-S-H gel in concrete is calculated. The research results showed that the the C-S-H content formed in binder paste of RPC is proportional to compressive strength development. The Ordinary Portland Cement (OPC) with higher C_3S content have compressive strength development earlier.

Introduction

As we know, the concrete is construction material that used as most widely. In the properties of concrete, compressive strength is the most important characteristic. The Reactive Powder Concrete (RPC) is designed towards using fine aggregate such as sand and increases the density. This basic principles for the development of RPC have been explained in 1990's by French company Bouygues. Conventional RPC is composed of cement and ultra-fine powders such as Crushed Quartz (CQ) and Silica Fume (SF) for the purpose of enhancing the density. On the other hand, the addition in the concrete by the active puzolans such SF as aims to improve the performance of concrete as well as contributing to reduce environmental pollution. With the good formulas designed for RPC aims to the best packing density, RPC can achieve over 150 MPa in compressive strength for the samples without fiber reinforced. Therefore, RPC is also classified as Ultra High Performance Concrete (UHPC).

The OPC is a heterogeneous fine grained material consists of four main solid phases namely Tricalcium Silicate ($C_3S = 3CaO.SiO_2$, Alite), Dicalcium Silicate ($C_2S = 2CaO.SiO_2$, Belite), Tricalcium Aluminate ($C_3A = 3CaO.Al_2O_3$), Tetracalcium Alumino Ferrite ($C_4AF = 4CaO.Al_2O_3.Fe_2O_3$). In the above symbols, using cement technology notation for the main oxides are following: $C = CaO$; $S = SiO_2$; $H = H_2O$; $A = Al_2O_3$ and $F = Fe_2O_3$. According to the same notation, SiO_3 is symbolized by $\overline{S}$ for Calcium sulphate dihydrate

($C\bar{S}H_2$ = CaO.SO_3.2H2O, gypsum), it added to the clinker to control "flash set".

When water is added to cement, the chemical reactions (called hydration) takes place and the paste passes from a fluid and workable state to a solid one that binds aggregates together. During this reaction, cement and water are consumed to form several hydrated compounds, having the appearance of a rods network structure, which envelops aggregates and is responsible for the final strength of concrete.

Of course, the final strength of concrete does not depend only on the water amount (W/C ratio), but also on *the characteristics of cement*. The timescales and contributions of the reactions of the individual compounds to the development of the cement's strength are shown in *Fig. 1* This further emphasises the long-term nature of the strength-giving reactions of the calcium silicates, particularly of the C_2S. In *Fig. 2* shown the cumulative amounts of individual products formed over timescales a few days and we can see the dominance of the C-S-H after a day or so is readily apparent. From *Fig. 1* and *Fig. 2*, we can notice that C-S-H gel is a major hydration product as well as is the main strength forming phase in the concrete. The *Fig. 1* referenced in *[2]* and *Fig.2* referenced in *[3]*.

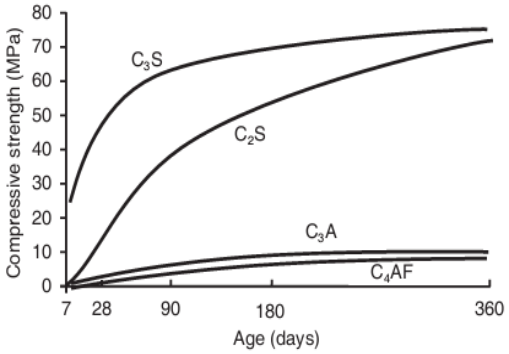


Figure 1. *Development of strength of compounds in Portland cement on hydration (after Bogue, 1955).*

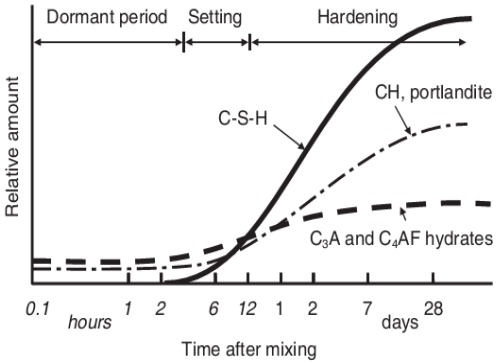


Figure 2. *Typical development of hydration products of Portland cement (after Soroka, 1979).*

In this study, three concrete formulas were estimated on compressive strength which were made from three different types of cement ownership different mineral compositions content. It was noted that due to the pozzolanic reaction of SF, the CH that is produced during cement hydration reacts with the SiO_2 (silicate of the SF) thus produces more C-S-H gel. The amount of C-S-H is calculated considering the contributions from cement hydration and SF reaction. Then, by using the C-S-H contents, the compressive strength of the SF-blended concrete is evaluated. The amount of C-S-H calculated base on a program of hydration kinetic model for Portland cement containing the silica fume. The results of the program allow determined the evolution of phase volume fractions in binder paste of RPC as well as caculated the C-S-H content in binder paste. The program of hydration kinetic model for Portland cement containing the silica fume is verified through testing on heat flux emitted from hydration process by isothermal calorimetry for all specimens of the concrete.

Materials

For producing concrete, the materials used are: the SF; the Quartz crushed (QB) with a maximum nominal size of 0.41 mm; the fine sand (SB) and the OPC type CEM I 52.5N. Three clinkers were chosen from three types of OPC: Type I, Type II/V and Type IV (according to the ASTM classification) and their chemical compositions, physical properties, Bogue's composition are given

in the *Table 1*. The characteristics of the concrete mixtures containing different amounts of SF are given in the *Table 2*.

Table 1. *Chemical composition and physical properties of cementitious materials*

Chemical composition ratio by weight, (%)				**Mineral composition ratio by weight:** $r(t_0)_{i/c}^{mass}$**, (%)**			
Item	OPC Type I	OPC Type II/V	OPC Type IV	Item	OPC Type I	OPC Type II/V	OPC Type IV
SiO_2	21.86	21.00	25.13	C_3S	62.501	60.08	44.23
Al_2O_3	5.31	4.10	2.51	C_2S	15.522	14.87	38.67
Fe_2O_3	3.43	3.70	3.48	C_3A	8.268	4.60	0.76
CaO	66.34	63.50	63.03	C_4AF	10.437	11.25	10.59
MgO	0.96	2.3	1.66	$C\overline{S}H_2$	1.3	1.3	1.3
Cl	0.02	-	0.01	**Physical properties**			
SO_3	0.30	2.10	2.05	Item	OPC Type I	OPC Type II/V	OPC Type IV
K_2O	0,28	0.67	0.64	Density: ρ_c, (g/cm^3)	3.18	3.20	3.15
Na_2O	0,10	0.09	0.04	Blaine fineness: m^2/kg	372	382	347
LOI	0,09	2.01	1.25				

Table 2. *Mixture proportions of concrete containing different amounts of silica fume*

	Mass to cement ratio, [-]			**Mass of 1 m^3, [kg/m^3]**		
Mix No.	B1 (Type I)	B2 (Type II/V)	B3 (Type IV)	B1 (Type I)	B2 (Type II/V)	B3 (Type IV)
Cement	1.00	1.00	1.00	1030.68	1032.77	1027.51
Sand	1.10	1.10	1.10	1133.75	1136.05	1130.26
Silica fume	0.10	0.10	0.10	192.40	103.27	102.75
Crushed quartz	0.05	0.05	0.05	51.53	51.63	51.37
Superplasticise	0.018	0.018	0.018	18.55	18.59	18.49
Water	0.16	0.16	0.16	164.91	165.24	164.40

Methods

Compressive Strength. All mixture concrete were tested on compressive strength at the ages of 2, 3, 7, 14 and 28 days for each time according to EN 196-1 *[1]*. First, a 3-point bending test was carried out and secondly in order to determine the compressive strength, 6 cubes – 40x40x40 mm3 in dimensions – were cut out from the broken beams and subjected to loading at the constant rate 2.4 kN/s. The specimens in prisms of 40 ×40 ×160 mm were casted with no vibration and curing process was at 20^0C with Relative Humidity (RH) 100%. The compressive strength is calculated as show in *Eq. 1* and the schematic of measuring on compressive strength as shown in *Fig. 1*.

$$R_c^{Test} = \frac{F_c^{Test}}{1600} \quad (1)$$

where: R_c^{Test} is the compressive strength, $(\frac{N}{mm^2})$; F_c^{Test} is the maximum load at fracture, (N).

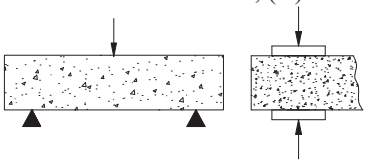


Figure 1. *Schematic of measuring on compressive strength*

Isothermal calorimetry. All mixture concrete were tested on heat flux emitted from chemical reaction process by isothermal calorimeter (TAM Air) as shown in *Fig. 2*. In order to control the test condition, the isothermal calorimeter was placed in a temperature control chamber at $20^0 C$ and RH 75%. The isothermal calorimeter contains eight separate channels, each hold a single specimen during a test and the heat of hydration in the first 7 days was recorded by the computer. The value of heat release from binder paste during the reaction process ($Q(t)_L^{Test}$) is calculated as show in *Eq. 2*. The chemical reactions in binder paste containing the SF are the exothermic processes, the total amount of heat generated is used to measure the reaction degree of binder paste following *Eq. 3*. In *Eq. 3*, the Q_L^{com} is the total heat generated when the binder paste completely reaction and calculated according to the *Eq. 4*.

$$Q(t)_L^{Test} = \int_0^t q(t)_L^{Test}.dt \quad (2)$$

$$\xi(t)_{binder}^{Test} = \frac{Q(t)^{Test}}{Q_L^{com}} \quad (3)$$

$$Q_L^{com} = P_c \cdot \sum r(t_0)_{i/c}^{mass} \cdot Q_i^{com} + P_{SF} \cdot \sum r(t_0)_{S/SF}^{mass} \cdot Q_S^{com} \quad (4)$$

where the $q(t)_L^{Test}$ is rate of heat development at the instant (t); P_c is the percentage by mass of cement in dry binder (cement-silica fume); the P_{SF} is the percentage by mass of silica fume in dry binder; the $r(t_0)_{i/c}^{mass}$ is the mineral composition ratio by weight of each phase "i" in cement; the $r(t_0)_{S/SF}^{mass}$ is the silic composition ratio by weight in silica fume; the Q_i^{com} is the maximum heat liberated when a mass unit of the phase "i" has hydrated completely; the Q_S^{com} the maximum heat liberated when a mass unit of the silica fume completely solubilized by pozzolanic reaction; the phase "i" is the clinker phase (i = C_3S, C_2S, C_3A, C_4AF) and the phase "S" is the silica dioxide (S = SiO_2 of silica fume). The values of Q_i^{com} and Q_S^{com} are referenced in *[2, 3, 4, 5, 6]*.

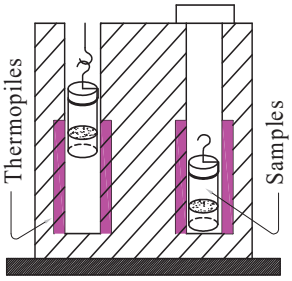


Figure 2. *Schematic of measuring on heat flux emitted by the Isothermal Calorimeter*

Hydration kinetic model for Portland cement containing the silica fume

Mechanism of the hydration of cement containing the silica fume. The four main components of cement minerals include: C_3S, C_2S, C_3A, C_4AF. These mineral composition are hydrated when interacted with water. These chemical reactions of the mineral components are shown by simple *chemical equations* as describes for each compound with coexisting $C\bar{S}H_2$ (gypsum) in OPC at ordinary temperature following from *Eq. 5 to Eq.10*.

$$C_3S + 5.3H \rightarrow C_{1.7}SH_4 + 1.3CH \quad (5)$$

$$C_2S + 4.3H \rightarrow C_{1.7}SH_4 + 0.3CH \quad (6)$$

$$C_3A + 3C\bar{S}H_2 + 26H \rightarrow C_6A\bar{S}_3H_{32} \quad (7)$$

$$C_3A + 0.5C_6A\bar{S}_3H_{32} + 2H \rightarrow 1.5C_4A\bar{S}H_{12} \quad (8)$$

$$C_3A + CH + 12H \rightarrow C_4AH_{13} \quad (9)$$

$$C_4AF + 2CH + 10H \rightarrow C_3AH_6 + C_3FH_6 \quad (10)$$

$$S + 1.7CH + 2.3H \rightarrow C_{1.7}SH_4 \quad (11)$$

For a pozzolanic reaction, the chemical reaction between S (silica fume) and CH described through the *Eq. (11)*. The chemical reactions from *Eq. 5* to *Eq.11* have been described according to references in *[2, 3, 4, 5, 6]*. According *[2, 3, 4, 5, 6]*, these chemical reactions are occurring in a certain order is described as shown in *Fig. 3*.

Model of the reaction degree of blended cement systems. As we know, the degree of hydration of cement is defined as the fraction of Portland clinker (including gypsum addition) that has already fully reacted with water relative to the final reacted cement. And on the other hand, the reaction degree of blended cement systems is defined as the fraction of dry binder that has already fully reacted with water relative to the complete reacted blended cement systems.

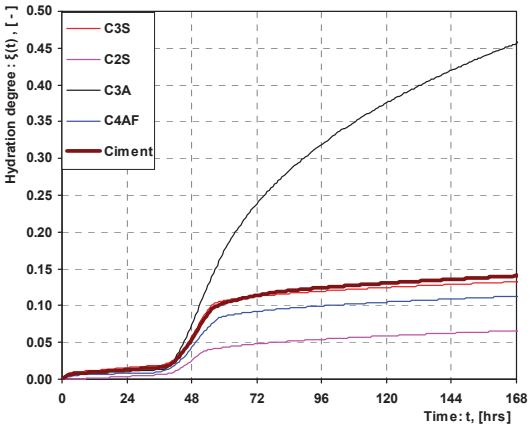


Figure 4. *The model of the hydration degree of cement and of four main components minerals.*

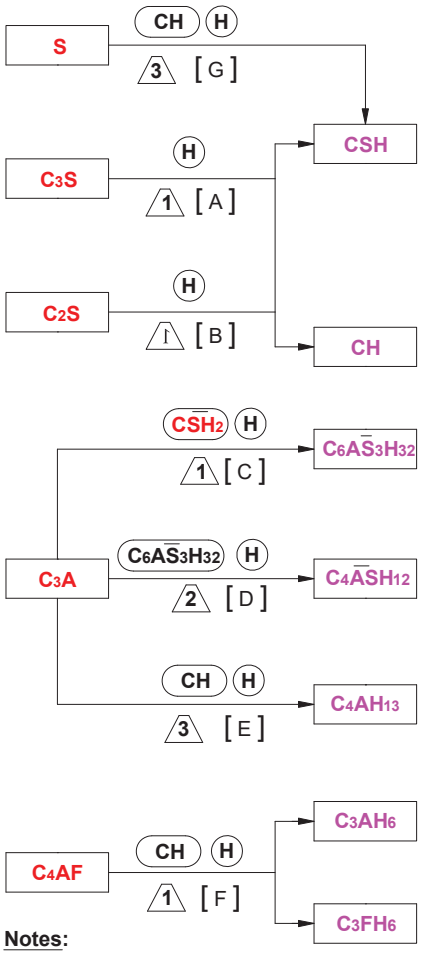
With these definitions, the model of the hydration degree of pure cement and the model of the reaction degree of blended cement systems are presented in *Eq. 12* and *Eq. 13*, respectively. The reaction degree of pozzolan is calculated as follows *Eq. 14*.

$$\xi(t)_c^{Model} = \frac{\sum_i [r(t_0)_{i/C}^{mass} . \xi(t)_i^{Model}]}{\sum_i [r(t_0)_{i/c}^{mass}]} \quad (12)$$

$$\xi(t)_{binder}^{Model} = P_c . \xi(t)_c^{Model} + P_{SF} . \xi(t)_s^{Model} \quad (13)$$

$$\xi(t)_s^{Model} = \frac{M(t)_s}{M(t_0)_s} \quad (14)$$

where: $\xi(t)_c^{Model}$ is the hydration degree of cement paste; $\xi(t)_{binder}^{Model}$ is the reaction degree of binder paste; $\xi(t)_s^{Model}$ is the reaction degree of Silica Fume; the $M(t)_s$ is the mass of SiO_2 (in silica fume) dissolved by the *Eq. (11)* at the instant t (this value is calculated according reaction mechanism as described in *Fig. 3*); the $M(t_0)_s$ is the initial mass of SiO_2 in dry binder (Cement- Silica Fume);



Notes:

[A] ... [G] : The chemical equations

1 : Priority order of the reactions (*)

C3S : Mineral composition of cement

C6AS3H32 : The products of hydration

(C6AS3H32) : Participating in the reaction

(H) : The water

→ : Orientation of chemical reactions

(*) : It is meaning that the chemical reactions will occur in order of the priority (at first 1, then 2, then 3), if at a certain moment there are several different oriented of chemical reactions in the possibility.

Figure 3. *Chemical reaction mechanism in a binder systems C-SF*

$\xi(t)_i^{Model}$ is the hydration degree of the phase i of four main components minerals in cement (C_3S, C_2S, C_3A, C_4AF). The $\xi(t)_i^{Model}$ are reference in *[7]* and the *Fig . 4* is a typical for B1.

Model of the heat liberated and the rate of heat evolution. When the blended cement is mixed with water, the chemical reactions occur with the exothermic. The predictive model of the heat liberated at time t for binder system during the reaction process are calculated following from *Eq. 15 to Eq. 19*. And the rate of heat evolution at time t for binder system is determined according as the *Eq. 20*.

$$Q(t)_L^{Model} = Q(t)_c^{Model} + Q(t)_s^{Model} \quad (15)$$

$$Q(t)_c^{Model} = P_c.[\sum_i r(t_0)_{i/c}^{mass}.Q(t)_i] \quad (16)$$

$$Q(t)_s^{Model} = P_{SF}.[r(t_0)_{s/SF}^{mass}.Q(t)_s] \quad (17)$$

$$Q(t)_i^{Model} = \xi(t)_i.Q(t)_i^{com} \quad (18)$$

$$Q(t)_s^{Model} = \xi(t)_s.Q(t)_s^{com} \quad (19)$$

$$\frac{dQ(t)_L^{Model}}{dt} = P_c.\left[\sum_i r(t_0)_{i/C}^{mass}.Q_i^{com}.\frac{d\xi(t)_i}{dt}\right] + P_{SF}.\left[r(t_0)_{s/SF}^{mass}.Q_s^{com}.\frac{d\xi(t)_s}{dt}\right] \quad (20)$$

where: $Q(t)_L^{Model}$ is the heat liberated at time t of binder paste during the occurrence of chemical reactions; $Q(t)_c^{Model}$ is the heat liberated at time t of cement; $Q(t)_s^{Model}$ is the heat liberated at time t of the Silica Fume. The $Q(t)_i^{Model}$ is the heat liberated at time t of the each minerals constituent "i" in cement; the $Q(t)_s^{Model}$ is the heat liberated at time t of the S in silica fume during the reaction process; $\frac{dQ(t)_L^{Model}}{dt}$ is the rate of heat evolution at time t for binder system.

Model of the evolution of phase volume fractions in binder paste of RPC. The model of the evolution of phase volumes in binder paste (un-hydrated cement and hydrated) are calculated basing on the evolution of the hydration degree of each mineral phase in cement. These formulas are shown in the equations from *Eq. 21 to Eq. 29*.

$$V(t)_{Hy\_i,s}^{Model} = \xi(t)_{i,s}^{Model}.V(t_0)_{i,s} \quad (21)$$

$$V(t)_{Unhy\_i,s}^{Model} = [1-\xi(t)_{i,s}^{Model}].V(t_0)_{i,s} \quad (22)$$

$$V(t)_{\mathrm{Pr}o\_hy\_j}^{\overset{e}{\longleftrightarrow}} = r_{i,s/j\_\mathrm{stoichiometry}}^{\overset{c}{\longleftrightarrow}}.(M_{i,s}^{molar}/M_j^{molar}).(\rho_{i,s}/\rho_j).V(t_0)_{i,s}.\xi(t)_i^{Model} \quad (23)$$

$$V(t)_{Hy}^{Model} = \sum V(t)_{Hy\_i,s}^{Model} \quad (24)$$

$$V(t)_{Un\_hy}^{Model} = V(t_0)_{Dry\_binder} - V(t)_{Hy}^{Model} \quad (25)$$

$$V(t)_{\mathrm{Pr}o\_hy}^{Model} = \sum V(t)_{\mathrm{Pr}o\_hy\_j}^{\overset{e}{\longleftrightarrow}} \quad (26)$$

$$V(t)_{E\_gel}^{Model} = V(t)_{Pore\_gel}^{Model} = 0.28.V(t)_{CSH}^{Model} \quad (27)$$

$$V_{E\_cap}^{Model} = V_{Pore\_cap}^{Model} = V(t_0)_E - V(t)_{E\_gel}^{Model} - V(t)_{E\_non\_\mathrm{evaporable}}^{Model} \quad (28)$$

$$V(t)_{Hy\_pore}^{Model} = V(t_0)_{Binder} - V(t)_{Unhy}^{Model} - V(t)_{\mathrm{Pr}o\_hy}^{Model} - V(t)_{Pore\_cap}^{Model} - V(t)_{Pore\_gel}^{Model} \quad (29)$$

where: $V(t)_{Hy\_i,s}^{Model}$ is the volume of hydrated of phase i of clinker at t (or S of SF); $V(t)_{Unhy\_i,s}^{Model}$ is the volume of un-hydrated of phase "i" (or S) of clinker at time t; $\sum V(t)_{\mathrm{Pr}o\_hy\_j}^{\overset{e}{\longleftrightarrow}}$ is the volume of hydration products of phase j at t by the equation of chemical reaction e (e = (5) , (6), (7), (8), (9),

(10), (11); $V(t)_{Hy}^{Model}$ is the total volume of four major phases hydrated of dry-binder at t; $V(t)_{Un\_hy}^{Model}$ is the total volume of un-hydrated dry-binder at time t; $V(t)_{Pro\_hy}^{Model}$ is the total volume of the solid products of hydration in binder paste at time t; $V(t_0)_{i,s}$ is the initial volume of minerals constituent "i" (or S); $r_{i,s/j\_\text{stoichiometry}}^{e\longleftrightarrow}$ is the stoichiometry ratio between phase "j" and phase "i" in the reaction at the equation "e" ("j" is the phases of products of hydration: C-S-H, CH, ...); $M_{i,s,j}^{molar}$ is the molar weight of each phase "i", "S" and "j"; $\rho_{i,S,j}$ is the density of each phase "i" , "S" and "j"; $V(t_0)_{Dry\_binder}$ is the initial dry-binder volume; $V(t)_{E\_gel}^{Model}$ is the volume of gel water at time t; $V(t)_{Pore\_gel}^{Model}$ is the volume of gel pore at time t; $V(t)_{E\_cap}^{Model}$ is the volume of capillary water at time t; $V(t)_{E\_non\_\text{evaporable}}^{Model}$ is the volume of non-evaporable water at time t; $V(t)_{Pore\_cap}^{Model}$ is the volume of capillary pores at time t; $V(t)_{Hy\_pore}^{Model}$ is the volume of hydration pore at time t. In the *Eq. 27*, the value of 0.28 is referenced in *[4]*.

The volume fraction of each phase (Φ_{Phase}^{Model}) in binder paste (un-hydrated cement, products of hydration, insoluble silica fume, water in gel pore, water in capillary pore) is defined as the volume of a constituent (V_{Phase}) divided by the volume of all constituents of the binder paste ($\sum V_{Phase}$), and the sum of all volume fractions of binder paste is equal to 1. This definition is shown in *Eq. 30* and *Eq. 31*.

$$\Phi_{Phase}^{Model} = \frac{V_{Phase}}{\sum V_{Phase}} \qquad (30)$$

$$\sum V_{Phase} = 1 \qquad (31)$$

Model for the C-S-H content in binder paste. The C-S-H content (W_{CSH}) is evaluated as shown in *Eq. 32*. In the *Eq. 32*, $M(t)_{CSH}$ is the weight of C-S-H in binder paste at time t; $M(t_0)_{Binder}$ is the weight of initial binder paste.

$$W(t)_{CSH} = \frac{M(t)_{CSH}}{M(t_0)_{Binder}} \qquad (32)$$

Results and Discussions

Evaluation of hydration kinetic model for Portland cement containing the silica fume. From the results of the heat liberated model and the rate of heat evolution model as described above, we perform comparison to the experimental results according to *Eq. 2, Eq. 15, Eq. 20*. A typical result is shown in *Fig. 5* for sample No. B1.

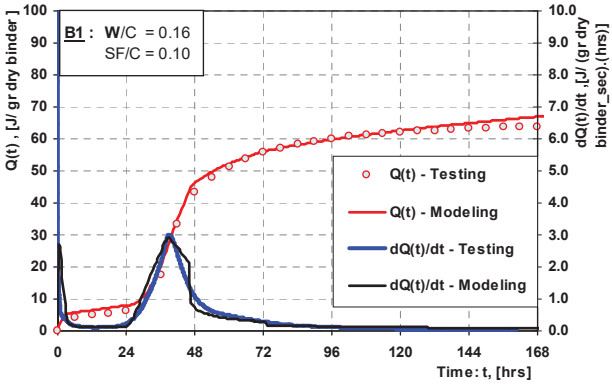


Figure 5. *Comparison between measuring and calculating results on the heat liberated and the rate of heat evolution*

We can clearly find that good agreement between predicted value and experimental value. This allows us to believe in the hydration kinetic model for Portland cement containing the silica fume as mentioned above. In addition, we can see the model of the evolution of the phases in binder paste of RPC according from *Eq. 21 to Eq. 29* is shown in *Fig. 6* for sample No B1.

In *Fig. 6,* the volume fraction of each phase in binder paste is calculated following *Eq. 30*. We

can find that with the proceeding of cement hydration and SF reaction, the volumes of un-reacted cement and SF are decreased, the volumes of $C-S-H$ and other reaction products are increased, and due to the filling effects of reaction products, the volume of capillary pore decreases, and so compressive strength increase.

In addition, we can find that component C-S-H gel is highest proportion in the hydration products of binder paste and the amount of this hydration product is due to hydration of components minerals C_3S, C_2S in cement according to the equations from *Eq. 5* to *Eq. 10* as well as the *Eq. 11* for pozzolanic reaction.

Quantitatively for C-S-H gel, we can see the C-S-H content in binder paste of three RPCs as shown in *Fig 7*. In *Fig 7*, the values C-S-H content were calculated according to the *Eq. 25*.

Compressive strength of RPC. *Fig. 8* shows the compressive strength development of three RPCs from the test results in relation to the time. If we pay attention to *Fig. 4* and *Fig. 7*, we find that the development of compressive strength accompanies the hydration degree development of cement and is similar to the increase in C-S-H content.

Fig. 9 presents the compressive strength of the RPCs as a function of the calculated C-S-H contents. As shown in *Fig. 9*, for RPC with different C_3S, C_2S, C_3A, C_4AF contents in cement (OPC: Type I, Type II/V and Type IV) and at different ages (2, 3, 7, 14 and 28 days), there is single linear relationship

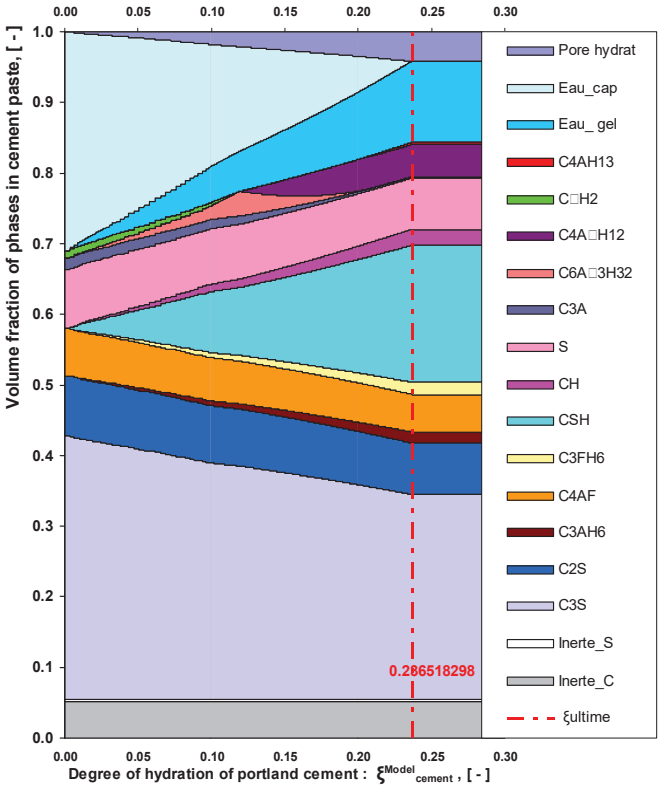


Figure 6. *The evolution of the volume fractions of the different component phases of a binder paste as function of the hydration degree of pure cement.*

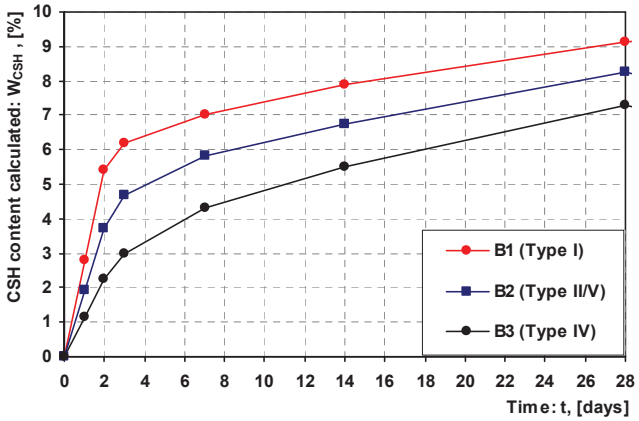


Figure 7. *Development of the C-S-H content in binder paste by time.*

between the compressive strengths and the calculated C-S-H amounts:

$$R_c^{Test} = 13.13 x CSH\ content$$

In a similar way, based on the compressive strength of the RPCs by testing results and the C_3S content in each type of cement, the relationship between them is shown in *Fig. 10*. In this figure, the compressive strength of concrete is always increased with the increase of C_3S content in cement and suggests that the C_3S content plays a decisive role in the production of C-S-H gel.

This is more noticeable when we consider the C_2S content in B3 (OPC Type IV) is very high but its compressive strength develops slower than B1 (OPC Type I) and B2 (OPC Type II/V). This can be explained by the C_3S content in each type of cement always occupies a high proportion and its hydration degree is higher than the hydration degree of C_2S in early age (as shown *Fig. 4*). On the other hand, the compressive strength of C_3S mineral develops faster than the compressive strength of C_2S mineral as shown *Fig. 1*.

Another comment in *Fig. 10*, RPCs compression strength increases rapidly at 2 days and 3 days because the hydration degree of cement and of four main components minerals increase rapidly in this term (as shown *Fig. 4*).

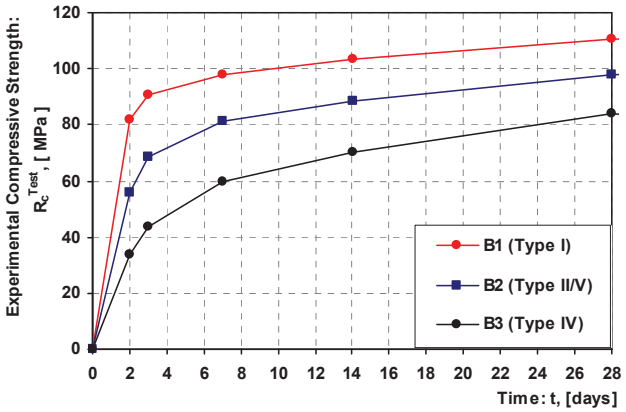


Figure 8. *Development of the compressive strength by time.*

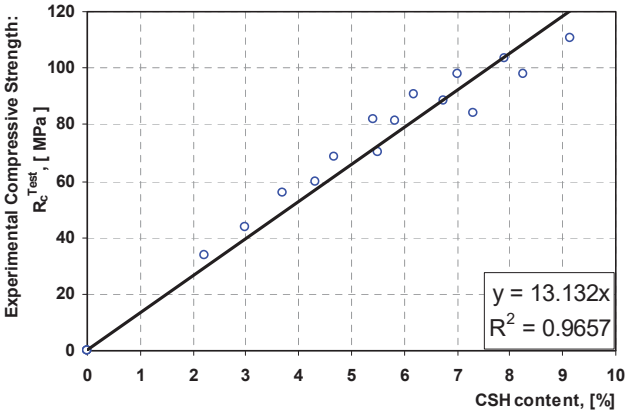


Figure 9. *Compressive strength of RPCs as a function of calculated C-S-H content.*

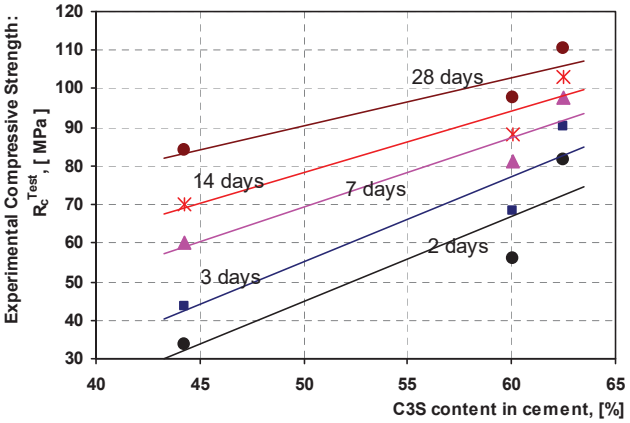


Figure 10. *Compressive strength of RPCs as a function of C_3S content in cement.*

Conclusions

The paper presents a kinetic hydration model of Cement-Silica Fume blends and a numerical procedure to evaluate the phases development of binder pastes containing Silica Fume. Using blended hydration model and the reaction degrees of cement (as well as the reaction degrees of C_3S, C_2S, C_3A, C_4AF), the calcium silicate hydrate (C-S-H) content and phase volume fractions are calculated as functions of curing age. Furthermore, the compressive strength of hardening concrete is evaluated through C-S-H contents as well as the quantity of C-S-H is quantitatively analyzed with the hydration of C_3S, C_2S.

Acknowledgements

This research is funded by Funds for Science and Technology Development of the University of Danang under grant number B2016-DNA-30-TT. The author gratefully acknowledge for this financial support.

References

[1] EN 196-1:2005, Methods of testing cement (Part 1): Determination of strength. British Standards Institute/The European Committee for Standardisation. Chiswick, London, 2005

[2] H.F.W. Taylor, Cement Chemistry, Thomas Telford, London, (1997).

[3] I. Soroka, Portland Cement Paste and Concrete, Macmillan, London, 1979.

[4] K. Maekawa, T. Ishida, T. Kishi, Multi-scale Modeling of Structural Concrete. Taylor & Francis, London, (2009).

[5] P.C. Hewlett, Lea's Chemistry of Cement and Concrete, 4th edition, Elsevier, 2013.

[6] R.H. Bogue, Chemistry of Portland Cement, Van Nostrand Reinhold, New York. 1955.

[7] Q.S. Bach, Développement, caractérisation et modélisation des Bétons de Poudres Réactives à impact environnemental réduit. Thèse de Doctorat, Université de Nantes, France. 2014.

A Study on Local Induction Hardening for Flat Surfaces

Pham Son Minh[1,a*], Nguyen Vinh Du[2,b], Tran Trung Truc[1,2,c],
Thanh Trung Do[1,d], and Ho Cong Minh[1,e]

[1]*HCMC University of Technology and Education, Ho Chi Minh City, Vietnam*

[2]*Department of Science and Technology, Ho Chi Minh city, Vietnam*

[a]minhps@hcmute.edu.vn, [b]nvdu.skhcn@tphcm.gov.vn, [c]trungtruc1977@yahoo.com,
[d]trungdt@hcmute.edu.vn, [e]hocongminhck@gmail.com

Keywords: Steel hardening, Induction heating, Flat surface, Heat treatment, Mold plate.

Abstract

Induction hardening for flat surface carbon steel specimens can be used in various fields of industry. This is a heat treatment process that can be used to increase the hardness on the surface of a steel component. To investigate the effects of this method, some specimens of C45 and SS400 steel were used. Experience data and results were simulated and set up by 3D electromagnetic model coupled temperature fields of COMSOL Multiphysics 5.0 software. A three-turn copper coil receiving a Foucault current from a power supply was used to heat the specimens during the experiments. The effect of this process will be evaluated by assessing the hardness and metallographic techniques of the material. Results showed that martensite affects the hardness of the material. The distribution of the hardness area is dependent on the result of the achieved temperature on the surface, which is in accordance with the shape of the induction coil. In the annular zone, martensite phase appears almost at the surface areas of the annular zone, whereas pearlite causes the lowest hardness in the central zone. To upgrade the hardness on all surfaces, the induction coil must affect all the areas of the specimens. For this purpose, we can move the coil point by point to increase the temperature opposite to the face or we can use continuous induction hardening by moving the coil along the *x*- and *y*-axes. A CNC machine is modified to carry out this task. Results show that the method of moving the coil point by point yields the best solution for induction hardening for flat surfaces.

Introduction

In the field of injection molding, the mold manufacturing process is very important. In this field, to reduce the cost, the mold is usually cut by common steel, and then heat treatment is used at the needed position. In general, heat treatment is a process that involves a combination of time-controlled heating and cooling operations of metal without changing the product shape, which will produce the desired mechanical properties and help observe the microstructure after heat treatment [1]. In almost all cases, the product performance will improve when the strength of the material increases [2]. This procedure can be divided into four main processes: annealing, normalizing, hardening, and tempering. These processes are the most important heat treatments that are often used to modify the microstructure and the mechanical properties of engineering materials, especially steels [3]. Annealing is defined as a type of heat treatment that consists of heating up to a suitable temperature and then holding at this temperature, followed by cooling at an appropriate rate, which is most frequently applied to soften iron or steel materials and refine its grains caused by the ferrite–pearlite microstructure; this method is used when elongations and an appreciable level of tensile strength are required in engineering materials. Hardening is a heat treatment process in which the

hardness of a steel piece increases by heating it to a certain temperature and then cooling it down rapidly to room temperature [4]. Tempering is the process of imparting toughness at the cost of hardness to an already hardened piece of steel by reheating it to a certain temperature and then cooling it rapidly [5]. The heating temperature depends on the toughness to be imparted and the hardness to be reduced. In the normalizing process, the material is heated to the austenitic temperature range, followed by air cooling. This type of treatment is usually carried out in order to obtain a pearlite matrix, which results in strength and hardness higher than those in the as-received condition. It is also used to remove the undesired free carbide present in the as-received sample [6].

Simulation and Experimental Method

In the field of metal heat treatment, the application for the complex part geometry or the large part is always challenging for engineers. In the first case, trouble appears in the magnetic control in the heating method. In the second case, the trouble lies in the power needed to heat a large area. In this research, the local hardening method using an induction heating coil will be applied on flat surfaces in order to increase the temperature up to a critical value, and then the coil is moved slowly to another area for tempering the whole flat surface. The research model is shown in Fig. 1 and the experimental model is shown in Fig. 2.

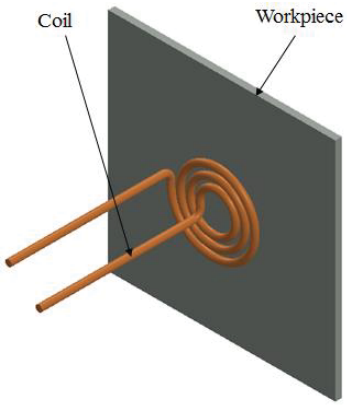


Figure 1: The research model for local induction hardening.

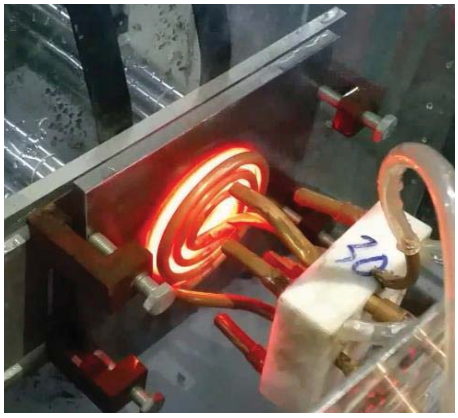


Figure 2: The experimental model for local induction hardening.

In this paper, in order to investigate the effects of the induction hardening method on the flat part, specimens of C45 and SS400 steel were used in the tempering process. Based on the ASTM E23, the chemical composition of these steel types is shown in Table 1. First, local induction hardening will be applied at the center of the C45 steel plate with a size of 150 mm × 150 mm × 10 mm. The main purpose of this step is to assess the effect of the heating step for flat surfaces with the heating position as in Figs. 1 and 2. Then, the specimens have the size of 200 mm × 200 mm × 10 mm with the materials of C45 and SS400 that are used in the experiment. The experiment is carried out using five samples for each case. The hardness will be measured by the Rockwell Hardness Testing Machines. Measurements will be carried out for all tempering surfaces by the dividing method as in Fig. 3. For each small area as in Fig. 3, hardness will be measured 20 times, and then the average value will be represented for the hardness of this area.

Table 1: Chemical composition of medium carbon steel [7, 8].

Content (%)	C	Si	Mn	P	S	Cr	Mo	Ni	Cr + Mo +
SS400	0,30	0,05	0,05	---	---	---	---	---	---
C45	0.42–0,50	0.40	0.50–0.80	0.045	0.045	0.40	0.10	0.40	0.63



Figure 3: Hardness measurement areas.

On the basis of the heat treatment experiments for C45 steel, the induction heating parameters are chosen as follows:

- Heating speed: 50–100°C/s.
- Temperature requirement: 850–950°C.
- Time of heat holding: 5–10 s.
- Cooling speed: 200–250°C/s.

To observe the induction heating process as well as the moving speed of the coil, a simulation of the 3D electromagnetic model was carried out with the model as shown in Fig. 4. In this model, the workpiece and the induction coil will be covered by the air volume. The COMSOL Multiphysics 5.0 software will be applied with the Heat Transfer and Electro-Magnetic module. Then, the boundary conditions will be set up as in the real experiment with the main parameters set as follows:

- Frequency: 20,000 Hz.
- Current: 350 A.
- Distance between the induction coil and the workpiece's surface: 3 mm.
- Moving speed of the workpiece: 3.5 mm/s.
- Total heating time: 60 s.

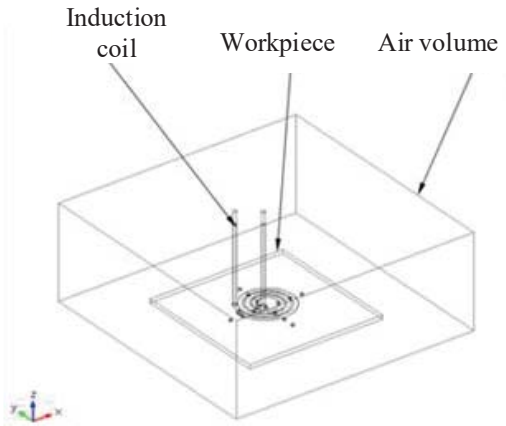


Figure 4: The 3D electromagnetic model for the induction heating process.

Results and Discussions

(*) Induction Hardening for the Local Position on a Flat Plate

In this paper, to verify the capability of heating with the position as in Figs. 1 and 2, the simulation and experiment of induction heating were carried out with a C45 steel workpiece. In this case, the coil will not be moved, and heating will be achieved within 30 s. At this step, the simulation shows the temperature distribution at the end of the heating step as in Fig. 5. The result shows that a high temperature is distributed in the ring area. The highest temperature reached was 905°C; this temperature is high enough for tempering steel. However, owing to the characteristics of the spiral coil, the temperature at the coil center is very low. So, this influence will reduce the capability of the hardening process on the steel material. By simulation, the center's temperature is just around 600°C.

In order to verify the simulation result, the experiment was carried out using the model as shown in Fig. 2. The temperature of the workpiece will be measured by an infrared sensor as shown in Fig. 6. The result shows that, after 30 s of heating, the highest temperature reached was 905.8°C. This result demonstrates that the simulation was properly carried out with the proper boundary conditions. Based on this result, the hardening process was applied on the C45 workpiece in order to observe the hardness increment. At this step, five workpieces were tested with the same parameters. Fig. 7 shows the workpiece after tempering. Surface hardness was measured by the Rockwell Hardness Testing Machines. Then, the hardness value was averaged and collected as in Table 2. The hardness of these plates is shown in Fig. 8. Based on these results, it is shown that the hardness could be increased from 15 HRC to over 65 HRC after 30 s of tempering using a stationary induction coil. Similar to the temperature distribution, the high hardness is also distributed on a ring area. At the center of the ring, the hardness is much lower than that in the neighboring area, which is only around 25–42 HRC. This is due to the fact that the center area is just heated to around 600°C during the tempering process; at this temperature, the phase of the steel could not be changed.

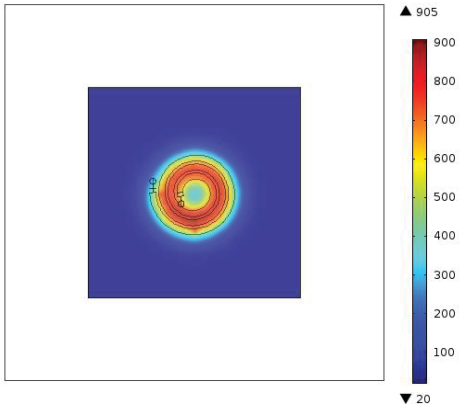


Figure 5: Temperature at the end of induction heating with the stationary coil.



Figure 6: Temperature measurement at the end of induction heating.



Figure 7: Workpiece after hardening with the stationary coil.

Table 2: The hardness of C45 steel with the stationary coil tempering (HRC).

Position	1	2	3	4	5	6	7	8	9	10	11	12	13
A	14.9	15.7	14.5	16.3	15.1	15.8	20.2	17.1	15.4	16.1	14.4	15.8	14.7
B	15.4	15.8	14.9	14.7	**57.4**	**59.5**	**60.3**	**57.1**	17.6	13.9	15.2	14.9	15.4
C	14.7	15.8	14.5	**59.5**	**62.1**	**61.3**	**58.2**	**58.7**	**57.9**	**56.2**	16.8	15.6	14.9
D	18.2	15.7	**59.3**	**61.5**	**64.2**	**61.8**	**62.5**	**63.1**	**59.7**	**61.4**	**55.1**	14.3	15.8
E	20.1	22.3	**62.8**	**61.5**	**57.9**	**58.4**	**59.1**	**60.2**	**64.6**	**60.5**	**57.8**	15.2	14.5
F	17.3	**58.4**	**61.2**	**60.6**	**57.7**	41.5	30.4	**61.3**	**51.8**	**59.5**	**54.8**	15.7	13.6
G	16.7	**59.1**	**66.2**	**62.7**	**59.3**	31.8	25.1	**59.4**	**60.5**	**60.8**	**54.3**	17.1	14.8
H	18.5	17.8	**65.1**	**60.3**	**61.5**	**59.6**	**58.9**	**59.1**	**57.6**	**58.2**	**56.1**	14.7	14.2
I	15.5	14.8	**58.6**	**63.5**	**56.3**	**63.4**	**60.7**	**60.1**	**59.2**	**57.8**	33.2	15.7	14.6
J	16.3	15.2	14.3	**60.5**	**51.8**	**56.3**	**61.2**	**60.1**	**57.4**	**48.5**	15.2	16.4	15.3
K	15.4	14.8	14.9	14.4	27.3	**61.5**	**57.8**	**45.7**	17.6	15.1	14.9	15.6	14.5
L	16.2	15.8	17.3	16.2	15.6	16.3	15.4	18.3	15.9	16.7	14.5	15.9	15.8
M	18.5	16.3	16.9	15.7	14.6	15.9	16.3	14.3	15.5	16.3	18.5	14.2	17.8

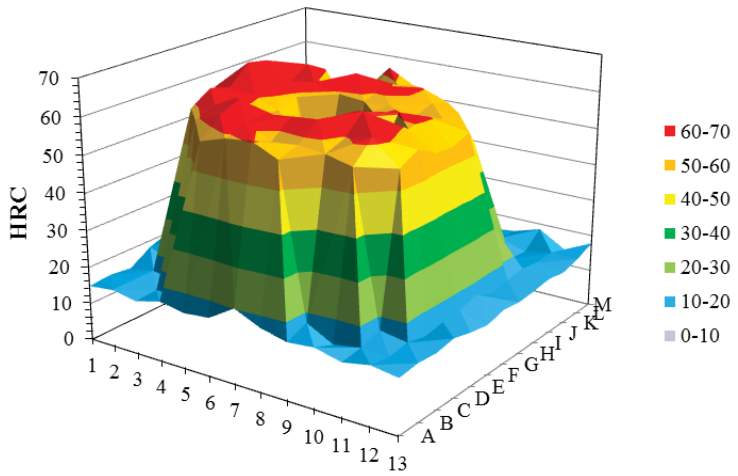


Figure 8: Hardness distribution of the C45 plate after tempering with the stationary coil.

To detect the effects of tempering on the grains of steel, after the hardening process, the workpiece will be cut as shown in Fig. 9. With the goal of observing the effect of temperature on the grains, areas Q7 and J7 (Fig. 9) will be used in the tests with depths of 3.5 mm and more. All tests follow the standard of ASTM E112-1996. The microstructural results of these testing samples are shown in Figs. 10–13. Results show that the microstructure at area J7 with the depth of 3.5 mm (Fig. 10) has a martensite phase quite clearly because of the tempering effect, with the maximum temperature reached being over 900°C. The longer the martensite phase, the higher the hardness of the plate. However, with the same J7 location, at a depth beyond 3.5 mm from the heating surface, the percentage of martensite exhibits a strong decrease. Figure 11 shows that the martensite phase almost disappeared. This result could be attributed to the temperature distribution on the depth of the plate. Due to the fact that we used the induction heating method in this research to raise the plate's temperature, the heating effect only appeared on the surface of the plate. At a deeper area, heat treatment will be strongly reduced. This microstructure result also shows that the tempering process has an influence on the heating surface, and this effect will decrease with greater depths. At the center of the heating area, the microstructure was also observed within the area of Q7. These microstructure results are shown in Figs. 12 and 13. These results show that the percentage of the martensite phase is very low due to the fact that heating is not as strong as in the ring area.

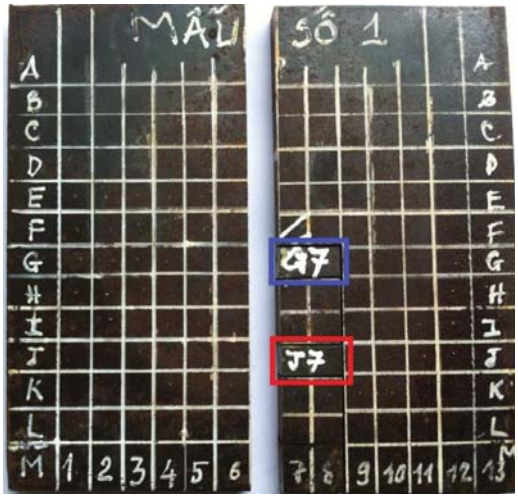


Figure 9: Q7 and J7 for microstructure testing.

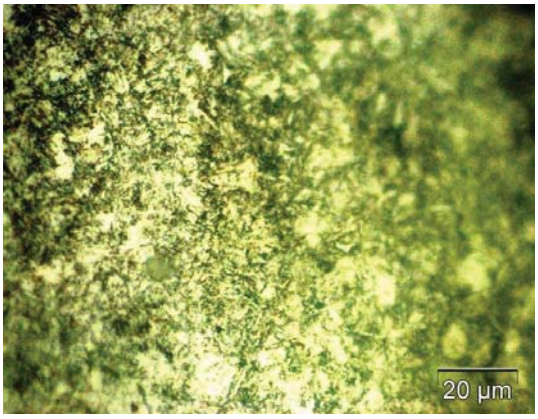


Figure 10: The microstructure at location J7 at the depth of 3.5 mm.

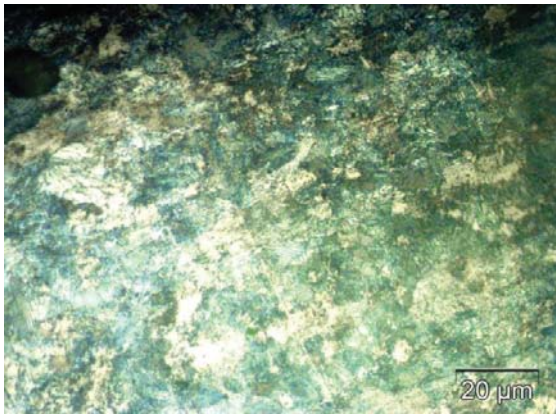


Figure 11: The microstructure at location J7 at a depth greater than 3.5 mm.

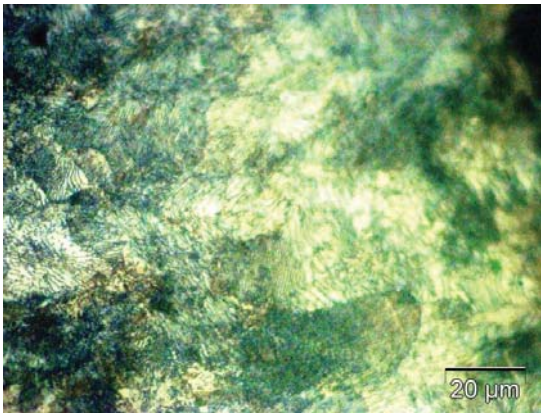


Figure 12: The microstructure at location G7 at a depth of 3.5 mm.

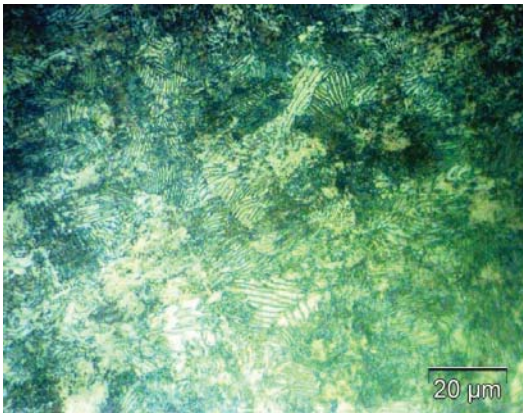


Figure 13: The microstructure at location G7 at a depth of 3.5 mm.

(*) Induction Hardening for Flat Plates with a Moving Coil

Based on the result of induction hardening in the local position on the flat plate, in this part of the paper, with the same induction coil and workpiece of 200 mm × 200 mm × 10 mm, the plate material of C45 and SS400 will be used in the hardening tests. In these cases, the coil will heat the plate in the beginning until reaching a temperature of over 900°C, and then the coil will be moved to the end of the plate. To determine the speed of moving the coil, some simulations were carried out. These simulations used the same boundary conditions as in the case of the stationary coil; however, the coil will be set up with different moving speeds. These simulations will be repeated until the hardening temperature stays at a value higher than 900°C. These simulations show that, with a total moving time of 30 s for a distance of 200 mm, heating will satisfy the requirement of the hardening process, as shown in Fig. 14.

For the experiment, Fig. 15 shows the plate after hardening. The workpiece of C45 and SS400 will be divided as in Fig. 16 in order to determine the hardness. The result of hardness is shown in Tables 3 and 4 and Figs. 17 and 18 with the C45 and SS400 plate, respectively. These results show that hardening with the moving coil could increase the hardness of steel within a rectangular area; in particular, hardness was quite uniform because this area was heated up to a proper temperature. In addition, when comparing the hardening of C45 and SS400 steel with the same parameters, the hardness of the C45 steel was higher than that of the SS400 steel. This result is due to the fact that the percentage of carbon in C45 is around 0.42–0.5 %, which is higher than that in the SS400 steel, which is lower than 0.3%. The lower hardness of SS400 may be due to the heat transfer coefficient. The heat transfer coefficient of the C45 steel is 30 W/m·K, whereas that of SS400 is 50 W/m·K. This property will make the temperature decrease faster in the SS400 steel, so the heat cannot stay accumulated at the hardening area, and thus hardening will be worse than in the C45 case. This can explain the reason for the hardness increment outside the heating area in the case of SS400, which increased from 15 HRC to around 30 HRC as shown in Table 4.

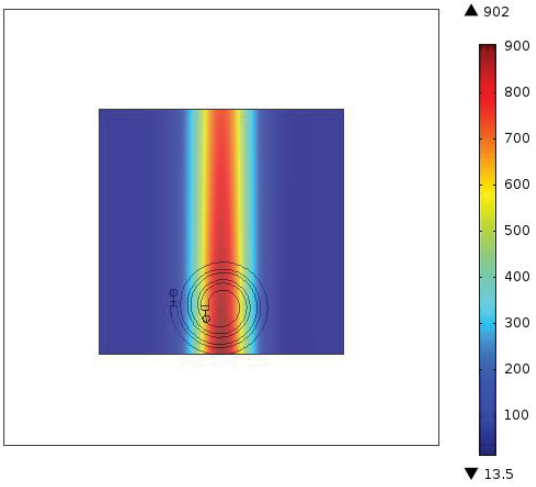


Figure 14: Temperature at the end of induction heating with the moving coil.



Figure 15: Workpiece after hardening with the stationary coil.



Figure 16: Hardness measurement areas with the moving coil cases.

Table 3: Hardness (HRC) of the C45 steel with the moving coil tempering.

Position	1	2	3	4	5	6	7	8
A	15.3	61.6	**54.3**	**76.5**	**58.1**	34.1	16.9	15.8
B	15.6	47.9	**54.9**	**51.2**	**46.6**	26.3	17.3	16.2
C	14.3	53.5	**58.8**	**56.2**	**47.1**	25.7	12.3	14.6
D	15.1	58.9	**51.7**	**58.0**	**55.3**	23.0	16.6	17.2
E	14.0	33.2	**31.1**	**25.8**	**40.9**	25.0	25.0	19.3
F	32.2	32.8	**55.4**	**50.5**	**46.9**	44.0	17.6	17.2
G	21.0	33.3	**49.5**	**50.0**	**56.2**	22.4	17.1	16.9
H	22.0	36.1	**59.6**	**35.3**	**35.8**	22.9	15.6	16.1
I	7.6	25.5	**55.6**	**53.5**	**20.6**	13.2	18.6	17.3

Table 4: Hardness (HRC) of the SS400 steel with the moving coil tempering.

Position	1	2	3	4	5	6	7	8
A	39.3	31.4	**34.5**	**35.3**	**34.8**	36.5	40.1	14.8
B	38.5	42.9	**42.3**	**38.5**	**42.4**	33.7	34.8	15.3
C	39.8	41.8	**42.1**	**38.9**	**42.8**	32.7	35.1	14.8
D	35.7	37.6	**30.9**	**41.3**	**30.7**	38.5	38.9	16.4
E	33.4	29.7	**38.2**	**42.7**	**41.3**	40.8	30.8	18.3
F	36.2	35.8	**35.8**	**39.8**	**40.7**	43.2	31.2	17.8
G	34.9	36.5	**37.3**	**43.5**	**42.6**	39.7	32.5	16.5
H	40.5	42.2	**40.1**	**40.6**	**47.3**	47.3	43.6	17.1
I	30.3	32.3	**41.4**	**40.9**	**39.7**	40.1	39.9	16.7

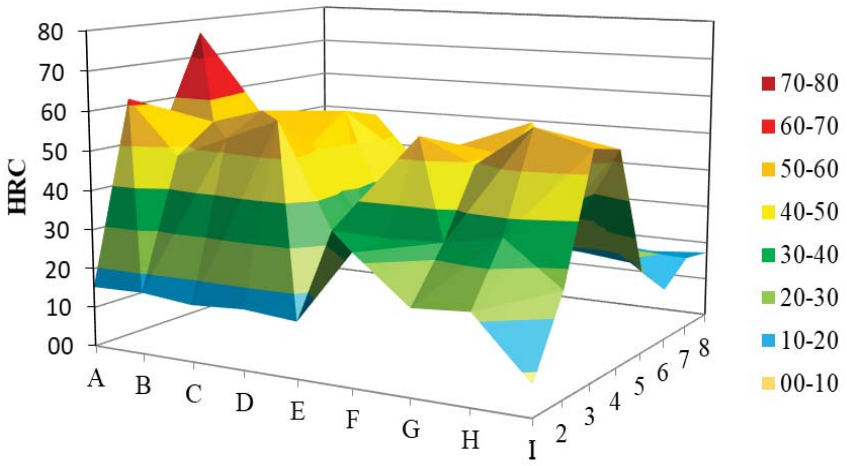


Figure 17: Hardness distribution of the C45 plate after tempering with the moving coil.

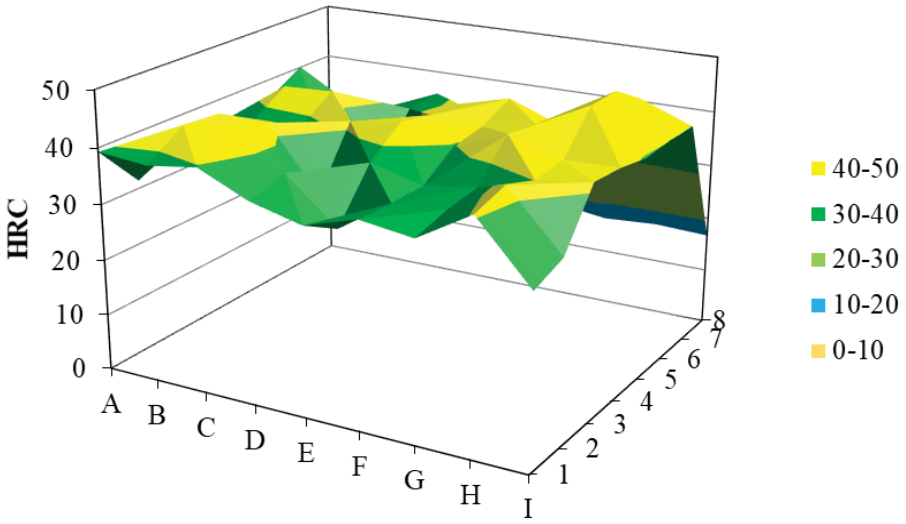


Figure 18: Hardness distribution of the SS400 plate after tempering with the moving coil.

Conclusion

In this study, an induction hardening process for flat surface carbon steel specimens was performed with both a stationary coil and a moving coil. A simulation method was applied to observe the temperature distribution and the moving speed of the coil. Then, the experiment was carried out with the same parameter as in the simulation. Based on these results, the following conclusions were obtained:

- *With the Stationary Coil*. C45 steel was tested. The result showed that the temperature was distributed on the ring area with a temperature of over 900°C, which is high enough for hardening steel. The hardness test showed that the tempering process increased the hardness of steel from 15 HRC to over 65 HRC within the ring area. Tempering has an influence on steel at a depth of 3.5 mm. The microstructure of steel was observed. This result showed that the martensite phase appeared at the ring area quite clearly. Both of the experiment and the

simulation show that when the stationary coil was used, the hardening effect was not as strong as in the ring area.

- *With the Moving Coil*. C45 and SS400 steels were used for testing. The result shows that hardness was increased in the testing area. This method improved the surface hardness of the plate from 15 HRC to 40 HRC in the SS400 steel and to 50 HRC in the C45 steel. In this case, hardness was quite uniform within a rectangular area.

References

[1] A. Bhateja. A. Varma. A. Kashyap. B. Singh. Study of the effect on the hardness of three sample grades of tool steel after heat treatment process. Int. J. Eng. Sci. 1 (2012) 253-259.

[2] B. L. Ennis. C. Bos. M. P. Aarnts. P. D. Lee. E. Jimenez-Melero. Work hardening behavior in banded dual phase steel structures with improved formability. Mater. Sci. Eng. A 713 (2018) 278-286.

[3] M. F. Hasan. Analysis of mechanical behavior and microstructural characteristics change of ASTM A-36 steel applying various heat treatment. J. Mater. Sci. & Eng. (2018) 2-6.

[4] M. S. I. N. Kamariah. W. S. W. Harun. N. Z. Khalil. F. Ahmad. M. H. Ismail. S. Sharif. Effect of heat treatment on mechanical properties and microstructure of selective laser melting 316L stainless steel. IOP Conference Series: Mater. Sci. Eng. 257 (2017) 1 – 11.

[5] Y. R. Ma. H. J. Yang. Y. Z. Tian. J. C. Pang. Z. F. Zhang. Hardening and softening mechanisms in a nano-lamellar austenitic steel induced by electropulsing treatment. Mater. Sci. Eng. A 713 (2018) 146-150.

[6] Y. Fu. J. Hu. X. Shen. Y. Wang. W. Zhao. Surface hardening of 30CrMnSiA steel using continuous electron beam. Nucl. Instr. Meth. Phys. Res. 410 (2017) 207-214.

[7] https://www.matbase.com/material-categories/metals/ferrous-metals/high-grade-steel/material-properties-of-high-grade-steel-c45.html

[8] http://www.steel-plate-sheet.com/Steel-plate/JIS/SS400.html

Design, Manufacturing and Testing of Magnetorheological Brake for Small Size Motorcycle

LE Duc Thang[1, a], NGUYEN Ngoc Diep[2, b], LE Duy Tuan[2, c], NGUYEN Ngoc Tuyen[2, d], PHAM Van Vinh[2, e], NGUYEN Quoc Hung[1,*]

[1]Faculty of Engineering, Vietnamese-German University, Binh Duong, Viet Nam

[2]Industrial University of Ho Chi Minh City, HCM, Viet Nam

[a]thang.ld@vgu.edu.vn, [b]pdiep66@yahoo.com, [c]leduytuan1986@gmail.com, [d]nguyenngoctuyen@iuh.edu.vn, [e] phamvanvinh.tcnntn@gmail.com

*Corresponding author: Mail: hung.nq@vgu.edu.vn, Tel: (+84)938485812.

Keywords: Magneto-rheological Fluid (MRF); MR brake; motorcycle, optimal design

Abstract. In this research, a new type of magneto-rheological brake (MRB) is proposed for small size motorcycle. The proposed MRB consists of a rotor with multiple trapezoidal teeth acting at multiple magnetic poles of the brake. In order to generate a magnetic field for controlling braking torque, a magnetic coil is placed on each side-housing of the brake. The inner face of each side-housing also has trapezoidal shape mating with the trapezoidal teeth of the rotor via MRF layer. By applying countercurrents to the coils, a magnetic fluid is generated with some magnetic flux going across the MRF layer (MRF duct) between the rotor teeth and their mating poles on the housing. By using multiple poles with trapezoidal shape, a high braking torque of the brake is expected while the size of the brake is still kept to be compacted. After an introduction about the development of MRBs in automotive engineering, the configuration of the proposed MRB is presented and its braking torque is derived based on Bingham rheological model of MRF. The proposed MRB is then optimally designed based on finite element analysis (FEA). Its optimized MRB is then manufactured and its braking performance is experimentally investigated. The MRB is then installed in a prototype motorcycle and the field test of this prototype motorcycle integrated with the MRB is then conducted.

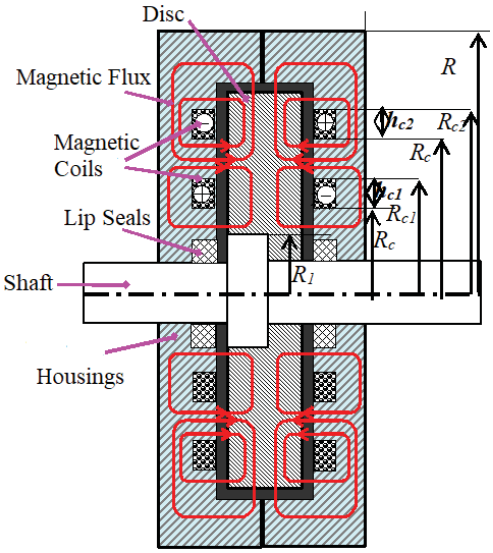
Introduction

In the past two decades, some studies in development and application of smart brake featuring magneto-rheological fluid (MRF) have attracted the attention of many researchers. The application for automotive vehicles or motorcycles is an interesting field in design MRB. Some researches on improving the performance of MRB for the above applications can be listed here. Park *et al.* [1] investigated a magneto-rheological brake design which is operated via a sliding-mode controller. Karakoc *et al.* [2] proposed the design considerations for building a feasible automotive MRB. Nguyen *et al.* [3] performed an optimal design of different disc-type MRBs considering the geometric volume and the off-state temperature constraints. After that, Nguyen *et al.* [4] proposed a hybrid MRB configuration for motorcycles which considered the radial and axial magnetic flux in order to increase its braking force and simultaneously decrease its mass. Although all abovementioned literature shows the high potential abilities of MRBs in automotive and motorcycle applications, the experimental results on examining their actual performance are still lacked. Recently, Nguyen *et al.* [5] designed a new MRB in which two magnetic coils is fixed on both sides of the MRB housings (in this work, it is called as double side-coil MRB). The optimal results showed that some disadvantages of the traditional ones such as the "bottle-neck" problem of magnetic flux, the nonmagnetic bobbin are required, and the difficulties in manufacturing and maintenance can be eliminated or minimized by using this configuration. In addition, the optimal solutions also performed that in providing the same braking torque, the mass of the double side-coil MRB was significantly improved in comparison with the conventional ones. Nevertheless, all of abovementioned MRB configurations just consider the disc which has the simple rectangular shape. Thus, in this study, the rotor which has a more complex profile created by many trapezoids is considered to apply to a typical MRB. Its MRB with a rotor having multiple trapezoidal teeth and multiple coils placed on the side housings is expected to provide the significantly better performance than the previous ones in the literature.

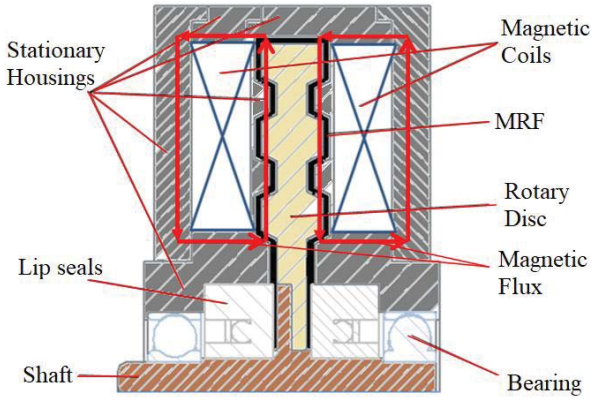
The remainder of the paper is displayed as follows. Section 2 shows the proposed multiple trapezoidal-teeth MRB with two coils placed on the side housings and some equations for estimating its braking torque. Section 3 presents the optimal design problem and the optimization procedure for the proposed MRB. Results and discussions are then described in section 4. Finally, some conclusions are performed in section 5.

The multiple trapezoidal-teeth MR brake with coils placed on the side housings

A configuration of an MRB with a rotor having multiple trapezoidal teeth and two coils placed on the side housing (in this research, it named as the multiple trapezoidal-teeth side-coil MRB) is proposed. Fig. 1a displays a typical double side-coil MRB and Fig. 1b presents the multiple trapezoidal-teeth side-coil one. Each abovementioned MRB has a disc (rotor) made of magnetic steel is fixed to the flange of the shaft made by nonmagnetic steel. The disc is also covered by a stationary envelope (housing) made of magnetic steel. In both two configurations, the coils are placed directly on side housing of the brake. As countercurrents are applied to the coils, a mutual magnetic field is generated to produce the braking force. It can be seen that the profile of the rotor and the inner housings in the case of the double side-coil MRB are rectangular while the respective ones in the case of the proposed MRB are made by some continuous trapezoidal contours. This trapezoidal-teeth profile makes the contact surface between the MRF and the disc increase; thereby, the induced braking torque of the multiple trapezoidal-teeth side-coil MRB is expected to increase notably.



(a) The double side-coil MRB



(b) The multiple trapezoidal-teeth side-coil MRB

Figure 1. Configurations of the double side-coil and the multiple trapezoidal-teeth side-coil MRBs

In order to calculate braking torque generated by the MRB, a small ring element in the inclined MRF gap as displayed in Fig. 2 is considered. The friction torque applied to this element can be evaluated as:

$$dT = r\tau \mathrm{d}A = 2\pi r^2 \tau \mathrm{d}l = 2\pi(R_1 + l\sin\varphi)^2 \tau \mathrm{d}l \quad (1)$$

Where r is the radius of the sloping small ring element with respect to the rotation axis of the MRB; R_1 and R_2 are respectively the radius calculated from the first end and the last end of the slope gap with respect to the rotation axis; L_a is the projected length of the slope gap with respect to the rotation axis; φ is the angle between the slope gap and the rotation axis; l is the length of the slope gap. In addition, the shear rate of MRF in the duct can be approximated as:

$$\dot{\gamma} = \frac{r\Omega}{d} \quad (2)$$

where Ω is the angular velocity of the disc.

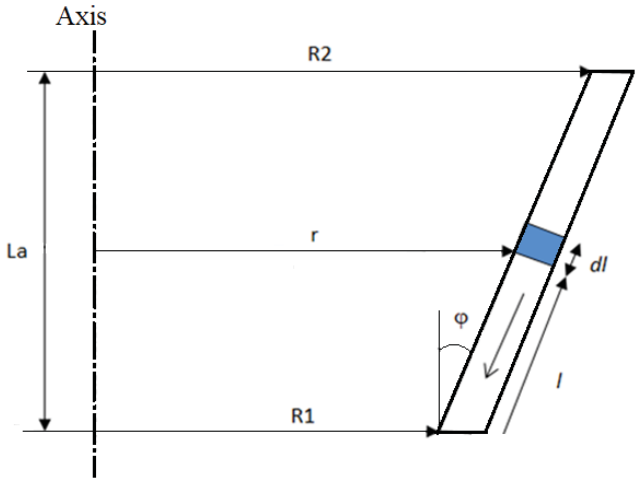


Figure 2. Annular ring element of MR fluid in the slope duct

The Bingham model of MRF along the axial direction can be expressed as:

$$\tau = \tau_y + \mu \frac{r\Omega}{d} = \tau_y + \mu \frac{\Omega(R_1 + l\sin\varphi)}{d} \tag{3}$$

where τ is the shear stress acting on the MRF; τ_y and μ_0 are respectively the zero-field yield stress and the viscosity of the MRF. Replacing some variables defined by Eqs. (2) – (3) to the corresponding ones in Eq. (1), the following equation is gained:

$$T = 2\pi \int_0^{L_a/cos\varphi} (R_1 + lsin\varphi)^2 \tau d = 2\pi \int_0^{l} (R_1 + lsin\varphi)^2 \left(\tau_y + \mu \frac{\Omega(R_1 + l\sin\varphi)}{d}\right) d$$

$$= 2\pi \left(R_1^2 l + R_1 l^2 sin\varphi + \frac{1}{3} l^3 sin^2\varphi\right) \tau_y + \frac{1}{2}\pi\mu \frac{l\Omega}{d} (4R_1^3 + 6R_1^2 lsin\varphi + 4R_1 l^2 sin^2\varphi + l^3 sin^3\varphi) \tag{4}$$

Fig. 3 shows the description for the division of the MRF ducts in order to estimate the total braking torque of MRB. The total braking torque is generated into three different kinds of the MRF ducts including the inclined gaps A1, A2, A3, A4 and A5, the annular gap C1 and the radial end-face gaps E1, E2, E3, E4, E5, and E6. Based on Eqs. (4) , the induced partial braking torque generated into each MRF duct can be estimated as follows:

$$T_{ve1} = \frac{\pi\mu_{e1} R_1^4}{2d} [1 - (\frac{R_i}{R_1})^4]\Omega + \frac{2\pi\tau_{ye1}}{3} (R_1^3 - R_i^3) \tag{5}$$

$$T_{ve2} = \frac{\pi\mu_{e2} R_3^4}{2d} [1 - (\frac{R_2}{R_3})^4]\Omega + \frac{2\pi\tau_{ye2}}{3} (R_3^3 - R_2^3) \tag{6}$$

$$T_{ve3} = \frac{\pi\mu_{e3} R_5^4}{2d} [1 - (\frac{R_4}{R_5})^4]\Omega + \frac{2\pi\tau_{ye3}}{3} (R_5^3 - R_4^3) \tag{7}$$

$$T_{ve4} = \frac{\pi\mu_{e4} R_7^4}{2d} [1 - (\frac{R_6}{R_7})^4]\Omega + \frac{2\pi\tau_{ye4}}{3} (R_7^3 - R_6^3) \tag{8}$$

$$T_{ve5} = \frac{\pi\mu_{e5}R_9^4}{2d}[1-(\frac{R_8}{R_9})^4]\Omega + \frac{2\pi\tau_{ye5}}{3}(R_9^3-R_8^3) \tag{9}$$

$$T_{ve6} = \frac{\pi\mu_{e6}R_d^4}{2d}[1-(\frac{R_{10}}{R_d})^4]\Omega + \frac{2\pi\tau_{ye6}}{3}(R_d^3-R_{10}^3) \tag{10}$$

$$\begin{aligned} T_{a1} &= 2\pi(R_1^2 l + R_1 l^2 \sin\varphi + \frac{1}{3}l^3\sin^2\varphi)\tau_{ya1} \\ &+ \frac{1}{2}\pi\mu_{a1}\frac{\pi}{d}(4R_1^3 + 6R_1^2 l\sin\varphi + 4R_1 l^2\sin^2\varphi + l^3\sin^3\varphi) \end{aligned} \tag{11}$$

$$\begin{aligned} T_{a2} &= 2\pi(R_3^2 l + R_3 l^2 \sin\varphi + \frac{1}{3}l^3\sin^2\varphi)\tau_{ya2} \\ &+ \frac{1}{2}\pi_{a2}\mu\frac{\pi}{d}(4R_3^3 + 6R_3^2 l\sin\varphi + 4R_3 l^2\sin^2\varphi + l^3\sin^3\varphi) \end{aligned} \tag{12}$$

$$\begin{aligned} T_{a3} &= 2\pi(R_5^2 l + R_5 l^2 \sin\varphi + \frac{1}{3}l^3\sin^2\varphi)\tau_{ya3} \\ &+ \frac{1}{2}\pi\mu_{a3}\frac{\pi}{d}(4R_5^3 + 6R_5^2 l\sin\varphi + 4R_5 l^2\sin^2\varphi + l^3\sin^3\varphi) \end{aligned} \tag{13}$$

$$\begin{aligned} T_{a4} &= 2\pi(R_7^2 l + R_7 l^2 \sin\varphi + \frac{1}{3}l^3\sin^2\varphi)\tau_{ya4} \\ &+ \frac{1}{2}\pi\mu_{a4}\frac{\pi}{d}(4R_7^3 + 6R_7^2 l\sin\varphi + 4R_7 l^2\sin^2\varphi + l^3\sin^3\varphi) \end{aligned} \tag{14}$$

$$\begin{aligned} T_{a5} &= 2\pi(R_9^2 l + R_9 l^2 \sin\varphi + \frac{1}{3}l^3\sin^2\varphi)\tau_{ya5} \\ &+ \frac{1}{2}\pi\mu_{a5}\frac{\pi}{d}(4R_9^3 + 6R_9^2 l\sin\varphi + 4R_9 l^2\sin^2\varphi + l^3\sin^3\varphi) \end{aligned} \tag{15}$$

$$T_{c1} = 2\pi R_d^2(b+2hh)(\tau_{yc1} + \mu_{c1}\frac{\Omega R_d}{d}) \tag{16}$$

The total braking torque is expressed by:

$$T_b = 2(T_{ve1}+T_{ve2}+T_{ve3}+T_{ve4}+T_{ve5}+T_{ve6}+T_{a1}+T_{a2}+T_{a3}+T_{a4}+T_{a5}) + T_{c1} + 2T_s \tag{17}$$

where T_s is the lip seal friction force which can be approximately evaluated by [6]

$$T_s = (f_c L_c + f_h A_r)R_s \tag{18}$$

In the above equation, T_s is the friction torque of a lip seal acting on the shaft of the MRB, f_c is the friction force per unit length of the shaft perimeter due to O-ring compression depending on the percentage of seal compression and the hardness of the O-ring material, L_c is the friction length of the inner face of the lip seals (shaft perimeter), f_h is the O-ring friction based on the fluid pressure applying to a unit projected area of the brake shaft, A_r is the seal projected area and R_s is the shaft diameter at the sealing.

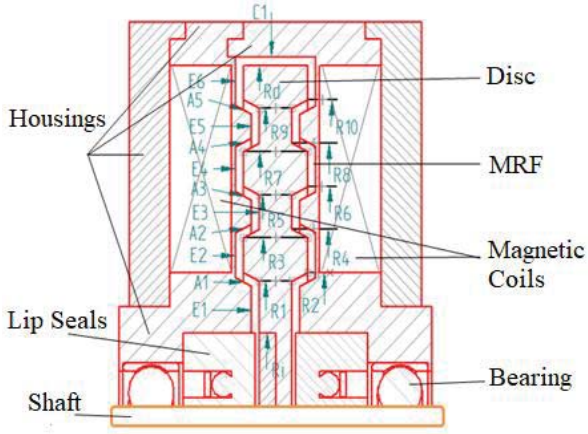


Figure 3. The division of MRF ducts for evaluating the braking torque

Optimal design of the proposed MRB

In this section, the optimization problem of the multiple trapezoidal-teeth, the double and the triple side-coil MRBs is considered for the small-sized motorcycles. It is noteworthy that the braking torque and the mass of MRBs are two important factors which their objectives are opposite. In detail, an MRB structure should be as small as possible in providing a required braking torque for minimizing its size and cost [5,8]. Therefore, in this paper, the objective of the MRB optimal design is to find the lightest MRB structure which can produce a critical braking torque for a determined small-sized motorcycle. Generally, the optimal design of MRBs can be expressed as [5,6,8]

$$\text{Minimize} \quad m_b = V_d\rho_d + V_h\rho_h + V_s\rho_s + V_{MR}\rho_{MR} + V_c\rho_c \tag{19}$$

$$\text{Subject to} \quad x_i^L \le x_i \le x_i^U,\ i = 1, 2 \ldots n$$

$$[T_0] \le T_b$$

where V_d, V_h, V_s, V_{MR}, $V_{bob,}$ and V_c are the volume of the disc, the housing, the shaft, the MRF, the bobbin and the coil of the brake, respectively; ρ_d, ρ_h, ρ_s, $\rho_{MR,}$ ρ_{bob} and ρ_c are the density of the discs, the housing, the shaft, the MRF and the coil material, correspondingly; x_i^L and x_i^U are the lower and upper bounds of the corresponding geometric dimensions of MRBs; n is the number of design variables; $[T_0]$ and T_b are respectively the required and the induced braking torque of the MRBs for a predetermined small-sized motorcycle.

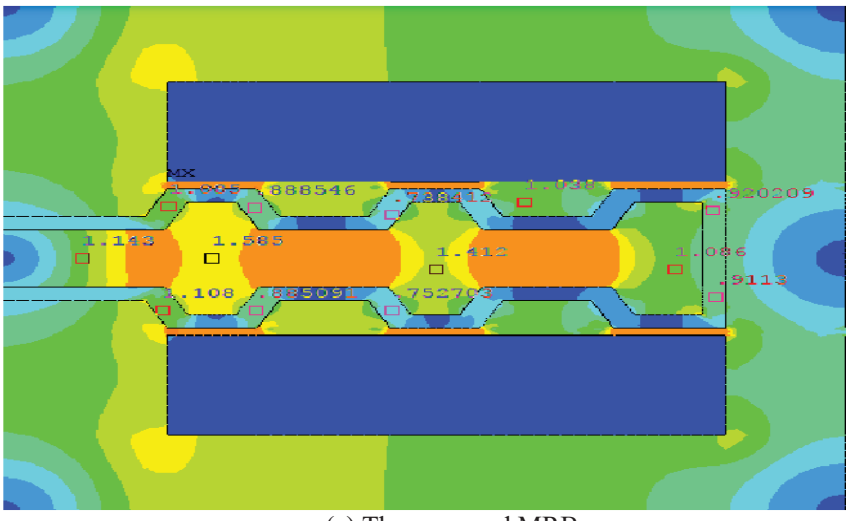
This section shows the optimal results of all abovementioned MRBs and some relative discussions are performed in detail. The magnetic components (the housing and the disc) of the MRB are made by the commercial steel C45. The MRF used in this study is MRF132-DG and its rheological parameters obtained by using curve fitting method from experimental results are shown as: $\mu_0 = 0.1pa \cdot s$; $\mu_\infty = 3.8pa \cdot s$; $\alpha_{s\mu} = 4.5T^{-1}$; $\tau_{y0} = 15pa$; $\tau_{y\infty} = 40000pa$; $\alpha_{sty} = 2.9T^{-1}$. The size of copper coil wires is 24-gage (diameter = 0.511mm) and its maximum working current is around 3A. However, in this research, a current of 2.5A is applied to the coil to investigate the MRB performance. In the optimal design problem, some important geometric dimensions of the MRBs such as the coil height (h_c, h_{cj}), the coil width (w_c, w_{cj}), the inner radius R_i and outer radius R_d of the MRF duct, the disc thickness t_d, outer radius of the brake R, the housing thickness t_h and the inner radius of the coils R_{ci} are considered as design variables. The required braking torque is 150Nm [4].

Table 1 shows the optimal solutions of the MRBs. In this table, it can be seen that the mass of the multiple trapezoidal-teeth side-coil MRB is significantly smaller than the double side-coil MRB.

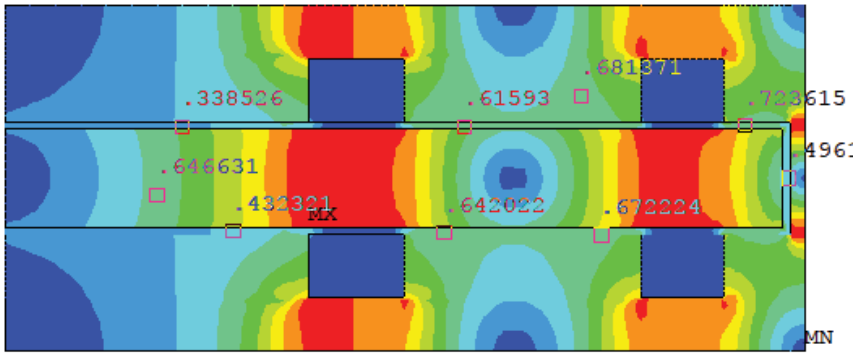
In detail, the optimal mass of the proposed MRB is 4.55kg while the ones of the double side-coil MRB is 12.47kg. In addition, the coil resistance in the case of the multiple trapezoidal-teeth side-coil MRB is the lowest (12.6Ω for the multiple trapezoidal-teeth side-coil MRB; 15.3Ω for the double side-coil MRBs); therefore, its power consumption is also smaller. Fig. 4 shows magnetic density distribution of the MRBs at their optimal configurations. It is observed that the magnetic distribution in the housing of the multiple trapezoidal-teeth side-coil MRB is more uniformed than that of two remaining ones.

Table 1 Optimal solution of the MRBs when the required torque is 150Nm

MRB types	Design parameter [mm]	Characteristics
Trapezoidal-teeth side-coil MRB	**Coil:** Width w_c=*7.7*; Height h_c,=24; No. of turns: 493 **Housing:** R_s=30, R=68.5, t_h=5, L=36.3 **Disc:** Radius R_i=32.5, R_d=63.5; Thickness t_d= 4.8 **MRF duct gap**: 1.0	**Max. Torque:** 150.06 [Nm] **Mass:** 4.55 [kg] **Total Coil Resistance:** R_c=12.6 [Ω]
Double side-coil MRB	**Coil:** Width w_{c1} =w_{c2}=*6.7*; Height h_{c1} =10; h_{c2}=8.7; No. of turns: 180 + 156 = 336 **Housing:** R_s=30, R=118.9, t_h=12.5, L=37.1 **Disc:** Radius R_i=32.5, R_d=116.4; Thickness t_d= 10.6 **MRF duct gap**: 1.0	**Max. Torque:** 150.42 [Nm] **Mass:** 12.47 [kg] **Total Coil Resistance:** R_c = 6.7 + 8.6 = 15.3 [Ω]



(a) The proposed MRB



(b) The double side-coil MRB

Figure 4. Magnetic flux density of the brakes at the optimum

Experimental results

To validate the precision of all above optimal results, the experiments should be performed to examine their actual performance. In this study, the prototype of the proposed MRB is manufactured based on the results which are shown in Table 1. The major parts of the prototype are shown in Fig. 5.

The experimental setup for testing the performance of the prototype is proposed in Fig. 6. A gear-box DC motor revolving the shaft of the MRB rotor at a constant angular speed of 19π *rad/s*. A force sensor is used to measure the acting load generated by the MRB. The analog output signal from the force sensor is then sent to the computer for evaluation. When the experiment process is stated, step current signals from the computer are transferred to the current amplifier. Various currents from 0A to 2.5A with a step of 0.25A are finally applied to the coils of the proposed MRB to create the braking forces.



Figure 5. prototype of the multiple trapezoidal-teeth side-coil MRB for experimental testing

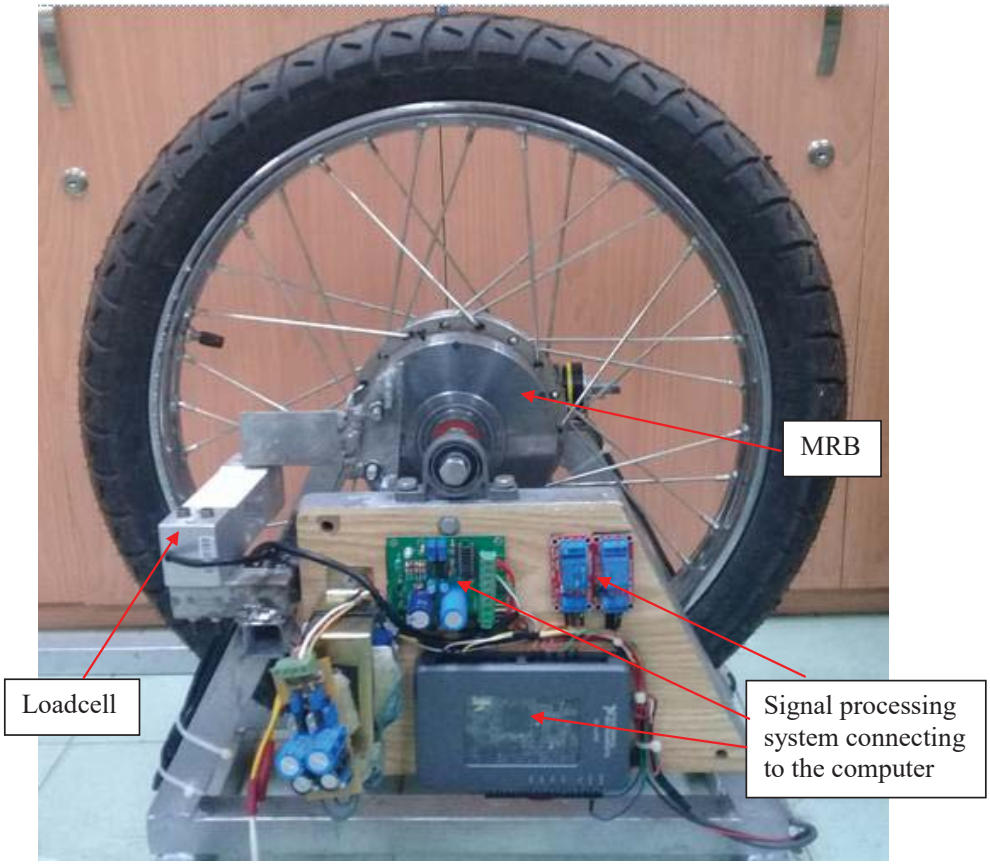


Figure 6. Experiment setup to test the performance of the prototype of proposed MRB

Fig. 7 shows step response of the multiple trapezoidal-teeth side-coil MRB prototypes at the step time of 0.5 sec with various currents from 0A to 2.5A being applied to the coils. It is realized that the response time of the induced braking torque also tends to increase with respect to the growth of the values of the applied currents. In detail, the response times in the cases of the current magnitude of 0.5A and 1A are respectively 0.3s and 0.4s; while those in the remaining cases are above 0.5s. In addition, the higher the current magnitude is, the greater the average value of torque will be. Fig. 8 shows braking torque of the MRB as a function of the applied current. The results show quite good agreement between the simulated and experimental results. The errors of the braking torque between the simulation and the experiment is around 11%. This error is mainly come from the coil filling ratio of the prototype, the loss of magnetic field to the ambient and at the contact between the magnetic parts of the MRBs. In addition, inaccurate estimation of the proposed MRBs can be also a potential reason.

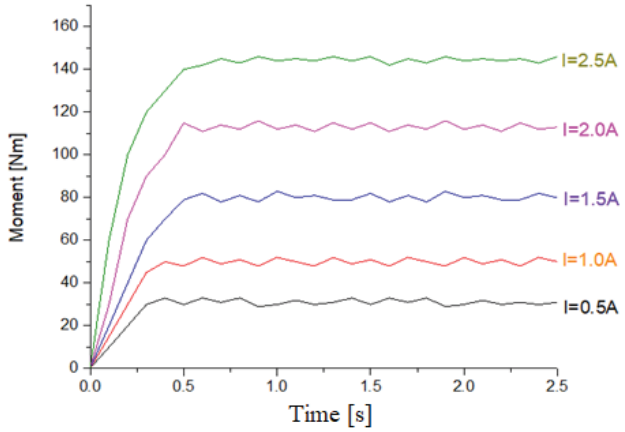


Figure 7. Step response of the proposed MRB

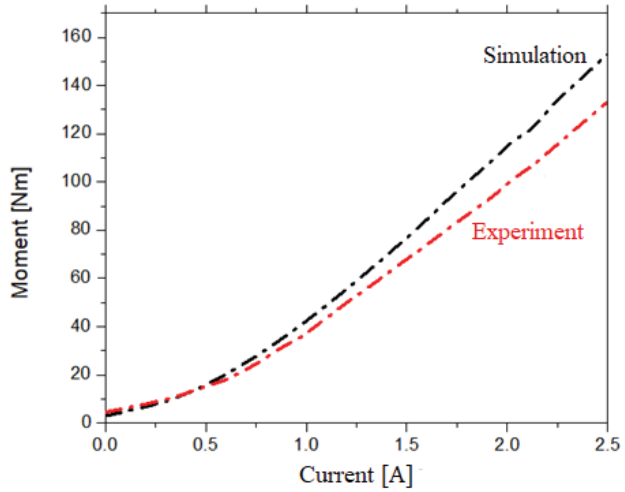


Figure 8. The braking torque of the proposed MRB as a function of the applied current magnitude

Conclusions

In this work, the MR brake with a rotor having multiple trapezoidal teeth and two coils placed on both side housings, which was referred as multiple trapezoidal-teeth side-coil MRB, was proposed and evaluated for the small-sized motorcycle application. Based on Bingham rheological model of the MR fluid, the braking torque of the proposed MRB was derived analytically. After that, the optimization procedure of three considered MRBs involving the multiple trapezoidal-teeth and the double side-coil was performed based on magnetic FEA module in ANSYS software. The optimal results showed that with the same braking torque constraint, the multiple trapezoidal-teeth side-coil MRB is significantly lighter than the double side-coil MRB. Moreover, the coil resistance in the case of the proposed MRB is also notably smaller which results in lower power consumption. Experimental solutions on the proposed MRB showed that the errors of the achieved braking torque between the analytical results and the experimental ones is around 11%, which agreed quite well with each others. As second phase of this research, a field test of the proposed MRB is conducted and heating, durability of the proposed MRB are considered.

Acknowledgement

This work was supported by the Vietnam National Foundation for Science and Technology Development (NAFOSTED) under grant no. 107.01-2016.32.

References

[1] E.J. Park, D. Stoikov, L. Falcao da Luz, A. Suleman, A performance evaluation of an automotive magnetorheological brake design with a sliding mode controller, Mechatronics **16** (2006) 405–416

[2] K. Karakoc, E. J. Park, A. Suleman, Design considerations for an automotive magnetorheological brake, Mechatronics **18** (2008) 434–47

[3] Q. H. Nguyen, S. B. Choi, Optimal design of an automotive magnetorheological brake considering geometric dimensions and zero-field friction heat, *Smart Materials and Structures* **19** (2010) 115024

[4] Q. H. Nguyen, S. B. Choi, Optimal design of a novel hybrid MR brake for motorcycles considering axial and radial magnetic flux, Smart Materials and Structures **21** (2012) 55003

[5] Q. H. Nguyen, N. D. Nguyen, S. B. Choi, Design and evaluation of a novel MR brake with coils placed on side housings, Smart Materials and Structures **24** (2015) 90590I

[6] Q. H.Nguyen, V. T. Lang, N. D. Nguyen, S. B. Choi, Geometric optimal design of a magneto-rheological brake considering different shapes for the brake envelope, Smart Materials and Structures **23** (2014) 15020

[7] M. Zubieta, S. Eceolaza, M. J. Elejabarrieta, M. M. Bou-Ali, Magnetorheological fluids: characterization and modeling of magnetization, Smart Materials and Structures **18** (2009) 95019

[8] D. T. Le, H. V. Ho, T. T. Nguyen and Q. H. Nguyen, A new design approach based on differential evolution algorithm for geometric optimization of magnetorheological brakes, Smart Materials and Structures **25** (2016) 125020

[9] Q. H. Nguyen, S. B. Choi, Optimal design of a vehicle magnetorheological damper considering the damping force and dynamic range, Smart Materials and Structures **18** (2009) 15013

[10] Q. H. Nguyen, Y. M. Han, S. B. Choi and N. M. Wereley, Geometry optimization of MR valves constrained in a specific volume using the finite element method *Smart Materials and Structures* **16** (2007) 2242–52

Researching on Measurement Strategies of Fuel Tank Corrosion Using Phased Array Technology

To Thanh Tuan[1, a *], Dang Thien Ngon[2,b]

[1, 2]Ho Chi Minh City University of Technology and Education, Viet Nam

[a]13252010306@student.hcmute.edu.vn, [b]ngondt@hcmute.edu.vn

Keywords: Fuel tank, corrosion, ultrasonic phased array, measurement strategy, robot.

Abstract. Measurement strategies for testing fuel tank corrosion using the ultrasonic Phased Array technology, these have been developed by companies producing ultrasonic measuring instruments, are only applied when performing manual measurement. Therefore, the applying of these measurement strategies for self-propelled robot carrying ultrasonic transducers to automate the testing process have not met the demand. This article presents the results of a study to develop a measurement strategy for testing fuel tank corrosion based on the specification of the self-propelled robot, the ability to build a corrosion map from collected image data by robot. Experimental results show that, with the three proposed measurement strategies using robot, the measurement strategy for moving the robot from bottom to top up will have the shortest testing time, image data are next and data coupling to build a corrosion map is easy. In addition, the process of building a corrosion map can be automatically perform on the computer, making the assessment process more convenient, accurate and faster.

1. Introduction

High capacity storage tanks play an important role in business and manufacturing activities of oil and gas field in term of maintaining and storing fuel. These fuel tanks are often manufactured by weld joints between metal sheet horizontally or vertically. After being operated for a period of time, the tanks should have quality checks periodically, especially their corrosion, in order to have a maintenance plan to ensure operation safety and supply fuel for the economy of the country.

Oil tank have meet corrosion defect in operating process under affecting by tank filling and emptying schedule. Corrosion occurs as general metal loss, pitting corrosion, localized corrosion adjacent to welds. Corrosion is caused by H_2O condensation, dissolved oxygen, chlorides and sulfates from atmosphere.



Figure 1. Examples of internal corrosion found to the steel of the tank including on welds [1]

Most tank corrosion inspections are primarily done by ultrasonic technology and perfromed manually. Therefore, the results depend much on technicians' level and mesuarement strategy [2]. In fact, technicians will localize areas where corrosion defect is likely to occur and carry out corrosion checks to have a direct assessment without building a corrosion map. In addition, the large size petrol tank needs to install a scaffold, remove and move to a new location after measuring a part of the tank body so it takes time.



a) Storage Tank inspection in Jakarta [3]



b) PAUT Corrosion Mapping for Column C-01 (Dinh Co GPP, Vietnam) [4]

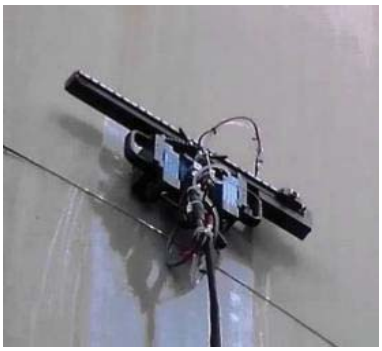
Figure 2. Manual tank inspection

The current ultrasonic technology still has some limitations:

- No corrosion map is built;
- Only produce a local assessment of the tank condition, not overall;
- Has high potential of unsafety and requires technicians with a lot of experience;
- Take long time to check and high cost.

In order to address these issues, some overseas NDT companies have recently applied robots to the process of tank corrosion inspections using ultrasonic technology. By localizing the areas likely to have corrosion, robots with ultrasonic probes will replace humans to test for these areas and be evaluated directly by technicians [5, 6].

However, how to build a corrosion map from the image data and corrosion map for the entire tank have not been paid much attention and there is not much information about this issue.



a) Robot Acctrak [5]



b) Robot Scorpion [6]

Figure 3. Tank inspections by robots in overseas

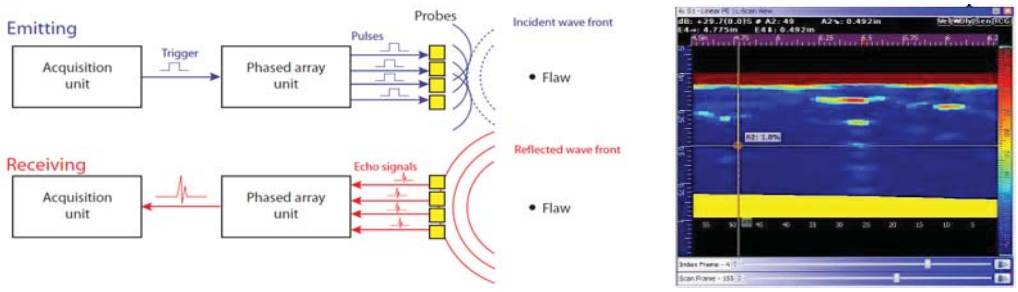
In Vietnam, building a corrosion map for a part of equipment or pipelines to monitor and assess the metal corrosion over time using the OmniScan MX2, Scanner, HydroFROM Probe, and Tomoview software is to determine the different thickness of the material due to the corrosion process in the form of images (maps). These strategy is applied on the ships, pipe systems (curve pipelines)... to determine accurately the corroded areas well as defects on the metal surface [7].

Besides, corrosion assessment for the gas pipelines of Ca Voi Xanh gas field (block 118, Vietnam) was performed in the laboratory using weight-loss method [8].

2. Theoretical background

2.1 Phased Array ultrasonic testing

To generate a beam in phase and with a constructive interference, the various active probe elements are pulsed at slightly different times. As shown in Fig. 4, the echo from the desired focal point hits the various transducer elements with a computable time shift. The echo signals received at each transducer element are time-shifted before being summed together. The resulting sum is an A-scan that emphasizes the response from the desired focal point and attenuates various other echoes from other points in the material [9].



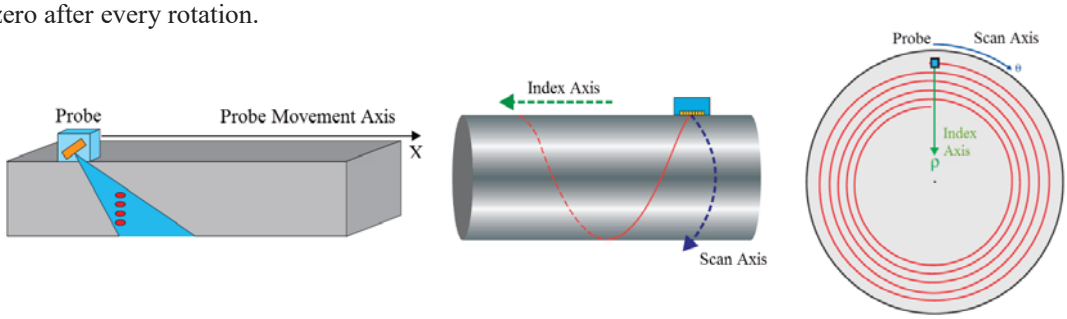
a) Principle *b) Corrosion map (Image form)*

Figure 4. Principle and Data of Phased Array Ultrasonic Testing [9]

2.2 Scanning patterns

The alternate move of Phased Array probe include [8]:

- Linear scan: a linear scan is a one-axis scanning sequence using only one position encoder to determine the position acquisition.
- Helical scan: the helical sequence is used to inspect cylindrical surfaces. The scanner performs a helicoidal movement around the cylinder.
- Spiral scan: the spiral sequence is designed to inspect circular surfaces such as disc surfaces. The inspection mechanism performs a spiral movement on the circular surface. Two independent encoders control the sequence. The scan-axis encoder controls the theta angle (θ) in the continuous rotation around the surface center; while the index-axis encoder controls the rho position (ρ) in the continuous movement along the radius. A signal can be used to reset the scan-axis encoder to position zero after every rotation.



a) Linear scan b) Helical scan c) Spiral scan

Figure 5. Scan patterns for probe characterization [9]

2.3 Corrosion mapping 2 axis encoded acquisition

When a scanner with 2 encoders is used, the A-scan and C-scan data is recorded to include the position on the scan and index axis.

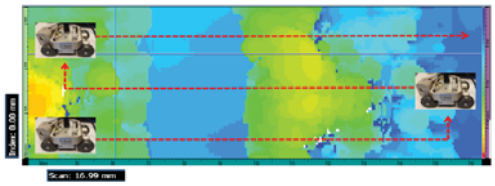


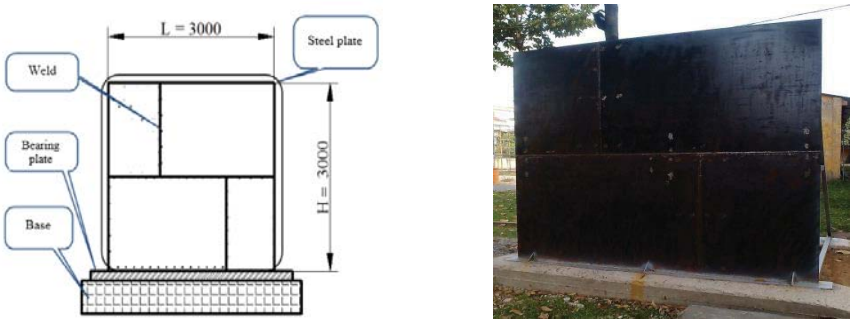
Figure 6. Data acquisition with two axis data [9]

3. Experiment and results

3.1 Experiment

3.1.1 Experimental model

A storage tank model is a very small part of a real tank (diameter 30 m, height 14 m). It is 3 m in length and 3 m in height (Fig. 7).



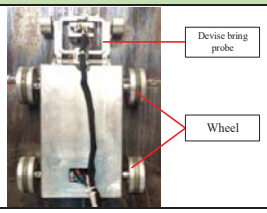
a) Storage tank model design *b) Storage tank model finish*

Figure 7. Storage tank model

3.1.2 The testing equipment

- OmniScan MX2 ultrasonic machine.
- 5L32-A31 probe.
- SA3-0L wedge.
- Figure form C-scan data.
- Robot with ultrasonic probe.

Table 1. Robot with ultrasonic probe [10]

Robot	Specifications	
	General dimension (DxR)	315×247 mm
	The force of permanent magnet	180 N
	Engine capacity	1,4 - 5,7 W
	Velocity	25 - 100 mm/s
	Revolution of wheel	6,6 - 26,8 rev/min

3.2 Recommendations for corrosion inspections

With the tank model and the size of the robot system with the ultrasonic probe, we can determine the scope which the robot will have corrosion checks [11, 12].

The width of the obtained data is equal to active probe length. The 5L32-A31 probe has a length of 32 mm but the active aperture is only 25 mm. The active aperture (A) = 25 mm is the total active probe length. Aperture length is calculated by the following equation:

$$A = n \times p \quad (1)$$

Where: + n: number of elements in the PA probe.
+ p: elementary pitch-distance between the centers of two adjacent elements.

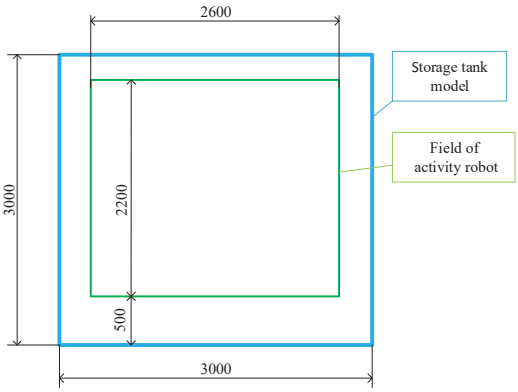


Figure 8. Working scope of robot on the tank

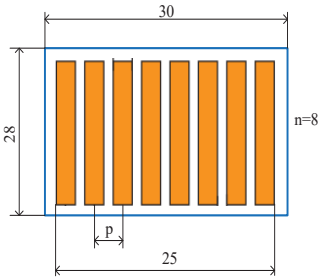


Figure 9. Probe parameters

3.2.1 The robot moving vertically from bottom to top

By using this strategy, the robot with ultrasonic probe is cotrolled to move vertically from bottom to top as shown in Fig. 10.

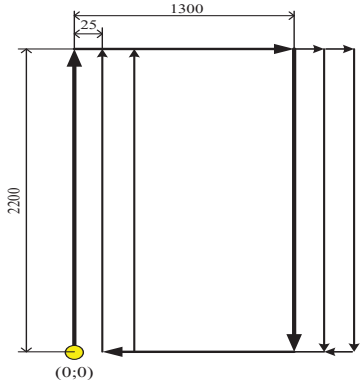


Figure 10. Vertical movement pattern of the robot

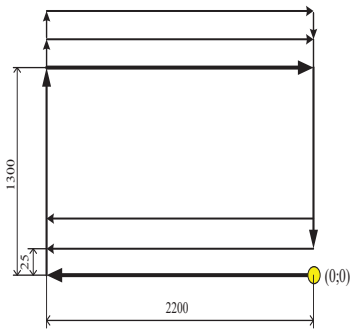


Figure 11. Horizontal movement pattern of the robot

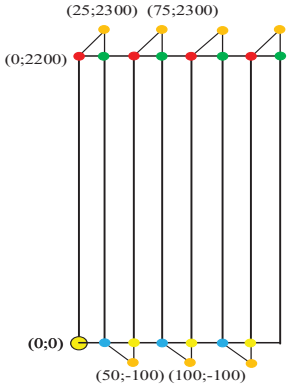


Figure 12. Vertical movement pattern of the robot from bottom to top and from top to bottom

How the robot works:

- From the initial position with the coordinates (0, 0) the robot with ultrasonic probe moves vertically at a distance of 2200 mm;
- At the coordinates (0, 2200) from the original position, the robot rotates 90 degrees to the right. Then, the robot continues to move horizontally with a distance of 1300 mm;
- At the coordinates (1300, 2200) the robot rotates 90 degrees in clockwise direction. Then, the robot moves downward with a distance of 2200 mm;
- At coordinates (1300, 0) the robot rotates 90 degrees in clockwise direction and continues to move horizontally to the coordinates (25, 0). At this point, the robot will be 25 mm away from the original position and end a cycle of robot activity;
- The robot will continue to move the next cycles in a similar way to the end of the tank length.

Disadvantages:

- The robot may slip when rotating 90°;
- It takes time for the robot to move horizontally;
- The stability of the robot is at medium level;
- It is difficult to determine the exact position of the image;
- The process of data collection is discontinuous;
- Difficulties in data integration;
- It is not possible to apply data integration software in building corrosion map.

3.2.2 The robot moving horizontally

With this strategy, the robot with ultrasonic probe moves horizontally to collect the data. The robot moves horizontally from bottom to top as shown in Fig. 11.

How the robot works:

- From the initial coordinates (0, 0) the robot with ultrasonic probe moves horizontally with a distance of 2200 mm;
- At coordinates (-2200, 0) from the original position, the robot rotates 90 degrees in clockwise direction. After that, the robot continues to move vertically at a distance of 1300 mm;
- At coordinates (-2200, 1300) the robot rotates 90 degrees in clockwise direction. Then, the robot moves horizontally at a distance of 2200 mm;
- At coordinates (0, 1300) the robot rotates 90 degrees clockwise and continues to move downward at a distance of 1275 mm to the coordinates (0, 25). At this point, the robot will be 25 mm away from the vertical position and ends a cycle of robot activity;
- The robot will continue to move the next cycles in a similar way to the end of the tank length.

Disadvantages:
- The robot may slip when rotating 90°;
- It takes time for the robot to move horizontally;
- The stability of the robot is at medium level;
- It is difficult to determine the exact position of the image;
- The process of data collection is discontinuous;
- Difficulties in data integration;
- It is not possible to apply data integration software in building corrosion map.

3.2.3 The robot moving vertically from bottom to top and from top to bottom

With this strategy, the robot with ultrasonic probe is controlled to collect data vertically by two-way movement: up and down. The robot moves from bottom to top, then from top to bottom as shown in Fig. 12.

How the robot works:

- From the initial position with the coordinates (0, 0) the robot with ultrasonic probe moves vertically at a distance of 2200 mm;
- At the coordinates (0, 2200) from the original position, the robot performs two movements: rotate and move to the coordinates (25, 2300);
- Then the robot rotates a 4 ° counter-clockwise and continue to move backward vertically from top to bottom with a distance of 2300 mm. At this time, the robot is 25 mm from the original position horizontally;
- At coordinates (0, 25) the robot performs two movements: rotate and move to the coordinates (50, - 100);
- Then the robot rotates a 4° clockwise. After finishing rotating movement, the robot continues to move vertically with a distance of 100 mm to the coordinates (50,0) which is 50 mm away from the original position horizontally and end a cycle of robot activity;
- The robot will continue to move the next cycles in a similar way to the end of the tank length.

Advantages:
- Spending less time when the robot moves;
- Robot can move flexibly;
- Reduce slipping during movement;
- The collected data is more accurate;
- More convenient in controlling robot;
- Easily locate the exact image.

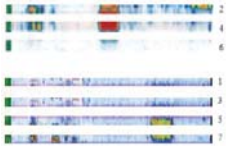
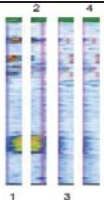
Disadvantages:
- Spending more time as the robot rotates.

3.3 Results

In order to evaluate the strategies above, we will carry out experiment for each one with data processing by experimental planning.

Conducting experiments to collect data with the equipment indicated for the three recommended strategies, the results of the experiments are presented in Table 2.

Table 2. Time and collected data pattern

Strategy	**1 (vertical movement)**	**2 (horizontal movement)**	**3 (bottom-up and top-down movement)**
Time	3h42m	3h42m	2h34m
Data pattern			

From the results of collected data in Table 2, we have the following comments:
- Collected data is stable;
- Option 1 is suitable for all three strategies;
- Option 2 can not be applied to strategy 1 and 2.

After gathering data for each strategy, the data is evaluated by two ways: 1-axis data integration in Table 3 and 2-axis data integration in Table 4.

Table 3. Evaluate option 1 (One-axis data integration for the three recommended strategies)

No	Compared criteria	Strategies		
		Strategy 1 (vertical movement)	**Strategy 2 (horizontal movement)**	**Strategy 3 (bottom-up and top-down movement)**
1	Data pattern	Data is performed vertically.	Data is performed horizontally.	Continuous data is performed vertically.
2	Data integration	Difficulties in data integration.	Difficulties in data integration.	Advantages in data integration.
3	Measurement time	Take more time for robot movement.	Take more time for robot movement.	Take less time for robot movement.
4	Level of data evaluation	Difficult to evaluate due to errors in data integration.	Difficult to evaluate due to errors in data integration.	Advantages to evaluate thanks to countinous data collection process.

Table 4. Evaluate option 2 (2-axis data integration for the three recommended strategies)

No	Compared criteria	Strategies		
		Strategy 1 (vertical movement)	**Strategy 2 (horizontal movement)**	**Strategy 3 (bottom-up and top-down movement)**
1	Data pattern	Not available	Not available	Collected data is continuity.
2	Data integration	Not available	Not available	Collected data is integrated automatically.
3	Measurement time	Not available	Not available	Take less time for robot movement.
4	Level of data evaluation	Not available	Not available	Building map is conducted automatically so it is convinient for evaluation process.

4. Conclusion

- The article has proposed 3 testing strategies using robots to measure the erosion level of gasoline tank using phase array ultrasonic technique: the robot moving vertically from bottom to top, the robot moving horizontally, the robot moving vertically from bottom to top and from top to bottom.
- Specific orbit of movement has been proposed to help robot to move easily and to obtain the image data completely (Fig. 12).
- An automatic data-coupling method based on the image-coupling function of the software on OmniScan MX2 ultrasonic machine that was proposed. Collected images are automatically processed and coupled to form a corrosion map for diagnostics and determine the erosion level of the tank.
- The testing strategy with the robot moving vertically from bottom to top and from top to bottom

that takes the shortest testing interval and helps image data to be obtained continuously and the data to be coupled to form the corrosion map easily.

References

[1] Paul Glister, Why is tank lining important?, Abfad Ltd, 2016,
Link: https://www.abfad.co.uk/editorial/why-is-tank-lining-important/

[2] Alobaidi W. M., Alkuam, E. A., Al-Rizzo H. M. and Sandgren E., Applications of Ultrasonic Techniques in Oil and Gas Pipeline Industries: A Review, American Journal of Operations Research, 5, 2015, pp. 274-287.

[3] SGS Industrial Services, Case Study - Storage Tank inspection in Jakarta Using Industrial Rope Access, SGS IND Oil and Gas, 10/2010.

[4] Alpha Inspection JSC, PAUT Corrosion Mapping for Column C-01 of PV Gas, Alpha NDT, 2015.

[5] AUT solutions, Acctrak, 2017. Link: http://www.autsolutions.net/ndt-products/automated-ndt-scanners/accutrak-automated-steerable-3-axis-scannertank-crawler-for-corrosion-mapping-weld-inspection-tofd-phased-array/

[6] Silverwing, Scorpion2, 2017 Link: http://www.silverwingndt.com/ultrasonic-testing/scorpion2-remote-ut-thickness-measurement.

[7] Phan Cong Thanh, Dang The Tung, Nguyen Dinh Dzung, Truong Quang Truong, Le Thi Hong Giang, Nguyen Thi Le Hien, Application of phased array technology on corrosion mapping for petroleum facilities, PETROVIETNAM Journal, Vol 5 - 2015, pp. 61-65.

[8] Le Thi Phuong Nhung, Nguyen Thi Le Hien, Pham Vu Dung, Le Thi Hong Giang, Nguyen Dinh Dung, Pham Thi Huong, Corrosion assessment for gas pipelines of Ca Voi Xanh gas field, PETROVIETNAM Journal, Vol 10 - 2017, pp. 43-49.

[9] Olympus, Introduction to Phased Array Ultrasonic Technology Applications, Advanced Practical NDT Series, Fourth printing, Olympus, 2017.

[10] To Thanh Tuan, Dang Thien Ngon, Nguyen Duy Anh, The study of proposal structure and control robot with ultrasonic probe for testing storage oil tank, National conference on machines and mechanisms 2015 (NCOMM 2015) Ho Chi Minh, VN, pp. 220-231, 2015.

[11] Philippe Rioux, Comparison Corrosion Mapping Solutions using Phased Array and Conventional UT Techniques, NDT in Canada 2015 Conference, 2015, 1-11

[12] Przemysław Magda, Tadeusz Stepinski, Corrosion Assessment Using Ultrasonic, Diagnostyka, Vol. 16, No. 1 (2015), 2015, pp. 15-17.

Influence of nitride hard coating on friction and soldering on surface of aluminum high pressure die casting core

Luu Thuy Chung[1,3, a *], Dinh Thanh Binh[2,3,b], Nguyen Thi Phuong Mai[3,c] and Pham Hong Tuan[4,d]

[1] Vinh University of Technology, No.117 Nguyen Viet Xuan, Vinh city, Nghe An province, Vietnam

[2] *Defense industrial college, Thanh Vinh, Phu Tho, Phu Tho, Viet Nam*

[3] *Hanoi University of Science and Technology, No. 1, Dai Co Viet, Hai Ba Trung, Hanoi, Viet Nam*

[4] *National Center for Technological Progress, C6-Thanh Xuan Bac, Thanh Xuan, Ha Noi, Viet Nam*

[a] lthuychung@gmail.com, [b] thanhbinh2183@gmail.com, [c] mai.nguyenthiphuong@hust.edu.vn, [d] phamhongtuan1@yahoo.com

* Corresponding author: Tel.: (+84) 98.234.1350

Keywords: Mold release work, average friction force, nitride hard coating, soldering.

Abstract. Wear and soldering are the two common failure types of high pressure die casting molds. Surface treatment solutions are often offered to limit these two forms of failure. In this study, the authors compare the average frictional force occurring when the die casting core is removed from the aluminum block to evaluate the effect of the chromium nitride and titanium nitride coating on the friction properties of the mold surface. Experience has shown that hard nitride coating significantly reduces the friction between the core and castings by aluminum alloys as well as significantly reduces the amount of adhesive applied on the mold surface. The experiment also showed that the coating of chromium nitride also reduced the level of damage to the core surface in real working conditions.

Introduction

Friction is the property that always exists between the contact surfaces. The friction between the surfaces with relative motion greatly affects their abrasion during work. Researches show that friction depends on the velocity of the slide, the pair of friction materials, the normal force on the surfaces [1, 2].

Erosion, corrosion / adhesion, thermal cracking and mold breakage are all major failures of High Pressure Die Casting (HPDC) dies [3, 4, 5]. Study [6] has shown that, HPDC mold's material should be non-wetted with molded materials, wear and corrosion resistant, and some other properties. In order to increase the working capacity of the HPDC molds, a number of surface treatment methods, especially hard coatings, have been applied to the mold surface [5, 6]. This study evaluated the effect of chromium nitride and titanium nitride hard coating to friction and adhesion of the high pressure die casting mold core surface with aluminum alloy.

The force to release product out from the mold after molding process, the products in the metal mold needs to be greater than the friction between the molded product and the mold (or core) and the adhesion of the metal molded to the mold surface. When releasing the mold in vertically direction, the normal force on the mold surface does not include the gravity of the casting but only the elastic force due to the thermal expansion of the casting. Under the same casting conditions, it is possible to view this pressure as a constant quantity. Equation 1 shows the relationship between surface forces, friction coefficient and sliding friction between surfaces.

$$F = \mu.N \quad (1)$$

where N is the normal force, μ is the coefficient of friction and F is the friction force.

When the molten metal is poured into the mold, wetting of the mold surface occurs, so that the surface of the mold product and the mold surface reach a state of sufficiently small distances to show adhesive strength. The process of pulling the sample takes 2 steps. In the first stage, the force increases linearly, in this period there is no relative motion between the casting product and the molding surface, the bonding force in this period is mainly the adhesion force. The second stage takes place after the release force reaches its maximum value, the force drops rapidly and reaches a steady state. During this period, the shear force is the friction force between the casting and mold surface.

The energy of the motion processes are expressed as in the equation 2 or can be calculated as equation 3 with small enough steps.

$$A = \int_{x_0}^{x_n} \vec{F} d\vec{x} = \int_{x_0}^{x_n} F dx \tag{2}$$

$$A = \int_{x_0}^{x_n} F dx \approx \sum_{i=1}^{n} \frac{1}{2} \left(F_{i-1} + F_i\right)\left(x_i - x_{i-1}\right) \tag{3}$$

Where A is the mechanical work of the mold release process, F is the friction force, x_i is the displacement of the component during the pulling process at time i.

By the above equation, it is possible to derive the average friction force as the equation 4.

$$\overline{F} = \frac{A}{\Delta x} \approx \frac{\sum_{i=1}^{n} \frac{1}{2} \left(F_{i-1} + F_i\right)\left(x_i - x_{i-1}\right)}{x_n - x_0} \tag{4}$$

By evaluating the extrusion force, average friction and adhesive force, we can evaluate the wear resistance of the mold surface during work.

In the same condition work, the core of mold usually hotter than mold wall and it usually stand in the flow of liquid metal, so it was often the faster damage part of the mold. Besides, the core is easy to manufacture and measure, so in the experiment, we usually use the core in the experiment.

Experiment

1. Samples

Table 1 shows the components of SKD61, the material that is used in the mold halves and cores to cast the product as shown in Fig. 2. The experimental samples are the cores in high pressure die casting that used to create holes for aluminum alloy products as shown in Fig. 2. Fig. 1 is the drawing of the core.

Table 1: Components of SKD61

Component	C	Si	Mn	S	Cr	Mo	V
Percent	0.32-0.42	0.8-1.2	≤0.5	0.12	4.5-5.5	1.0-1.5	0.8-1.2

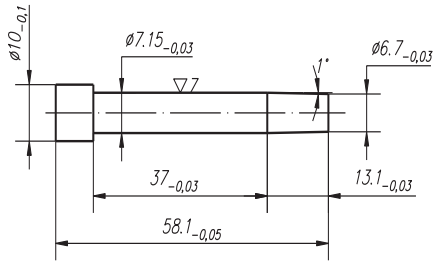


Figure 1. Drawing of the core



Figure 2. Products after molding process (has 6 details)

Number of samples: 03 samples. The 1st sample (Sample No. 26) is no coating layer SKD61, the second sample (Sample No. 22) is coated by TiN and the 3rd sample (Sample No. 17) is sample that coated by CrN. Both of two thin film are made by pulsed DC magnetron method in the same device B30 by Centre for optoelectronics, National Center for Technological Progress, Vietnam.

These core samples are mounted vertically in the graphite cup and poured liquid aluminum and then solidified. Release force is measured by releasing the core samples from the aluminum block.

2. Results and discussions

2.1. Mold release force. Release force shown as Fig. 3 shows that the uncoated sample (sample No. 26) had the largest extrusion force, 1831.87 kgf, while the extrusion force in the other two cases was smaller and approximately equal, 1208.23 kgf for the CrN coated sample and 1224.48 kgf for the TiN coated sample.

Before reaching the maximum point, the bonding force between the product and the core includes friction and molecular forces. This force is much greater than the pure friction between the product and the core. When the traction reaches its maximum value, it mean that the bonding force reaches the maximum value, so the bonding force is not sufficient to hold the position between the two components and start moving. At this time the molecular link forces are broken, the pair of molded parts and cores have only pure friction. Fig. 3 shows that after reaching the maximum point, the nitride coated core has a rapid pull-down force while the uncoated sample has a slower pull force and is maintained at a higher level in the case of overlaying, which demonstrates that the force In the case where the core sample is not covered higher than in the case of coated core samples.

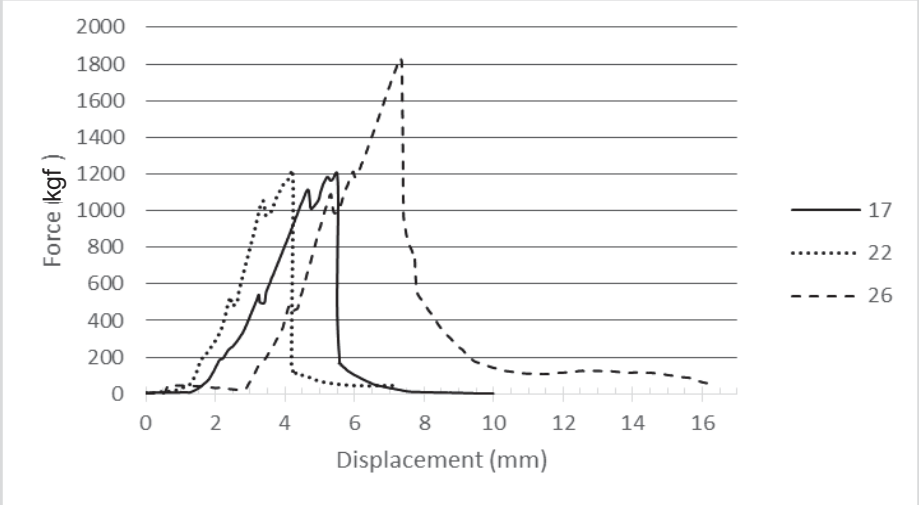


Figure 3. Force-Displacement chart during mold release

Mechanical energy of mold release in three cases is shown as Fig. 4, 5, 6. These three figures show that the mold release energy is mainly made for breaking the adhesive between the mold product and the core. Applying equation 3, release energies are calculated and drawn by the chart in the Fig. 7.

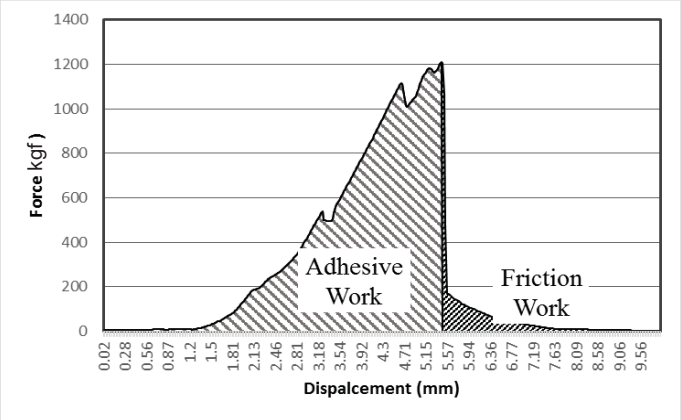


Figure 4. Release work for CrN coated sample

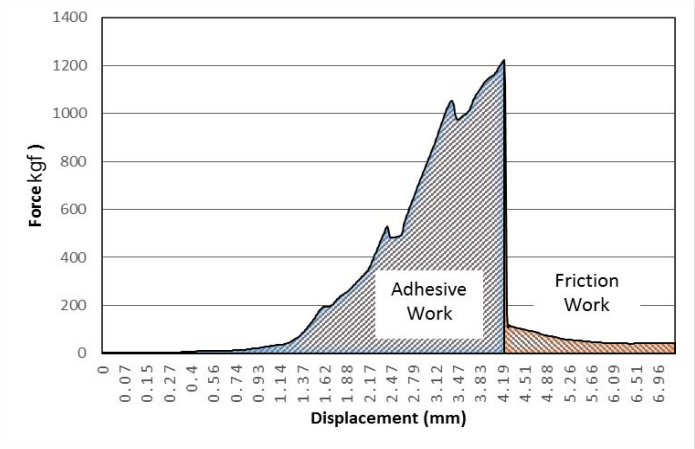


Figure 5. Release work for TiN coated sample

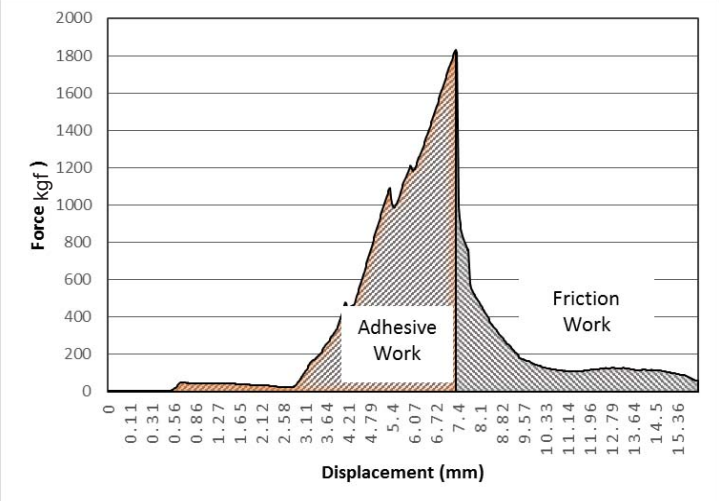


Figure 6. Release work for non-coated sample

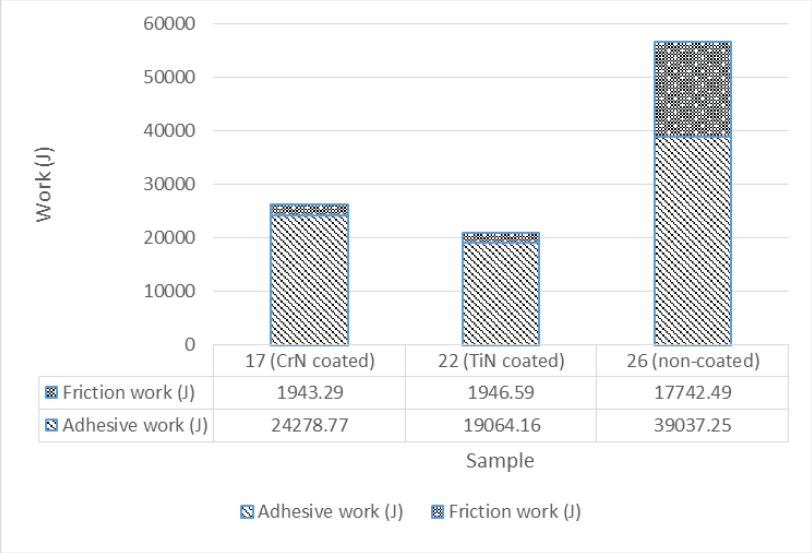


Figure 7. Compare the work of mold release in the cases

Based on analysis the above chart, it was found that nitride coated samples' mold release energy were approximately equal and relatively small compared to uncoated sample. Applying average friction equation 4, the average friction between the cores and the casting products (excluding the molecular linkage) of the nitride coated samples was 429.9303 N (CrN coated sample) and 632.01 N (TiN coated sample) are also very small compared to the non-coated model with an average force of 2009.343 N.

From the above experimental data, we can confirm that the nitride coating reduces the friction between the molding material and the mold surface, which would reduce the surface abrasion of the mold compared to the case. [1, 2, 7].

2.2. Evaluation of mold soldering. Figure 8 is the core sample images after pulling out of the aluminum block. Observation of both front and back sides of samples showed that the uncoated core had aluminum scales occupying most of the surface, while the coated core had much less aluminum on the surface. It can be asserted that the nitride coating can limit the type of defects caused by the adhesive on the mold surface. This result is consistent with previous study [6].



Figure 8. Samples after removing the mold with aluminum scales on the surface
a) front side, b) back side, c) details of soldering
c-1. Non-coated, c-2. TiN coated, c-3. CrN coated

2.3. Evaluation of mold wear and soldering in real test. As above analysis, nitride hard coating can be wear and soldering resistance. But titanium nitride is oxidized in high temperature, so TiN cannot be used in HPDC mold that used to cast the high molten temperature materials. The molten

temperature of aluminum is higher than working range temperature of TiN, so in this real test, we don't use TiN coated sample. To estimate the effect of nitride hard coating to mold wear and soldering, we put a pin that is coated by CrN in a mold as shown in the Fig.9. After about 50000 cycles, when there are some serious fails occurs in products the casting process stopped, we use microscope to measure and capture the surfaces of 2 pins, which are the nearest to the gate as shown in the Fig.9. Fig.10 illustrates the pictures of CrN coated pin's surface and non-coated pin's surface after 50000 cycles of real casting. Fig. 11 is the picture of the worn out of the non-coated pin's surface after it's damaged and Fig.12 is the picture of the CrN coated pin's worn out on the surface after the same working time.

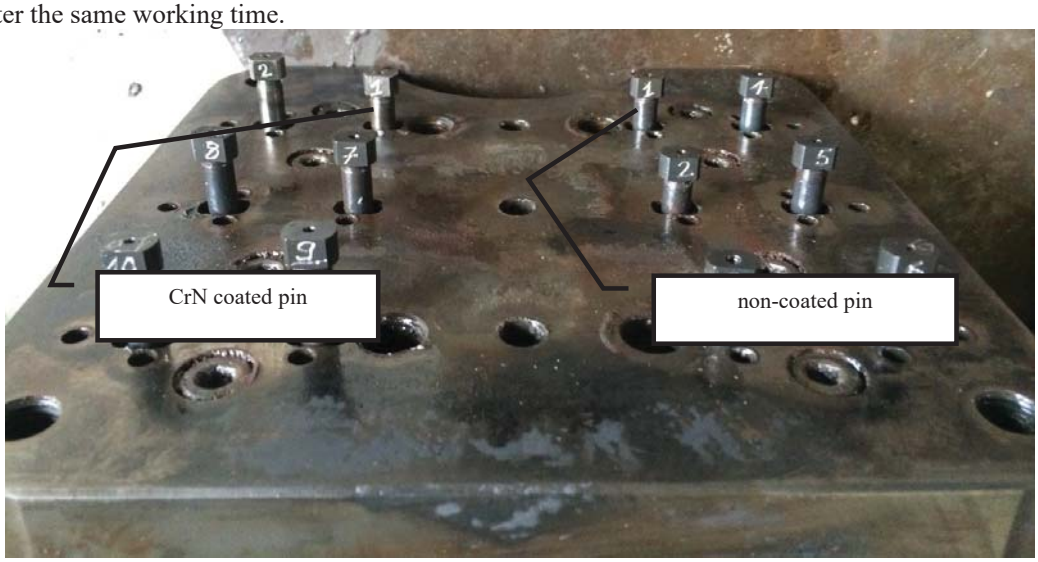


Figure 9: Pins in the real metal mold to cast

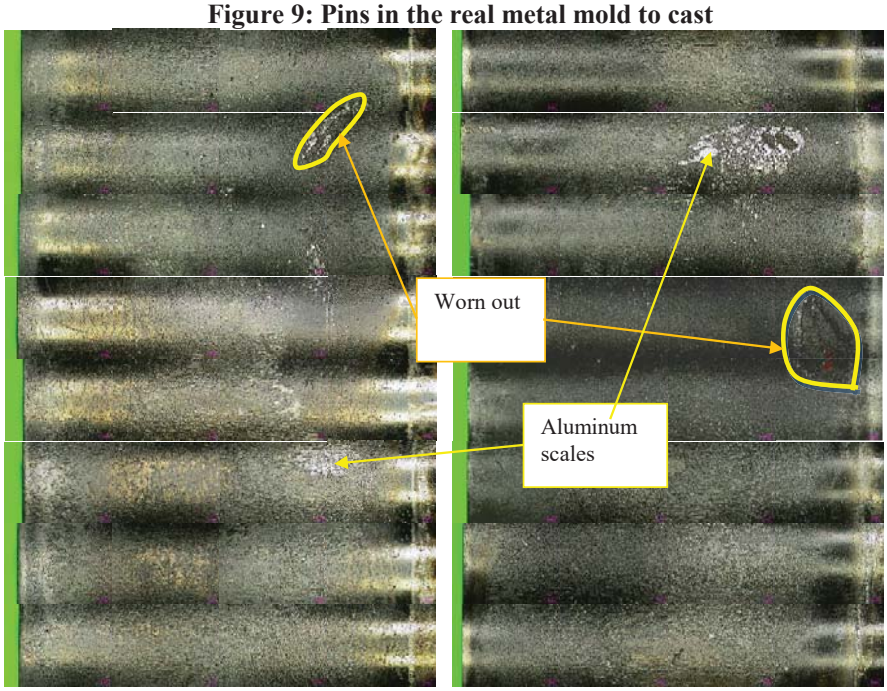


Figure 10: Pictures of pins' surfaces after 50000 cycles.



Figure 11: Non-coated core's worn-out after 50000 cycles



Figure 12: Chromium nitride coated core's worn-out after 50000 cycles

Figure 10 shows the comparing of coated and non-coated cores' surface after the same working time, the welded aluminum scraps on the uncoated core surface are more clearly and larger than on the CrN coated core. Wear on uncoated core is also much larger than on coated core. Figure 11

shows the wear on uncoated core up to 2.4mm in length and 1.53mm in width while Fig.12 shows the worn-out on the CrN coated core's surface with 1.86mm in length and 0.59mm in width.

Conclusions

Hard nitride coatings affect the friction and adhesion of aluminum alloy die casting surface.

- Hard nitride coating significantly reduces the removal force from over 18000 kgf to about 12000 kgf.
- The average friction force of the core covered with chromium nitride is smaller than the average friction force of the titanium nitrided core and is much smaller than the uncoated core.
- Nitrite hard coating significantly reduces the amount of aluminum scale that adheres to the core surface after casting from over 80% of the surface to ~50% with CrN coated core or less than 50% with TiN coated core.
- The real test shows that the damage of non-coated core is heavier than CrN coated core in the same working time.

References

[1]. Nguyễn Anh Tuấn, Phạm Văn Hùng, Ma sát học, nhà xuất bản khoa học và kỹ thuật, Hà Nội, 2007
[2]. Bharat Bhushan, INTRODUCTION TO TRIBOLOGY – 2nd edition, A John Wiley & Sons, Ltd., Publication, 2013
[3]. Đinh Ngọc Lựa - Kỹ thuật đúc – NXB KHKT, 1980
[4]. Z.W. Chen, M.Z. Jahedi – Die erosion and its effect on soldering formation in high pressure die casting of aluminum alloys – Materials & Design – April 1999
[5]. R. Shivpuri, Y.-L. Chu, K. Venkatesan, J.R. Conrad, K. Sridharan, M. Shamim, R.P. Fetherston – An evaluation of metallic coating for erosive wear resistance in die casting applications – Wear 192 (1996)
[6]. J. Lin, S. Carrera, A.O. Kunrath, D. Zhong, S. Myers, B. Mishra, P. Ried, J.J. Moore, Design methodology for optimized die coatings: The case for aluminum pressure die-casting, Surface & Coatings Technology 201 (2006) 2930–2941
[7]. Nguyễn Trọng Hiệp – Chi tiết máy – NXB Giáo dục, tập 1 – 2006

Applied Studies on Material of Biocomposite Biological Origin Prepared from Oxide Nano and Biogum (Extracted from Osaka Seeds (Cassia Fistula Linn)) for the Treatment of Methylene Blue

Dao Minh Trung[1a*], Pham Mai Ly[1b], Nguyen Vo Chau Ngan[2c]

[1]Thu Dau Mot University, Binh Duong province, Viet Nam

[2]Can Tho University, Can Tho City, Viet Nam

[a]moitruongviet.trung@gmail.com, [b]mt.lypham@gamil.com, [c]nvcngan@ctu.edu.vn

* Dao Minh Trung

Keywords: color treatment, Gum OH nano, materials of biological origin, methylene blue, Nano Gum, treatment efficiency

Abstract. Researching on Methyllen Blue dye treatment ability with Nano material ($CoFe_2O_4$ synthesized by co-precipitation method) combined with Biogum (extracted from Osaka Seeds (*Cassia Fistula Linn*). Research results show that with Biogum base material fully covered by magnetic nanoparticles of size 70 - 95 nm (SEM) and the presence of several specific functional groups for biogum and ferromagnetic oxide nano (FT-IR). When adding OH group to nano material, the adhesive ability to biogum and the size of the particle does not change. Results of comparative studies on the application of Nano-Biogum and Nano-OH-Biogum materials showed that when studying the dyeing color of Methylene blue, the treatment efficiency is from 62.43 to 78.72%, decreasing from 349.67 Pt-Co, 74.41 Pt-Co at pH 6 - 7 and dosage at 1.5 g/L. Based on the above results, Nano - Biogum is able to treat dyeing color better than Nano OH - Biogum. Therefore, Nano - Biogum can become suitable material for the application of color treatment in practice.

Introduction

Dyeing textile industry is one of the chemical industry contains many pollutants discharged after several dyeing phases [1]. Wastewater from the dyeing process is discharged with relatively high color [2], [3], [4]. According to color research [2], it is capable of obstructing light and slow down the process of photosynthesis, inhibiting the growth and reproduction of organisms as well as tend to generate metal chelate ions causing toxic to bacteria in the water. Therefore, the direct discharge into areas such as rivers, lakes... not only affect the entire ecosystem in the water [5] but also affect the lives of the people in the neighborhood [2], [4].

Currently, many materials of biological origin used in dyeing textile wastewater treatment such as activated carbon [6]; wheat; fly ash, zeolite clay, unburnt carbon [8], in addition to current Biogum extracted from osaka seeds (Cassia fistula linn) is being studied and applied widely in many fields of wastewater [9], etc. materials are being used instead of the physical methods or chemical previously used because such materials are capable of completely biodegradable without generating any toxic ingredient [10], [11], low cost, easy to use, easy to operate and high treatment efficiency [12].

Research on using Nano Gum and Nano OH Gum prepared from Cassia fistula seeds [13] and ferromagnetic oxide nano [14] to examine the methylene blue treatment efficiency in dyeing textile wastewater.

Research methodology

Research means

- Research object: Methyllen Blue ($C_{16}H_{18}ClN_3S.3H_2O$, China) with concentration of 25 mg/L.

- Research Chemicals: $CoC_{l2}.6H_2O$ (China, 99%); $FeC_{l2}.4H_2O$ (China, 98%); NaOH (China, 96%), SDS (India, 85%); Cassia fistula seeds (collected from Huynh Van Luy street, the New city, Binh Duong province); n - hexane (China, 97%); C_2H_5OH (China, 99.7%); NH_4OH (China, 25 - 28%); $(CH_3)_2CO$ (China, 95%), HCl (1M - China), NaOH (1M - China).
- Researched materials: Nano Gum and Nano OH Gum are prepared from Cassia fistula seeds [13] and ferromagnetic oxide nano [14].
- Research device: Jartest.

Research method

- Determination of pH is measured directly using pH Meter Toledo (2017).
- Determination of color in accordance to Vietnamese standard of TCVN 6185:2005.
- Determination of particle size by scanning electron microscope (SEM).
- Determination of functional groups in molecules by the equipment of Fourier Transformation Infrared Spectrometer (FT-IR).

Experimental layout

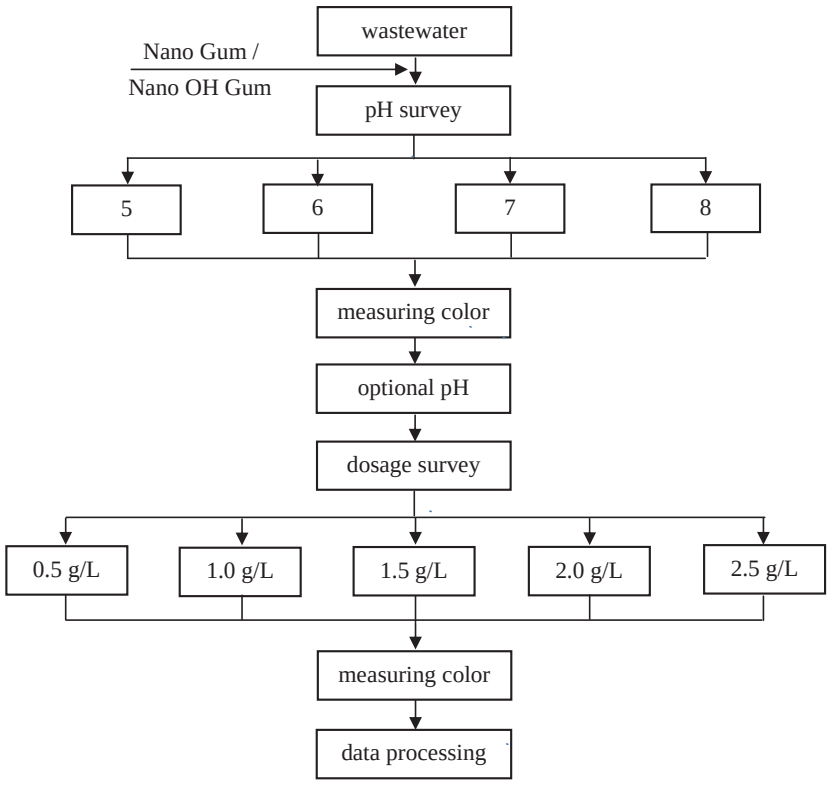


Fig. 1 Methylene Blue processing experiment layout with two types of materials, Nano - Nano biogum and OH – biogum

Results and discussion

Material preparation results

Survey results of particle size (SEM)

According to SEM results obtained in Fig. 2 (a) and (b), MHY gum material is observed with a rough, dry surface. According to research [15], it has been shown that biogum is readily dispersible

in water and has the ability to bind with water rather strongly to produce high viscosity materials that increase adhesion to contaminants. In addition, according to research results that biogum is a type of natural conglomerate, so they are able to decompose from the 2nd day at high humidity.

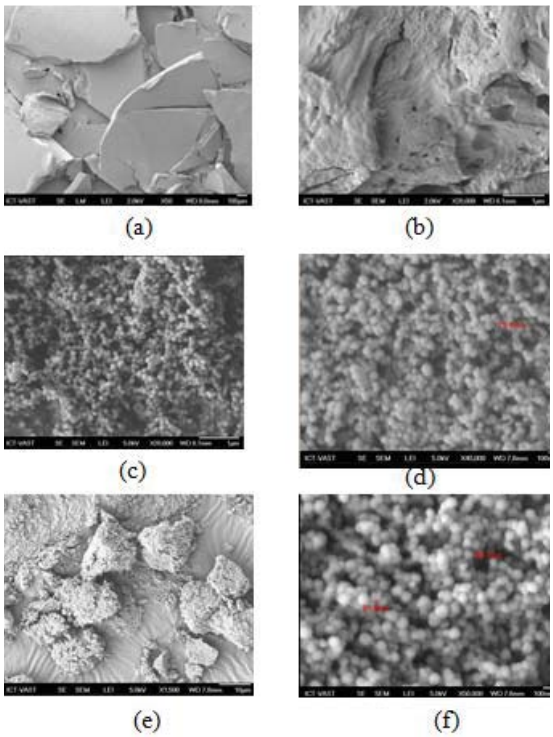


Fig. 2 SEM images of the material
(a), (b): biogum material; (c), (d): magnetic nano; (e), (f): Nano-Gum Materials

The Fig. 2 (c) and (d) shows ferromagnetic oxide nano is highly porous with the connection between the particles quite dense and relatively similar in size with the diameter of particles from 70 - 95 nm. But this size is still much larger than some other studies such as the study of [16] and [17] synthesized by the method of micro-emulsion obtained mixed particles $CoFe_2O_4$ with size of 13 nm. The seed size is 15 - 48 nm but it is the same size with the study of [18]. According to summary from multiple studies, the size of ferromagnetic oxide nano particles depends on many factors such as pH, salt concentration, temperatures, stirring speed, concentration of SDS [19].

For Nano - Biogum material, in Fig. 2 (e) and (f), it is shown that nanoparticle size is unchanged and highly porous clinging around Biogum bases material forming a rigid cohesive block. Because the particles bind to Biogum thickly, gravity of the particles is decreased markedly. Thereof, it shows that the solid binding ability between the nanoparticles and biogum may increase the material treatment ability.

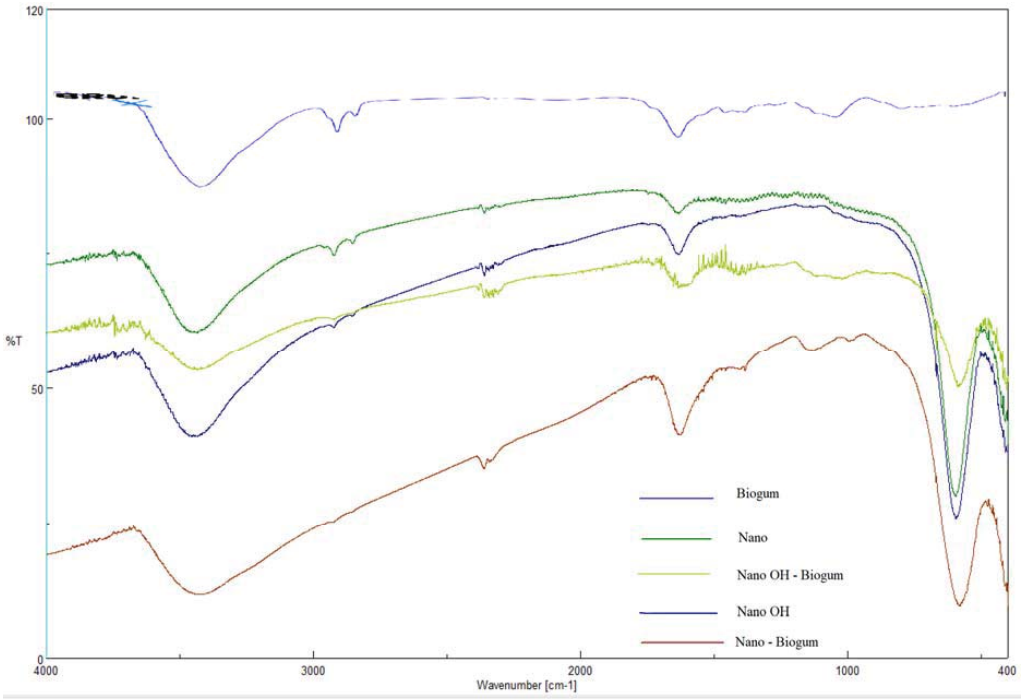


Fig. 3 FT-IR diagram of researched materials

From the infrared absorption diagram, it is seen that the presence of functional groups in the structure of Biogum as at the oscillation peaks of 3446.90 cm^{-1} and 1636,17 cm^{-1}, these are the characteristic oscillations of the original -OH and the original -COO - [20, 21]; In addition, some other oscillation peaks such as C-N fluctuations occurred at peak 1460.27 cm^{-1} and 2925,36 cm^{-1} characterizes C-H bond in CH_2 group; there is a slight oscillation at 1409.44 cm^{-1} is the oscillation of the two groups -OH and -CH; Group C = O was observed with slight oscillation in 1385 cm^{-1}; 1550 cm^{-1} appeared light bonding band with amide III (group $-NH_3^+$) [22]; 1271.08 and 1040.21 cm^{-1} oscillation correspond to the bond of C-O (CH_2OH) [22]; 790,1 cm^{-1}, it shows that this is the bond (1-4), (1-6) of galactose and mannose. Through the results of the infrared spectrum analysis FT-IR, We determined the structure of the bio-polymer extracted from osaka seeds (Cassia Fistula Linn) with similar functional groups as analyzed by [20] and [23].

For $CoFe_2O_4$ particle, there was an occurrence of an oscillation peak at 3456 cm^{-1}. It is thought the oscillation peak for free-water binding and absorption on the surface of the nanoparticles (-OH group). C-H oscillation groups are observed at peak 2920 cm^{-1} and at peak 2857 cm^{-1} shows the presence of SDS on the surface of $CoFe_2O_4$ particle [16], 2357,55 cm^{-1}, 628,59 cm^{-1} corresponding to the presence of -OH group [24]. The wavelengths observed at 595.41 cm^{-1} and 446.44 cm^{-1} correspond to the concave-convex vibration at the octahedral and tetrahedral compounds in the spinel structure containing Fe^{2+} and Co^{2+} groups [24]. Compared to previous studies such as [16] and [24], there is a similarity on functional groups between the research results.

When attaching the functional groups to the surface of the nanoparticles, the oscillations at the peak of -OH group at 3456 cm^{-1} wavelength is wider than those of the previous material. This could prove that nanoparticles are attached -OH-group functional groups by intermolecular hydrogen bonding. There is also a strong oscillation at the wavelengths of 595.41 cm^{-1} and 446.44 cm^{-1} corresponding to the internally strong oscillation of the tetrahedral structure coordinated with the octahedron in the spinel structure. It is thought that the bonding length of oxygen to metal ions (O-Me) in the octahedral holes is shorter than O-Me bonding length in the tetrahedral hole [16]. At

1628.59 cm^{-1} wavelength, the expansive oscillation of -OH group may be due to the adsorption of H_2O onto the surface of the particle.

From Fig. 3, the presence of characteristic peaks of magnetic nanoparticles at 595.41 cm^{-1} and 446.44 cm^{-1} wave lengths is the presence of metal bonds in tetrahedral and octahedral holes. In addition, there is the presence of -OH group characterizing for bio-gum at 3446.90 cm^{-1} and 1636,17 cm^{-1}. However, because the heated stirring process partly causes the evaporation of water molecules on the surface of the material and the breakdown of the chemical liquid bonds in the material. With the biogum cover, the magnetism of the composite material is considerably reduced.

According to the survey results of SEM and FT-IR image, it shows that the material has a combination of biogum and ferromagnetic oxide nano, it shows that the material can treat dyeing color.

Survey results of Biocomposite's Methylene Blue Color treatment

Determine optimal pH for Biocomposite

The research results from Fig. 4 show that the color treatment efficiency is highest at pH = 6 for Nano-material with - OH group attached to osaka gum and at pH 7 for Nano material. Combined with osaka gum. With the treatment efficiency of Nano gum and Nano-gum added –OH reaching at 31.42% and 30.41%. It can be explained that the influence of H^+ ion on the material's absorption through the protonation process of the functional group [25].

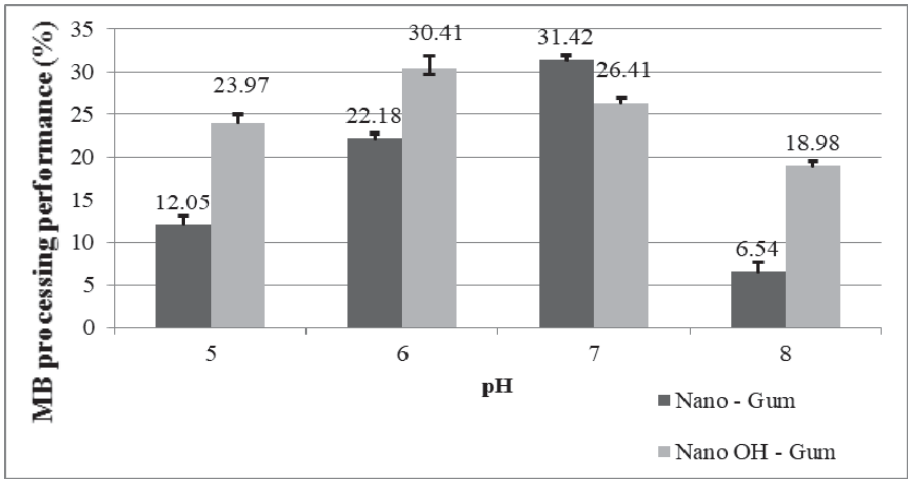


Fig. 4 Color treatment efficiency of Nano Gum and Nano OH Gum material by pH

Some studies show that at low pH, the surface of Biocomposite material is positively charged due to the presence of excess H^+ ions and these ions compete with dye cations and reduce the absorption of Methylene Blue while at high pH, -COOH functional groups on the material surface are ionized and interact with the molecules of Methylen Blue, in addition -COOH groups contained in acrylate are separated to form -COO group which increases the ionizing groups and creates an electrostatic repulsion, which causes the polymer chains to expand and enhance the cationic absorption of the dye [26], [27].

Based on several studies of other biologically derived materials such as almond gum [28] and guar gum [29], it is shown pH in the range of 6 to 10 is the appropriate pH rate for color absorption of Methylene Blue with achieved efficiency of 55%.

Thus, when compared with previous studies, it is showed that there is a similarity of pH suitable for the treatment process of Methylene Blue wastewater between the materials studied. This proves that the research material is capable of treating the dyeing color.

Determining the optimal dosage for Biocomposite

From Fig. 5, appropriate dosage survey studies show that Methylene Blue's color treatment ability is increased from 0.5 g/L to 1.5 g/L, the highest concentration is at 1.5 g Biocomposite/L, with the efficiency of Nano OH gum reaches 62.43% and Nano gum reaches 78.72%. From the initial coloring concentration (349.67 Pt-Co) via the treatment of Nano Gum and Nano OH Gum material is reduced to 74.41 Pt-Co for Nano Gum and 131.37 Pt-Co for Nano OH Gum.

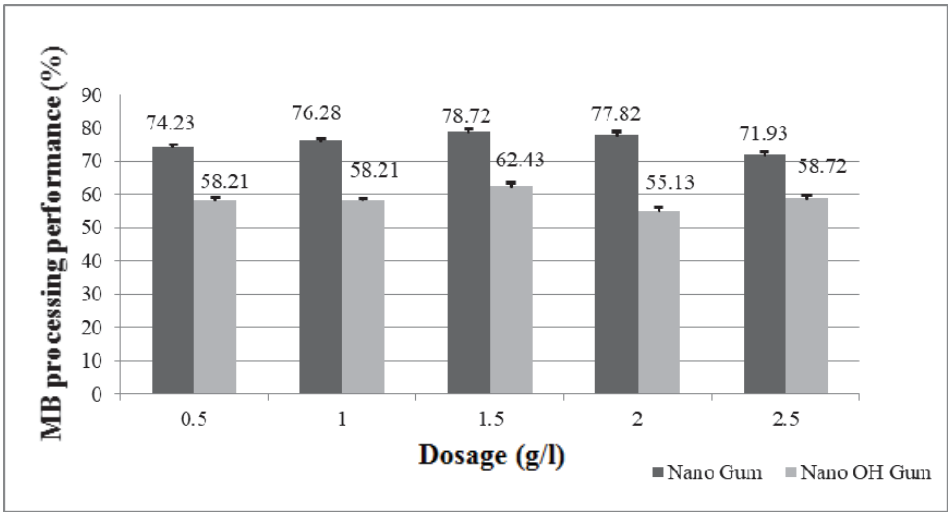


Fig. 5 The color treatment efficiency of Nano Gum and Nano OH Gum by dosage

The research result on Biocomposite material is compared with the previous researches shows that the efficiency of color treatment in dyeing textile wastewater is similar as the research result on the use of sludge after domestic wastewater treatment process [30] achieved 81% or research project on Shewanella putrefaciens cell of [31] has eliminated 80% of color out of the solution or research results of almond gum of [32] shows that at concentrations of 0.05 - 2 g/L the treatment ability reaches 89% [33].

However, some research results such as the research results of [34] achieved 56% eliminating efficiency when using Kurthia sp or the research of [35] on anaerobic microorganisms with a 70% color eliminating ability; it is shown that Biocomposite treatment ability is better.

Conclusion

Nano Gum and Nano OH Gum is a material of biological origin which is combined by $CoFe_2O_4$ magnetic Nano and treatment ability of Osaka gum. In this study, Nano Gum and Nano OH Gum are used to examine the color treatment ability of the initial concentration of 349.67 Pt-Co. The results show that Nano Gum is used to treat color at pH = 6 and 1.5 mg/L dosage reaches the efficiency of 78.72%, it is reduced from initial color concentration down to 74.41 Pt-Co. At the same dosage, Nano material added OH-group combined with gum gave an efficiency of 62.43% at pH = 7 lower than the material without functional group.

Based on the research results, it shows that Nano Gum and Nano OH Gum material is capable of treating Methylene Blue in dyeing textile wastewater. The research result is the scientific basis to guide the expansion of applied research on Nano Gum and Nano OH Gum in dyeing textile wastewater treatment.

References

[1] B. Y. Gao, Q. Y. Yue, Y. Wang, W. Z. Zhou, Color removal from dye-containing wastewater by magnesium chloride, Journal of Environmental Management, 82 (2007) 167–172.
[2] V. K. Garg, M. Amita, R. Kumar, and R. Gupta, Basic dye (methylene blue) removal from simulated wastewater by adsorption using Indian Rosewood sawdust: a timber industry waste, Dyes and pigments, 63 (2004) 243–250.
[3] S. K. A. Solmaz, A. Birgul, G. E. Ustun, T. Yonar, Colour and COD removal from textile effluent by coagulation and advanced oxidation processes, Coloration Technology, 122 (2006) 102 –109.
[4] A. K. Verma, R. R. Dash, P. Bhunia, A review on chemical coagulation/flocculation technologies for removal of colour from textile wastewaters, Journal of Environmental Management, 93 (2011) 154–168.
[5] S. K. A. Solmaz, A. Birgül, G. E. Üstün, T. Yonar, Colour and COD removal from textile effluent by coagulation and advanced oxidation processes, Coloration Technology, 122 (2006) 102–109.
[6] S. Wang, Z. H. Zhu, A. Coomes, F. Haghseresht, G. Q. Lu, The physical and surface chemical characteristics of activated carbons and the adsorption of methylene blue from wastewater, Journal of Colloid and Interface Science, 284 (2005) 440–446.
[7] Y. Bulut, H. Aydın, A kinetics and thermodynamics study of methylene blue adsorption on wheat shells, Desalination, 194 (2006) 259–267.
[8] S. Wang, L. Li, H. Wu, Z. H. Zhu, Unburned carbon as a low-cost adsorbent for treatment of methylene blue-containing wastewater, Journal of colloid and interface science, 292 (2005) 336–343.
[9] Dao Minh Trung, Le Hung Anh, Nguyen Thi Khanh Tuyen, Nguyen Vo Chau Ngan, Effectiveness on color and COD of textile wastewater removing by biological material obtained from Cassia fistula seed. J. Viet. Env. 8 (2016) 121–128.
[10] S. H. Lee, S. Wang, Biodegradable polymers/bamboo fiber biocomposite with bio-based coupling agent, Composites Part A: Applied Science and Manufacturing, 37 (2006) 80–91.
[11] Dao Minh Trung, Nguyen Vo Chau Ngan, Ngo Kim Dinh, Effect of dye textile wastewater treatment of chemical and biological coagulants, Journal of Science, 2016.
[12] B. Y. Gao, Q. Y. Yue, Y. Wang, W. Z. Zhou, Color removal from dye containing wastewater by magnesium chloride, Journal of Environmental Management, 82 (2005) 167–172.
[13] V. T. P. Vinod, R.B. Sashidhar, Bioremediation of industrial toxic metals with gum kondagogu (Cochlospermum gossypium): A natural carbohydrate biopolymer, 2011.
[14] A. Pui, D. Gherca, G. Carja, Characterization and magnetic properties of capped $CoFe_2O_4$ nanoparticles ferrite prepared in carboxymethylcelullose solution, Dig. J. Nanomater. Bios, 6 (2011) 1783–1791.
[15] S. K. Singh, S. Singh, Evaluation of Cassia fistula Linn. Seed Mucilage in tablet formulations, International Journal of PharmTech Research, 2 (2010) 1839–1846.
[16] A. Pui, D. Gherca, G. Carja, Characterization and magnetic properties capped $CoFe_2O_4$ nanoparticles ferrite prepared in carboxymethylcelullose solution, Digest Journal of Nanomaterials and Biostructures, 6 (2011) 1783–1791.
[17] K. Maaz, A. Mumtaz, S. K. Hasanain, A. Ceylan, Synthesis and magnetic properties of cobalt ferrite ($CoFe_2O_4$) nanoparticles prepared by wet chemical route, Journal of magnetism and magnetic materials, 308 (2007) 289–295.
[18] F. Sadri, A. Ramazani, A. Massoudi, M. Khoobi, V. Azizkhani, R. Tarasi, Magnetic $CoFe_2O_4$ nanoparticles as an efficient catalyst for the oxidation of alcohols to carbonyl compounds in the presence of oxone as an oxidant, Bullein of the Korean Chemical Society, 35 (2014) 2029– 2032.

[19] Y. I. Kim, D. Kim, C. S. Lee, Synthesis and characterization of $CoFe_2O_4$ magnetic nanoparticles prepared by temperature - controlled coprecipitation method, Physica B, 337 (2003) 42–51.
[20] V. T. P. Vinod, R. B. Sashidhar, A. A. Sukumar, Competitive adsorption of toxic heavy metal contaminant by gum kondagogu (Cochlospermum gossypium): A natural hydrocolloid, Colloids and Surfaces B: Biointerfaces, 75 (2009) 490–495.
[21] V. T. P. Vinod, R. B. Sashidhar, Surface morphology, chemical and structural assignment of gum Kondagogu (Cochlospermum gossypium DC.): An exudate tree gum of India, Indian Journal of Natural Products and Resources, 1 (2010) 181–192.
[22] H. E. Andrews, O. S. Castilla, H. V. Torres, E. J. V. Carter, C. L. Calleros, Determination of the gum arabic-chitosan interactions by fourier transform infrared spectroscopy and characterization of the microstructure and rheological features of their coacervates, Carbohydrate Polymers, 79 (2010) 541–546.
[23] D. Mudgil, S. Barak, B. S. Khatkar, X-ray diffraction - IR spectroscopy and thermal characterization of partially hydrolyzed guar gum, International Journal of Biological Macromolecules, 50 (2012) 1035–1039.

Removal of Metal Ions from Plating Wastewater by Ferromagnetism Nano-Oxide ($CoFe_2O_4$) and Ferromagnetism Nano-OH Material

Nguyen Vo Chau Ngan[1a*], Dao Minh Trung[2b]

[1]Can Tho University, Can Tho City, Viet Nam

[2]Thu Dau Mot University, Binh Duong province, Viet Nam

[a]nvcngan@ctu.edu.vn, [b]moitruongviet.trung@gmail.com

* Nguyen Vo Chau Ngan

Keywords: Chemical flocculants, ferromagnetism Nano, plating wastewater

Abstract. Study on using of ferromagnetic nano particles ($CoFe_2O_4$) and ferromagnetic nano –OH materials evaluated the efficiency of plating wastewater treatment with initial parameters: pH = 5; Ni^{2+} = 25 mg/L, Cu^{2+} = 25 mg/L, Zn^{2+} = 25 mg/L. Research results showed that Ni^{2+}, Cu^{2+}, Zn^{2+} ions removal efficiency of Nano material are respectively 62,53%; 69,32% and 61,47% while the efficiency of Nano – OH material are 65,45%; 67,85% and 84,2%. These results showed that the new materials have potential in wastewater treatment.

Introduction

Heavy metal pollution is one of the most serious environmental problems [1]. Most of heavy metal ions such as copper, nickel, zinc, chromium, etc. are present in wastewater of many industries (alloys, battery manufacturing, plating, mining operations… [2]). These heavy metal ions are highly soluble in water and are not biodegradable as other organic wastes, so they can easily accumulate in living tissue causing serious health effects for organisms on the earth [3], [4], [5].

Many methods have been used to remove heavy metal ions before they were released into the environment such as precipitaion, ion exchange, electrolytic filtration and membrane separation [6]. Adsorption is one of the physical and chemical treatment methods that is found to be effective in removing heavy metals from aqueous solutions without giving rise to any harmful products after treatment [5], [7].

At present, the adsorption process combined with magnetic materials was widely used in many applications such as biochemistry, biomolecules, analytical chemistry, mining and recently they were applied in water treatment and environmental applications. Pollutants can be readily removed from magnetic particles by a simple magnetic field and through research reports of [8]; [9]; [10] showed that magnetic particles are capable of removing heavy metals in wastewater.

This study used $CoFe_2O_4$ magnetic materials synthesized with nano size by co-precipitation method and investigated Ni^{2+}, Cu^{2+}, Zn^{2+} heavy metal ions adsorption in plating wastewater.

Materials and Method

Research subjects

Plating wastewater (Ni^{2+}, Cu^{2+}, Zn^{2+}) with concentration of 25 mg/L.

Research Chemitry

H_2SO_4 1N (China), $CuSO_4.5H_2O$ (China, 99%), $CoCl_2.6H_2O$ (China, 99%); $FeCl_2.4H_2O$ (China, 98%); NaOH (China, 96%), SDS (India, 85%); n – hexan (China, 97%); C_2H_5OH (China, 99.7%); NH_4OH (China 25 – 28%); $(CH_3)_2CO$ (China, 95%).

Research Materials

Magnetic nano particles ($CoFe_2O_4$) and nano – OH at dosage of 12,5 g/L.

Research Methods

- Determinination of pH measured directly with Mettler Toledo pH Meter (2017).

- Determinination of heavy metal concentration on Atomic Absorption Spectrometer (AAS) (2016).

Materials Preparation

Based on research report of Pui *et al*. [11], ferromagnetic nano oxide ($CoFe_2O_4$) were synthesized by co-precipitation method with SDS as the surfactant. The mixture contained 250 mL of 0,02M $CoCl_2.6H_2O$ and 0,04M $FeCl_2.4H_2O$ solution and they was stirred with 250 mL of 111M SDS solution for 30 min, heating to 70 ± 5^oC. According to the study results of Vijayaraghavan *et al*. [12] explainted that SDS was added as a agent to control particle size and evenly distributed during synthesis. After 5 hours, the nano particles were separated from the solution using an external magnet. The nano was washed with water, ethanol and n-hexan to remove impurities on the particle surface.

Preparation of ferromagnetic nano –OH oxide particles: the nano particles obtained after synthesising process were dispersed by ultrasound in a mixture of water and ethanol (350 mL, 1 : 1) for 30 min. After that, 35 mL of Ammonia was added and stirred at 60 ± 5^oC for 24 hours. The resulting mixture was washed with water, ethanol and n-hexan to remove impurities.

Results and discussion

Material preparation results

Analysis of SEM

The results of SEM in Fig. 1 (a) and (B) showed that ferromagnetic nano particles have a high porosity with relatively dense interconnected particles and they are relatively homogenerous in size with a particle diameter of 70 – 95nm. For nano – OH particles, the SEM in Fig. 1 (c) and (d) showed that when the –OH groups were added, the size and shape of nano particles are changed negligible.

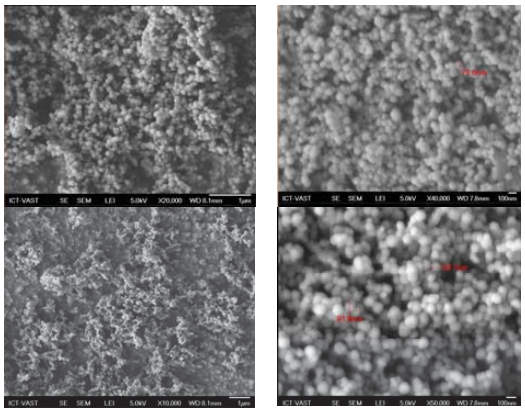


Fig. 1 SEM images of materials
(a), (b): magnetic nano particles (c), (d): nano – OH particles

Comparation to the results of Sadri *et al*. [13] suggested that these two sudies have a similarity in particle size. However, the results of particle size in this study are better than those of Pramanik *et al*. [14], in results of study of Pramanik et al., the materials reached the size of 400 - 500 nm. Based on the results of several studies, size of ferromagnetic oxide nano particles depended on many factors such as pH, salt concentration, density, stirring speed and SDS concentration [15].

Analysis of FT-IR

The results of analysis in Fig. 2 (a) showed that fluctuating peaks featured functional groups mounted on the surface of $CoFe_2O_4$ material. The –OH group is present at different wavelengths such as 3384 cm^{-1}, which is the oscillating peak of the free water bond and ther are absorbed on the surface of nano particles and at 1625,39 cm^{-1} wavelength may be due to the adsorption of H_2O on the surface of particle [11]. There are also strong fluctuations at 618,62 cm^{-1}, 446,99 cm^{-1} and 417,97 cm^{-1} wavelengths corresponding to network fluctuations within the tetrahedral structure of the spinel structure can be thought of as the bonding length of oxygen to metal ions (O-Me) in octahedral holes shorter than the O-Me bond length in the tetrahedral hole [11].

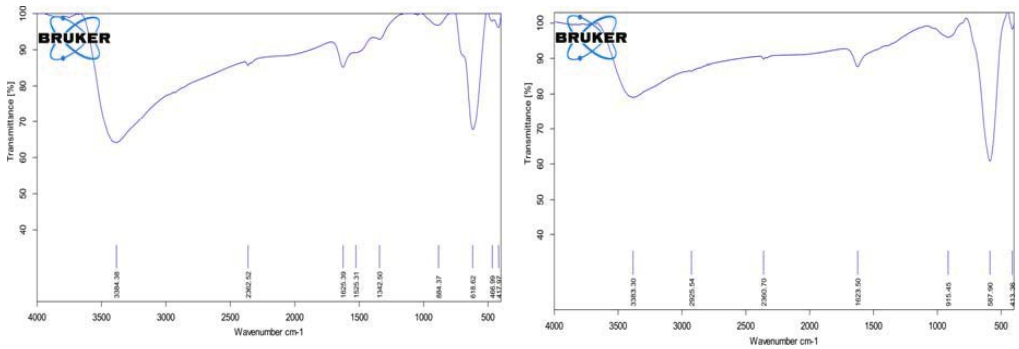


Fig. 2 FT-IR schema of materials
a) Ferromagnetic nano oxide b) Ferromagnetic nano –OH oxide

When attaching –OH function groups to the surface of nano particles, the fluctuating peak of –OH group at 3383,3 cm^{-1} [11] were wider than Nano material. This could prove that the nano particles attached the –OH functional group by intermolecular hydrogen bonding. There are also strong oscillations at 587,9 cm^{-1} and 413,36 cm^{-1} wavelengths corresponding to the internal oscillation of the tetrahedral structure coordinates with the octahedron in the spinel structure. It is thought that the bonding length of oxygen to metal ions (O-Me) in the octahedral holes is shorter than the O-Me bond length in the tetrahedral holes [11]. At the 1623,5 cm^{-1} wavelength, that is also due to the oscillation of the –OH group, this may be due to the adsorption of H_2O onto the surface of the particle [11].

Determination of optimum operating parameter of materials on plating wastewater

Determination of optimum pH

The results of Fig. 3 (a) showed that at three differrent pH levels as in the graph, the heavy metal ions removal efficiency of magnetic nano material was the best at pH = 5. The Ni^{2+}, Cu^{2+}, Zn^{2+} ions removal efficiency was 38,11%; 42,40% and 34,53%.

Fig. 3 (b) showed that the heavy metal ions removal at many pH levels. It also showed that pH = 5 was the optimum pH for Nano – OH material. The Ni^{2+}, Cu^{2+}, Zn^{2+} ions removal efficiency was 45,03%; 40,12% and 46,53%.

In order to explain for the effect of pH on the removal capable of metal ions, the study showed that metal ion removal capable at the initial pH was the best of the effluent is due to the acidic environment of the H + Nano-iron oxide competition with metal ions, with the smallest size of ions, easily enters and occupies gaps in the ferromagnetic nanoparticle molecules, locating in the molecule Filled and ferromagnetic Nanofibers are no longer capable of capturing metal ions, resulting in reduced treatment efficiency. In addition, the protonation of the -OH groups also reduces the complexity and reduces the metal removal efficiency of the Nano material.

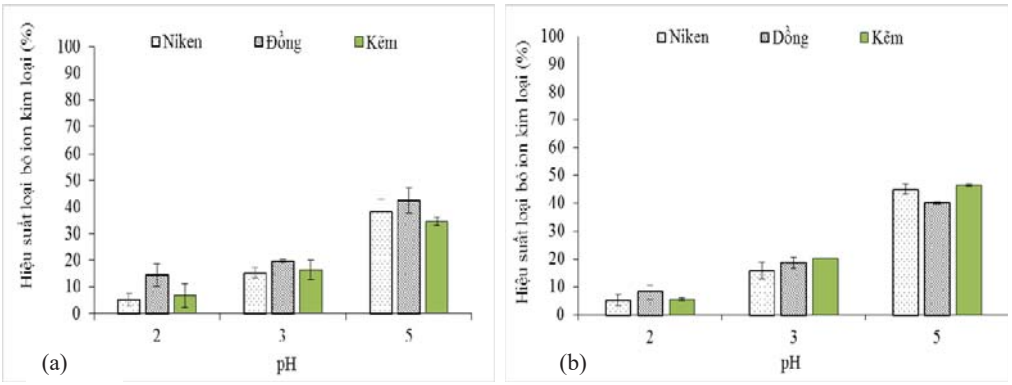


Fig. 3 The results of determination of optimum pH

a) Magnetic Nano b) Nano – OH

This results showed that the same optimum pH condition, however, the heavy metal ions removal efficiency of Nano – OH and magnetic nano materials were significantly different. Nano materials were added –OH group for better removal capable. They proved that the addition of –OH group allowed material to easily covalently bond with many other metal ions in the solution, resulting in better initial treatment efficiency [17].

According to research results of [18] reported on the use of activated carbon to adsorb Ni^{2+}, Zn^{2+} ions with 37% and 11%. Comparation with the research results of using Nano and Nano - OH materials, they were able to treatment better than the research results of Warner *et al*. [18].

The research results of Cu^{2+} ions removal efficiency of using Nano and Nano – OH materials showed that they have a similarity with the study results of Önnby *et al*. [19], $HN(CH_2CO_2H)_2$ iminodiacetic acid could be removed 38% Cu^{2+}.

Determination of optimum dosage

The study results from Fig. 4 (a) showed that the optimum pH = 5 and nano particles concentration at 50 mL had the highest heavy metal ions removal efficiency in assumed plating wastewater. The results reached 61.47% Zn^{2+}; 62.53% Ni^{2+} and 69.32% Cu^{2+}.

In Fig. 4 (b), this study showed that dosage of material were surveyed from 20 to 60 mL and optimum pH at 5, the removal efficiency was the best at Nano -OH material concentration of 40 mL. The research results reached 84.20% Zn^{2+}; 65.45% Ni^{2+} and 67.85% Cu^{2+}.

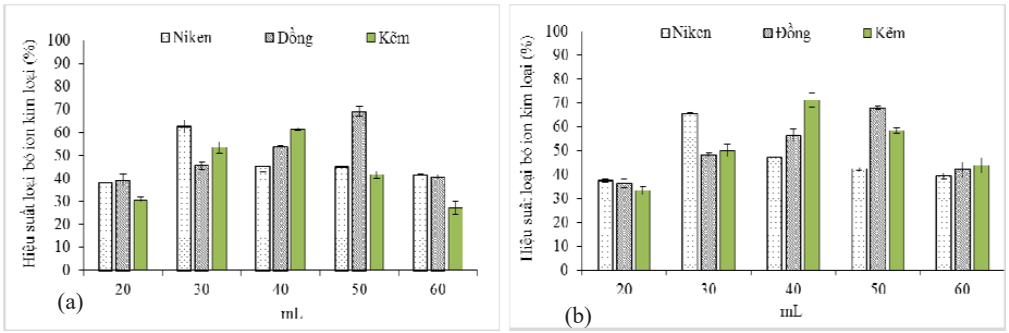


Fig. 4 The results of determination of optimum dosage

a) Magnetic Nano b) Nano – OH material

When changing the dosage of Nano and Nano –OH materials, the performance of Nano – OH material was better the efficiency of Nano material with significantly higher Zn^{2+} treatment efficiency.

For Cu^{2+} ion removal results, this study was a similarity with the study results of Önnby *et al*. [19] when using TBA adsorption gel to treatment Cu^{2+} and reach 63% removal efficiency. The other reported results of Warner *et al*. [18], the use of ferromagnetic oxide mixed with 4,5%Mn material treatmented 61% Cu^{2+}.

In addition, this materials had Ni^{2+} removal capable better than UF membrane of Akita *et al*. [20]. According to Akira *et al*., the study results showed that Ni^{2+} removal efficiency reached 60%.

When comparing the results of Zn^{2+} removal in the effluent solution, it was found that the removal capable of two research materials in this study was more favorable than activated carbon of Önnby *et al*. [19], the study showed that activated carbon only reached 11% of the heavy metal ions treatment efficiency.

Conclusion

The research results showed that there is a difference in plating wastewater treatment application of Nano and Nano – OH materials. The treatment efficiency of Nano material was quite high with treatment concentration $Zn^{2+} < Ni^{2+} < Cu^{2+}$ corresponding 61.47%; 62.53% and 69.32% at optimum pH = 5 and dose range at 50 mL. For Nano – OH material, the removal efficiency of Zn^{2+} was 84.20%, while treatment efficiency of Ni^{2+} was 65.45% and Cu^{2+} was 67.85% at pH = 5 and Nano - OH concentration was 40 mL.

The results of the study are the basis for scientific studies to improve the quality of waste water containing other metal components in the future. In addition, the creation of recovered and environmentally friendly bio-materials can be a research direction in the future.

References

[1] V. Dushenkov, P. B. A. N. Kumar, H. Motto, I. Raskin, Rhizofiltration: the use of plants to remove heavy metals from aqueous streams, *Environmental science & technology,* 29 (1995) 1239-1245.

[2] K. Kadirvelu, K. Thamaraiselvi, C. Namasivayam, Removal of heavy metals from industrial wastewaters by adsorption onto activated carbon prepared from an agricultural solid waste, *Bioresource technology,* 76 (2001) 63-65.

[3] E. Bååth, Effects of heavy metals in soil on microbial processes and populations (a review), *Water, Air, and Soil Pollution,* 47 (1989) 335-379.

[4] M. A. Barakat, New trends in removing heavy metals from industrial wastewater, *Arabian Journal of Chemistry,* 4 (2011) 361-377.

[5] W. S. W. Ngah, M. A. K. M. Hanafiah, Removal of heavy metal ions from wastewater by chemically modified plant wastes as adsorbents: a review, *Bioresource technology,* 99 (2008) 3935-3948.

[6] F. Akbal, S. Camcı, Copper, chromium and nickel removal from metal plating wastewater by electrocoagulation, *Desalination,* 269 (2011) 214-222.

[7] J. Hu, I. M. C. Lo, G. Chen, Comparative study of various magnetic nanoparticles for Cr (VI) removal, *Separation and Purification Technology,* 56 (2007) 249-256.

[8] X. Guo, B. Du, Q. Wei, J. Yang, L. Hu, L. Yan, Synthesis of amino functionalized magnetic graphenes composite material and its application to remove Cr (VI), Pb (II), Hg (II), Cd (II) and Ni (II) from contaminated water, *Journal of hazardous materials,* 278 (2014) 211-220.

[9] Y. Zhang, L. Yan, W. Xu, X. Guo, L. Cui, L. Gao, Adsorption of Pb (II) and Hg (II) from aqueous solution using magnetic $CoFe_2O_4$ - reduced graphene oxide, *Journal of Molecular Liquids,* 191 (2014) 177-182.

[10] A. Mittal, R. Ahmad, I. Hasan, Poly (methyl methacrylate)-grafted alginate/Fe_3O_4 nanocomposite: synthesis and its application for the removal of heavy metal ions, *Desalination and Water Treatment,* 57 (2016) 19820-19833.

[11] A. Pui, D. Gherca, G. Carja, Characterization and magnetic properties capped $CoFe_2O_4$ nanoparticles ferrite prepared in carboxymethylcelullose solution, *Digest Journal of Nanomaterials and Biostructures,* 6 (2011) 1783-1791.
[12] G. Vijayaraghavan, T. Sivakumar, A. V. Kumar, Application of plant based coagulants for waste water treatment, *International Journal of Advanced Engineering Research and Studies,* 1 (2011) 88-92.
[13] F. Sadri, A. Ramazani, A. Massoudi, M. Khoobi, V. Azizkhani, R. Tarasi, Magnetic $CoFe_2O_4$ nanoparticles as an efficient catalyst for the oxidation of alcohols to carbonyl compounds in the presence of oxone as an oxidant, *Bullein of the Korean Chemical Society,* 35 (2014) 2029-2032.
[14] N. C. Pramanik, T. FujiI, M. Nakanishi, J. Takada, Preparation and magnetic properties of the $CoFe_2O_4$ thin films on Si substrate by sol-gel technique, *Journal of materials science,* 40 (2005) 4169-4172.
[15] Y. I. Kim, D. Kim, C. S. Lee, Synthesis and characterization of $CoFe_2O_4$ magnetic nanoparticles prepared by temperature - controlled coprecipitation method, *Physica B,* 337 (2003) 42-51.
[16] S. Maensiri, C. Masingboon, B. Boonchom, S. Seraphin, A simple route to synthesize nickel ferrite ($NiFe_2O_4$) nanoparticles using egg white, *Scripta Materialia,* 56 (2007) 797-800.
[17] Ayhan Demirbas, Heavy metal adsorption onto agro-based waste materials: a review, *Journal of hazardous materials,* 157 (2008) 220-229.
[18] C. L. Warner, W. Chouyyok, K. E. Mackie, D. Neiner, L. V. Saraf, T. C. Droubay, Manganese doping of magnetic iron oxide nanoparticles: tailoring surface reactivity for a regenerable heavy metal sorbent, *Langmuir,* 28 (2012) 3931-3937.
[19] L. Önnby, C. Giorgi, F. M. Plieva, B. Mattiasson, Removal of heavy metals from water effluents using supermacroporous metal chelating cryogels, *Biotechnology progress,* 26 (2010) 1295-1302.
[20] S. Akita, L.P. Castillo, S. Nii, K. Takahashi, H. Takeuchi, Separation of Co (II)/Ni (II) via micellar-enhanced ultrafiltration using organophosphorus acid extractant solubilized by nonionic surfactant, *Journal of Membrane Science,* 162 (1999) 111-117.

Effects of some parameters on properties of Cu-Al_2O_3 composite materials synthesized by internal oxidation process

Ho Ky Thanh[1, a *], Nguyen Duc Duy[2,b]

[1]Thai Nguyen University of Technology, Thai Nguyen City, Vietnam

[2]The College of Mechanics and Metallurgy, Thai Nguyen City, Vietnam

[a]hkythanh@tnut.edu.vn, [b]nguyenducduyckllk@gmail.com

Keywords: composite materials; internal oxidation; dispersion; electrical conductivity.

Abstract. The Cu-Al_2O_3 composite materials applying for electrode materials were successfully synthesized by internal oxidation process. The process included steps: producing solid solution α-Cu[Al] and oxidizing completely solid solution α-Cu[Al] as powders, then adding pure Cu powders and mixing in planetary ball milling, the mixtures were compressed into cylindrical samples, reduced at 750°C in 3h and sintered at 950°C in 2h in reduction atmosphere. The XRD patterns showed that total Al in Cu-matrix were completely oxidized in range of 20÷25h. After reducing and sintering process, the final products were Cu-Al_2O_3 composite materials. The results showed that micro-hardness, porosity and compress strength of Cu-Al_2O_3 materials increased with increasing of Al_2O_3 content, which were the result of dispersion of the fined Al_2O_3 grain size in Cu-matrix. When Al_2O_3 content was unchanged, the porosity of received materials decreased with increasing of compress pressure. Whereas, the electrical conductivity of Cu-Al_2O_3 composite materials decreased comparing with pure Cu and it decreased with increasing of Al_2O_3 content.

Introduction

Cu-matrix composite strengthened by fine ceramic particles applying for electrode materials have attracted much scientists' attention to enhance mechanical properties of Cu-matrix through impeding motion of dislocation [1,2], such as tensile and compress strength, hardness, temperature resistance, wear resistance,... Many kind ceramic particles used to disper or to strengthen Cu-matrix, including Al_2O_3, TiC, TiB_2... [1-5]. To fabricate Cu-matrix, many process have been to research and to characterise mechanical and electrical properties, such as internal oxidation [1-3], in situ [4], hot press [5], mechanochemical process [6]...

Among these methods, internal oxidation process is most common. Internal oxidation method have many advantages in fabricating Cu-Al_2O_3 composite because this process was based on the chemical reaction between Al with O_2 in Cu-matrix or Al with Cu oxides to form Al_2O_3. The Al_2O_3 particles were dircetly formed in Cu-matrix so that they were very fine, can be reach to nano size [2], micro size without milling in a long time. In addition, the formation of Al_2O_3 particles in Cu-matrix was definitely received clear surface between them, so that mechanical and electrical properties of Cu-Al_2O_3 composite material.

This paper presented the process to fabricate Al_2O_3 particles from α-Cu[Al] by internal oxidation and investigation results about effect of compressive pressure, Al_2O_3 content on the porosity, micro hardness, compress strength and electrical conductivity of Cu-Al_2O_3 composite material.

Experimental procedure

The experimental materials were 91% Cu (purity of 99.9%) and 9% Al (purity of 99.9%). The alloy was prepared by induction melting in a monoxide atmosphere. The samples were cutting and foils were milling in Pulverisette planetary ball milling in range of 5.0h in alcohol atmosphere. The speed rotation was 300rpm, the ratio of ball and materials was 10 : 1. Then the powders were oxidized in electrical furnace in range of time from 15.0h to 25.0h at 950°C. The received product

powders were mixture of CuO and Al_2O_3. To reduce Al_2O_3 content in the mixture powders to lower 2.0%, Cu pure powder (purity of 99.9%) was added, then they continuously were mixed in planetary ball milling to be homogenous and cold pressed to form cylinder samples (50mm in height and 10mm in diameter) with 100MPa compressive pressure. The raw cylinder samples was reduced at 750°C in 3.0h, then sintered in reduction atmosphere (carbon monoxide atmosphere) at 950°C in 2.0h. After that, the samples were cold pressed by a hydraulic press with compressive pressure of 200MPa, 400MPa and 600MPa.

The composition of materials was determined by X-ray diffractometer (D5005 – Siemens). The microstructure of the samples was examined using scanning electron microscope (Hitachi S - 4800). The porosity of materials was test by Archimedes method. The micro-hardness of materials was tested by Duramin Struers (diamond indenter, 1kgf). The specific resistance of materials was determinded by comparative method, then calculating the conductivity of materials.

Experimental results and discussion

The phase composition:

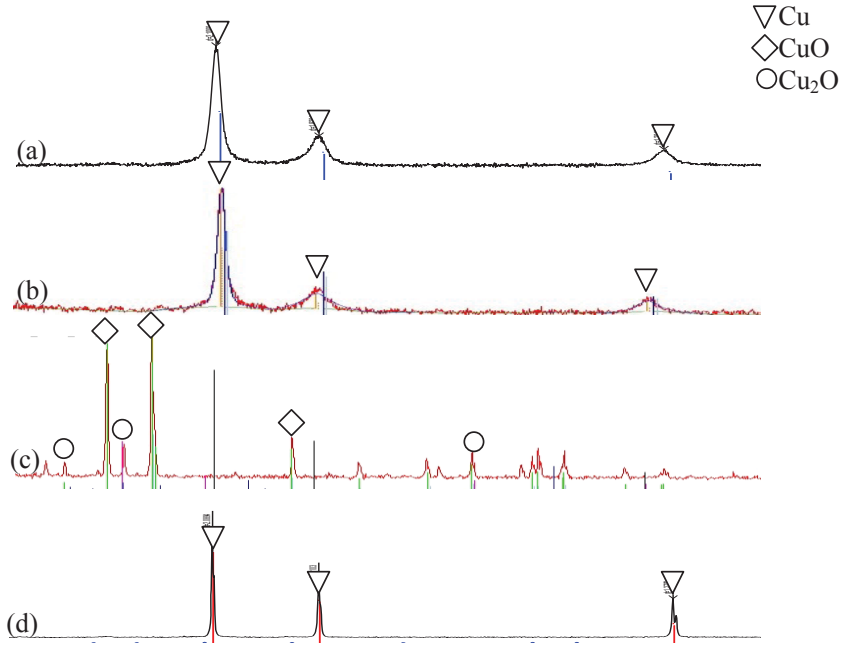


Fig. 1: XRD pattern results of (a) Cu-Al alloy; (b) powder Cu-Al alloy after 15.0h oxidizing; (c) powder Cu-Al alloy after 25.0h oxidizing, and (d) Cu-Al_2O_3 composite after sintering.

The XRD pattern result in Fig.1a showed that none of the peaks of Al content appeared. In addition, peaks of Cu were moved. It is said that Al completely dissolved into Cu-matrix to form α-Cu[Al] solution (Cu-Al alloy) after melting. When the oxidizing time was shot, almost Cu-Al alloy was not oxidized (Fig. 1b). When oxidizing time was elongated to 25.0h, all peaks of Cu disappeared, and the peaks of CuO, Al_2O_3 appeared on XRD patterns (Fig. 1c). After reduced process, the XRD pattern existed only Cu peaks, the peaks of Al, Al_2O_3 and Cu oxides were not showed (Fig. 1d). This can be explained that, at high temperature (950°C), the Al and Cu content in Cu-Al powers were completely oxidized to form Al_2O_3, CuO and Cu_2O, and then in the carbon monoxide atmosphere, Cu oxides were completely reduced, but Al_2O_3 phase was not reduced because it was resistant temperature phase. However, Al_2O_3 content was smaller than 2.0%, thus its peaks did not show in XRD pattern.

The porosity of Cu-Al_2O_3 composite was presented on Fig. 2. The results showed that, at the same compressive pressure, the porosity of Cu-Al_2O_3 composite increased with the increasing of Al_2O_3 composition. The porosity was reduced remarkably with the increasing of compressive pressure from 200MPa to 400MPa. Howerver, to raise pressure upper 400MPa, the decreasing of porosity was not significant. When the pressure reached to 600MPa, the porosity of most of the samples was smaller than 5%.

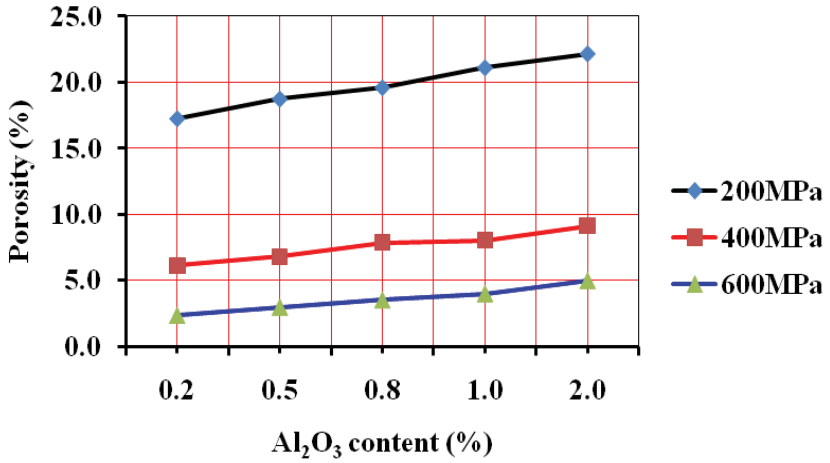


Fig. 2. Effects of compressive pressure and Al_2O_3 content on the porosity of Cu-Al_2O_3 composite.

The micro-hardness of Cu-Al_2O_3 composite was showed on the Fig. 3. Fig. 4 presented the results of compressive strength of Cu-Al_2O_3 composite. It is obviously that the micro hardness of composite was enhanced more significantly than that of Cu pure. When Al_2O_3 composition increased, both micro-hardness and compressive strength of Cu-Al_2O_3 composite increased. These results can be explained by the dispersed Al_2O_3 particles in the Cu-matrix, they restricted the motion of dislocation in the materials. When raising compressive pressure,

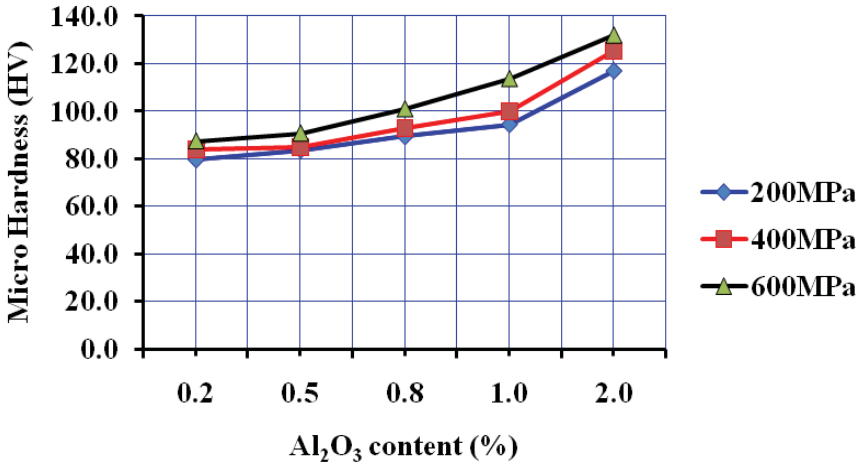


Fig. 3. Effects of compresive pressure and Al_2O_3 content on the micro hardness of Cu-Al_2O_3 composite.

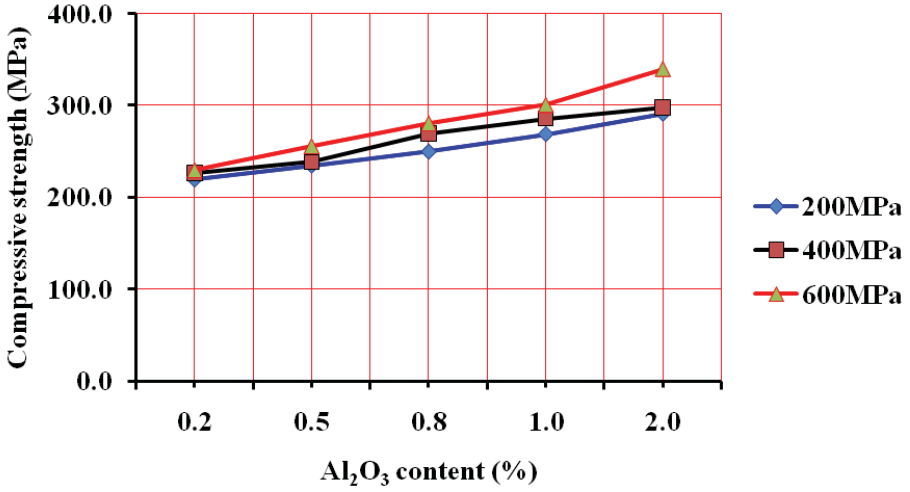


Fig. 4. Effects of compressive pressure and Al_2O_3 content on the compressive strength of Cu-Al_2O_3 composite.

Fig. 5 was the tested result of electrical conductivity of Cu-Al_2O_3 composite. It is clearly that when raising Al_2O_3 content, the electrical conductivity of composite decreased. This can be existence of Al_2O_3 particles, they reduced the section area of material. In addition, when raising Al_2O_3 content, the porosity of materials increased and the porosity also caused bad affect on the electrical conductivity.

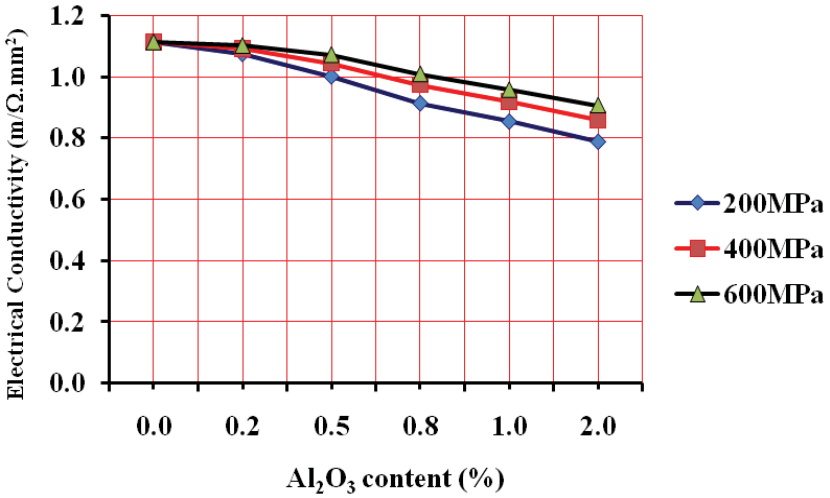


Fig. 5. Effects of compressive pressure and Al_2O_3 content on the electrical conductivity of Cu-Al_2O_3 composite.

The SEM images (Fig. 6) showed that, the Al_2O_3 particles (bright colour) were very fine (about < 0.5μm). They dispersed in Cu-matrix and strengthened Cu-matrix. So that, the dispersion of Al_2O_3 effected strongly on the porosity, the micro hardness and the compressive strength of Cu-Al_2O_3 composite, enhancing mechanical properties through impeding dislocation movement [1]. In addition, the SEM images also showed the pore in the materials. The pore sizes were very small, but can be bad affect on the electrical conductivity of Cu-Al_2O_3. So that, the electrical conductivity of materials decreased with increasing of Al_2O_3 composition.

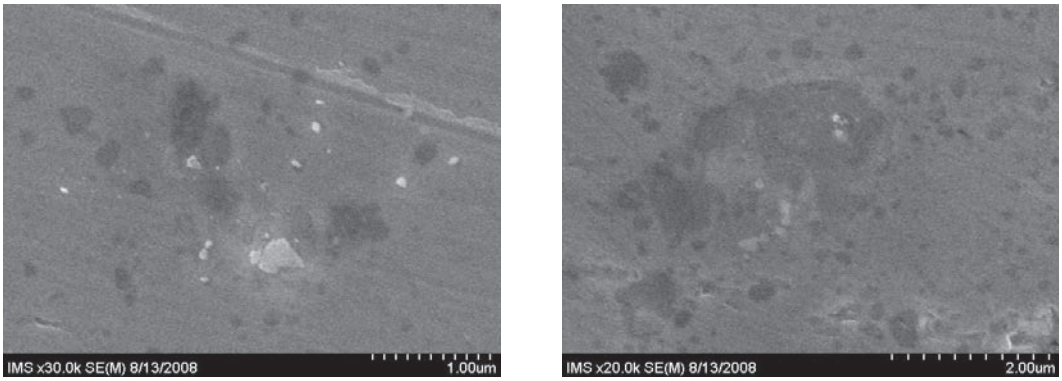


Fig. 6. SEM microstructure of Cu-1.0%Al_2O_3 composites: (a) 30.000X; (b) 10.00X.

Summary

The Cu-Al_2O_3 composite materials were successfully synthesized by internal oxidation process from α-Cu[A] powder. The XRD patterns showed that Al in Cu-matrix were completely oxidized in range of 20÷25h. After reduced (at 750°C in 3.0h) and sintered (in 2.0h at 950°C) process in carbon monoxide atmosphere, the final products were Cu-Al_2O_3 composite materials. The results showed that micro-hardness, porosity and compress strength of Cu-Al_2O_3 materials increased with increasing of Al_2O_3 content, which was the result of dispersion of the fined Al_2O_3 grain size in Cu-matrix. When Al_2O_3 content was unchanged, the porosity of received materials decreased with increasing of compressive pressure. Whereas, the electrical conductivity of Cu-Al_2O_3 composite materials decreased comparing with pure Cu and it decreased with increasing of Al_2O_3 content.

References

[1]. Ziyuan Shi, Maofang Yan; *The preparation of Al_2O_3–Cu composite by internal oxidation*; 1998, vol. 134, Issues 1–4, pp. 103-106.

[2]. Li Guobin, Sun Jibing, Guo Quanmei, Wang Ru; *Fabrication of the nanometer Al_2O_3/Cu composite by internal oxidation*; Journal of Materials Processing Technology, 2005, vol.170, pp. 336–340.

[3]. Viseslava Rajkovic, Dusan Bozic, Milan T. Jovanovic; *Effects of copper and Al_2O_3 particles on characteristics of Cu–Al_2O_3 composites*; Materials and Design, 2010, vol.31, pp. 1962–1970.

[4]. J.H. Kim, J.H. Yun, Y.H. Park, K.M. Cho, I.D. Choi, I.M. Park; *Manufacturing of Cu-TiB_2 composites by turbulent in situ mixing process*; Materials Science and Engineering A 449–451, 2007, pp. 1018–1021.

[5]. S. Islak, D. Kir, S. Buytoz; *Effect of Sintering Temperature on Electrical and Microstructure Properties of Hot Pressed Cu-TiC Composites*; Science of Sintering 46, 2014, pp. 15–21.

[6]. Seung J. Hwang, Jin-hyung Lee; *Mechanochemical synthesis of Cu–Al2O3 nanocomposites*; Materials Science and Engineering A 405, 2005, pp. 140–146.

A comparative investigation of the porous NiTi alloys synthesized by self-propagating high-temperature synthesis and combined process of decomposition and sintering

Nguyen Dang Thuy[1,a], Ho Ky Thanh[2,b*], Tran Van Dung[1,c]
1 Hanoi University of Science and Technology, Hanoi, Vietnam
2Thai Nguyen University of Technology, Thai Nguyen City, Vietnam
[a]nguyendangthuy.ndt@gmail.com, [b]hkythanh@tnut.edu.vn, [c]dung.tranvan@hust.edu.vn

Keywords: porous NiTi; SHS process; decomposition; sintering; porosity; mechanical property.

Abstract. Porous NiTi alloys were successfully synthesized by two different processes, including self-propagating high-temperature synthesis (SHS), and combined process of decomposition and sintering. A systematic comparison of micro-structures and mechanical properties of these alloys was investigated. The results showed that the SHS process was better than decomposition – sintering process. By controlling the processing parameters of SHS, the received porous NiTi alloys showed that the porosity and pore were larger, and ratio of opened-pore reached up to 80%. The porous NiTi alloys fabricated by SHS process also exhibited good properties, such as a high compressive strength (up to 250MPa), and elastic modulus in range of 6.1-7.0GPa. The porous NiTi alloys synthesized by decomposition – sintering process have lower porosity (26-43%), lower compressive strength (< 110MPa), lower elastic modulus (< 1.2GPa) but the strain could be reached to 10%.

Introduction

Porous NiTi alloys have attracted much of scientists' attention because of its common benefits such as low density, small modulus, high wear resistance, super-elastic and shape memory behaviors, bio-compatibility [1]. So that, porous NiTi alloys were proposed in many applications, especially biomedical materials for medical applications such as implant tissues [2], dental and orthopaedic appliations [3,4],….

Because the melting point of NiTi is high (1310°C), thus porous NiTi alloys are often fabricated by metallurgy methods from element or pre-alloyed powder [2], including conventional sintering (CS), vacuum sintering (VS), hot isostatic pressure (HIP), spark-plasma sintering (SPS), self-propagating high-temperature synthesis (SHS), thermal explosion. In addition, by combination processes of decomposition and sintering, porous NiTi alloy was successfully synthesized from Ni and TiH_2 powders [5,6]. To control the pore sizes and porosity of porous NiTi alloy, some researchers used space holder powder to mix with elemental (Ti and Ni) or pre-alloyed (NiTi) powder before sintering. The space holder powders are eliminated during sintering. Thus the received products have pores with well-defined sizes, shape and volume fraction.

This paper introduces some researches on comparing investigation processes of the porous NiTi alloys fabricated by self-propagating high-temperature synthesis (SHS) and combined processes of decomposition and sintering.

Experimental procedure

Fabricating porous NiTi by SHS process: Each sample was prepared by mixing 9.573 gram of commercial Titanium (Ti) powder (purity > 99.9%, average particles size 100μm) with 11.739 gram Nickel (Ni) powder (purity > 99.9%, average particles size 10μm). This ratio was to get the atomic ratio 1 : 1 of Ni and Ti. The powders were then mechanical activation (MA) for 2.0 hours by using Attritor milling. The balls to powder ratio was 10 : 1. The purpose of first mixing step was to make the mixed powder become homogeneous and reduce the energy of the reaction between Ni and Ti. It ensures that Ni and Ti particles contact to each others. The more homogeneous the powder mixture was the more surface area of contact can be, so the easier the reaction can be happened. During this

step the energy was stored in the powder, which makes the reaction in the combustion process easier to occur. After that, the mixing powder was then cold pressed with pressure of 120MPa to form a cylindrical shape (radius d = 16mm and height h = 30mm). The green compact was then put into the resistance furnace to reach the preheating temperature (T_p) from 400°C to 600°C in Argon environment gas. Finally, samples were ignited by using ignitor made by tungsten alloy wire at T_{ig} = 2000°C.

Fabricating porous NiTi by combination of decomposition and sintering process: TiH_2 powder (purity > 99,9%, average particles size 300nm) and Ni powder (purity > 99,9%, average particles size 10μm) were mixed with ratio 9.25gram TiH_2 and 10.73gr Ni to ensure that the atomic ratio of Ni and Ti in porous NiTi alloy was balance. Then the mixture powders were mixed in ball milling in 2.0 hours. The balls to powder ratio was 10 : 1. Then the powders were cold pressed with pressure of 150MPa to become a cylindrical shape (radius d = 16mm and height h = 60mm). The decomposition process was carried out in tube furnace using Ar+CO_2 atmosphere protection in range of 400°C ÷ 500°C in 1.0 hour. After that, the sintering process was taken in tube furnace in range of 900°C ÷ 1000°C in 1.0hour or in vacuum furnace at 1180°C in 2.0hours.

Experimental tests: The phase constituents of products received from preparing were analyzed by XRD. Pores sizes and micro structure were investigated by SEM. The porosity were measured by Archimedes method. The compressive tests were carried out to define Young modulus and mechanical behavior of materials.

Results and discussion

Fig. 1 showed the XRD patterns of porous NiTi synthezised by SHS process (Fig. 1a), by conventional sintering at 1000°C in 1.0h (Fig. 1b) after decomposition process and by vacuum sintering at 1180°C in 2.0h (Fig. 1c) after decomposition process.

In SHS process (T_{pre} = 400°C and T_{ig} = 2000°C), when samples were ignited at some pre-heating temperature, the reaction between Ni and Ti elements happened and released heat and this heat source help self-sustaining the reaction. Due to the reaction happened very fast, reaction time was very short then the reaction nearly completed. So that NiTi phase in XRD pattern was dominant. In addition, before igniting the powders were activation in 2.0h so that the reaction was easier to occur.

In conventional sintering (at 1000°C in 1.0h), the XRD pattern of samples showed that many peaks appear, including peaks of NiTi, Ni_3Ti, Ni_4T_3, $NiTi_2$, Ti, Ni and TiO_2. It meant that the diffusion between Ti and Ni was happened, but it was not complete. This can be explained that the the sintering time was too short, so that Ni and Ti elements cannot diffuse in each other completely. Otherwise, the atmosphere (Ar + CO_2) was not pure, and Ti element was oxidized to form oxide (TiO_2 phase), and TiO_2 impeded the diffusion process between Ti and Ni. So that on the XRD pattern (Fig. 1b), the peaks of Ti, Ni elements still appear.

In vacuum sintering (at 1000°C in 1.0h), the XRD pattern of samples showed that the peak of Ni and Ti disappear. It can be explained in vacuum furnace was complete did not exist oxidation gas, so that Ni and Ti element was easier to diffuse to each other and form Ni-Ti compound. But the sintering time was long and sintering temperature was not high enough so that the samples have both balance phase (NiTi) and not ($NiTi_2$, Ni_3Ti).

Fig.2 showed the SEM images of crack planes of porous NiTi. With the SHS samples, it is clearly that the porosity was high volume, and pores connect to each other so that opened porosity of received porous NiTi was very high, could be reached up to 80% total porosity of materials. Otherwise, pore sizes were quite homogenous. The SEM image also showed that the samples completely formed continuous material. Thus it may give the material the high strength.

Fig. 2c showed the crack plane of conventional sintering samples. We can recognize that the powders connect weakly, so that it maybe affect not good on mechanical properties of porous NiTi alloys.

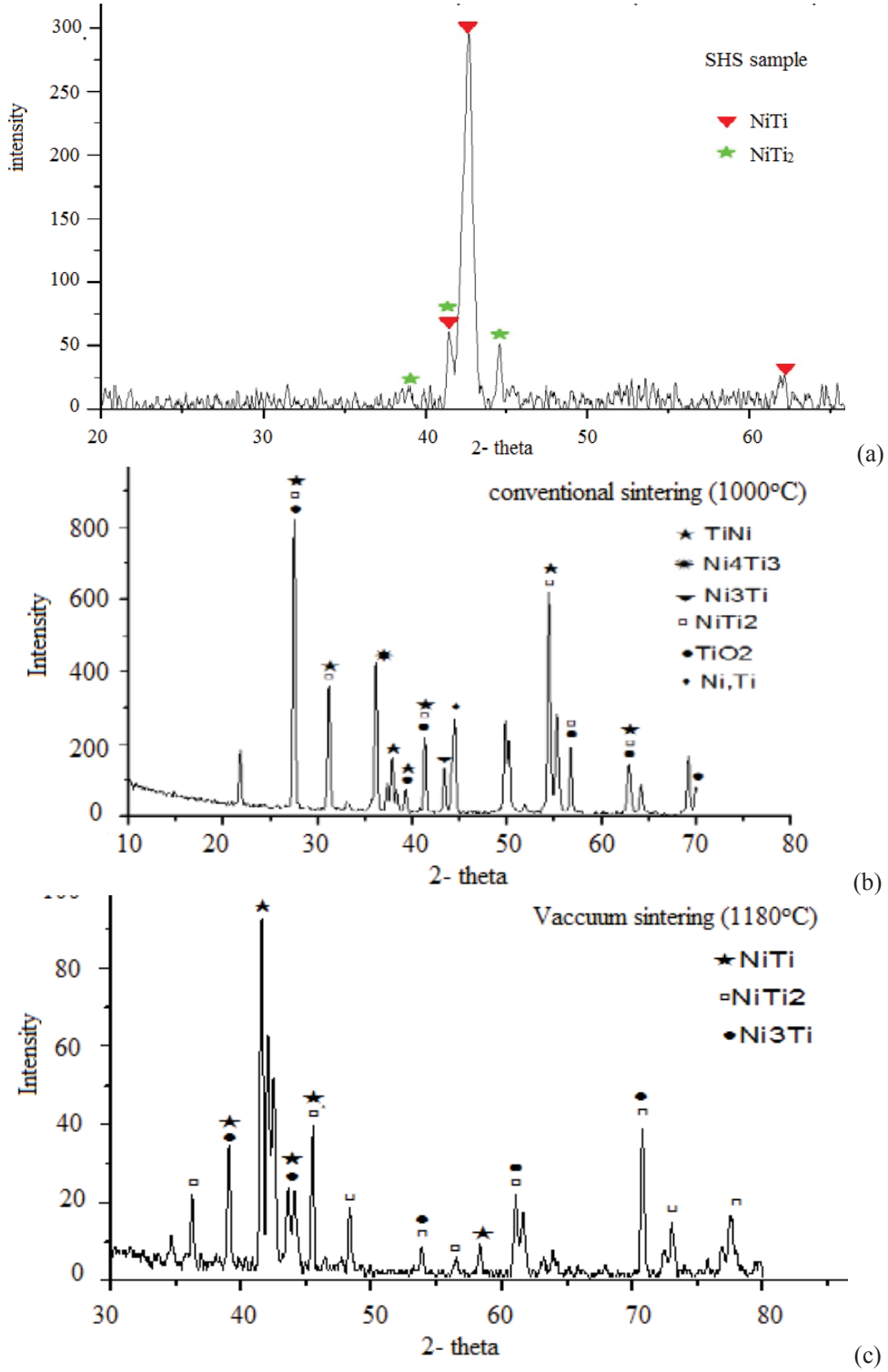


Fig.1. XRD patterns of porous NiTi: (a) SHS samples, T_{ig} = 2000℃, T_{pre} = 400℃; (b) Conventional sintering, T_{sin} = 1000℃, 1.0h; (c) Vacuum sintering, T_{sin} = 1180℃, 2.0h.

Fig. 2d shows that, the porosity of materials was low, it meant that the density of material was high. Thus, it maybe enhances mechanical properties of porous NiTi.

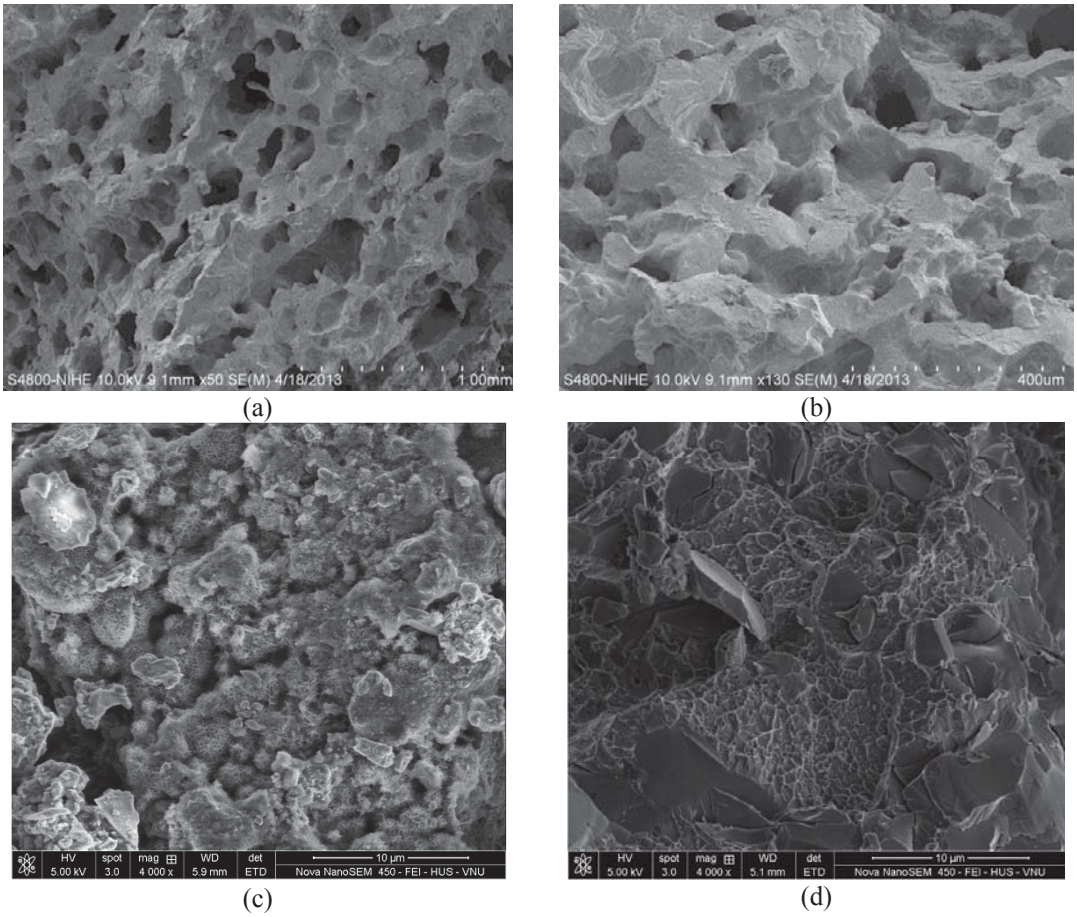


Fig. 2. SEM images of crack plane of: (a) SHS sample, T_{ig} = 400℃; (b) SHS sample, T_{ig} = 500℃; (c) conventional sintering sample (1000℃; 1.0h); (d) vaccuum sintering sample (1180℃; 2.0h).

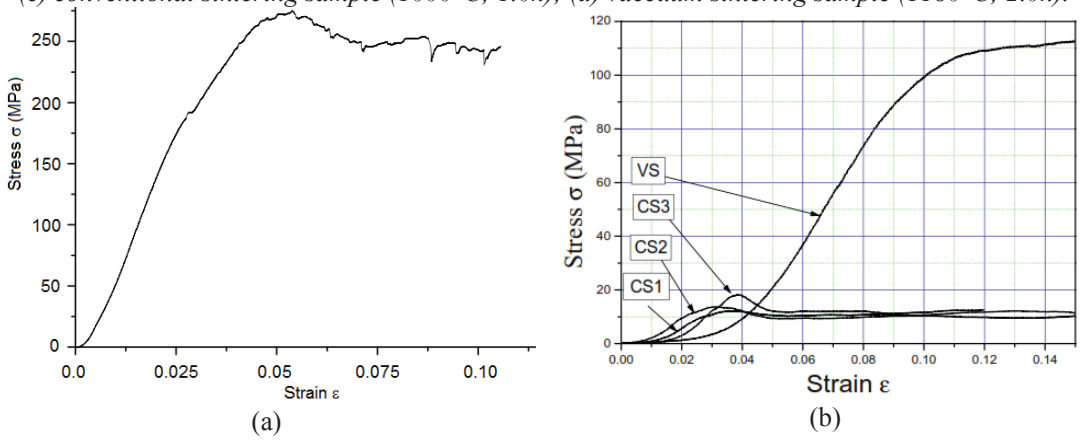


Fig. 3. Stress – Strain curves of porous NiTi: (a) SHS sample (porosity 47%); (b) conventional and vacuum sintering samples: CS1 (1000℃ and porosity 35%); CS2 (900℃ and porosity 36%); CS3 (1100℃ and porosity 38%); VS (1180℃ and porosity 26%).

The stress – strain curves in compress test of porous NiTi samples showed on Fig. 3. The SHS samples exhibited stronger than conventional and vacuum sintering samples (> 250MPa with SHS samples and about 110MPa with vacuum sintering samples and < 20MPa with conventional sintering samples). But SHS samples were more brittle than those, they was cracked when the

degree deformation reached to 5% (with sintering samples > 10%). It can be explained that SHS samples have higher porosity, due to reaction time was very short, the reaction temperature was high so that the pores of samples have complex geometry, and it was easier to form acute angles on surface of pores and cause stress concentration phenomena. When the stress excess maximum stress, the samples will crack. This maybe decrease deformation ability of porous NiTi fabricated by SHS process. Elastic modulus of SHS samples were also higher than sintering samples (about 6.1 – 7.0GPa comparing with < 1.2GPa).

Conclusion

Porous NiTi alloys were successfully synthesized by two different processes, including self-propagating high-temperature synthesis (SHS), and combined processes of decomposition and sintering. By controlling the processing parameters of SHS, the received porous NiTi alloys showed that the porosity and pores were larger, and ratio of opened-pore reached up to 80%. The porous NiTi alloys fabricated by SHS process also exhibited good properties, such as a high compressive strength (up to 250MPa), and elastic modulus in range of 6.1-7.0GPa. The porous NiTi alloys synthesized by decomposition – sintering process have lower porosity (26-43%), lower compressive strength (< 110MPa), lower elastic modulus (< 1.2GPa) but the strain could be reached to 10%.

References

[1]. Christian Greiner, Scott M. Oppenheimer, David C. Dunand; High strength, low stiffness, porous NiTi with superelastic properties; Acta Biomaterialia 1, 2005, pp. 705–716.

[2]. A. Bansiddhi, T.D. Sargeant, S.I. Stupp, D.C. Dunand; Porous NiTi for bone implants: A review; Acta Biomaterialia 4, 2008, pp. 773 – 782.

[3]. Meenakshi Mour, Debarun Das, Thomas Winkler, Elisa Hoenig, Gabriela Mielke, Michael M. Morlock and Arndt F. Schilling; *Review*: Advances in Porous Biomaterials for Dental and Orthopaedic Applications; Materials 2010, 3, pp. 2947 – 2974.

[4]. Lorenza Petrini and Francesco Migliavacca; Review Article: Biomedical Applications of Shape Memory Alloys; Journal of Metallurgy, Volume 2011 (doi:10.1155/2011/501483).

[5]. BING-YUN LI, LI-JIAN RONG, YI-YI LI, and V.E. GJUNTER; An Investigation of the Synthesis of Ti-50 At. Pct Ni Alloys through Combustion Synthesis and Conventional Powder Sintering; METALLURGICAL AND MATERIALS TRANSACTIONS A, VOLUME 31A, JULY 2000, pp. 1867 – 1871.

[6]. Gang Chen, Peng Cao, Neil Edmonds; Porous NiTi alloys produced by press-and-sinter from Ni/Ti and Ni/TiH_2 mixtures; Materials Science and Engineering A, vol.582, 2013, pp. 117-125.

Effects of sintering and compress on porosity, mechanical properties and conductivity of Cu-Al_2O_3 composite materials fabricated by mechano-chemical method

Ho Ky Thanh[1*], Nguyen Duc Duy[2,3], Tran Van Dung[3]

[1]Thai Nguyen University of Technology, Thai Nguyen City, Vietnam

[2]The College of Mechanics and Metallurgy, Thai Nguyen City, Vietnam

[3]Hanoi University of Science and Technology, Hanoi, Vietnam

[a]hkythanh@tnut.edu.vn; [b]nguyenducduycklk@gmail.com; [c]dung.tranvan@hust.edu.vn

Keywords: Cu-matrix composite; mechano-chemical process; dispersion; porosity; conductivity.

Abstract. Nano Al_2O_3 dispersion - strengthened Cu-matrix composite materials were fabricated by mechano-chemical method. The method carrys out at room temperature by mechanical milling in attritor in 16h using mixtures of CuO, Al and Cu powder ingredients, then the mixtures were cold pressed into cylindrical samples and then sintered at various temperatures (from 700°C to 900°C) and time (from 1 to 3 hours) in argon atmosphere. The XRD pattern and EDS results revealed that Al_2O_3 phase were formed and dispersed into Cu-matrix during mechano-chemical process. The Al peak disappeared at the end of mechano-chemical process and th final received products were Cu-Al_2O_3 composite materials with Al_2O_3 content of 3-10% volume. The SEM and EDS results also showed that the particle sizes of Al_2O_3 were in about (50÷100)nm and uniformly dispersed within the C-matrix. The porosity of materials strongly depended on pressure compress, sintering time and temperature, it decreased with increasing of these parameters and reached about 5%. The porosity and Al_2O_3 content affected on mechanical properties of materials, such as micro-hardness and compress strength, due to the dispersion of nano-Al_2O_3 into Cu-matrix. The conductivity of materials decreased with increasing porosity and Al_2O_3 content.

1. Introduction

Copper matrix composite associated with high strength and high electrical conductivity is widely used in industrial applications. Today, different methods have been developed for production of metal matrix composites (MMCs) such as in situ and ex situ methods. In situ reaction has high potential for preparing MMCs with nano-reinforced particles.

MMCs are one of the groups of such type of materials. Copper based metal matrix composites are being used in many industrial applications such as contact supports, electrode materials for lead wires, spot welding and others [1, 2].

Copper matrix composite reinforced by Al_2O_3, TiC, TiB_2 and so on has been widely investigated because: with a certain amount of content, they remain stable, good conductivity, but increased durability, low abrasion resistance at high temperatures.Among common reinforcing phases, Al_2O_3 is well-known for enhancing stiffness, hardness, mechanical strength and wear resistance of copper alloy.

Dispersion strengthened Cu-Al_2O_3 composite materials are extensively used as materials for products which require high-strength and electrical properties, such as electrode materials for lead wires and spot welding, relay blades, contact supports that require high strength at a high temperature, wear-resistance for electrical discharge as well as electrical properties and bearing materials for industry [3]. Studies on the synthesis and characterization of nano-scale alumina dispersed copper metal matrix composites have been attracting scientific interest in recent years, since nanostructure-type materials are expected to have special physical and mechanical properties. In the copper-alumina system, the nano-scale Al_2O_3 particulate dispersion provide unique characteristics, such as high thermal and electrical conductivities, as well as high strength and excellent resistance to high temperature annealing.The main requirement for structure of dispersion

strengthened materials is homogeneous distribution of very fine oxide particles (dispersoids) in the copper matrix [3, 4]. In nano-crystalline materials, the main role of the dispersoids is to limit grain growth at elevated temperatures and to attain a very small grain size, resulting in high strength due to the fine-grain strengthening mechanism [5]. Electrode tips made of this composite material which operating temperature is approximately 800°C demonstrate much higher softening (recrystallization) temperature than tips made of standard high-strength and high conductivity copper alloys. Copper-based composite with a fine dispersion of nano-Al_2O_3 particles produced by high-energy milling has been extensively studied in recent years due to attained better properties than pure copper and precipitation or solid solution hardened copper. Further, high energy milled powders are characterized by very fine, nano-scaled grain structure, which may be retained even during compaction. This fine-grained structure contributes to copper matrix strengthening together with Al_2O_3 particles.

In this study, Cu-Al_2O_3 nano-composites have been fabricated by mechano-chemical process, wherein the alumina contents were adjusted represents 5 vol.%. Some of mechanical and physical properties such as microstructure and density, hardness of Cu-Al_2O_3 composite was the object of this paper. Also, the results demonstrated that nano Al_2O_3 can be able to synthesize by a mechano-chemical process in attritor balls milling.

2. Experimental procedure

The starting materials used in this work were CuO (purity ≥ 99.0%, average size about 40÷50 μm), Cu (purity ≥ 99.7%, average size about 40÷50 μm) and Al (purity ≥ 99.7%, average size about 40÷50 μm) powders. For in-situ powder composite, mixed powder Cu-CuO-Al was milled for 16 hours in argon atmosphere in the attritor ball mill at 720 rpm speed to creating mixture powder Cu-20vol.% Al_2O_3 nano-composites. Then, add Cu powder into the Cu-20vol.%Al_2O_3 mixture was milled for 3 hours in the drum ball mill at 300 rpm speed to produced homogeneous mixture of Cu-5vol.%Al_2O_3 powder.

Then, the nano-composite powders were cold pressed into the compaction mold at pressures 200 to 400 MPa. The compact samples were conventionally sintered at various temperatures (700°C to 900°C) and time (1 to 3 hours). The compact samples were characterized for phase analysis by X-ray diffraction (XRD) and scanning electron microscope (SEM) with energy dispersive spectrometer (EDS). Sintered density of the compact samples was determined by Archimedes method and microhardness of the compact samples was measured by Vickers hardness tester.

3. Results and discussion

3.1. Microstructure

The Cu-20vol.%Al_2O_3 nano-composites was prepared by the mechano-chemical in the attritor ball milling with phase transformations of the precursors. The preparation is described in detail in our works [6]. Obtained by in-situ Al_2O_3 particles are ultrafine - about 50÷100 nm in diameter.

On the Fig.1 shows the results of X-ray diffraction diagram analysis of mixed powder material samples Cu-5vol.%Al_2O_3, that only the appearance of the peak of Cu phase, the peak of Al_2O_3 phase difficult to determine, due to concentration and small size.

With the results of the analysis SEM as shown in Fig.2, Al_2O_3 phase created and dispersed homogenous in the Cu matrix. But here also to note further, in the process of milling, the grain of the constituents will be smaller, leading to the intensity of the peaks are reduced, and the width of the peak increases.

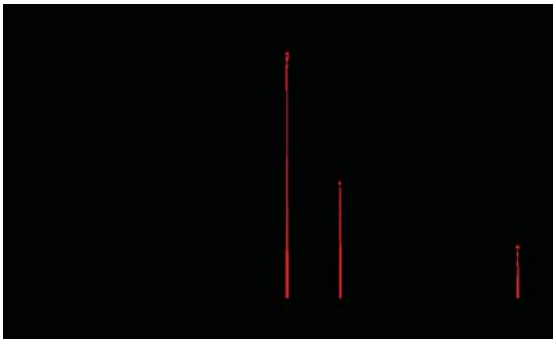


Fig.1. *The X-ray diffraction diagram of mixed powder material samples, Cu-5vol.%Al_2O_3*

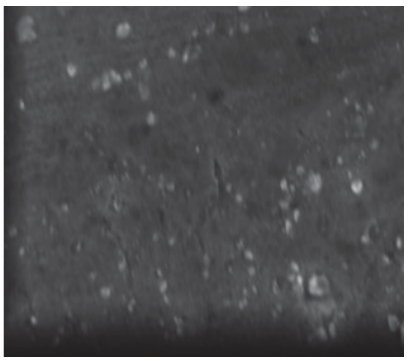


Fig.2. *SEM images of the sample Cu-5vol.%Al_2O_3 sintered at 800°C, 2h*

Fig.3 shows images of SEM-EDS of the sample sintered Cu-5vol.%Al_2O_3. The SEM image indicates fairly homogeneous distribution of Al_2O_3 in Cu matrix. EDS image scan indicates that uniform distribution of Cu, Al and O elements all over surface. The level of copper is much higher than that of aluminum and oxygen. The EDS results revealed locations with a relatively high concentration of Al and O elements. These locations were thought as being "Al_2O_3-rich" which may represent the presence of a third phase of $CuAlO_2$ at interface between alumina particles and copper crystallites matrix.

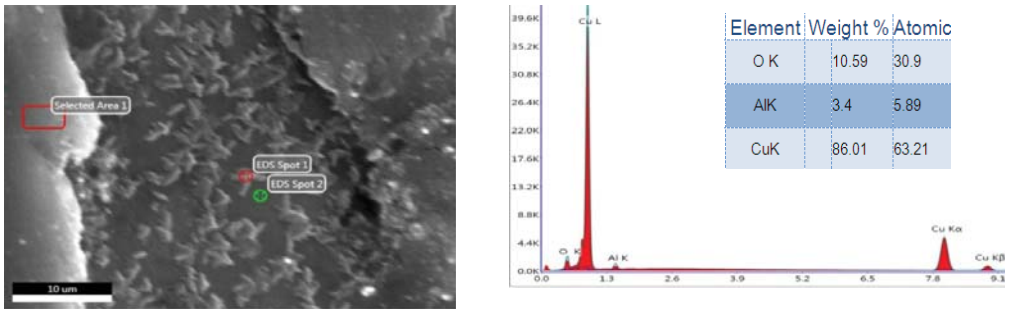


Fig.3. *SEM image and EDS analysis for spot 1 of the sample Cu-5vol.%Al_2O_3 sintered at 800°C, 2 h*

3.2. Material properties

Density is very important information of materials, especial in metal and powder metallurgy engineering. The density is much related to the mechanical properties, friction,... of material. People usually use Archimedes rule to estimate the density.

Micro-hardness is ability of materials to prevent some deformation such as elastic deformation, and bent by reacting with other objects. It is clearly, the higher micro-hardness the harder material to be deformed.

The results of relative density and micro-hardness of the samples of Cu-Al_2O_3 with different alumina content, sintered temperature at 800°C are show in the Table 1.

In the Table 1, the result density and hardness of the material Cu-Al_2O_3 shows that, when Al_2O_3 dispersed in the Cu matrix, the micro-hardness of Cu-Al_2O_3 material much larger than sample blocks are pressed sintered from pure Cu powder, with relative density of about 95%, particle size less than 1 µm crystal, hardness of about 60 HV. This demonstrates that Al_2O_3 dispersed phase is very effective hardening. Thereby, it can be stated effective hardening of Al_2O_3 phase in Cu-Al_2O_3 composite material, the hardness of the sample microstructure Cu-Al_2O_3 nano-composite materials was quite high compared to pure Cu.

Table 1. *Relative density and micro-hardness values of nano-composite Cu-Al_2O_3*

Composites	Relative density (%)	Micro-hardness (HV)
Cu	95.2	58.9
Cu-5vol.%Al_2O_3	85	80
Cu-20vol.%Al_2O_3	75	120

In Fig.4, it is shown that the pressure of the pressures has a strong influence on increasing the density of the nano-composite material, which means that the porosity of the Cu-20% Al_2O_3 nano-composite is reduced. Other, it can be seen from Fig.5 that sintering at high temperatures and sintering time will increase the density of the nano-composite and the porosity will increase due to the development of fine cracks on the surface contact surface between Cu and Al_2O_3. However, the pressures increase in the range of 100 ÷ 400 MPa, the density of Cu-20% Al_2O_3 nano-composite increases from 4.75 g/cm^3 to 6.25 g/cm^3.

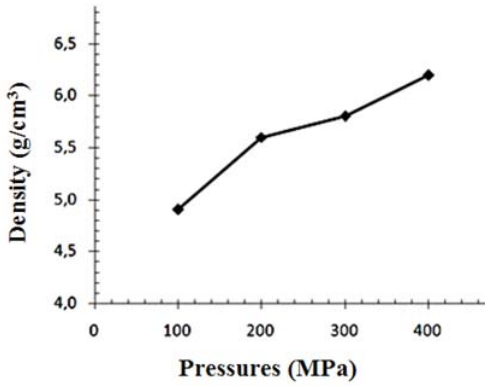


Fig.4. *Effect of pressure on the density of nano-composite Cu-20% Al_2O_3*

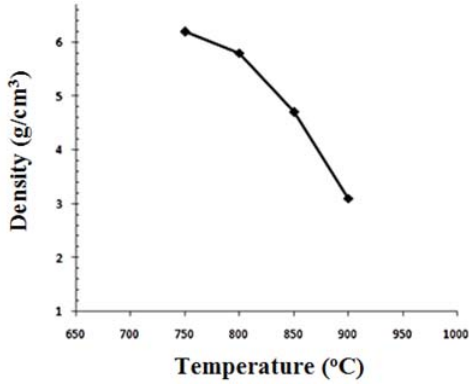


Fig.5. *Effect of sintering temperature on the density of nano-composite Cu-20% Al_2O_3*

The nano-composite hardness with different is shown in Fig.6 and Fig.7. The analysis results show that with the presence of Al_2O_3 phase dispersed in the Cu matrix, the pressures increase from 100 MPa to 400 MPa, the hardness of the Cu-20% Al_2O_3 nano-composite increased from 95 HV to 175 HV. Other, if the temperature increase from 750^{0}C to 900^{0}C and increase the sintering time from 1h to 3h, the porosity increased to 34.05% due to the development of fine cracks on the contact surface between Cu and Al_2O_3. Due to the difference in thermal expansion coefficient between metal Cu and Al_2O_3 ceramic at high temperature, when their temperature returns to normal temperature will appear cracks and holes on the contact surfaces make the degree the hardness of the material also decreased to about 100 HV.

However, the hardness of the Cu-20%Al_2O_3 nano-composite is much higher than that of pure Cu. It can be confirmed that the durability of nano-Al_2O_3 dispersed in Cu matrix and the technology parameters was defined as: milling time of 16h, curing press pressure of 300 MPa, sintering temperature 750 ÷ 850 oC, sintering time 1 ÷ 3 hours.

It can be seen the presence of nano-Al_2O_3 particles significantly increased hardness of Cu-Al_2O_3 materials compared to pure Cu material. Confirm the effectiveness of hardening Cu with dispersed Al_2O_3 phase. The increasing in mechanical properties is analyzed by considering the increation between dispersed of nano-Al_2O_3 particles in the Cu matrix.

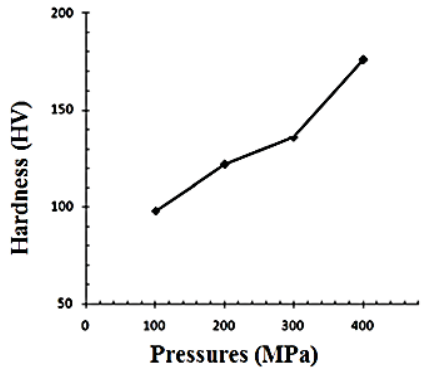


Fig.6.*Effect of pressure on the hardness of nano-composite Cu-20%Al_2O_3*

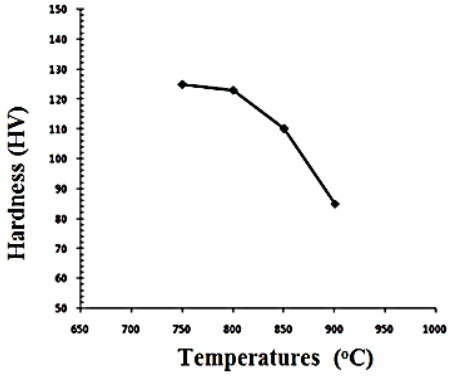


Fig.7.*Effect of sintering temperatures on the hardness of nano-composite Cu-20%Al_2O_3*

4. Conclusion

Composite copper matrix - nano Al_2O_3 dispersion were produced by a mechano-chemical method. The results analysis such as micro-structural and some technological characteristics of the sample Cu-Al_2O_3 materials to draw the following conclusions:

- Copper matrix composite reinforced by nano-Al_2O_3 particles was prepared by in situ reaction on the mechano-chemical methods.
- The process of manufacturing nano-composite Cu-Al_2O_3 by mechanical methods - which have already been set up as perfectly reasonable.
- Al_2O_3 reinforced particles significantly improved hardness and mechanical properties of composite relative to pure Cu material.
- Hardness of Cu-Al_2O_3 materials increased significantly compared to pure Cu material. Confirm the effectiveness of hardening Cu with dispersed Al_2O_3 phase.

References

[1]. Hao Wu, Qiang Li; *Application of mechanochemical synthesis of advanced materials*; Journal of Advanced Ceramics, 2012, vol.1, Issue 2, pp. 130–137.
[2]. D.W. Lee, B.K. Kim; *Nanostructured Cu-Al_2O_3 composite produced by thermochemical process for electrode application*; Mater. Lett. 58, 2004, p. 378-383.
[3]. Seung J.Hwang, Jin-hyung Lee; *Mechanochemical synthesis of Cu-Al_2O_3 nanocomposites*; Materials Science and Engineering A, 2005, vol. 405, pp. 140-146.
[4]. P.K. Jena, E.A. Brocchi, M.S. Motta; *In-situ formation of Cu–Al_2O_3 nano-scale composites by chemical routes and studies on their microstructures*; Materials Science and Engineering A313, 2001, pp. 180–186.
[5].D.Y. Ying, D.L. Zhang; *Processing of Cu-Al_2O_3 metal matrix nanocomposite materials by using high energy ball milling*; Materials Science and Engineering A286, 2000, 152-156.
[6] Nguyen Duc Duy, Tran Van Dung, Nguyen Dang Thuy;*Effect of parameters on microstructure and properties of copper-Al_2O_3 composite by mechanochemical*, Vietnam Mechanical Engineering Journal, ISSN 0866-7056, No.12, 2014, p. 88-93.

Chapter 10. Science and technology developments towards sustainability

A multiple objective model for vehicle routing problem with time windows: A case study

Ho Thi Thu Ai[1, a], Nguyen Truong Thi [2, b], Nguyen Van Can[3, c]

[1,2,3]Department of Industrial Management, College of Engineering and Technology, Can Tho University, Vietnam

[a]: hothithuai2014@gmail.com, [b]: ntthi@ctu.edu.vn, [c]: vancan@ctu.edu.vn

Keywords: green vehicle routing, transportation, carbon emissions.

Abstract

Green transportation has emerged as an efficient way to promote a sustainable supply chain. Transportation activities have significant impact on the whole supply chain at any decision levels. At an operational level, vehicle routing decisions are one of the most critical determinants of the release of transportation emissions. Therefore, this study develops a mathematical model, with an aim to construct routes that simultaneously minimize total cost and total CO_2 emissions from the transportation activities of a case study located in Can Tho City, Vietnam. A multiple-objective model with the consideration of different vehicle loading capacity, and time windows is then solved using a Weighted Tchebycheff method. Results show that route selection has a positive contribution toward a better balance between economic and environmental objectives.

1. Introduction

Transportation has become one of the important sectors in economic development as its direct influence to customer satisfaction levels. However, significant concerns, regarding negative impact on both human health and the environment, have emerged from transportation activities [1]. The release during the combustion of fossil fuels from transportation is a major source of hazardous air pollutants emissions, such as: nitrogen oxides (N2O), particulate matter (PM), and carbon dioxide (CO2). According to United States Environmental Protection Agency (EPA), the amount of CO2 emissions accounts for about 14% of global in 2014 (EEA [2]). Road transport is the biggest contributor to greenhouse gas emissions (GHGs) among all transport modes due to its flexibility and lower weather effects. This leads to a lot of efforts by researchers and practitioners in recent years to reduce these impacts at any decision levels. At strategic level, decision making focuses on long term impacts on the environment, such as facility location, facility capacity, etc. On the other side, operational decisions mainly related to ordering planning, designing and scheduling routing.

VRP (Vehicle Routing Problem) is a well-known problem in routing design, it focuses on minimizing the total travelling distance or the overall transportation cost. Dantzig and Ramseur (1959) [3] are two authors firstly proposed VRP based on Travelling Salesman Problem (TSP). This resulting optimization problem helps decision makers to determine the optimal set of routes for a fleet of vehicles to serve a set of customers. To illustrate, Kara and et al (2007) [4] mention the Capaciated VRP with the new objective. They calculated realistic cost by considering the load of the vehicle and distances. Authors developed integer linear programming but the way solved problem was not presented. Then, Xiao and et at (2011) [5] proposed a fuel consumption rate which considered in Capaciated VRP case. In that model, they taken both distances traveled and load as the factors impacting fuel costs. The load of the vehicle is one of the factors effect to fuel consumption. So, Tavares et al. [6] three levels of vehicle loads are considered: half load, full load, and empty load. Beside that, the effect of the road gradients and speed of the vehicle also should be studied in the next time. The above researches focus on minimizing the amount of fuel consumption as a factor

contributing to minimizing operation costs. However, minimizing the amount of fuel consumed has an importance in minimizing environmental impacts.

Green VRP (GVRP), an extension of VRP, is arising an efficient way to promote a sustainable supply chain as its ability to identify the best route with cost and environment minimization. Green VRP often focus on objective of harmonizing the environmental and economic costs which contribute to sustainable development and improved competitiveness of the company. There are numerous studies on GVRP aiming at lower GHGs by reducing the fuel consumption and improving the transportation efficiency [7]. As stated in the report by the US Department of Energy, travel speed, carrying load weight, and travelling distance are one of the main factors affecting fuel consumption [8]. Ubeda and et.al [9] introduced "green logistics" term in logistics management. Authors considered minimization of distances and pollutant emissions in real case at a company of the Spanish food distribution. Kuo and et al [10] add the transportation speed to the fuel consumption calculation model with time-dependent VRP (TDVRP). In that study, scholar indicated trade-offs between fuel consumption, transportation time and transportation distance when given a vehicle routing plan. Koc¸ and et al. (2014) [11] studied with the objective is a linear combination of vehicle, fixed cost, fuel cost and GHGs, and driver cost. Computational experiments are conducted to show the potential trade-offs between various performance indicators, such as fuel and GHGs emissions, vehicle fixed cost, distance, and total cost. When types of vehicle is considered, Kwon and et al. (2013) [12] expand the Heterogeneous Fleet (HF) when considering environmental impact. The results show that carbon emissions can be reduced with increasing costs due to the benefits of carbon trading. Then, carbon constraint's economy in HF-VRP model is explored in the scholar of Kopfer (2013) [13]. Most GVRP studies have only developed a single objective model based on integrating environmental factors in an objective function. Consequently, affect environment in single objective is not big. Only a few studies have built up a multi-objective model for solving GVRP problems. Following this interest, Racero and et al. (2013) [14] propose a linear programming mathematical model of the Heterogeneous Fleet VRP (HF-VRP) with time windows and backhauls. Paper proposed a multi-objective model minimize the total internal costs, CO_2 and NOx emissions. Moreover, study considered constraints about different capacities and emissions factors.

As the previous work, studies on HF-VRP rarely consider time windows restrictions when mentioning environmental objective. Although there are numerous studies on GVRP, their models consider a single objective function including total cost of transportation and CO_2 emissions or fuel consumption. This paper is distinguished from the previous work in this area by developing a mixed integer linear programming (MILP) model under the consideration of the difference vehicle capacity. This model focuses on minimizing the amount of emissions based on travelled distance and weighted load for each vehicle of type. The multi-objective is then solved using the Weighted Tchebycheff method, which is able to generate Pareto solutions. Furthermore, this study not only optimizes total transportation cost and CO_2 emissions, but also considers regional effect of CO_2 emissions from transportation activities to residential areas through a case study located in Can Tho city.

The structure of the remaining paper is arranged as follows: Section 2 describes the methodology used for emission estimates in MILP and affected region estimates. Section 3 presents the case study description and the mathematical model is presented in section 4. The last sections provide results and conclusion of the research.

2. Methods

2.1. Emission estimates

The formulation is adapted to estimate the amount of CO_2 emissions as follows:

$$\bar{\varepsilon} = \left[\left(E^k_{full} - E^k_{empty} \right) * \frac{\text{loading weight}}{\text{loading capacity}} + E^k_{empty} \right] \quad (1)$$

The calculation of E^k_{full} and E^k_{empty} for different vehicle loading capacity is based on the data provided by DEFRA [15]. The main required parameters for the formulation are the amount of CO_2 emissions (gr CO_2/km) for empty and full vehicle load.

2.2. Affected region estimates

ArcGIS is a Geographic Information System (GIS) tool that allows us to create map and analyze spatial data, while the proposed project is composed of different data, such as census, roads, sub-district outline, and facility location. Once these data are compiled into ArcGIS, both a geodatabase and an electronic map is generated. Here, the approach to obtain affected regions around the road segments is applied by coupling ESRI ArcGIS (Version 10.2). The buffer within 5,000 m of each road segment is generated in order to determine the affected areas. This distance has been addressed in several previous studies to estimate the number of population exposed to fine particulate emissions [16].

3. Problem description (Case study)

Can Tho is the biggest city located in the center of Mekong Delta region, Vietnam. As of 2017, the city has a population of 1.45 million citizens residing in the total land areas of 1,439.2 km^2, including 9 districts [17]. Here, the road transportation system is quite convenient with the national road connecting the city to the rest of country and hence create opportunities for enterprises to exploit their business. The demand for cargo, transported by vehicle from and to the city, has become greater in proportion as the number of people has increased. It is well aware that the emissions from these transportation activities is considered as one of the leading causes of air pollution, which can result in serious issues related to the health effect on residents living in surrounding geographical areas.

In this study, we consider a distribution network, which aims to deliver a product to customers. This kind of network is composed of 1 depot and 13 delivery points. All these points are designed to place on urban and rural areas, as illustrated in Fig 1. A depot, located at central district - a very compact central area, is responsible for collecting and sorting products. This process allows to create a diversified and good products quality before delivering them to customers in different areas of Can Tho city. All products are transported by using a heterogenous fleet with different vehicle loading capacity, assumed to be original from a depot to customers and then from customers to a depot.

The parameters, including capacity, allowable time, driver cost, fixed cost and transportation cost for each vehicle type, are presented in Table 5.

Table 1. Fleet parameters

Vehicle (k)	**1**	**2**	**3**
q_k (tons)	7	10	18
p_k (VND/hour)	40,000	45,000	55,000
T_k (h)	8	8	8
fx_k (VND/vehicle)	200,000	450,000	600,000
tc (VND/km)	5,000	5,000	5,000

Data, related to location, demand, number of delivery points, and time restrictions, is summarized in Table 2.

Table 2. Arrival point location and their demand

Node	**Denomination**	**Demand (tons)**	**Service time (h)**	**Required time windows [e_i; l_i]**
0	Depot	-	0.00	[0; 8]
1	Ninh Kieu 1	5.0	1.00	[0; 4]
2	Ninh Kieu 2	4.5	0.90	[4; 8]
3	Ninh Kieu 3	4.7	0.94	[0; 4]
4	Cai Rang 1	3.0	0.60	[4; 8]
5	Cai Rang 2	1.5	0.30	[0; 4]

6	Binh Thuy 1	2.0	0.40	[4; 8]
7	Binh Thuy 2	2.3	0.46	[0; 4]
8	Phong Dien	0.7	0.14	[0; 4]
9	Thoi Lai	2.1	0.42	[4; 8]
10	O Mon	1.2	0.24	[4; 8]
11	Co Do	2.4	0.48	[0; 4]
12	Thoi Lai	1.4	0.28	[0; 4]
13	Vinh Thanh	0.3	0.06	[4; 8]

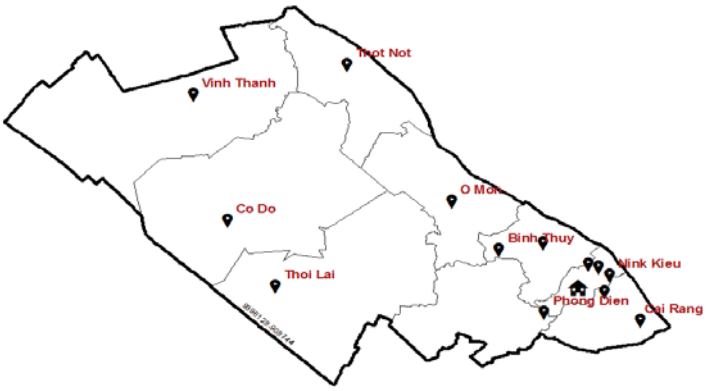


Fig 1. A depot and delivery point location

4. Model formulation

The problem above is formulated as an MILP model with the key following assumption as follow: (a) the product flow starts and finishes at a depot, (b) the number of depot, and customers is known. The customer's demand is deterministic and must be satisfied by a depot, (c) the vehicles used in the case study, are heavy goods vehicles with their payload of 7, 10 and 18 tons.
The indices, parameters and decision variables, used for mathematical model of supply chain network design problem, are formulated as follows.

Sets and indices

i, j	a set of nodes
k	a set of vehicle

Parameters

D_i	demand by node i ∈ {1…n}
q_k	capacity of vehicle k ∈ {1…m}
$[e_i, l_i]$	earliest and latest time to begin the service at node i
s_{ik}	service time in node i by vehicle k
d_{ij}	distance from node i to node j (i ≠ j)
t_{ij}	driving time between the node i and j
T_k	maximum allowable driving time for vehicle k
c_{ijk}	transportation cost per km of vehicle k from node i to j
ε	emission factor (amount of CO_2 emitted per km)
p_k	Pay of labor of vehicle k per unit time
fx_k	fixed cost of vehicle k

Decision variables

x_{ijk}	Equals 1 if vehicle k ∈ {1…m} travels from node i to j (i ≠ j) Otherwise, equals 0
y_{ik}	starting service time at node i ∈ {0, 1…n}

y_{0k} ending service time at a depot
f_{ijk} load carried by vehicle $k \in \{1…m\}m$ from node i to j ($i \neq j$)

Model

A mixed integer programming formulation of the problem can be stated as follows

$$\text{Min} \quad OF_1 = \sum_{k=1}^{m} 2 * p_k * y_{0k} + \sum_{i=0}^{N} \sum_{\substack{j=0 \\ j \neq i}}^{N} \sum_{k=1}^{m} c_{ijk} * d_{ij} * x_{ijk} + \sum_{i=1}^{N} \sum_{k=1}^{m} fx_k * x_{0jk} \qquad (2)$$

$$\text{Min} \quad OF_2 = \varepsilon * d_{ij} * f_{ijk} \qquad (3)$$

The constraints of the mathematical model are given from Equation (3) to Equation (14):

$$\sum_{j=1}^{n} x_{0jk} \leq 1 \qquad (k = 1…m) \qquad (4)$$

$$\sum_{\substack{j=0 \\ j \neq i}}^{n} x_{ijk} - \sum_{\substack{j=0 \\ j \neq i}}^{n} x_{jik} = 0 \qquad (k = 1…m;\ i = 1…n) \qquad (5)$$

$$\sum_{k=1}^{m} \sum_{\substack{j=0 \\ j \neq i}}^{n} x_{ijk} = 1 \qquad (i = 1…n) \qquad (6)$$

$$\sum_{i=1}^{n} D_i * \sum_{\substack{j=0 \\ j \neq i}}^{n} x_{ijk} \leq q_k \qquad (k = 1…m) \qquad (7)$$

$$y_{ik} + s_{ik} + t_{ij} \leq y_{jk} + T_k * (1 - x_{ijk}) \qquad (i = 1…n;\ j = 0…n;\ j \neq i;\ k = 1…m) \qquad (8)$$

$$t_{0j} \leq y_{jk} + T_k * (1 - x_{0jk}) \qquad (j = 1…n;\ k = 1…m) \qquad (9)$$

$$e_i \leq y_{ik} \leq l_i \qquad (i = 1…n;\ k = 1…m) \qquad (10)$$

$$y_{0k} \leq T_k \qquad (k = 1…m) \qquad (11)$$

$$\sum_{k=1}^{m} \sum_{\substack{j=0 \\ j \neq i}}^{n} f_{jik} - \sum_{k=1}^{m} \sum_{\substack{j=0 \\ j \neq i}}^{n} f_{ijk} = D_i \qquad (i = 1…n) \qquad (12)$$

$$f_{ijk} \leq (q_k - D_i) * x_{ijk} \qquad (i = 0…n;\ j = 0…n;\ j \neq i;\ k = 1…m) \qquad (13)$$

$$D_j * x_{ijk} \leq f_{ijk} \qquad (j = 1…n;\ i = 0…n;\ i \neq j;\ k = 1…m) \qquad (14)$$

$$\sum_{i=0}^{N} x_{4ik} + \sum_{i=0}^{N} x_{i4k} + \sum_{i=0}^{N} x_{i10k} + \sum_{i=0}^{N} x_{10ik} = 0 \qquad k = 1, i = 0 \ldots n \qquad (15)$$

The objective function (2) minimizes the total transportation cost including driver cost, transportation cost based on total distances and fixed cost for each vehicle is used The objective function (3) minimizes the total CO_2 emissions caused by transportation activities. Constraint (4) means that each vehicle departs from the depot once or doesn't. Constraint (5) are the flow conservation on each node. Constraint (6) guarantees that each customer and supplier is visited exactly once. Constraint (7) ensures that no vehicle can be overloaded. Starting service times are calculated in constraints (8) and (9), where y_{0k} is the ending time of the tour for vehicle k. Time windows are imposed by constraints (10). Constraint (11) avoids exceeding the maximum allowable driving time. The flow balance is described in constraint (12). Constraints (13) and (14) are used to restrict the total carrying load of a vehicle. Constraint (15) means that vehicle 1 cannot serve at node 4 and 10 due to the limitation of infrastructure to these nodes.

This paper generally focuses on finding the compromise solutions that can minimize cost and environmental impact represented by OF_1 and OF_2 respectively. Each of these solutions is described as a Pareto solution, which represents a trade-off between conflicting objectives. This means that any improvement in one objective results in the other objective to be worse. The Pareto frontier, created by linking all Pareto solutions, is the curve that divides the Pareto shape into feasible and infeasible domain. Afterwards, the best suite solution for the problem is typically selected based on decision makers experience to analyze and evaluate the Pareto set. In this paper, one of the common methods, proposed to solve these two conflicting objectives, is Augmented weighted Tchebycheff method, as firstly suggested by Steuer and Choo [18]. Augmented weighted Tchebycheff method formulation for this approach are shown as follows:

$$\text{Minimize} \qquad \gamma + \rho * \sum_{k=1}^{2} (OF_k - z_k^{**}) \qquad (16)$$

$$\text{Subject to} \qquad w_1 * \left(OF_1 - z_1^{**}\right) \le \gamma$$
$$w_2 * \left(OF_2 - z_2^{**}\right) \le \gamma \qquad (17)$$
Equation (4) to Equation (15)

$$\text{in which} \qquad w_1, w_2 \ge 0 \text{ and } w_1 + w_2 = 1 \qquad (18)$$

Note: ρ: very small and positive
z_k^{**}: reference point (approximate to the ideal solution)
γ: zero or positive

5. Results

In order to solve the proposed model, the value of ρ is assumed to be 0.01 for all problem types. Since the size of the problem is not quite large, the optimal solution can be found at a reasonable time. In this paper, we use CPLEX optimization software version 12.6 to solve each sub-problem on 1.70 GHz Intel ® Core ™ i3-4005 CPU. There are total of 11 sub-problems corresponding to 11 Pareto solutions obtained along the Pareto frontier, as given in Fig 2. Each Pareto solution allows decision makers to verify the dependency between economic and environmental objectives.

Different solutions result in different delivery routes. It worth noting that the proximity of the depot to customers is one of factors affecting a lower the total transportation cost. Here, the location of the depot at Ninh Kieu district is close to delivery points, and hence creates the advantages in

transportation cost savings. However, environmental and human impact, caused by these transportation activities, are large due to a higher population density of this area. Minimizing the impact always results in the higher transportation cost, as represented in solution 11. A total decrease in environmental impact of 46.7% can be obtained at a cost increase of only about 0.1%. For solution 6, 39.3% reduction in environmental impact leads to approximate savings of 0.03% in transportation cost.

Another interesting point is to investigate the areas affected by transportation activities. The supply chain configuration of solution 6 is selected due to its less CO_2 emissions and transportation cost among the others, as depicted in Fig 3. The product from the depot to delivery points is transported by using 3 vehicles with different payloads. Customers have higher demand will be served to reduce fuel consumption and fuel cost. That the reasson why total cost increase a little by increase travel time and total distances. Vehicle 1 and 3 with their payload of 7 and 18 tons starts from the depot to the customer in Ninh Kieu, Cai Rang, Binh Thuy district. Vehicle 2 with a payload of 10 tons from the depot to Phong Dien, Thot Not, Co Do, Vinh Thanh, Thoi Lai, and O Mon.

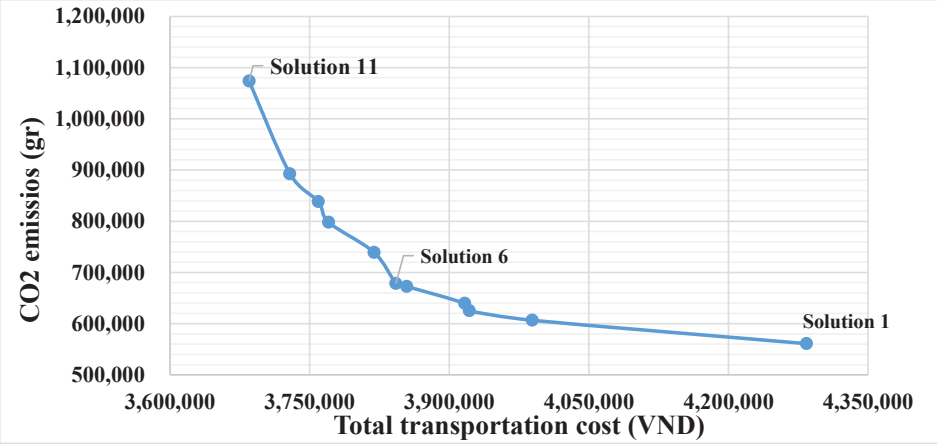


Fig 2. Trade-offs between total transportation cost and CO_2 emissions

6. Conclusion and discussion

This paper focuses on the design of supply chain network. A bi-objective model for a distribution network problem with the consideration of different vehicle loading capacity 7 tons, 10 tons and 18 tons is presented. The first objective of the model is to minimize total transportation cost, while the second one is to minimize CO_2 emissions. The relationships between these objectives are represented to assist decision makers in developing a sustainable supply chain. The resulting model demonstrates that a slight increase in total transportation cost results in a significant reduction of environmental impact. The use of Arcgis is very effective in estimating the affected areas by transportation operations. Beside that, transportation is main source congestion, noise and other pollution in area. Future research can be extended to include demand uncertainty in a tri-objective model when considering simultaneously economic, environmental, and social impact.

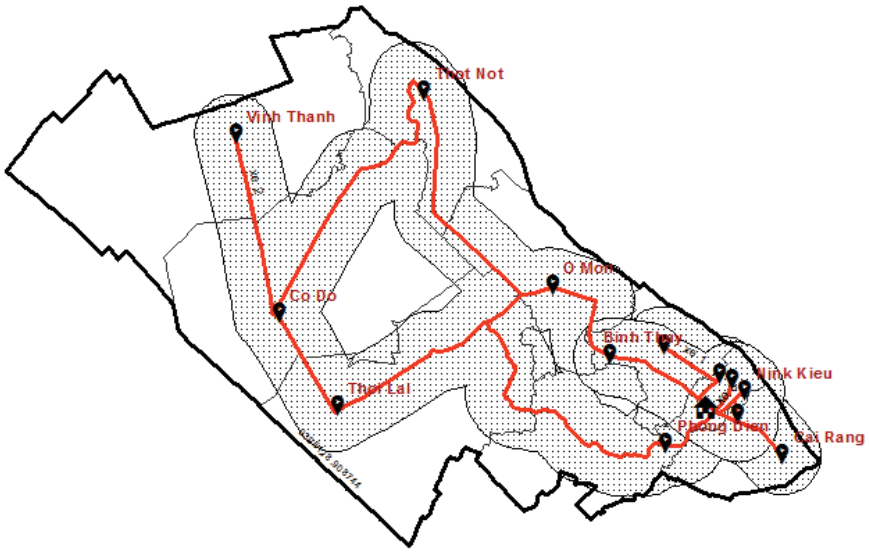


Fig 3. Areas affected by transportation activities

References

1. Dekker, R., J. Bloemhof, and I. Mallidis, *Operations Research for green logistics – An overview of aspects, issues, contributions and challenges.* European Journal of Operational Research, 2012. 219(3): p. 671-679.
2. EEA, *EEE Greenhouse Gas Data (2008).* 2011.
3. Dantzig, G.B. and J.H. Ramser, *The Truck Dispatching Problem.* Management Science, 1959. 6(1): p. 80-91.
4. Kara, I., B. Kara, and M. Yetis, *Energy Minimizing Vehicle Routing Problem*. Vol. 4616. 2007. 62-71.
5. Xiao, Y., et al., *Development of a fuel consumption optimization model for the capacitated vehicle routing problem.* Computers & Operations Research, 2012. 39(7): p. 1419-1431.
6. Tavares, G., et al., *A case study of fuel savings through optimisation of MSW transportation routes*. Vol. 19. 2008. 444-454.
7. Erdoğan, S. and E. Miller-Hooks, *A Green Vehicle Routing Problem.* Transportation Research Part E: Logistics and Transportation Review, 2012. 48(1): p. 100-114.
8. *Fuel economy guide.* US Department of Energy 2008.
9. Ubeda, S., F.J. Arcelus, and J. Faulin, *Green logistics at Eroski: A case study.* International Journal of Production Economics, 2011. 131(1): p. 44-51.
10. Kuo, Y., *Using simulated annealing to minimize fuel consumption for the time-dependent vehicle routing problem*. Vol. 59. 2010. 157-165.
11. Koç, Ç., et al., *The fleet size and mix pollution-routing problem.* Transportation Research Part B: Methodological, 2014. 70: p. 239-254.
12. Kwon, Y.-J., Y.-J. Choi, and D.-H. Lee, *Heterogeneous fixed fleet vehicle routing considering carbon emission.* Transportation Research Part D: Transport and Environment, 2013. 23: p. 81-89.
13. Kopfer, H. and H. Kopfer, *Emissions minimization vehicle routing problem in dependence of different vehicle classes*. 2013. 49-58.
14. Racero, J., *Environmental issues in vehicle routing problems*. 2013. 215-241.
15. DEFRA, *Guidelines to Defra's GHG Conversion Factors: Methodology Paper for Transport Emission Factors.* Technical Report, Department of Environment, Food and Rural Affairs, 2008.
16. Waygood, E.O.D., T. Chatterton, and E. Avineri, *Comparing and presenting city-level transportation CO2 emissions using GIS.* Transportation Research Part D: Transport and Environment, 2013. 24: p. 127-134.
17. Wikipedia, 2017.
18. E. Steuer, R. and E. Choo, *An Interactive Weighted Tchebycheff Procedure for Multiple Objective Programming*. Vol. 26. 1983. 326-344.

Producing of Carbon Fibers from Commercial Viscose Fibers

NGUYEN Huu Son[1,a], VU Le Hoang[2,b], PHAM Van Cuong[2,c], LE Thai Hung[1,d*]

[1]*The School of Materials Science and Engineering – Hanoi University of Science and Technology, Nº1 Dai Co Viet Street, Hanoi, Vietnam*

[2]*Institute of Technology, Hanoi, Vietnam*

[a] email: son28tccnqp@gmail.com, [b] email: vulehoangvl@gmail.com,

[c] email: cuong.pv@gmail.com, [d*] email: hung.lethai@hust.edu.vn

Keywords: Carbonization, carbon fibers, Viscose, cellulose, stabilization

Abstract. In this work, commercial Viscose fibers (cellulosic based precursor) were used for making carbon fibers. The experimental procedures include two main steps: Stabilization in air atmosphere and Carbonization in inert gas atmosphere. In the first step, the Viscose fibers are stabilized with the catalyst of mixture urea/diamonium hydrogen phosphate in air at temperature of 250 ºC. The stabilized fibers are then carbonized in argon at heating rates of 3 ºC.min^{-1} (below 600 ºC) and 5 ºC.min^{-1} (above 600 ºC). Ultimate carbonization temperature is 1200 ºC. Commercial Viscose fibers possessed carbon content about 40 wt% and fiber dimension about 18 μm. After carbonization, obtained fibers have carbon content above 94 wt% and diameter of about 8μm. The Thermogravimetry Analysis (TGA), Carbon analysis, SEM imaging and XRD analysis are used for this study.

1. Introduction

Viscose rayon fiber (Cellulosic based precursor), PAN fiber (Polyacrylonitrile) and Pitch based precursor are widely used materials to manufacture carbon fibers [1, 2]. Among them, Viscose rayon fiber is the most common precursor for commercial carbon fibers production. Developing carbon fiber from Viscose fiber is generally subjected to three processes namely stabilization, carbonization, and graphitization to structural materials or activation to activated materials.

The experimental works on stabilization of Viscose fibers have recently been reported in litteratures [3, 4], in which suitable catalyst contents and dehydration temperature of cellulose have been determined. The objective of this study is to investigate carbonization process of Viscose fibers after stabilization step, and effective factors on carbon-cellulose transformation process.

Carbonization is a pyrolysis process at a temperature higher than that of the cellulosic based precursor. During the carbonization process, the cellulose mainly transforms into carbon. Pyrolysis of cellulose is an oxidation process in air at temperature below 350 ºC to stabilize fibers, which improves carbon fibers properties and prevents the undesirable formation of pitch. During the pyrolysis process of cellulose, suitable catalyst is used in order to increase dehydration rate, lower stabilization temperature, and prevent the elimination of carbon in residual fibers. In this stage, several chemical reactions take place at the same time, which bring about a significant reduction of fibers's weight. The formation of pre-structure proceeds subsequently at elevated temperatures to make carbon matrices [2, 5, 6, 7].

After stabilization, residual fibers possesses about 60 – 70 wt% carbon. When the fibers is carbonized at temperatures 900 – 1500 ºC, the carbon content increases continuously to reach of 90

– 95 wt%. In this stage, all physical and mechanical properties of fibers have been changed, therefore, it can be controlled to make carbon fibers with desirable characteristics.

This paper presents experimental results of making carbon fibers from commercial Viscose fibers. Changes in crystalline structure, the variation of fiber diameter and carbon content are investigated.

2. Experiments

2.1. Materials

Cellulosic based precursor is commercial Viscose fibers possessed carbon content of 40.70 wt% and fiber diameter about 18 μm (fig 1, 2).

The catalyst mixture for stabilization includes as follows: urea $CO(NH_2)_2$, diamonium hydrogen phosphate $(NH_4)_2HPO_4$ and pure water.

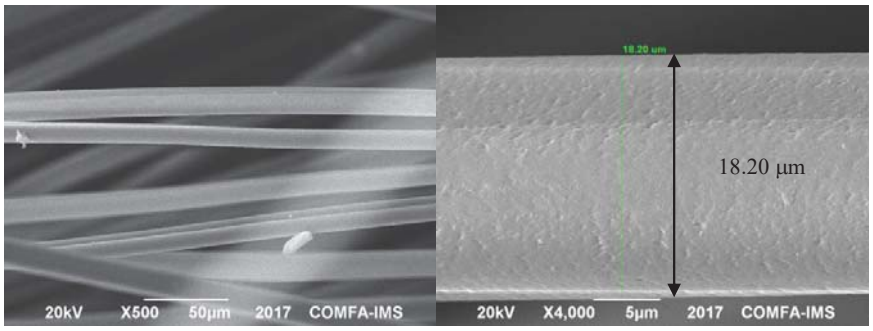


Fig. 1. SEM images of commercial Viscose fibers.

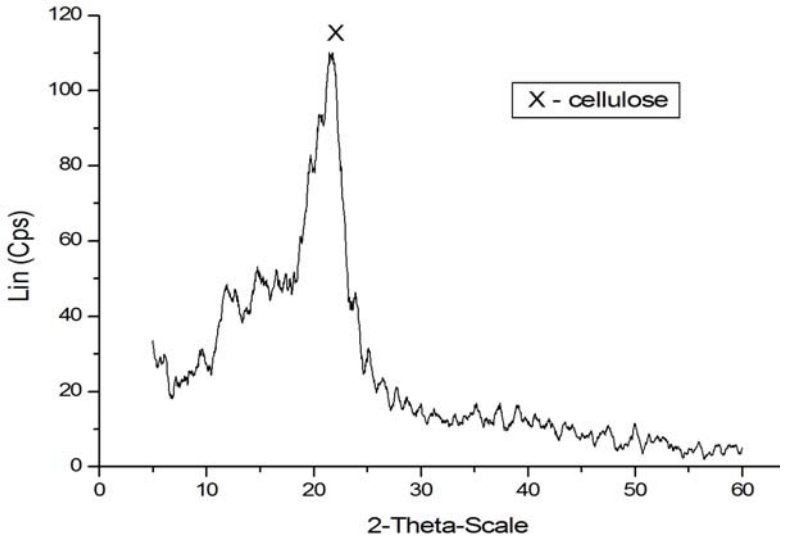


Fig. 2. XRD patterns of commercial Viscose fibers.

2.2. Experimental procedures

Stabilization step

Cellulose pyrolysis, dehydration and stabilization of Viscose fibers are firstly done [3, 4]. Fibers are immersed into solution of mixtured urea/diamonium hydrogen phosphate (weight ratio of 2/1), then heated at temperature of 250 ^oC for 60 min in air.

Carbonization step

Carbonization experiments are conducted in in tube furnace system of Nabertherm RSRC, Germany. Its maximum temperature can reach 1300 ºC. Carbonization process is conducted in argon at temperature ranging from 250 to 1200 ºC . Heating rate are 3 ºC.min^{-1} at temperature from 250 to 600 ºC and 5 ºC.min^{-1} at temperature from 600 to 1200 ºC. Temperature holding time is of 60 min.

Carbon content of the fibers samples are analyzed by Leco CS230CSH equipment. Viscose fibers and carbonized fibers are observed by SEM images and the fiber diameter is measured based on the SEM images. The phase of the fibers are analyzed by Brucker D8 Advance X-ray diffraction equipment.

3. Results and discussions

3.1. Stabilization step

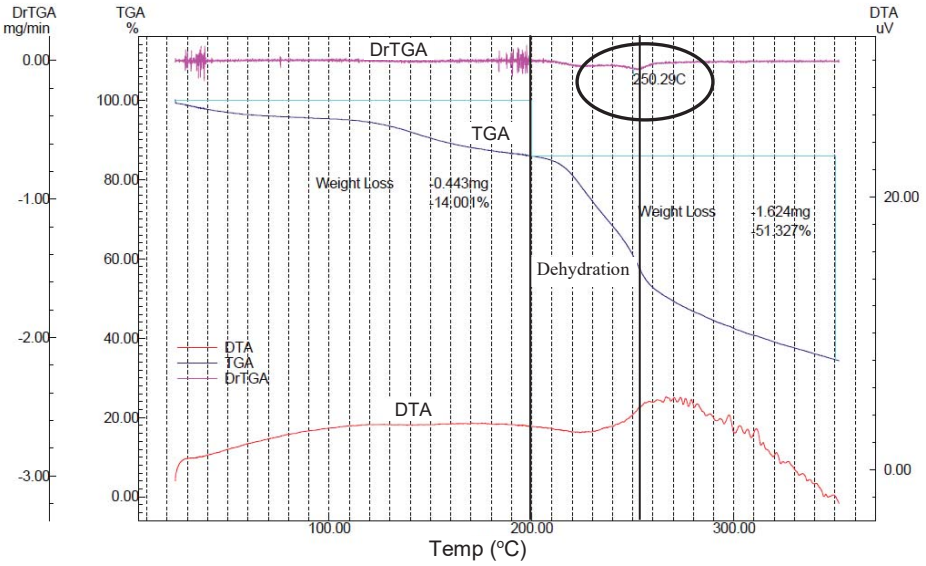


Fig. 3. TGA scans of commercial Viscose fibers in stabilization step (with catalyst).

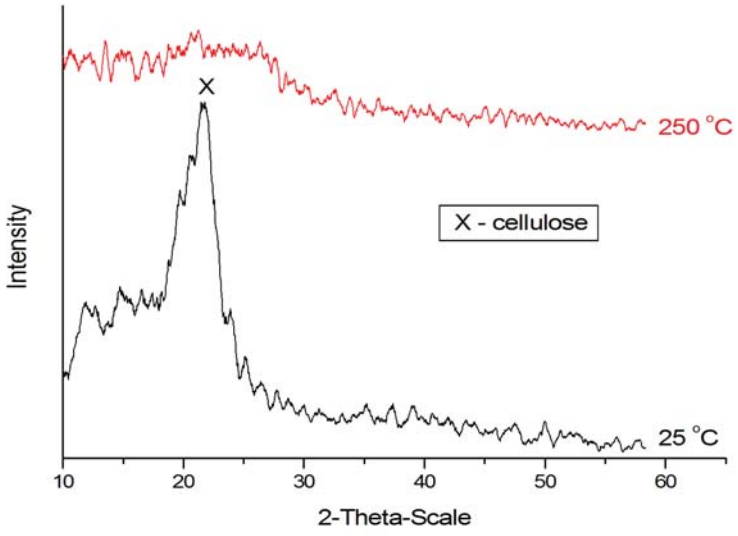


Fig. 4. XRD-patterns of fibers in stabilization step.

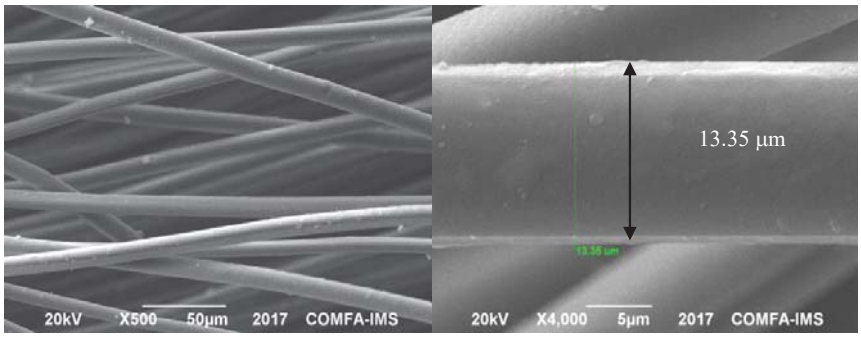


Fig. 5. SEM images of stabilized fibers.

Physical desorption of water and dehydration from cellulose unit happened in this step. Cellulose was pyrolyzed at low temperature with elimination of hydroxyl groups (-OH). The results showed that weight loss was high (25.23 %), carbon content in residue enhanced fast (40.70 to 59.72 wt%). Dehydration reaction reached maximum rate at 250 ºC in TGA scans (see fig. 3).

Changes in crystalline structure of fibers are conducted in XRD-patterns (fig. 4). The dehydration of Viscose fibers changed the crystal structure partially. The pyrolysis of cellulose unit made the structure become chaotic at 250 ºC. The fiber structure was non-crystalline, like amorphous fibers.

Figure 5 shows SEM images of stabilized fiber sample at temperature 250 ºC. Fiber diameter decreased strongly (18.20 to 13.35 µm) after stabilization step, corresponding to significant weight loss.

3.2. Carbonization step

Carbonization is pyrolysis process at higher temperature than pyrolysis of the cellulose. The weight of fibers will decrease slower, carbon content increases simultaneously with the gradual elimination of oxygen and hydrogen in residue.

Table 1: Experimental results of carbonization step.

No	Carbonization temp, [ºC]	Carbon content, [wt%]	Weight loss, [%]
1	250	59.72	25.23
2	600	77.10	45.69
3	700	79.95	46.89
4	800	83.30	49.50
5	900	86.65	50.65
6	1000	90.00	52.62
7	1100	93.05	55.53
8	1200	94.15	56.43

The results in table 1 showed that oxygen and hydrogen were eliminated vigorously in pyrolysis stage from 250 to 600 ºC, weight loss (25.23 to 45.69 %) and enhancement of carbon content (59.72 to 77.10 wt%) were still significant. In stages of higher temperatures from 600 to 1200 ºC, weight loss and carbon enhancement are slower because amount of oxygen is very little in residue. The elimination of hydrogen, aromatization and polymerization are the essential processes in these stages. At ultimate temperature of 1200 ºC, carbon content reached 94.15 wt% and residual weight (carbonization efficiency) of 43.57 % whereas precursors possessed 40.70 wt% carbon (see figure 6). These showed a high carbonization efficiency and a low amount of eliminated carbon only. Carbonization efficiency is the ratio of carbonized fibers's weight to starting fibers's weight.

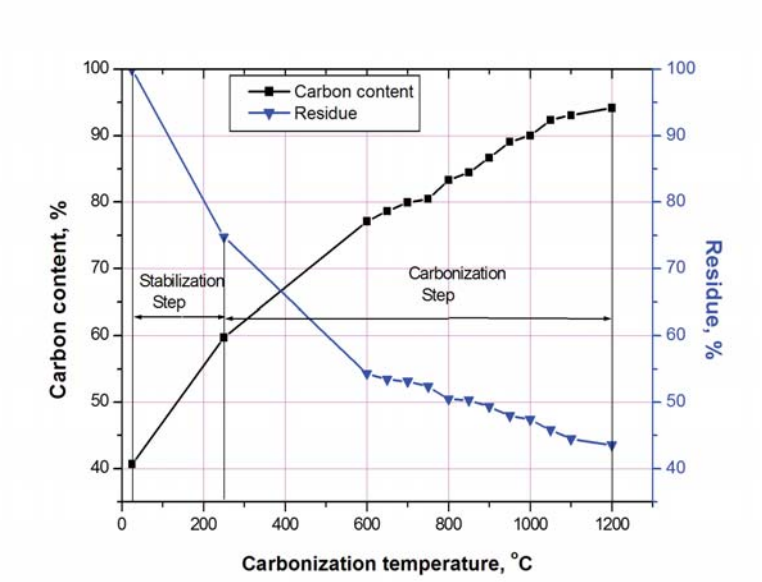


Fig. 6. Relationship between carbonization temperature and carbon content, residue.

Changes in crystalline structure of fibers are indicated in XRD-patterns (fig.7). Amorphous structure existed in pyrolysis stage from 250 to 600 ºC with a large elimination of oxygen and hydrogen. Order structure developed gradually above 600 ºC. Evidence of turbostratic structure might be in the whole crystalline structure of carbon fiber which is carbonized at 1200 ºC (see XRD-patterns in fig.7).

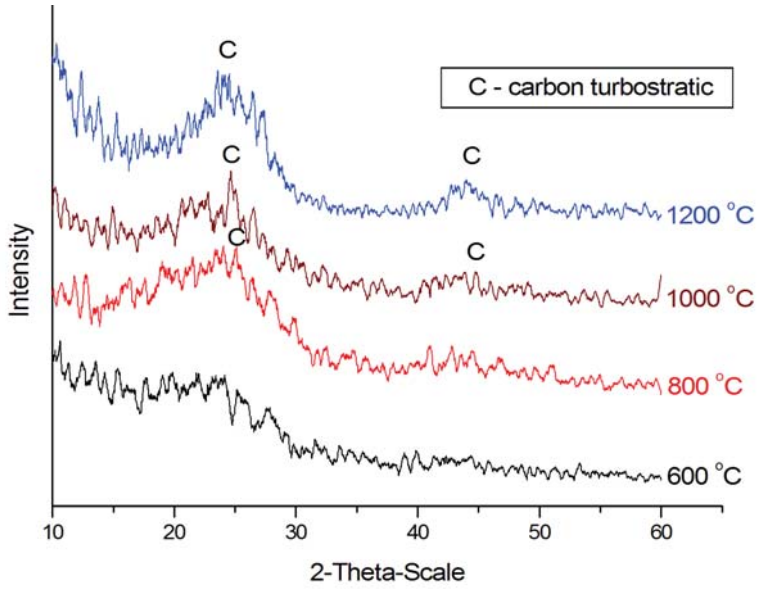


Fig. 7. XRD-patterns of fibers in carbonization step.

Fiber diameter decreased in carbonization step slower than it did in stabilization step, corresponding to smaller weight loss. These quite accorded with mechanism of carbon-cellulose transformation. A large amount of oxygen and hydrogen were removed in stages of dehydration at

250 ºC and pyrolysis below 600 ºC. The removal of hydrogen, aromatization and polymerization were the essential processes in higher temperature stages. After carbonization at 1200 ºC, fiber diameter decreased of 56.05 % (down to 8.00 µm), while it reduced of 26.65 % in stabilization step (room to 250 ºC) and 29.40 % in carbonization step (250 - 1200 ºC). Changes in fiber diameter are showed in figures 8 and 9.

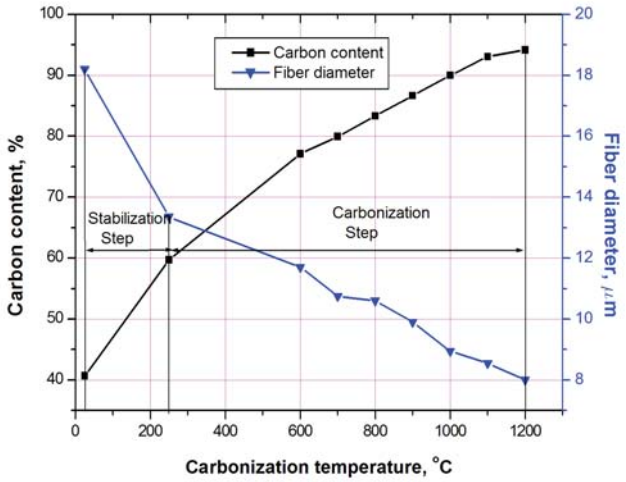


Fig. 8. Relationship between carbonization temperature and fiber diameter, carbon content.

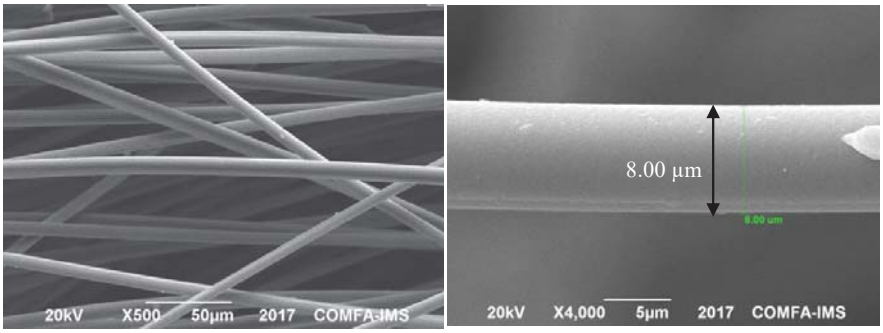


Fig. 9. SEM images of carbon fibers (carbonized at 1200 ºC).

4. Conclusions

- Commercial Viscose fibers (Cellulosic based precursor) have been carbonized in argon at temperature of 1200 ºC to get carbon fibers, which possess carbon content above 94 wt%.

- The suitable heating rate is chosen for carbonization process, as follow: 3ºC.min^{-1} in the below 600 ºC stages; 5 ºC.min^{-1} in the above 600 ºC stages. When carbonizing with this heating mode, carbonization efficiency reaches 43.57 % (precursor possessed 40.70 % carbon) and carbon content reaches 94.15 wt%.

- Carbon fibers have diameter of about 8.00 µm after carbonizing at 1200 ºC in unstrained condition. It decreases of 56.05 % as one of Viscose fibers (18.20 µm). Fiber diameter decreases quickly with 26.65 % (down to 13.35 µm) in stabilization stage, subsequently it decreases slower in carbonization stages.

- Weight loss is larger and carbon content increases quickly in carbonization stages below 600 ºC. In carbonization stages at temperatures in a range from 600 to 1200 ºC, weight loss is smaller and carbon content enhancement is slower.

- Crystalline structure of fibers are changed throughout the making process. Cellulose units became amorphous at 250 ºC. Subsequently, order structure developed gradually above 600 ºC and finally, crystalline structure of carbon fibers has been carbon turbostratic at 1200 ºC.

Acknowledgements

We thank the school of Materials Science and Engineering – Hanoi University of Science and Technology for research supports.

References

[1] Peter Morgan, "Carbon Fibers and their Composite – Chapter 4: Precursor of Carbon Fiber Manufacture", Taylor & Francis Group, 2005.

[2] D. D. Edie & R. J. Diefendort, "Carbon Fiber Manufacturing", Carbon-Carbon Materials and Composite, Edited by John D. Buckley & Dan D. Edie, Noyes Publications, 1993.

[3] Nguyen Huu Son, Pham Van Cuong, Vu Le Hoang, Le Thai Hung, "Stabilization of commercial viscose fiber for making carbon fibers", Proceedings of the Metallurgical Engineering & Advanced materials technology, HUST, pp.34-39, 2016, ISBN: 978-604-95-0019-0.

[4] Nguyen Huu Son, Pham Van Cuong, Vu Le Hoang, Le Thai Hung, "Effect of catalyst content on stabilization of commercial viscose fibers used as carbon fiber precursor", J. Science and Technology of Metals, No76, (2018) pp.38-43.

[5] Peter Morgan, Carbon Fibers and their Composite – Chapter 6: Carbon Fiber Production using Cellulosic based Precursor", Taylor & Francis Group, 2005.

[6] Bacon, R. and M. Tang, Carbonization of Cellulose Fibers-I: Low Temperature Pyrolysis, Pergamon Press Ltd, Carbon, vol 2, (1964) pp. 211-220.

[7] S. J. Allen, L. Whitten, G. Mckay, The Production and Characterisation of Activated Carbons: A Review, Asia-Pacific Journal of Chemical engineering, Vol6, (1998), pp.231-261.

The influence of alumina filler on mechanical, thermal and electrical properties of Bulk Moulding Compounds (BMCs) composite

LE Thai Hung[1, a *], NGUYEN Hien Trang[1, b]

[1]Hanoi University of Science and Technology, N°1 Dai Co Viet Street, Hanoi, Vietnam

[a*] hung.lethai@hust.edu.vn, [b] hientrang955@gmail.com

Keywords: BMC; mechanical properties; electrical properties; thermal resistance; alumina filler.

Abstract. Bulk moulding compounds (BMCs) are composite materials of thermosetting polymer matrix reinforced by short glass fibers. BMCs have known as the alternative of the traditional materials thanks to their optimal properties such as lightweight, durability, corrosion under certain environment, formable, high electrical resistance... The previous study mentioned the process of manufacturing composite materials BMCs from unsaturated polyester resin reinforced with short glass fiber and $CaCO_3$ filler by Z axis mixer and applying in the circuit breaker bottom, [1, 2]. To improve the thermal resistance of BMCs under high temperature condition in the industry, in this research, alumina filler was added to investigate the influence of alumina with the different content of 15wt.% and 20wt.% on the mechanical, thermal and electrical properties of BMCs. Specimens manufactured with and without alumina filler content were compared. The results show clearly that adding alumina could improve the thermal properties whereas this might decrease the tensile strength of BMCs. The experimental results also indicated the influence of mass fraction of alumina filler content on properties of BMCs.

1. Introduction

Bulk moulding compounds (BMCs) are composite materials that are made up of a pasty filled thermoset polymer matrix reinforced by entangled short glass fibers. BMC's are widely used by the electric industry to produce small components with good surface quality and complex shapes, as well as by the automotive industry to produce for example car panels. Their processing consists of three main phases: (i) the compounding phase, i.e. mixing uncured polyester resin, mineral fillers, glass-fiber bundles and other additives, (ii) the injection or compression moulding phase (1–10 s) during which these compounds are forced to fill a hot mould 150 °C), (iii) the resin cure within the hot mould (60–180 s).

In the previous study mentioned the process of manufacturing composite materials BMCs from unsaturated polyester resin reinforced with short glass fiber and $CaCO_3$ filler by Z axis mixer and applying in the circuit breaker bottom, [1, 2]. For obtaining this high flame retardancy, many additives can be used in thermoset polymer matrix composite, [3-10].

One of additives used to reduce smoke generation and improve the fire resistance of the system is nanoclay (NC). Wu et al. [4] researched about using NC in conjunction with epoxy adhesives to provide fire resistant properties for the epoxy. This research investigated various flame spread and high-temperature exposure tests. They found that the fire retardancy can be improved by 2%-3% NC. Moreover, NC which was distributed into the epoxy using a mixer was better at enhancing fire properties than NC distributed by hand. Nazare et al. [5] investigated the use of NC in polyester resin and found that the addition of NC helps reduce the flammability because the dispersion of clay in the polymeric matrices produces a nanocomposite structure which allows for reduced flammability and improved mechanical properties.

Dholakiay [6] studied the effects of four different additives: hydroxyapatite or calcium phosphate, zinc borate, class C fly ash, and antimony trioxide. They tested for their flame resistance using LOI, TGA and IR spectroscopy. They concluded that with the increase of amount of fillers, the fire resistance of the composite also increases. According to the results from Rockwell hardness

test and flexural strength test, the mechanical properties was improved as the filler content increased. The exception was for antimony trioxide and fly ash. Zhang et al. [7] investigated the mechanical properties and thermal properties of wood-fiber/polypropylene (PP) composites. Cone colorimeter data (CONE) and LOI results showed that Ammonium Polyphosphate (APP) and silica are effective flame retardant materials for wood-fiber/PP composites. Liang et al. [8] studied mechanical properties and flammability performance of polypropylene (PP) composites filled with Microencapsulated of polypropylene (MRP) and Magnesium Hydrate [$Mg(OH)_2$]/Aluminum Hydrate $Al(OH)_3$. They found that when weight fraction of MRP increases the index of limit oxygen, the rank of smoke density, the Young's modulus and tensile elongation; but decreases the horizontal burning speed and tensile yield and fracture strengths.

Jeencham et al. [9] studied the effects of flame retardant fillers: APP, $Mg(OH)_2$, zinc borate (Zb), and silica are effective flame retardant materials for wood-fiber/ PP composites. Michaela R. Petersen et al. [10] studied the effect of alumina tri-hydrate (ATH) filler on mechanical properties of Glass FRP (GFRP) material, based on compression, tension, shear and flexural test results from different materials with the amount of 0%, 25% and 50% ATH filler by weight of resin. They concluded that adding ATH generally the strength and make FRP more brittle but develop fire-resistant FRP systems.

All outstanding above studies has been shown that the fire resistance of FRP can be improved by adding various additives to the resin. Surprisingly, even if BMC are widely used in the industry for two decades, only limited studies concern their mechanical behavior, thermal and electrical properties as adding fire resistant. From above researches, an idea to add alumina filler to glass fiber reinforced composite brings benefits of enhancing thermal properties. Theoretically speaking, when adding alumina filler and remaining the initial ratio of matrix and reinforcement, mechanical properties of BMC can be predicted to decrease, but it still has the limitation.

Thus, the aim of this paper is to improve the thermal resistance of BMCs under high temperature condition in the industry. For that purpose, alumina filler was added to investigate the influence of alumina with the different content of 15wt.% and 20wt.% on the mechanical, thermal and electrical properties of BMCs. Specimens manufactured with and without alumina filler content were compared.

2. Materials and experimental procedures

The matrix material was made up of polyester resin (20-40 wt. %), zinc stearate (2.65 wt. %), moulding agents (8.8 wt. %) and was filled with high content (40-60 wt. %) of mineral fillers (calcium carbonate and alumina particles). The matrix was reinforced by 20-30 wt. % of short entangled glass fibers (E-glass type, 25 mm in length and 14μm in diameter).

The matrix compound was mixed in 20 minutes under shear to produce a viscous paste. Glass fibers were added to this paste and mixed by Z-blade mixer in 30 minutes with rotational speed of 25 rev/min. The production is done by applying pressure of 10 MPa in 10 minutes at 150°C to molds in which the raw materials are placed.

Table 1: Samples and notations

Test	0 wt.% alumina	15 wt.% alumina	20 wt.% alumina
Tensile (6 samples)	0L	15L	20L
Flexural (6 samples)	0F	15F	20F
Impact (6 samples)	0I	15I	20I

Initial samples with different amount of alumina filler were two plates of BMC. Tensile, flexural and impact samples were manufactured based on ISO527, ISO178 and ISO180, respectively. The number of samples and their notations are given in table 1. The tensile and flexural strength were estimated by using MTS 793 machine while impact test was conducted by Tinus-Olsen. Thermal properties were measured by Memmert US 450 equipment, electrical properties were estimated by measurement of breakdown voltage by Phenix 660-10P, and resistivity by Advantest R8340A Ultra-High Resistance Meter.

3. Results and discussions

3.1. Mechanical properties

- *Tensile testing*

Fig.1a shows the stress-strain curve of 15 wt.% alumina sample. It indicated that the mechanism of fracture was brittle. Only slight plastic deformation occurred after elastic deformation before breakage. There is a decrease in tensile strength from the 0 wt.% alumina, 15 wt.% alumina, 20 wt.% alumina samples shown in Fig.1b. The maximum stresses of the 15 wt.% and 20 wt.% alumina samples are 11 and 18 MPa lower than the samples without alumina filler, respectively. It is acceptable with previous study [5] that when adding alumina filler to BMC, the tensile strength decreases. In other words, adding alumina filers makes samples more brittle in tension.

SEM pictures in Fig.2 illustrate the surface at breaking point of tensile samples with different alumina filler content. The particle size of alumina measured is about 4 µm. From SEM images, the content of alumina particles in BMC increases while the content of glass fiber and resin remain. This results in the poorer distribution of load from matrix to reinforcement. Therefore, tensile samples added alumina particles are more brittle than those do not contain alumina.

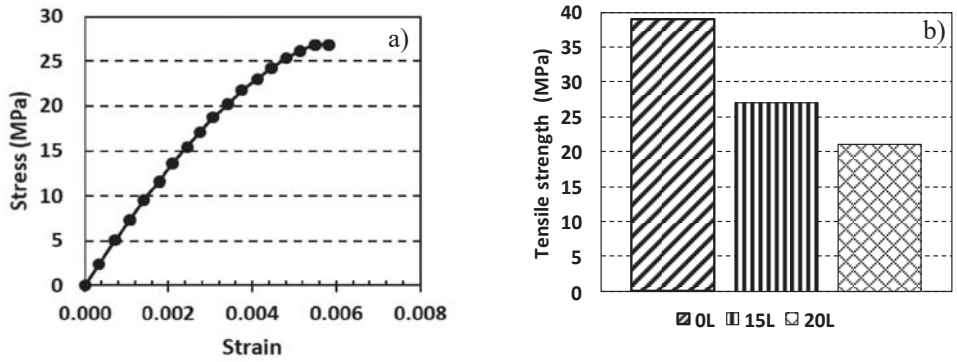


Figure 1: Stress-strain curve for tensile test on BMC samples with: 15 wt.% alumina (a); Comparison for tensile strength (b)

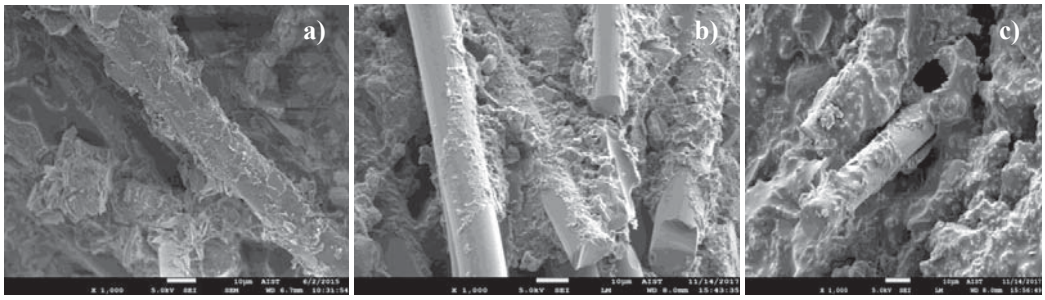


Figure 2: SEM images of BMC manufactured with: (a) 0 wt.%, (b) 15 wt.% and (c) 20 wt.% of alumina

- *Flexural testing*

Fig.3a shows the flexural strength with different alumina filler content. It can be seen that strength of the 0 wt.% alumina is the highest while strength of samples added alumina are nearly the same, with 4 MPa difference. Comparing to samples without alumina, there are decreases by 17.5 MPa and 12.7 MPa for 15 wt.% and 20 wt.% alumina samples. The decrease can be considered small or even nonexistent when considering standard deviation of the flexural strength values. The values flexural strength are acceptable with related research done by A.Aruniit [11]. Flexural strength of BMC samples added alumina is lower than that without alumina due to the poorer distribution of load from the matrix to reinforcement after adding alumna particles.

- *Impact testing*

The Charpy impact test method works by placing a notched specimen (with the notch facing away from the point of contact) into a large machine with a pendulum of a known weight. The pendulum is raised to a known height and allowed to fall. As the pendulum swings, it impacts and breaks the specimen, rising to a measured height. The difference in the initial and final heights is directly proportional to the amount of energy lost due to fracturing the specimen. The total energy of fracture is determined, and the data is recorded in Fig.3b. When the content of alumina filler increases from 0 wt.% to 15 wt.% and 20 wt.%, the impact strength decreases from 20.8 KJ/m^2 to 18.8 KJ/m^2 and 15.5 KJ/m^2, respectively since the distribution of fiber in resin is not good with lots of vacancy inside.

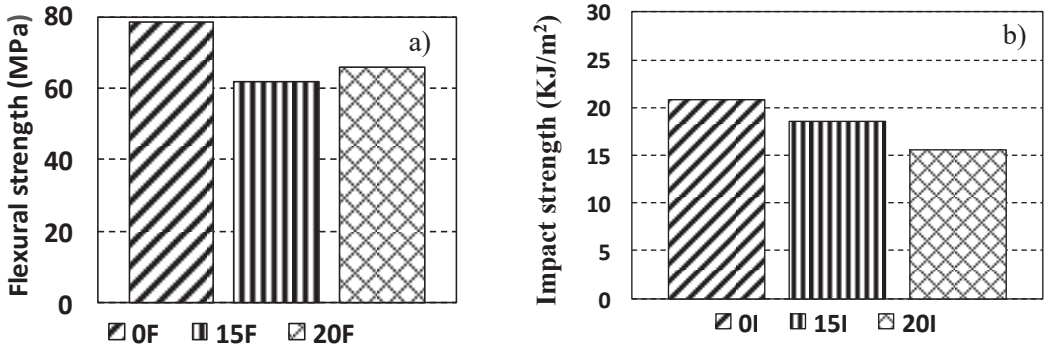


Figure 3: Comparison for flexural strength (a) and impact strength (b)

3.2. Thermal properties

The fabricated samples were tested for thermal properties. Table 2 and table 3 show the effects of alumina filler with different content on thermal properties of BMC and compare those values with properties of BMC manufactured in the world.

From two tables, it can conclude that adding alumina filler improved the thermal properties of BMC. Moreover, these properties were improved to withstand thermal condition at 190°C, which reached the thermal properties of BMC in the world. The explanation is that alumina is the most well-known fine material having high heat resistance, which enhanced the thermal properties of BMC after adding to matrix compound.

3.3. Electrical properties

Electrical properties were measured based on IEC 60093 standard. Table 2 and table 3 also show that there is an increase in electrical properties of BMC manufactured after adding alumina in terms of resistivity and specific electrical resistance. BMC still possesses dielectric properties.

Table 2: Comparison thermal and electrical properties of BMC samples without alumina fillers and samples with 15 wt.% alumina fillers

Properties of BMC manufactured	BMC samples with 15 wt.% alumina	BMC samples without alumina	Properties of BMC in the world, [12]
Tensile strength [MPa]	27.0	39.0	30-70
Flexural strength [MPa]	61.1	78.6	75-150
Impact strength [KJ/m²]	18.8	20.8	10-50
Maximum Temperature [°C]	190	180	190
Breakdown voltage at 30kV	No breakdown	No breakdown	No breakdown
Resistivity [Ω]	5.4×10^{13}	10^{10}	10^{12}
Specific electrical resistance [Ωm]	$>10^{10}$	$>10^{10}$	10^{10}

Table 3: Comparison thermal and electrical properties of BMC samples without alumina fillers and samples with 20 wt.% alumina fillers

Properties of BMC manufactured	BMC samples with 20 wt.% alumina	BMC samples without alumina	Properties of BMC in the world, [12]
Tensile strength [MPa]	21.0	39.0	30-70
Flexural strength [MPa]	65.9	78.6	75-150
Impact strength [KJ/m²]	15.5	20.8	10-50
Maximum temperature [°C]	190	180	190
Breakdown voltage at 30kV	No breakdown	No breakdown	No breakdown
Resistivity [Ω]	5.4×10^{13}	10^{10}	10^{12}
Specific electrical resistance [Ωm]	$>10^{10}$	$>10^{10}$	10^{10}

4. Summary

The results shown clearly that adding alumina could improve the thermal properties whereas this might decrease the tensile strength of BMCs. Adding alumina filler into BMC material could enhance thermal and electrical properties while reduced mechanical properties through tensile, flexural and impact tests. With 15 wt.% alumina filler content, the values of mechanical properties are still acceptable compared to the values of BMC fabricated in the world. The experimental results also indicated the influence of mass fraction of alumina filler content on properties of BMCs.

References

[1] Le Thai Hung, Vu Van Thong, Nguyen Thi Lan, Producing and evaluation of mechanical properties of BMC composite from unsaturated polyester resin and reinforced with short glass fiber, Proceedings of the National conference on Mechanics, Duy Tan University, 6-7/08/ (2015), pp.646-651.

[2] Le Thai Hung, Nguyen Kim Chinh, Nguyen Duc Thai, Vu Dinh Thang et al, Fabrication of the circuit breaker bottom using BMC composite material from unsaturated polyester resin and reinforced with short glass fiber, J. Sci. and Tech. of Metals, No64, (2016), pp.34-38.

[3] Laurent Orgeas, Pierre Dumont, Thai-Hung Le and Denis Favier "Rheology of Bulk Molding Compounds, a concentrated and fibre reinforced granular polymer suspension", J. Rheologica Acta, vol. 47, 2008, pp.677-688.

[4] Wu L, Hoa SV, Wuang H. Improvement of flammability resistance of epoxy adhesives used in infrastructure applications, Canadian Journal of Civil Engineering (2007), pp323-330.

[5] Nazare S, Kandola B, Horrocks A. Flameretardant unsaturated polyester resin incorporating nanoclays. Pol Adv Technol. (2006), pp.294-303.

[6] Dholakiya BZ, Use of non-traditional fillers to reduce flammability of polyester resin composites, Polimeri (2009), pp.10-17.

[7] Zhang ZX, Zhang J. Lu BX, Xin ZX, Kang CK, Kim JK, Effect of flame retardants on mechanical properties, flammability and foamability of PP/wood-fiber composites, Composite Part B (2012), pp.150-158.

[8] Liang JZ, Feng JQ, Tsui CP, Tang CY, Liu DF,…et al. Mechanical properties and flame-retardant of PP/MRP/$Mg(OH)_2$/$Al(OH)_3$ composites, Composite part B (2015), pp.74-81.

[9] Jeencham R, Suppakarn N, Jarukumjorn K. Effect of flame retardants on flame retardant, mechanical, and thermal properties of sisal fiber/polypropylene composites, Composite part B (2014), pp.249-253.

[10] Michaela R. Petersen, An Chen, Mark Roll, S.J. Jung, Mostafa Yossef, Mechanical properties of fire-retardant glass fiber-reinforced polymer materials with alumina tri-hydrate filler, Composite part B (2015), pp.109-121.

[11] A. Aruniit, J. Kers and K. Tall, Influence of filler proportion on mechanical and physical properties of particulate composite, Agronomy Research Biosystem Engineering (2011), pp.23-29.

[12] Information on http://www.bulkmolding.com/

Study on reasonable ratios of straight vegetable oil and diesel oil as an alternative fuel for marine diesel engine application in Vietnam

Tran The Nam*, Dang Van Uy and Nguyen Dai An

Vietnam Maritime University, 484 Lach Tray Street, Haiphong City, Vietnam

thenam@vimaru.edu.vn, vanuydang@gmail.com, nguyendaiandhhh@gmail.com

Keywords: Vegetable oil; combustion simulation; marine diesel engine.

Abstract. At present time, the climate change has been effecting on the over world. There are many reasons to make the climate changed including the emissions from the diesel engines equipped on board the ships. The International Maritime Organization through the Annex VI of the MARPOL 73/78 Convention strongly requests the all Governmental Parties to take a part in the reduce the emissions from their fleet to the atmosphere. However, how to reduce the emissions from the ships is always a rather difficult question for the whole governments. Responding to global strategic mission on effectively energy utilization and environment protection, biofuel is a positive selection attracting almost scientists and researchers in the world. For diesel engine, such renewable energy is mainly including biodiesel and pure plant oil (PPO) or vegetable oil. When vegetable oil is used directly as a fuel, in either modified or unmodified equipment, it is referred to as straight vegetable oil (SVO). SVOs have some advantages in comparison with fossil fuel oils such as: renewability, local availability, lower sulfur content, etc. avoiding the environmental effects caused by sulfuric acid, lower aromatic content and high biodegradability. However, SVOs are also attached to several disadvantages such as: high viscosity, low heating value, high fatty contents, influencing on injection process and causing engine coking if misused. In order to prevent such negative effects of diesel engine fuelled by SVO, one of potential solutions is using blends of SVO with diesel oil (DO). In such case, the reasonable ratio of SVO and diesel oil plays a very important role for normal running condition, but also seems to be challenge to identify. The article shows results of a study on defining the ratio for marine diesel application. It is firstly based on the assessment on the heat release processes inside the diesel engine cylinder upon a specific simulation with different blends of SVO and diesel oil. In comparison with the particular requirements for fuel of marine engines, the preferable percentage of vegetable oil in the fuel mixture is pointed out. And finally, the experiments with fuel system of a typical marine diesel engine, HANSHIN 6LU32, installed at the lab of Vietnam Maritime University in terms of checking real engine's operation and reducing harmful emissions.

1. Introduction

The idea of using natural pure plant oils as a fuel for engines is certainly not new, but is as old as the diesel engine itself. When Rudolf Diesel invented the diesel engine over 100 years ago, he operated his first engines with pure plant oil (PPO). In light of the current developments in the oil industry and the associated oversupply of low-priced oil products, it will soon be the case that PPOs will no longer be competitive. When PPO is used directly as a fuel, in either modified or unmodified equipment, it is referred to as straight vegetable oil (SVO). Production of SVO is quite simple by mechanical extraction of oil from an oil-bearing biomass as feedstock. The quality of SVO for fuel use depends on the feedstock and the processing conditions. SVOs have a chemical composition of triglycerides that mainly consist of one glycerol combined with three molecules of fatty acids [1]. The latter contains a long chain of carbon atoms, linked by single bonds and combined with hydrogen, ending with carboxyl group. Therefore, it owns disadvantages such as high viscosity, low heating value, high fatty contents, influencing on injection process. However, there is no shortage of reasons for using SVO as a fuel, especially the benefit on environment protection can be definitely pointed out. Renewability, local availability, lower sulphur content, etc. are positive properties avoiding the

environmental effects caused by sulphuric acid, lower aromatic content and high biodegradability. In order to effectively use PPO for diesel engines, blend of PPO with fossil diesel oil (DO) is one of preferable solution. In such case, the most important thing is the reasonable ratio of PPO for normal running condition which is quite difficult to identify.

2. Proposal for selecting PPO's ratio in marine applied fuel blends

Depending to technical characteristics of diesel engine, fuel using in each application will be different from others and standardized by ISO based on physical specifications, such as density, heat value, Cetane number, sulfur content, etc. In marine field, almost of diesel engines are medium or large size that supports for using more "dirty" and cheaper fuels than one of other application modes. It doesn't mean that every fuel can be used for maritime sector. Actually, marine fuel has to strictly meet the extra requirements relating to safety on fire/explosion prevention and stability in storage. All of such requirements can be list as follows:

- Regulations of Ship Classifications as well as of engine makers on fuel supplying system;
- Quality assessment standards of fuel mixture;
- Regulations of SOLAS 74 and Annex VI of International Convention MARPOL 73/78 on environmental protection;

In case of utilizing the PPO, even mixture of PPO and DO as alternative fuel for marine diesel, the authors have studied and summarized issues of fuel blends applying to maritime sector as followings:

- Homogeneousness of PPO in diesel oil has to be over 95% and no separation in layer between PPO and DO is recorded in fuel supply system;
- Heat release process and ignition delay;
- Emissions of exhaust gas must be comply with concerned regulations.

By assessment on the heat release processes, ignition and emissions formation inside the diesel engine cylinder upon a combustion modelling-based simulation with different blends of SVO and diesel oil, in regards to the particular requirements for fuel of marine engines, the preferable percentage of vegetable oil in the fuel mixture is pointed out. And finally, the experiments with fuel system of a typical marine diesel engine, HANSHIN 6LU32, installed at the lab of Vietnam Maritime University in terms of checking real engine's operation and reducing harmful emissions. The main parameters of this engine are shown in the Table 1.

Table 1. Technical specifications of experimental diesel engine [2]

No	Engine characteristics	Value
1	Engine HANSHIN	6LU32
2	Number of cylinders	i = 6
3	Nominal revolution	n = 340 rpm
4	Nominal power	Ne = 1,300HP/970 kW
5	Bore	B = 320 mm
6	Stroke	S = 510 mm
7	Average speed of piston	W = 5.78 m/s
8	Max. Pressure	Pz = 90 kG/cm^2

Table 2. Fuel features of blended palm oil [2]

No	Fuel characteristic	Blended fuels and DO				
		DO	PO10	PO20	PO30	PO100
1	Density at 15°C, [kg/dm^3]	0.8464	0.8538	0.8599	0.8668	0.9225
2	Viscosity at 40°C, [cSt]	2.6	3.42	5.31	6.45	40.24
3	Cetane number	42.89	50.13	50.91	52.11	52.92
4	Flash point, [^{o}C]	72	73	75	77	135
5	Freezing point, [^{o}C]	-6	-1	1	2	16
6	Lower Heating Value, [MJ/kg]	43.4	39.72	39.55	38.69	37.11

3. Modelling the combustion process

3.1. Theoretical study

To calculate parameters of fuel combustion happened inside a cylinder of a diesel engine, a single zone model based on mathematical formulas was selected. This is developed in accordance with the first thermodynamic law that can be expressed as follow [3, 4, 5]:

$$dU = \partial Q - \partial W \tag{1}$$

In case the formula (1) is applied for ideal gas and converted into differential equation depending on a engine crank angle, also using some related relations such as $R = C_P - C_v$ và $k = C_P / C_v$, then the energy conservation equation is as follows:

$$\frac{dP}{d\theta} = \frac{k-1}{V}\frac{dQ}{d\theta} - k\frac{P}{V}\frac{dV}{d\theta} \tag{2}$$

a. Pressure in cylinder

$$\frac{dP}{d\theta} = \frac{k-1}{V}\left[Q_{in}\frac{df}{d\theta} - \frac{hA}{\omega}(T_g - T_w)\frac{\pi}{180}\right] - k\frac{P}{V}\frac{dV}{d\theta} \tag{3}$$

Where: Q_{in} _Energy input, [kJ/kg]; $dV/d\theta$ _Change of a cylinder volume depending on crank angle and calculated by formula (4).

$$Q_{in} = m_f \eta_f q_{HV} = \frac{1 - x_r}{1 + \lambda(A/F)_s}\frac{p_{IVC}V_{IVC}}{RT_{IVC}}\eta_f q_{HV} \tag{4}$$

b. Heat release

The deferential equation for the real heat release can be created as follows :

$$\frac{dQ_{gross}}{d\theta} = \frac{dQ_{net}}{d\theta} - \frac{dQ_{loss}}{d\theta} \tag{6}$$

Where:

Q_{net} _Total input energy of one cylinder that can be calculated as follows:

$$\frac{dQ_{net}}{d\theta} = \frac{C}{r}\left(P\frac{dV}{d\theta} + V\frac{dP}{d\theta} - \frac{PV}{m}\frac{dm}{d\theta}\right) + P\frac{dV}{d\theta} \tag{7}$$

Q_{loss} _Lost energy to surrounding construction that can be expressed by formula (7):

$$\frac{dQ_{loss}}{d\theta} = A\left(a_c\frac{K}{B}R_e^b(T_g - T_w) + c_r(T_g^4 - T_w^4)\right) \tag{8}$$

c. Temperature in cylinder

Formula (1) or (2) can be expressed to calculate the combustion temperatures inside a diesel engine cylinder as follows:

$$\frac{dT}{d\theta} = \frac{1}{mC_v} Q_{in} \frac{df}{d\theta} - \frac{hA(T_g - T_w)}{mC_v} - \frac{RT}{C_v V} \frac{dV}{d\theta} \tag{9}$$

d. Formation of NOx emissions

The formation of thermal NOx is determined by a set of highly temperature-dependent chemical reactions known as the extended Zeldovich mechanism. The net rate of formation of NO via reactions governing the formation of thermal NOx from molecular nitrogen are as follows [3]:

$$\frac{d[NO]}{dt} = 2k_{1f} \frac{K_{P(O)}}{(RT)^{1/2}} [O_2]^{1/2} [N_2] \tag{10}$$

$$\frac{d[NO]}{dt} = \frac{6.10^{16}}{T^{1/2}} \exp\left(-\frac{69{,}09}{T}\right) [O_2]^{1/2} [N_2] \tag{11}$$

3.2. Simulation software

GT-Power is a professional tool and widely used for modelling the combustion process. This is able to link with others in order to increase the accuracy of results, such as CFD Star-CD, Fluent, Simulink, MS-Excel, etc. Main applications of GT-Power can be listed as follows:

- Building the characteristic curves of moment and fuel consumption of engine;
- Calculation of combustion progress and emissions;
- Modelling the turbine charging system;
- Etc.

For HANSHIN 6LU32 engine, modelling scheme is created by the GT-Power Version 7.3 as shown in the Fig. 1.

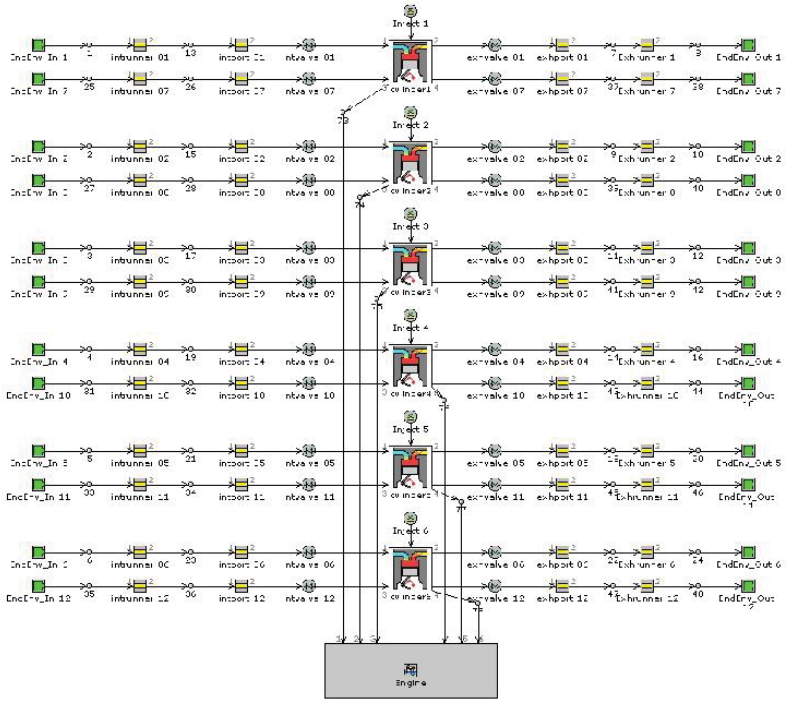


Figure 1. Combustion modelling scheme of HANSHIN 6LU32 diesel by GT-Power

3.3. Results of simulation

The internal combustion process and the different blends of diesel oil with PPO shown in Table 2 simulated by GT-Power at operational regimes of 50% to 100% load. The results are shown as Fig. 2, 3.

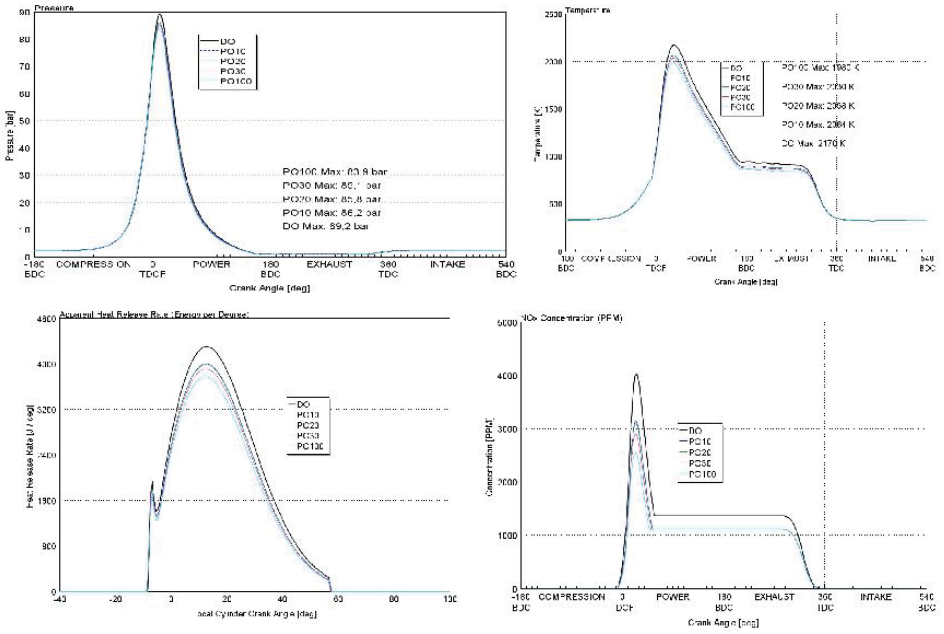


Figure 2. Diesel combustion characteristics at regime of 100%

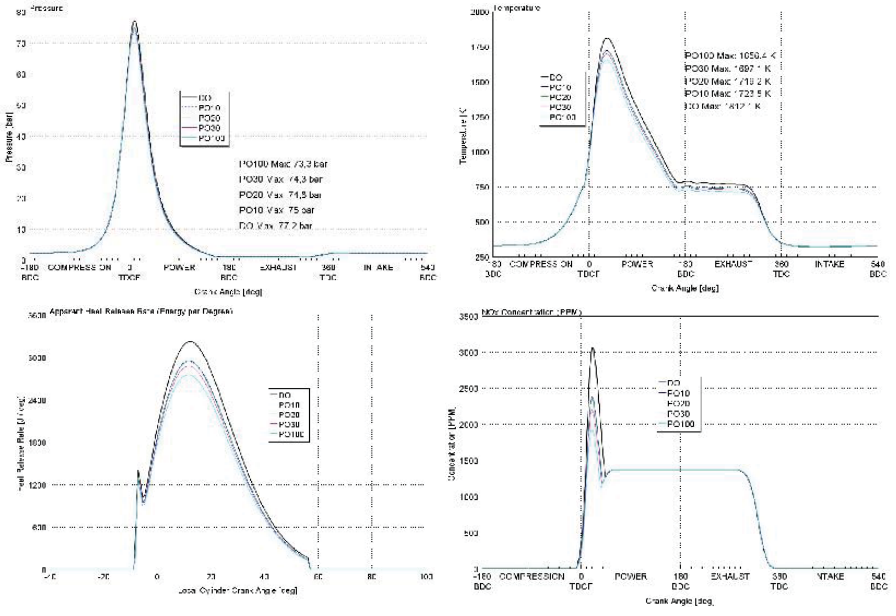


Figure 3. Diesel combustion characteristics at regime of 75%

It can be seen that the internal combustion processes inside a cylinder of fuels follows the same curve, however maximum values are much different and decreased in corressponding with the ratio of PPO (10%, 20%, 30% and 100%) in blends of PO10, PO20, PO30 and PO100. The difference between these parameters also depends on operation regime as follows:

- Decrese of peak pressure of PO100 in comparison with those of DO is recorded 5.94% at regime of 100% and 5.03% at 75%;
- The biggest diversion in the simulation of varied fuels is the speed of NOx formation. It is over 20% at all of operation regimes and higher ratio of SVO in blends is, more decreasingly the NOx emission forms.

Actually, the real experiments on HANSHIN 6LU32 diesel engine with an analysis of exhaust emissions show the similarity of variable trend to those of simulation. The results summarized by special measuring system AVL AMA i60 R1 are plotted in Fig. 4.

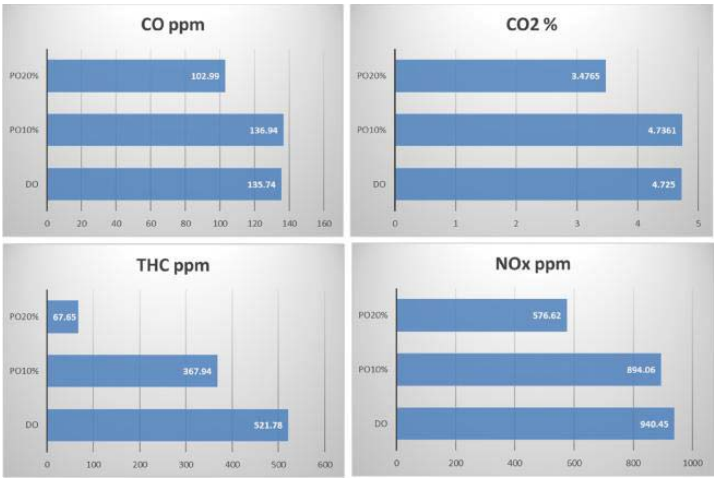


Figure 4. Emissions depending on kind of fuels

4. Study on Ignition delay

The ignition delay of a fuel can be calculated on base of mathematical model. In this paper, the authors applied a a model of ignition delay proposed by two scientists Hardenberg and Hase as follow [2]:

$$\tau_{id}(GQTK) = (0{,}36 + 0{,}22\overline{S}_p \exp\left[E_A\left(\frac{1}{\overline{RT}_{cyl}} - \frac{1}{17.190}\right)\left(\frac{21{,}1}{P_{cyl} - 12{,}4}\right)^{0{,}63}\right] \quad (12)$$

In which: τ_{id} _Ignition delay time [s] or [^{o}CA]; $\overline{S}_p$ _Average speed of piston [m/s]; E_A _Activation energy [kJ/mol]; T_{cyl} _Temperature of burned mixture inside cylinder [^{o}K]; P_{cyl} _Pressure of burned micture inside cylinder [Pa]; R=*8.314* [J/mol.^{o}K] _Real gas constant.

By using the analysis software during experiment period, the results of ignition delay of blended palm oil are showed in Table 4.

Table 4. Ignition start of fuels before top dead center (TDC)

No	Engine load [kW]	Ignition start of blended fuels before TDC [s]		
		DO	PO10	PO20
1	485	0.0017	0.0017	0.0008
2	730	0.0021	0.0016	0.0012

It can be recognized that the ignition start of PO10 before TDC is the same as that of DO at low load and delayed 1.31 times at higher one. Also, the delay increases approximately linearly with raising volume of palm oil in the blended fuels. Based on the captures of combustion process shown in Fig. 5 by the Video Scope equipment, such conclusion is confirmed again.

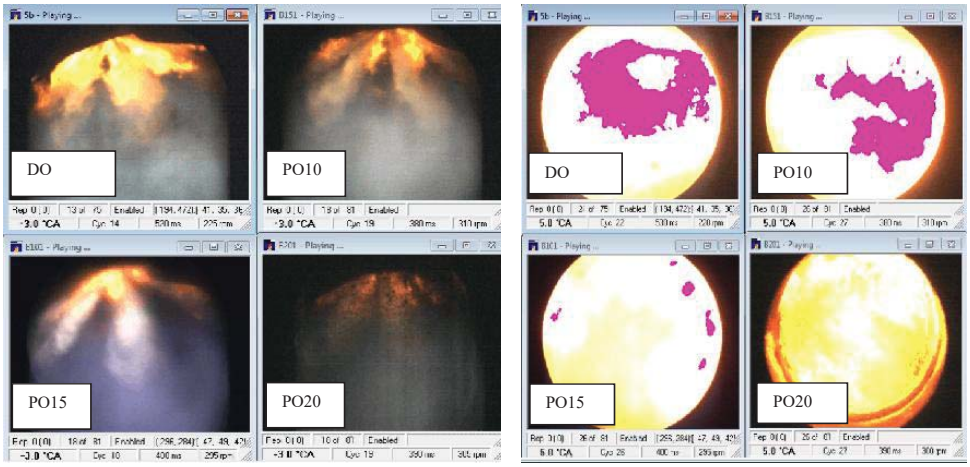


Figure 5. Ignition start and burning of fuels [2]

5. Conclusions

To use straight vegetable oil is more and more spread in the maritime field due to important advantages of PPO as fuel alternatives. On base of a comprehensive study, some conclusions can be figured out for marine application of PPO's blends as follows:

- The difference of ignition delay times of varied SVO blends affected much to burning process. Therefore, the volume of PPO in blends should not exceed 20%.
- The impressive results associated with emissions in exhaust gas also were recorded positively. The values of contents of CO, CO_2, THC and NO_x decrease corresponding with increase of PPO rate in the blends;

Finally, the reasonable ratio of PPO in mixture with DO should be less than 20% in regards to keep the normal operation of marine diesel engines.

References

[1] Stan McMillen, Philip Shaw, Nicholas Jolly, Bryant Goulding, Victoria Finkle, "*Biodiesel: Fuel for Thought, Fuel for Connecticut's Future",* CCEA (Connecticut Center for Economic Analysis), March 24, 2005.

[2] Dang Van Uy and research team, *"Research and develop a technology solution in order to convert marine diesel engines of small and medium scale to use blended straight vegetable oils as alternative fuel",* No.04.11/NLSH, 2014.

[3] John B. Heywood, *"Internal Combustion Engine Fundamentals"*, McGraw-Hill Book Company, 1988;

[4] Bernard Challen, Rodica Baranescu, *"Diesel Engine Reference Book"*, Butterworth-Heinemann, Oxford OX2 8DP, 1999.

[5] P.A. Lakshminarayanan, Yogesh V.Aghav, *"Modelling Diesel Combustion"*, Springer, 2009.

Biocompatibility of Ultrafine Grained Pure Titanium Fabricated by Equal Channel Angular Pressing

Dinh Van Hai[1]*, Ho Quang Sang[1], Le Van Lich[1], Nguyen Viet Nam[2]

[1] *School of Materials Science and Engineering, HaNoi University of Science and Technology, Ha Noi - VIETNAM*
[2] *108 Military Central Hospital, Ha Noi – VIETNAM*

*hai.dinhvan@hust.edu.vn

Keywords: ultrafine grained pure titanium, ECAP, biocompatibility, in-vitro.

Abstract. This research presents results on the biocompatibility evaluation of ultrafine grained (UFG) pure Titanium (Ti) fabricated by Equal Chanel Angular Pressing (ECAP). The ECAP process is conducted to make UFG pure Ti, and then the microstructure and mechanical properties of the obtained materials are evaluated. The results indicate that the grain size of material decreases from 150 μm to 5 μm and the tensile strength of the material increases three times to 900MPa. The mechanical properties of the UFG pure Ti fabricated by ECAP meet the requirements for biomedical applications. Two in-vitro tests are carried out to examine the biocompatibility of obtained material. The results show that the material is safe with the cells in the in-vitro medium.

1. Introduction

Titanium [1,2] based materials have been emerged as potential functional materials for biomedical applications due to their good mechanical properties, superior corrosion behavior and excellent biocompatibility [3-5]. Demands of divest combination of requisite properties encourage the researchers to develop new materials and processing techniques for materials in the field of implantology. Micro-structural characteristics, including grain sizes, phase combinations, grain boundary density, and lattice defects, play crucial roles in improving the desired biomedical properties [3-5]. However, conventional processes such as solution treatment, cold rolling, and aging treatment are difficult to achieve simultaneously required properties such as high strength while maintaining low Young's modulus [6]. On the other hand, severe plastic deformation (SPD) techniques have recently been developed with the objective of creating ultrafine-grained (UFG) materials [7]. SPD is one of the most efficient metalworking technologies for fabrication of bulk nanocrystalline materials [8-11].

The aim of the present work is improvement of the mechanical, structural aspects of pure Titanium by Equal Channel Angular Pressing (ECAP) and assesses the in vitro biocompatibility of pure Titanium. The biocompatibility of titanium material is evaluated by means of MTT assay and the trypan-blue technique. Through the results of experiments to assess the extent of cell damage and survival, cell death due to the influence of ultrafine grained pure Titanium.

2. Experimental procedure

2.1. Material

The raw material used in the present study is commercially pure Titanium. The composition is analyzed and listed in Table 1. The average grain size of the original material sample is around 150 μm.

Table 1. The chemical composition of commercially pure Ti (wt%).

Ti	Fe	Al	Sn	Zn	Mo	V	Si	Mn	Cr	Ni	Cu	Nb	W	Pb
99.5	0.22	0.007	0.067	0.06	0.01	0.01	0.025	0.009	0.004	0.03	0.005	0.005	0.02	0.02

2.2. Ultrafine grained Titanium fabricated by ECAP

The ECAP processing is conducted at temperature of 425°C using the solid die, which have two channels with equal cross-section intersecting at an angle of 90˚ [12,13]. This configuration imparts a supplementary strain of about 1 on each pass of the specimen through the die. Since grain refinement by ECAP is usually saturated at an equivalent strain of about 4, ECAP is performed up to 4 passes, which can provide an accumulated strain of 4, using processing Route A where the sample does not rotate between consecutive passes.

2.3. Assesses the in vitro biocompatibility of pure Titanium

MTT assay: Based on the oxidation reaction between MTT (3- (4,5-dimethylthiazol-2-yl) 2,5-diphenyltetrazolium bromide compound) with mitochondria of the cell forming colored formazan compounds [14-15]. After immersing the titanium plate into the AAAAAA cellular fiber solution, cells are cultured on the plate with a density of 2×104 cells/plate for 24, 48, and 72 hours. MTT solution is then added to determine the level of injury of the input. Three groups are divided and considered; that are material group (culture medium containing 1 piece of material), positive verification group (culture medium with 1% formon (Formaldehyde)), and negative verification group (only culture medium). The plate containing the cell solution is placed in the incubator for 4 hours to convert the yellow MTT to purple by the action of mitochondria. Dissolved crystals are added, then shook for 10 min at 20 rpm and determining the optical density of the Beckman counter DTX 880 at 570 nm. Based on the results of the measured spectral level, comparisons with positive and negative predictors will reveal the extent of cellular damage to the material.

Trypan-blue Test: Based on the selective permeability of the living cell membrane, trypan-blue absorbent cell membrane ($C_{34}H_{28}N_6O_{14}S_4$). The living cells are not colored, while the dying cells are dyed blue. This characteristic can be used to accurately determine the number of living cells die. One ml of cell solution at a density of 106 cells/ml is added to the plate. The specimens are divided into two groups: material group and control group (culture medium). The experiment is carried out for 1 hour at temperature of 37°C and with the presence of 5% CO_2, in which 1ml of trypan-blue solution 0.4% is added. The solution of live cells is prepared by Neubauer counting.

3. Experimental procedure

3.1. Result of ultrafine grained Titanium fabricated by ECAP

Since the present study mainly focuses on the biocompatibility of ultrafine grained Titanium materials, the mechanical properties of ultrafine grained Titanium materials is briefly described for clarity.

Fig. 3.1 and 3.2 show the microstructures of the original Titanium specimen and the specimen after four times pressing, respectively. Fig. 3.1 shows that the specimen contains grains with the size of about 150μm. After four times of pressing, the grain size of titanium dramatically decreases to about 5μm, as shown in Fig. 3.2. Therefore, ultrafine grained Titanium can be achieved by means of ECAP.



Fig. 3.1. *Microstructure of original titanium specimen*



Fig. 3.2. *Microstructure of titanium specimen after 4 times pressing.*

The hardness of Ti specimens are then examined by Vickers hardness tests. The obtained results shows that the hardness of the original Ti specimen is of about 228 Hv, however the hardness increases to 248 Hv after 4 times of pressing.

To examine the mechanical strength of Ti specimens, several tensile tests are then carried out. Fig. 3.3 shows stress-strain curves of Ti specimens before and after ECAP process. Fig 3.3 shows that the tensile strength of Ti specimen increases from 350 MPa in the original specimen to 900 MPa after ECAP process, while the maximum strain decreases from 0.18 to 0.14. This suggests that the ultrafine grained titanium material improves mechanical properties of Ti specimens. Therefore, the ultrafine grained pure titanium can meet the requirements for biomedical implant applications.

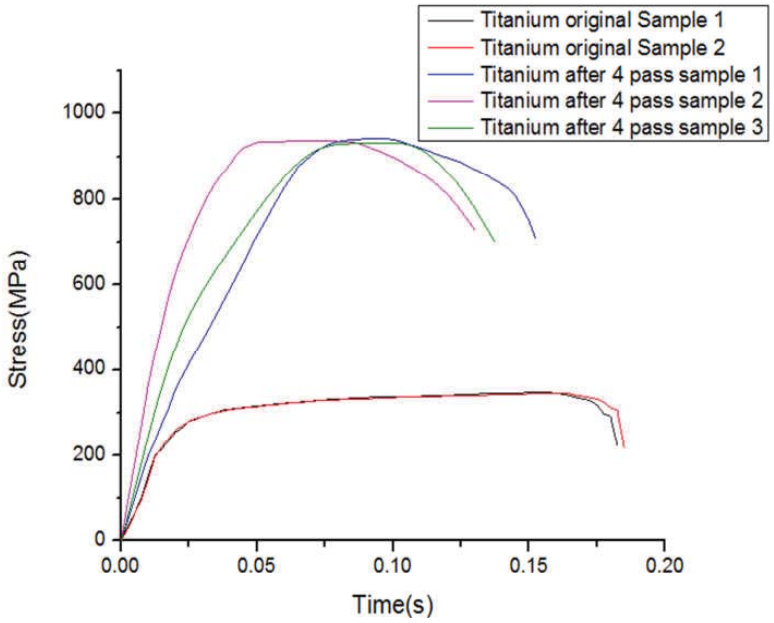


Fig. 3.3. Stress-strain curves before and after ECAP process

3.2. Result of viability assay of cell for titanium

3.2.1. Experimental results by MTT assay

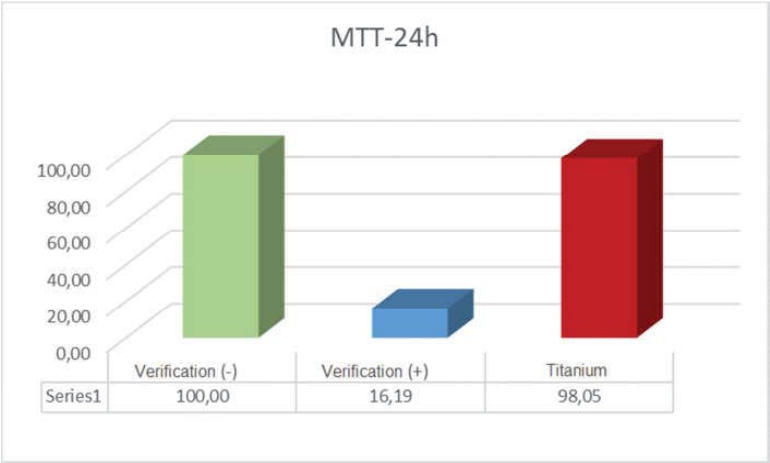


Fig. 3.4. *Optical density at plates after 24 hours of testing(%)*

Fig. 3.4 shows optical density at plates in three testing groups after 24 hours of testing. The fibrous cells in the material group show no signs of injury. Optical density at the discs in the material group is almost the same with that in the verification group. On the other hand, positive verification groups (1% formon medium) has very low optical density, which indicates a low survival rate of 16.19% in comparison to that in the negative verification group. There is no cell scored on titanium test plates after 24 hours.

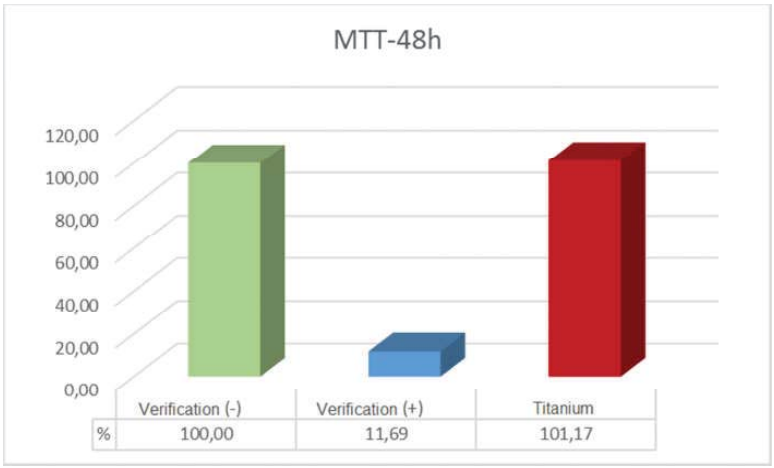


Fig. 3.5. *Optical density at plates after 48 hours of testing(%)*

Similarly, after 48 hours testing, optical densities at titanium is almost the same with that in negative verification group. However, in the positive verification group, the optical density is only of 11.69% compared to the negative control, showing very low cell density in cultured plates. Evaluation points in the material test wells reached 0 points after 48 hours.

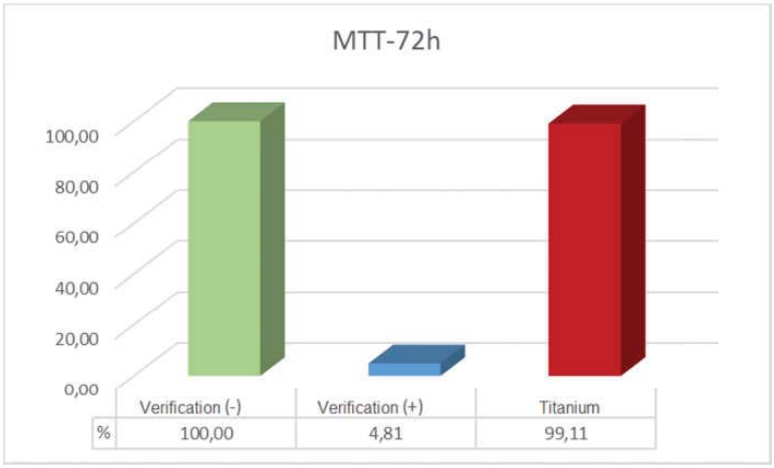


Fig. 3.6. *Optical density at plates after 48 hours of testing(%)*

After 72 hours of test, the optical density of group has titanium has no difference in comparison with that in negative verification group. The optical density of the positive verification group is only 4.81% compared with that in the negative verification group. The score on the material test discs scored 0 points after 72 hours.

The material is therefore very safe for fibrous cells in the culture medium of in-vitro. Cells can survise without damage or limitation of growth rate in the culture medium with the material. The cell score is 0 points at all 24, 48 and 72 hours test.

3.2.2. Experimental results of the Trypan-Blue method

Table 2: Trypan Blue test results

Group	Total cells	Number of dead cells	p
Group Ti	421,7 ± 20,8	26,3 ± 1,2	p >0,05
Group verification	415,0 ± 16,5	22,0 ± 4,4	

Trypan-Blue test results show that Titanium material has no effect to the cells.

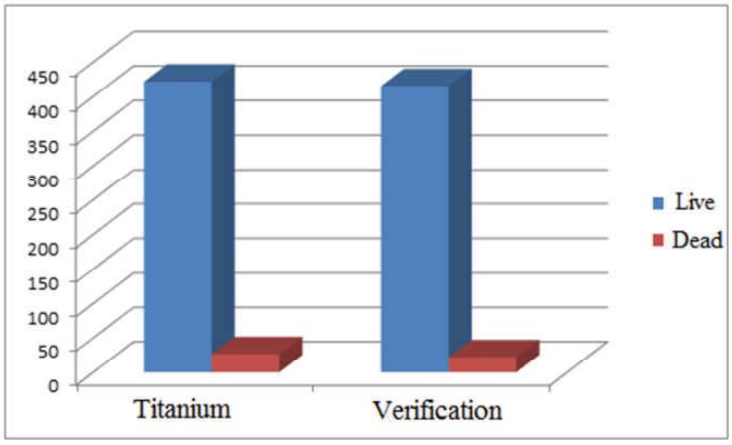


Fig. 3.7. *The number of cells in culture medium compared between Ti material and verification group*

Fig. 3.7 shows a comparison of cell numbers in culture medium between the Ti material group and the verification group. The diagram shows the cell death rate and total number of cells between two cultured plates is almost the same ($p>0.05$). Therefore, material is safe with cells, very good applicability to biomedical materials.

4. Conclusions

The fabrication process of ultrafine grained pure titanium with a grain size of 5μm has been developed. Mechanical properties are improved with hardness from 228 Hv to 248 Hv and the tensile strength from 350 MPa to 900 MPa. Obviously, the mechanical properties of ultrafine grained pure titanium fabricated by ECAP meet the requirements for biomedical applications. Two in-vitro tests shows that the Ti material is very safe for fibrous cells in the culture medium of in-vitro without damage or limitation of growth rate. The results of this research imply that mechanical properties ultrafine grained pure titanium fabricated by ECAP are sufficient for biomedical application and highly safe for fibroblast cells in the in-vitro medium. Therefore, ultrafine grained pure titanium by ECAP is a very potential candidate for biological implantation.

Acknowledgements

This research was financially supported by Moet-VIETNAM grant (05/HĐ-HTQTSP)

Reference

[1] C. Leyens, M. Peters. Titanium and Titanium Alloys Fundamentals and Applications. Wiley-VCH, Weinheim 2003.

[2] G. Lütjering, J. C. Williams. Titanium. Springer, New York 2003.

[3] D. M. Brunette, P. Tengvall, M. Textor, P. Thomsen. Titanium in Medicine. Springer, Berlin and Heidelberg, 2001.

[4] H. L. Freese, M. G. Volas, J. R. Wood. Metallurgy and Technological Properties of Titanium and Titanium Alloys. Springer, Berlin 2001.

[5] V. Latysha, G. Krallicsb, I. Alexandrovc, A. Fodorb. Application of bulk nanostructured materials in medicine. Curr. Appl. Phys. 6 (2006), 262-266.

[6] R. Z. Valiev, A. V. Korznikov, R. R. Mulyukov. Structure and properties of untrafine–grained materials produced by severe plastic defomation. Mat. Sci. Eng. A 168 (1993), 141-148.

[7] R. Z. Valiev. Nanostructuring of metals by severe plastic deformation for advanced properties. Nat Mater, 3 (2004), 511.

[8] I. Sabirov, N. A. Enikeev, M. Y. Murashkin, R. Z. Valiev. Bulk Nanostructured Materials with Multifunctional Properties. Springer (2015).

[9] R. Z. Valiev, R. K. Islamgaliev, I. V. Alexandrov. Bulk Nanostructured Materials from Severe Plastic Deformation. Prog. Mater. Sci. 45 (2000), 103–189.

[10] C. C. Koch. Nanostructured Materials: Processing, Properties and Applications. William Andrews Publishing, New York, NY, 2002.

[11] M. J. Zehetbauer, Y. T. Zhu. Bulk nanostructured materials. Wiley-VCH Verlag GmbH & Co. KGaA, Weinheim (2009).

[12] R. Z. Valiev, T. G. Langdon. Principles of equalchannel angular pressing as a processing tool for grain refinement. Prog. Mater. Sci. 51 (2006), 881–981.

[13] B. Ravisankar, J. K. Park. ECAP of Commercially Pure Titanium: A Review. Trans. Indian Inst. Met., 61 (2008), 51-62.

[14] T. Mosmann. Rapid Colorimetric Assay for Cellular Growth and Survival: Application to Proliferation and Cytotoxicity Assays. J. Immunol. Methods 65 (1983), 55-63.

[15] M. V. Berridge, P. M. Herst, A. S. Tan. Tetrazolium dyes as tools in cell biology: New insights into their cellular reduction. Biotechnol. Annu. Rev. 11 (2005), 127–152.

Transient numerical simulation for solid-liquid flow in a centrifugal pump using dense discrete phase model-DDPM

Hoang Bui Minh[1,a*], Mich Nguyen The[2], Duc Nguyen The[3]

[1]University of Mining and Geology, Hanoi, Vietnam;

[2]Hanoi university of Science and Technology;

[3]Vietnam Petroleum Institute;

[a]buiminhhoang@humg.edu.vn

Keywords: two-phase flow; solid-liquid pump; DDPM.

Abstract. The two phase solid - liquid flow in the computational fluid dynamic (CFD) method is generally analyzed by treating the solid particles as a quasi - fluid element, but this does not take into account the effects of the physical features of the solid particles. In this study, the dense discrete phase model (DDPM) in Fluent software was used to analyze the transient two phase solid - liquid flow in a centrifugal pump. The research also refered to the particle - particle and particle - structure interactions. Therefore it is possible to provide structural solutions to reduce erosion of impeller and pump. Simulations were performed for the water at the continuous phase together with 25% of the volume as spherical solid particles (density $\rho = 2260 kg/m^3$) with the diameter ranging from 3.0 to 5.0 mm in a random order. The results illustrate the motion of the solid particles in the pump and their effect on the flow performance of the pump in terms of time variation in the head. The results in this study are limited to the solid, liquid and two phase flows in a centrifugal pump which used in thermal power plants; it would be desirable to compare these with those obtained from the other multiphase flow approach so as to assess the relative errors. Further studies on the applications of the results for predicting pump component wear due to interactions with solid particles are also desirable.

1. Introduction

Centrifugal pumps are widely used to deliver solid-liquid two-phase media in agriculture, pharmacy industry, petrochemical industry,... Compared with the case delivering pure liquid such as water, centrifugal pumps not only have lower efficiency but also are subject to severe abrasion when delivering solid-liquid two-phase flow, leading to the damage of the flow components and even the decrease of the service life. Therefore, how to improve the hydraulic performance of solid-liquid two-phase centrifugal pumps becomes an important task. The "relative block, relative draw" theory was used to design solid-liquid two-phase flow centrifugal pump by Baoyuan [1]. In this theory, the liquid phase was considered as referential parameter, the solid phase as moving boundary condition. Even so, the existing results are still not satisfactory, and the problems, such as low efficiency, severe abrasion, and worse reliability, are still unsolved satisfactorily. Because of the complexity of solid-liquid two-phase flow in pumps, the theory and the method of design are still under development at two-phase flow conditions. Experimental measurement and theoretical analysis have the advantage of high reliability, but both of them need too long time and huge expenses. With the rapid development of computer technique and computational fluid dynamics (CFD), the numerical simulation method has become a very important tool to investigate the flow field in pumps and to predict the performance. Based on numerical simulation, EBAYASHI, et al [2], revealed the backflow phenomenon in a screw-type centrifugal pump. MEDVITZ, et al [3], applied a multi-phase CFD method to predict and analyze the performance of centrifugal pumps under developed cavitation conditions. BONAIUTI, et al [4], employed all the three approaches including numerical simulation to accomplish the parametric design of a mixed-flow water-jet pump. In addition, the CFD method was also successfully used to solve the transient flows during transient operating periods, such as startup and stopping periods [5]. It can be clearly seen that the

above-mentioned studies mainly concentrate at the single phase flow or gas-liquid two-phase flow. For the general solid-liquid two-phase flow, the studies are relatively minor up to now. At present, the most effective way to study pumps is to simulate and analyze the internal flow field by means of CFD, and then to establish CFD-based design theory and method.

In this paper, in order to investigate the flow characteristics and predict the abrasion of the flow components, a typical centrifugal pump is chosen as research model. The solid-liquid two-phase flow field of model pump is numerically simulated by using the algebraic slip mixture model under non-cavitation condition. Meanwhile, the effect of solid phase properties on hydraulic performance and abrasion are also presented.

2. Model and calculating method

2.1. Modeling tools and calculating method

The Ansys Fluent software was used for simulation of the solid-liquid two-phase flow in the model centrifugal pump. The multiphase flow simulations are performed in the dense discrete phase model (DDPM). In the standard formulation of the Largrangian multiphase model, the assumption is that the volume fraction of the discrete phase is sufficiently low: it is not take into account when assembling the continuous phase equations. The general form of the mass and the momentum conservation equations is given in equations Eq.1 and Eq.1.

$$\frac{\partial \rho}{\partial t} + \nabla.(\rho \vec{v}) = S_{DPM} + S_{other}. \quad \text{(Eq.1)}$$

$$\frac{\partial \rho \vec{v}}{\partial t} + \nabla.(\rho \vec{v}\vec{v}) = -\nabla p + \nabla.\tau + \rho.\vec{g} + \vec{F}_{DPM} + \vec{F}_{other}. \quad \text{(Eq.2)}$$

To overcome this limitation of the Largrangian multiphase model, the volume fraction of the particulate phase is accounted for by extending Eq.1 and Eq.1 to the following set of equations (written for phase *p*):

$$\frac{\partial}{\partial t}(\alpha_p \rho_p) + \nabla.(\alpha_p \rho_p \vec{v_p}) = \sum_{q=1}^{npha} (\dot{m}_{qp} - \dot{m}_{pq}). \quad \text{(Eq.3)}$$

$$\frac{\partial}{\partial t}(\alpha_p \rho_p \vec{v}_p) + \nabla.(\alpha_p \rho_p \vec{v}_p \vec{v}_p) = -\alpha_p \nabla p + \nabla.[\alpha_p \mu_p (\nabla \vec{v}_p + \nabla \vec{v}_p^T)] + \alpha_p \rho_p \vec{g} + \vec{F}_{vm,lift,user} + \sum_{q=1}^{npha} (\vec{K}_{qp}(\vec{v}_q - \vec{v}_p) + \dot{m}_{qp}\vec{v}_{qp} - \dot{m}_{pq}\vec{v}_{pq}) + K_{DPM}(\vec{v}_{DPM} - \vec{v}_p) + S_{DPM,other}. \quad \text{(Eq.4)}$$

Where: ρ_p is the phase reference density for the p phase (defined as the total volume average density of phase p); $\vec{v}_p$ is the velocity for the p phase ; S_{DPM}, S_{other} is the mass added to the continuous phase from the dispersed second phase and any user-defined mass source for each phase; p is the static pressure; τ is the stress tensor; $\rho\vec{g}$ and $\vec{F}$ are the gravitational body force and external body forces (also contains other model-dependent source terms such as porous-media and user-defined source); α is the phase volume fraction; μ_q is the viscosity of phase q; $\dot{m}_{qp}$ characterizes the mass transfer from the phase q to phase p; $\dot{m}_{pq}$ characterizes the mass transfer from the phase p to phase q; K is the interphase momentum exchange coefficient; $\vec{F}_{vm,lift,user}$ is the total force; $\vec{v}_{pq}$ is the interphase velocity.

The Realizable $k-\varepsilon$ (RKE) model is chosen as the turbulence model to close Reynolds averaged equations. The flow simulation is simulation is iterated until convergence is achieved for a given time step ($t = 10^{-3}$s). The simulations determine the instantaneous position, velocity and forces developed by the particle. The coordinates of the particles are subsequently updated and transferred.

In the process, the iterations are performed in an independent integration time step following the convergence corresponding to each CFD. The total simulation time is thus significantly higher, especially when the dynamic motion of a large number of solid particles is tracked. The total simulation time for a single iteration, however, is affected not only by the number of particle elements but also by the surface and geometric properties of the elements, and the contact conditions.

2.2. Material and the coefficient of interaction between phases

The simulations were performed for water at 25^0C as the continuous phase, while the solid particles formed the discrete phase. The physical parameters of the solid particles were chosen so as to approximately simulate the physical properties of the fly ash at Vietnamese thermal power plants [7]. The density of the particles was taken as 2260 kg/m^3, while the sizes of the particles were varied from 3.0 to 5.0 mm in diameter in a random manner. The volume fraction of the solid particles was set to 25% at the pump inlet. Some of the material properties of the particles and pump structure are presented in Table 1 [8].

Table 1. Material properties of the solid particles and the pump structure

Inlet Diameter- D1 (mm)	Outlet Diameter-D2 (mm)	Inlet width- b_1 (mm)	Blade thickness - δ (mm)
140	400	60	15
Inlet angle-β_1	Outlet angle-β_2	Outlet width- b_2 (mm)	Blade number- Z
28	34	60	5

2.3. Computational domain and meshing

The computational domain consisted of the inlet pipe, impeller, volute and outline pipe of a centrifugal pump, as shown in Fig.1. A single stage centrifugal pump was selected for the study of two-phase flow and the interactions of the solid particles. The flow rate capacity of the pump was 200 m^3/h with the head being 54mH_2O, when operating at 1450 rpm. The pump structure is showed in Table 1. The tetrahedral meshes were created using ANSA software and a total of 1,300,118 cells constituted the entire computational domain with mesh sizes are from 3.0 to 6.0 mm. Sliding meshes were adopted at the interfaces of the rotating impeller with the stationary components of the pump for the transient analyses. In addition, the acceleration due to gravity (g = 9.81 m/s^2) was taken into account and its direction was considered to be opposite to the flow entering the pump inlet.

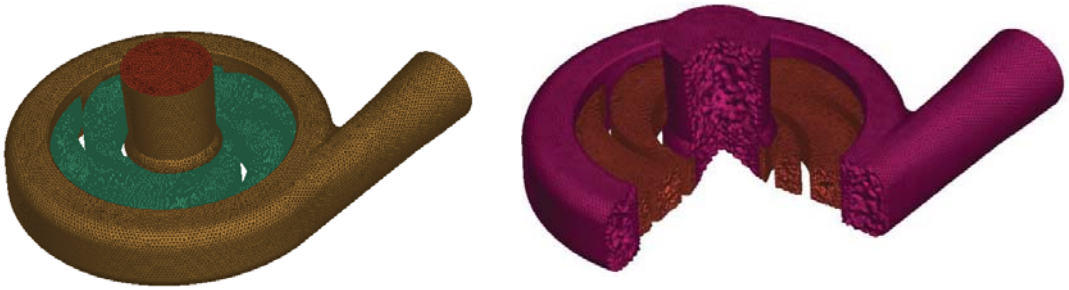


Fig.1a. Computational domains and grids *Fig.1b. The cross section of computational grids*

Fig.1: Computational domains and grids

2.4. Transient analysis

Both the pump and the fluid medium were considered to be in a static state prior to start-up. Once the pump starts, the impeller rotational speed grows with time until the design value and the flow field inside the pump gradually enter a stable circulating state. The simulations were designed to study the transient solid-liquid flow fields but without factoring in the contributions due to the transient response of the impeller, in order to preserve reasonable computational efficiency. A steady impeller speed of 1450 rpm was thus considered in the transient analysis. The initial velocity of the liquid phase was set as zero in all computational domains. Computations were initiated with solid particles being released continuously at the pump inlet, while the volume of solid particles was maintained at 25%. The inlet boundary condition in FLUENT included the design flow rate of the

pump, while the outlet boundary was given by the outlet pressure (p = 54mH_2O). The computations in FLUENT were performed using the time step $\Delta t = 10^{-3}$s.

3. Results and discussion

3.1. Trajectories of the solid particles

Fig.2,3 and Fig.4 show the trajectories of the solid particles inside the pump at various instants during the simulation. The computational domains of the inlet and the outlet pipes are omitted so as to clearly observe the distributions of the solid particles phase around the impeller and the volute. The trajectories clearly show a gradually increasing particle volume with time for $t \leq 0.2s$. The solid particles tend to distribute more uniformly in the inlet section and enter the impeller along the pressure sides of the vanes. In general, the particles tend to maintain a steady trajectory during flow towards the volute that corresponds with the shape of the impeller vanes. The particles tend to cluster along the volute outside wall and move downstream towards the outlet.

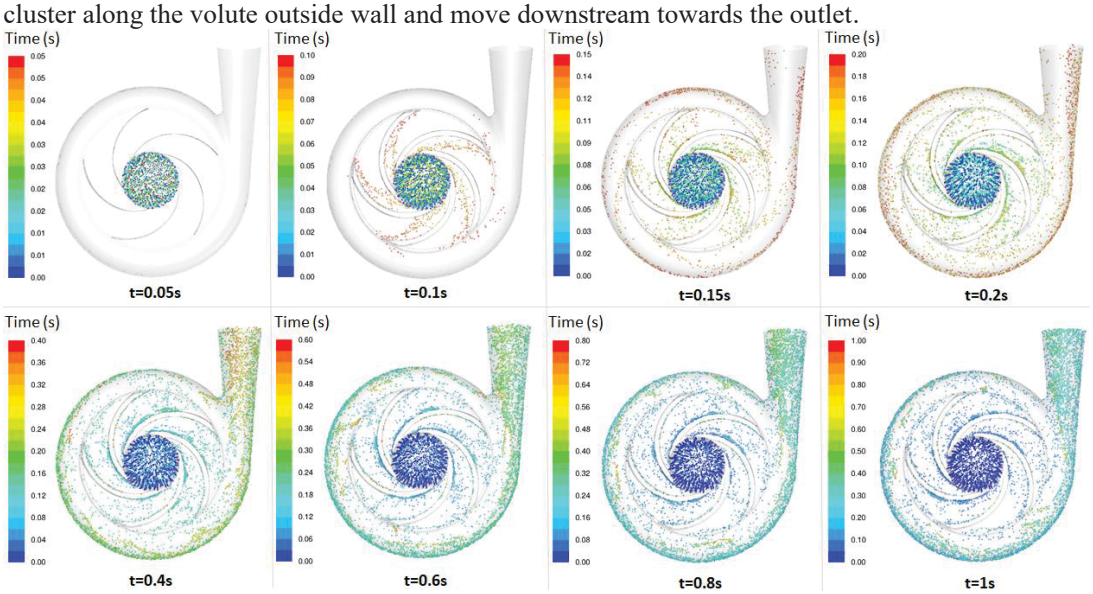


Fig.2: Trajectories of the solid particles inside the pump at different selected instants

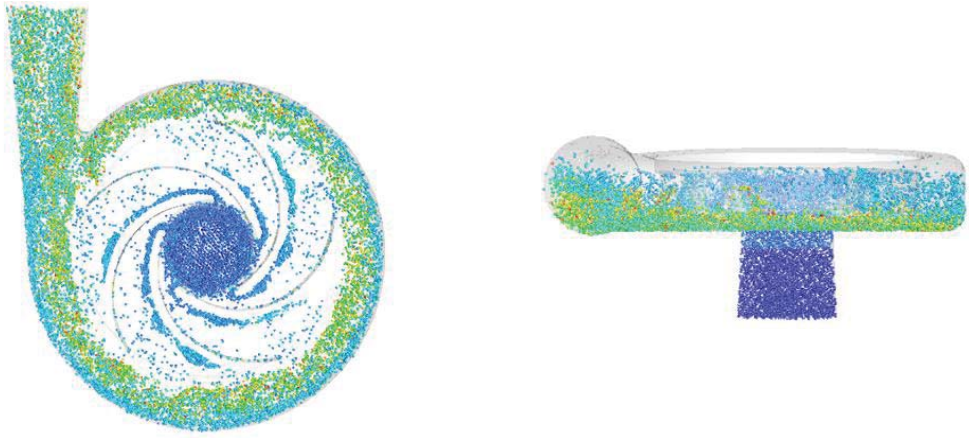


Fig.3: Trajectories of the solid particles in sections (t=1s)



Fig.4: Trajectories of the solid particles (in case d=4mm)

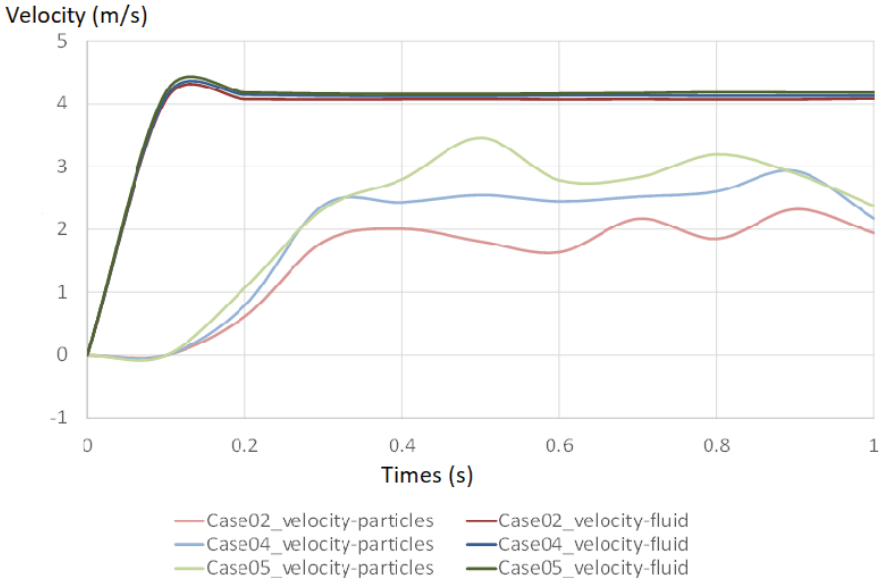


Fig.5: Comparison of the velocity of two phase with the time



Fig.6: Velocity fields of the particles inside the pump

3.2. Velocity fields of the flow phases

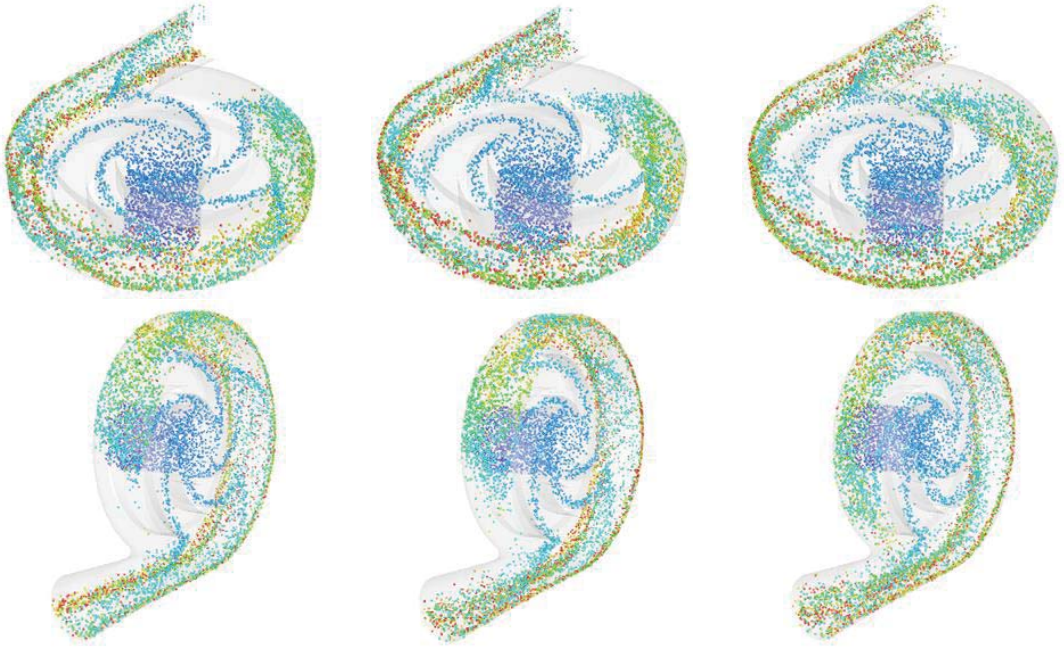
Fig.5 shows the variations in the volume-average velocities of both flow phases in the pump domains. The results show that the average velocity of the liquid phase approaches a nearly steady value of 4.2 m/s, while that of the solid phase approaches a considerably lower value of 2.2 m/s. There are apparently whole slip velocities between the liquid and solid phase flows inside the pump.

Fig.6 shows the velocity fields of the particle phase inside the pump at different selected instants. The figures show quite similar velocity fields for the liquid phase at all of the selected instants. This is due to the fact that the volume volumeaverage average velocity of the liquid phase in the pump

domain rapidly approaches a steady value after t =0.15s, as seen in Fig.5. The flow velocity magnitude near the impeller outlet tends to be relatively high due to the rotating impeller, while the maximum was obtained near 18.5m/s. In contrast, the velocities of the solid particles are substantially lower, particularly at the inlet. The particle velocity is only about 2 m/s in the inlet pipeline, while they tend to accelerate in the impeller and discharge from the impeller outlet at a speed of about 10 m/s. While the higher velocity of the liquid phase compared to that of the particle phase in the inlet pipeline and the impeller is clearly evident, the velocity slips between both the phases are not obvious in the volute. This is due to the fact that the liquid-phase velocity decreases considerably with increase in the cross-sectional area of the volute, while the solid particles, as the dispersed phase, retain their inertia from the impeller.

3.3. Solid-phase volume distribution

The distributions of the particle volume fraction, as well as the trajectories of the solid particles inside the pump, can provide important guidelines for identifying potential locations of wear caused by the solid particles. More particles tend to cluster together on the inlet-downward side of the volute wall due to the gravity effect, especially in the downstream path of the volute, since the kinetic energy of the two-phase flow decreases gradually.



Case 01 – d_p=3mm *Case 02 – d_p=4mm* *Case 03 – d_p=5mm*

Figure 7: Solid-phase distribution depend on diameter of the particles

3.4. Conclusions

The transient two-phase solid-liquid flow in a centrifugal pump which was analyzed using the DDPM model shows that:

1. For the two-phase flow with densely distributed particles (2260 kg/m3 in density, 3.0–5.0 mm in diameter, 25% volume fraction at the pump inlet), the results show that the pump head in the equilibrium state is considerably lower compared to that for the liquid-only flow. The two-phase flow also results in substantially higher amplitude oscillations in the pump head, an effect which is attributed to collisions among the particles in the densely distributed state.

2. The results further show an increase in the total volume of the particles inside the pump during the start-up period, suggesting that the particles entering the pump are greater than those discharged in the same period. The velocity fields of the flows also reveal whole slip velocities between the two phases inside the pump.

3. The solid particles are more uniformly distributed in the inlet section, and enter the impeller along the pressure sides of the vanes. The trajectories of the particles are consistent with the shape of the impeller vanes when moving towards the volute. Furthermore, most of the particles along the outside wall of the volute move to the downstream towards the outlet.

The results in this study are limited to the solid, liquid and two-phase flows in a pump; it would be desirable to compare these with those obtained from the pseudo-fluid multiphase flow approach so as to assess the relative errors.

References

[1] Baoyuan C. (1991), New design theory of solid-water two-phase flow for hydraulic machinery,Journal of Engineering Thermophysics, 12, (3), (1991),pp. 261-266.

[2] Tatebayashi Y., Tanaka K., Kobayashi T. (2005), Pump performance improvement by restraining back flow in screw-type centrifugal pump,ASME Journal of Turbomachinery,127, (4), pp. 755-762.

[3] Medvitz R. B., Kunz R. F., Boger D. A., Pauley L. L. (2002), Performance analysis of cavitating flow in centrifugal pumps using multiphase CFD,ASME Journal of Fluids Engineering, 124, (2), pp. 377-383.

[4] Bonaiutid D., Zangeneh M, Aartojarvi R., Eriksson J. (2010),Parametric design of a water jet pump by means of inverse design, CFD calculations and experimental analyses,ASME Journal of Fluids Engineering, 132, (3),pp.103-114.

[5] Liu J., Li Z., Wang L., Jiao L. (2011), Numerical simulation of the transient flow in a radial flow pump during stopping period,ASME Journal of Fluids Engineering, 133,(11), pp.101-111.

[6] ANSYS, Inc. (2009),Ansys Fluent 12.9 – Theore Guide.

[7] Viện Khoa học Công nghệ Mỏ - Vinacomin (2016), Nghiên cứu lựa chọn vật liệu chèn hợp lý trong công nghệ chèn lò bằng sức nước để bảo vệ bề mặt tại các mỏ hầm lò vùng Quảng Ninh.

[8] Bùi Minh Hoàng, Nguyễn Thế Mịch, Vũ Nam Ngạn (2017), Một số đặc điểm tính toán, thiết kế bánh công tác bơm ly tâm vận chuyển chất thải rắn trong các nhà máy nhiệt điện. Tạp chí cơ khí Việt Nam, 1, (2017), pp. 134-139.

Effect of Geometric parameters on the performance of H-type Darrieus turbine

Tuan Nguyen Quoc[1]*, Mich Nguyen The[2], Cuong Do Huy[3]

[1]Institute for hydro power and renewable, Hanoi, Vietnam

[2]Hanoi university of Science and Technology

*Corresponding author. Tuan Nguyen Quoc Tel: (+84) 989588892;

Email: nguyentuan.afm@gmail.com

Keywords: Simulation, H-type Darrieus turbine turbine, hydro power, renewable energy, Ansys-Fluent software.

Abstract.

For the H-type Darrieus turbine turbine runner, the geometry parameters such as runner diameter, blade height, number of blades, blade profiles... have certain effects on the ability to working situation and the performance of the turbine. Therefore to give the runner samples with good efficiency and working ability, it need to design, simulate and test many runner samples, hence we can select the most optimal one. The paper main purpose is to investigate the effect of geometric parameters on the performance of H-type Darrieus turbine by using Ansys-Fluent simulation software, K-ε turbulence model and NACA 0018 airfoil are chosen. The results are collected into relation curves to show the turbine working characteristics, thereby evaluating and selecting the optimum geometry parameters for H-type Darrieus turbine that is suitable for calculation water flow conditions.

1. Introduction

Blade profiles much affect on power performance of the turbine. There are many kinds of aerodynamic profiles with high quality have been studied at famous research institutions about aero-dynamic on the world. The currently most popular that are NACA profiles of National Aeronautics and Space Administration (NASA) are used for H-type Darrieus turbine turbine. NACA profiles have more suitable characteristics of aero-dynamics as Reynolds number, angle of attack, chord length, coefficients of lift and thrust, sliding scale, largest and smallest pressure coefficient.

Currently, the theoretical basis of H-type Darrieus turbine which used to exploit water flow energy is entirely based on the theoretical basis of straight bladed vertical-axis Darrieus wind turbine. As such, research works about this turbine type are mainly used for exploiting wind power, with very few research studies for exploiting the water flow power. In addition, the geometry parameters of runner also affect the working characteristics of H-type Darrieus turbine turbine. One of geometric parameters such as D/H aspect ratio – the ratio between diameter and blade height of the runner. When changing the D/H aspect ratio will affect to blade rotation, turbine efficiency and its are changed and reach a maximum value and then decrease gradually[1]

The article contents presents some research results on effect of D/H aspect ratio change on turbine energy characteristics that used to exploit water flow power by using simulation of software ANSYS – Fluent.

2. Research Methodology.

The article using Ansys-Fluent software to calculate, simulate energy exchange process between water flow and turbine runner by models with the changing cases of aspect ratio as H/D = 0.9; H/D = 1; H/D = 1.1 and l/t = 0.25(Z = 8); l/t = 0.32(Z = 10); l/t = 0,38(Z = 12). The computational models studied with flow velocites on changes in the range of 1.5 m/s - 3.5 m/s [2], Meanwhile, straight-blade vertical-axis wind turbine researchs usually has a wind speed up to 9 m/s with turbine efficiency is 32%[1]. Simulation calculations can evaluate turbine performance characteristics, thus possibly select a model of high-energy performance turbine.

3. Model Geometry

3.1. Blade profile Selection

There are many NACA sample profiles, however in the research results shown that NACA0018 profile to be best suitable for H-type Darrieus turbine vertical axis turbines[2].

The tip speed ratio, defined as:

$$\lambda = \frac{R\omega}{v} \tag{1}$$

(R: Runner radius; ω: Angular velocity: V: Water flow speed; A: Turbine swept area; P: Shaft power)

The power coefficient, defined as:

$$C_p = \frac{P}{P_{max}} = \frac{P}{\frac{1}{2}.\rho.V_\infty^{\,3}.A} \tag{2}$$

The blade density, defined as:

$$t = \pi.D/Z \tag{3}$$

(D: Runner diameter; Z: blade number)

3.2. Physical model building

This paper simulate the dynamic relationship between the changing cases on ratio D/H of H-type Darrieus turbine turbine runner to different velocities, specifically 05 cases of change that are H/D = 0.9; H/D = 1; H/D = 1.1 and l/t = 0.25(Z = 8); l/t = 0,38(Z = 12). From there we built the calculation physical model for 05 cases with the parameters as by table 1 and figure 1:

Case / Items	D/H = 0.9	D/H = 1	D/H = 1.1	l/t = 0.25	l/t = 0,38
Diameter D (mm)	1000	1000	1000	1000	1000
Height of blade H (mm)	1110	1000	910	1000	1000
Blade No. Z	10	10	10	8	12
Profiles	NACA 0018	NACA 0018	NACA 0018	NACA 0018	NACA 0018
Chord length c (mm)	100	100	100	100	100

Table 1. Runner parameters for 05 studied cases

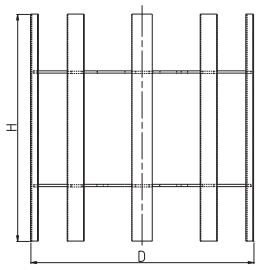


Fig 1. The runner of H-type Darrieus turbine

3.3. Calculation and simulation methods

Fluid dynamic calculation with computer support (CFD) is a useful tool to analyze flow energy characteristics. The CFD can predict properties of torque, pressure on turbine runner, from which we can predict the turbine energy characteristics. In this paper we use ANSYS - Fluent software to simulate problem.

3.3.1. Turbulence model

There are many models of turbulence flow, including k-ω model and k-ε model is most commonly used currently. K-ω model used with the problem in boundary layer, near the wall while the more distant regions, need to use k-ε model. When using k-ε model, must use a wall function to resolve the boundary layer. This means that the mesh density near the wall should be included in order to obtain all of viscous boundary layer.

In the most cases, k-ε model give the same results as other models when use a coarser mesh density near the wall, which reduces the time to complete the calculations[3].

This paper uses k-ε turbulent flow model to simulation calculate, shown by 02 equations on kinetic energy k and ε turbulent loss rate as following [4]:

$$\frac{\partial(\rho\varepsilon)}{\partial t}+\frac{\partial(\rho\varepsilon u_t)}{\partial x_t}=\frac{\partial}{\partial x_t}\left[\left(\mu+\frac{\mu_t}{\sigma_\varepsilon}\right)\right]\frac{\partial\varepsilon}{\partial x_t}+C_1\frac{\varepsilon}{k}G_k-C_2\rho\frac{\varepsilon^2}{k} \tag{4}$$

$$\frac{\partial(\rho k)}{\partial t}+\frac{\partial(\rho k u_t)}{\partial x_t}=\frac{\partial}{\partial x_t}\left[\left(\mu+\frac{\mu_t}{\sigma_k}\right)\frac{\partial k}{\partial x_t}\right]+G_k-\rho\varepsilon \tag{5}$$

With: C_1, C_2, σ_k are empirical constants, G_k is the quantity express formation of kinetic energy, it depends on the velocity gradients and turbulence viscosity.

$$G_k=\mu_t\left(\frac{\partial u_t}{\partial x_j}+\frac{\partial u_j}{\partial x_t}\right)\frac{\partial u_j}{\partial x_t} \tag{6}$$

Turbulent viscosity is derived from k and ε, including a constant is determined empirically by $C_\mu = 0.09$,

$$\mu_t=\rho C_\mu\frac{k^2}{\varepsilon} \tag{7}$$

3.3.2. Meshing model

We mesh 03 models with same type of triangle and structureless mesh before we proceed to run the simulation. The models meshed after will shown as following figure 2 and figure 3:

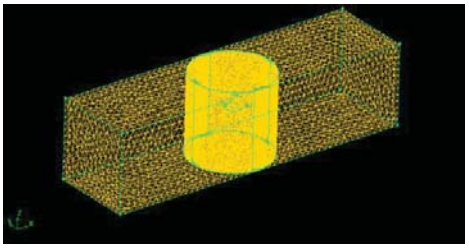


Fig 2. The turbine runner model after meshed

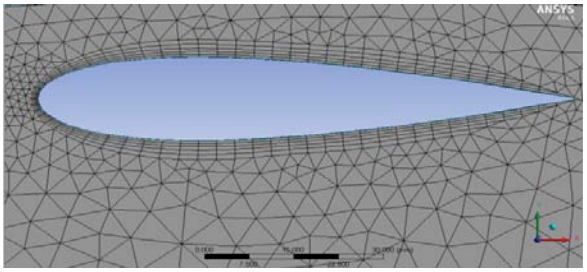


Fig 3. Structureless mesh model on blade profile

The meshing is done on Gambit software, the thickest mesh density at blade profile and blade tip locations, in these areas the mesh is thicker than the others such as inlet and outlet. The Meshing parameters on models as shown by table 2.

Case / Items	D/H = 0.9	D/H = 1	D/H = 1.1	l/t = 0.25	l/t = 0,38
Mesh node No.	2184799	1934879	1706923	1402134	1903979
Mesh element No.	9323392	8125898	7232985	5221829	9256785

Table 2. Meshing parameters of 05 models

The meshing effects the accuracy of calculation results. When the mesh density reaches convergence value, then the simulation results ensure reliability. The meshing parameters as shown in table 2 are convergence values.

3.3.3. Solution method

The selection of solver, viscous model, material properties, boundary conditions are carried out as follows:

Solver:

Interpolation method: Implicit; Direction: 3D; Time: Steady; Turbulence model: k-ε; Heat exchanger: None; Material: salt water with ρ=1000 kg/m3.

To set up conditions for problem calculation: Velocity, to ignore the influence of gravitational acceleration

Boundary condition:

Inle condition: inlet velocity in range 1.5 – 3.5 m/s

Blade condition: Wall

Symmetrical surfaces

Outlet condition: Residual pressure (variance between outlet and inlet pressures) $P_{res} = 0$

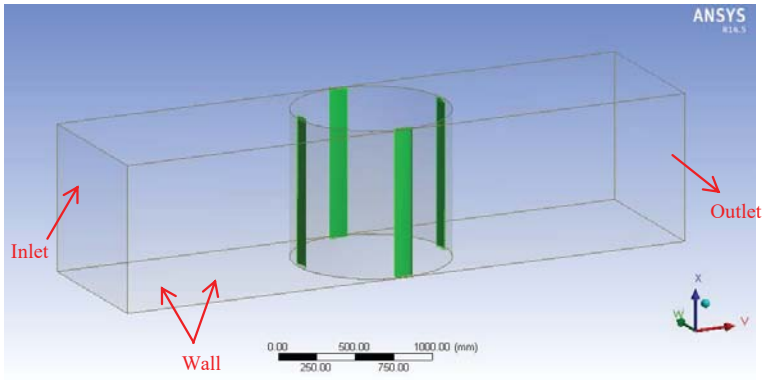


Fig 4. Problem model with Boundary condition

Figure 4 shows the 3D problem model with setting boundary conditions before we proceed to run and simulate models by Ansys-Fluent software

4. Results and Discussion

After simulation running for above research cases, we obtain the results of velocity distribution through the turbine runner.

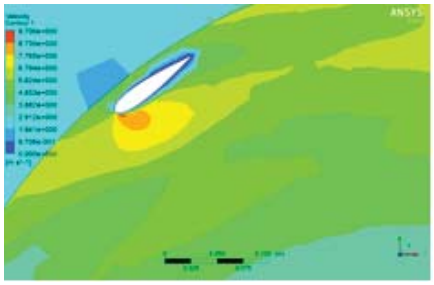


Fig 5. Velocity distribution around blade profile for case of H/D = 0.9

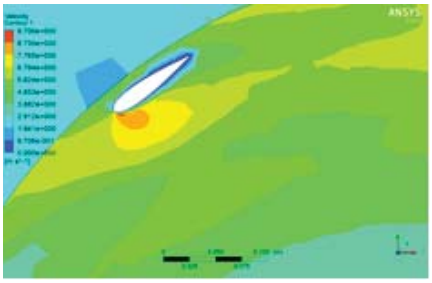


Fig 6. Velocity distribution around blade profile for case of H/D = 1

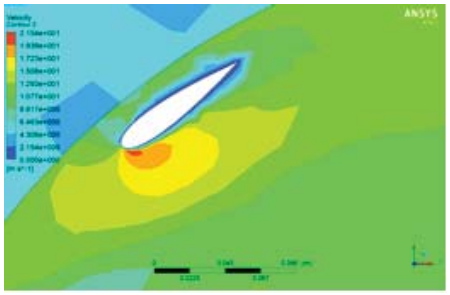


Fig 7. Velocity distribution around blade profile for case of H/D = 1.1

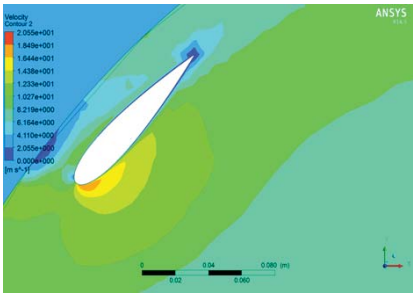


Fig 8. Velocity distribution around blade profile for case of l/t = 0.25

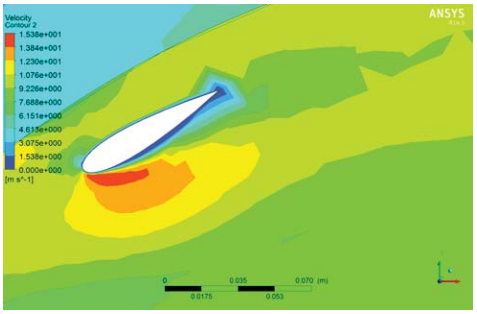


Fig 9. Velocity distribution around blade profile for case of l/t = 0.38

As shown in Figures 5, 6, 7, 8 and 9 we see that the field of velocity distribution change into several distinct regions when flowing through blade profile. There is phenomenon of turbulent flow at blade profile. After simulation, we obtain the calculated results for corresponding research cases and then we build the relationship curves C_p-λ to consider performance characteristics of H-type Darrieus turbine.

The simulation results will be shown in Fig.10 and Fig.11, the results show relation between water flow speed and turbine working efficiency. Since, we can select working range of turbine with highest efficiency and assess turbine characteristics.

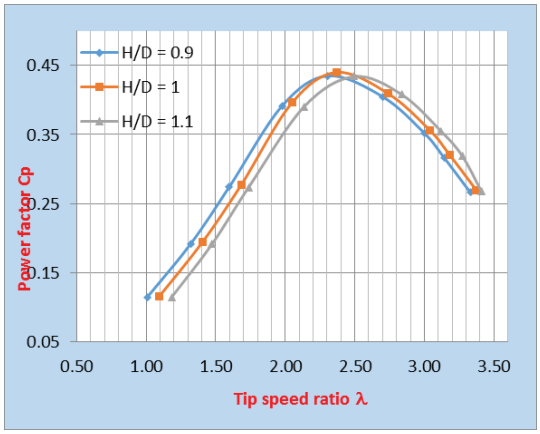


Fig 10. Relationship curves Cp-λ of H/D changing cases

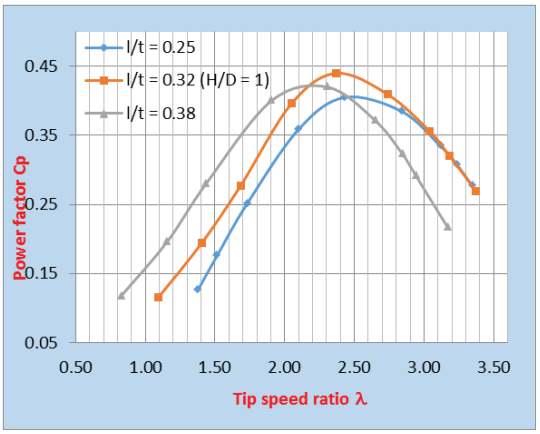


Fig 11. Relationship curves Cp-λ of l/t changing cases

As shown in Figure 10 and 11, it is found that when flow velocity or tip speed ratio increases, the power coefficent C_P or turbine efficiency increases and reaches its maximum value and then decreases. When changing the H/D aspect ratio, the turbine's energy characteristics also change. Based on the simulation and calculation results, we see that case of aspect ratio D/H = 1 that is one has highest performance efficiency at value C_P = 0.440, λ = 2.5 compared to the two remaining cases that are D/H = 0.9 and D/H = 1.1 under the same flow velocity research condition. Similar, when changing the H/D aspect ratio, the turbine's energy characteristics also change, we see that case of aspect ratio l/t = 0.32 that is one has highest performance efficiency at value C_P = 0.44, λ=2.5 compared to the two remaining cases that are l/t = 0.25 and l/t = 0.38.

5. Conclusion

This paper presents the research results on influence of H/D and l/t aspect ratio on H-type Darrieus turbine efficiency by using Ansys-Fluent software. Based on the results of simulation and calculations on turbine runner models with cases of H/D = 0.9; H/D = 1; H/D = 1.1; l/t = 0.25 and l/t= 0.38 respectively, we see that:

- When the flow velocity increases, the turbine efficiency also increases and reaches to maximum value and then decreases. The greatest performance values of research cases corresponding to bellow:

The case of H/D = 0.9: C_{Pmax} = 0.435; λ = 2.5
The case of H/D = 1: C_{Pmax} = 0.434; λ = 2.5
The case of H/D = 1.1: C_{Pmax} = 0.440; λ = 2.5

- When changing H/D aspect ratio, turbine efficiency also change. The case of H/D = 1 the turbine efficiency reach max value compared by remaining research cases.

- When changing l/t aspect ratio, turbine efficiency also change. The case of l/t = 0.32 the turbine efficiency reach max value compared by remaining research cases.

With range of water flow speed that is 1.2 - 3.5 m/s, we can fully choose H-type Darrieus turbine with aspect ratio D/H = 1; l/t = 0.32 to exploit the water flow energy, ensuring that turbine has highest performance. These research results can be fully applied in order to serve the turbine runner geometric parameters selection that used to exploit water flow energy.

References

[1] J. van der Geer, J.A.J. Hanraads, R.A. Lupton, The art of writing a scientific article, J. Sci. Commun. 163 (2000) 51-59.

Reference to a book:

[2] W. Strunk Jr., E.B. White, The Elements of Style, third ed., Macmillan, New York, 1979.

Reference to a chapter in an edited book:

[3] G.R. Mettam, L.B. Adams, How to prepare an electronic version of your article, in: B.S. Jones, R.Z. Smith (Eds.), Introduction to the Electronic Age, E-Publishing Inc., New York, 1999, pp. 281-304.

[4] R.J. Ong, J.T. Dawley and P.G. Clem: submitted to Journal of Materials Research (2003)

[5] P.G. Clem, M. Rodriguez, J.A. Voigt and C.S. Ashley, U.S. Patent 6,231,666. (2001)

[6] Information on http://www.weld.labs.gov.cn

Analyzing rotor profile's effects to performance of roots vacuum pump applied the CFD method

Nguyen Thanh Tung[1,2,a*], Bui Ngoc Tuyen[2,b], Tran The Van[3,c]

[1]Ha Noi University of Mining and Geologys
[2]Ha Noi University of Science and Technology
[3]Hung Yen University of Technology and Education, Hung Yen, Viet Nam

[a]Nguyenthanhtung@humg.edu.vn, [b]tuyen.buingoc@hust.edu.vn, [c]Vanct4.hut@gmail.com

Keywords: Lobe pump, CFD, circular profile, epi-cyloidal profile, CIC profile

Abstract

The article is mainly focused on analysis characteristics of lobe pump with three different tooth profiles: Circular, Epicycloidal and Circular–Involute–Circular (CIC) rotor profiles. Based on the geometric analysis and mathematical model, the CIC rotor profile combined Circular–Involute–Circular is generated. In this paper, the CFD techniques are used to estimate the effects of tooth profile and number of lobes to the pump performance. The simulation results obtained from FLUENT software illustrated that the rotor profile effects remarkably to the pump performance. The CIC rotor profile provided an outlet pressure higher than that of the circular and epi-cycloidal rotor profiles. The numerical outcomes also showed that higher rotor's speed resulted in higher outlet pressure and velocity nearly linearly. Beside, this study also indicated that number of lobes on rotor effect slightly to the pump performance.

1. Introduction

Lobe pump is a kind of the positive displacement pumps such as gear pump and vane pump. It is applied to transport high viscosity fluid and gas in many applied industries, the food, medicine, biotechnology. The basis units of the lobe pump consist of two rotors non-contact rotating in opposite direction with small gap. So lubrication for two rotors is unnecessary during its operating even high-speed. In recent years, there are many studies concentration on designing rotor profile of the lobe pump and using the CDF (Computer Fluid Dynamics) technique to analyse pump performance. Jan et al. [1] have revised the involute rotor with Feviation function method that can obtain high efficiency effect. Jung et al. [2] focused on the involute and ellipse profiles to make smooth and continuous. Litvin and Feng [3] developed geometry for roots blowers in which the addendum tooth profile is a single circular arc. The estimate volumetric efficiency of leakage in roots blower has attended by various researchers [4-8]. Mimmi and Pennachi [9, 10] focused on the load dynamics on three–lobe roots blowers and show that increasing the reservoir and using helical shaped rotors improves dynamic load regularity and decreased system vibrations.

Nowadays, computer simulation has developed significantly and applied widely in section of industries. The simulation dynamics is supported by the strong software and hardware. Many researchers have developed model algorithm to deal with analysis load dynamic and flow fluid mechanics. Houzeaux et al. [11] developed an innovative algorithm to simulate the fluid mechanics of rotary pumps such as gear pumps. Voorde et al. [12] applied the fictitious domain method to study a three- lobe pump and tooth compressor.

Computational Fluid Dynamics method are numerical methods that find out flow behaves when setting inlet and outlet conditions. CFD method approaches to analyze flow dynamic in lobe pump. In this research, authors would like to compare lobe pump performance as estimated head pressure and velocity in three model profile with the CFD techniques with 2D profile.

2. Mathematical model

2.1 The base rotor profile

The base rotor profile can be generated by some base curves: circle arc and epi-cycloidal curve. The coordinate system for generating the rotor profile is presented in Fig. 1. The coordinate systems $O_1X_1Y_1$ (S_1) and $O_2X_2Y_2$ (S_2) are rigidly applied to rotor 1 and rotor 2, respectively. The $O_fX_fY_f$ (S_f) is the fixed coordinate systems with the center of the rotor 1($O_1 \equiv O_f$). The $M_1(x_1, y_1)$ in the tip of rotor is defined [13] by vector $\overrightarrow{O_1M_1} = r_1$:

$$r_1 = \begin{bmatrix} (r_p + r)\cos\theta - r\cos\dfrac{r_p + r}{r}\theta \\ (r_p + r)\sin\theta - r\sin\dfrac{r_p + r}{r}\theta \\ 1 \end{bmatrix} \quad (1)$$

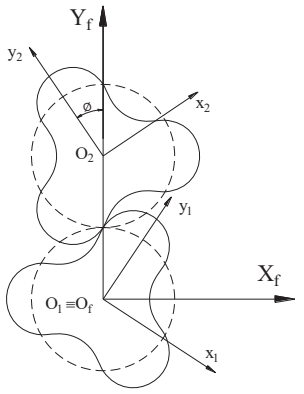


Fig. 1: The coordinate systems

The $M_2(x_2,y_2)$ in the root of rotor is defined by Eq. 2

$$r_2 = \begin{bmatrix} (r_p + r)\cos(\theta - 2\phi) + r\cos(\dfrac{r_p + r}{r}\theta - 2\phi) - 2r_p\cos\phi \\ (r_p + r)\sin(\theta - 2\phi) + r\sin(\dfrac{r_p + r}{r}\theta - 2\phi) + 2r_p\sin\phi \\ 1 \end{bmatrix} \quad (2)$$

Where: r and r_p are radius of rolling circle and base circle, respectively. θ is the geometric parameter, ϕ is the motion parameter and n is the number of lobes.

The relationship between design parameters is defined as [13]:

$$f(\theta,\phi) = r_p\sin(\theta - \phi) + r_p\sin(\frac{r_p + r}{r}\theta\text{-}\phi) + r\sin\frac{r_p}{r}\theta - (r_p + r)\sin\frac{r_p}{r}\theta = 0 \quad (3)$$

Similar to the epi-cycloidal profile, circular rotor profile is generated by circular arc. The equations of the point at the vertex curve in the coordinate system S_1 is represented by vector r_1 and r_2 as follows [13]:

$$r_1 = \begin{bmatrix} x_1 \\ y_1 \\ 1 \end{bmatrix} = \begin{bmatrix} a + \rho\cos\theta \\ \rho\sin\theta \\ 1 \end{bmatrix} \quad (4)$$

$$r_2 = \begin{bmatrix} \rho\cos(\theta\text{-}2\phi) + a\cos 2\phi - 2r_c\cos\phi \\ \rho\sin(\theta\text{-}2\phi) - a\sin 2\phi + 2r_c\cos\phi \\ 1 \end{bmatrix} \quad (5)$$

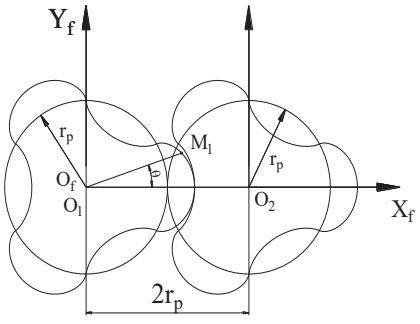


Fig. 2: The epi-cycloidal rotor profile

where θ is the angle parameter of circular arc of rotor 1, θ' is limited angle, n is the number of lobes. According to the geometric relationship, design parameters a, ρ and radius of pitch circle r_c are related as follow:

$$\rho^2 = r_c^2 + a^2 - 2a.r_c\cos\frac{\pi}{2n} \quad (6)$$

The geometric parameter θ and motion parameter ϕ must satisfy the equation [13]:

$$f(\theta,\phi) = r_c \sin(\theta-\phi) - a\sin\theta = 0 \quad (7)$$

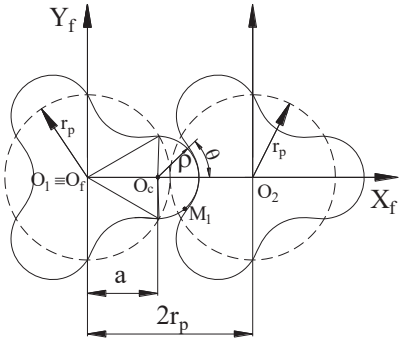


Fig. 3: The circular rotor profile

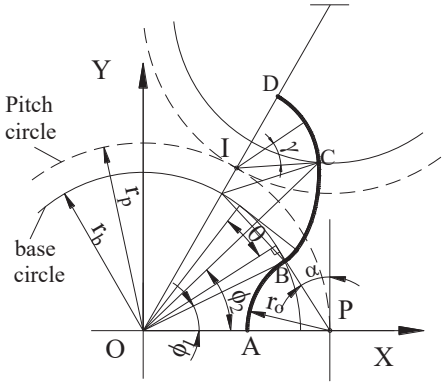


Fig. 4: The CIC rotor profile

2.2 The CIC Rotor profile

The CIC rotor profile is generated by three curves circular, involute and circular curves. The addendum and dedendum rotor are circle arcs that has provided small gap and stable clearance between rotor and chamber pump. The flank of rotor is an involute curve that is easily to get higher precision. The tooth profile of lope pump is geometric symmetry, so rotor profile is conducted in partial section. Fig. 4 shows the portion of rotor profile in the coordinate systems OXY. The one-half of tooth rotor profile is divided into three segments: circular arc CD, involute curve BC and circular arc AB.

The addendum circle curve is circular CD that is confirmed as equation (8):

$$\begin{cases} x = r_p.\cos\dfrac{\pi}{2n} + r_v.\sin\gamma \\ y = r_p.\sin\dfrac{\pi}{2n} + r_v\cos\gamma \end{cases} \quad (8)$$

where γ is the motion parameter of the vertex circle of rotor. r_p and r_v are the radius of pitch circle and circular tip, respectively.

The side of tooth is an involute curve BC

$$\begin{cases} x(\phi) = x_M.\cos(\phi_1) + y_M\sin(\phi_1) \\ y(\phi) = x_M.\sin(\phi_1) - y_M\cos(\phi_1) \end{cases} \quad (9)$$

$$\text{Here} \quad \begin{cases} x_M = r_b.\left[\cos(\alpha+\theta) + (\alpha+\theta).\sin(\alpha+\theta)\right] \\ y_M = r_b.\left[\sin(\alpha+\theta) - (\alpha+\theta).\cos(\alpha+\theta)\right] \end{cases} \quad (10)$$

where r_b is the radius of base circle; θ is the geometric parameter of involute curve; α is the angle pressure; ϕ_1 is the motion parameter and r_p is the pitch radius, $r_b = r_p.\cos\alpha$.

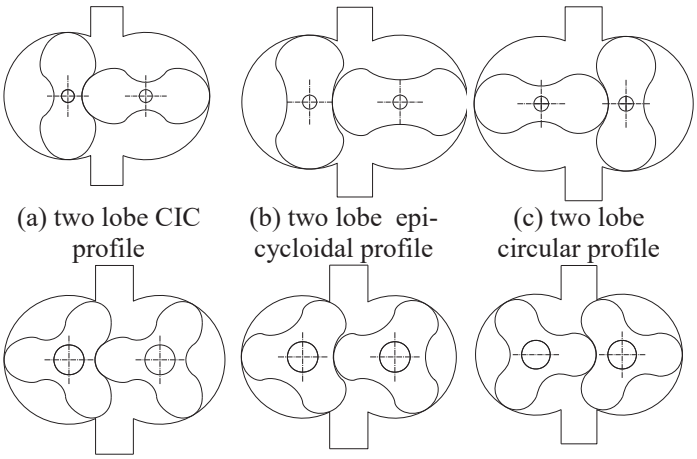
In operating process of the lope pump, the involute flank of the two rotors run in contact full times on the pitch circles. The involute portion starts from the base circle and the pressure angle is critical pressure. In the involute meshing, the actual line of contact of two rotors less than theoretical line of contact in the base circle.

$$r_o = \frac{\pi}{2n} r_b \le r_b \tan\alpha \Rightarrow \tan\alpha \ge \frac{\pi}{2n} \Rightarrow \alpha_{min} = \arctan\frac{\pi}{2n} \quad (11)$$

The dedendum circle is arc AB with the radius r_c

$$\begin{cases} x = r_p + r_c \sin\gamma_c \\ y = r_c \cos\gamma_c \end{cases} \quad (12)$$

CAD data of the rotor profiles is built by using MATLAB program. This data is exported into point data and converted to script file that can be ran in AutoCAD for generating drawing file and generation rotor profile (Fig. 5).



(a) two lobe CIC profile (b) two lobe epi-cycloidal profile (c) two lobe circular profile

(d) three lobe CIC profile (e) three lobe epi-cycloidal profile (f) three lobe circular profile

Fig. 5: Multi – rotor profile

2.3 The CFD simulation

2.3.1 Calculation method with the CFD

The CFD method (Computer Fluid Dynamics) is based on the finite volume method to solve conservation equations of mass and momentum. The continuity equation is defined as [14]:

$$\frac{\partial \rho}{\partial t} + \nabla.\rho\vec{V} = 0 \quad (13)$$

The momentum equation is defined as:

$$\rho\left[\frac{\partial\left(\vec{V}\right)}{\partial t} + \left(\nabla.\vec{V}\right)\vec{V}\right] \nabla p + \left(\nabla_{\vec{T}}\right) = \rho.\vec{g} + \vec{f} \quad (14)$$

where ρ is the static pressure, $\vec{T}$ is the stress tensor, $\rho.\vec{g}$ is the gravitational force, $\vec{f}$ is surface force and $\vec{V}$ is the velocity.

The Newton fluid is used to transport into pump by applying the standard K-Epsilon model (k-ε), which is based on assumptions. The standard k-ε model is as follows:

$$\frac{\partial}{\partial t}(\rho k) + \nabla.(\rho k V) = \nabla.\left[\left(\mu + \frac{\mu_t}{\sigma_k}\right)\nabla k\right] + G_k + G_b - \rho\varepsilon - Y_M + S_k \quad (15)$$

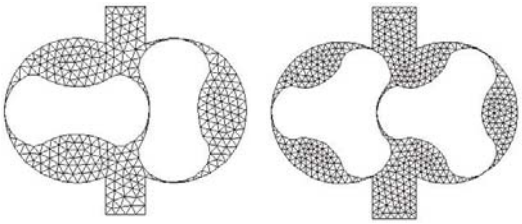
$$\frac{\partial}{\partial t}(\rho\varepsilon) + \nabla.(\rho\varepsilon V) = \nabla.\left[\left(\mu + \frac{\mu_t}{\sigma_k}\right)\nabla\varepsilon\right] + C_{1\varepsilon}\frac{\varepsilon}{k}\left(G_k + C_{3\varepsilon}.G_b\right) - C_{2\varepsilon}.\frac{\varepsilon^2}{k} + S_\varepsilon \quad (16)$$

where μ_t is the turbulent viscosity, $\mu_t = \rho.C_\mu k^2/\varepsilon$ and $C_{1\varepsilon} = 1.44$, $C_{2\varepsilon} = 1.92$, $C_\mu = 0.09$, $\sigma_k = 0.3$, $\sigma_\varepsilon = 1.3$ are model constants.

2.3.2 Boundary conditions

The 2D model rotor for lobe pump was conducted with supporting MATLAB program and AutoCAD. The grid of lobe pump was generated by using software ANSA version 13.1.2. The size of grid selects 0.4mm with triangle in all area (Fig 6)

In the CFD simulation, the water-liquid is Newtonian and incompressible, its viscosity of 0.001003 kg/m-s, the density is 998.2 kg/m^3. The range of the rotational speeds of rotors is 1000 rpm – 3000 rpm. Inlet pressure is set equals 100 Kpa. The UDF function is used to define the rotational angles of rotors, which are opposite direction with each other. The parameters of geometric pump are set: inlet and outlet diameters are same equals 25 mm, pitch circle radius equals 30 mm. The gap of two rotors is 0.2 mm and the gap rotor to chamber is 0.1 mm.



a) two lobe b) three lobe

Fig. 6: The grid model for lobe pump

3. Results and discussion

3.1 The volumetric efficiency

The volumetric efficiency of a pump is defined by proportion of discharged volume to the volume of the chamber that includes the mating rotors. The volumetric efficiency can be estimated as area efficiency. The area efficiency is an important scale index to evaluate the profile of the lobe pump rotor. It is defined by:

$$\eta_V = \frac{A_o - A}{A_o}.100 = \frac{2(\pi R_c^2 - A_{rotor})}{\pi R_c^2 + 4R_p R_c}.100 \qquad (16)$$

where R_c is the radius of chamber; A_{rotor} is the cross-sectional area of rotor; R_p is the radius of the pitch circle. Geometric parameter of rotor profile: pitch circle radius R_p = 30 mm. number of lobes n = 2, 3.

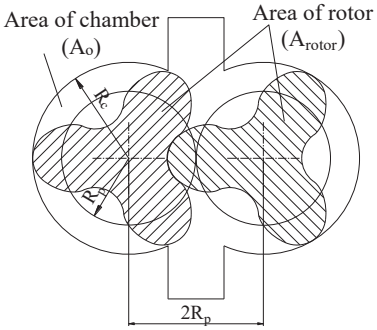


Fig. 7: The Cross section area

Table 1 indicated that if the number of lobes is increased, the volumetric efficiency η_V will be decreased at all rotor profiles. For rotor with two lobes, the CIC profile rotor can be improved the volumetric efficiency higher than that of the circular and epi-cycloidal rotor profile, 55.6%, 53.7% and 48.4%, respectively. Similar for rotor with three lobes, the CIC rotor profile can be improved the volumetric efficiency 49.5%, which is the highest value compare to that of the circular, epi-cycloidal profile with 47.8% and 44.6%, respectively. However, pump efficiency depends on many factors, gap between both rotors, gap between rotor and chamber, the discharge volume, rotor profiles, ...etc. Thus, number of lobes affects slightly to pump efficiency.

Table 1: Volumetric efficiency η_V

Multi lobes	Two lobes	Three lobes
The CIC profile	55.64%	49.54%
The circular profile	53.73%	47.83%
The cycloidal profile	48.42%	44.67%

3.2 Analysis pressure and velocity

The outlet head pressure depends significantly on rotor profiles that are improved tiny clearance between two rotors and between rotor and chamber of lobe pump. Figure 8 shows outlet pressure of lobe pump for three different kinds of rotor profiles: epi-cycloidal, CIC, circular rotor profiles. The rotational speed of rotors is set equal 2000 rpm. Overall, the variation of pressure is steady in periodic time for all three different rotor profiles. In the beginning working process of lobe pump about less 0.01s periods, the outlet pressure is unsteady. After that, the pressure distribution is homogeneous throughout the remainder of the period pump. The outlet pressure reached peak point at t = 0.042 s (140269 Pa), at t = 0.092s (134155 Pa) and 0.057s (123015 Pa) with CIC, circular and epi-cycloidal profiles, respectively. The graph also illustrated the pressure outlet in the CIC rotor profile is the highest compares to that of the circular and epi- cycloidal rotor profile with the same parameter geometries and speed of rotor (Fig. 9). The result suggest that the clearances are

remained as a constant for the CIC profile on all time cycles and it is an evidence shows that the compound profile has much more advance than single profiles (circular and epi-cycloidal profiles).

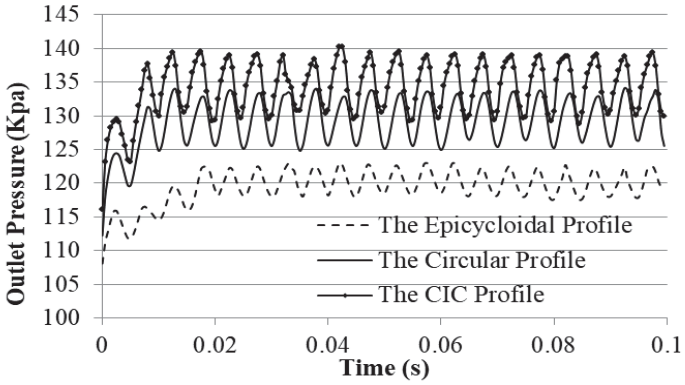


Fig. 8: The variation in outlet pressure at 2000 rpm

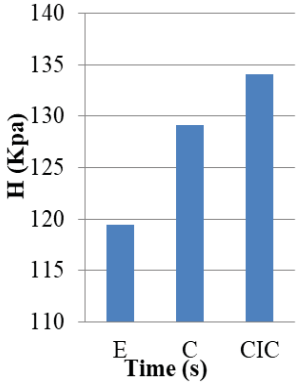


Fig.9: The average in outlet pressure at 2000 rpm

Figure 10 presented outlet velocity for three tooth profiles of the rotors with the same geometry and boundary conditions. The rotational speed of rotors is set equal 2000 rpm. The outlet velocity shows cyclic fluctuation with the same frequencies and amplitudes for all profile models. The average velocity of the CIC rotor profile is higher than that of the circular and epicycloid rotor profile and the epi-cycloidal rotor profile provided the smallest average velocity (Fig. 11). The head pressure and velocity are suitability and correspondence with volumetric efficiency of multi-lobes.

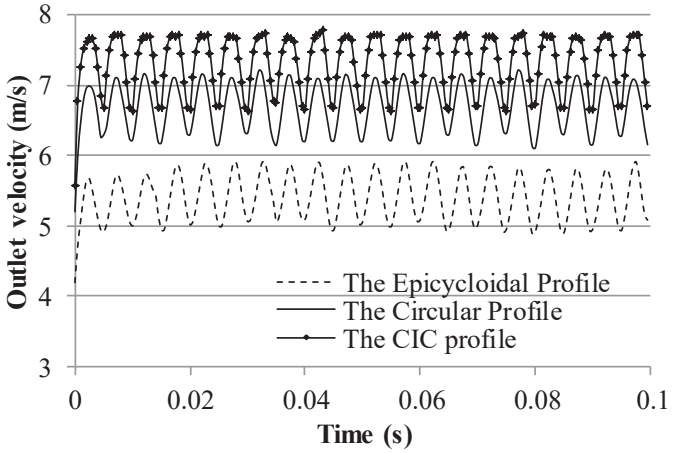


Fig. 10: The variation in outlet velocity at 2000 rpm

E – Epicycloidal;
C – Circular;

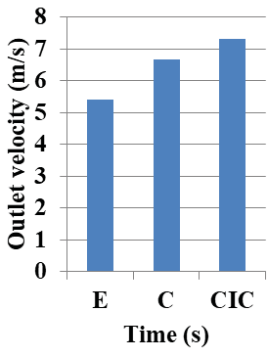


Fig.11:The average in outlet velocity at 2000 rpm

3.3 Analysis the effects of rotor speed

Figure 12 shows that the outlet pressures for three rotor profiles (epi-cycloidal, circular and CIC) with three lobes are compared when the rotor speed of pump is changed. The three different rotor speeds is selected sequentially 1000 rpm, 2000 rpm and 3000 rpm. The pressure of pump is increased when the rotor speed have increased for all rotor profiles. The outlet pressure of the epi-cycloidal rotor profile is less than that of the circular rotor profile and the CIC rotor profiles can be provided the highest pressure and the same with outlet velocity (Fig. 13). The difference from pressure, the velocity increased linearly with rotor speed.

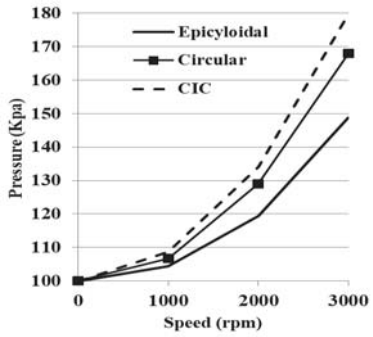


Fig.12: the outlet pressure for three rotors

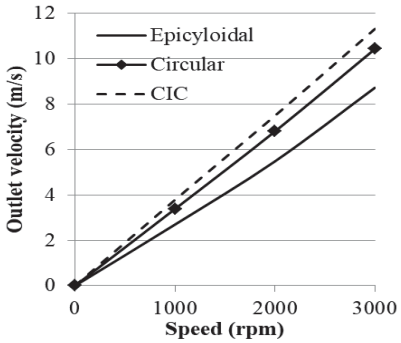


Fig.13: the outlet velocity for three rotors

3.4 Analysis the effects of lobe number

This section focused on analysis effects of the lobe number on rotor to pump performance based on the outlet pressure and velocity in a range of 1000 rpm to 3000 rpm for the CIC rotor profile. Overall, the pressure in output declined when number of lobes increased at all case speed (Fig. 14). At 1000 rpm, the two lobe provided pressure higher about 18.2%, 24.6% more than that of three lobes and four lobes, respectively. The trend was similar in terms of a general decline velocity (Fig. 15). The two lobe provided the highest in terms of velocity and pressure. However, working with high speed often damages the rotor'surface and reducing the durability of pump. Thus, using number of lobes more than two lobes is more appropriate.

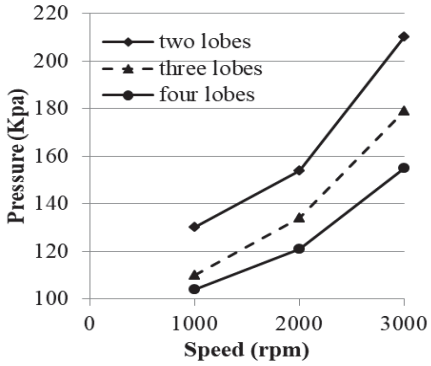


Fig. 14: the outlet pressure for multi-lobes

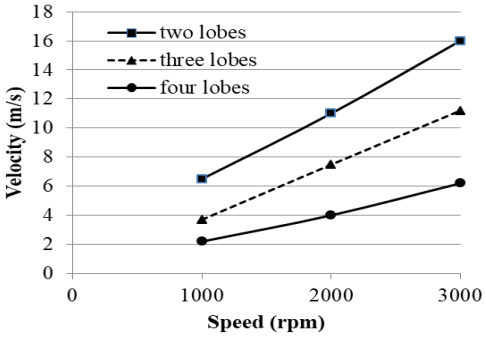


Fig. 15: the outlet velocity for multi-lobes

4. Conclusion

The main target of this article performs for analyzing effects of rotor profile, rotor speed and number lobe of rotor to pump performance by using the CFD technique. The volumetric efficiency, outlet pressure and outlet velocity of roots pump are considered in analytical process. The analytical results reveal that the outlet pressure and outlet velocity are significant difference for the CIC, circular and epi-cycloidal rotor profiles. The pressure obtained from CIC rotor profile is much higher than that of two other rotor profiles. The obtained analysis data has showed that the rotors with three lobes have more advantages than the rotors with two lobes. Furthermore, the paper provided the mathematical model that can be used to design the rotor profile of roots pump. The present paper also gives some factors to find the suitable rotor profile.

REFERENCES

1. Yan J, Daniel C H Yang and Tong S H 2009 *J. of Mechanical Design, Vol.* 131, 0926011.
2. Jung S Y, Bae J H, Kim M S and kim C 2011 *Int. Journal of Precision Engineering and Manufacturing* 12(5), pp835-41.
3. F.L Litvin, P.H. Feng, Computer design and genration of cycloidall gearings, Mech,Theory 31 (1996).
4. Cole, B.N, Crooves, J.F Imrie, B.W Performace Characterics tics of Roots Blower Systems, Proc. Inst. Mech. Eng. 1967-1970, Vol. 189, pp. 114-127.
5. Winter, E.F., The effect of Running Clearances on the Performance of Roots type Superchargers R.A.E Rept. Eng. 1945.
6. Ritchie, J.B., Pattorson, J. Geometry and Leakage Adpects of Involute rotors for the roots blower, Proc. Inst. Mech. No. 36, Eng 1968 -1969 .
7. Patterson, J., Ritchie, J.B., roots blower performace Int. J. Mech. Sci. pergamon Press, 1969, pp. 575-593.
8. Mc. Dougald, S. Imrie, B.W, Cole, B.N., An Investigation of the volumetric efficiency of roots blower, 1974 Purdue Compressor Techology Conference Proceedings.
9. G. Mimmi and P. Pennacchi, Compression load dynamics in a special helical blower: a modeling improvement, Transaction of ASME, J. Mech. Des., 123 (3) (2001) 402-407.
10. G. Mimmi and P. Pennacchi, Dynamics effects of pressure loads in three screw pump rotors, Transaction of ASME, J. Mech. Des., 120 (4) (1998) 589-592.
11. G. Houzeaux and R. Codina, A finite element method for the solution of rotary pumps, Comput. Fluids, 36 (2007) 667- 679.
12. J. V. Voorde, J. Vierendeels and E. Dick, Flow simulations in rotary volumetric pumps and compressors with the fictitious domain method, Comput. Method Appl. Math., 168 (2004) 491-499.
13. F.L. Litvin, A. Fuentes, Gear Geometry and Applied Theory, the second edition, Cambridge University Press (2004).
14. Fluent 15.0 Documentation, Fluent Inc, New York, 2013

The effect of turbocharging on the performance and pollutant emission level of the diesel engine

Cuong Duong Quoc [a *], **Thi Luong Dinh** [b] and **Thang Dao Trong** [c]

Faculty of Vehicle and Energy Engineering, Military Technical Academy, Ha Noi, Vietnam

[a]quoccuongqd13501@yahoo.com, [b]thidongluc33@yahoo.com, [c]daotrongthanghv@yahoo.com

Keywords: Turbocharger; brake specific fuel consumption; pollutant emissions; downsizing engine; GT-Suite.

Abstract. Air pollution is a serious problem in many developing country cities. The purpose of this study is to respond to the global concerns for the increase of the pollutant emissions and the necessaries of preventing their formation rather than cope with the consequences of them. Thus, the production levels of carbon monoxide (CO), unburned hydrocarbons (uHC), oxides of nitrogen (NOx) and Soot emissions of the 4BD1 diesel engine are evaluated by 1D simulation with the GT-Suite software. From there, a suitable combination of turbine-compressor is chosen to propose a turbocharger for the engine, and the resultant pollutant emissions are compared to the naturally aspirated diesel engine. It was found that the pollutant emission levels of CO, uHC and Soot are higher and NOx is lower in terms of their concentration in the exhaust gases of the turbocharged diesel engine, in comparison with the naturally aspirated diesel engine. Though, at the same time, the brake power of the turbocharged diesel engine are higher and the brake specific CO, uHC, Soot of the turbocharged diesel engine are lower than those of the naturally aspirated diesel engine. So, it is concluded that, for different modes, turbocharging provides the opportunity to achieve the performance higher a naturally aspirated diesel engine while generating lower pollutant emissions.

Introduction

Compression ignition engines have been widely used all over the world. Their chief application is for transportation such as vehicles, ships, agricultural machines,...Increasing the special capacity, minimizing environmental pollution of internal combustion engines is now one of the major concerns of experts in the vehicle dynamics. One of the most solutions to increase special capacity, down-size engine and reduce emissions pollutant is boosted intake air in engine by turbocharging. Nowadays, this is one of the most optimal and popular methods. Boosted engine pressure by the turbine-compressor is using a large amount of heat in the high-temperature engine exhaust that continues to expand and work in the turbine to rotate the compressor to provide high-pressure air. From there, intake air density and charging coefficient are increased, lead to rise the useful power and fuel economy of the engine [1]. Improved fuel economy when turbocharging engine is due to better fuel air mixing and combustion quality, the fuel burned out.

With a high demand for improved efficiency, fuel economy and reduced emissions pollutant of engines into the environment, this research proposes solutions to apply turbocharged technology in to the engine is necessary. The typical emissions of the turbocharged diesel engines are NOx, CO, soot and uHC. NOx includes all forms of oxides of nitrogen; however, in combustion engines it is dominated by nitric oxide (NO) followed by a small amount of nitrogen dioxide (NO_2).These pollutants form in extremely high temperature in-cylinder conditions of compression ignition engines in the presence of nitrogen and oxygen from the air and the fuel [1]. NO_2 form acid rain which harms human health, deteriorates structures, pollutes waters and marine ecosystems, and destructs forests [2,3]. Moreover, they can penetrate deeply into lung tissues and cause irritations, cause or worsen respiratory diseases, or deteriorate heart diseases [4]. CO is an odorless, colorless, and tasteless gas that is slightly less dense than air. It is a product of partial oxidation of carbohydrates and forms when there is not enough oxygen available to combustion. In the presence of enough oxygen CO burns to

produce carbon dioxide. CO has about 220 times greater potential to combine with hemoglobin in blood and thus lessens the oxygen delivery to the tissues and causes suffocation [5]. Unburned hydrocarbons are actually the fuel molecules not burned during the combustion process in cylinder. Situated inside the crevices of the combustion chamber or precipitate on the walls of the chamber, they avoid the flame zone and thus remain unburned. These unburned fuel molecules then find their way to the exhaust fume and eventually the atmosphere [1]. The uHC can cause respiratory problems, allergic issues or even immune deficiencies in children [6]. Carbon black is one of the particulate pollutants that are interest in engine exhaust. In the air, soot particles absorb and diffuse sunlight, reducing the transparency of the atmosphere. Thereby reducing visibility, which leads to unsafe traffic results. Diffusion combustion in the diesel engines is very convenient for the formation of soot. The combustion of liquid fuel pellets as they move in the combustion chamber and localization of the fuel vapors in high temperature areas is the main reason for carbon black production [7].

2. Methodology

2.1. Double Wiebe Function

The operation cycle of the internal combustion engine is affected by many parameters. The GT-Suite software allows the description of the burning process through a variety of models such as: heat release rate, theoretical combustion cycles, user defined combustion or predictive heat release properties [8,9]. In the GT-Suite software, the Wiebe function is used to impose the burn rate on CI engines. The Wiebe function [10] is often used to approximate the actual heat release characteristics of an engine:

$$\frac{dx}{d\alpha} = \frac{\alpha}{\Delta\alpha_c}(m+1).y^m.e^{-ay^{(m+1)}}. \quad (1)$$

$$dx = \frac{dQ}{Q}; y = \frac{\alpha-\alpha_0}{\Delta\alpha_c}. \quad (2)$$

with Q- total fuel heat input; α- crank angle; α_0- start of combustion; $\Delta\alpha_c$- combustion duration; m- shape parameter; a Wiebe parameter (a = 6,908). The integral of the Wiebe function gives the fraction of the fuel mass which was burned since the start of combustion:

$$x = \int \frac{dx}{d\alpha}.d\alpha = 1 - e^{-ay^{(m+1)}}. \quad (3)$$

where x - mass fraction burned. The superposition of two Wiebe functions (Double Wiebe) is used to approximate the measured heat release characteristics of a compression ignition engine more accurately: $x = x_1 + x_2$. (4)

2.2. Extended heat release approach

For the simulation of engine transients, the heat release characteristics change with engine speed and load. As the speed and load profile for a transient is not known prior to a simulation run, a model predicting the rate of heat release dependent on the operating point is required. For diesel engines the approach used is based on the model by Woschni and Anisits [11]. The Wiebe functions and the characteristic parameters of one operating point must be defined. The model predicts the change of the Wiebe parameters according to the actual operating conditions:

$$\Delta\alpha_c = \Delta\alpha_{c,ref}.\left(\frac{AF_{ref}}{AF}\right)^{0.6}.\left(\frac{n_{ref}}{AF}\right)^{0.6}. \quad (5)$$

$$m = m_{ref}.\left(\frac{id_{ref}}{id}\right)^{0.6}.\left(\frac{P_{IVC}}{P_{IVC,ref}}\right).\left(\frac{T_{IVC}}{T_{IVC,ref}}\right).\left(\frac{n}{n_{ref}}\right)^{0.3}. \quad (6)$$

with AF- air fuel ratio; n- engine speed; id- ignition delay; P_{IVC}- pressure at intake valve closes; T_{IVC}- in-cylinder temperature at intake valve closes; index "ref" at reference operating point. The ignition delay is calculated with the relations found by Andree and Pachernegg [12] which assume that the ignition of the injected fuel droplets takes place if the differential of gas temperature versus time exceeds a threshold.

2.3. Calculation of emission in CI engine

Emissions produced by internal combustion engines during laboratory are commonly compared in terms of emissions. In order to calculate emissions of the exhaust pollutants as well as O_2 levels and thermal capacity of the inducted charge, it is necessary to know the molar concentration of all the

constituents of the exhaust gases. As a variety of methods can be applied to compute the molar concentration of the species that are not measured in the exhaust, different results can be obtained in terms of specific emissions. These results are generally reported without any reference to the procedures and assumptions used. In addition, most of the methods used are applicable for a limited selection of fuels. The production levels of carbon monoxide, hydrocarbons, oxides of nitrogen and Soot emissions of the CI engine are callculated in [13].

2.4. Modeling the turbocharger diesel engine in GT-Suite software

GT-Suite is a software developed by Gamma Technologies that can simulate an entire internal combustion engine. The software is used by almost all major car and truck companies. The software can simulate all the parts of the engine and also be coupled with external software programs to study specific parts. This simulation software have the calculation methods and equations of the internal combustion, emission, heat release and friction losses. Furthermore, the specifications of the turbocharger and engine, atmospheric conditions and throttle designing considerations are described clearly. More information on this software is available in [8,14].

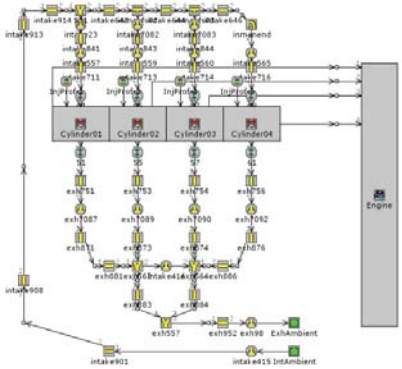


Figure 1. The natural diesel engine model_4BD1

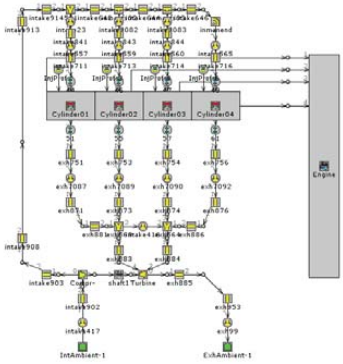


Figure 2. The turbocharger diesel engine model_4BD1T

Based on the calculations for the naturally aspirated (4BD1) engine model, the rated power in the calculation is 63.9 kW, while the actual engine power is 64 kW [15]. Thus, the calculated error of capacity is 0.2%. The calculated brake specific fuel consumption is 258.3 g/kWh, while the actual brake specific fuel consumption is 258 g/kWh [15]. Error brake specific fuel consumption in the calculation mode and catalogue data is 0.1%. It demonstrates that the building model was reliable. Based on that, the calculation model for the turbocharged 4BD1 engine was build as shown in Fig. 2.

General specifications of the engine are presented in Tables 2 [15]. Air enters the intake system from the atmospheric conditions of the working environment that are introduced in Table 3. The assumed values for these parameters are presented in Table 4. Then, guided by the manufacturer, a procedure is followed in order to find the proper turbo model [16,17]. Technical specifications of the selected turbo model are presented in Table 5. This model will not face surge or choke problems under the particular working conditions of this work.

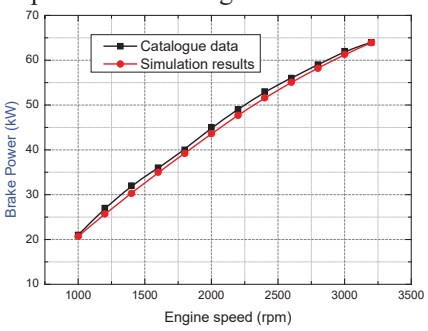


Figure 3. Catalogue and simulation power results

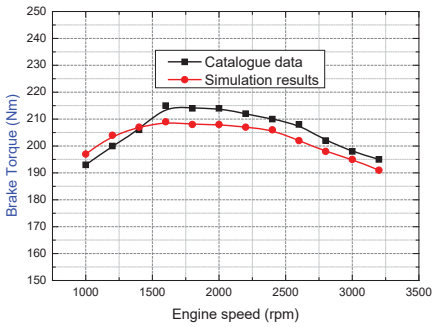


Figure 4. Catalogue and simulation torque results

Validation of the simulation results is based on the catalogue data reported. A graph is drawn in Fig. 3 to make a comparison between the results of the simulation and data of the experimental

researches. This graph depicts the full load brake power curve of the engine in different speeds (1000 to 3200 rpm). As is evident, the minimum and the maximum deviation percentages from the catologue data are 0.2 % and 5.3%, respectively. In order to further facilitate the investigation of the deviation, Table 6 reports the error percentages of the simulation in 12 discrepant engine speeds.

Brake torque derived from the simulation is put in comparison with the results from a catalogue data of the 4BD1 engine. Fig. 4 depicts both curves in one graph for comparing purposes, and Table 7 facilitates this comparison by revealing the data points. As can be clearly seen, the minimum and the maximum deviation percentages from the standard engine are 0.5% and 2.9%, respectively.

Table 1: Compare the performance of simulation and catalogue data at 3200 rpm

Performance	Simulation	Catalogue	Error %
Brake Power [kW]	63.9	64	0.2
Brake Torque [Nm]	191	195	2.1
BSFC [g/kWh]	258.3	258	0.1

Table 2: Engine Specification

Brand	ISUZU 4BD1
Engine type	Diesel, 4 cylinder
Bore	102mm
Stroke	118 mm
Total displacement	3.857 liter
Compression ratio	17.5
Max break Power	64 kW @ 3200 rpm
Max break Torque	215 N.m @1600 rpm

Table 3: Atmospheric conditions

Parameter	Measure
Absolute pressure	1 bar
Temperature	298K
Dry air pressure	0.99 bar

Table 4: Assumed parameters used in turbo selecion

Engine volumetric efficiency	95%
Intake manifold temperature	363K
BSFC of the turbocharger engine	0.38

Table 5: Technical specifications of TD05H-12G-8[16,17]

Frame: TD05H-12G-8			
Part Number	OE Number		
49178-03160	28230-45500		
Compressure			
Inducer Wheel Diameter	Exducer Wheel Diameter	Trim	Power indication
48.3 mm	68 mm	49.8	95-147 kW

Turbine			
Inducer Wheel Diameter	Exducer Wheel Diameter	Turbine Housing throat areas (T.H.R.A)	Trim
56 mm	49.1 mm	8.0 cm^2	76.9

Table 6: Producer and simulation data points for power

Engine speed (rpm)	Brake Power (kW)		Error %
	Catalogue data	Simulation results	
1000	21	20.7	1.4
1200	27	25.7	4.8
1400	32	30.3	5.3
1600	36	35.0	2.8
1800	40	39.2	2.0
2000	45	43.6	3.1
2200	49	47.7	2.7
2400	53	51.6	2.6
2600	56	55.1	1.6
2800	59	58.2	1.4
3000	62	61.3	1.1
3200	64	63.9	0.2

Table 7: Producer and simulation data points for torque

Engine speed (rpm)	Brake torque (kg.m)		Error %
	Catalogue data	Simulation results	
1000	193	197	2.1
1200	200	204	2.0
1400	206	207	0.5
1600	215	209	2.8
1800	214	208	2.8
2000	214	208	2.8
2200	212	207	2.4
2400	210	206	1.9
2600	208	202	2.9
2800	202	198	2.0
3000	198	195	1.5
3200	195	191	2.1

3. Results and discussion

Figs. 5 and 6 reveal that brake power and brake torque in the turbocharged diesel engine increase substantially to about 25% those in the naturally aspirated diesel engine. Maximum brake power in the turbocharged condition is 79.8 kW at 3200 rpm, while maximum brake power in the naturally aspirated diesel engine is 63.9 kW at 3200 rpm. Maximum brake torque in the turbocharged diesel engine is 267 Nm at 1600 rpm, while that of the naturally aspirated diesel engine is 215 Nm at 1600

rpm. In addition it is interpreted from these figures that greater ranges of brake power and torque are accessible with the turbocharged diesel engine.

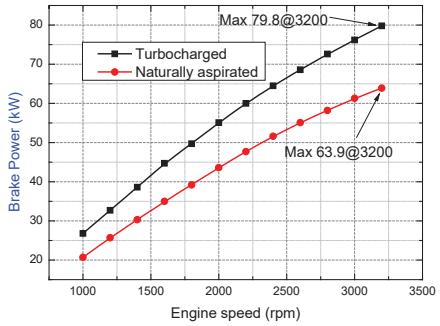


Figure 5. Brake power in turbocharged and naturally aspirated diesel engine

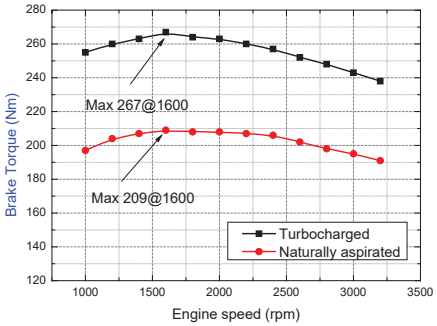


Figure 6. Brake torque in turbocharged and naturally aspirated diesel engine

Fig. 7 shows two quadratic curves of NOx concentrations in 3200 rpm engine speed. The formation of NOx emissions is substantially dependent on in-cylinder temperature during combustion and exhaust strokes, and also, to a lesser extent, on the concentration of oxygen inside the cylinder. In higher temperatures and oxygen concentrations, more NOx will be emitted. The climax of NOx concentration in exhaust gases is reached at just under the stoichiometric fuel-to-air ratio, since a compromise between maximum temperature and sufficient oxygen is established there [3]. Production of NO is of far higher level than that of NO_2; therefore, the trend of NOx concentrations is accurately traceable, considering the trend of NO concentrations. As is shown in Fig. 7, peaks in concentrations of the NOx emissions are observable; thus, the fuel-air equivalence ratios for both naturally aspirated and turbocharged diesel engines can be perceived to be close to the stoichiometric ratio, where NOx emissions typically peak [3,18].

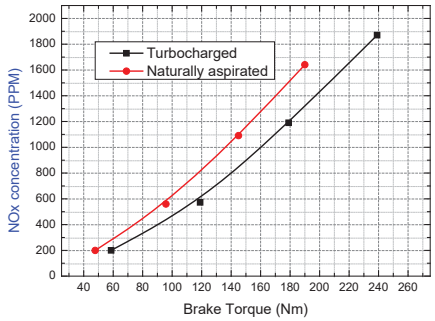


Figure 7. NOx concentration dependency on brake torque, in naturally aspirated and turbocharged diesel engine, at 3200 rpm

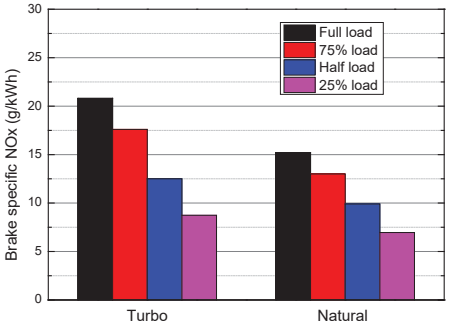


Figure 8. Brake specific NOx in turbocharged (left) and naturally aspirated (right) engine at 3200 rpm. Various loads are drawn in different colors.

The fact that these two curves are standing very far apart each other suggests that the turbocharged diesel engine produces significantly higher concentrations of NOx emission at incomparably higher brake torques (roughly 230 PPM and 47 Nm increments are observed at the peak points). Therefore, this type of comparison with concentrations does not seem very wise and dependable to an engineer, for it does not maintain a balanced and normalized perspective on the two prominent factors of power and emissions. In this day and age, reaching very high powers is sometimes essential and this will compromise the higher emission levels. Consequently, a normalized figure, called brake specific emission level, is also utilized for reporting the comparison between the emission levels. The unit for brake specific emission is grams per kilowatt-hour (g/kWh) and is derived from dividing the mass flow of the pollutant in g/h by the power in kW in the corresponding working condition. Fig. 8, this graph shows the comparison between the naturally aspirated (right) and the turbocharged diesel engine (left), in terms of g/kWh, various colors represent loads. As is evident, the brake specific NOx emissions level of the naturally aspirated and the turbocharged diesel engine are of the same order.

Considering the graph more meticulously, we can infer that the emission levels in the turbocharged diesel engine are rise at higher loads. Considering one of the bar groups, take the right one for example, for full load down to 25% load, the brake specific figures show a significant growth because of the rise in NOx concentrations. This rise in NOx concentrations is due to the falling fuel-air ratios toward stoichiometric ratio and rising temperature inside the cylinder.

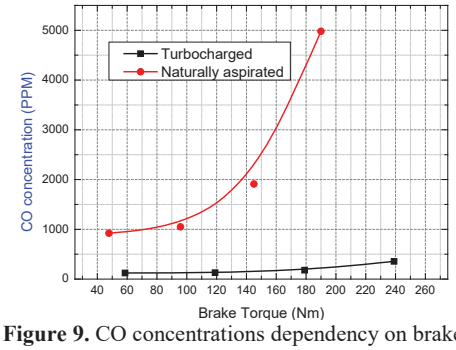


Figure 9. CO concentrations dependency on brake torque, in naturally aspirated (top) and turbocharged (bottom) engine, at 3200 rpm

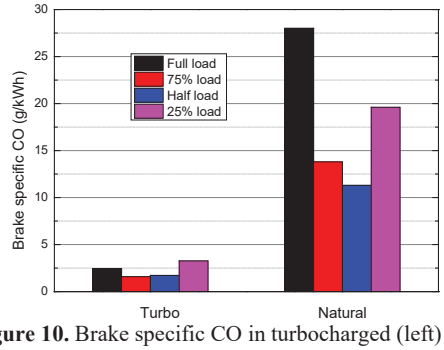


Figure 10. Brake specific CO in turbocharged (left) and naturally aspirated (right) engine at 3200 rpm. Various loads are drawn in different colors.

According to the graph in Fig. 9, we can assert that carbon monoxide concentration levels are lower in turbocharged diesel engine, when putting in perspective the results from the turbocharged and the naturally aspirated diesel engine. The utmost difference is about 4625 PPM in the full load condition. This suggests that turbocharging the 4BD1 diesel engine will influence the concentrations of carbon monoxide in the exhaust gas. CO emissions from internal combustion engines are controlled primarily by the fuel air equivalence ratio. For fuel-rich mixtures, CO concentrations in the exhaust fume increase steadily with increasing fuel air equivalence ratio, as the amount of excess fuel increases and combustion faces a more severe lack of oxygen [18]. For fuel-lean mixtures, CO concentrations in the exhaust vary little with fuel air equivalence ratio. Since compress ignition engines often operate far from stoichiometric at part load and fuel-rich at full load, CO emissions are significant and must be curbed. As is expected based on what is perceived from the graph of CO concentrations, the brake specific amounts of carbon monoxide dwindle in the turbocharged condition (Fig. 10). This is caused when the concentration decrease by minute amounts, while the power dwindles more influentially, as applies to this case.

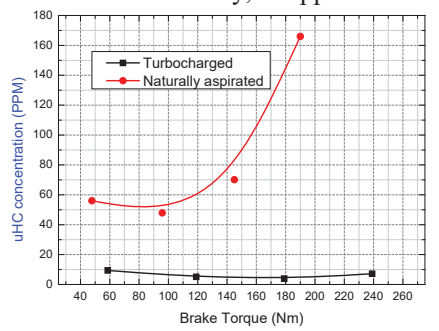


Figure 11. uHC concentration dependency on brake torque, in naturally aspirated (top) and turbocharged (bottom) engine, at 3200 rpm

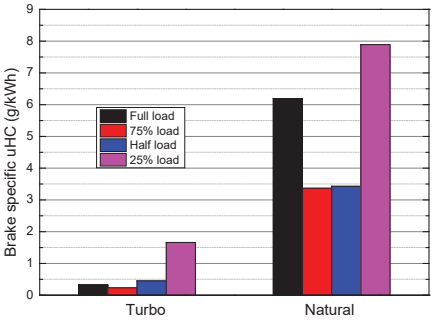


Figure 12. Brake specific uHC in turbocharged (left) and naturally aspirated (right) engine at 3200 rpm. Various loads are drawn in different colors.

The concentrations of unburned hydrocarbons (uHC) in the exhaust fume of the naturally aspirated and the turbocharged diesel engines at 3200 rpm are observable in Fig. 11. The main point in this figure is that the concentration of unburned hydrocarbons is exceptionally lower in the exhaust gas of the turbocharged diesel engine. This is apparently due to more pressure and temperature caused by the intense combustion in the turbocharged diesel engine, that impels the chemical equilibrium coefficient to further move toward oxidization of these molecules later in the power stroke and during the exhaust stroke. Enough oxygen should exist adjacent to the fuel molecules to oxidize them during the aforementioned procedure. Brake specific unburned hydrocarbon (uHC) pollutant emission,

follows the trend of concentrations and is minimum in 75% load (Fig. 12). In this Figure, starting from the full load condition and following the graph of either engines down to the 75% load condition. Then, from the 75% load condition on, the uHC concentration, as confirmed by Fig. 11, is on a slowly growth that causes the numerator of the brake specific to become greater and the brake specific graph (Fig. 12) depicts a rise in 25% load.

Moreover, having been scrutinized, the graph in Fig. 12 reveals that the turbocharged diesel engine leaves less unburned hydrocarbons for production of unit power. This is because of less uHC concentrations due to higher temperatures in the turbocharged condition that as elaborated in the previous section burns the hydrocarbon leftovers and prevents them to enter exhaust. So, the power levels in the turbocharged diesel engine are considerably higher.

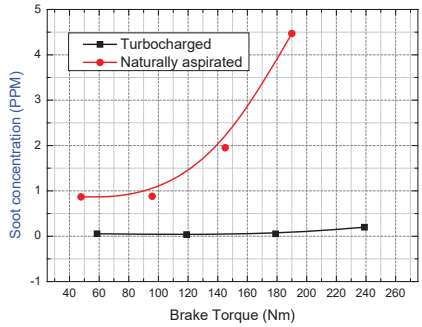


Figure 13. Soot concentration dependency on brake torque, in naturally aspirated (left) and turbocharged (right) engine, at 3200 rpm

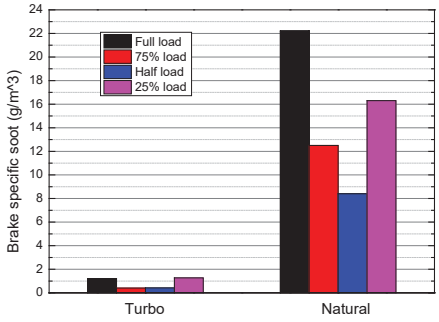


Figure 14. Brake specific Soot in turbocharged (left) and naturally aspirated (right) engine at 3200 rpm. Various loads are drawn in different colors.

Fig. 13 depicts the soot concentrations for the naturally aspirated and the turbocharged diesel engine, at 3200 rpm and various loads. Diffusion flame in diesel engines is very convenient for the formation of soot. The graph in Fig. 13 reveals that the soot concentration in the turbocharged diesel engine lower than naturally aspirated diesel engine due to higher temperatures in the turbocharged condition. Fig. 14 includes the brake-specific soot emissions of both naturally aspirated and turbocharged diesel engines at 3200 rpm. The naturally aspirated diesel engine stands significantly higher than the turbocharged diesel engine in brakespecific soot emission pollutant levels.

4. Conclusion

In this study, 1-D simulation code of GT-Suite software has been used to research the effects of turbocharging on emission pollutant as well as performance of 4BD1 diesel engine. In order to finish this purpose, a model of the engine was built and validated with catalogue data. The primary simulation show that this model acceptably represents the engine and deviates insignificantly from that. The most important conclusions of this research are as follows:

* For the turbocharged diesel engine, the maximum brake torque, 267 Nm, is produced at 1600 rpm, whereas the maximum power, 79.8 kW, is reached at 3200 rpm (Figs. 5 and 6). Turbocharging provides near-to-peak powers in a wider range of engine speeds, in comparison with the same diesel engine, naturally aspirated (Fig. 5). NOx emissions show different trends in different speed zones. In 3200 rpm, there is a peak in the curve at about 267 Nm of brake torque (Fig. 7). CO emission pollutants show different trends in different load at constant speed. At 3200 rpm, there is a minimal point in the curve at about 58.6 Nm of brake torque (Fig. 9). uHC emission pollutants also show various trends in different load. At 3200 rpm, there is a minimal point in the curve at about 179 Nm of brake torque (Fig. 11). The soot concentration in the exhaust gas also change with various brake torque. The lowest point in the curve at half load, about 119 Nm of brake torque (Fig. 13).

* For comparison between turbocharged and naturally aspirated diesel engine:

The peak torque and power are boosted roughly 25%. Their increase in other points of the engine speed range is lower, especially in low speeds. This is due to the policy in choosing the turbocharger which has been focused on boosting the maximum power. This policy leads to larger turbochargers

which operate well in high-end speeds (Figs. 5 and 6). Correspondingly, brake specific emissions of the turbocharged diesel engine are almost lower than those of the naturally aspirated diesel engine, and emission concentrations in the turbocharged diesel engine are lower, except for NOx concentrations.

This proves that the increase in power by turbocharging on the diesel engine will decrease in emission pollutants. It is clear that the reason behind the emission concentrations being lower in the turbocharged diesel engine is that turbocharging make more intake air in to in-cylinder (leading to more oxygen), so better fuel air mixing and combustion quality, the fuel burned out, leading to higher in-cylinder temperatures. This higher temperature eliminates the unburned hydrocarbons after the flame quench, and leads to lower uHC emissions in the turbocharged diesel engine. However, higher in-cylinder temperatures also leads to higher NOx emission pollutant levels.

References

[1]. John.B, Heywood, Internal Combustion Engines Fundamentals, McGraw-Hill, New York, 1988.
[2]. S. Eyssautier-Chuine, B. Marin, C. Thomachot-Schneider, G. Fronteau, A. Schneider, S. Gibeaux, P. Vazquez, Simulation of acid rain weathering effect on natural and artificial carbonate stones, Environ. Earth Sci. 75 (9) (2016).
[3]. G.E. Likens, C.T. Driscoll, D.C. Buso, Long-term effects of acid rain: response and recovery of a forest ecosystem, Science 272 (5259) (1996) 244–246.
[4]. U.S. Environmental Protection Agency, NOx: How nitrogen oxides affect the way we live and breathe, 1998.
[5]. D.G. Penney, Carbon Monoxide Toxicity, CRC Press, 2000.
[6]. M.J. Mendell, Indoor residential chemical emissions as risk factors for respiratory and allergic effects in children: a review, Indoor Air 17 (4) (2007) 259–277.
[7]. Gunter P. Merker, Christian Schwarz, Rudiger Teichmann, Combustion Engines Development, Mixture Formation, Combustion, Emissions and Simulation, Springer Heidelberg Dordrecht London New York, 2009.
[8]. GT, GT-Power Engine Performance Application Manual, Gamma Technologies, 2009.
[9]. Brahim Menacer, Mostefa Bouchetara, "Simulation and Modelling of a Turbocharged Compression Ignition Engine", International Journal of Energy and Power Engineering, Vol. 4, No. 3 (2015), pp. 129-145.
[10]. AVL Boost, user guide, version 4.0.4, 2004.
[11]. Woschni, G. and Anisits, F., Eine Methode zur Vorausberechnung der Änderung des Brennverlaufs mittelschnellaufender Dieselmotoren bei geänderten Betriebsbedingungen, MTZ 34, 1973.
[12]. Andree, A. and Pachernegg, S. J., Ignition Conditions in Diesel Engines, SAE 690253, 1969.
[13]. Stefano d'Ambrosio, Roberto Finesso, Ezio Spessa, Calculation of mass emissions, oxygen mass fraction and thermal capacity of the inducted charge in SI and diesel engines from exhaust and intake gas analysis, IC Engines Advanced Laboratory, Politacnico di torino, c.so Duca degli Abruzzi, 24, 10129, Torino, Italy.
[14]. GT-Suite, Engine Performance Tutorials, Gamma Technologies, Inc, 2012.
[15]. Isuzu model 4BD1, Workshop manual diesel engine, for automotive use, Isuzu Motor Co., Inc, 1979.
[16]. Information on http://www.turbomaster.info
[17]. Mitsubishi diesel eingines, Performance turbocharger list, 2006.
[18]. Constantine D. Rakopoulos, Evangelos G. Giakoumis, Diesel Engine Transient Operation, Principles of Operation and Simulation Analysis, 2009.

Finite element modeling method of centrifugally rotary processing

Soloviev A.N.[1,2,a*], Tho Nguyen Van [1,2], Tamarkin M.A.[3], Panfilov I.A.[1]

[1] Department of Theoretical and Applied Mechanics, Don State Technical University, Rostov-on-Don, Russia
[2] Electrical and Mechanical Engineering, Hai Phong University, Hai Phong City, Vietnam
[3] Department of Mechanical Engineering, Don State Technical University, Rostov-on-Don, Russia

[a] solovievarc@gmail.com

Keywords: Centrifugal-rotary processing; contact problem, CAE; FEM.

Abstract. In the present work, the process of interaction of an abrasive particle with the surface of a component is modeled in the framework of dynamic problems of the theory of thermoelasticity, considering plastic deformation, friction and wear of the surface in the contact region. Two boundary contact problems are considered. The first problem deals with the contact interaction of an element of an abrasive particle in the form of a truncated cone and the surface of a part. The circle of smaller diameter of the cone contacts the surface of the part taking into account the friction and plastic deformation of this surface. Kinematic or force boundary conditions are applied to the circle of greater diameter. In the case of kinematic conditions, the normal and tangential displacements of the circle and its rotation are specified. In the case of force conditions, the force and moment are given. In the second task, the hard stamp slides at a constant speed along the flat boundary of the workpiece, the value of the die insertion is set. In the contact area, the sliding friction force is expressed through normal pressure and heating due to the friction and wear. The stress and temperature fields near the contact region are investigated.

Introduction

The method of centrifugal-rotational processing (CRC) in an abrasive medium is characterized by high productivity and low cost. The wide technological possibilities of the method refer to it as one of the most promising methods of finishing cleaning operation. Optimization of the process requires development of the refined models of frictional interaction between the abrasive particles and the metal component's surface. In this model, the heating and wear of the surface due to the impact and further sliding of the abrasive particle must be taken into account.

Contact interaction leads to the wear and warming of the detail's surface, when abrasive processing of the surface is done. The processes of friction and wear have been studied for a long time and its foundations are presented in [1]. The process of processing in a rotary chamber is described in the works of M.A. Tamarkin and his colleagues [2,3]. Study of the characteristics of this process were done in papers [4-6]. In this paper, the aspects of the contact interaction between an abrasive particle and the surface of a detail are studied.

The elemental models of the constructions under consideration are constructed in the CAE packages ANSYS and FlexPDE. Series of numerical experiments are performed, and dependences of contact pressures and temperatures are constructed depending on the input parameters (speed of the magnitude of the introduction of power characteristics, etc.).

Mathematical model

In the first problem, the contact interaction is considered in the framework of the axisymmetric deformation of a fragment of an abrasive particle with the surface of the work piece. The fragment of the abrasive particle is a circular truncated cone, the smaller circle of which interacts with the

surface of the detail (Figure 1). The abrasive particle (corundum) is modeled by a linearly elastic solid material whose Young's modulus is significantly larger than that of the material being processed. The material to be processed (steel) is modeled by an elastically plastic bilinear solid material, using the Von Mises plasticity criterion.

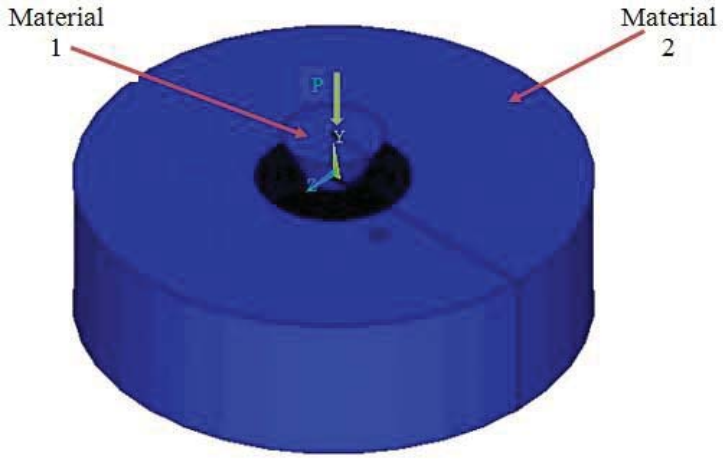


Figure 1. Particle model and details

The abrasive particle and the detail are contacted without friction. The top plane of the detail, the smaller circle and the lateral surface of the cone are contact surfaces. The bottom plane and the lateral surface of the detail are fixed along the normal. On the circle of the truncated cone, the force (uniformly distributed pressure) or kinematic (vertical displacement) boundary conditions are given. The intrusion of a particle into a detail is considered and the zone of plastic deformations and their maximum values are investigated.

In the second problem, sliding with a constant speed of a circular flat stamp (abrasive particle) on the surface of a detail is considered in the formulation of the linear theory of thermoelasticity, within the framework of a planar deformation. The temperature is included as mass forces in equations of motion, mechanical quantities are not included in the heat equation. The relationship between mechanical quantities and temperature is achieved by taking into account the heating under the stamp. The heating occurs through the specification of heat sources proportional to the normal pressure under the stamp, sliding speed and friction coefficient. The bottom edge of the layer is thermally insulated or the temperature is constant thereon, the heat exchange with the surrounding medium is specified on the top side.

Solution Methods

As a method for solving the above-described boundary-value problems, the finite element method implemented in the ANSYS package is used. Figure 2 shows the finite element grid in the first task. In the area of contact and possible plastic deformation the mesh is thickened. Finite elements PLANE183 (material 1), PLANE182 (material 2) and TARGET169, CONTA172 for contact surfaces are used.

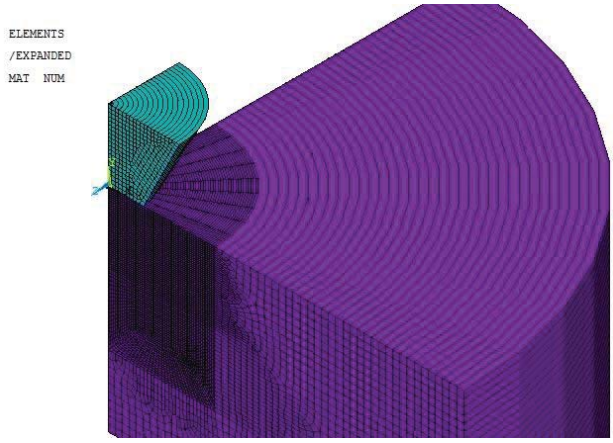
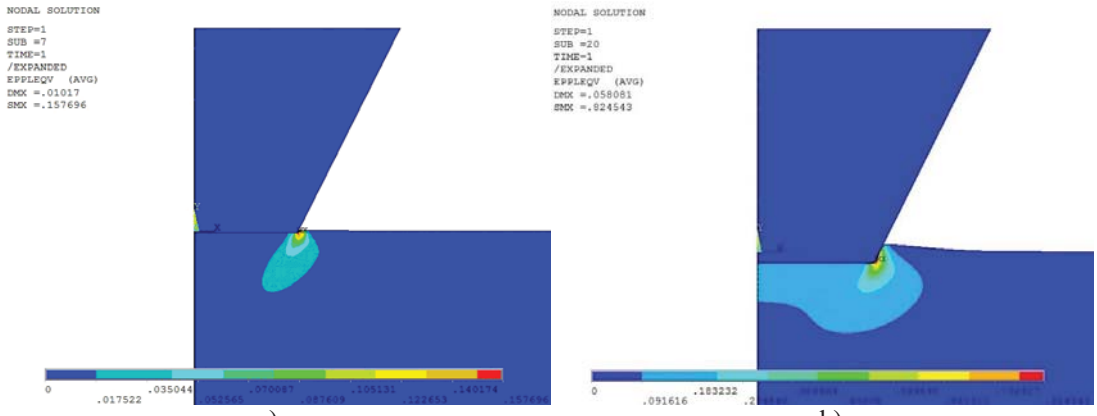


Figure 2. Element decomposition in the contact problem

Results of numerical experiments

In numerical calculations, the following data were used in the first problem: the radii of a truncated cone of 0.5 mm and 1 mm, the height of a cone of 1 mm, the radius of a detail of 5 mm, the thickness of 3 mm, the Young's modulus of material 1 is 2×10^6 GPa, the Poisson's ratio is 0.3, for material 2 – 2×10^2 GPa and 0.28, respectively, the yield stress is 0.22 GPa. Figure 3 shows the distribution of equivalent plastic deformations at the penetration depths of the cone 0.01 mm (Figure 3a) and 0.05 mm (Figure 3b)



a) b)

Figure 3. Distribution of equivalent plastic deformations

Investigations of the dependence of the maximum value of the equivalent plastic deformation on the penetration depth are shown at Fig. 4. The dependences of the dimensions of the region for which the plastic deformation is greater than 1% are determined (Figures 5-7)

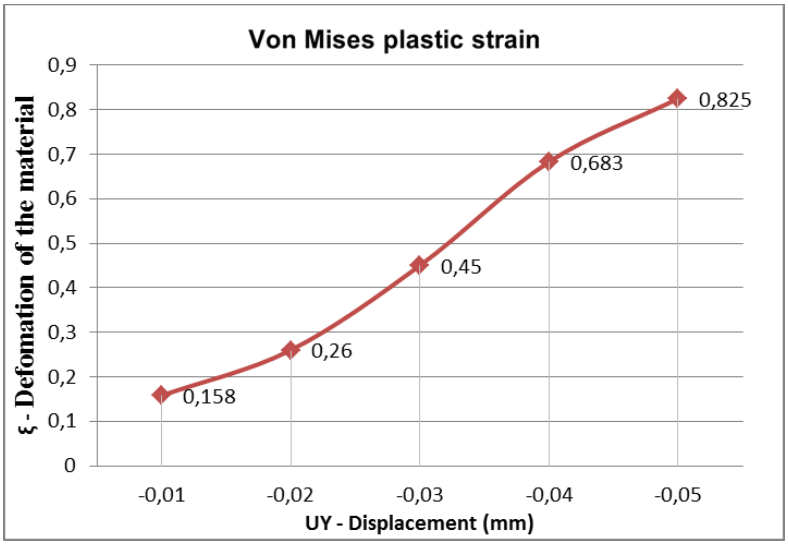


Figure 4. Maximum plastic deformation depending on the depth of penetration

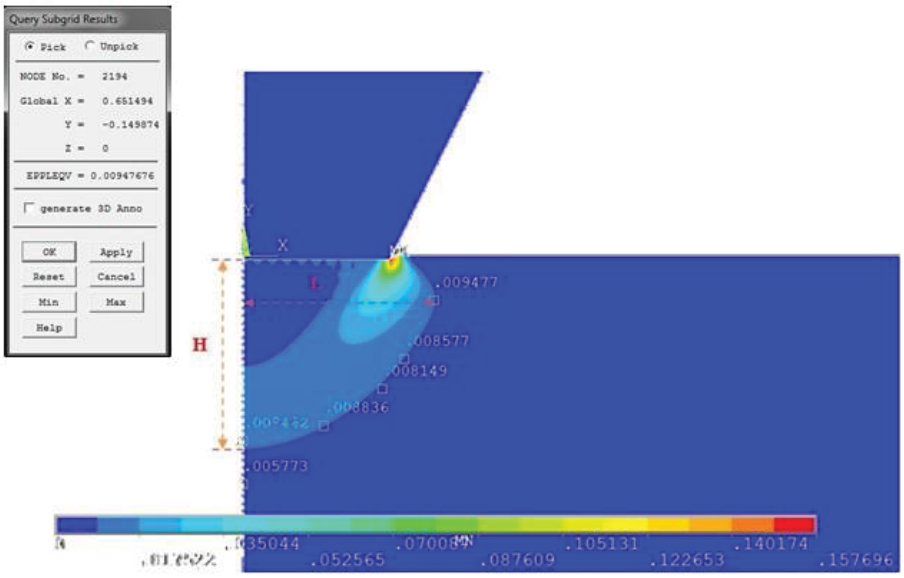


Figure 5. Dimensions of the plastic deformation zone

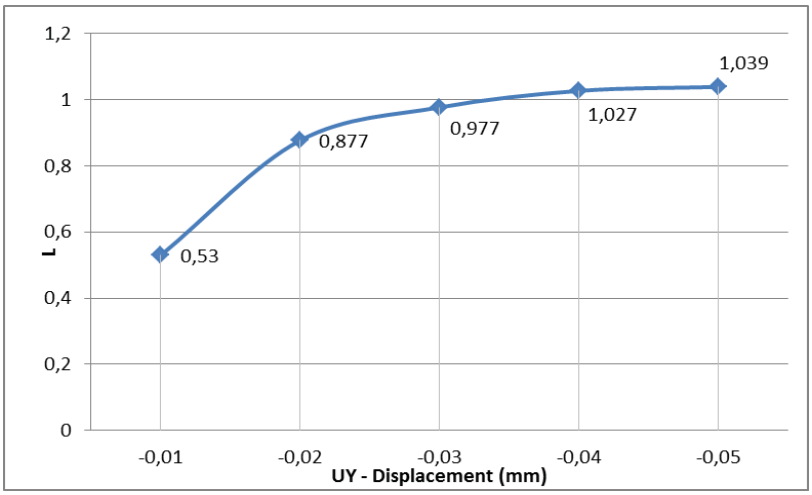


Figure 6. Dependence of the radius of the plastic deformation region

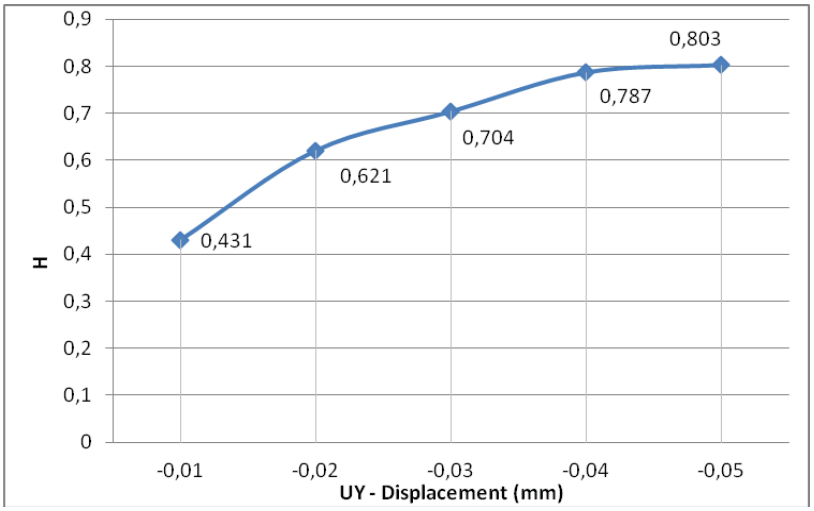


Figure 7. Dependence of the depth of the plastic deformation region

In the second problem, the following mechanical and temperature characteristics were used in the SI system: Young's modulus - $E = 2 \times 10^{11}$, Poisson's ratio - $\nu = 0.3$, coefficient of thermal expansion - $\alpha_T = 11.9 \times 10^{-6}$, density - $\rho = 7.8 \times 10^3$, thermal conductivity $\lambda_q = 52$. Specific heat $c_\varepsilon = 462$, heat transfer coefficients $h_1 = 1791.3$, $h_2 = 1791.3$, initial and external temperatures - $T_1 = T_2 = T_3 = 20^0 C$, strip length $b = 25h$, slip speed - $v = 0.2$, strip height - $h = 0.04$, diameter of the stamp $2a = 0.02$, coefficient of friction - $v = 0.2$, penetration depth $\delta = 1.0 \times 10^{-4}$.

The following figures show the distribution of the stress-strain state of the layer and the temperature fields.

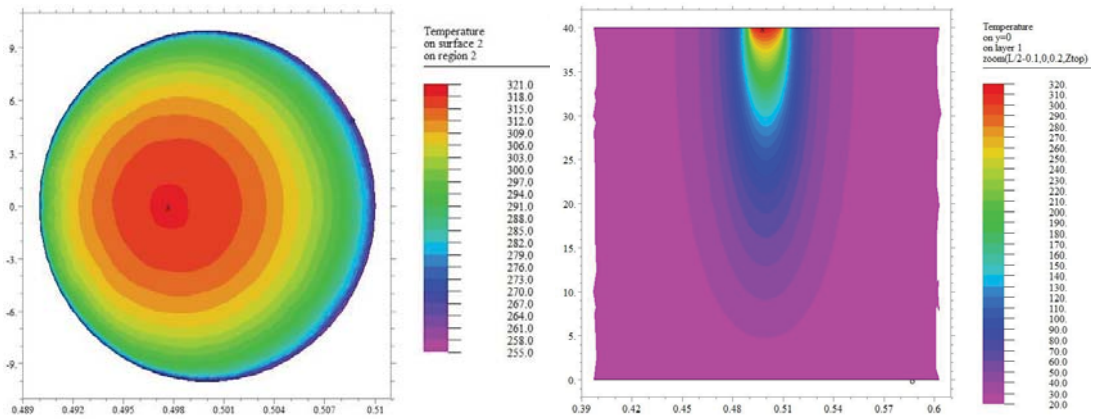


Figure 8. Temperature distribution under the stamp.

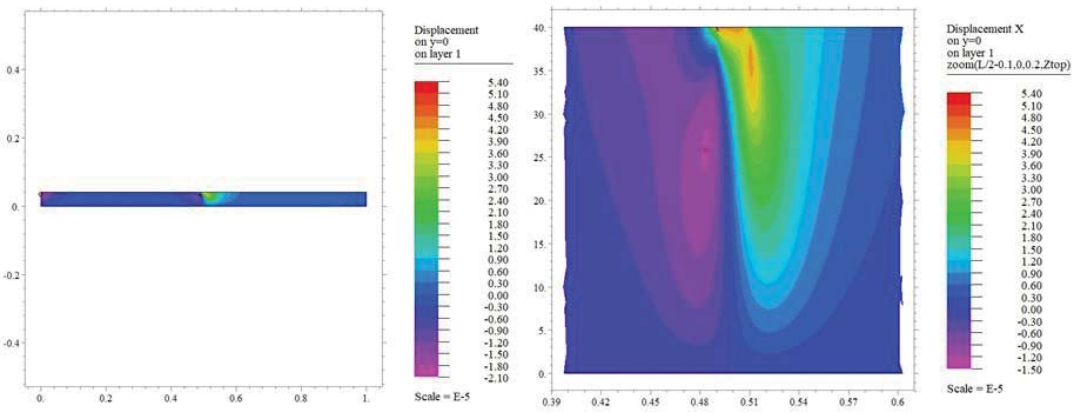


Figure 9. Distribution of horizontal displacement in the layer

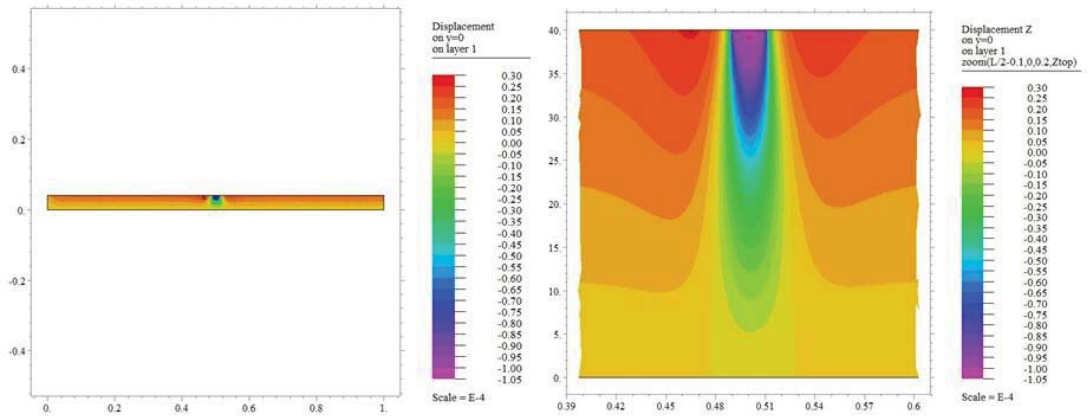


Figure 10. Distribution of vertical displacement in the layer

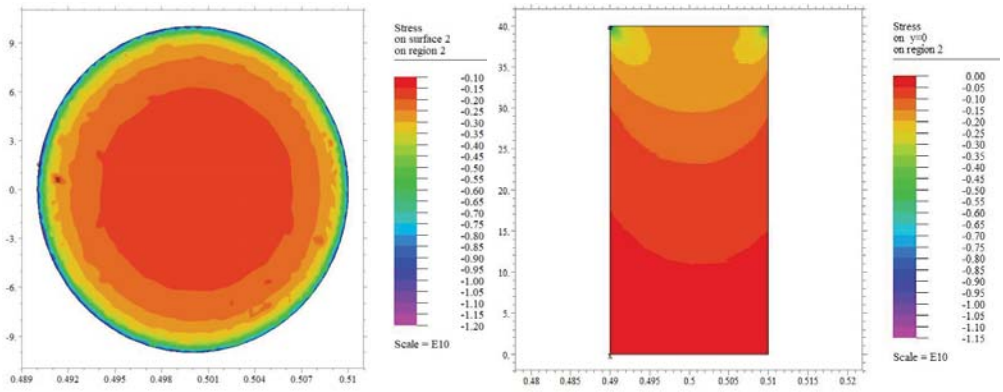


Figure 11. Stress σ_y distribution in the area under the stamp

Conclusion

Analysis of the stress-strain state of the layer on the basis of the presented calculations allows us to notice the following features. The stresses under the stamp and the temperature increase with increasing Young's modulus. The stresses under the stamp and the temperature increase with increasing Poisson's ratio. The stresses under the stamp and the temperature increase with increasing coefficient of friction. With a linear relationship between the coefficient of friction and the temperature, the stresses under the stamp increase and decrease with increasing and decreasing friction coefficient as a function of temperature, respectively. The stresses under the stamp and the temperature decrease with increasing layer thickness. The stresses under the stamp decrease with increasing width of the stamp, and the maximum temperature increases. The stresses increase with increasing speed with a constant coefficient of friction. The asymmetry of the stress distribution and the temperature under the stamp is disclosed with increasing speed.

References

[1] Kragelskiy I.V. Friction and wear. Moscow " Mashinostroenie " 1968. 480 p. (in Russia)

[2] Tamarkin M.A., E.E.Tishenko, V.V. Druppov. The study of metal removal during centrifugal-rotary processing in an abrasive medium // Vestnik Rybinskoy gosudarstvennoy aviacionnoy tehnologicheskoy akademii im. P.A. Solov'eva. - 2007. - №1 (11). P. 169-186. (in Russia)

[3] Tamarkin M.A., E.E.Tishenko, V.V. Druppov. Formation of surface quality parameters for centrifugal-rotary processing in an abrasive medium // Uprochniaiushie tehnologii i pokrytiia, №10, 2007, p. 19-23 (in Russia)

[4] Ph. G. Grützmacher, A. Rosenkranz, S. Rammacher, C. Gachot, F. Mücklich. The influence of centrifugal forces on friction and wear in rotational sliding // Tribology International 116 (2017) 256–263.

[5] Wenhui Li, Li Zhang, Xiuhong Li, Shengqiang Yang, Fengfeng Wu, Theoretical and Simulation Analysis of Abrasive Particles in Centrifugal Barrel Finishing: Kinematics Mechanism and Distribution Characteristics, Powder Technology (2017), doi:10.1016/j.powtec.2017.06.033

[6] J.C. Aurich, B. Linke, M. Hauschild, M. Carrella, B. Kirsch. Sustainability of abrasive processes // CIRP Annals - Manufacturing Technology 62 (2013) 653–672.

Determining the Optimal Parameters of Chip Shrinkage Coefficient and Cutting Force in High-Speed Machining for Aluminum Alloy A6061

Pham Duc Thanh[2,d], Nguyen Duc Toan[1,b], Doan Thi Huong[1,c], Phạm Thị Hoa[1,a*,]

[1]Hưng Yen University of Technology and Education,

[2] University of Transport and Communications,

[a]hoapt2108@gmail.com, [b] ductoancae@gmail.com, [c]doanhuong2009@gmail.com
[d]thanhphamstc@gmail.com

Keywords: Bao-Wierzbicki model, high-speed milling, cutting force, chip shrinkage coefficient.

Abstract

Nowadays, increasing the productivity and the quality of machining become major challenges of the metal cutting process. Due to the complexity of the chip formation process, in particular, at high cutting speeds, finite element model (FEM) has been frequently used as an alternative solution. Chip shrinkage coefficient and cutting force are the two basic parameters of the cutting process, which determines the productivity and quality of the workpiece. This study uses a Grey correlation relationship to analyze and select the common set of parameters for cutting force and chip shrinkage coefficient of the chip. Simulation of the A6061 aluminum alloy high-speed milling is done by Bao-Wierzbicki's (B-W) model. The optimal parameters are determined cutting depth 1 mm, clearance angle 6° and rake angle 10°. This parameter set adjusts the cut parameters so that the cutting process achieves the highest machining efficiency.

Introduction

Nowadays, high-speed machining has received a great deal of attention in modern industry to achieve high quality and productivity in manufacturing. The chip formation mechanism in high-speed machining is one of the most important factors influencing the surface finish of machining product and other cutting parameters, such as cutting force, temperature, vibration, wear and life of the cutting tool. Due to the complexity of the chip formation process, in particular, at high cutting speeds, finite element method (FEM) has commonly been used as an alternative approach. Various studies on the chip formation process are based on the J-C fracture model [1]. Several authors have employed different fracture models for simulation of material cutting processes, such as constant fracture strain model [2], Wilkins model [3], and modified Cockcroft-Latham model [4]. In general, all the models can provide the consistent predictions of cutting forces, chip thickness, and shear angle with adequate accuracy. The empirical B-W model, on the other hand, indicates that the fracture of a ductile material is strongly depended on the stress triaxiality. The B-W fracture model is distinguishable from the other models by the fact that a ductile material would never fail if the stress triaxiality is less than -1/3 [5]. So far, the B-W fracture model has been often adopted for the general purpose of material testing [6]. Recently, Liu *et al*. [7] evaluated different fracture models using finite element simulation. The simulated results of 2024-T3 aluminum alloy show that the best prediction of chip removal behavior of ductile metals is obtained by using the B-W fracture model with the consideration of the rate dependency, temperature effect, and damage evolution.

This work develops FE models based on B-W fracture model to simulate the metal cutting in the high-speed milling of aluminum alloy. The simulations are performed under different combinations of tool geometries and cutting conditions. Then, a design optimization is implemented using the Taguchi method to determine optimal cutting depth, rake angle, and clearance angle with the objectives of the cutting force and chip shrinkage coefficient. The obtained results are presented and discussed.

Workpiece material properties

The A6061 aluminum alloy was used for workpiece material in this work. Tables 1 shows the chemical formula, and Table 2 displays the physical properties of the A6061 aluminum alloy, respectively, which are used as the inputs of the FE model. The tensile stress-strain curve is shown Fig. 1. The tensile flow stress $(\bar{\sigma})$ is determined as a function of the equivalent plastic strain $(\bar{\varepsilon}^P)$ by [20]

$$\bar{\sigma} = 284(1+125\bar{\varepsilon}^P)^{0.1} \quad (1)$$

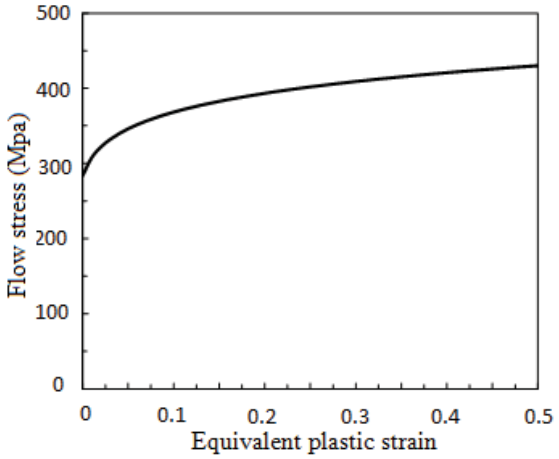


Fig. 1 Tensile stress-strain curve of A6061 aluminum alloy

Table 1: Chemical formula of A6061 aluminum alloy (%) [28]

Si	Fe	Cu	Mn	Mg	Cr	Zn	Ti	Al
0.4-0.8	0.7	0.15-0.4	0.15	0.8-1.2	0.04-0.35	0.25	0.15	remaining

Table 2: Physical properties of A6061 aluminum alloy

Physical properties	Value	Physical properties	Value
Melt temperature (^{0}C)	582-652	Elastic modulus (Gpa)	68.9
Thermal conductivity coefficient (W/m.K)	167	Fracture strength (Mpa)	96.5
Density (kg/m^3)	2.7	Tensile strength (Mpa)	276
Poisson's ratio	0.33		

Numerical model

Material fracture model

The B-W fracture model indicates the fracture occurring at a point in a body when the accumulated plastic strain reaches a critical value. The accumulated equivalent plastic strain or damage parameter based on the B-W model is given by [5]

$$D = \int_0^{\bar{\varepsilon}_f} \frac{\sigma_H}{\bar{\sigma}} d\bar{\varepsilon} = \left(\frac{\sigma_H}{\bar{\sigma}}\right)_{av} \bar{\varepsilon}_f \quad (2)$$

where $\left(\frac{\sigma_H}{\bar{\sigma}}\right)_{av}$ is the average stress triaxiality.

The equivalent strain to fracture can be denoted by the fit curve formulas given as follows [5]

$$\bar{\varepsilon}_f = 0.1225\left(\frac{\bar{\sigma}_H}{\bar{\sigma}} + \frac{1}{3}\right)^{-0.46} \text{ for } \frac{\bar{\sigma}_H}{\bar{\sigma}} = -\frac{1}{3} \div 0 \quad (3)$$

$$\bar{\varepsilon}_f = 0.19\left(\frac{\bar{\sigma}_H}{\bar{\sigma}}\right)^2 - 0.18\left(\frac{\sigma_H}{\bar{\sigma}}\right) + 0.21 \text{ for } \frac{\bar{\sigma}_H}{\bar{\sigma}} = 0 \div 0.4 \quad (4)$$

$$\bar{\varepsilon}_f = 0.15\left(\frac{\bar{\sigma}_H}{\bar{\sigma}}\right)^{-1} \text{ for } \frac{\bar{\sigma}_H}{\bar{\sigma}} = 0.4 \div 0.95 \quad (5)$$

The variation of the equivalent strain to fracture as a function of average stress triaxiality is shown in Fig. 2 shows, which is determined using Eqs. (3-5) and applying for A6061 aluminum alloy.

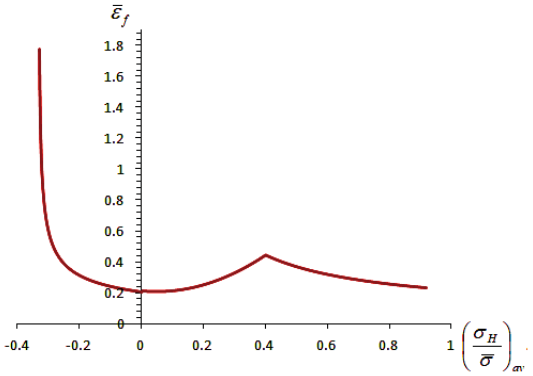


Fig. 2 Fracture curve of an A6061 aluminum alloy based on the B-W model

Simulation model

The numerical analyses were carried out in the commercial software Abaqus/Explicit 6.13.1. A 2D finite-element model for the cutting problem is shown in Fig. 3. The workpiece was modeled by 4-node bilinear elements with reduced integration (CPE4R). The cutting tool was modeled by the rigid element, and therefore, the tool wear was eliminated.

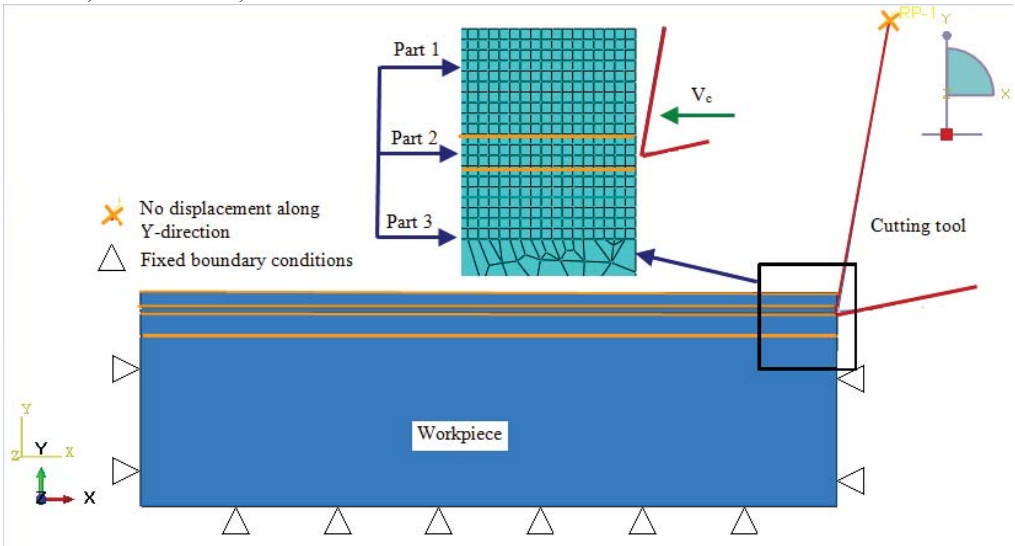


Fig. 3 Finite element model of the cutting problem

In order to optimize the contact management during simulation, the model consisting of four geometrical parts, as shown in Fig. 3, was developed. It consisted of three parts 1: the chip, parts 2: the tooltip passage zone that is a narrower band, and parts 3: the workpiece support. Part 2 played a role of the sacrificial layer, which directly interacted with a cutting tool. This layer was modeled by a mesh of

three elements with the total thickness larger than the cutting edge radius. A major part of the chip was formulated from the elements in the uncut chip portion. Another part arises from the elements in the sacrificial layer if they were not completely damaged. The remaining elements in the damaged zone, which were completely damaged, would be removed, while V is kept constant at V = 1500 m/min.

Determination chip shrinkage coefficient (*K*)

The effect of machining parameters on chip morphology and the deformability of metal can be described using the chip shrinkage coefficient. The formula for K can be written as following [30]

$$K = \frac{t_p}{t} \tag{6}$$

where t and t_p represent the un-deformed thickness and the chip thickness (Fig.4), respectively.

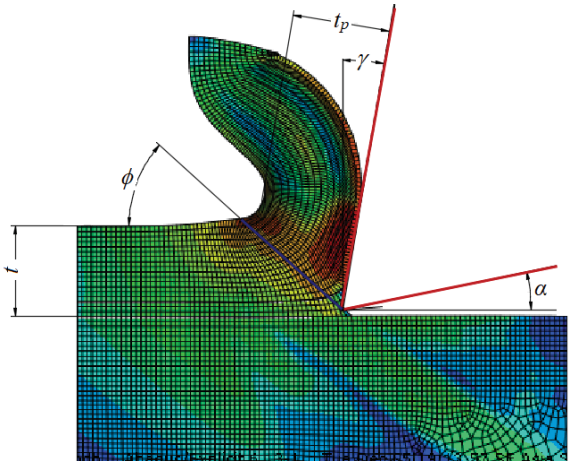


Fig. 4 Measurement of the chip thickness of the cutting model

Results and discussion

Taguchi orthogonal array

The Taguchi method is commonly used to improve the design and further product quality. Taguchi method based on the signal to noise ratio (S/N ratio) as a performance quantity to choose control levels that best cope with noise. To implement the method, the S/N ratio needs to estimate through both the mean and the variability and then is to be optimized. The formula of the S/N ratio is shown in Eq. (7). Purpose of the study is to reduce simultaneously the both of chip shrinkage coefficient (K) and cutting force (F). Therefore, the design problem is subjected to a smaller-the-better design for all experiments.

$$S/N = -10\log\frac{1}{n}\left(\sum y^2\right) \tag{7}$$

where n is the number of measurements in an experiment, and y the observed data of n measurements.

Table 3 lists the different levels of three-factor including depth of cut (t), clearance angle (α) and Rake angle (γ). The L9 orthogonal array experiment results are then presented in table 4.

Table 3: Cutting parameters and their levels

Symbol	Factor	Unit	Levels		
			1	2	3
A	Depth of cut (t)	mm	1.0	1.5	2.0
B	Clearance angle (α)	°	2	6	12
C	Rake angle (γ)	°	6	8	10

Table 4: L9 orthogonal array and calculated observed values

Trial no.	Column number and factor assignment			Chip Shrinkage Coefficient		Cutting Force	
	t (mm)	α (^{o})	γ(^{o})	(K)	S/N (K)	(F)	S/N (F)
1	1(1.0)	1(2)	1(6)	1.412	-2.9967	91.8128	-39.258
2	1(1.0)	2(6)	2(8)	1.394	-2.8853	117.006	-41.364
3	1(1.0)	3(12)	3(10)	1.376	-2.7724	178.052	-45.011
4	2(1.5)	1(2)	2(8)	1.349	-2.6002	176.836	-44.951
5	2(1.5)	2(6)	3(10)	1.344	-2.568	228.088	-47.162
6	2(1.5)	3(12)	1(6)	1.31	-2.3454	150.877	-43.572
7	3(2)	1(2)	3(10)	1.327	-2.4574	255.06	-48.133
8	3(2)	2(6)	1(6)	1.32	-2.4115	167.965	-44.504
9	3(2)	3(12)	2(8)	1.34	-2.5421	216.954	-46.727

After having a value of the S/N ratio, the Statistical Analysis of Variance (ANOVA) is employed to evaluate the contribution percentage of each design parameter. The ANOVA results for K are shown in Table 5. From Table 5, it reveals that the Depth of cut (t) has the highest contribution to the overall performance with 84.0%. The rake angle (γ) and clearance angle (α) have lower contribution with 11.8% and 4.3%, respectively. Based on the analysis, the optimum condition for the K is A3B3C1, respectively sign (*).

Table 5: Results of ANOVA for K

Factor	Mean S/N ratio of each level			The total squared	Contribution
	1	2	3		
A	-2.885	-2.579	-2.470*	0.283	0.840
B	-2.685	-2.622	-2.525*	0.040	0.118
C	-2.585*	-2.676	-2.599	0.014	0.043

Similarly, the ANOVA results and the S/N ratio responses for the cutting force F are given in Table 6. It is seen that F has a minimum value corresponding to the cutting parameters at levels A1B3C1 (respectively sign (*)). The results are indicated that the contribution of each factor is different. The contributions magnitude respect to the depth of cut (t), rake angle (γ) is 44.4% and clearance angle (α) subsequently is 53.1%, 44.4%, and 2.5%. Again, depth of cut (t) also has the biggest contribution.

Table 6: Results of ANOVA for F

Parameters	Mean S/N ratio of each level			The total squared	Contribution
	1	2	3		
A	-41.878*	-45.229	-46.455	33.682	0.531
B	-44.114	-44.344	-45.104*	1.609	0.025
C	-42.445*	-44.348	-46.769	28.175	0.444

Grey relational generation

The above analysis identifies the optimal factor for each objective individually. In fact, the optimal factor for K and F should be simultaneously optimized. For the purpose is "lower-the-better" the original sequence is rewritten in normalized form as follows:

$$x_i(k) = \frac{\max y_i(k) - y_i(k)}{\max y_i(k) - \min y_i(k)} \quad (8)$$

where, i = 1, 2, 3,…m, m is the number of experimental runs in Taguchi orthogonal array, k = 1,2,…n, n is the number of quality characteristics or process responses. *max* $y_i(k)$ is the largest value of y_i *(k)* for the kth response. *min* y_i (k) is the smallest value of y_i *(k)* for the response. $x_i(k)$ is the value after the Grey relational generation.

Grey relational coefficient *GZi(k)* is introduced in Eq. (9). Clearly, *GZi(k)* estimated through the best and actual experimental results.

$$GZ_i(k) = \frac{x(k)_{\min} - \zeta x(k)_{\max}}{x_i(k) + \zeta x(k)_{\max}} \quad (9)$$

where ζ is the distinguishing coefficients, $0 \le \zeta \le 1$. In the present case, ζ=0.5 is utilized due to the moderate distinguishing effects and good stability of outcomes.

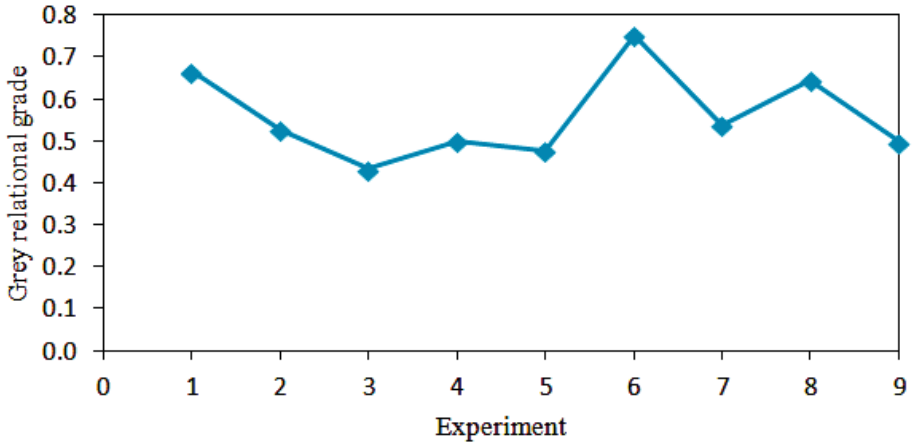


Fig. 5 Ranking of the Grey relationship

Summation of the Grey relational coefficient, the Grey relational grade (G_j), which represents an overall evaluation of experimental data for multivariable optimization design, will be obtained by Eq. (10). Optimization of a factor is to become finding the level of the highest grey relational grade.

$$G_i = \frac{1}{n}\sum_{k=1}^{n} GZ_i(k) \quad (10)$$

where, i=1,2,3 …9, *Gzi(k)* is the Grey relational coefficient of kth response in i^{th} experiment, n is the number of responses.

Table 7: Grey relational analysis results

Trial no.	x_i (for K)	x_i (for F)	GZ (for K)	GZ (for F)	G	Order
1	1.000	0.000	0.333	1.000	0.667	2
2	0.829	0.237	0.376	0.678	0.527	5
3	0.656	0.648	0.433	0.435	0.434	9
4	0.391	0.642	0.561	0.438	0.500	7
5	0.342	0.891	0.594	0.360	0.477	8
6	0.000	0.486	1.000	0.507	0.754	1
7	0.172	1.000	0.744	0.333	0.539	4
8	0.101	0.591	0.831	0.458	0.645	3
9	0.302	0.842	0.623	0.373	0.498	7

Table 8: Grey relational analysis results

Symbol	Factor	Grey relational grade			Max-min	Rank	Sum of squares	Mean square
		1	2	3				
A	t	0.543*	0.577	0.561	0.018	3	0.0006	2.236
B	α	0.568	0.550*	0.562	0.019	2	0.0002	0.700
C	γ	0.688	0.508	0.483*	0.205	1	0.0250	97.063

By using Eqs. (9) and (10), The Grey relational coefficients is determined and present in Table 7. In addition, the Grey relational grade is drawn in Fig. 5. The higher value of Grey relational grade means that the corresponding combination of process parameters reaches closer to the desired level. Therefore, a higher Grey relational grade results are favorable to better quality characteristics. From Table 7, the trial number 6 possesses the highest Grey relational grade, which holds the first preferred order, subsequently to the trial numbers 1 and 8.

Consequently, A1B2C3 is the optimal combination of parameters for obtaining the objectives of minimum K and F among others, respectively sign (*). From Table 8, it displays that the factor C (rake angle) has the highest contribution to overall performance with 97.06%. The cutting depth of 2.24% as a second contribution is observed. And the factors B (clearance angle) with 0.7 % is the smallest contribution.

Conclusions

The high-speed milling of aluminum alloy has been performed based on an FE model in this study. Based on the BW ductile model, the proposed numerical model was able to determine various parameters in the high-speed milling of the aluminum alloy such as cutting force, chip shrinkage coefficient. By apply the Taguchi method, the optimal conditions for the cutting process have been acquired. Optimal design carried out for identifying the cutting parameters with the objective of cutting force and chip shrinkage coefficient revealed that the optimum values obtained for high-speed milling process were cutting depth 1 mm, clearance angle 6° and rake angle 10°.

Acknowledgments

This research was supported by Center for Research and Applications in Science and Technology, Hung Yen University of Technology and Education, under grant number UTEHY.T016.P1718.02.

References

[1] T. Data, " Facture characteristics of three matals subjected to various strains, strain rates, temperatures and pressures," *Eng. Mech.*, (1985)vol. 21, no. I,.

[2] O. Article, "On predicting chip morphology and phase transformation in hard machining," *Int Adv Manuf Technol*, (2006) pp. 645–654.

[3] M. L. Wilkins, R. D. Streit, and J. E. Reaugh, "Cumulative-Strain-Damage model of ductile fracture: Simulation and prediction of engineering fracture tests," *Lawrence Livermore Natl. Lab.*, (1980)pp. 1–68.

[4] J. Lorentzon, N. Järvstråt, and B. L. Josefson, "Journal of Materials Processing Technology Modelling chip formation of alloy 718," *J. Mater. Process. Technol.*, vol. 209, (2009)pp. 4645–4653.

[5] Y. Bao and T. Wierzbicki, "On fracture locus in the equivalent strain and stress triaxiality space," *Int. J. Mech. Sci.*, vol. 46, no. 1, (2004) pp. 81–98.

[6] M. Giglio, A. Manes, and F. Viganò, "Numerical simulation of the slant fracture of a helicopter's rotor hub with ductile damage failure criteria," *Fatigue Fract. Eng. Mater. Struct.*, vol. 35, no. 4, (2012), pp. 317–327.

[7] J. Liu, Y. Bai, and C. Xu, "Evaluation of Ductile Fracture Models in Finite Element Simulation of Metal Cutting Processes," *J. Manuf. Sci. Eng.*, vol. 136, no. February, (2013), p. 11010.

[8] Banh Tien Long, Tran The Luc and Tran Sy Tuy. Metal Cutting Principles, 2nd Ed, Scienceand Technics Publishing House, (2013) (InVietnamese)

Preparation of high porous aerogel nanocomposites as electrode materials supercapacitors

Van Hoa Nguyen*, Pham Anh Dat, Tran Quang Ngoc, Nguyen Huu Nghia, Tran Ngoc Le

Department of Chemistry, Nha Trang University, 2 Nguyen Dinh Chieu, Nha Trang, Vietnam.

*Corresponding author. Tel: (+84) 966337972; E-mail: hoanv@ntu.edu.vn.

Keywords: Nanocomposites; Electrochemical peformance; Supercapacitors; Energy storage and conversion.

Abstract. Supercapacitors have attracted considerable attention as a unique class of energy storage devices with high power capability, long cyclic life, low maintenance, and rapid dynamics of charge propagation. One of the most important factors that affects on the performance of supercapacitors is electrode materials. It reported that the idea materials for supercapacitors should have a high surface area, high conductivity, high porousity and proper pore size. Aerogels are know to have very high surface area and high porousity with very low density. In fact, the design and fabrication of hierarchical aerogel nanocomposites were developed by various techniques, such as chemical vapor deposition, hydrothermal and electrodeposition processes for supercapacitor applications. In this study, taking advantages of the highly conductive, mesoporous nature of graphene and high capacitance of V2O5, polyaniline, NiCo2S4 and open framework of the three-dimensional nickel foam, the as-prepared electrodes exhibited rapid electron and ion transport, large electroactive surface area, and excellent structural stability. The specific capacitance of the obtained electrodes was as high as 1950 F g−1 at a high current density of 7.5 A g−1, suggesting its promising applications as an efficient electrodes for supercapacitors.

Acknowledgements. This research is funded by Vietnam National Foundation for Science and Technology Development (NAFOSTED) under grant number 103.99-2015.01.

Design of a Novel Adaptive Prescribed Controller for MR Suspension

DO Xuan Phu[1, a *], TA Duc Huy[1,b], LE Tran Huy Thang[1,c], MAI Bui Quoc Long[1,d]

[1]MediRobotics Laboratory, Department of Mechatronics and Sensor System Technology, Vietnamese-German University, Binh Duong, Vietnam

[a]phu.dx@vgu.edu.vn; [b]msst2016_huy.td@student.vgu.edu.vn; [c]me2015_thang.lth@student.vgu.edu.vn; [d]me2015_long.mbq@student.vgu.edu.vn

Keywords: adaptive control; prescribed performance; sliding mode control; vibration control; MR suspension.

Abstract. This work proposes a novel adaptive controller based on the prescribed performance of the sliding surface and applies it to a vehicle seat suspension system. The interval type 2 fuzzy neural networks system is used as a model establishment and two sliding surfaces are defined: conventional surface and prescribed surface. Then, an equivalent control is determined by assuming the derivative of the prescribed surface is zero, followed by the design of a control which can guarantee both stability and robustness. Two controllers are combined and integrated with adaptation laws which can make the proposed control system be stable in the sense of Lyapunov. After formulating the controller, the effectiveness of the proposed control is validated through simulation by adopting a semi-active seat suspension system with a magneto-rheological damper. A road profiles of random step wave road is adopted to evaluate the proposed controller. Simulation results show that the proposed controller provides excellent vibration control performances with a small tracking error between the proposed and prescribed (objective) controls.

Introduction

Nowadays, modern technical devices integrating with various controllers are popularly applied to numerous dynamic systems to achieve desired performances in a real time. Therefore, the development of a new control methodology which can bring enhanced desirable performances is one of crucial and attractive topics in control engineering society. Especially, the design of a composite controller which is defined as a combination of more than two different control methods is one of the attractive research topics. This is because the composite controller is much more robust against external disturbances or/and parameter uncertainties than a single controller. There are several approaches to develop a new composite controller. The indirect and direct adaptive control based on a sliding surface and the modified Riccati-like equation was presented in [1,3,4,5,6,7,8,13]. These controls were applied for control vibration of smart actuators based on magneto-rheological fluid. A review of controls for magneto-rheological fluid actuators was studied in [2]. It is remarked that the adaptive controllers were combined with the fuzzy model for prevent the severe disturbance environment. From the above controllers, the fuzzy model is always a good solution for uncertainty of the system. Recently, the interval type 2 fuzzy model has been used in design of control [10,11]. The advantage of this model is its flexible and optimized value which are different from the classical fuzzy with fixed value and non-optimization [40, 41]. To improve the fuzzy model, clustering method [9] should be used. The data-driven for fuzzy rules was studied in [10]. From the above surveys, this study presents a new control with more than one sliding surface: one is the conventional sliding surface, the other is designed from the prescribed definition. After that, these surfaces are combined with the fuzzy model and H infinity technique. In design of new controller, the online fuzzy model is built with an optimized computational cost algorithm and its rules are established by using clustering method. The contributions of the new controller are summarized as follows:

(1) A new connection between the conventional and prescribed sliding surface is suggested.

(2) A new novel adaptive control with two sliding surface functions is presented.
(3) The new novel sliding surface with modified Riccati-like equation is applied to design of new adaptation laws.

Design of a New Composite Adaptive Controller

Interval Type 2 Fuzzy Model

The fuzzy model is the interval type 2 fuzzy [10], and this model is developed following online method for updating rules through application. The rule base of OIT2F can be expressed as follows [10].

$$R_f^j: \text{If } h_1 \text{ is } \boldsymbol{H}_{f1}^j \text{ and } \ldots \text{ and } h_n \text{ is } \boldsymbol{H}_{fn}^j \text{ Then } g \text{ is } a_0^j + \sum_{i=1}^{n} a_i^j h_i \quad (1)$$

Where, $\boldsymbol{H}_{fi}^j \left(i = 1,\ldots,n; j = 1,\ldots,m\right)$ are fuzzy sets, m is the number of rules, and a_i^j are interval sets. It is noted that the calculation process of OIT2F is clearly depicted in [10]. The defuzzified output is then determined by

$$g_f = \frac{g_l + g_r}{2} = \frac{\boldsymbol{\theta}_l^T \boldsymbol{\xi}_l^f + \boldsymbol{\theta}_r^T \boldsymbol{\xi}_r^f}{2} \quad (2)$$

In the above, $\boldsymbol{\theta}_l^T = \left[w_1^l\ w_2^l\ w_3^l \ldots w_n^l\right]$ and $\boldsymbol{\theta}_r^T = \left[w_1^r\ w_2^r\ w_3^r \ldots w_n^r\right]$ are the weighting vectors, which symbolize the relation of the rule layer and type-reduction, and the weighted firing strength vectors are given by

$$\boldsymbol{\xi}_l^f = \left[\frac{\underline{f}_1}{\sum_{i=1}^{n}\underline{f}_i}\ \frac{\underline{f}_2}{\sum_{i=1}^{n}\underline{f}_i}\ \frac{\underline{f}_3}{\sum_{i=1}^{n}\underline{f}_i} \ldots \frac{\underline{f}_n}{\sum_{i=1}^{n}\underline{f}_i}\right]^T,\quad \boldsymbol{\xi}_r^f = \left[\frac{\overline{f}_1}{\sum_{i=1}^{n}\overline{f}_i}\ \frac{\overline{f}_2}{\sum_{i=1}^{n}\overline{f}_i}\ \frac{\overline{f}_3}{\sum_{i=1}^{n}\overline{f}_i} \ldots \frac{\overline{f}_n}{\sum_{i=1}^{n}\overline{f}_i}\right]^T$$

Adaptive Prescribed Performance

In order to formulate a new composite controller, consider a single-input single-output (SISO) nonlinear system governed by the following equation:

$$\dot{\mathbf{x}} = \mathbf{f}(\mathbf{x}) + \mathbf{g}(\mathbf{x})u(t) + \mathbf{d}(\mathbf{t}) \quad (3)$$

where $\mathbf{f}(\mathbf{x}) \in R^n$ and $\mathbf{g}(\mathbf{x}) \in R^n$ are two unknown non-linear function vectors, $u(t) \in R^1$ is control function, $\mathbf{d}(\mathbf{t}) \in R^n$ is an external disturbance vector, $|\boldsymbol{d(t)}| \le \boldsymbol{\delta d}$ where value $\boldsymbol{\delta}\mathbf{d} \in R^n$ is upper bound of $\mathbf{d}(\mathbf{t})$, $\mathbf{x} = \left[x_1, x_2, \ldots, x_n\right]^T = \left[x_1, \dot{x}_1, \ldots, x_1^{(n-1)}\right]^T \in R^n$ is the state vector of the system. The first sliding surface s_s is defined as follows:

$$s_s = k_1 x_1 + k_2 x_2 + k_3 x_3 + \ldots + k_n x_n = \sum_{i=1}^{n} k_i x_i \quad (4)$$

Where, $\mathbf{K} = \left[k_n, k_{n-1}, k_{n-2}, \ldots, k_1\right]$ is defined as the coefficients such that all of the roots of the polynomial, $\sigma^n + k_{n-1}\sigma^{n-1} + k_{n-2}\sigma^{n-2} + \ldots + k_1$ are in the open left-half complex plane. It is noted that $k_n = 1$ in this analysis following the property of sliding surface [53]. The sliding surface (4) is rewritten using the state variables as follows:

$$x_n = -k_1 x_1 - k_2 x_2 - k_3 x_3 - \ldots - k_{n-1} x_{n-1} + s_s \quad (5)$$

A new vector $\tilde{\boldsymbol{x}}$ is defined by $\tilde{\boldsymbol{x}} = \left[x_1\ x_2\ x_3\ \ldots\ x_{n-1}\right]^T$, and thus the system (3) is rewritten as follows:

$$\dot{\tilde{\boldsymbol{x}}} = \boldsymbol{S}_1 \tilde{\boldsymbol{x}} + \boldsymbol{S}_2^T s_s \quad (6)$$

Where,

$$S_1 = \begin{bmatrix} 0 & 1 & 0 & \dots & 0 \\ 0 & 0 & 1 & \dots & 0 \\ . & . & . & \dots & . \\ -k_1 & -k_2 & -k_3 & \dots & -k_{n-1} \end{bmatrix}, \quad S_2 = \begin{bmatrix} 0 \\ 0 \\ . \\ 1 \end{bmatrix}$$

The tracking error is then defined as $e(t) = x_1 - x_d$, x_d is the desired value. It is noted that x_1 is also x in the Eq. (3). Error performance function is defined as follows.

$$\lambda(t) = (\lambda(0) - \lambda_\infty)e^{-lt} + \lambda_\infty \tag{7}$$

Where $l > 0, 0 < |e(0)| < \lambda(0), \lambda_\infty > 0, \lambda_\infty < \lambda(0)$ then $\lambda_t > 0$ and $\lambda(t)$ tend to λ_∞ exponentially. The value e in the Eq.(7) is exponential function. In order to guarantee fast convergence of tracking error, and obtain a certain convergence accuracy, the tracking error is also set as follows:

$$e(t) = \lambda(t)S(\varphi) \tag{8}$$

Where the prescribed error performance function of $S(\varphi)$. So the function $S(\varphi)$ is found as:

$$S(\varphi) = \frac{e(t)}{\lambda(t)} \tag{9}$$

From the above conditions (10), the function $S(\varphi)$ can be determined as follows:

$$S(\varphi) = \frac{e^{\varphi} - e^{-\varphi}}{e^{\varphi} + e^{-\varphi}} \tag{10}$$

It is noted that e in the Eq. (10) is exponential function. From the conditions (10) and using the Eq. (8), the tracking error is obtained as:

$$-\lambda(t) < \lambda(t)S(\varphi) < \lambda(t) \Leftrightarrow -\lambda(t) < e(t) < \lambda(t) \tag{11}$$

Hence, the tracking error can be summarized as follows.

$\Xi = \{e \in R : |e(t)| < \lambda \ \ \forall t \geq 0 \ \ and \ e(t) < \lambda_\infty \ \ for \ t \to \infty\}$. Now, the inverse function of (10) is expressed by

$$\varphi = \frac{1}{2} ln \frac{1+S}{1-S} = \frac{1}{2}\left[ln(\lambda + e(t)) - ln(\lambda - e(t))\right] \tag{12}$$

Hence, the derivatives of Eq. (12) are obtained as follows.

$$\dot{\varphi} = \frac{1}{2}\left[\frac{\dot{\lambda} + \dot{e}(t)}{\lambda + e(t)} - \frac{\dot{\lambda} - \dot{e}(t)}{\lambda - e(t)}\right] \tag{13}$$

$$\ddot{\varphi} = M_1 + M_2 + M_3\ddot{e}(t) \tag{14}$$

$$M_1 = \frac{\ddot{\lambda}(\lambda + e(t)) - (\dot{\lambda} + \dot{e}(t))^2}{2(\lambda + e(t))^2}, \qquad M_2 = -\frac{\ddot{\lambda}(\lambda - e(t)) - (\dot{\lambda} - \dot{e}(t))^2}{2(\lambda - e(t))^2},$$

$$M_3 = \left(\frac{\lambda + e(t)}{2(\lambda + e(t))^2} + \frac{\lambda - e(t)}{2(\lambda - e(t))^2}\right).$$

To realize the convergence of $\varphi \to 0$, the second (prescribed) sliding surface is defined as follows:

$$\sigma_s = \dot{\varphi} + c_s\varphi \tag{15}$$

Where, $c_s > 0$. Then, the derivative of Eq. (15) is obtained as follows.

$$\dot{\sigma}_s = \ddot{\varphi} + c_s\dot{\varphi} = M_1 + M_2 + M_3\left(f(x) + g(x)u(t) + d(t) - \ddot{x}_d\right) + c_s\dot{\varphi} \tag{16}$$

The lumped uncertainty of system is then defined by

$$w = M_3\tilde{\gamma}_f\xi_f + M_3\tilde{\gamma}_g\xi_g u + M_3 d(t) \tag{17}$$

Where, $\gamma_f = f(x) - f^*(x)$, $\gamma_g = g(x) - g^*(x)$. Using Eq. (17) and Eq. (17), the derivative Eq. (16) is rewritten as follows:

$$\dot{\sigma}_s = M_1 + M_2 + M_3 f^*(x) + M_3 g^*(x) u(t) - M_3 \ddot{x}_d + c_s \dot{\varphi} + w \quad (18)$$

Based on Eq. (2), the relationship between Eq. (18) and OIT2F model is expressed as follows:

$$\dot{\sigma}_s = M_1 + M_2 + M_3 \theta_f^* \xi_f + M_3 \theta_g^* \xi_g u - M_3 \ddot{x}_d + c_s \dot{\varphi} + w \quad (19)$$

Where,

$\theta_f^* = arg\,min_{\theta_f \in \Delta\theta_f} \left[sup_{x \in \Delta x} \left| f(x) - f^*(x) \right| \right]$, $\theta_g^* = arg\,min_{\theta_g \in \Delta\theta_g} \left[sup_{x \in \Delta x} \left| g(x) - g^*(x) \right| \right]$,

$\Delta\theta_f = \left\{ \theta_f \in R^n, \left\| \theta_f \right\| \le \Theta_f \right\}$, $\Delta\theta_g = \left\{ \theta_g \in R^n, \left\| \theta_g \right\| \le \Theta_g \right\}$, $\Delta x = \left\{ x \in R^n, \left\| x \right\| \le \Theta_x \right\}$

In the above definitions, Θ_f, Θ_g, Θ_x are constant boundaries. Now, an equivalent control is determined from Eq. (19) based on the assumption $\dot{\sigma}_s \approx 0$:

$$u_1 = \frac{1}{M_3 \hat{\theta}_g \xi_g} \left(-M_1 - M_2 - M_3 \hat{\theta}_f \xi_f + M_3 \ddot{x}_d - c_s \dot{\varphi} \right) \quad (20)$$

The equivalent control u_1 cannot control the system because it cannot compensate the error from the fuzzy approximation. To guarantee the robustness and stability in control, a robust control part u_2 should be added as follows:

$$u_2 = \frac{1}{M_3 \hat{\theta}_g \xi_g} \left(-\sum_{i=1}^{n-1} P_{(n-1)i} x_i - \frac{\sigma_s}{\beta} + \frac{1}{2} M_3 \Gamma \xi_z \tilde{\boldsymbol{x}} \boldsymbol{P} \boldsymbol{S}_2 \boldsymbol{S}_2^T \boldsymbol{P} \tilde{\boldsymbol{x}}^T \right) \quad (21)$$

Thus, the total control u of the system is determined as follows.

$$u = u_1 + u_2 \quad (22)$$

The control u_2 is the combination of two sliding surfaces s_s and σ_s. The value Γ is the adaptive parameter where its boundary is given by $\Delta\Gamma = \left\{ \Gamma \in R, \left\| \Gamma \right\| \le \Theta_\Gamma, \sigma_s \Gamma \xi_{fz} \le \rho \right\}$, and Θ_Γ is constant boundary. The matrix $\boldsymbol{P} = \boldsymbol{P}^T \ge 0$ in which its result is a solution of Riccati-like equation given by

$$\boldsymbol{P}\boldsymbol{S}_1 + \boldsymbol{S}_1^T \boldsymbol{P} + \boldsymbol{Q} - \sigma_s \Gamma \xi_z \boldsymbol{P}\boldsymbol{S}_2 \boldsymbol{S}_2^T \boldsymbol{P} + \rho \boldsymbol{P}\boldsymbol{S}_2 \boldsymbol{S}_2^T \boldsymbol{P} = 0 \quad (23)$$

Where, $\rho \ge \sigma_s \Gamma \xi_z$, ρ is the prescribed attenuation level, $\boldsymbol{Q} = \boldsymbol{Q}^T \ge 0$, ξ_z is consequent membership value of the OIT2F. When the value $\rho = \sigma_s \Gamma \xi_z$, the Riccati-like equation is rewritten as:

$$\boldsymbol{P}\boldsymbol{S}_1 + \boldsymbol{S}_1^T \boldsymbol{P} + \boldsymbol{Q} = 0 \quad (24)$$

Now, the Eq. (19) can be analyzed as follows:

$$\dot{\sigma}_s = M_1 + M_2 + M_3 \theta_f^* \xi_f + M_3 \theta_g^* \xi_g u - M_3 \ddot{x}_d + c_s \dot{\varphi} + w - M_3 \hat{\theta}_f \xi_f + M_3 \hat{\theta}_f \xi_f - M_3 \hat{\theta}_g \xi_g u + M_3 \hat{\theta}_g \xi_g u$$

$$\Leftrightarrow \dot{\sigma}_s = M_1 + M_2 + M_3 \tilde{\gamma}_f \xi_f + M_3 \tilde{\gamma}_g \xi_g u - M_3 \ddot{x}_d + c_s \dot{\varphi} + w + \left[M_3 \hat{\theta}_f \xi_f + M_3 \hat{\theta}_g \xi_g u \right] \quad (25)$$

Where, $\tilde{\gamma}_f = \theta_f^* - \hat{\theta}_f, \tilde{\gamma}_g = \theta_g^* - \hat{\theta}_g$. Using Eq. (22) and Eq. (25), the following equation is obtained.

$$\dot{\sigma}_s = \left[-\sum_{i=1}^{n-1} P_{(n-1)i} x_i - \frac{\sigma_s}{\beta} + \frac{1}{2} M_3 \Gamma \xi_z \tilde{\boldsymbol{x}} \boldsymbol{P}\boldsymbol{S}_2 \boldsymbol{S}_2^T \boldsymbol{P} \tilde{\boldsymbol{x}}^T \right] + \left[M_3 \tilde{\gamma}_f \xi_f + M_3 \tilde{\gamma}_g \xi_g u + w \right] \quad (26)$$

Theorem: The stability and robustness of the proposed control system are guaranteed if the main control function is designed as given in Eq. (20), (21) and (22), and adaptation laws are suggested as follows:

$$\dot{\tilde{\gamma}}_f = -\mu_1 M_3 \sigma_s \xi_f, \; \dot{\tilde{\gamma}}_g = -\mu_2 M_3 \sigma_s \xi_g u, \; \dot{\Gamma} = -\mu_3 M_3 \sigma_s \xi_z \tilde{\boldsymbol{x}} \boldsymbol{P}\boldsymbol{S}_2 \boldsymbol{S}_2^T \boldsymbol{P} \tilde{\boldsymbol{x}}^T \quad (27)$$

Proof of the theorem is shown in Appendix.

Application to Vibration Control

In this work, the vehicle suspension system with MR damper is adopted to demonstrate control effectiveness of the proposed composite adaptive controller. The mechanical model of the seat suspension system is shown in Fig. 1. The governing equations of the MR seat suspension system are derived as follows.

$$m_s\ddot{x}_s = -k_s\left(x_s - x_0\right) - c_s\left(\dot{x}_s - \dot{x}_0\right) + k_1\left(x_1 - x_s\right) + c_1\left(\dot{x}_1 - \dot{x}_s\right) + F_{MR} \tag{28}$$

$$m_1\ddot{x}_1 = -k_1\left(x_1 - x_s\right) + c_1\left(\dot{x}_1 - \dot{x}_s\right) \tag{29}$$

The above equations can be rewritten using the state variables as follows.

$$\begin{aligned} \dot{x}_{11} &= \dot{x}_s = x_{22} \\ \dot{x}_{22} &= f_{11}\left(x_{11}, x_{22}, x_{33}, x_{44}\right) + g_{11}\left(x_{11}, x_{22}, x_{33}, x_{44}\right)u \\ \dot{x}_{33} &= \dot{x}_1 = x_{44} \\ \dot{x}_{44} &= f_{22}\left(x_{11}, x_{22}, x_{33}, x_{44}\right) \end{aligned} \tag{30}$$

Where,

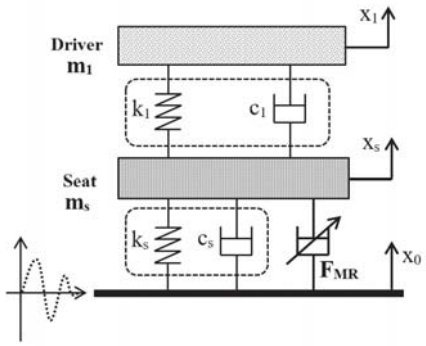


Fig. 1. Mechanical model of the seat suspension with MR damper

$f_{11}\left(x_{11}, x_{22}, x_{33}, x_{44}\right) = -\frac{k_s}{m_s}\left(x_{11} - x_0\right) - \frac{c_s}{m_s}\left(x_{22} - \dot{x}_0\right) + \frac{k_1}{m_s}\left(x_{33} - x_{11}\right) + \frac{c_1}{m_s}\left(x_{44} - x_{22}\right)$,

$g_{11}\left(x_{11}, x_{22}, x_{33}, x_{44}\right) = \frac{1}{m_s}$, $u = F_{MR}$, $f_{22}\left(x_{11}, x_{22}, x_{33}, x_{44}\right) = -\frac{k_1}{m_1}\left(x_{33} - x_{11}\right) - \frac{c_1}{m_1}\left(x_{44} - x_{22}\right)$. It is noted that $x_{11}, x_{22}, x_{33}, x_{44}$ are variables related x_s and x_1 of the system which are pointed out in both Fig. 1 and Eq. (30).

Table 1. Parameters of desired prescribed performance and applied prescribed performance

Parameter	**Desired Prescribed Performance**	**Applied Prescribed Performance**
Initial value $\lambda(0)$	0.5	0.5
Infinity value λ_∞	0.001	0.001
Exponential value l	1	0.00047

Simulation Results and Discussions

The proposed controller is simulated with two different excitations: random step wave road and regular bump road. The first excitation is collected from the real road, and the second excitation is achieved from the model given in [13].The process of the controller is expressed as follows: the objective trajectory is a desirable one to be tracked in the control action [13]. The outputs of the proposed control and the objective will be used for calculating the error. This error will be checked by desired prescribed performance. It is remarked that the desired prescribed performance is different from the applied prescribed performance which is given Eq.s (7-12). The parameters of both the

desired and the applied prescribed performance are listed in Table 1. The damping force of MR damper is designed 1000 N (±5%) at 2 A. The values of the sliding surface $[k_1, k_2]$ are chosen by $[1,\ 20]$ for both road profiles. The constant value Γ of the Riccati-like equation is chosen by 10 for both road profiles. The constant c_s is chosen by 500 and 5000 for the regular bump road and the random step wave road, respectively. In addition, the matrix **Q** of the Riccati-like equation is chosen as $Q = [-2 \quad 0; 0 \quad -2]$. The constants μ_1, μ_2, μ_3 of adaptation laws are chosen as 10 for all road profiles.

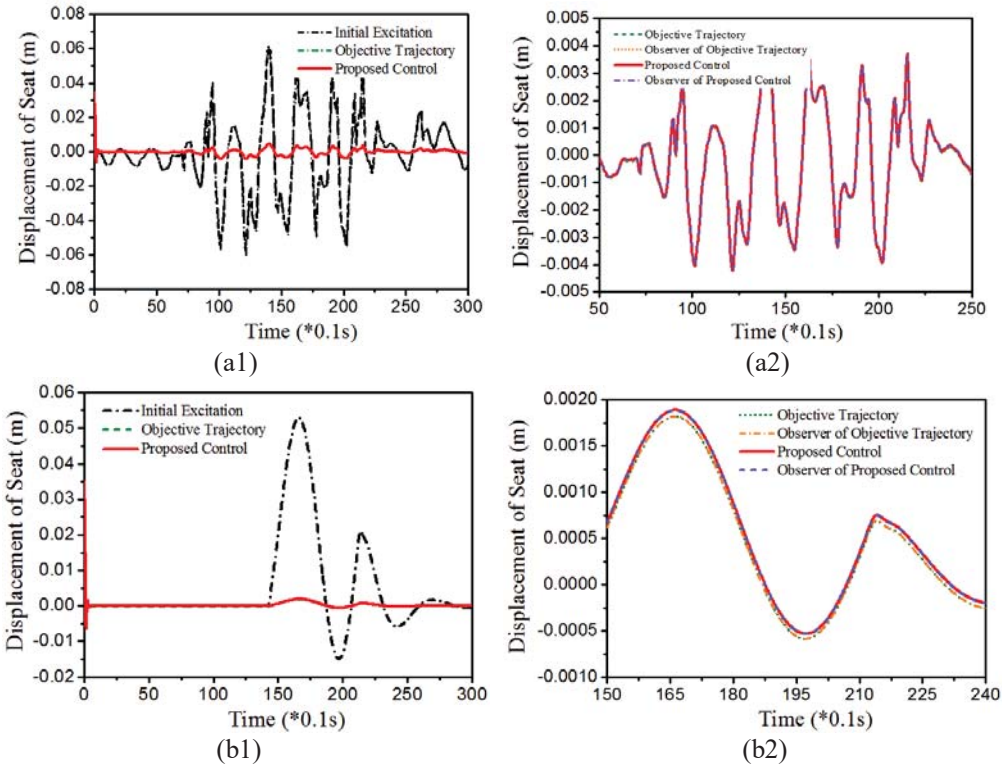


Fig. 2. Simulation results of the displacement at the seat (x_s) with the proposed control: (a1) (a2) random step wave road, (b1) (b2) regular bump road

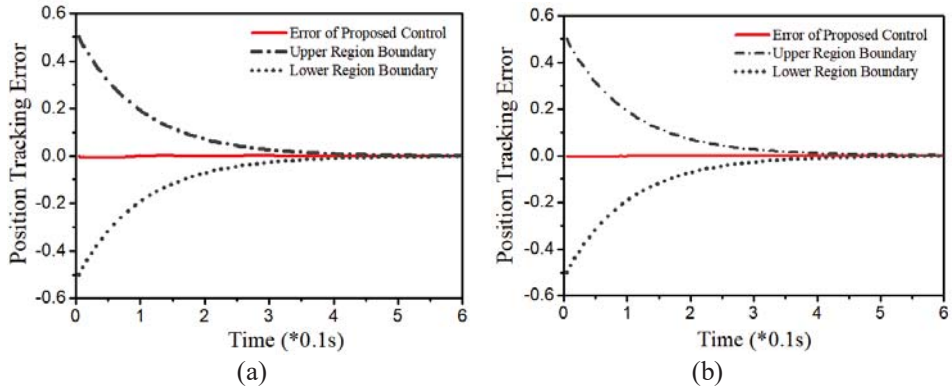


Fig. 3. Simulation results of position tracking error: (a) random step wave road, (b) regular bump road

Simulation results includes displacement of seat, displacement of driver, prescribed sliding surface and error responses. These are presented from Fig. 2 to Fig. 3. It is seen from Fig. 2 that the displacement responses at the seat and driver positions of the proposed controller are good

performance following the objective trajectory under two different road excitations. This is attributed by combination of the conventional surface and the prescribed surface proposed in this work. It is noted here that the response of the driver belongs to the controlled result of the seat and two parameters of k_1 and c_1. The error performance of the proposed controller is shown in Fig. 3. It is clearly observed that the proposed controller provides excellent performances with the error within the limit of the desired prescribed performance (boundary). More specifically, the tracking error satisfies the objective vibration permitting the error limitation of 0.001 mm as given in Table 1.

Conclusions

In this study, a new composite adaptive controller was proposed and applied to vibration control of a semi-active vehicle seat suspension system featuring MR damper. In order to formulate the composite controller, the on-line type of the interval type 2 fuzzy model was used. Basically, the proposed controller has two sliding surfaces: one is conventional surface for the initial states of the system and the other is the prescribed surface for the objective performance. It has been shown from simulation results that the proposed controller provides excellent vibration control performances as well as good tracking performance with a small error in range of the defined boundary. This proposed control will be applied in practical model to evaluate its performance in the future.

Acknowledgement

This research is funded by Vietnam National Foundation for Science and Technology Development (NAFOSTED) under grant number 107.01-2017.28.

References

[1] Do Xuan Phu and Seung-Bok Choi, Vibration control of a ship engine system using high-load magnetorheological mounts associated with a new indirect fuzzy sliding mode controller, Smart Materials and Structures 24 (2015) 025009

[2] Seung-Bok Choi, Weihua Li, Miao Yu, Haiping Du, Jie Fu and Phu Xuan Do, State of the art of control schemes for smart systems featuring magneto-rheological materials, Smart Materials and Structures 25 (2016) 043001

[3] Do Xuan Phu, Do Kyun Shin and Seung-Bok Choi, Design of a new adaptive fuzzy controller and its application to vibration control of a vehicle seat installed with an MR damper, Smart Materials and Structures 24 (2015) 085012

[4] Do Xuan Phu, Kruti Shah and Seung-Bok Choi, Design of a new adaptive fuzzy controller and its implementation for the damping force control of a magneto-rheological damper, Smart Materials and Structures 23 (2014) 065012

[5] Do Xuan Phu, Seung-Bok Choi, Yang-Sub Lee and Moon-Sihk Han, Vibration control of a vehicle's seat suspension featuring a magneto-rheological damper based on a new adaptive fuzzy sliding-mode controller, Proc IMechE Part D: J Automobile Engineering 230(4) (2016) 437-458

[6] Do Xuan Phu, Nguyen Vien Quoc, Joon-Hee Park and Seung-Bok Choi, Design of a novel adaptive fuzzy sliding mode controller and application for vibration control of magneto-rheological mount, J Mechanical Engineering Science 228(13) (2014) 2285–2302

[7] Xuan Phu Do, Kruti Shah, and Seung-Bok Choi, Damping force tracking control of MR damper system using a new direct adaptive fuzzy controller, Shock and Vibration (2015) 947937

[8] Do Xuan Phu, Jin-Hee An, Seung Bok Choi, A novel adaptive PID controller with application to vibration control of a semi-active vehicle seat suspension, Applied Sciences 7(10) (2017) 1055

[9] Xianchang Wang, Xiaodong Liu, Lishi Zhang, A rapid fuzzy rule clustering method based on granular computing, Applied Soft Computing 24 (2014) 534–542

[10] Chia-Feng Juang and Yu-Wei Tsao, A self-evolving interval type-2 fuzzy neural network with online structure and parameter learning, IEEE Transactions on Fuzzy Systems 16(6) (2008) 1411-1424

[11] Dongrui Wu, Approaches for reducing the computational cost of interval type-2 fuzzy logic systems: overview and comparisons, IEEE Transactions on Fuzzy Systems 21(1) (2013) 80-99

[12] Jinkun Liu, Sliding mode control using Matlab, Tsinghua University Press, 2017

[13] Do Xuan Phu, Sang-Min Choi and Seung-Bok Choi, A new adaptive hybrid controller for vibration control of a vehicle seat suspension featuring MR damper, Journal of Vibration and Control 1-22 (2016) Doi: 10.1177/1077546316629597

Appendix

Proof: To proof the above theorem, a Lyapunov function candidate is proposed as follows:

$$L_v = \frac{1}{2}\sigma^2{}_s + \frac{1}{2}\tilde{\boldsymbol{x}}\boldsymbol{P}\tilde{\boldsymbol{x}}^T + \frac{1}{2\mu_1}\tilde{\gamma}_f^2 + \frac{1}{2\mu_2}\tilde{\gamma}_g^2 + \frac{1}{2\mu_3}\Gamma^2 \tag{A1}$$

The derivative of Eq. (A1) is obtained as:

$$\dot{L}_v = \sigma_s\dot{\sigma}_s + \frac{1}{2}\dot{\tilde{\boldsymbol{x}}}\boldsymbol{P}\tilde{\boldsymbol{x}}^T + \frac{1}{2}\tilde{\boldsymbol{x}}\boldsymbol{P}\dot{\tilde{\boldsymbol{x}}}^T + \frac{1}{\mu_1}\tilde{\gamma}_f\dot{\tilde{\gamma}}_f + \frac{1}{\mu_2}\tilde{\gamma}_g\dot{\tilde{\gamma}}_g + \frac{1}{\mu_3}\Gamma\dot{\Gamma} \tag{A2}$$

Substituting Eq. (27) into Eq. (A2) yields the following.

$$\begin{aligned}
\dot{L}_v &= \sigma_s\left[\left(-\sum_{i=1}^{n-1}P_{(n-1)i}x_i - \frac{\sigma_s}{\beta} + \frac{1}{2}M_3\Gamma\xi_z\tilde{\boldsymbol{x}}\boldsymbol{P}\boldsymbol{S}_2\boldsymbol{S}_2^T\boldsymbol{P}\tilde{\boldsymbol{x}}^T\right) + \left(M_3\tilde{\gamma}_f\xi_f + M_3\tilde{\gamma}_g\xi_g u + w\right)\right] + \frac{1}{2}\dot{\tilde{\boldsymbol{x}}}\boldsymbol{P}\tilde{\boldsymbol{x}}^T + \\
&\quad + \frac{1}{2}\tilde{\boldsymbol{x}}\boldsymbol{P}\dot{\tilde{\boldsymbol{x}}}^T + \left[\frac{1}{\mu_1}\tilde{\gamma}_f\dot{\tilde{\gamma}}_f + \frac{1}{\mu_2}\tilde{\gamma}_g\dot{\tilde{\gamma}}_g + \frac{1}{\mu_3}\Gamma\dot{\Gamma}\right] \\
\Leftrightarrow \dot{L}_v &= \left[M_3\sigma_s\tilde{\gamma}_f\xi_f + \frac{1}{\mu_1}\tilde{\gamma}_f\dot{\tilde{\gamma}}_f\right] + \left[M_3\sigma_s\tilde{\gamma}_g\xi_g u + \frac{1}{\mu_2}\tilde{\gamma}_g\dot{\tilde{\gamma}}_g\right] + \\
&\quad + \left[M_3\Gamma\xi_z\sigma_s\tilde{\boldsymbol{x}}\boldsymbol{P}\boldsymbol{S}_2\boldsymbol{S}_2^T\boldsymbol{P}\tilde{\boldsymbol{x}}^T + \frac{1}{\mu_3}\Gamma\dot{\Gamma}\right] + \left[\sigma_s w - \frac{\sigma^2{}_s}{\beta} - \frac{1}{2}\rho\boldsymbol{P}\boldsymbol{S}_2\boldsymbol{S}_2^T\boldsymbol{P} - \frac{1}{2}\tilde{\boldsymbol{x}}^T\boldsymbol{Q}\tilde{\boldsymbol{x}}^T\right]
\end{aligned} \tag{A3}$$

It is noted that Eq. (24) is used in finding Eq. (A3). Now, substituting Eq. (28) into Eq. (A3) yields the following.

$$\begin{aligned}
\dot{L}_v &= \sigma_s w - \frac{\sigma^2{}_s}{\beta} - \frac{1}{2}\rho\boldsymbol{P}\boldsymbol{S}_2\boldsymbol{S}_2^T\boldsymbol{P} - \frac{1}{2}\tilde{\boldsymbol{x}}^T\boldsymbol{Q}\tilde{\boldsymbol{x}}^T \\
\Leftrightarrow \dot{L}_v &= \left[-\frac{1}{2}\tilde{\boldsymbol{x}}^T\boldsymbol{Q}\tilde{\boldsymbol{x}}^T - \frac{1}{2}\left(\frac{\sigma_s}{\sqrt{\beta}} - \sqrt{\beta}w\right)^2 + \frac{1}{2}\beta w^2\right] - \frac{1}{2}\rho\boldsymbol{P}\boldsymbol{S}_2\boldsymbol{S}_2^T\boldsymbol{P} \le -\frac{1}{2}\tilde{\boldsymbol{x}}^T\boldsymbol{Q}\tilde{\boldsymbol{x}}^T + \frac{1}{2}\beta w^2
\end{aligned} \tag{A4}$$

The above equation cannot be used for conclusion of stability. Hence, it needs to be integrated from $t = 0$ to $t = T$;

$$L_v(0) - L_v(T) + \frac{1}{2}\beta\int_0^T w^2 dt \ge \frac{1}{2}\int_0^T \tilde{\boldsymbol{x}}\boldsymbol{Q}\tilde{\boldsymbol{x}}^T dt \tag{A5}$$

Where, $L_v(0) = \frac{1}{2}\sigma^2{}_s(0) + \frac{1}{2}\tilde{\boldsymbol{x}}(0)\boldsymbol{P}\tilde{\boldsymbol{x}}^T(0) + \frac{1}{2\mu_1}\tilde{\gamma}_f^2(0) + \frac{1}{2\mu_2}\tilde{\gamma}_g^2(0) + \frac{1}{2\mu_3}\Gamma^2(0)$. The value $L_v(T)$ is always positive, so Eq. (A5) is determined as:

$$L_v(0) + \frac{1}{2}\beta\int_0^T w^2 dt \ge \frac{1}{2}\int_0^T \tilde{\boldsymbol{x}}\boldsymbol{Q}\tilde{\boldsymbol{x}}^T dt \ge 0 \tag{A6}$$

Design of a Novel Magnetorheological Damper for Exoskeleton Suspension

DO Xuan Phu[1, a *], MAI Bui Quoc Long[1], TA Duc Huy[1], LE Dai Hiep[1]

[1]MediRobotics Laboratory, Department of Mechatronics and Sensor System Technology, Vietnamese-German University, Binh Duong, Vietnam

[a]phu.dx@vgu.edu.vn; [b]me2015_long.mbq@student.vgu.edu.vn
[c]msst2016_huy.td@student.vgu.edu.vn; [d]ledaihiep1993@gmail.com

Keywords: MR damper; MR exoskeleton; knee exoskeleton; vibration control; outside electrical coil.

Abstract. This study presents a novel MR damper for control vibration of exoskeleton. The exoskeleton includes two dampers that are used for the human thigh frame and the lower leg. The geometry of exoskeleton is analyzed to present the stroke of dampers. With the determined forces and moments of the exoskeleton, the configuration of the dampers is shown. The required damping force from the dampers are calculated and optimization process is carried out with ANSYS ADPL. It is shown that the results of the optimization is good compared with the initial requirement of damping force.

Introduction

After over a decade of the MR-Fluid application in industry, especially in automobile, the application of MR fluid in medical devices has been of major interest recently. The design of MR actuators also follows the three modes of MR fluid. The flow mode and shear mode were applied in the design of MR mount in [1]. A full review of MR configuration was studied in [2]. It is noted that these configurations [1,2] can also be applied for dampers. The saturation problem and various impactive conditions in design of damper are also presented in [3] and [4], respectively. The bi-fold flow mode and bypass hole for damper are studied in [5] and [6]. In addition, the control of MR actuators is also studied in [7-10]. From the those analyses, the modes of MR fluid are activated with electrical coils that are placed inside of the actuator. This study suggests a new design of MR damper with outside electrical coils for high efficiency of vibration control. The MR damper is used for the human-support exoskeleton.

Configuration of the proposed exoskeleton

The structure of the proposed exoskeleton is shown in figure 1. It includes two parts: the first part is the frame AKE_1F_1 with one MR damper for the vibration control of the thigh, the second part is the frame DCF_2E_2 with one MR damper for the vibration control of the lower leg and foot. The role of the damper is controlling the vibration and supporting the patient walking movement. The stroke of damper is defined by the length x_{AB} and x_{BC}.

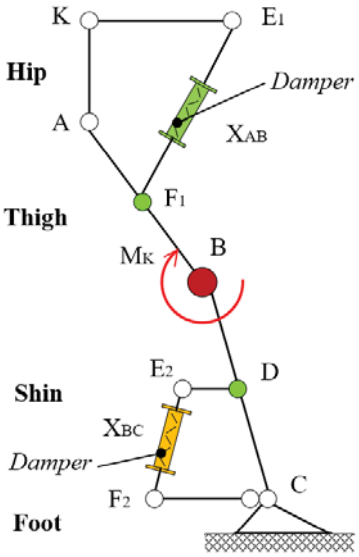
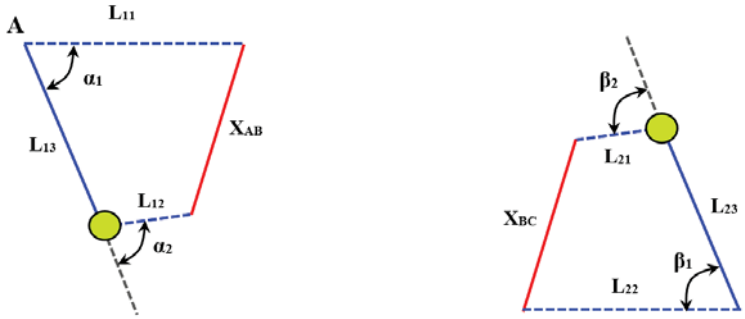


Fig. 1. Mechanical model of the proposed exoskeleton

Calculation of forces and moments of the proposed exoskeleton

From the figure 1, the geometry, forces and moments of the structure are shown in figure 2 and 3, respectively. The stroke of damper x_{AB} and x_{BC} are determined following the geometries as shown in figure 2.



(a) (b)

Fig. 2. Geometric parameters of the first frame AKE_1F_1 (a) and the second frame DCF_2E_2 (b)

The length x_{AB} is determined as follows:

$$x_{AB} = \sqrt{L_{12}{}^2 + L_{13}{}^2 + 2L_{12}L_{13}\cos\alpha_2 + L_{11}^2 - 2\left(L_{11}\cos\alpha_1\left(L_{13} + L_{12}\cos\alpha_2\right) + L_{11}L_{12}\sin\alpha_1\sin\alpha_2\right)} \quad (1)$$

Similarly, the length x_{BC} is determined as follows:

$$x_{BC} = \sqrt{L_{22}{}^2 + L_{23}{}^2 + 2L_{22}L_{23}\cos\beta_1 + L_{21}^2 - 2\left(L_{21}\cos\beta_2\left(L_{23} + L_{22}\cos\beta_1\right) + L_{21}L_{22}\sin\beta_1\sin\beta_2\right)} \quad (2)$$

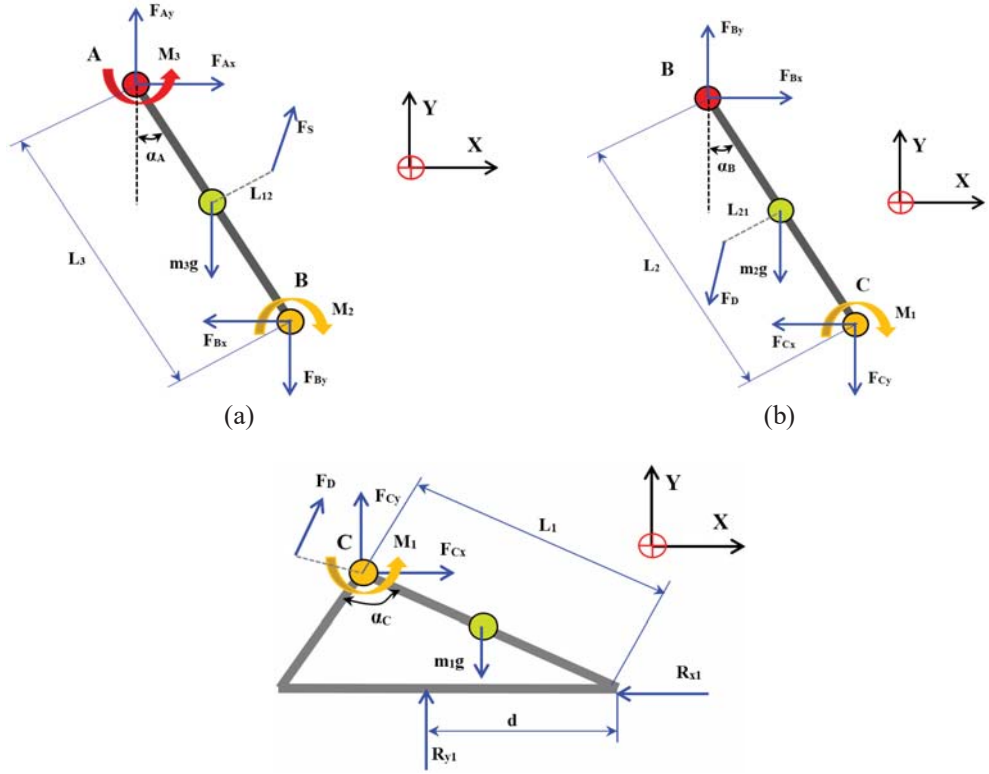


Fig. 3. Forces and moments analysis: (a) Thigh, (b) Lower leg, (c) Foot

From figure 3, the force and moment of the proposed are found. Forces and moment of the foot are found as follows:

$$\begin{aligned} F_{CX} &= R_{X1} + m_1 a_{CX} - F_D \sin\alpha_B \\ F_{CY} &= -R_{Y1} + m_1 g + m_1 a_{CY} - F_D \cos\alpha_B \\ M_1 &= F_{CX}\left(L_1 \cos\alpha_C\right)p_1 - F_{CY}\left(L_1 \sin\alpha_C\right)p_1 - R_{Y1}\left(d - L_1\left(1-p_1\right)\sin\alpha_C\right) - R_{X1}\left(L_1 \cos\alpha_1\right)\left(1-p_1\right) + \\ &\quad + I_1\gamma_1 + F_D L_{22}\cos\alpha_B \end{aligned} \tag{3}$$

Similarly, forces and moment of the lower leg are calculated as follows:

$$\begin{aligned} F_{BX} &= R_{X1} + m_1 a_{CX} + m_1 a_{BX} \\ F_{BY} &= -R_{Y1} + \left(m_1 + m_2\right)g + m_1 a_{CY} + m_2 a_{BY} \\ M_2 &= M_1 - F_{BX}\left(L_2 \cos\alpha_B\right)p_2 - F_{BY}\left(L_2 \sin\alpha_B\right)p_2 + F_{CY}\left(L_2 \sin\alpha_B\right)\left(1-p_2\right) - F_{CX}\left(L_2 \cos\alpha_B\right)\left(1-p_2\right) + \\ &\quad + I_2\gamma_2 + F_D L_{21}\cos\alpha_B \end{aligned} \tag{4}$$

From the results (3) and (4), the forces and moments of the thigh are obtained as follows:

$$\begin{aligned} F_{AX} &= R_{X1} + m_1 a_{CX} + m_1 a_{BX} - F_S \sin\alpha_A + m_3 a_{AX} \\ F_{AY} &= -R_{Y1} + \left(m_1 + m_2 + m_3\right)g + m_1 a_{CY} + m_2 a_{BY} + m_3 a_{CY} - F_S \cos\alpha_A \end{aligned} \tag{5}$$

$$M_3 = -M_2 - F_{AX}\left(L_3 \cos\alpha_A\right)p_3 - F_{AY}\left(L_3 \sin\alpha_A\right)p_3 + F_{BY}\left(L_3 \sin\alpha_A\right)\left(1-p_3\right) - F_{BX}\left(L_3 \cos\alpha_A\right)\left(1-p_3\right) + \\ + I_3\gamma_3 + F_S L_{12}\cos\alpha_A$$

Where m_1, m_2, m_3 are masses of the thigh, the lower leg, and the foot respectively; a_{AX}, a_{BX}, a_{CX} are the accelerations of the thigh, the lower leg, and the foot, respectively; p_1, p_2, p_3 are dimensionless parameters referring the foot, the lower leg, and the thigh, respectively. The equations (3), (4) and (5) are elementary for the calculation of the force and moment of the exoskeleton.

Configuration and optimization of MR damper

The configuration of the MR damper is shown in figure 4 that includes 8 separated coils. In this design, the group of coils can move up and down following the vibration of the attached system. This mechanism improves the vibration control capacity and is energy efficient. With this structure, the coils are easily replaceable for maintenance purpose. The parametric model is shown in figure 5.

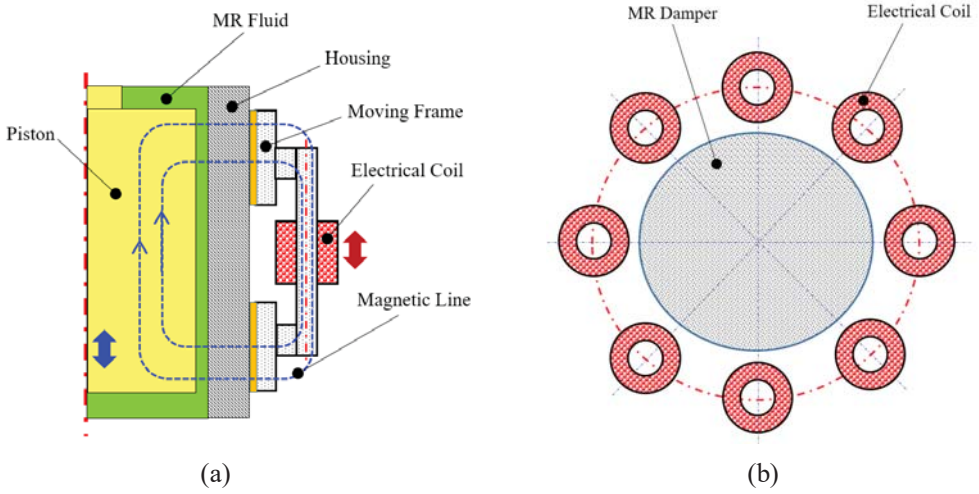


Fig. 4. Configuration of MR damper: (a) cross-section, (b) Distribution of electrical coils

The force of MR fluid inside the damper is calculated as follows:

$$F_{MR} = 8\tau A = 32\pi\tau rt \tag{6}$$

Where τ is the shear stress of the MR fluid, A is the charged area of the damper, r is the axial radius of the piston, t is the thickness of the magnetic pole. Hence, the total damping force of the MR damper is:

$$F_{damper} = (F_{MR} + 2f)\,\mathrm{sgn}(\dot{x}) \tag{7}$$

Where f is the Coulomb friction force between the piston and the seals. The relation between total shear stress and yield stress is determined according to the Bingham model:

$$\tau = \left(\tau_y(H) + \eta\left|\dot{\gamma}\right|\right)\mathrm{sgn}(\dot{\gamma}) \tag{8}$$

Where $\dot{\gamma}$ is the shear rate, H is the magnetic field strength of a transverse applied magnetic field, η is the effective bulk viscosity of the MR Fluid, τ_y is the yield strength. From equation (8) and some manipulations, the formulation of yield stress can be rewritten as follows:

$$\tau = C_0 + C_1\left(H_{magnet} + \frac{NI}{2d}\right) + C_2\left(H_{magnet} + \frac{NI}{2d}\right)^2 + C_3\left(H_{magnet} + \frac{NI}{2d}\right)^3 + \frac{\eta}{d}\dot{x} \quad (9)$$

From equation (6), the force is finally found as:

$$F_{MR} = 32\pi rt\left(C_0 + C_1\left(H_{magnet} + \frac{NI}{2d}\right) + C_2\left(H_{magnet} + \frac{NI}{2d}\right)^2 + C_3\left(H_{magnet} + \frac{NI}{2d}\right)^3 + \frac{\eta}{d}\dot{x}\right) \quad (10)$$

In this study, the objective damping force of the second damper is 250 N. After optimization, the value of damping force is 256.47 N. It is noted that the maximum applied current is 2 A for the proposed damper. The results of optimization are shown in figures (6) and (7).

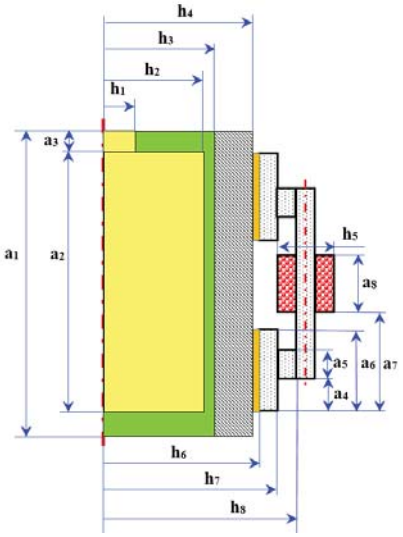


Fig. 5. Parametric model of the proposed MR

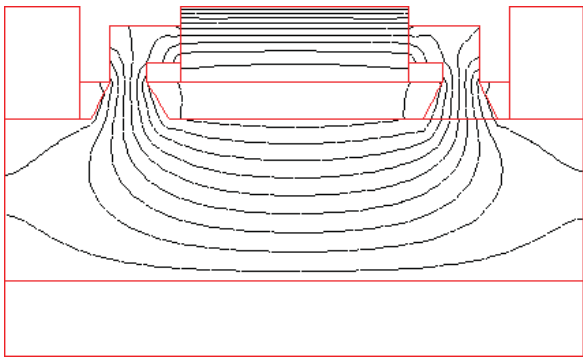


Fig. 6. Magnetic lines of MR damper damper after optimization

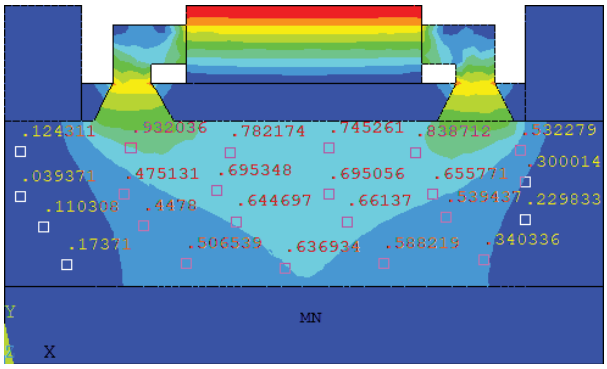


Fig. 7. Magnetic flux density of MR damper after optimization

Conclusion

In this study, a leg exoskeleton with novel MR damper configuration is presented. This design includes two MR dampers for the thigh and the lower leg positions. The design includes eight electric coils which are distributed around the outside of the housing damper. The coils have their position vary as the patient moves, making the damper more flexible and more efficient in vibration control. After calculating the forces and moments of the exoskeleton, the damping force of the damper is derived. The optimization of the MR damper is carried out. It is shown that the force requirement of the dampers is fulfilled and the saturation of damping force is within the range of the design materials. In the future, the structure of the exoskeleton and the damper will be manufactured and tested.

Acknowledgement

This research was funded by Vietnam National Foundation for Science and Technology Development (NAFOSTED) under grant number 107.01-2017.28

References

[1] D.X.Phu, S.B.Choi, Y.S.Lee, M.S.Han, Design of a new engine mount for vertical and horizontal vibration control using magnetorheological fluid, Smart Mater. Struct. 23 (2014) 117001
[2] Xuan Phu Do, Seung Bok Choi, High loaded mounts for vibration control using magnetorheological fluids: review of design configuration, Shock and Vibration 915859 (2015) 1-19
[3] Xiangcheng Zhang, Xu Zhang, Yixiao Zhao, Jun Zhao, Zhaodong Xu, Experimental and numerical studies on a composite MR damper considering magnetic saturation effect, Engineering Structures 132 (2017) 576-585
[4] Louise A Ahure Powell, Young T Choi, Wei Hu, Norman M Wereley, Nonlinear modeling of adaptive magnetorheological landing gear dampers under impact conditions, Smart Mater. Struct. 25 (2016) 115011
[5] Kyongsol Kim, Zhaobo Chen, Dong Yu, Changhyon Rim, Design and experiments of a novel magnetorheological damper featuring bifold flow mode, Smart Mater. Struct. 25 (2016) 075004
[6] Jung Woo Sohn, Jong Seok Oh, Seung Bok Choi, Design and novel type of a magnetorheological damper featuring piston bypass hole, Smart Mater. Struct. 24 (2015) 035013
[7] Seung Bok Choi, Weihua Li, Miao Yu, Haiping Du, Jie Fu, Phu Xuan Do, State of the art of control schemes for smart systems featuring magneto-rheological materials Smart Mater. Struct. 25 (2016) 043001
[8] Do Xuan Phu, Kruti Shah, Seung Bok Choi, Design of a new adaptive fuzzy controller and its implementation for the damping force control of a magnetorheological damper, Smart Mater. Struct. 23 (2014) 065012
[9] Do Xuan Phu, Seung Bok Choi, Vibration control of a ship engine system using high-load magnetorheological mounts asscociated with a new indirect fuzzy sliding mode controller, Smart Mater. Struct. 24 (2015) 025009
[10] Do Xuan Phu, Kruti Shah, Seung Bok Choi, A new magnetorheological mount featured by changeable damping gaps using a moved-plate valve structure, Smart Mater. Struct. 23 (2014) 125022

A New Novel Magnetic Damper using Flexible Gap for Knee Exoskeleton Suspension

LE Dai Hiep[1, a] , NGUYEN Quoc Hung[2,b] and DO Xuan Phu[3,c*]

[1]MediRobotics Laboratory, Department of Mechatronics and Sensor System Technology, Vietnamese-German University, Binh Duong, Vietnam

[a]ledaihiep1993@gmail.com, [c]hung.nq@vgu.edu.vn, [c]phu.dx@vgu.edu.vn

*Corresponding author, E-mail: phu.dx@vgu.edu.vn

Keywords: MR damper; flexible damping gap; force optimization; exoskeleton damper; MR suspension.

Abstract. This study proposes a new design of magnetic damper with flexible gap. The damper uses magneto-rheological fluid for control vibration of knee exoskeleton. In this proposed design, the damping gap is considered based on the idea of the flexible position which can changes following the vibration of the system. Hence the damping force is also changed such as its amplitude is high if the vibration is large, and inversely. The new configuration of damper was optimized the shape to get minimum the mass and the desired maximum damping force. The analysis and optimization of magneto-rheological fluid (MR in short) damper are conducted in Finite Element Method software like ANSYS ADPL. The results show that the prototype reaches the force in some position are the same with simulation on software.

Introduction

It is well-known that MR is potential smart material which has characteristic depend on magnetic flux through on it. It gets many achievement on research and application such as employ it on the brake, clutch or damper, so on. Recently, there have been a large of number research and improvement of MR Damper. In order to improve performance and optimize the off-state damping force, many configuration of MR damper were proposed and valuated such as [1][2]. However, a lot of research only focus on designing and manufacturing MR damper with constant size of MR duct. Moreover, to control the damping force, the system needs more sensors like displacement sensor or acceleration sensor. The controller has the important role to adjust continuously the current through the coils. With this one, the coils with various current generates the eddy currents which causes the heat on material. Furthermore, the time response of MR damper is also a factor to consider.

In order to resolve this problem, we propose the new novel configuration of MR damper which has flexible duct of MR fluid. Instead of adjusting the magnetic field through the MR gap by adjust the current through the coils, flexible gap is employed. This this configuration, the current applies for the coils is constant by the time. When the system is vibrated at small amplitudes with small damping force. By contrast, large damping force at large amplitudes.

The Proposed New Configuration of MR Damper

In this work, the new configuration of MR damper with flexible gap is proposed and analyzed damping force base on Bingham model

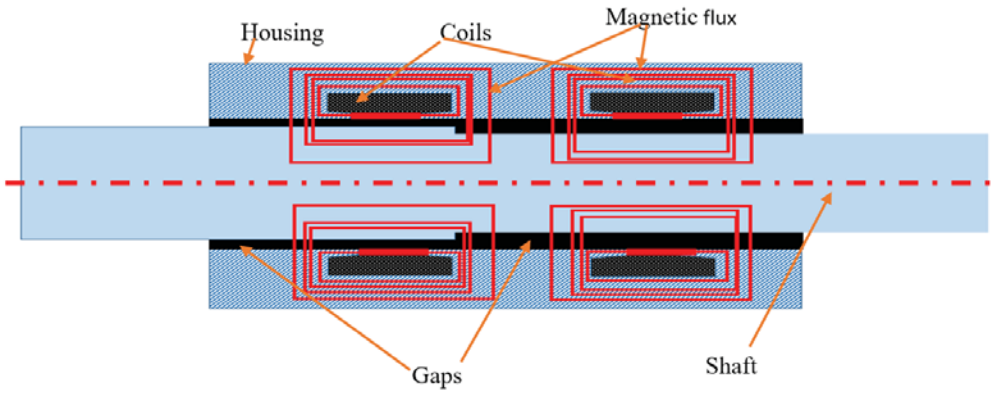


Fig. 1. New configuration of the proposed MR damper

Fig.1 shows the proposal configuration of MR damper. In this configuration, two coils are wounded directly on the coil grooves of the housing. The section of the thin wall between the coil grooves and the MR gap is designed to have a small area so that the magnetic flux going through it promptly reaches to saturation and hence is forced to go across the MR gap. MR gap has two distinguished regions with different size of narrow gaps. In response to the magnetic field, the MR fluid solidifies and resists the relative movement between the shaft and the housing producing the damping force. In the literature, a configuration with more than two coils can be used to increase the magnetic flux density across the MR gap. On this configuration, the damping force includes 3 phases with various damping force. Fig.2 shows the first stage of MR damper. When the system vibrates with small amplitude, it doesn't need more damping force. In this stage, with the large MR gap, the damping force is small. Fig.3 shows the second stage of MR damper. Obviously, it comprises two different regions gap. This is transition region of damping force from the small force caused by large gap to large force generated by small gap. In this stage, the damping force increases gradually depended on different gap sizes and the length of damper. Fig.4 demonstrates the last stage of MR damper. At this position, high amplitude of system affects to damper, large damping force is generated by small gap. The different damping force between stage 1 and stage 3 depend on ratio size of the flexible gaps.

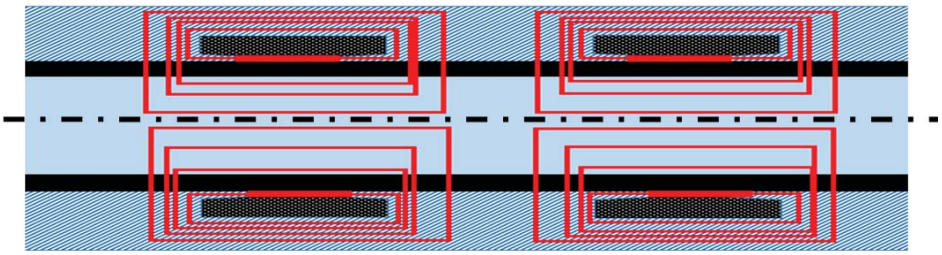


Fig. 2. First stage of the proposed damper

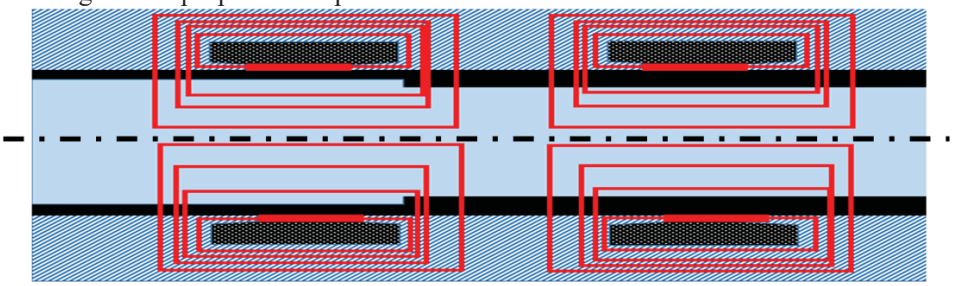


Fig. 3. The second stage (transition phase) of the proposed damper

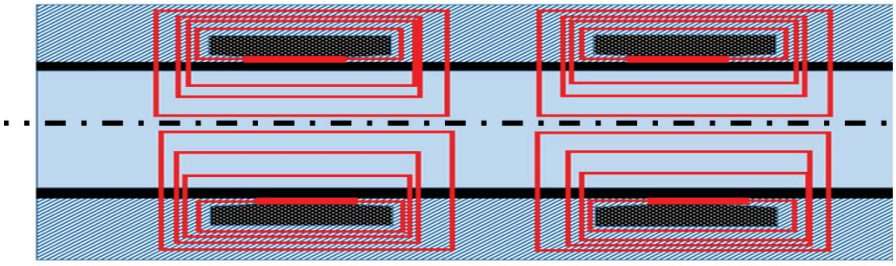


Fig. 4. Final stage of the proposed damper

In order to evaluate the damping force of MR damper, it is assumed that MR follows Bingham plastic model and velocity profile of MR fluid is linearly distributed from the shaft to the housing. The induce damping force can be respectively determined by:

$$F_d = 2\pi R_{s1} L_1 (\tau_{y1} + \eta \frac{v}{d_1}) + 2\pi R_{s2} L_2 (\tau_{y2} + \eta \frac{v}{d_2}) + 2F_{or} \quad (1)$$

$$F_{do} = 2\pi R_{s1} L_1 (\tau_{yo} + \eta \frac{v}{d_1}) + 2\pi R_{s2} L_2 (\tau_{yo} + \eta \frac{v}{d_2}) + 2F_{or} \quad (2)$$

where R_{s1}, R_{s2} are the shaft radius of region 1 and region 2, respectively. Variables d1,d2 are the gap size of the MR fluid duct , v is the relative velocity between the shaft and the housing, η and τy are, respectively, the field-dependent post yield viscosity and yield stress of the active MR fluid in the duct, L_1,L_2 are the length of the MR fluid duct .For is the coulomb friction force between the shaft and the oring which can be approximately calculated by [3].

Optimal Design of New Novel Configuration MR Damper and Discussion

In this work, the damping force generated on stage 1 is considered to optimize to obtain the off-state damping force is the smallest. After optimizing the geometry dimensions, the damping force is analyzed at some other positions from first stage to final stage.

In order to determine the damping for of the MR damper using Eq.1. Firstly, the magnetic density across the MR fluid ducts of MR damper is determined using FEA. In this study, finite element models using a 2D-axisymmetric couple element (Plane13) of commercial ANSYS software are exerted to solve magnetic circuits of the MR damper. The FE models used in this study are shown in Fig.5. The off-state damping force of the MR damper is also determined from Eq.2. The first-order optimization method using the gradient descent algorithm is employed to find the optimal solution. A detailed description of this algorithm integrated with ANSYS software has been mentioned in several studies [4,5]. The 1008 steel is employed for magnetic components of the MR damper such as shaft and housing. The coil wires are sized as 21-gage (diameter=0.511mm) whose maximum working current is around 3A and during the optimization process, a current of 1.5 A is applied for the coils. It is noteworthy that the cross section area of the coil is assumed to be fully wounded. In addition, the commercial MR fluid, MRF132-DG, made by Lord Corporation is used in this research. In the optimization, the following significant geometric dimensions are considered as design variables: the coil peak height $h_{co,}$ the coil peak width w_{co}, the height chamfer ch, the width chamfer ch1, the distance from coil to centerline tfi, the outer radius of the MR damper R and the housing thickness t_o. The MR fluid duct and velocity is set by 1.5 mm and 0.5m/s, respectively. Table 1 shows the optimal solution of MR damper. In this case, the damping force is constrained to be greater than 200 Nm with 2% of accuracy, the convergence rate is set by 0.1%. As mentioned above, the MR fluid gap size is not considered as a design variable and determined based on manufacturing advantages which is set by 0.8mm. As shown in the results, at the optimum, the damping force of MR damper can reach up to 200 Nm as constrained and the off-state damping force of optimized is Fig.6(a)(b) show the optimal solution of the MR damper. Obviously, the convergence occurs after 45 iterations, at which the braking torque can reach up 200 Nm as constrained. The magnetic distribution of the optimized MR damper is shown in Fig.7 and the magnetic distribution in the MR fluid gap is non -

uniform. The magnetic density near the coils almost reaches the magnetic saturation of the housing material

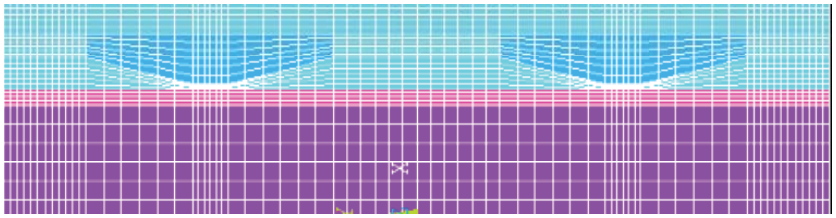
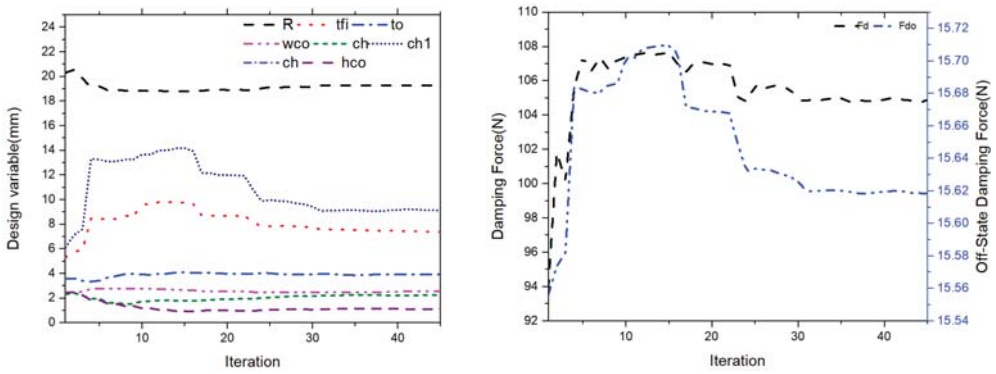


Fig 5. Finite element method model for MR damper

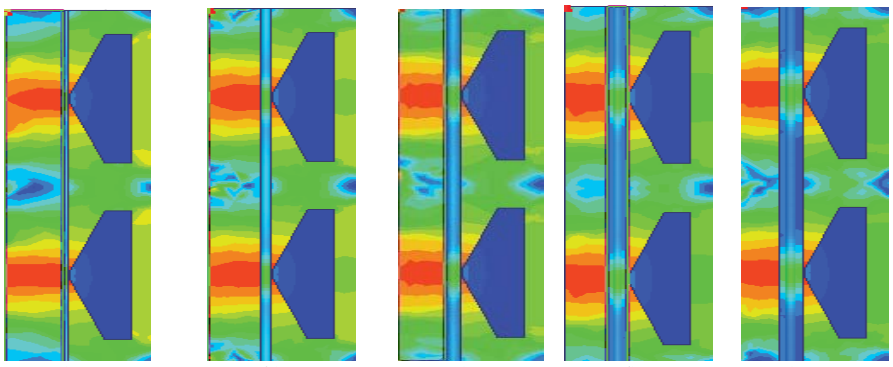


(a) (b)

Fig.6. Convergence of optimization process

Table 1. Results of optimization

Parameters			
Off-state force F_{d0} [N]	18.754	Coil width w_{c0} [mm]	2,7666
Max damping force F [N]	198.55	Axial chamfer ch_1 [mm]	21,484
MR duct length L_d [mm]	125,57	Shaft radius R_s [mm]	11,711
Outer radius R [mm]	29,930	MR duct gap tg [mm]	0.80
Coil groove height h_c [mm]	1,2339	Thin wall ti [mm]	0.50
Coil height h_{c0} [mm]	5,3653	Sliding housing t_0 [mm]	4,5799
Radial chamfer ch [mm]	6,9741	Coil to centerline tfi [mm]	85,248



a)0.8 mm b)1.8 mm c)2.8 mm d)3.8 mm e) 4.8mm

Fig.7. Magnetic distribution on MR damper with various gaps

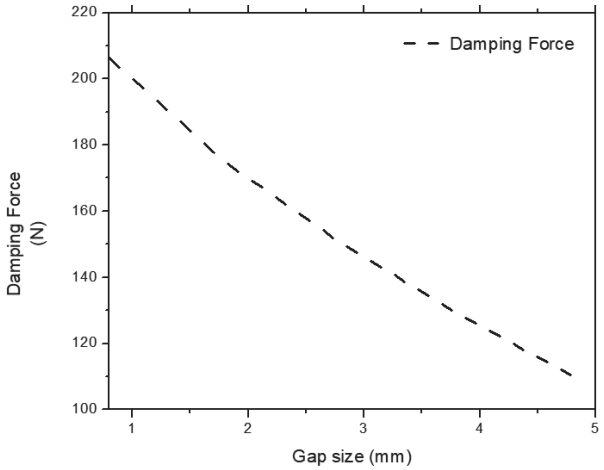


Fig.8. Damping force with various gaps

Fixing optimal value of dimensions housing of MR damper, surveying the effect of gap size MR is conducted with changing dimension of shaft. Fig.8 shows the results of the force generated with various gap sizes. Obviously, the damping force decreases with increasing gap sizes.
In this work, after survey affection of gap sizes to the damping force, the shaft with flexible dimensions is exerted on MR damper to adjust dimension of the gap MR. Fig.9 shows the transition force of stage 2 when the gap size changes gradually from total large size regions to total small size regions (from 0.8mm to 4.8 mm). Fig.10 demonstrates the flux magnetic distribution in some positions.

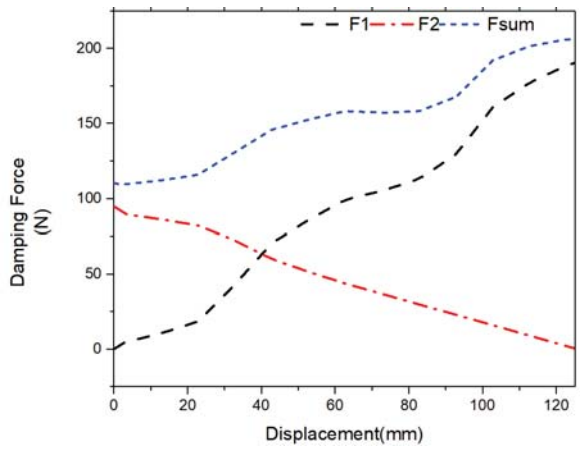


Fig.9. Relation of force and transition phase

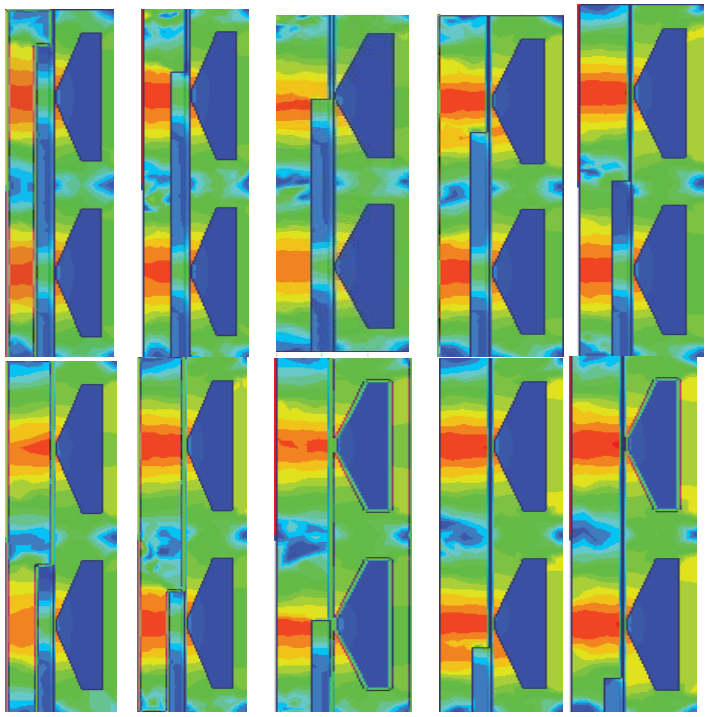


Fig.10. Magnetic distribution of some positions in transition phase

Fig.11 shows the force with displacement of MR damper. The damping force of MR damper depends on the length of the shaft with various regions. According to other purposes, the shaft has different of the length regions.

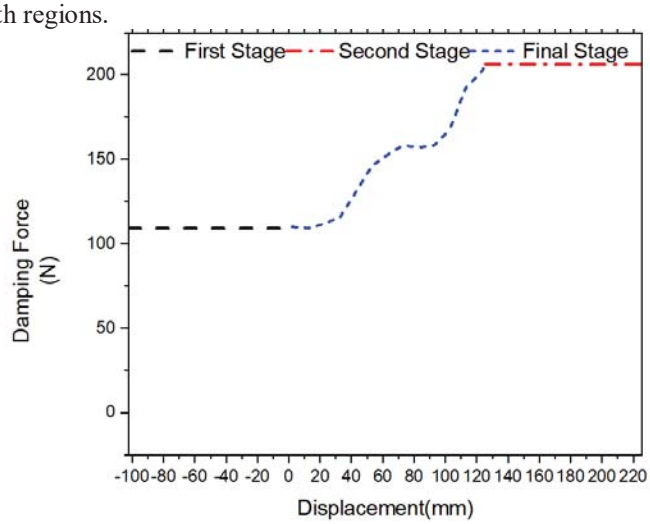


Fig.11. Damping force depends on displacement

Conclusion

This paper presents a new configuration of MR damper which can adapt the force depend on amplitude vibration. Optimization the MR damper with high damping force is conducting and simulating with various gap. Besides, transition phase of MR damper gets effective about damping force when changing displacement of flexible shaft. In this ones, self-adaptation for vibration is effective trend. In the future research, we will fabricate the prototype and test it to valid the performance

Acknowledgement
This research is funded by Vietnam National Foundation for Science and Technology Development (NAFOSTED) under grant number 107.01-2017.28

Reference

[1]QH Nguyen, SB Choi and JK Woo, Optimal design of magnetorheological fluid-based dampers for front-loaded washing machines, Proceedings of the Institution of Mechanical Engineers, Part C: Journal of Mechanical Engineering Science 228 (2014) 294-306
[2] D.X.Phu, S.B.Choi, Y.S.Lee, M.S.Han, Design of a new engine mount for vertical and horizontal vibration control using magnetorheological fluid, Smart Mater. Struct. 23 (2014) 117001
[3] EPS Division, Rotary seal design guide, Parker Hannifin Corporation, Catalog EPS 5350, 2006
[4] Nguyen Q H, Han Y M, Choi S B and Wereley N M, Geometry optimization of MR valves constrained in a specific volume using the finite element method, Smart Mater. Struct. 16 (2007) 2242
[5] Nguyen Q H, Choi S B and Wereley N M, Optimal design of magneto-rheological valves via a finite element method considering control energy and a time constant, Smart Mater. Struct. 17 (2008) 025024
[6] Xuan Phu Do, Seung Bok Choi, High loaded mounts for vibration control using magnetorheological fluids: review of design configuration, Shock and Vibration 915859 (2015) 1-19
[7] Do Xuan Phu, Kruti Shah, Seung Bok Choi, Design of a new adaptive fuzzy controller and its implementation for the damping force control of a magnetorheological damper, Smart Mater. Struct. 23 (2014) 065012
[8] D.X.Phu, S.B.Choi, Y.S.Lee, M.S.Han, Design of a new engine mount for vertical and horizontal vibration control using magnetorheological fluid, Smart Mater. Struct. 23 (2014) 117001
[9] Do Xuan Phu, Do Kyun Shin and Seung-Bok Choi, Design of a new adaptive fuzzy controller and its application to vibration control of a vehicle seat installed with an MR damper, Smart Materials and Structures 24 (2015) 085012
[10] Do Xuan Phu, Jin-Hee An, Seung Bok Choi, A novel adaptive PID controller with application to vibration control of a semi-active vehicle seat suspension, Applied Sciences 7(10) (2017) 1055

Preparatio of chitosan chloride salt in solid state using hydrogen chloride gas

Nguyen Cong Minh[1,*], Van Hoa Nguyen[2], Pham Thi Dan Phuong[2], Trang Si Trung[2]

[1]Institute of Biotechnology and Environment, Nha Trang University, Vietnam

[2]Faculty of Food Technology, Nha Trang University, 2 Nguyen Dinh Chieu, Nha Trang, Vietnam

*Corresponding author. Tel: (+84) 974099771; E-mail: minhnc@ntu.edu.vn.

Keywords: Water soluble chitosan; Low viscosity; Low molecular weight.

Abstract. Chitosan is prepared by the deacetylation process of chitin. Chitosan has many applications in food, agriculture, environment, pharmacy, medicine. However, chitosan is insoluble in water but dissolves in diluted acid solutions such as acetic acid, hydrochloric acid that it limits their applications. In order to improve soluble ability of chitosan in water, chitosan was converted to water soluble chitosan forms. These chitosan forms can be oligochitosan or chitosan salt or chitosan adsorbed H+ proton. Oligochitosan was very short chain of chitosan with only 2 to 10 monomers, while chitosan salts were products of reaction between amin groups and acid groups. Water soluble chitosans can be preppared using in solution or solid state methods. In solution method, chitosan was dissolved in a diluted acid solution and then spaied at high temperature. In solid-state method, chitosan was reaction with concentrated acid (acetic acid, hydrochloric acid) or acid gas (hydrochloric gas). The solution method provides products with a high yield and good uniformity but it is difficult to produce in large scale with a high cost. On the other hand, the solid state method can be applied in large scale easily.

In this study, water soluble chitosan was obtained by reaction between chitosan and hydrogen chloride gas in solid-state. The effects of the solubility, molecular weight and pH of the chitosan solution were investigated. The temperature shows a strong effect on the depolymerization of chitosan and chloride salt formation. The formation of chloride salt observed after 3 h at all temperature. The water solubility of the chloride salts (> 98% for all samples obtained after 3 h) was found to be much higher than the initial chitosan. The average molecular weights of 100-600 kDa were much depended on reaction time and temperature. The antibacterial of chitosan chloride against Bacillus Cereus, Vibrio Parahaemolyticus, Staphylococcuss Aureus and Escherichia Coli also evaluated. This production process can be scaled up in industry.

Acknowledgements. This research is funded by the Ministry of Science and Technology and Leibniz-Institute of Polymer Research Dresden, Germany for analytical supports.

Preparation of nanochitosan using chitosan extracted from squid pens and its antibacterial property

Hoang Ngoc Cuong[1,*], Van Hoa Nguyen[2], Trang Si Trung[2]

[1]Binh Duong University, 504 Binh Duong Boulervard - Thu Dau Mot - Binh Duong, Vietnam

[2]Nha Trang University, 2 Nguyen Dinh Chieu, Nha Trang, Vietnam

*Corresponding author. Tel: (+84) 918920369; E-mail: hncuong@bdu.edu.vn

Keywords: Nanochitosan; Squid pens; Antibacterial property.

Abstract. Chitosan was produced commercially from shrimp and crab shells with different degree of deacetylations (DD) and molecular weights (Mw), which were the important parameters for applying the chitosan in special cases. Due to its unique biological characteristics, including biocompatibility, biodegradability and nontoxicity, many applications have been found either alone or blended with other natural polymers (alginates, starch, gelatin) in the food, agriculture, textile, water treatment, cosmetics and other industries. Recently, squid pens have been reported to be a main source forthe production of β-chitin. This chitin has a higher solubility, higherreactivity and higher affinity towards solvents and swelling than β-chitin. These are important properties with regard to the chemicalderivatization of β-chitin for different applications. Moreover, β-chitin, isolated from squid pens, was more amenable to deacetylation to form chitosan with a high DD and Mw.

Chitosan nanoparticles have been synthesized and mainly used as controlled-release drug carrier for gene transfer in artificial organs and for immune prophylaxis. In addition, it has shown its capacity for the encapsulation and delivery of polyphenolic compounds hydrophilic and hydrophobic drugs and proteins. In this study, nanochitosan was prepared from squid pen chitosan with different Mw and DD. The antibacterial activity of prepared nanochitosans was tested against three pathogenic bacteria including: P. fluorescens, causing bacterial head rot of broccoli, E. carotovora, causing soft mould disease and E. coli, causing bloody diarrhea.

Predictive Surface Roughness of Workpiece in Cylindrical Grinding

Do Duc Trung[1,a*], Phung Xuan Son[2,b]

[1]Faculty of Mechanical Engineering, Hanoi University of Industry, Ha Noi, Vietnam

[2]Faculty of Mechanical Engineering, Hanoi University of Industry, Ha Noi, Vietnam

[a]Email: dotrung.th@gmail.com

[b]Email: phungxuanson@gmail.com

Keywords: cylindrical grinding, predictive surface roughness, cutting parametrs, wheel parameters

Abstract

In this paper, based on the theory of grinding process, the relationship between surface roughness (R_a) of workpice in cylindrical grinding and cutting parametres (grinding wheel velocity - v_G, workpiece velocity - v_w, depth of cut - t) and grinding wheel parameters (diameter - d_G, the mesh number used in the grading sieve – M, volume fraction - ϵ) are developed. This relationship used to predict surface roughness of workpiece, its value is good agreement experiment value. So, results of this paper can be used for predictive the surface roughness in practical cases.

Introduction

Like other machining methods, the quality of the surface finish by grinding is evaluated using many parameters. Of which, the surface roughness of the workpiece surface is the most important element which may significantly impact the usefulness of the workpiece. The surface roughness of workpiece forming mechanism is complex and mostly dependent on other factors (cutting parameters, dressing parameters, cooling and lubrication) and the machining factors (geometrical parameters, stability and contact behavior). Simulating the grinding process to predict the value of surface roughness in particular cases will help reduce the time spent for machine adjustment and trial processing, which will lead to the processing cost reduction and the enhancement of the product quality [1].

In the empirical method, surface roughness models are normally developed as a function of kinematic conditions [2]. The empirical model developed by Suto et at. [3] relates surface finish to the number of active cutting edges using the experimental data and it has been found to be having a logarithmic relationship. Although empirical models have the advantage that they require minimum efforts to develop and are used in all fields of grinding technology but the inherent problem associated with this method is that the model developed under one grinding condition, can not be used for surface roughness prediction at other conditions, i.e. it can be used for accurate description of the process within the limited range of chosen parameters only. Hence the scope is limited.

To overcome the above-mentioned problem, analytical models for surface roughness were tried out to predict the surface roughness at different grinding conditions. The analytical models are always preferred to empirical models as these models are based on the fundamental laws which use mathematical formulations of qualitative models. Hence, these results can be made applicable to a wide range of process conditions. The analytical models for surface roughness have always been characterized by the description of the microstructure of the grinding wheel in one dimensional form taking the grain distance, the width of cutting edge and the grain diameter into account and in two dimensional forms by considering the grain count and the ratio of width of cut to depth of cut. Lal et at. [4] used similar approach to describe the surface roughness based on chip thickness model. But this model does not require the microstructure of the grinding wheel, thus it is moresuccessful in industry as it does not need the effort of wheel characterization. Cui et at. [5] have built dynamic model of material removal process in grinding process. Described the state of art in the modeling and simulation of grinding processes comparing different approaches to

modeling by Tonshoff et al. [6]. Furthermore, the benefits as well as the limitations of the model applications and simulation were discussed. This work identified one simple basic model where all the parameters such as wheel topography, material properties, etc. are lumped into the empirical constant. Models developed forthe grinding process in the surface roughness analysis [7–9] have assumed an orderly arrangement of the abrasive grains on the grinding wheel. Have used a conventional method to determine the surface roughness based on the model using the mean value of the grain protrusion heights by Zhou et at. [10]. However, the predicted value of the surface roughness based on traditional method is found to be less than the measured value. To overcome this problem, some authors proposed method takes into consideration the random distribution of the grain protrusion heights. Used fuzzy set theory to predict surface roughness in grinding process operations by Tzu-Liang Tseng et at. [11]. But, this method had used many values of experimental processes, so it method is difficult for application in manufacturing. Developed the relationship between grinding tool surface characterization and surface roughness by E. Uhlmann et at. [12]. But, cutting parameters have more signifficant on surface roughness, that were absented in this work. Predictive surface of roughness with the form of grinding wheel as a pineapple had proposed by Haiyue Yu et at. [13]. But this form of wheel it is unsuitable for cylindrical grinding process. Investigation of different grain shapes and dressing to predict surface roughness in grinding by YuemingLiu [14]. But, like as reference 12, cutting parameter were absent in this work.

Several random models have been proposed to simulate the surface profile generated during grinding based on the stochastic nature of the grinding process [15–18]. In these models, the abrasive grains on the grinding wheel have been thought of as a number of small cutting points distributed randomly over the wheel surface. Assuming a particular probability distribution of these random cutting points, output surface profiles have been generated for known input surface profile and input grinding conditions. To simulate the relative cutting path of grains, Performed a closed loop simulation, presupposing that thermo-mechanical equilibrium has been established during the grinding process by Steffens [19]. The input for this simulation program will be the quantities like grinding wheel topography, physical quantities of the system, set-up parameters of the machine tool, and the temperature dependent material properties, etc. Simulations can closely reproduce the ground surface using probabilistic analysis; however, the applicability of this programme is limited since the simulation programme is based on the measurement of microstructure of grinding wheel. This method is timeconsuming. Although many analytical models have been developed based on the stochastic nature of the grinding process but Basuray et al. [20] have proposed a simple model for evaluating surface roughness in fine grinding based on probabilistic approach. The concept of radial distribution parameter and an effective profile depth associated with the stochastic model have been used to obtain the distribution of the grains on the wheel surface. Results of the approximate analysis yield values that agree reasonably well with the experimental results. However many parameters and properties of materials were merged into the empirical constants in this analysis.

Developed an analytical model for the prediction of the arithmetic mean surface roughness based on the probabilistic undeformed chip thickness model by Hecker et at. [21]. This model uses ground finish as a function of the wheel microstructure, the process kinematic conditions and the material properties. The material properties and the wheel microstructure are considered in the surface roughness through the chip thickness model. A simple expression that relates the surface roughness with chip thickness was found, which was verified using experimental data from cylindrical grinding. However, in this work, form of grain has been assumed to be triangular. And, as in opinion of Sanchit Kumar Khare et at. [22] a simple abrasive grain on the wheel surface generally has many tiny cutting points on its surface. Therefore, it is evident that the groove produced by an individual grain can be better approximated by an arc of a circle. Then, they had developed a method to predict value of surface roughness with form of grain assumed to be an arc.

Based above analysis, suggestion that method of Sanchit Kumar Khare et at. [22], which has most advancement.

In this paper, based on the theory of grinding process, the relationship between surface roughness of workpice in cylindrical grinding and grinding wheel velocity, workpiece velocity, depth of cut, wheel diameter, mesh number used in the grading sieve and structure number of the wheel are developed. This relationship used to predict surface roughness of workpice, its value is good agreement experiment value. So, results of this paper can be used for predictive the surface roughness in practical cases.

Establishment of Surface Roughness Equation

The analyzing of chip forming in grinding by probabilistic approach, Sanchit Kumar Khare et al. [22] proposed the surface roughness equation:

$$R_a = 0{,}471.h_m \quad (1)$$

Where: h_m is maximum of undeformed chip thickness.

The existing chip thickness model proposed by Anne Venu Gopal et al. [23]. The equation is as follows:

$$h_m = 2\sqrt{\frac{1}{Nr}\frac{v_w}{v_G}\sqrt{\frac{t}{d_e}}} \quad (2)$$

Where:

v_w – workpiece velocity.

v_G – grinding wheel velocity.

t – depth of cut.

d_e – equivalent wheel diameter. In cylindrical grinding, the equation is as follows:

$$d_e = d_G.d_w/(d_G + d_w) \quad (3)$$

With d_G, d_w are grinding wheel diameter and workpiece diameter respective.

r - is the chip width to thickness ratio. The value of 'r' is difficult to determine and is assumed in the range of 10-20 [24]. In this work 'r' was assumed to be equal to 10 [24, 25].

N - The number of active grits per unit area 'N' derived by Xu. Hockin et al [26] is as follows:

$$N = 4f\frac{1}{d_g^2}\frac{1}{\sqrt[3]{\left(\frac{4\pi}{3\epsilon}\right)^2}} \quad (4)$$

Where:

f – the fraction of diamond particles involved in active grinding. The value of 'f' is difficult to determine. For calculating the number of active grits per unit area, it is assumed that only one half of diamond particles are engaged in cutting [27], $f = 0.5$.

d_g – The equivalent spherical diameter of diamond grit, is given [2] as:

$$d_g = 15.2/M \quad (5)$$

Where:

M is the mesh number used in the grading sieve.

ϵ- volume fraction of diamond in grinding wheel. The grinding wheels used in the present study have a concentration of 60, or volume fraction $\epsilon = 0.18$ [28].

Substituting the eq (2), (3), (4), (5), (5) in (6) and after mathematical simplification, the value of

surface roughness will be:

$$R_a = 3{,}2148.\frac{1}{\mathrm{M}}.t^{1/4}.\left(\frac{1}{f.r}\right)^{1/2}.\left(\frac{v_w}{v_G}\right)^{1/2}\left(\frac{4\pi}{3\epsilon}\right)^{1/3}.\left(\frac{d_G+d_w}{d_G.\mathrm{d_w}}\right)^{1/4} \quad (6)$$

From equation (6) so that, value of surface roughness will be increase if value of workpiece velocity and volume fraction are increased. Beside, if value of the mesh number used in the grading sieve, the fraction of particles involved in active grinding, grinding wheel velocity and chip width to thickness ratio are increased, these make surface roughness will be reduced. This equation will be used for calculating value of surface roughness in next part of this paper.

Result and Discussion

For evaluation the predictive value of surface roughness, the comparison between value of surface roughness of experimental [29] and predictive value, with the same in-put parameters in 27 tests.

Table 1. *Experimental $R_{a(1)}$ and calculated $R_{a(2)}$ of surface roughness.*

Runs	$n_G(rev/min)$	$v_w(m/min)$	$t(mm)$	$Ra_{(1)}$ (μm)	$Ra_{(2)}$ (μm)
1	1250	7.5	0.005	1.03	1.09
2	1250	7.5	0.01	1.44	0.88
3	1250	7.5	0.15	1.62	1.74
4	1250	10	0.05	1.34	1.52
5	1250	10	0.1	1.59	1.81
6	1250	10	0.15	1.72	2.00
7	1250	12.5	0.05	1.38	1.70
8	1250	12.5	0.1	1.68	2.03
9	1250	12.5	0.15	1.94	2.24
10	1650	7.5	0.05	1.18	1.15
11	1650	7.5	0.1	1.56	1.37
12	1650	7.5	0.15	1.68	1.51
13	1650	10	0.05	1.49	1.33
14	1650	10	0.1	1.64	1.58
15	1650	10	0.15	1.72	1.75
16	1650	12.5	0.05	1.50	1.48
17	1650	12.5	0.1	1.70	1.76
18	1650	12.5	0.15	1.83	1.95
19	2050	7.5	0.05	1.36	1.03
20	2050	7.5	0.1	1.58	1.23
21	2050	7.5	0.15	1.70	1.36
22	2050	10	0.05	1.46	1.19
23	2050	10	0.1	1.63	1.41
24	2050	10	0.15	1.81	1.57
25	2050	12.5	0.05	1.51	1.33
26	2050	12.5	0.1	1.73	1.58
27	2050	12.5	0.15	2.07	1.75

The kinematic parameters considered for each experiment are depth of cut (t) workpiece velocity (v_w) and wheel velocity (v_G). The value of surface roughness in experimental $(R_{a(1)})$ and of predictive $(R_{a(2)})$ as shown in Table 1 and Figure 1. From these so that there is a good agreement between $R_{a(1)}$ and $R_{a(2)}$.

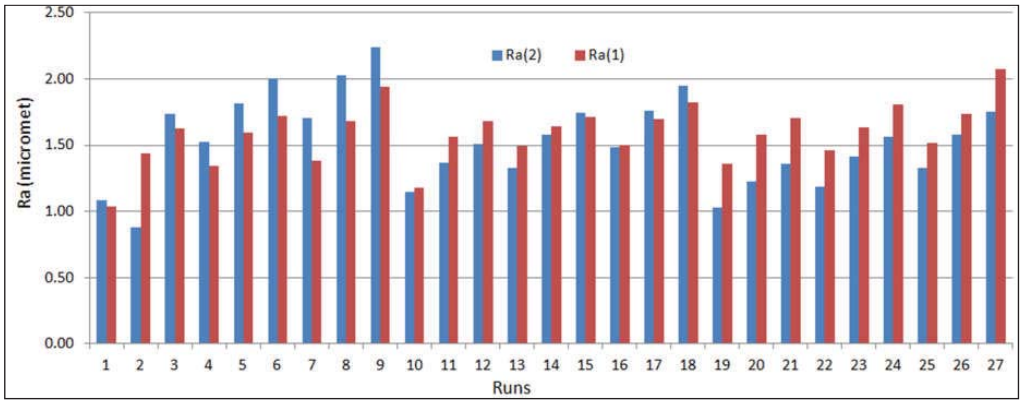


Figure 1. *Comparison of experimental and calculation of surface roughness.*

Conclusions

The value of surface roughness is depended many factors, of which are cutting parameters, wheel parameters, interaction parameters between wheel and workpiece surrface. The value of surface roughness is expensive to determine by experimental processes.

In this paper, a simple equation is proposed for predicting the surface roughness in cylindrical grinding. From that equation so that, value of surface roughness will be increased if value of workpiece velocity and volume fraction are increased. Beside, if value of the mesh number used in the grading sieve, the fraction of particles involved in active grinding, grinding wheel velocity and chip width to thickness ratio are increased, these make surface roughness will be reduced. Predictive surface roughness is good agreement with experiment value. This result of this work can be used for predictive the surface roughness in practical cases.

Acknowledgements

To obtain the results of this research, the authors would like to thank to Dr. Rogelio L. Hecker (Facultad the Ingenieria, Universidad Nacional de La Pampa, General Pico, LP, 6360, Argentina) who helped during the research process.

References

[1] Do Duc Trung, Study on identifying the machining parametesrs in centerless grinding of the 20X- carbon infiltrated steel to reduce its roundness error and surface roughness, The thesis completed at Thai Nguyen University of Technology (2016).

[2] Malkin S, Grinding technology. theory and applications of machining with abrasives. Ellis Horwood. Chichester (1989).

[3] T. Suto, T. Sata, Simulation of grinding process based on wheel surfacecharacteristics, Bulletin of Japan Society of Precision Engineering 15(1) (1981) 27–33.

[4] G. K. Lal, M. C. Shaw, The role of grain tip radius in finegrinding, Journal of Engineering for Industry August (1975) 1119–1125.

[5] Qi Cui, Shijin Chen, Hui Ding, Kai Cheng, Dynamic Model of Material Removal Process in Through – feed Grinding Based on the Lagrange Equation, Trans tech Publications, Switzwerland, Vol. 667 (2016), 173-180.

[6] H. Tonshoff, J. Peters, I. Inasaki, T. Paul, Modeling and simulation ofgrinding processes, Annals of CIRP 41 (2) (1992) 677–688.

[7] K. Nakayama, M. C. Shaw, Study of finish produced in surface grinding, part 2, Proceeding of the Institution of Mechanical Engineers 182(1967–68) 179–194.

[8] [8] K. Sato, On the surface roughness in grinding, Technology Reports, Tohoku University 20 (1955) 59–70.

[9] [9] C. Yang, M. C. Shaw, The grinding of titanium alloys, Transactions ofASME 77 (1955) 645–660.

[10] X. Zhou, F. Xi, Modeling and predicting surface roughness of thegrinding process, International Journal of Machine Tools andManufacture 42 (2002) 969–977.

[11] Tzu-Liang Tseng, Udayvarun Konada, Yongjin Kwon, A novel approach to predict surface roughness in machining operations using fuzzy set theory. Journal of Computational Designand Engineering (2015), http://dx.doi.org/10.1016/j.jcde.2015.04.002.

[12] E. Uhlmanna, b, S. Koprowski, W. L. Weingaertner, D. A. Rolon, Modelling and simulation of grinding processes with mounted points: Part I of II - Grinding tool surface characterization, 7th HPC 2016 – CIRP Conference on High Performance Cutting, Procedia CIRP 46 (2016) 599 – 602.

[13] Haiyue Yu, Jun Wang and Yushan Lu, Simulation of grinding surface roughness using the grinding wheel with an abrasive phyllotactic pattern, Int J Adv Manuf Technol (2016) 84:861–871.

[14] YuemingLiu, AndrewWarkentin, RobertBauer, YadongGong, Investigation of different grain shapes and dressing to predict surface roughness in grinding using kinematic simulations, Precision Engineering, Volume 37, Issue 3, July (2013), 758-764.

[15] H. Yoshikawa, T. Sata, Simulated grinding process by Monte-Carlomethod, Annals of CIRP 16 (1968) 297–302.

[16] J. Peklenik, Contribution to the correlation theory for the grindingprocess, Journal of Engineering for Industry 86 (1964) 85–94.

[17] S. J. Deutsch, S. M. Wu, Selection of sampling parameters for modelinggrinding wheels, Journal of Engineering for Industry 92 (1970) 667–676.

[18] S. S. Law, S. M. Wu, Simulation study of the grinding process, Journal ofEngineering for Industry 95 (1973) 972–978.

[19] K. Steffens, Closed loop simulation of grinding, Annals of CIRP 32 (1)(1983) 255–259.

[20] P. Basuray, B. Sahay, G. Lal, A simple model for evaluating surface roughness in fine grinding, International Journal of Machine Tool Design and Research 20 (1980) 265–273.

[21] R. L. Hecker, S. Liang, Predictive modeling of surface roughness in grinding, International Journal of Machine Tools and Manufacture 43 (2003) 755–761.

[22] Sanchit Kumar Khare, Sanjay Agarwal, Predictive modeling of surface roughness in grinding, 15th CIRP Conference on Modelling of Machining Operations - Procedia CIRP 31 (2015) 375 – 380.

[23] Anne Venu Gopal, P. Venkateswara Rao. A new chip-thickness model for performance assessment of silicon carbide grinding. Int J Adv Manuf Technol (2004) 24: 816–820.

[24] J. E. Mayer. G. P. Fang, Effect of grit depth of cut on strength of ground ceramics. Annals CIRP (1994). 43. 309-312.

[25] S. Somasundaram1. C. Thiagarajan, Experimental Evaluation of a Chip Thickness Model Based on the Fracture Toughness of Abrasive and Work Material in Grinding of Alumina Ceramics. International Journal of Modern Engineering Research (2013). Vol. 3. Issue. 6. Nov

– Dec. pp-3825-3829.

[26] Xu. Hockin, S. Jahanmir, L. K. Ives, Effect of grinding on strength of tetragonal zirconia and zirconia-toughned alumina'. Journal of Machining Science Technology. 1. (1997). 49-66.

[27] Hockin HKX. Jahanmir S. Ives LK, Effect of grinding on strength of tetragonal zirconia and zirconia-toughened alumina. Mach Sci Technol (1997) 1:49–66.

[28] X. Chen, Strategy for the selection of grinding wheel dressing conditions. Ph.D. Thesis. Liverpool John Moores University (1995).

[29] Rajani Sharma, Promise Mittal, Kuldeep Kaushik, Pavan Agrawal, Optimization of Surface Roughness in cylindrical grinding, International Research Journal of Engineering and Technology, Volume: 03 Issue: 12 (2016).

A Machine Vision Based Automatic Optical Inspection System for Detecting Defects on Electronic Boards

Từ Vương Bảo Ngọc[1,a], Nguyễn Huỳnh Minh Hải [2,b], Cao Minh Trí [3,c], Lê Ngọc Huẩn[4,d*]

[1]International University, Linh Trung, Ho Chi Minh City, Viet Nam
[2] Eastern International University, Binh Duong, Viet Nam
[3] Eastern International University, Binh Duong, Viet Nam
[4] Mechatronic Department, Eastern International University, Binh Duong, Viet Nam

[a] ngoc.tu.k1set@eiu.edu.vn, [b] hai.nguyen.k2set@eiu.edu.vn, [c] tri.cao.k2set@eiu.edu.vn, [d] huan.le@eiu.edu.vn

Keywords: Detect defects; 2D calibration; Electronic board; Automatic Optical Inspection (AOI).

Abstract. To improve the yield rate and reduce manufacturing costs, the optical inspection devices are widely installed in the design, layout, fabrication, assembly, and testing processes of production lines. This study proposed a prototype of computer vision based system for automatically detecting defects on electronic boards, which includes a conveyor system and a capturing room. The system can run in two modes: manual and auto. A control algorithm was built to run on the Arduino Microcontroller for speed control of a DC motor and Visual Studio C# to analyze data of captured image and display the final result. To improve the lens distortion rectification, a novel, easy calibration method using image local transformations defined by both sets of points, the points detected in the distorted image and the undistorted ones without using a model for a wide-angle and low-cost lens camera was proposed. For dealing with the rotation of input boards, we developed a set of algorithm including: Speeded up robust features (SURF) for detecting local features; a combination of k-nearest neighbors algorithm (k-NN) and Random sample consensus (RANSAC) for matching corresponding features, deleting outliers and generating rotation and translation parameters. As a result, the defective electronic board detection system can detect two common defects: missing electronic components and wrong position of electronic components. Moreover, the users can create new data files for different board types and they also can be edited, saved and reused later.

1. Introduction

In most manufacturing industries, one main goal is to achieve 100% quality assurance of the parts, subassemblies, and finished products also. Product inspection is an important step in the manufacturing process. However, inspection tasks are time consuming, and mostly performed by human inspectors these days. Compared to machines, the working hours of human inspectors are short, the cost of labor is high, and the performance of the inspectors is inadequate. Automatic optical inspection (AOI) system has been developed for decades. The system can detect the surface-related defects. The product would be inspected by sensors, and visual data would be collected and analyzed by the system. The main inspection process often involves a measurement of assembly integrity, surface finish, and geometric dimensions. AOI system is a good choice compared to the effectiveness of manual inspection.

To inspect the quality of printed circuit board assembly (PCBA), a Fourier descriptor based image alignment algorithm (FDBIA) for applications of AOI system performed in real-time environment was presented [1]. Besides, in order to improve the comprehensive performance of solder joints inspection in three aspects, i.e. high recognition rate, detailed classification of defect types and fast inspection speed, a new detection and classification algorithm of the chip solder joints based on color grads and Boolean rules is developed [2]. The detection and classification method is designed and presented using Boolean rules. Then, eight common solder joint types, including the

acceptable solder joint, pseudo, no solder, lacked solder, excess solder, shifted, tombstone, and miss component can be classified and detected by the proposed algorithm. In [3], to improve the performance of AOI system, a neural network combined with genetic algorithm for the diagnosis of solder joint defects on printed circuit boards (PCBs) assembled in surface mounting technology (SMT) is presented. Six types of solder joint have been classified in respect to the reality in the manufacture.

In all above researches, detailed studies on the welding of the component parts have been made. In which, the authors used the accurate mechanical systems to assist in the imaging process, which is equipped by expensive CCD-camera and light illumination systems. The devices can identify up to seven different types of solder joint of PCBAs. And, the processing time is higher than 15 seconds for a PCBA.

Today, advances in technology and manufacturing devices have resulted in cheaper industrial visual inspection equipment. So, AOI systems served in companies tend to use low-prize and wide-angle lens camera that is a main component deciding the quality of inspection system. A wide-angle lens has become popular for various digital imaging devices such as surveillance systems, vehicle rearview cameras, endoscopes and automatic optical inspection systems recently. One disadvantage of wide-angle lens is that wide-angle view images acquired by a single camera still cannot avoid radial distortion in the peripheral region, which results in significant degradation of the image quality. Several lens distortion correction methods have been studied for a long time in the context of the camera calibration for solving this problem [4-8]. These mentioned methods deal the common problems such as the non-uniform image resolution and gradually increasing aliasing artifact in the radial direction since conventional interpolation methods cannot completely cover the non-uniform distortion. As a result, the image quality and the performance of object recognition are degraded by aliased high frequency components in the central region and blurred details in the peripheral region.

In addition, it is a costly and time consuming investment for the system so that the circuit board position is fixed and the camera moves to the desired locations as in expensive AOIs. We can place the PCBA freely on the conveyor belt and the detection algorithm will rotate the board to the desired position using the software. For dealing with the input image registration, we developed a set of algorithm including: SURF [9] for detecting local features; a combination of k-NN [10] and RANSAC [11] for matching corresponding features, deleting outliers and generating rotation and translation parameters.

In order to match the actual requirements of the enterprise for an efficient system that needs a low cost and can identify the common types of defect such as missing or wrong components, this paper proposed a low cost AOI system. The main objective of this research is to develop algorithms to automatically detect defects of the PCBAs as closely and robustly as possible to the result of a human grading expert. A mobile image acquisition and processing system was developed for on-site application. The system was composed of an image acquisition unit and a mobile computing unit mounted on a laptop computer. The developed algorithms were implemented on the mobile processing unit as a supplementary checking device.

2. Materials and methods

(A) Mobile Image Processing Unit

The developed mobile unit was composed of an image acquisition unit, conveyor and a mobile computing unit mounted on a 15" Notebook (Intel Core i7, 2.2GHz, RAM 8 Gb) as in Fig. 1(a). An illumination system was composed of a white LED rectangular-type direct lighting device. A web camera was placed at the center of the rectangular-type LED lighting at the top site of image acquisition unit. PCBAs were supported by a big automation company which was making several types of PCBA. The analysis software was made with C# and sample PCBA images, Fig. 1(b), were taken directly from the conveyor. A photo sensor was used for relatively checking position of PCBA

in front of camera. The speed of conveyor is changeable and controlled by an Arduino Mega 2560 controller.



(a) (b) (c)

Figure 1. (a) a full prototype of defective detection system, (b) a PCBA image captured by the system, (c) the chessboard using for calibration.

B. Image calibration

a. Plane calibration

In this system, the camera is always normal and keeps a constant distance to the conveyor. So, we proposed a quick calibration method based on non-metric scheme. As in [12, 13], the nearer the area around image center is, the lower the radial distortion is. In this research, a checkerboard with its rectangular size of 10mm×10mm (56x56 pixels) was used to analyze the distribution law of the error. To use the suggested method, it is supposed that the horizontal edges of the rectangles in the checkerboard are parallel relatively to the horizontal axis of image frame.

Calibration and error obtained process is shown below:

1) Get the calibration plate image;

2) Calculate the size of centroid rectangular;

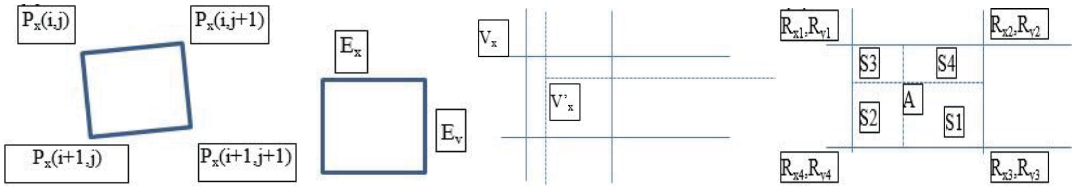
3) Get the grid map based on the size of centroid rectangular and the position of image center;

4) Get the shrinkage coefficients of the intersection points versus corresponding undistorted points or grid vertices;

5) Recover the input image by combining with shrinkage coefficients and the grid vertices.

b. Theory and method of generating the grid

In the 23*13 grid of Fig. 1(c), X coordinate values of four vertices of each grid cell change into abscissa as in Fig. 2(a). Firstly, center of image can be found. From this, four intersection points around the center are estimated.



(a) (b) (c) (d)

Figure 2. (a) vertex-deviation in input image, (b) grid cell, (c) vertex of grid cell and intersection point, (d) vertex of grid cell and a point inside grid cell.

The value of center point in X and Y direction should be calculated as in Eq. 1 and 2.

$$C_x(i,j) = (P_x(i, j)+ P_x(i, j+1)+ P_x(i+1, j+1)+ P_x(i+1, j))/4 \quad (1)$$

$$C_y(i,j) = (P_y(i, j)+ P_y(i, j+1)+ P_y(i+1, j+1)+ P_y(i+1, j))/4 \quad (2)$$

Recalculate the size of rectangular as in Fig. 2(b) by using Eq. 3 and 4.

$$E_x = (P_x(i, j+1) + P_x(i+1, j+1) - P_x(i+1, j) - P_x(i, j))/2 \quad (3)$$

$$E_y = (P_y(i+1, j) + P_y(i+1, j+1) - P_y(i, j+1) - P_y(i, j))/2 \quad (4)$$

From the center' rectangular, the grid of rectangular having the same size with center' rectangular is generated. At each cell of the grid, the shrinkage coefficients in X and Y direction R_x and R_y can be achieved as in Eq. 5 and 6.

$$R_x = V_x / V'_x \quad (5)$$

$$R_y = V_y / V'_y \quad (6)$$

Where V is the distance of the vertices (distorted and undistorted vertices) to the image center, Fig. 2(c). From now on, each grid vertex contains two shrinkage coefficients in X and Y direction.

c. Construction of the error compensation model

To recover the input image, a new null calibration image is created firstly. Then, at each pixel belongs to a grid cell as in Fig. 2(d) from input image, the formula below is used for estimating shrinkage coefficients R_xA and R_yA at point A.

$$R_xA = (S1/S)*R_x1 + (S2/S)*R_x2 + (S3/S)*R_x3 + (S4/S)*R_x4 \quad (7)$$

$$R_yA = (S1/S)*R_y1 + (S2/S)*R_y2 + (S3/S)*R_y3 + (S4/S)*R_y4 \quad (8)$$

Where, $S = S1 + S2 + S3 + S4$

Then, a corresponding position (AP) in calibration image can be calculated as below equations.

$$XAP = XA / R_xA \quad (9)$$

$$YAP = YA / R_yA \quad (10)$$

Where, XAP and YAP are X, Y coordination of AP point. However, the XAP and YAP are not integer values. So, to get the exact color value at AP point, we need to do interpolation one more time as in below equation.

$$CA = CAP = (S1)*C1 + (S2)*C2 + (S3)*C3 + (S4)*C4 \quad (11)$$

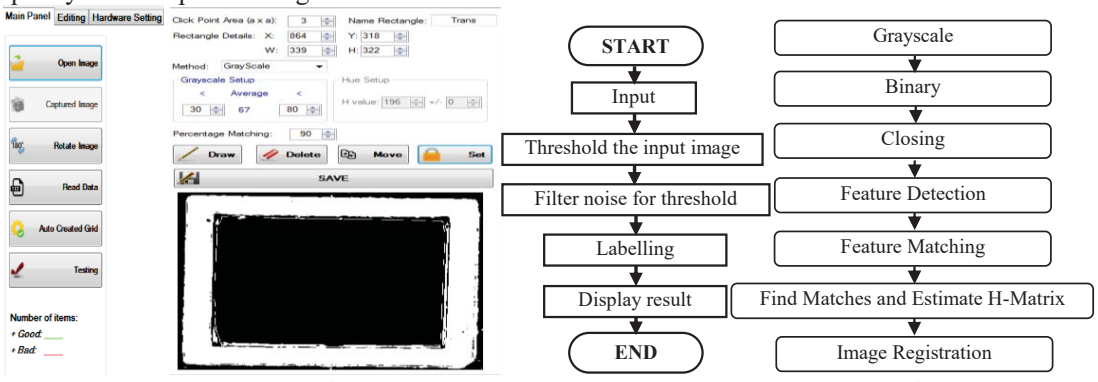
Where S1, S2, S3 and S4 calculated as in Fig. 2(d) are the area of corresponding rectangles. And, C1, C2, C3, C4 are grayscale values (0-255) of four pixel surrounding AP point.

C. Editing and Automatic defect detection algorithm

Before testing PCBA's quality, we firstly have to edit the test mode for each component on a standard PCBA. In general, the user can usually get a file storing the coordination values of the components from the PCB maker. From there, the program can locate the components exactly and the users edit the test mode for each component after that. However, most PCBAs that need to be tested do not have the coordination data file. Therefore, in this paper, the authors have proposed two manual and semi-automatic methods to locate the components on each PCBA image.

a. Manual editing

In Fig. 3(a), the Hardware Setting tab gives the user the ability to configure the serial port, DC servo parameters and the motor's speed. In addition, it also allows the user to change the Kp, Ki, Kd coefficients for the PID control, the exposure of the camera and control the lighting to ensure the quality of the captured image.



(a) (b) (c) (d)

Figure 3. (a) the main tab of user interface, (b) setting area for each component, (c) the flow chart of automatic component registration, (d) the flow chart of automatic image registration method.

To edit the component's configuration manually, firstly, we capture a standard image (image without errors) of the PCBA and go to the Editing tab, Fig. 3(a). In the user interface, there supports a button for generating rectangles with variable sizes. We can click and drag the rectangle to the desired position of component and begin to configure the values for detecting the component such as: threshold value, matching percentage, type of used color (grayscale or hue), and so on before

saving for later use, Fig. 3(b). At each rectangle, the user can adjust a proper threshold value by seeing the segmentation result directly below the SAVE button. The functions to find the average value and hue (H) are shown in Eq. 12 and 13, respectively. Then we continue configuring sequentially for all necessary components. Finally, an information file including the location and test mode of all components on the PCBA will be saved and used for actual inspection.

$$AverageValue = \frac{\mathrm{Re}\,d + Green + Blue}{3} \tag{12}$$

$$\begin{aligned} &R' = \frac{\mathrm{Re}\,d}{255}; G' = \frac{Green}{255}; B' = \frac{Blue}{255} \\ &C_{\max} = \max(R', G', B') \\ &C_{\min} = \min(R', G', B') \\ &\Delta = C_{\max} - C_{\min} \end{aligned} \qquad H = \begin{cases} 0^0, \Delta = 0 \\ 60^0 \times \left(\dfrac{G' - B'}{\Delta} \right), C_{\max} = R' \\ 60^0 \times \left(\dfrac{B' - R'}{\Delta} + 2 \right), C_{\max} = G' \\ 60^0 \times \left(\dfrac{R' - G'}{\Delta} + 4 \right), C_{\max} = B' \end{cases} \tag{13}$$

In which, Red is the intensity of the image in the red color frame. Green is the intensity of the image in the red color frame. And, Blue is the intensity of the image in the blue color frame.

b. Semi-automatic component registration

Manual editing task takes a lot of time when the number of components on a PCBA is large. Therefore, the authors suggested a semi-automatic editing mode for finding the location and displaying the rectangle surrounding the existing components on the PCBA. We proposed an automatic object registration method with the flowchart as below, Fig. 3(c). In which, we firstly select a threshold value suitable for each PCBA and segment the image to separate the components off the background. The image after thresholding is processed successively by dilation and erosion morphological algorithms, 2 erosions and 2 dilations. Then, we continue labelling the remain blobs. At each blob we draw a rectangle around it. Finally, we get the location and size of all the rectangles and superimpose these rectangles over the original image for re-editing manually done by the users.

c. Image Registration

With an input image placed randomly, there will be two kinds of rotation compared to the reference image. First, the input image can rotate 180 degree from the reference image. Then, even if placed in the same direction, the input image can be rotated a little compared to the reference image. Therefore, before proceeding to find the local errors in the board, we must rotate the input image to the same direction and parallel to the reference image. To solve this problem, firstly we convert the color to grayscale image. Then, we use the Otsu method [14] to find adaptive threshold value for segmentation step. We use closing morphological scheme for keeping the general shape of the object and from that we can find features in both input and reference image using SURF. Then, RANSAC algorithm will be used to filter matches from previous step. From these matches, we find the homography matrix (H-matrix) and use it to rotate and translate the test image to match with the reference image. Figure 3(d) shows the flow chart of automatic image registration.

d. Matching operation

In each rectangle, using the saved data including threshold value range and type of color to run thresholding operation for both the reference image and captured image. Then, we compare the value of each pixel on both images. If the value is similar (both black and white), the counter will increase one. After that, we calculate the real matching percentage by using Eq. 14:

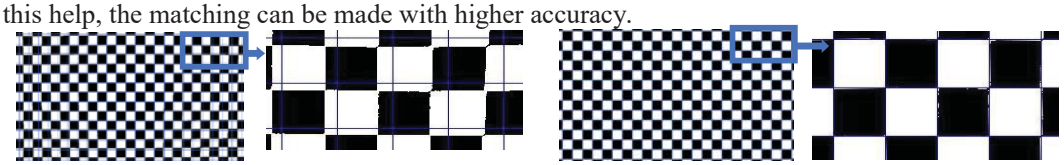
$$\mathrm{Re}\,alMatchingPercentage = \frac{TheValueOfTheCounter}{TheAreaOfThe\,\mathrm{Re}\,c\tan gle} \tag{14}$$

The final step is the comparison of the real matching percentage (RMP) and the default matching percentage (DMP) of this rectangle. If RMP is greater than or equal to DMP, this rectangle will be displayed in green color. And if RMP is less than DMP, this rectangle will be displayed in red color.

3. Results and Discussion

a. Image calibration

Figure 4(a)&4(b) show the images of the checkerboard before and after calibration respectively. In this, if the object is put in the same plane of the checkerboard while calibration, the image distortion will be corrected as in the traditional calibration. By contrast, using the checkerboard's surface as a standard, the object's surface will be bended to coincide with the reference plane. With this help, the matching can be made with higher accuracy.

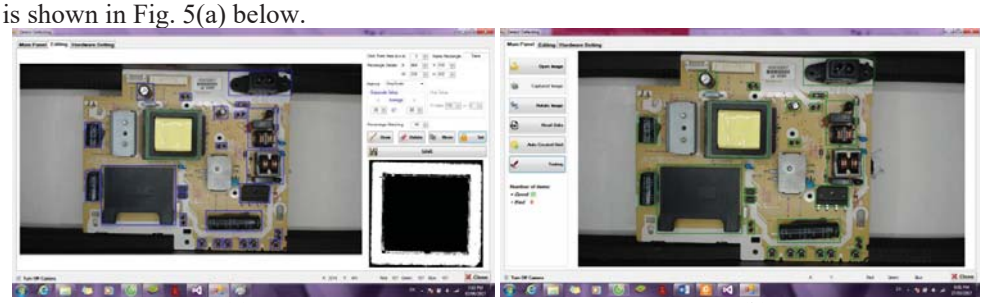


(a) (b)

Figure 4. (a) the image of the checkerboard before calibration, (b) the image of the checkerboard after calibration.

b. Manual editing

When we need to test a new PCBA, calibration is done firstly. Then, based on a standard board, we determine the position of the components to be tested and the necessary parameters such as gray-color or hue, percentage matching. The result after configuring all the components on a sample board is shown in Fig. 5(a) below.



(a) (b)

Figure 5. (a) the result after configuring all the components on a sample board, (b) superimposing rectangles into the PCBA after automatic component registration.

c. Semi-automatic component registration

To start registering the components semi-automatically, we find the appropriate threshold value and proceed to segment the image. Then, because of the noise that appears in the binary image, we implement an opening morphological algorithm to eliminate the noise from the binary image. After implementing the steps as the flow chart in Fig. 3(c), we have the result with all components having the rectangles around them, Fig. 5(b).

After automatically finding PCBA components, it is normal to have components marked incorrect or the sizes of the rectangle that are too small or too large to the components. Therefore, we need to check for these errors and edit again manually. For PCBAs with more than 100 components, implementing a semi-auto method for positioning components saves a lot of time compared to doing manually.

d. Image Registration

The image registration process is implemented as the flow chart in Fig. 3(d). The input image, Fig. 6(a), will be converted to the grayscale image and the result is shown in Fig. 6(b). We then proceed to segment the grayscale image using the Otsu scheme and continue implementing a closing morphological algorithm to keep the general shape of the object, Fig. 6(c). Figure 6(d) shows the result of the features detected in both the image and the reference image using SURF. Then, after using K-NN algorithm to find similar feature points on reference and test images, we got the result as in Fig. 6(e). In Fig. 6(f), we filter matches from previous step using RANSAC algorithm. Finally,

using Homography matrix obtained on previous step, we rotate and translate the test image to match with the reference image, Fig. 6(g).

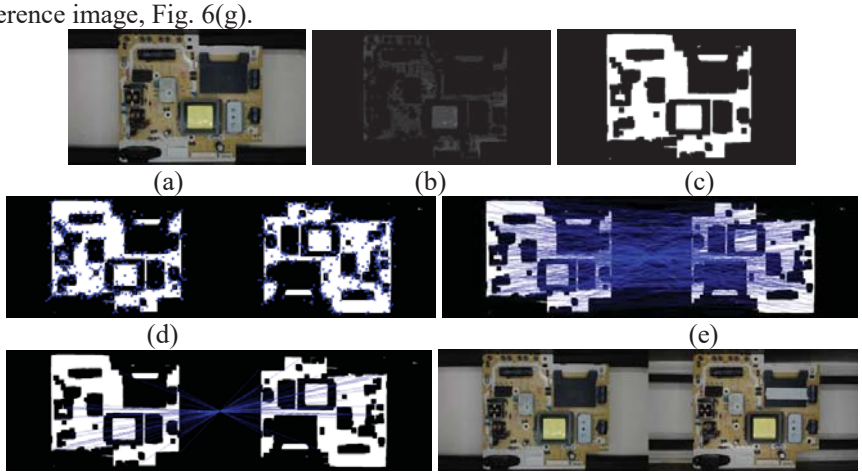


Figure 6. (a) input image, (b) grayscale image, (c) binary image, (d) using SURF finding feature in both test image and reference image, (e) using K-NN algorithm to find similar feature points on reference and test images, (f) using RANSAC algorithm to filter matches from previous step, (g) using Homography matrix obtained on previous step to rotate and translate the test image to match with the reference image.

e. The final result

Once having configuration data file of standard PCBA, we run the proposed algorithm to determine the error of the PCBA running on the conveyor. The program can check exactly two common mistakes that are lack of components and wrong type of components. Figure 7(c)&8(d) are the results after examining the defective PCBA boards in Fig. 7(a)&(b), respectively.

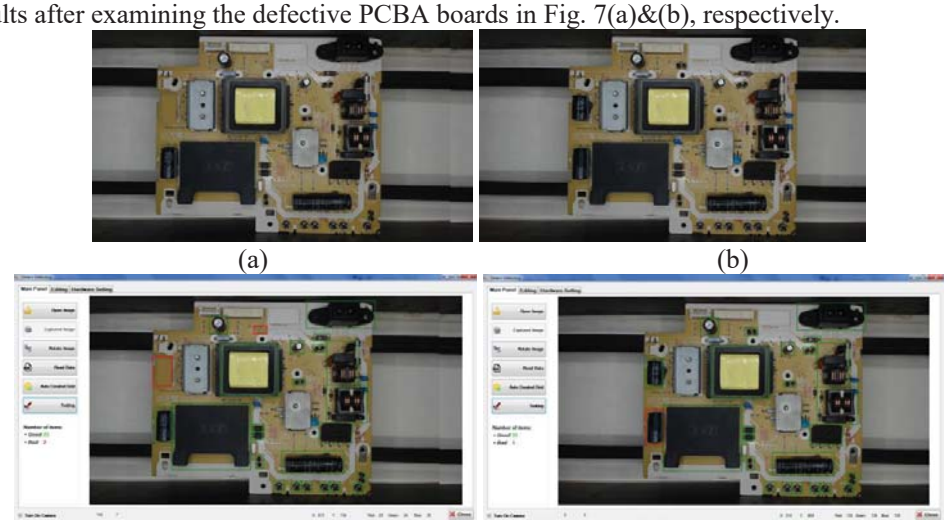


Figure 7. (a) & (b) two test images, (c) & (d) two results of (a) & (b), respectively.

4. Conclusion

Using computer vision systems to assist in detecting defect of industrial products is used widely in the world, especially in industry 4.0 era. In this paper, a research was fully carried out to solve all issues related to defects of PCBA with a cheap system compared to commercial expensive AOIs

system. The program works well even if the input board is rotated somehow to the reference board by searching and rotating the input board automatically. Besides, the authors proposed a quick calibration method without using a model for a wide-angle and low-cost lens camera. In this, the object's surface will be bended to coincide with reference plane used in calibration process. So, the size of all objects at any position in the image will be the same even if they are not put in the same plane. This proposed method showed a significant result and gave the chance for speeding up the whole process to real-time processing. A mobile computer-based system was developed and it showed significant results with the time consuming about 9 seconds per a PCBA with over 50 objects. The user interface also permits the users to easily create new data files for different board types of PCBA by positioning the component manually and semi-automatically. Although the proposed algorithms worked successfully, further improvement in speeding up the whole process has been carrying out continuously.

References

[1] C. S. Chen, C. W. Yeh, P. Y. Yin, A novel Fourier descriptor based image alignment algorithm for automatic optical inspection, J. Vis. Commun. Image R. 20 (2009) 178–189.

[2] F. Wu, X. Zhang, An inspection and classification method for chip solder joints using color grads and Boolean rules, Robotics and Computer-Integrated Manufacturing 30 (2014) 517–526.

[3] W. Hao, Z. Xianmin, K. Yongcong, O. Gaofei, X. Hongwei, Solder joint inspection based on neural network combined with genetic algorithm, Optik 124 (2013) 4110–4116.

[4] G. Klančar, M. Kristan, R. Karba, Wide-angle camera distortions and non-uniform illumination in mobile robot tracking, Robotics and Autonomous Systems 46 (2004) 125–133.

[5] U. Tiwari, U. Mani, S. Paul, Non-Linear Method Used For Distortion Correction Of Fish-eye Lens: Comparative Analysis Of Different Mapping Functions, IEEE, International Conference on Man and Machine Interfacing (MAMI) (2015) 978-1- 5090-0225-2.

[6] D. Kim, J. Park, J. Jung, T. Kim, J. Paik, Lens Distortion Correction and Enhancement Based on Local Self-similarity for High-quality Consumer Imaging Systems, IEEE Transactions on Consumer Electronics, Vol. 60, No. 1 (2014).

[7] C. Ricolfe-Viala, A. José, S. Salmerón, Correcting non-linear lens distortion in cameras without using a model, Optics & Laser Technology 42 (2010) 628-639.

[8] S. Aritan, Efficiency of non-linear lens distortion models in biomechanical analysis of human movement, Measurement 43 (2010) 739–746.

[9] H. Bay, A. Ess, T. Tuytelaars, L. V. Gool, Speeded Up Robust Features, ETH Zurich, Katholieke Universiteit Leuven (2008).

[10] N. S. Altman, An introduction to kernel and nearest-neighbor nonparametric regression, The American Statistician 46 (3) (1992) 175–185.

[11] T. Strutz, Data Fitting and Uncertainty, 2nd ed., Springer Vieweg (2016).

[12] C. R. Viala, A. J. S. Salmerón, Using the camera pin-hole model restrictions to calibrate the lens distortion model, Optics & Laser Technology 43 (2011) 996-1005.

[13] Q. Sun, Y. Hou, J. Chen, Lens distortion correction for improving measurement accuracy of digital image correlation, Optik 126 (2015) 3153–3157.

[14] N. Otsu, A threshold Selection Method from Gray-Level Histograms, 1979.

Effects of different drying techniques on drying characteristics and quality of dried Moringa oleifera leaves

Tran Dinh Khai [1], Le Anh Duc [2*], Nguyen Hay [3]

[(1)] PhD student, Ly Tu Trong College Ho Chi Minh City, Vietnam

[(2)] Assoc. Prof., Dr., Nong Lam Univerisity Ho Chi Minh City, Vietnam

[(3)] Prof., Dr., Nong Lam Univerisity Ho Chi Minh City, Vietnam

*Corresponding author. Tel: (+84) 0908.470.490; E-mail: leanhduc@hcmuaf.edu.vn

Abstract

The objective of the study was to investigate the effects of different drying techniques on drying characteristics and quality of Moringa oleifera leaves. The fresh moringa leaves were dried by using heat pump (HP), heat pump assisted infrared (IHP) and heat pump assisted microwave (MHP) method at three different temperature levels of 35, 40 and 45°C. Three methods were performed at the same drying air velocity of 0.5 m/s. The drying characteristics and quality attributes, namely, drying time, drying rate, color and calcium contents, were analyzed and compared.

Among the three drying techniques studied, the MHP drying method at the temperature of 40ºC is the best suitable for moringa leaves drying. The drying time of 180 minutes, the average drying rate reached 22.9 %/h. The dried moringa leaves have good quality than other drying methods on calcium content and color, the highest calcium contents reached 1.06% and the lowest color index ΔE of CIELab value of 4.79.

Keywords: moringa oleifera, heatpump, infrared, microwave, color index

1. INTRODUCTION

Moringa oleifera is also called the drumstick plant. The moringa leaves are the plentiful sources of vitamin A and C, calcium, essential amine acid, instance of methionine, tryptophan and lysine with protein contents. However, the fresh moringa leaves sustain only for about form 2 to 3 days. So that, drying must be a preserving method safely.

Now, drying methods for moringa leaves mainly are expose in the sunlight or convective heating, therefore it takes too long time for drying. Besides, high temperature drying changes the attributes of the moringa leaves such as the aroma, color, decreased nutritious values.

Microwave drying is a substitute method because it has the inner increased heat, conducting drying process exactly, saving energy, reducing the drying time and improving the quality of products after drying (Soysal, 2004).

For many years ago, drying with assistance of microwave heating has been used by many researchers for crops such as parsley (Soysal, 2004), Bina (Ozkan et al., 2007), mushrooms in pieces (Lombrana et al., 2010). The researchers showed that assisted microwave brought about many good points such as short drying time, equal levels of products moisture content are being better, the quality of drying products being improved from the nutritious quality and saving energy.

II. MATERIAL AND METHODS

Moringa leaves were plucked off stems after harvesting, cleaned completely and stored in refrigerator at the temperature 4 ± 1ºC until the experiments could be fulfilled (Dev et al., 2011). The initial moisture content of fresh moringa leaves of 77 ± 0.5% (wb.).

Experimental method: three methods include heat pump (HP), heat pump assisted infrared (IHP) and heat pump assisted microwave (MHP) were performed at the ranges of drying air temperature of 35ºC,

40°C and 45°C, drying air velocity of 0.5 m/s. The proper drying method was determined base on evaluating the drying time, drying rate, color and calcium contents of the dried moringa leaves.

The moisture content of moringa leaves were determined by oven method at temperature of 105°C until the sample mass is constant (Dev et al., 2011) and used formulate to calculate. The drying rate was determined the percentage of evaporated water of drying materials according to the corresponding drying time.

The calcium contents of the dry moringa samples were analyzed by the HPLC method (High Performance Liquid Chromatography method).

Measuring color: using the colorimeter X–rite MR200 to measure the values L^*, a^*, b^* of the moringa leaves samples by using the three drying methods to determine color index $\Delta L^*, \Delta a^*, \Delta b^*$. The experiments were repeated three times for each sample and calculate the average value. The changes of color were commonly represented by indices of ΔE* index (Dev et al., 2011).

$$\Delta E^* = \sqrt{\Delta L^{*2} + \Delta a^{*2} + \Delta b^{*2}} \quad (1)$$

The heatpump dryer has technical parameters: the size of drying cabin is designed as 330 x 330 x 180 mm. The heatpump has the power of 1 HP, drying centrifugal fan has the power of 200 W, the emitting microwave head has the power 700 W (has 5 adjusted levels of emitted power), emitting microwave frequency is 2450 MHz (Tran Dinh Khai et al., 2016).

III. RESULTS AND DISCUSSIONS

3.1. Drying time of three methods at three drying temperatures

Drying time of three methods at the temperature of 35°C:

The moisture content of the moringa leaves required after drying is 8 ± 0,5% (wb.) (Ali et al., 2014). The experiment results were determined the drying time of three drying methods for the moringa leaves shown in the figure 1.

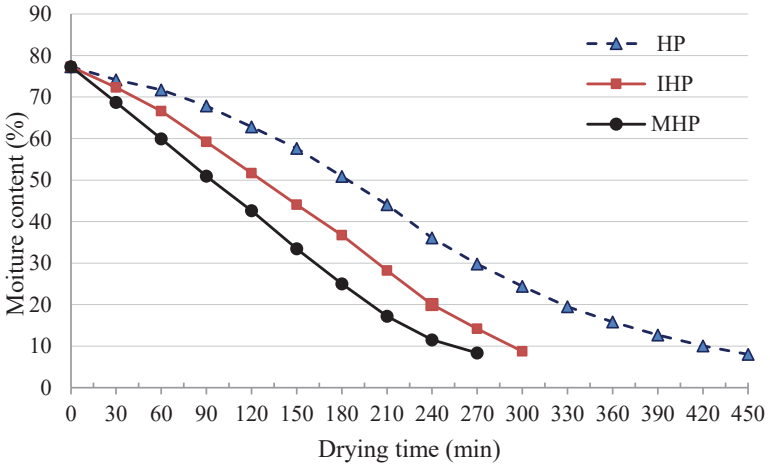


Fig 1. Moisture content versus drying time of three drying methods at the drying temperature of 35°C

The result showed that at the same drying temperature, drying process by the heat pump assisted microwave shortened 40% drying time versus the heat pump and 33% drying time versus the heat pump

assisted infrared.

Drying time of three methods at the temperature of 40°C:

The experiments of three drying methods at the temperature of 40°C, the results in comparison with drying time of moringa leaves shown in the figure 2.

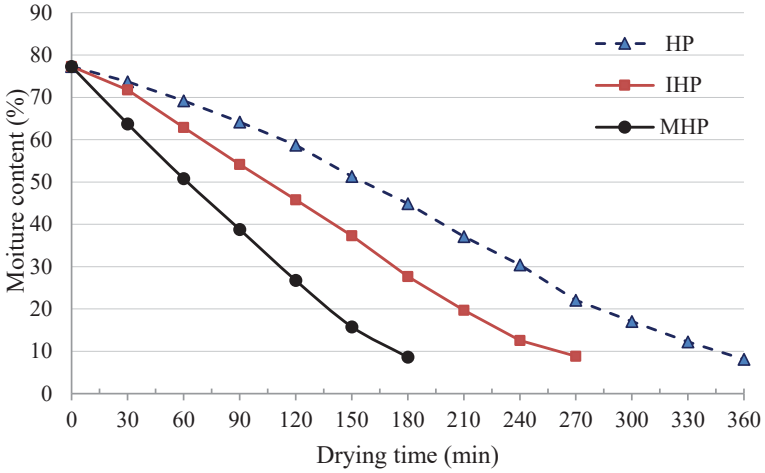


Fig 2. Moisture content versus drying time of three drying methods at the drying temperature of 40°C.

The result showed that at the same drying temperature, drying process by the heat pump assisted microwave shortened 50% drying time versus the heat pump and 25% drying time versus the heat pump assisted infrared.

Drying time of three methods at the temperature of 45°C:

The experiments of three drying methods at the temperature of 45°C, the results in comparison with drying time of moringa leaves shown in the figure 3.

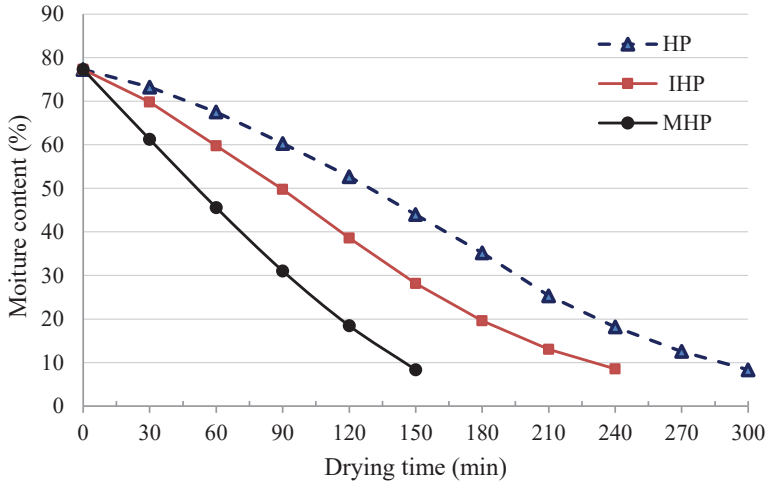


Fig 3. Moisture content versus drying time of three drying methods at the drying temperature of 45°C.

The result showed that at the same drying temperature, drying process by the heat pump assisted

microwave shortened 50% drying time versus the heat pump and 22% drying time versus the heat pump assisted infrared.

The experiment results shown that the drying time of three methods decreased when the drying temperature increased. In order to determine the drying process properly for the moringa leaves needs to compare more with the moisture rate of moringa leaves.

3.2. The drying rate of three methods at three drying temperatures

At the drying temperature of 35^0C, the drying rate of drying method by heat pump assisted microwave increased more rapid than 40% versus by the heat pump and 18% versus by the heat pump assisted infrared.

At the drying temperature of 40^0C, the drying rate of drying method by heat pump assisted microwave increased distinctly and more rapid than 50% versus by the heat pump and 33% versus by the heat pump assisted infrared.

At the drying temperature of 45^0C, the drying rate of drying method by heat pump assisted microwave increased nearly, more rapid than 50% versus by the heat pump and 38% versus by the heat pump assisted infrared.

The results of the average drying rate of three drying methods showed in table 1.

TABLE 1. The average drying rate (%/h) of three drying methods.

Drying method	Drying temperature		
	35ºC	40ºC	45ºC
HP	9.2	11.5	13.8
IHP	12.5	15.3	17.2
MHP	15.3	22.9	27.6

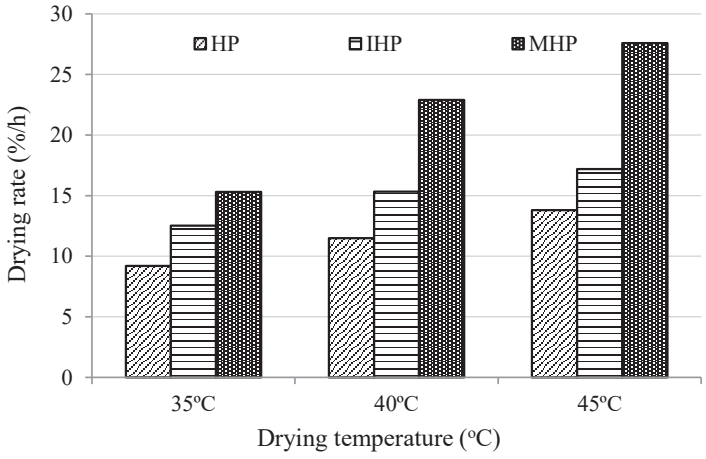


Fig 4. Compare the results of the average drying rate of three drying methods.

3.3. The effects of drying methods to calcium contents in moringa leaves

By method HPLC one determines Calcium content in moringa leaves after drying. The sample of moringa leaves dried by the drying method of the heat pump assisted infrared at the ranges of temperatures

35ºC, 40ºC and 45ºC, Calcium contents in dried moringa leaves were 0.87%, 0.99% and 0.62%. When drying heat pump assisted microwave, Calcium contents in moringa leaves at the corresponding temperatures were 1.02%, 1.06% and 1.01%.

TABLE 2. Calcium contents (%) of two drying methods (%).

Drying method	Drying temperature		
	35ºC	40ºC	45ºC
IHP	0.87	0.99	0.62
MHP	1.02	1.06	1.01

Comparing the Calcium contents in dried moringa leaves of two methods at three temperatures shown in figure 5.

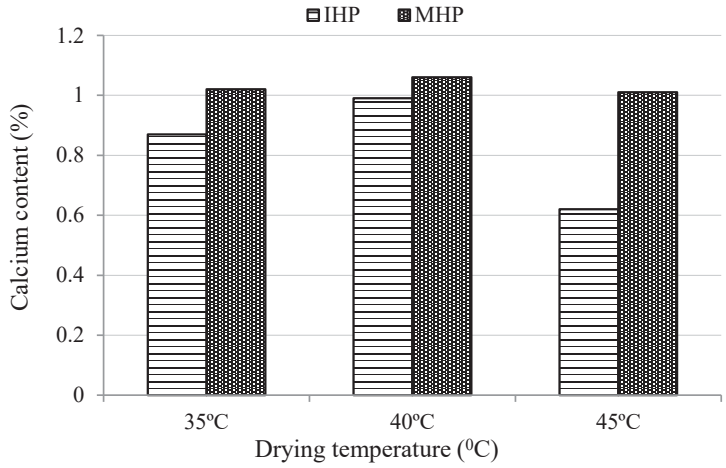


Fig 5. Calcium content of two drying methods at three drying temperatures.

The results shown that the heat pump assisted microwave has effects to Calcium contents in moringa leaves in drying process.

3.4. The effects of three drying methods to the color of moringa leaves

The determination of the color of dried moringa leaves of three drying methods which were conducted by using the colorimeter X-Rite, model MR200. The measuring the color index of heat pump assisted infrared drying method showed in table 3.

TABLE 3. The color values of drying method by the heat pump assisted infrared at three temperatures

Drying method	L*	a*	b*	a*/b*	ΔE*
IHP 35ºC	42.78	-4.70	24.19	-0.19	9.65
IHP 40ºC	43.12	-4.69	23.98	-0.20	9.26
IHP 45ºC	41.43	-4.13	25.26	-0.16	11.45
Fresh moringa leaves	50.37	-6.48	18.51	-0.35	-

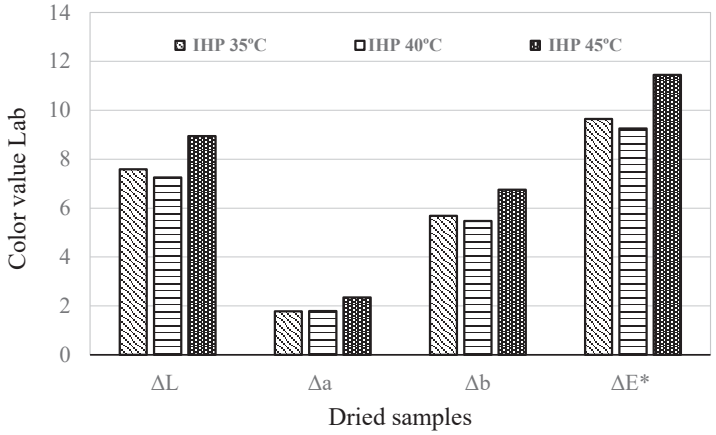


Fig 6. Changed color of dried moringa by the heat pump assisted infrared at three drying temperatures.

The variety of the value L* of dried moringa leaves was not even at the temperature 40ºC, that had the lower at the temperature 35ºC.

The measuring the color index of heat pump assisted microwave drying method showed in table 4.

TABLE 4. The color values of drying method by the heat pump assisted microwave at three temperatures

Drying method	L*	a*	b*	a*/b*	ΔE*
MHP 35ºC	46.74	-5.72	22.32	-0.26	5.32
MHP 40ºC	46.81	-5.93	21.65	-0.27	4.79
MHP 45ºC	45.66	-4.72	24.11	-0.20	7.52
Fresh moringa leaves	50.37	-6.48	18.51	-0.35	-

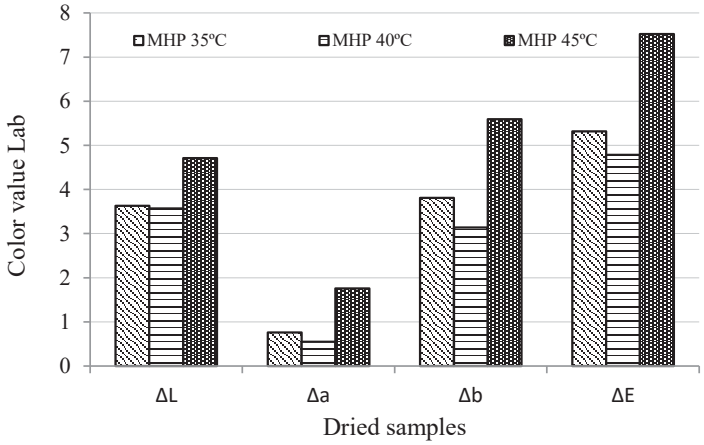


Fig 7. Changed color of dried moringa by the heat pump assisted microwave at three drying temperatures

When drying by the heat pump assisted microwave at three temperatures conduced the values L*, a*, b* and ΔE which were highest in the drying samples at 45˚C. Those showed that the products were colorless and more yellow than when they were dried at this temperature. At the temperature 40˚C drying time shortened very much was 3 h in comparison with 4.5 h at the temperature 35˚C . So that the value ΔE was the lowest 4.79. The value a*/b* was higher and the value ΔL* was lower so that these were favored in the dried food products.

Thus, the results determined drying method by the drying principle in heat pump assisted microwave at the temperature of 40ºC there was the rate of color ΔE, the lowest reach the value of 4.79.

IV. CONCLUSIONS

The experiments were performed for drying moringa leaves by the heat pump, heat pump assisted infrared and heat pump assisted microwave at three drying temperatures of 35, 40 and 45˚C. The estimation based on the technical criterions of the drying process and the quality of the product after drying to claim that the microwave was able to heat rapidly materials, shortened drying time, and really improved the quality of products from nutritious contents and good color in comparison with no combined microwave.

The suitable drying temperature was determined that at the temperature of 40˚C, drying air velocity of 0.5 m/s, drying time 3 h, the moringa leaves reached to the required moisture content of 8%, the average drying rate reached to 22.9 %/h, Calcium contents of dried moringa leaves reached to 1.06%.

CONFERENCES

[1] Ali M.A, Yusof Y.A, Chin N.L, Ibrahima M.N, Basra S.M.A, 2014. Drying kinetics and color analysis of Moringa Oleifera Leaves. Agriculture and Agricultural Science Procidia.

[2] Barminas J.T, Charles M., Emmanuel D., Mineral composition of non-conventional leafy vegetables, 1998. Plant foods for human nutrition.

[3] Dev S.R.S, Geetha P., Orsat V., Gariépy Y., Raghavan G.S.V., 2011. Effects of Microwave-Assisted hot air drying and Conventional hot air drying on the drying kinetics, color, rehydration, and volatiles of Moringa oleifera. Drying technology.

[4] Lombrana J.I., Rodriguez R., Ruiz U., 2010. Microwave drying of sliced mushroom. Analysis of temperature control and pressure. Innovative Food Science and Emerging Technologies, Vol. 11, 652 - 660.

[5] Nadiah N.I., Uthumporn U., Syahariza Z.A., 2016. Effect of Microwave Heater on Potato and Tapioca Starches in Water Suspension. International Journal on Advanced Science Engineering Information Technology.

[6] Ozkan I.A., Akbudak B., Akbudak N., 2007. Microwave drying characteristics of spinach. Journal of Food Engineering, Vol.78, 577 - 583.

[7] Soysal Y., 2004. Microwave drying characteristics of parsley. Biosystems Engineering, Vol.89, 167 - 173.

[8] Tran Dinh Khai, Mai Xuan Dieu, Le Anh Duc, 2016. Design, manufacture and testing heat pump assisted microwave drying of Moringa oleifera leaves. Journal of Rural industry.

Rhythmical Behavior Analysis for Vision Inspection Using Perception Neuron and Unity

Vo Nhu Thanh, Tran Ngoc Hai, Dang Phuoc Vinh and Nguyen Linh Giang
University of Science and Technology, The University of Da Nang, Viet Nam
vnthanh@dut.udn.vn*, tnhai@dut.udn.vn, dpvinh@dut.udn.vn, nlgiang@dut.udn.vn

Keywords: Peripheral visual inspection, Unity, Perception Neuron, Production quality control, Operator health.

Abstract. The purpose of this study is to evaluate rhythmic behavior of operators who inspect products using peripheral vision inspection method. Measurements have been realized using a motion capture suit called Perception Neuron. The suit has been implemented into Unity, software for 3D application development. Thus, the authors develop a virtual skeleton moving in real-time according to the operator's motion, with a custom environment (with objects to inspect, neon light) which reproduces inspection's working conditions. Moreover, Unity allows extracting data from measurements, so they can be analyzed and evaluated directly. In this study, we propose a new inspection method by applying PVI which improves operator's health and comfort at work. It would be a big help for production quality control in industry regarding to the improvement of working condition of the workers. This proposal can help to increase the productivity by improving inspection's efficiency and speed.

1. Introduction

Classical visual inspection consists of focusing the looking on particular points of a product, to check if there is any defect. Operators checks products one by one, or sometime two by two, by toggling their look between both products. Visual inspection is thus often used as a part of quality control of production. It is a very tiring process for the eyes, which can cause health problems. The operators who realize these visual inspections may get visual fatigue and bad postures such as eyestrain, stiff in neck and/or shoulders, pain in the lower back, gastric problems… etc. These health problems are unfortunately very often noticed [1].

Peripheral vision inspection (PVI) is a specific method of visual inspection using peripheral vision [2],[3],[4]. This method is developed to improve work conditions and health of inspection operators. It requires training, but once acquired, inspection is faster, more efficient and less tiring. To achieve peripheral vision inspection, the operator needs to reach a relaxed state of mind; and to perform the inspection nearly unconsciously, the inspection operator feels more than he thinks.
PVI differs from classical inspection by two important aspects which are the motion and the look. In details, the motion is important to achieve the smooth, repetitive and rhythmic state. This requires the inspectors always do the same motions to take a rhythm. Handling of parts is also concerned. With training, these movements become more natural, so he can do it unconsciously which help him more relaxed in his job. Secondly, the look needs to remain fixed and wide when the operator moves parts to inspect in front of his eyes. More precisely, look remains fixed slightly behind the location where the operator moves parts. It means that he doesn't need to look at them directly.

For the brain, each inspected part becomes an "event" and an "experience", which is stored in memory with all associated feelings, impressions. By training with compliant parts, the brain memorizes more and more inspection events, with relatively constant feelings. The inspection process becomes gradually automatic. At each new inspection, the unconsciousness compares the present inspection to all the memorized inspections, and to all the associated feelings. While the feeling is the same, inspection process stays unconscious, but if the feeling is somewhat different, consciousness is alerted that something is abnormal, and very often, it means that there is a defect.

In this study, we apply PVI method to analyze the rhythmic of the movement in product inspection. The authors use Perception Neuron equipment as the motion capture device and connect it to Unity3D software to analyses the rhythmic in the working behavior of expert, intermediate, and beginner user. From analysis results, the training processes for inspection operators using PVI can be derived. It would be a big help for production quality control in industry regarding to the improvement of working condition of the workers. This proposal can help to increase the productivity by improving inspection's efficiency and speed. This could be applied as standardization for PVI method that every company could use, especially when the Automation 4.0 evolution is coming.

2. Experimental equipment

2.1 Motion capture device: Perception Neuron

To evaluate body motion of a PVI operator, we use a motion capture device made by Noitom Ltd, called Perception Neuron (PN) [5] as shown in Figure 1. It is a suit composed of different straps all over the body, from head to feet. There are slots on these straps, provided for 31 sensors. These sensors, called Neurons (one is presented on Fig.1), house an Inertial Measurement Unit (IMU), which means a 3-axis gyroscope, a 3-axis accelerometer and a 3-axis magnetometer. Neurons are clipped in the slots. All neurons are linked to a hub, placed on the belt. It transmits data to a compute via USB cable or Wi-Fi, or records data with an embedded micro-SD.

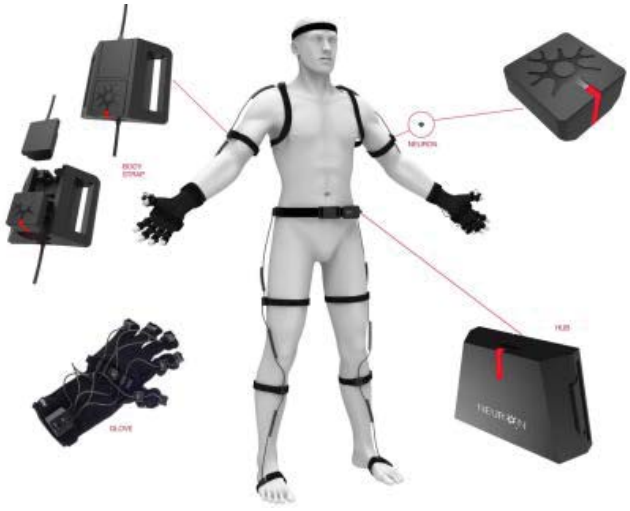


Fig.1. Perception Neuron motion capture system, by Noitom Ltd.

Figure 2 shows the distribution of all 31 neurons in the system. The finger sensors represent nearly half of all sensors (14 of 31), the thumb and index fingers have two neuron and the other fingers have one neuron. This PN system is adaptive which means the user can connect only the neurons as he needs, from only one arm (3 neurons) to the full body, fingers included or not. It is very affordable system which cost only 1500 USD in comparison with other conventional motion capture system using cameras and markers (cost between 20,000 USD up to 50,000USD).

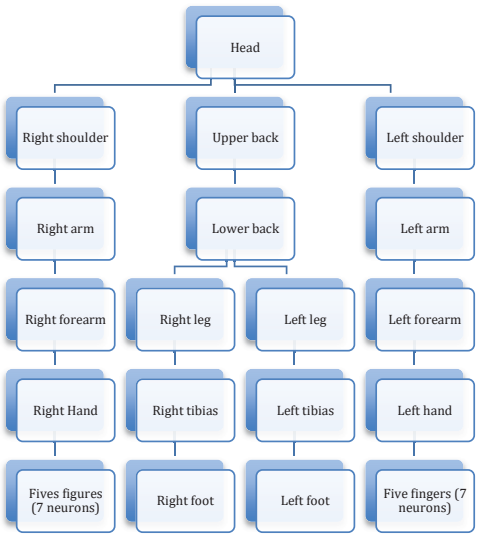


Fig.2. Distribution of all 31 neurons in Perception Neuron system

2.2 Unity3D software and connection to Peripheral Neuron

Unity3D is software developed by Unity Technologies. It is used to develop 3D application such as simulations for computers, virtual reality, and games. It supports both 2D and 3D, drag and drop functions and scripting in C# and JavaScript. It uses Unity Engine. Unity users have big community where plenty of assets and library are created and supported by Unity Technologies or community members. Thus, it can help saving a lot of time when developing an application.

Noitom Ltd. Developed a Unity asset, which is called Axis Neuron, to implement Perception Neuron's skeleton in developing application. In Axis Neuron, by activating broadcasting option, all position and orientation values are sent in real-time, at 60 frame per second (fps) if more than 18 neurons are connected, or 120 fps if less than 18 neurons are used. With the asset, Unity receives these data from Axis Neuron, and the skeleton in Unity moves exactly the same way than the one in Axis. By attaching the camera to the head of the skeleton, we can have a first person view, which is easier to understand for users. This is helpful considering that, to create a training application, it is better to have real time motion transmitted to Unity than to record motion and analyze them later (see Fig. 3) [5].

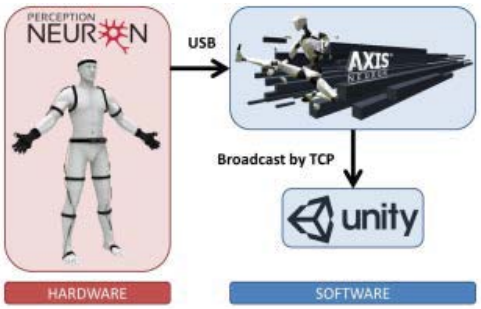


Fig. 3. Communication architecture from Perception Neuron device to Unity

3. Experiment and result

For analysis the rhythmic movement of different level, we need to get the data from industrial workers in quality control section at DENSO Corporation. Three different skill-level operators realize

this work that classified as expert, intermediate and beginner. The expert operators are the engineer and training manager for PVI method; Intermediate operators are the operators who used PVI method for about more than 1 year; and Beginner are the operators who used PVI method for about 3 months.

Three sets of motion measurements are made for each operator, namely two sets of measurements with a full plate and one set with two half plates. Thus, we are able to compare data between the three of them. First of all, the whole motion capture suit with 31 neurons is used as shown in Figure 4. However the gloves with all sensors on fingers are not convenient for operator's handling, because of the nine sensors on each hand. Therefore, we modify the system with simple gloves that have 2 neurons on it (instead of 9). Operator also wore other measurement equipment such as cameras, glasses with eyes camera, heart rate sensor and shoes equipped with sensors to calculate gravity central movement.



Fig. 4. Opertor with full measurement equipment

3.2 Data extraction

To be able to analyze recorded data, we extract them from raw file of Axis Neuron asset. For analyzing the central of gravity of the worker we select the lower back sensor. As the operator work while standing, it is a good approximation.

To analyze just rhythmic motion, hand's position and its orientation would be a good approximation. However, with the aims to create training application, in would be better to include the work piece's position and orientation. As there is no sensor on the object, we create a virtual cube in Unity. We make a program in Unity which calculates the central position between two hands and give that position to the cube and give the cube the same orientation as the right hand (see Fig. 5)

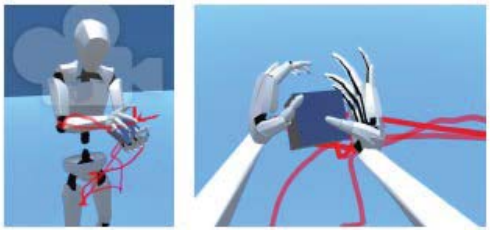


Fig. 5. Skeleton holding the cube in Unity (left) and first person view (right)

The orientation in Unity is a bit tricky because it is in quaternion. It is also possible to use Euler angle instead, but the problem of Euler angles in that kind of 3D application is range. If an angle has $0\text{-}360^0$ range, and if the object rotates of 2^0, from 359^0 to 361^0, the software will understand a rotation from 359^0 to 1^0, because 361^0 is out of range. Thus, the object will rotate 358^0 in the opposite direction of designed rotation of just 2^0. Because of this, it is advisable to use quaternions, which do not suffer from range limits. A quaternion is a set of 4 values x, y, z, and w, which can describe all orientations. The drawback is that it is not possible to touch one of the four values of a quaternion, as the four

values make a coherent whole. So it is not possible to apply offsets to quaternions by modifying just one value. Therefore, we only make the cube take orientation of just one hand.

Once what to extract is chosen, we visualize data with a Unity asset called Grapher. This asset allows drawing on a graph several components of Unity. By this, we can visualize at the same time object position (x, y and z), object orientation (alpha, beta and gamma) and operator's gravity central position (x, z).

3.2 Data processing

Data are gathered by operator and experiment. We obtain a table of six variables including time, object's position, operator central gravity position. We also derive the derivatives and acceleration of each variable to evaluate the smoothness of the motion.

The skeleton is orientated while calibrating, depending on north direction and not on a specific axis. To correct the orientation, we need to know what direction the skeleton is looking, to be able to align it with z-axis (depth axis), so graphs are easier to understand. We calculate the average orientation on the whole data table considering the looking direction as the projection on horizontal place of the vector formed by skeleton's central gravity as indicate in equation 1.

$$coef_{angle} = \arctan\left(\frac{ave(object_z) - ave(gravity_z)}{ave(object_x) - ave(gravity_x)}\right) \quad (1)$$

To correct position drift, we apply a linear regression on graphs to obtain drift coefficients *c* (see Fig. 6). The correction of position drift and orientation is obtained using equation 2 to 5.

$$newobj_x = \left(obj_x - c_{obj_x} \times t\right)\cos\left(c_{ang}\right) + \left(obj_z - c_{obj_z} \times t\right)\sin\left(c_{ang}\right) \quad (2)$$

$$newobj_z = \left(obj_z - c_{obj_z} \times t\right)\cos\left(c_{ang}\right) + \left(obj_x - c_{obj_x} \times t\right)\sin\left(c_{ang}\right) \quad (3)$$

$$newgra_x = \left(gra_x - c_{gra_x} \times t\right)\cos\left(c_{ang}\right) + \left(gra_z - c_{gra_z} \times t\right)\sin\left(c_{ang}\right) \quad (4)$$

$$newobj_x = \left(gra_z - c_{gra_z} \times t\right)\cos\left(c_{ang}\right) + \left(gra_x - c_{gra_x} \times t\right)\sin\left(c_{ang}\right) \quad (5)$$

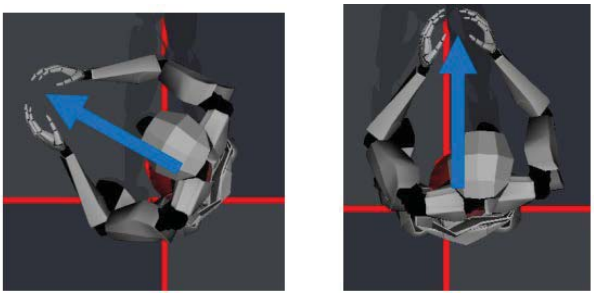


Fig. 6. Orientation correction before (left) and after (right)

With these corrections, the graphs are much clearer as shown in Figure 8,9,10, respectively represent for Expert, Intermediate, and Beginner data. Each figure shows three graph indicating the object position in horizontal plane, the object height, and operator gravity center.

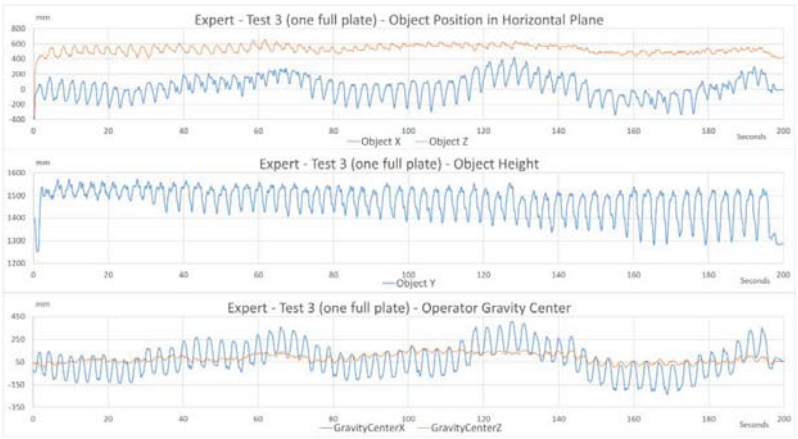


Fig. 8. Expert graphs

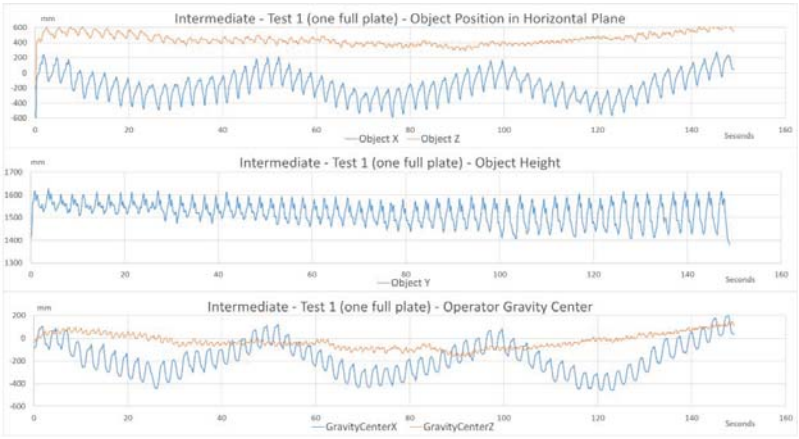


Fig. 9. Intermediate graphs

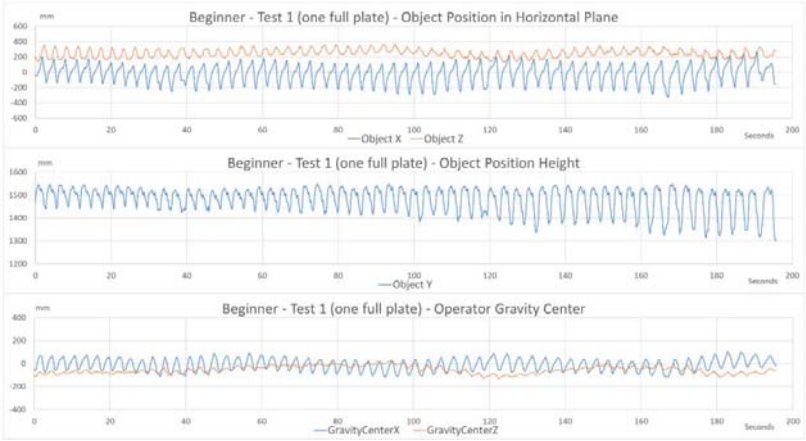


Fig. 10. Beginner graphs

4. Analysis and conclusion

In all three graphs, each little wave corresponds to one part's inspection which has 60 in total. We can also see it in operator central gravity as we apply the balancing from left to right. There is also a slow oscillation of three periods, which corresponds to the six rows of a plate. Indeed, the operator

moves progressively to stay between where he takes and where he put the work piece. Thus, the operator changes direction six times when he changes of rows. The depth (z-axis) is nearly constant compared to left-right displacement (x-axis). The height has more and more amplitude over time. To be more precise, the upper pictures of each graph are nearly aligned and correspond to the inspection height, and the lower pictures correspond to the height of the plate's row. As the plate is inclined, operator takes parts lower and lower. The fastest and most regular operator is the intermediate because he is the most used to this work. However, expert is the smoothest (see the sinus shape of curve on Fig. 25), maybe because he studies the most about the PIV and know how to optimize his movements. Beginner has less rhythm than the two others do. We cannot find the slow oscillation corresponding to the six rows. In addition, he has less amplitude in his movements. However, his movement is very stable. He probably just lacks of experience or has difficulties to synchronize balancing with inspection.

In this study, we apply PVI method to analyze the rhythmic of the movement in product inspection. The authors use Perception Neuron equipment as the motion capture device and connect it to Unity3D software to analyses the rhythmic in the working behavior of expert, intermediate, and beginner user. From analysis results, the training processes for inspection operators using PVI can be derived. In the next study, we will propose the training application applying this approach to improve work conditions and health of inspection operators. It would be a big help for production quality control in industry regarding to the improvement of working condition of the workers. The proposal can help to increase the productivity by improving inspection's efficiency and speed.

References

[1] N. Ryosuke, I. Ippei, M. Toshiyuki, Development of a Training System for Visual Inspection Method utilizing Peripheral Vision, Journal of Japan Industrial Management Association, Vol. 66, No. 3 p. 267-276, 2015.

[2] B.M. Kleiner and C.G. Drury, Design and Evaluation of an Inspection Training Program, Appl. Ergon., Vol. 24, No. 2, pp. 75-82,1993.

[3] N. Ryosuke, S. Keisuke, M. Toshiyuki, A Study on the Effect of Inspection Time on Defect Detection in Visual Inspection, Advances in Production Management Systems (APMS), IFIP Advances in Information and Communication Technology, AICT-414 (Part I), pp.29-39, 2013.

[4] M. Toshiyuki, S. Hideki and S. Keisuke, A Study on Effective Methods of Visual Inspection for Reused-Parts by Inspectors, Human Interface and the Management of Information. Designing Information Environments. Human Interface, pp. 131-139, 2009.

[5] Noitom Ltd.: Perception Neuron (2015). https://neuronmocap.com/

Study of the possibility of syngas making from the industrial scale continuous downdraft coffee husk gasifier

Associate Professor. Dr.-Ing. Nguyen Dinh Tung [1,*];

[1] Vietnam Research Institute Agricultural Machinery - RIAM, No 8- Tran Phu Road, Ha Dong-Hanoi-Vietnam; ndtung@riam.com.vn; ndtung.hn@gmail.com

[*] Correspondence: ndtung@riam.com.vn; ndtung.hn@gmail.com; Tel.: 0989741728

Academic Editor:

Keywords: Syngas, coffee husk gasifier, continuous downdraft gasification of coffee husk.

Abstract: The content of the article presents the research results of the possibility of syngas making from the industrial scale continuous downdraft coffee husk gasifier. Survey results show that in syngas, the ratio of main combustible gas components obtained is as follows: CO ≈ 29.07 %, H_2 ≈ 11.97 %, CH_4 ≈ 2.16 %, moreover, it was able to determine the effect of temperature on the ratio of some component gases made during gasification. Thanks to experimental optimization process, it was able to find optimal technological parameters so that the quality of syngas obtained is best achieved, specifically, the optimal parameters are: moisture content (10.52 %); wind flow (56.75 m^3/h); fuel consumption rate (100.35 kg/h).

1. Introduction

Vietnam is an agricultural country, currently a large proportion of its population is engaged in agriculture. Its technology, equipment for agricultural production is still backward, largely produced in craft form. Therefore, the advanced, modern technologies are not yet applied in agricultural production, especially in post-harvest processing area. Thus, currently in Vietnam, the process of producing, processing agricultural produce, besides the main products obtained after processing raw, there are other subproducts, for example in coffee processing field. For example with the current coffee area of Vietnam, every year it releases hundreds of thousand tons of coffee pods from the milling process [1-7]. However, the amount of that coffee husk is being considered natural "waste", which is being wasteful, more dangerously, it becomes a cause of environmental pollution such as the situation of its pouring into rivers, canals, or burned off right in the field (figure 1) [1-3],.… therefore, apart from causing environmental pollution (water environment, gas environment) it also causes energy waster, which most remarkably this renewable energy source can be used to replace fossil fuels such as coal, oil and natural gas are still used for processing. Therefore, it is necessary to select, find out technological solution to reuse this redundant coffee husk to be converted into alternative renewable enegy sources to replace fossil fuel sources is very necessary to Vietnam in the current period. Therefore, the application of coffee husk gasification in continuous downdraft principle will be an optimal solution, the results bring us economic results, improving the export product quality, and contribute to reducing environmental pollution.



Figure 1. Coffee husk after processing is released causing environmental pollution [2-4].

2. Material, Methodology

2.1. Research material

The materials served in this study is coffee husk in Taya Nguyen area, and in Son La province of Vietnam released after processing (Figure 2).



Figure 2. Research material (coffee husk) [2,3].

For coffee husk that has special physical, chemical possibilities, there are physical, chemical features, especially the components of such materials as: content of carbon (C), oxygen (O), hydro (H), nitrogen (N), sulfur (S), ash (a) and low heat value of H_u material is shown in table 1.

Table 1. Physio-chemical properties of coffee husk [1-7].

Composition (%)	**(C)**	**(H)**	**(O)**	**(N)**	**(S)**	**(a)**	**(w)**	**Hu (kj/kg)**
Coffee husk	44.8	6.2	36	0.96	-	3.1	8.87	16.22
Density	330 (kg/m^3)							

2.2. Methodology

The methodology in this article is combined between empirical research methods and optimal experimental planning.

2.3. Measurement equipment in the research

For the empirical research results of research results, the precision of results is affected by many factors, in which partly due to measurement equipment. The measurement equipment used in the experiment (figure 3), includes: a- table scale to verify quantity (VN); b- gun-type handheld temperature device (Ebro – Germany); c- Wind flow and velocity measuring machine (Testo – Germany); d- engine velocity controlling inverters; e- ammeter to measure the consumed electricity (Germany); f- pre-gasification material humidity measuring machine; g- environmental monitoring measurement equipment to measure syngas elements); h- deployment of syngas empirical experiment (syngas); besides there are temperature sensors measuring the inner temperature of reactors.

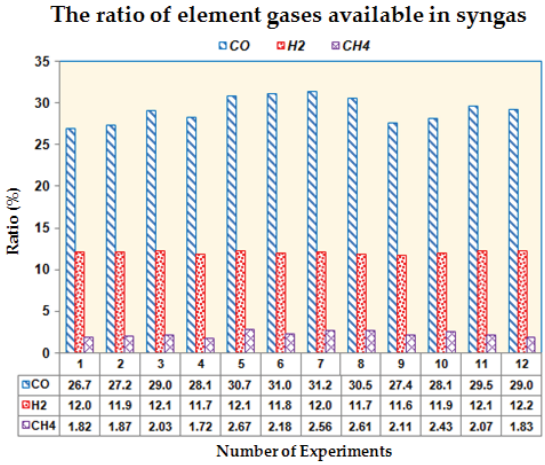


Figure 3. Gas measuring and analytic equipment in empirical research [2,3,11].

3. Research results and discussion

3.1. Empirical research results

The empirical experimental research of the coffee husk gasifier to evaluate the quality of syngas produced as the scientific base to evaluate the suitability with the types of gasifiers which have been designed, manufactured and/or necessary to renovate, redesign of equipment. The results of empirical research are monitored, analyzed to test the concentration of element gases (CO, H_2, CH_4…) included in syngas. The empirical results of analyzing the concentration of syngas during gasification process are shown on the diagram in Figure 4.



	1	2	3	4	5	6	7	8	9	10	11	12
CO	26.7	27.2	29.0	28.1	30.7	31.0	31.2	30.5	27.4	28.1	29.5	29.0
H2	12.0	11.9	12.1	11.7	12.1	11.8	12.0	11.7	11.6	11.9	12.1	12.2
CH4	1.82	1.87	2.03	1.72	2.67	2.18	2.56	2.61	2.11	2.43	2.07	1.83

Figure 4. Empirical results verifying the ratio of element gases available in syngas formed during gasification process.

The quality of syngas formed during gasification process is evaluated through the ratio of main element combustible gases such as (CO, CH_4, H_2). The empirical results reveals the value of gas elements of CO (29.07 %), H_2 (11.97 %), CH_4 (2.16 %). According to the author [10] Steinbrecht D. With the low calorific value of the gas components are as follows: for carbon monoxide CO (12.64 MJ/m^3(N)); methane CH_4 (35.88 MJ/m^3(N)); hydrogen H_2 (10.78 MJ/m^3(N)), comparing this result with research results published in documents [8], [9] and of some other authors published in the world for biomass gasification, it is shown that the quality of syngas when gasifying coffee husk is very good. However, during gasification, the ratio of element gases made also depends on temperature parameter. In Figure 5 it clearly shows the characteristic lines about the effect of gasification temperature to the ratio of element gases formed in syngas.

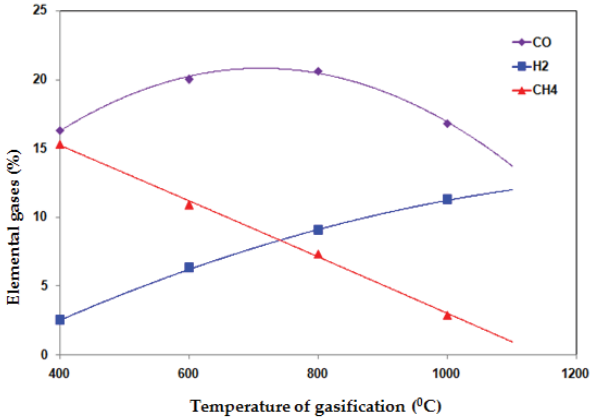


Figure 5. Diagram showing the effect of gasification temperature to the ratio of element gases made in syngas.

Through diagram 5 it is shown that the effect of gasification temperature to the forming ratio of CO and CH_4 is more than the gas element of H_2. On the other hand, the empirical results are carried out many times to find out the "optimal" value zone for technological parameters to define the most "reasonable" value to these gas elements. To find the optimal parameters but minimize the times of

experiments, saving costs for experiments, the author has used empirical planning method in research.

3.2. Optimal research results according to empirical planning method

The scientific basis of quality assessment of gasification process is evaluated through syngasifying capabilities, which should include key gas components such as (CO, H_2, CH_4), syngas quality is affected by some major technological elements such as moisture of the gasification material, airflow provided for gasification process (which is the primary oxygen amount), ratio of consumed fuel,... Actually during gasification process, due to many changing elements with different degrees, if one wishes to reduce to number of experiments but still ensure the precision of experiments, it is necessary to use empirical planning method, from which determining optimal parameters as bases to decide or select the technological process to create products suitable with results when doing empirical research. In this research, the author selects Box-Behnken matrix with 3 influential factors which have been coded to be used for research for coffee husk continuous gasification furnace, specifically.

Encrypted influential factors:

X_1 – Material humidity /coffee husk (%)

X_2 – Air flow (m^3/h)

X_3 – Consumed fuel ratio (Kg/h)

Conduct the experiment according to the method of building math functions based on regression equations in the form of degree 2 polynomy. The experimental results of several factors affecting the gasification process, according to the experimental matrix shown in the following table:

Table 2. Coded value of factors when experimenting coffee husk gasification.

Variable	Symbol	Unit	Level		
			-1	0	1
Material humidity /coffee husk	X_1	(%)	10	11	12
Airflow	X_2	(m^3/h)	50	55	60
Consumed fuel ratio	X_3	(kg/h)	90	100	110

On table 2 it is shown that the material humidity varied within 10 – 12 % moisture, the air flow varied within 50 - 60 m^3/h and the consumed fuel amount during gasification varied within 900 – 110 kg/h.

On the other hand, the gasification quality is rated through 3 factors:

Y_1 – Air quality/ratio of CO element (%)

Y_2 – Air quality/ratio of H_2 element (%)

Y_3 – Air quality/ratio of CH_4 element (%)

Build level 2 regression function for the targets:

$$Y_1 = a_0 + a_1X_1 + a_2X_2 + a_3X_3 + a_{12}X_1X_2 + a_{13}X_1X_3 + a_{23}X_2X_3 + a_{123}X_1X_2X_3 \quad (1)$$

$$Y_2 = b_0 + b_1X_1 + b_2X_2 + b_3X_3 + b_{12}X_1X_2 + b_{13}X_1X_3 + b_{23}X_2X_3 + b_{123}X_1X_2X_3 \quad (2)$$

$$Y_3 = c_0 + c_1X_1 + c_2X_2 + c_3X_3 + c_{12}X_1X_2 + c_{13}X_1X_3 + c_{23}X_2X_3 + c_{123}X_1X_2X_3 \quad (3)$$

Table 3. Empirical matrix of optimizing the coffee husk continuous gasification experiment.

N°Exp	X_1	X_2	X_3	Y_1	Y_2	Y_3
1	-1.0000	-1.0000	-1.0000	26.70	12.00	1.87
2	1.0000	-1.0000	-1.0000	29.00	11.70	2.03
3	-1.0000	1.0000	-1.0000	28.10	12.00	1.72
4	1.0000	1.0000	-1.0000	30.70	11.90	2.18
5	-1.0000	-1.0000	1.0000	31.00	11.60	2.54
6	1.0000	-1.0000	1.0000	31.20	12.10	2.62
7	-1.0000	1.0000	1.0000	30.50	11.80	2.11
8	1.0000	1.0000	1.0000	29.00	12.20	2.05

Building the regression coefficient value table of target functions as in table 4:

Table 4. Target function regression coefficient value.

Regression coefficient of function Y_1		**Regression coefficient of function Y_2**		**Regression coefficient of function Y_3**	
Coefficient	*Value*	*Coefficient*	*Value*	*Coefficient*	*Value*
a_0	29.525	b_0	11.912	c_0	2.140
a_1	0.450	b_1	0.062	c_1	0.080
a_2	0.050	b_2	0.062	c_2	-0.125
a_3	0.900	b_3	0.013	c_3	0.190
a_{12}	-0.175	b_{12}	0.012	c_{12}	0.020
a_{13}	-0.775	b_{13}	0.162	c_{13}	-0.075
a_{23}	-0.725	b_{23}	0.013	c_{23}	-0.125
a_{123}	-0.250	b_{123}	-0.038	c_{123}	-0.055

From which we can define the regression equation (1), (2), (3) as follows:

Air quality regression equation /ratio of CO gas element made:

$$Y_1 = 29,525 + 0,45X_1 + 0,05X_2 + 0,9X_3 - 0,175X_1X_2 - 0,775X_1X_3 - 0,725X_2X_3 - 0,25X_1X_2X_3$$

Air quality regression equation /ratio of H_2 gas element made:

$$Y_2 = 11,912 + 0,062X_1 + 0,062X_2 + 0,013X_3 + 0,012X_1X_2 + 0,162X_1X_3 + 0,013X_2X_3 - 0,038X_1X_2X_3$$

Air quality regression equation /ratio of CH_4 gas element made:

$$Y_3 = 2,14 + 0,08X_1 - 0,125X_2 + 0,19X_3 + 0,02X_1X_2 - 0,075X_1X_3 - 0,125X_2X_3 - 0,055X_1X_2X_3$$

On this basis, establish models expressing the values from the above regression equation.

Model reflecting CO air quality made of gasification is expression in equation (1), model reflecting H_2 air quality made of gasification is expressed in (2), mdel reflecting CH_4 air quality made of gasification is expressed in equation (3). The value of regression coefficients of target function is expressed in table 4. From here we have the effect diagram and interaction diagram of regression value to target function Y_1 , Y_2, Y_3 as in Figure 6 to Figure 17.

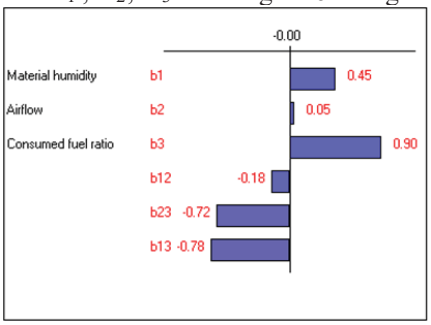


Figure 6. Diagram of the effect of regression value to the target function Y_1

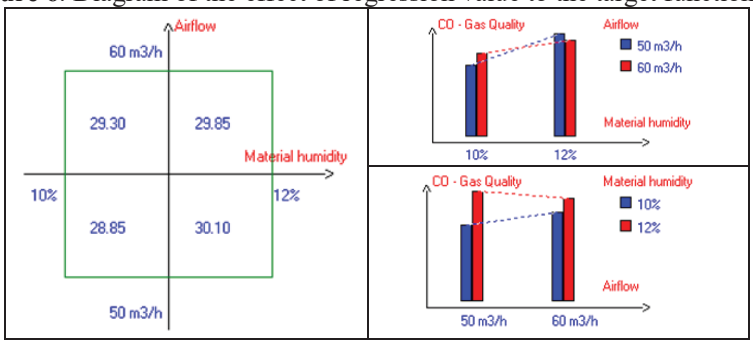


Figure 7. Diagram of the interaction (Y_1) between material moisture and air flow.

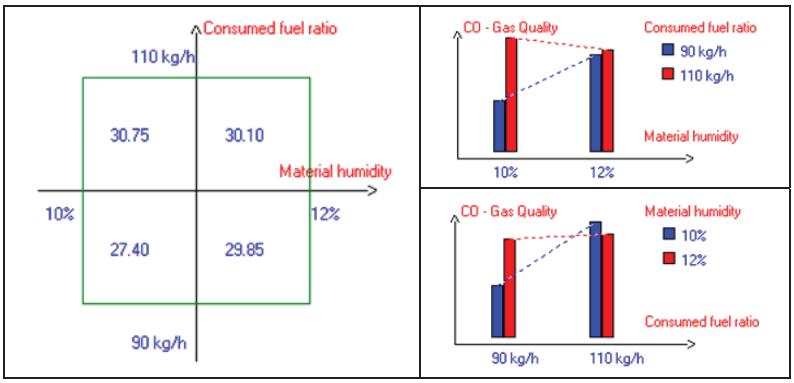


Figure 8. Diagram of the interaction (Y_1) between material moisture and consumed fuel ratio.

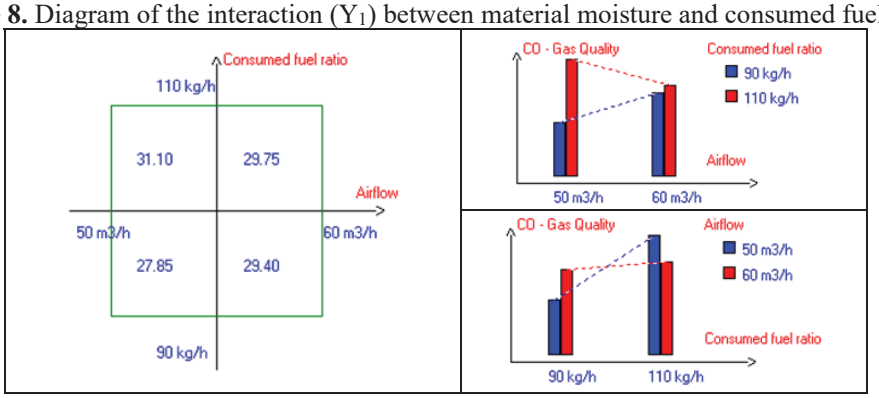


Figure 9. Diagram of the interaction (Y_1) between airflow and the consumed fuel ratio.

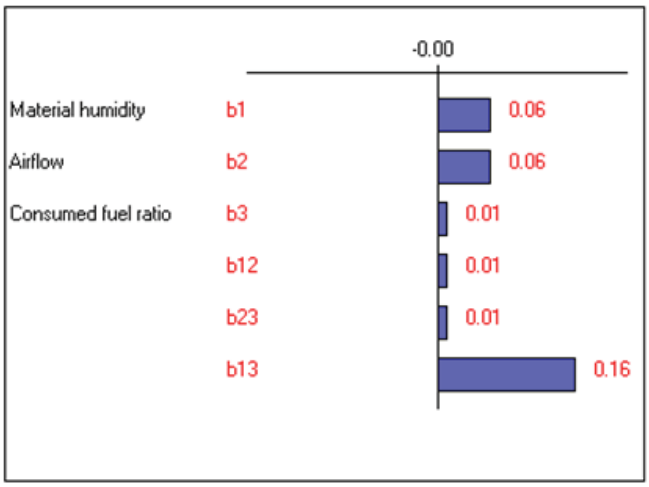
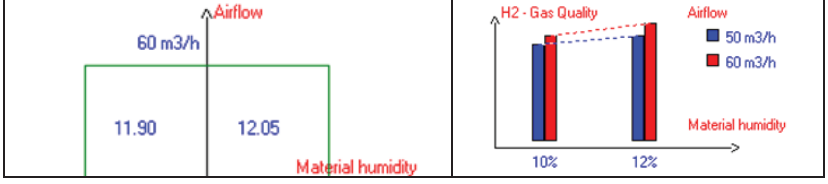


Figure 10. Diagram of the effect of regression value to the target function Y_2.



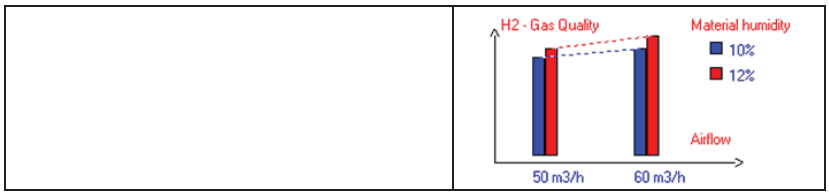


Figure 11. Diagram of the interaction of (Y_2) between material moisture and air flow

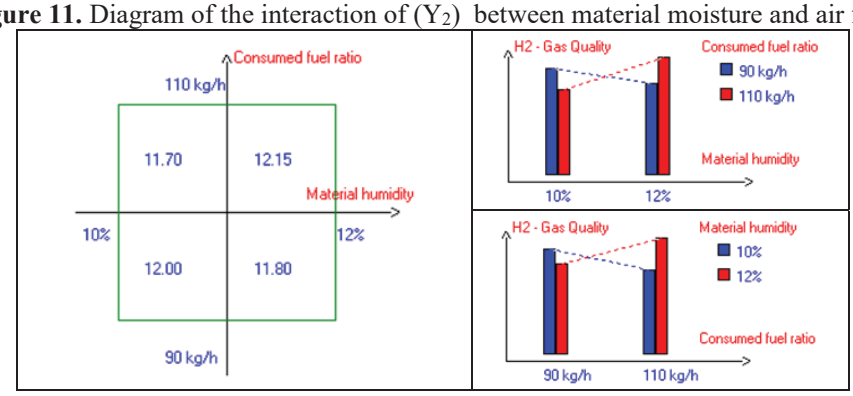


Figure 12. Diagram of the interaction of (Y_2) between material moisture and consumed fuel ratio.

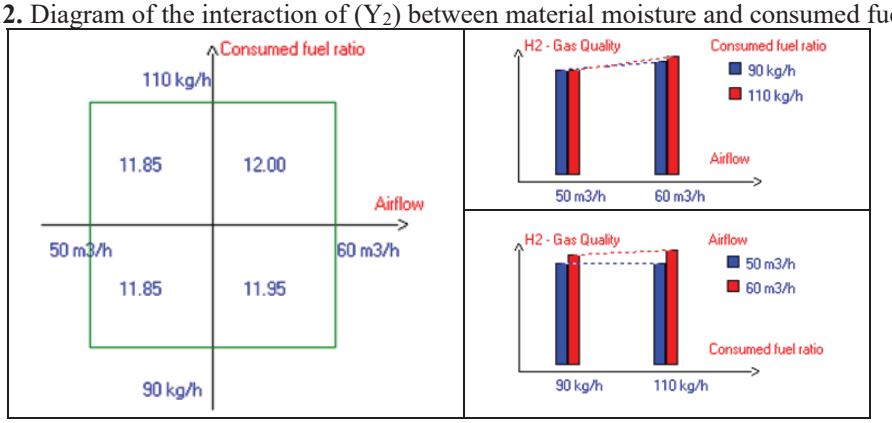


Figure 13. Diagram of the interaction of (Y_2) between the air flow and the consumed fuel ratio.

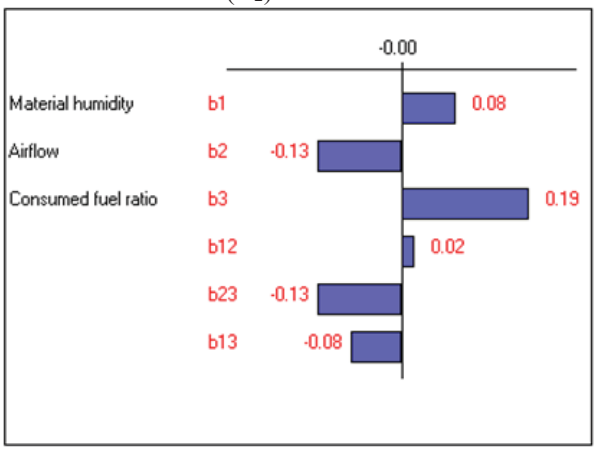


Figure 14. Diagram of the effect of regression value to the target function Y_3.

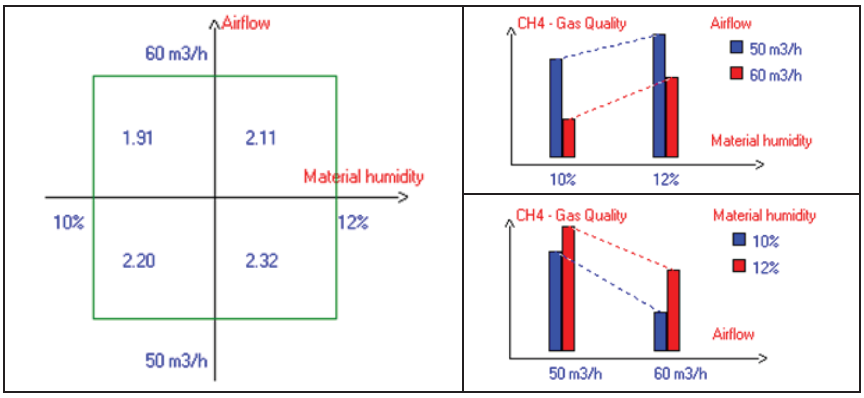


Figure 15. Diagram of the interaction of (Y_3) between material moisture and airflow

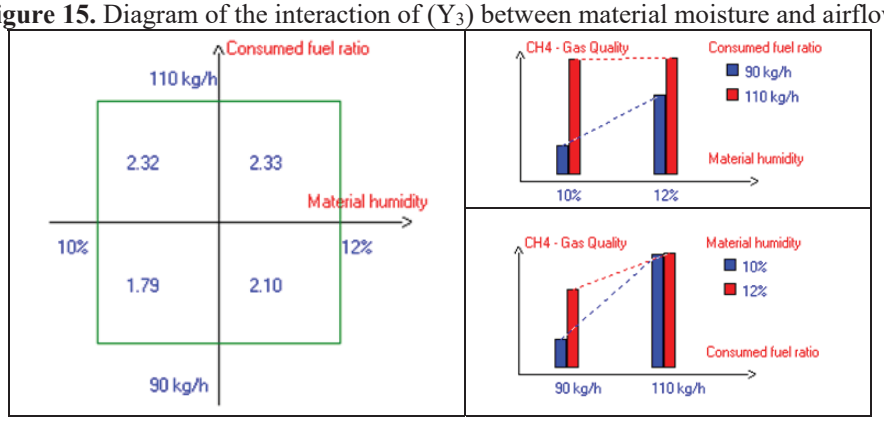


Figure 16. Diagram of the interaction of (Y_3) between material moisture and consumed fuel ratio.

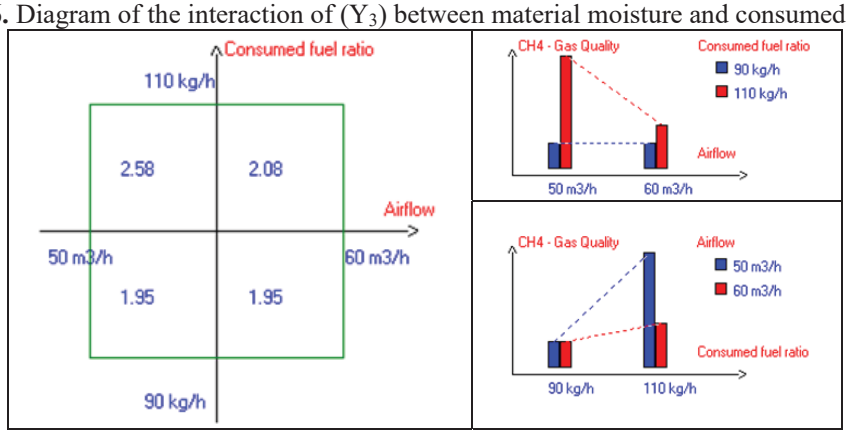


Figure 17. Diagram of the interaction of (Y_3) between airflow and consumed fuel ratio.

The results shown as in diagrams, from the diagram of Figure 7 to Figure 17, it reveals that the interaction/influential degree between technological elements (material moisture upon gasification, airflow (primary oxygen amount), consumed fuel amount) during gasification to the capabilities of making syngas. The variation in each diagram all reveals the effect on the optimization process. Here the author optimizing the factors affecting the quality of gasification process according to expect algorithmic function with 3 target functions as follow:

- *The quality of CO expected to achieve is the greatest,*
- *The quality of H_2 expected to achieve is the greatest,*
- *The quality of CH_4 expected to achieve is the greatest,*

The optimization results is expressed through Figure 18.

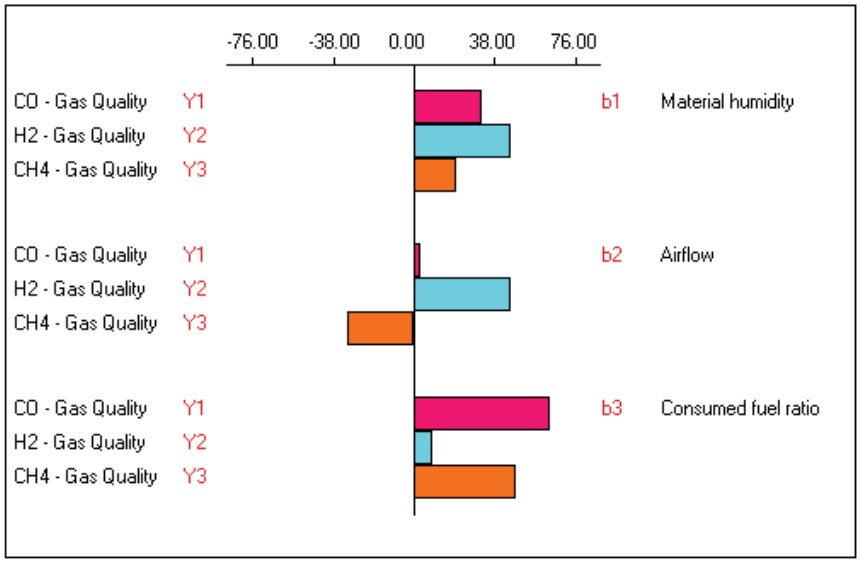


Figure 18. Optimal results of technological elements.

From the diagram in Figure 18 it is shown that, the optimal results in the quality of syngas produced during continuous coffee husk gasification with the coded elements such as the moisture of the selected material was **10.52 %** at this moisture, the consumed fuel ratio was **100.35 kg/h** and the wind flow needed to supply for gasification was **56.75 m^3/h**. With these values, the gasification process can find optimal value with the ratio of component gas ratio available in syngas, specifically *(CO is 29.1 %; H_2 is 12 %; CH_4 is 2.24 %)*. This result can achieve the expected outcome and suitable with the experimental results presented in item 3.1.

4. Conclusion

The experimental results have been identified: i)- the ratio of element gases inlcuded during gasification process, specifically CO (29.07 %), H_2 (11.97 %), CH_4 (2.16 %), comparing this result with the biomass gasification such as wood chips, rice husks, corn cobs,... shows that the quality of coffee husk gasification was excellent; ii)- from experimental results as in diagram 5, it reveals that the effect of gasification temperature to the formation ratio of CO and CH_4 more than the elements of H_2.

Thanks to the empirical planning model, it is possible to define the optimal value with technological parameters such as: material moisture (10.52 %), consumed fuel ratio (100.35 kg/h) and airflow needed to supply for the gasification process (56,75 m^3/h). With this technological regime, the ratios of element gases such as CO, H_2, CH_4 included in syngas reached the highest value, respectively corresponding to 29.1 %; 12 % and 2,24 %, this result has reached the expected result.

References

[1]. Martin Kaltschmitt, Hans Hartmann, Hermann Hofbauer, Energie aus Biomasse, Springer Verlag. (2011)

[2]. Nguyen Dinh Tung, Theoretische und experimentele Untersuchungen zur energietische Nutzung von landwirtschaftlichen Abfällen aus Vietnam. Dissertation Universität Rostock, Deutschland. (2009)

[3]. STEINBRECHT. D, Technische Verbrennung Emissionen Verfahrenstechnische Berechnungen mit Verbrennungsabgasen, Abschnitt 1. Universitaet Rostock. (2009)

[4]. Tung D. Nguyen, Present State, Potential and the Future of electrical Power Generation from Biomass Residues in Vietnam. Agricultural Engineering International: the CIGR Ejournal. (2009)

[5]. TUNG N.D.; STEINBRECHT D.; BEU J. and BACKHAUS E, Experimental Study on Hemp Residues Combustion in a small Scale Stationary Fluidized Bed Combustor, Agricultural Engineering International: the CIGR Ejournal. Manuscript EE 08 006. Vol. X. August, 2008, S. 1-11.
[6]. TUNG N.D. and STEINBRECHT. D, Modeling a Combined Heat and Power Cogeneration System in Vietnam with a Fluidized Bed Combustor Burning Biomass, Agricultural Engineering International: the CIGR Ejournal. Manuscript EE 08 008. Vol. X. December, 2008, S. 1-22.
Bei: http://www.cigrjournal.org/index.php/Ejounral/article/viewFile/1125/1040 (Dez. 2008).
[7]. TUNG N.D.; STEINBRECHT D. and VINCENT T, Experimental Investigations of Extracted Rapeseed Combustion Emissions in a Small Scale Stationary Fluidized Bed Combustor, Energies, Vol. 2(1), February 2009, pp 57-70.
[8]. Tung Nguyen Dinh et al, Research, design and manufacture the continuous gasification furnace from coffee husk used for coffee coffee drying device capacity 7-8 ton/batch, Ministerial level research topic of 2014, Ministry of Agriculture, Vietnam. (2014)
[9]. Tung Nguyen Dinh, Thanh Nguyen Van, Research, design and manufacture coffee husk gasification furnace operating continuously, heat capacity 100kWh. Vietnam Mechanics Journal, July 2012.
Bei:http://www.mdpi.com/1996-1073/2/1/57; http://www.mdpi.com/journal/energies.
[10]. Tung Nguyen Dinh et al, Research, design and manufacture agricultural residues gasification furnace *(rice husks, corn cobs) on an industrial scale*, State-level research topic of 2014, Ministry of Industry and Trade. (2014)
[11]. UNDP, Biomas Energy for Heating and Hot Water Supply in Belarus. Best Practice Guidelines, Part A: Biomass Combustion. (2005)

Experimental investigation and optimization of machine parameters in high speed cutting of titanium alloys

Ducnam Nguyen[a]
Industrial University of Ho Chi Minh City, Ho Chi Minh City, Vietnam
[a]nguyenducnam@iuh.edu.vn

Keywords: Titanium alloys, surfaces roughness, high speed machining, cutting force

Abstract. Titanium alloys have been widely used in the aerospace, biomedical, chemical, automotive and many other industries, because of their good specific strength, high toughness, high corrosion resistance, low density and bio-compatibility. However, it is very difficult to machine them due to their poor machining conditions. In this study, the influence of machining parameters in high speed machining on cutting force and surface roughness of titanium alloys when turning using TNGT308-AK tool in dry environment were investigated by experiments. The experimental results revealed that the feed rate, nose radius and tool geometries have the greatest influence on the machining process. An L8 orthogonal array and analysis of variance (ANOVA) are used in this study for finding the optimal parameters. The mathematical model obtained as a result of regression analysis can be reliable to predict cutting force and surface roughness. The most significant parameters for cutting force Pz, Py are cutting edge angle and nose radius. The surface roughness Rz is mainly affected by nose radius. The best setting of input process parameters for surface roughness and cutting force in turning are presented in this study.

Introduction

Nowadays, high speed machining method has been widely applied in many industries such as automotive, mold, semiconductor, electronics and aerospace industry. This method is often used for machining difficult-to-cut materials such as titanium alloys, ceramics and hard steel alloys. Especially thin-walled workpieces were processed by high speed machining [1]. Titanium alloys have their excellent properties including excellent corrosion resistance, high strength-to-weight ratio, low density and high temperatures resistance, therefore it is widely used in the industries. However, it is very difficult to machine them due to their poor machining conditions such as low thermal conductivity, low modulus of elasticity and high chemical reactivity at segmented chip formation with other materials at elevated temperatures [2-4]. As a result, the surface quality of workpieces will not be satisfactory, especially in that surface roughness is an important requirement related to the quality of product. Good surface quality of product improves fatigue strength, corrosion resistance, hardness toughness, or creep life. Surface roughness are affected by many factors such as the machining variables, the tool geometry, coolant and vibrations. It is very difficult to take all the parameters that control the surface roughness in the high speed machining. In this study, the influence of machining parameters in high speed machining on surface roughness of titanium alloys when turning using TNGT308-AK tool in dry environment were investigated by experiments. The model of the surface roughness and cutting force has been developed in terms of nose radius, tool geometries and feed rate. With the suitable parameters, the smoother surfaces of titanium alloys with better surfaces roughness can be obtained. Based on the results of experiments, optimize the cutting parameters to achieve the best surface roughness. An L8 orthogonal array of Taguchi method and analysis of variance (ANOVA) are used in this study for finding the optimized solution [5-6]. Selection of best process parameters using various optimization techniques will help to solve the problem of improper surface roughness.

Experimental Setup

Cutting tool insert and workpiece material

The turning experiments were carried out in dry cutting conditions using a Graziano CTX 310 CNC Lathe with a maximum spindle speed of 6000 rpm and the work piece material used was titanium alloys Ti-6Al-4V [7]. The diameter of workpiece was taken 35 mm and cutting length was 150 mm during experiments. The chemical composition of Ti-6Al-4V is given in Table 1. The cutting tool selected for machining is cutting inserts TNGT308-AK (see Fig. 1)

Table. 1 The chemical composition of Ti-6Al-4V

Elements	C	Si	Fe	Al	Ni	V	Cr	Sn	Zr	Ti
Wt %	0.369	0.022	0.112	5.48	0.006	4.22	0.0099	0.0625	0.0028	90.0



Fig.1 Cutting tool insert and workpiece material

Experimental Procedure

The workpiece was mounted by using a pneumatic chuck in CNC turning center and the clamping pressure was set as 8 bar. The machining parameters like feed, depth of cut, cutting speed, etc. were selected in the experiments. The Graziano CTX 310 CNC Lathe was used in the experiments as show in Fig.2.



Fig.2 Graziano CTX 310 CNC Lathe

In this study, except for cutting tool inserts, depth of cut, workpiece material and feed rate, the cutting parameters such as cutting speeds, cutting edge angle and nose radius were changed in the experiments. Based on the results of experiments, optimize the cutting parameters to achieve the best surface roughness and minimum cutting force. A cutting force installation was used to measure the cutting forces in the experiments (as shown in Fig.3). The cutting force in X – direction (Px) is quite small, so it is omitted during the experiment. The workpiece, cutting tool and cutting force installation were shown in Fig.4.

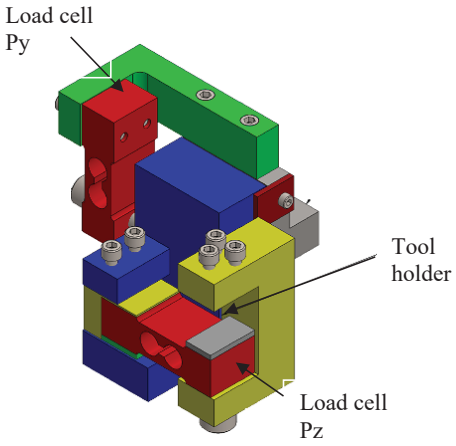


Fig.3 Cutting force installation

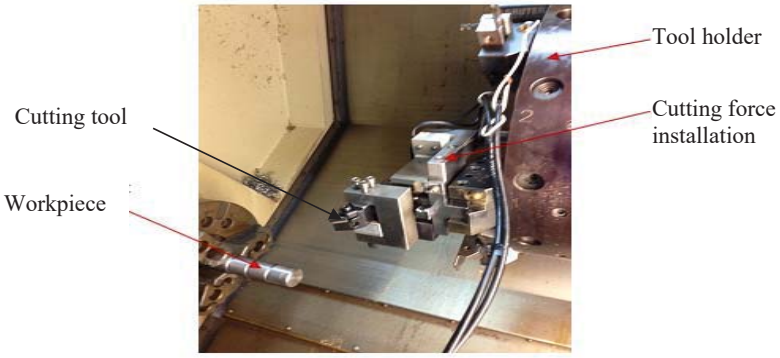


Fig.4 Workpiece, cutting tool and cutting force dynamometer

Design of experiment

The Taguchi method was used to reach more comprehensive a result with lesser experiments for design of experiment. Taguchi method is an efficient method for designing process that optimally over a variety of conditions to optimize designs for performance, quality and cost. The L8 orthogonal array for mixed level design for three parameters which are feed rate, cutting edge angle and nose radius (as presented in table 2). The following process parameters are selected for present work: feed rate (S), tool cutting edge angle (φ), nose radius (R). The depth of cut and velocity cutting are set as 0.2 mm and 220 m/min respectively.

Table.2 Process parameters

Process parameters	Factors	Level 1	Level 2
Feed rate: S (mm/min.)	A	80	160
Nose radius: R (mm)	B	0.2	0.8
Cutting edge angle: φ (^{0})	C	45^0	90^0

Results and Discussion

The experimental procedures were performed on cutting parameters in table 2. The experimental results used for the optimization process are presented in table 3.

Table.3 Process parameters

No.	S (mm/min)	φ (^{0})	R (mm)	Pz (N)	Py (N)	Rz (μm)
1	80	45	0.2	30.8353	17.9705	16.46
2	80	45	0.8	18.2058	14.039	5.4
3	80	90	0.2	11.9895	4.705	17.12
4	80	90	0.8	21.515	11.8935	5.76
5	160	45	0.2	43.9864	17.9361	22.18
6	160	45	0.8	29.4923	23.5635	14.67
7	160	90	0.2	18.7072	8.0148	4.73
8	160	90	0.8	40.2773	22.4622	5.96

The optimization analysis was applied for individual of Pz, Py, Ra parameters and then determine the optimal conditions for the whole parameters.

Optimal conditions for Pz

The ANOVA (Analysis Of Variance) technique is help to determine which parameter is most significant. Where, DF – Degree of freedom, SS – Sum of Square MS – Mean of Square, F – Statistical parameter, P- Percentage. The percentage distribution of parameters on the cutting force Pz are presented in table 4.

Table.4 Percentage distribution of parameters for Pz

Process parameters	% Contribution
Feed rate S (mm/min.)	35.11
Nose radius R (mm)	0.22
Cutting edge angle φ (^{0})	12.71
S.R	1.46
S. φ	0.02
R. φ	47.76

The most significant factor for the Pz is R.φ and its contribution is 47.76%. The second significant factor for Pz is feed rate S and its contributions is about 35.11%. After that the third significant factor for Pz is cutting edge angle φ and its contributions is about 12.71%. The interaction plot and main effect plot of S, R, φ (PHI) affected on Pz are shown in Figure 5. The mean effects plots are used to determine the optimal conditions for Pz. The ANOVA table for Pz are presented in table 5.

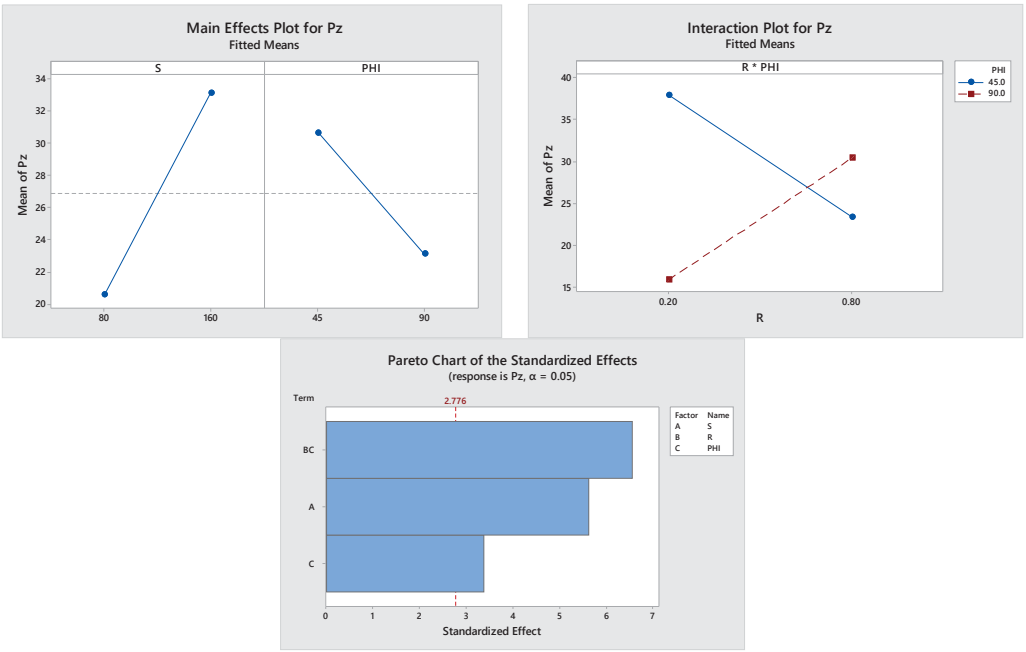


Fig.5 Interaction plot and main effect plot for Pz

Table.5 ANOVA table for Pz

Source	Sum of Squares	DF	Mean Square	F Value	P-value Prob > F
Model	847.8871	3	282.629	28.80688	0.0036
A-S	311.4708	1	311.4708	31.74657	0.0049
C-Phi	112.7304	1	112.7304	11.49001	0.0275
BC	423.6859	1	423.6859	43.18405	0.0028
Residual	39.24466	4	9.811165		
Cor. Total	887.1317	7			
Std. Dev.	3.132278	R-Squared	0.955762		
Mean	26.87611	Adj R-Squared	0.922584		

From the ANOVA table 5, The value of R-Sq (95.6%) implies that 95.6% of variation in response values can be explained by the variations in the control factors considered. The high value of determination coefficient confirms model adequacy, goodness of fit and high significance of model. The regression equation for Pz is:

$$Pz = 26.88 + 6.24\ S - 3.75\ \varphi + 7.28\ R\varphi$$

According to Ramp plots for Pz (as shown in Fig.6), the optimal conditions for cutting force Pz are analysed. The optimal parameters for cutting force Pz are list in table 6.



Fig.6 Ramp plots for Pz

Table.6 Optimal parameters for Pz

Feed rate S (mm/min.)	Nose radius R (mm)	Cutting edge angle φ (^{0})
80.36	0.27	88.49

Optimal conditions for Py

The percentage distribution of parameters affects on the cutting force Py are presented in table 7.

Table.7 Percentage distribution of parameters for Py

Process parameters	**% Contribution**
Feed rate S (mm/min.)	21.89
Nose radius R (mm)	21.83
Cutting edge angle φ (^{0})	28.01
S.R	11.34
S. φ	0.77
R. φ	15.94

The most significant factor for the Py is tool cutting edge angle φ, and its contribution is 28.01%. The second significant factor for Py are feed rate S, nose radius R and its contributions are about 21.89% and 21.83% respectively. After that the third significant factor for Pz is R.φ, S.R and its contributions are about 15.94% and 11.34% respectively. The interaction plot and main effect plot of S, R, φ affects on Py are shown in Figure 7. The ANOVA table for Py are presented in table 8.

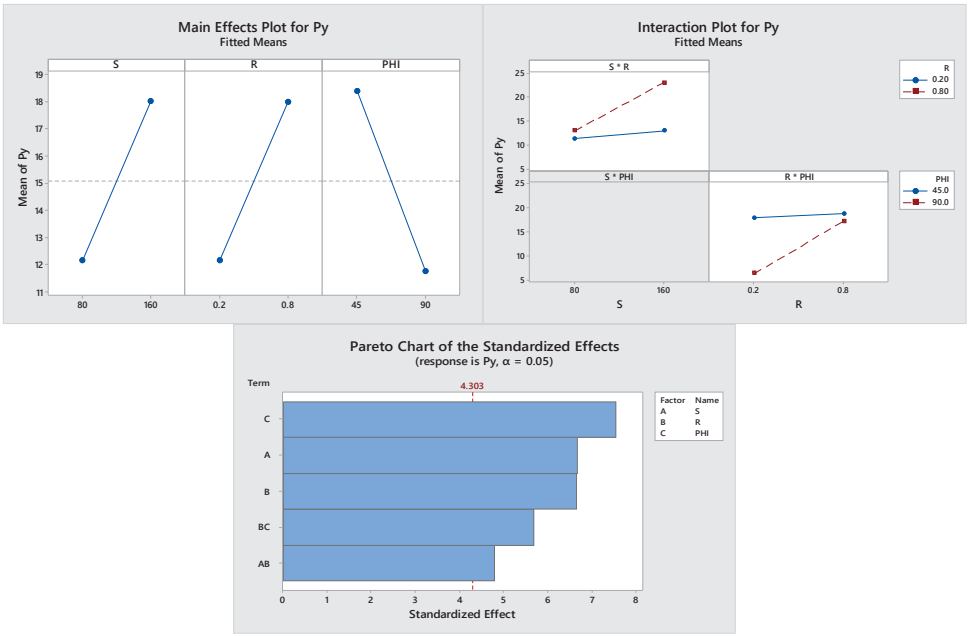


Fig.7 Interaction plot and main effect plot for Py

Table.8 ANOVA table for Py

Source	Sum of Squares	DF	Mean Square	F Value	P-value Prob > F
Model	308.7043	5	61.74087	40.24198	0.0244
A-S	68.26173	1	68.26173	44.4922	0.0217
B-R	68.04632	1	68.04632	44.3518	0.0218
C-Phi	87.34157	1	87.34157	56.92822	0.0171
AB	35.35501	1	35.35501	23.04398	0.0408
BC	49.6997	1	49.6997	32.39369	0.0295
Residual	3.068481	2	1.53424		
Cor Total	311.7728	7			
Std. Dev.	1.238645	R-Squared	0.990158		
Mean	15.07304	Adj R-Squared	0.965553		

From the ANOVA table 8, the value of R-Sq (99.1%) implies that 99.1% of variation in response values can be explained by the variations in the control factors considered. The value of R-Sq (adj) is 96.5 %. The regression equation for Py is:

$$Py = 15.07 + 2.92\ S + 2.92\ R - 3.3\varphi + 2.1\ S.R + 2.49.R.\varphi$$

Based on Ramp plots for Py, the optimal conditions for cutting force Py are presented in Figure 8. The optimal parameters for cutting force Py are list in table 9.

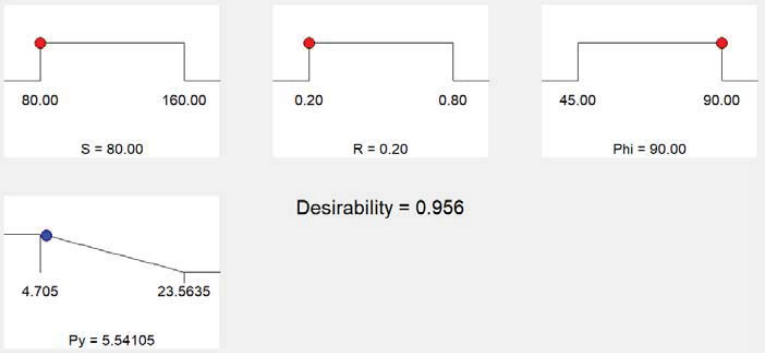


Fig.8 Ramp plots for Py

Table.9 Optimal parameters for Py

Feed rate S (mm/min.)	Nose radius R (mm)	Cutting edge angle φ (^{0})
80	0.2	90

Optimal conditions for Rz

The percentage distribution of cutting parameters affects on the surface roughness Rz are presented in table 9.

Table.9 Percentage distribution of parameters for Rz

Process parameters	**% Contribution**
Feed rate S (mm/min.)	0.30
Nose radius R (mm)	31.49
Cutting edge angle φ (^{0})	24.16
S.R	9.96
S. φ	28.24
R. φ	2.72

The most significant factor for the Rz is nose radius R, and its contribution is 31.49%. The second significant factor for Rz are tool tool cutting edge angle φ, S.φ and its contributions are about 24.16% and 28.24% respectively. After that the third significant factor for Rz is S.R and its contributions are about 9.96%. The interaction plot and main effect plot of S, R, φ affects on Rz are shown in Figure 9. The ANOVA table for Py are presented in table 10.

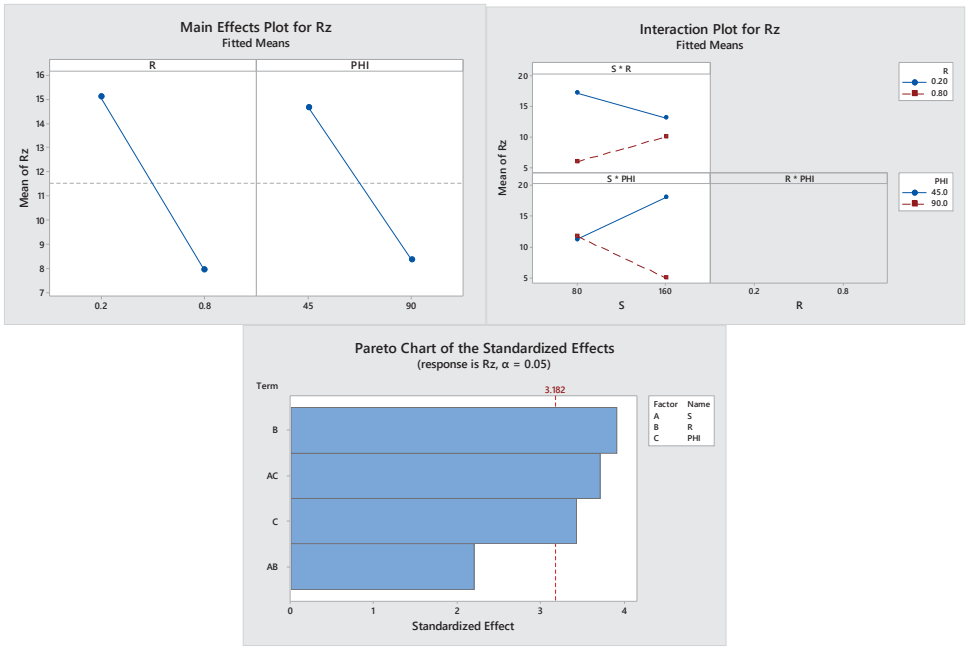


Fig.9 Interaction plot and main effect plot for Rz

Table.10 ANOVA table for Rz

Source	Sum of Squares	DF	Mean Square	F Value	P-value Prob > F
Model	306.8702	4	76.71755	11.45072	0.0367
B-R	102.9613	1	102.9613	15.36781	0.0295
C-Phi	79.00245	1	79.00245	11.79176	0.0414
AB	32.56245	1	32.56245	4.860212	0.1147
AC	92.34405	1	92.34405	13.78311	0.0340
Residual	20.0994	3	6.6998		
Cor Total	326.9696	7			
Std. Dev.	2.588397	R-Squared	0.938528		
Mean	11.535	Adj R-Squared	0.856566		

Base on the ANOVA table 10, the value of R-Sq and R-Sq (adj) are 93.8% and 85.6% respectively. The regression equation for Rz is:

$$Rz = 11.54 - 3.59\ R - 3.14.\varphi + 2.02\ S.R - 3.4\ S.\varphi$$

From Ramp plots for Rz, the optimal conditions for surface roughness Rz are presented in Figure 10. The optimal parameters for surface roughness Rz are list in table 11.



Fig.10 Ramp plots for Rz

Table.11 Optimal parameters for Rz

Feed rate S (mm/min.)	Nose radius R (mm)	Cutting edge angle φ (^{0})
159.29	0.64	89.51

Optimal conditions for Rz, Pz, Py

The order of priority in the optimization process were chosen as Rz, Pz and Py respectively. The optimal conditions for Rz, Pz, Py are presented in Ramp plots Figure 11. The optimal parameters for Rz, Pz, Py are list in table 12.

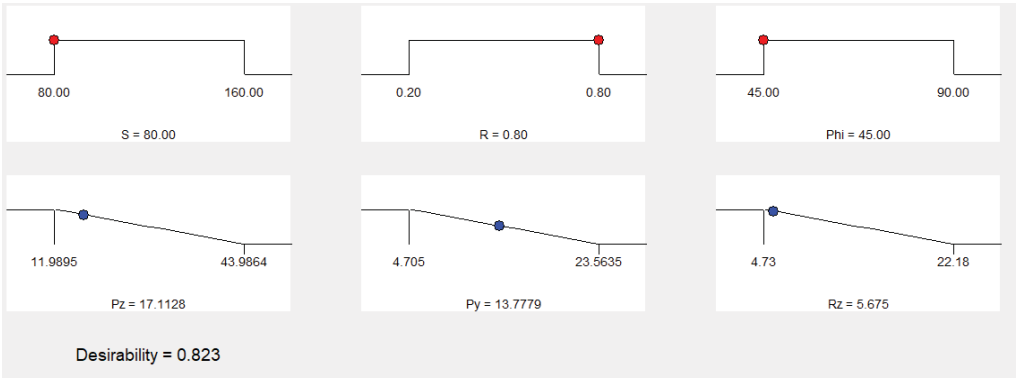


Fig.11 Ramp plots for Rz, Pz, Py

Table.12 Optimal parameters for Rz, Pz, Py

Feed rate S (mm/min.)	Nose radius R (mm)	Cutting edge angle φ (^{0})
80	0.8	45

Conclusions

The present study was carried out to study the effect of input parameters on cutting force and surface roughness. Based on the experiment results, the conclusions can be summarized as follows:

- The most significant parameters for cutting force Pz, Py are tool cutting edge angle and nose radius. The surface roughness Rz is mainly affected by nose radius.
- The mathematical model obtained as a result of regression analysis can be reliable to predict cutting force and surface roughness Rz.
- The best setting of input process parameters for surface roughness and cutting force in turning within the selected range is as follows: Feed rate: 80 (mm/min.), nose radius: 0.8 (mm) and tool cutting edge angle: 45^0.

References

[1] D. Umbrello 2008, Finite element simulation of conventional and high speed machining of Ti6Al4V alloy, Journal of Materials Processing Technology. 196 (2008) 79-87.

[2] S. Sun, M. Brandt, et al., Thermally enhanced machining of hard-to-machine materials - A review. International Journal of Machine Tools & Manufacture, 50 (2010) 663–680.

[3] S. Sun, M. Brandt, et al., Machining Ti–6Al–4V alloy with cryogenic compressed air cooling. International Journal of Tool & Manufacture, 50 (2010) 933–942.

[4] Z.G. Wang, Y.S Wong, et al., High-speed milling of titanium alloys using binderless CBN tools. International Journal of Machine Tools and Manufacture, 45 (2005) 105-114.

[5] U. K. Yadav, Deepak Narang, et al., Experimental investigation and Optimization of machine parameters for surface roughness in CNC turning by Taguchi method, International Journal of Engineering Research and Application. 2 (2012) 2060-2065.

[6] M.P. Vipindas, P. Govindan. Taguchi-Based Optimization of Surface Roughness in CNC Turning Operation, International Journal of Latest Trends in Engineering and Technology. 2 (2013) 454-463.

[7] C.H. Che-Haron, A. Jawaid. The effect of machining on surface integrity of titanium alloy Ti6Al4V. J. Mater. Process. Technol., (2005) 188–192.

Microstructure of FeS Layer Developed on Die Steels by Sulfonitridation

Truong To Quoc[1], Kazuya Horie[1], Makoto Nanko[1,*], Satoru Nishikawa[2], Yoshihiro Kuwabara[2]

[1]Department of Mechanical Engineering, Nagaoka University of Technology, Nagaoka, 940-2188 Japan

[2]Nagaoka Denshi Co., Nagaoka, 940-2188 Japan

*E-mail: nanko@mech.nagaokaut.ac.jp

Keywords: Sulfonitridation; Seizure; Die-steels; FeS; Microstructure.

Abstract. In the automobile industry, a hot hammer die forging method is often utilized for fabricating engine components. The forming method is able to shape metallic product without or with less cutting and grinding. Moreover, products fabricated by a hot hammer forging have the high mechanical strength and its reliability etc. In the forming process, the hot metallic material sometimes adhered to a die made of heat-treated die steel. This phenomenon is called "seizure". In order to prohibit seizure, liquid lubricants are often used but the effects of liquid lubricants are limited. Sulfonitridation of die surface is commonly used for prohibiting seizure of die and hot metallic material. A die made of die steel is heat-treated in gas mixture including NH3 and H2S at temperatures around 520°C. In the heat treatment process, sulfidation and nitridation of steel occur simultaneously. The FeS contentious layer as a solid lubricant layer is developed as the top layer on the nitrided steels. However, microstructure of the FeS layer was not investigated, for example, influences of heat treatment conditions such as temperature and time. In this report, microstructure of the FeS layer produced by sulfonitridation on the die steel (40CrMoV5, JIS-SKD61) is discussed, in particular, influences of nitridation.

Acknowledgements. The author express great appropriate to the financial support for cross-ministerial Strategic Innovation Promotion Program (SIP) supported by The Cabinet Office of Japanese government and Challenge Project in Nagaoka Activation Zone of Energy (NAZE). The author also thanks, Satoru Nishikawa and Yoshihiro Kuwabara, Nagaoka Denshi Co.

SYNTHESIS OF Mo-MODIFIED TiO_2 WITH ENHANCED PHOTOCATALYTIC ACTIVITY

LAN Nguyen Thi[1,a], NGOC Ngo Van[1,b], HA Tran Huu[1,c*], HANG Huynh Thi Thuy[1,d], THUY Le Thi Thanh[1,e], HUNG Nguyen Phi[1,2,f], VO Vien[1,3,g]
[1] Faculty of Chemistry, Quy Nhơn University, Binh Dinh, Vietnam
[2] Institute of Pedagogical and Educational Science, Quy Nhơn University, Binh Dinh, Vietnam
[3] Applied Research Institute for Science and Technology, Quy Nhon University, Binh Dinh, Vietnam
[a] nguyenthilan@qnu.edu.vn
[b] ngovanngoc4321@gmail.com
[c] tranhuuhaqn1992@gmail.com
[d] thuyhangsp93@gmail.com
[e] lethithanhthuy@qnu.edu.vn
[f] nguyenphihung@qnu.edu.vn
[g] vovien@qnu.edu.vn

Keyword: TiO_2, MoO_3, photocatalyst, Ilmenite, modified-TiO_2

Abstract

The Mo-modified TiO_2 was synthesized via facile impregnation combined with pyrolysis of mixtures in several different initial mass ratios of precursors as $m_{Ti(OH)_4}/m_{(NH_4)_6Mo_7O_{24}.4H_2O}$ equaling 5, 10 and 15 in 500 ^oC for an hour. The as-prepared samples, denoted as n-MT-500 within n for the initial mass ratio of precursors, were characterized by X-ray diffraction, scanning electron microscopy, ultraviolet-visible diffuse reflectance spectroscopy, Raman spectroscopy, as well as X-ray photoelectron spectroscopy, which all not only illustrate the presence of TiO_2 and MoO_3 components in the composites but also demonstrate the introduction of Mo hetero-atom into anatase lattice. All of the obtained samples performed higher photocatalytic activity under visible light than TiO_2 via the photodecomposition of RhB in aqueous solution, in which 10-MT-500 exhibits the highest degradation efficiency up to 87% after 5-hour illumination.

Introduction

Since the first time Fujishima and Honda published their work which inspired many scientists to conduct a variety of researches on the field of applying photo-catalytic activity of semiconductor for resolving global problems such as waste-water treatment, green energy generation, clean synthesis for chemical industry, etc., scientists still devolve themselves to bring this methods from academic investigation to real application. Among oxide semiconductors, titanium dioxide, TiO_2, has attracted much attention of researchers in use as photo-catalyst due to its unique properties such as non-toxicity, low-cost, high photo and chemical stability and so on [1]. However, practical application of pure TiO_2 confronts a number of limitations with two main reasons. Firstly, the wide band gap of approximately 3.2 eV causes that TiO_2 is mainly activated under excitation of photons in UV region which only accounts for about 5% in the solar energy spectrum. In order to overcome this inherent objection, various efforts have been conducted to narrow band gap of TiO_2 via doping hetero-elements [2-4]. Secondly, the low photo-catalytic activity of TiO_2 could be attributed to the high-rated recombination of photo-induced charge carriers. For the purpose of surmounting this disadvantage, the strategy of coupling TiO_2 with other semiconductors, which own appropriate conduction band (CB) and valence band (VB) positions is a promising way to assist separation of photo-generated electron-hole pair then enhance the photo-reactivity of TiO_2 [5-8]. Among oxide semiconductors which are suitable for coupling with TiO_2,

molybdenum trioxide, (MoO_3), as one of the most principal layered materials, is an ideal candidate due to its advantages such as high electron-stored ability [9], environmentally friendly as well as relative narrow band gap of 2.85 eV [10] leading to absorption of onset-visible irradiation which is very beneficial for the photo-catalysis.

In this communication, we synthesized the composite of MoO_3/TiO_2 with hierarchical electronic structure via the facile impregnation combined with calcination of precursors. Beside the forming of composites, the as-prepared samples were in a desire of Mo-doping into TiO_2 lattice, due to the smaller radius of Mo^{+6} compared to Ti^{+4}, leading to the reduction of the band gap.

Experiments

Chemicals

Ammonium molybdate tetrahydrate $(NH_4)_6Mo_7O_{24}.4H_2O$ was purchased from China with purity of 99% and used directly without any further modification. Ilmenite ore, as the TiO_2 precursor was collected in Binh Dinh Province, Vietnam.

Decomposition of Ilminite ore

The direct decomposition of Ilmenite ore collected in Binh Dinh, Vietnam, with chemical compositions presented in Table 1, was conducted via the procedure of Zenghe Li et al. [11] with some modifications. In a typical process, 50 g Ilmenite ore was added into concentrated solution of H_2SO_4 in 500 ml three-necked flask then the mixture was stirred continuously in the range of 200 to 210 ^oC for an hour. The dark-purple obtained dispersion, as a solution of $TiOSO_4$, was hydrolyzed and the collected precipitate, as $Ti(OH)_4$, was used as Ti precursor for the next steps.

Synthesis of TiO_2 and MoO_3/TiO_2 composites

The MoO_3/TiO_2 composite was prepared via impregnation combined with pyrolysis in solid-state. In detail, the constant amount of ammonium heptamolybdate tetrahydrate was added into a 50ml aqueous dispersion of $Ti(OH)_4$ within weight ratios of $m_{Ti(OH)_4}/m_{(NH_4)_6Mo_7O_{24}.4H_2O}$ equaling 5, 10 and 15. The obtained mixtures were stirred continuously at room temperature to evaporate solvent then treated the final solid in 500 ^oC for an hour. The as-prepared samples were denoted as nMT-500 in which n represents to the weight ratios of precursors. The pure TiO_2 was synthesized by the same procedure without Mo precursor and denoted as TiO_2. For comparison, the collating sample of pure MoO_3 was synthesized by heating separately ammonium heptamolybdate tetrahydrate following the aforementioned process.

Characterization

Powder X-ray diffraction (XRD) patterns of samples were recorded by a D8 Advance X-ray diffractometer with Cu Kα radiation (λ = 1.540 Å) at 30 kV and 0.01 A. X-ray photoelectron spectroscopy (XPS) was obtained by ESCALab spectrometer (Thermo VG, U.K.). The SEM images of samples were recorded on Nova Nano SEM 450. UV-Vis diffuse reflectance spectroscopy (UV-Vis-DRS) was carried out on Cary 5000 (Varian, Australia). Raman spectra were recorded on T64000 Raman with a 633 nm laser as an excitation source.

Photocatalytic Performance

The photo-catalytic activity of all samples was investigated via the photo-degradation of RhB in aqueous solution under visible light irradiation. In a typical experiment, 0.1 g of nMT500 was added into 80 mL RhB solution with the initial concentration of 20 mg/L. The 220V-100W wolfram bulb with UV cutoff filter provided the source of visible light. Prior to irradiation, the suspension was continuously stirred in the dark for 1.5 hours to ensure the establishment of absorption – desorption equilibrium. At every

irradiation time interval, about 10 mL of the suspension were taken up then centrifuged to remove the photo-catalyst. The concentration change of RhB was measured at 553 nm wavelength on UV-Vis spectrophotometer (CECIL CE2011).

Results and Discussions

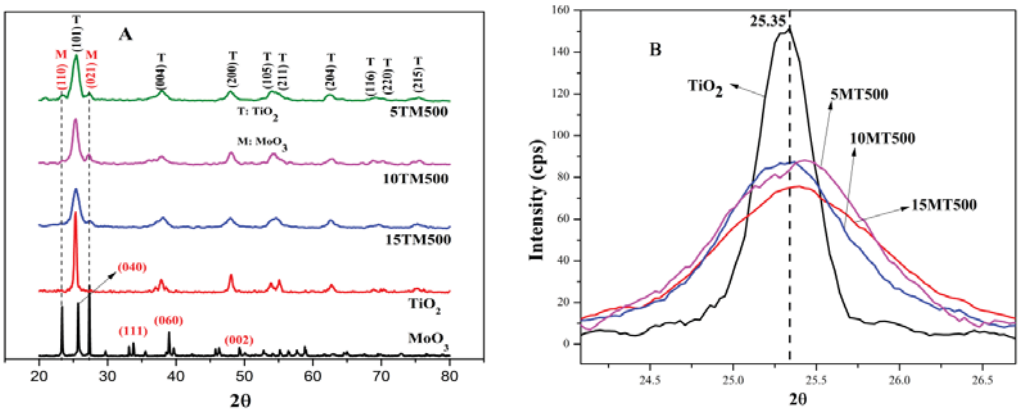


Fig. 1. (A) XRD patterns of TiO_2, MoO_3 and nMT500 (n=5, 10, 15); (B) Comparison in intensity, width and red shift of (101) peaks

Characterization

The XRD patterns of as-prepared samples were presented in Fig. 1. As shown in Fig. 1, the XRD pattern of TiO_2 includes peaks at 2θ = 25.35, 37.9, 48.09, 53.94, 55.06, 62.87, 69.0, 70.4 and 75.3° corresponding to the crystalline planes of (101), (004), (200), (105), (211), (204), (116), (220) and (215) which indicate the well-structured anatase phase of TiO_2 [2, 11-13]. The XRD pattern of collating sample MoO_3 shows peaks at 2θ = 23.4, 25.64, 27.3, 33.86, 39.03 and 49.33° which is consistent with crystalline planes (110), (040), (021), (111), (060) and (002) of orthorhombic MoO_3 (JCPDS Card no. 35-0609) [10, 14]. The nMT500 XRD patterns also include mainly peak system of TiO_2 anatase phase while the characterizing signals of MoO_3 could be only seen at 23.4 and 27.3°, with weak intensity illustrating the low content of this component, which demonstrates that successful formation of MoO_3 insignificantly alters crystallite structure of TiO_2.

Table 1. Crystallite parameter and lattice distortion of TiO_2 and nMT500 (n = 5, 10, 15)

Sample	Particles size (nm)	Lattice Parameters			
		d_{101} (nm)	a (nm)	c (nm)	Lattice distortion ε
TiO_2	21.91843	0.350013	0.378878	0.914248	0.011782
15MT500	6.960279	0.350421	0.379101	0.918379	0.041275
10MT500	8.957081	0.350827	0.377989	0.942502	0.036221
5MT500	7.886819	0.351236	0.378211	0.947005	0.047259

The low content of MoO_3 in the composites, however, could be assigned to another role of incorporating into the TiO_2 lattice of Mo-element. According to Fig 1A, it is obvious to declare that most of the peaks characterizing for TiO_2 in composite XRD patterns become lower in intensity as well as broader compared to pure TiO_2. Actually, particle size of nMT500 (Table 1) calculated via Debye – Scherrer equation is much smaller than that of bare component which could demonstrate that the introduction of Mo-constituent blocked the growth of TiO_2 particles [15-17]. This comment was also confirmed by SEM images in Fig 2. Accordingly, beside the existence of rod-liked blocks which could be attributed to the layered MoO_3, SEM analysis of representative 10MT500 shows that, the surface of materials was surrounded by sphere-liked particles of TiO_2 with much smaller size than pure TiO_2.

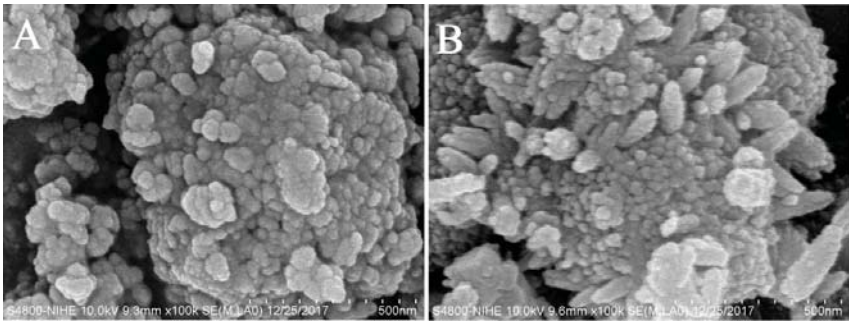


Fig. 2. SEM images of TiO_2 (A) and 10MT500 (B)

Furthermore, comparing to pure TiO_2, the highest intensity peak of (101) plane in nMT500 pattern shows a slight red shift to higher 2θ illustrating the effect of inhibiting crystallite growth. Diminution of anatase crystallite quality could be attributed to the change of anatase lattice parameters. In detail, the lattice parameters as *a* and *c* of building unit of tetragonal anatase TiO_2 was estimated by Bragg's law while the lattice distortion ε of crystal was inferred via Williamson – Hall equation [18] $\varepsilon = \frac{\beta_{hkl}}{4tan\theta_{hlk}}$ where β_{hkl} is full peak width at half maximum of *(hlk)* plane at angle of θ_{hlk}. As shown in Table 1, despite the independence of lattice parameter *a*, the *c* lattice constants as well as the interplanar spacing d_{101} values are in direct proportion to the content of Mo-precursor, which could be ascribed to the incorporation of Mo atom into the anatase lattice. As the result of Mo^{+6} radius (0.62 Å) [19] much smaller than Ti^{+4} (0.68 Å) [16], Mo-atoms could occupy titanium position in crystallite units. In addition, the increase of lattice distortion could be characterized for the introduction of Mo into TiO_2 lattice which could be confirmed in Table 1.

The further investigation on the structure of as-synthesized samples was conducted via Raman spectroscopy which is shown in Fig. 3A. The spectra of 10MT500 show the highest peak of Eg signal located at Raman shift of 143.9 cm^{-1} with a slight red shift compared to TiO_2. The other peaks at around 196, 393, 514 and 637 cm^{-1} are corresponding to signals as E_g, B_{1g}, A_{1g} and E_g [20]. The absence of signals for Mo-O bonding combining the above XRD results could deduce the low content of MoO_3.

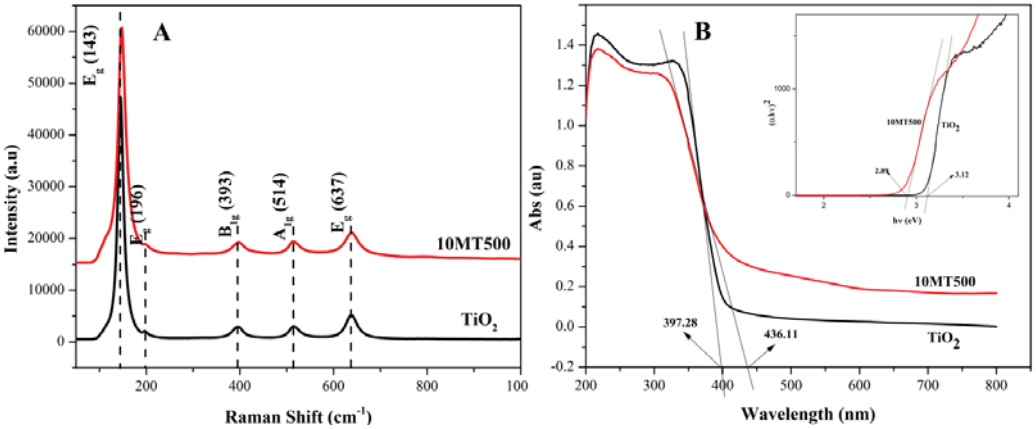


Fig. 3. Raman spectroscopy (A) and UV-Vis DRS (B) of TiO_2 and 10MT500

The insertion of hetero-atom was in the desire of narrowing band gap of TiO_2. The reduction of band gap value could be estimated by UV-Vis DRS analysis. As shown in Fig. 3B, the absorbance of representative 10MT500 in visible light region is much higher than TiO_2 which is favorable for photo-catalytic activity. Band gap values of sample were

calculated by using Kubelka – Munk function [21] and shown in box of Fig. 3B. The pure TiO_2 exhibits a band gap of 3.12 which concurs with the value of previous reports [2-4, 22]. The modified TiO_2 as 10MT500 performs a clear red shift of band gap energy to around 2.89 eV which could be explained by the formation of charge transfer transition at bottom of conduction band of Mo atom [15-17].

In order to clarify the presence of Mo in as-prepared samples, the XPS analysis had been conducted and shown in Fig. 4. Firstly, as shown in Fig5 4A, the Ti2p spectrum of TiO_2 include two peaks at a binding energy (BE) of 459.1 and 464.7 eV which are corresponding to the Ti^{4+} of TiO_2 crystalline [16, 23]. In comparison to the TiO_2, two similar peaks in the Ti2p spectrum of representative 10MT500 located at 459.3 and 465.1 eV, which performs a slight shift to higher BE, indicates the substitution of Mo-atom into anatase lattice [16, 22]. Secondly, in Fig. 4B, peaks at 232.4 and 235.6 eV are attributed to BE of Mo^{+6} in which the difference between these peaks is 3.2 eV in agreement with previous reports [24, 25]. The other state of Mo^{+5} could be confirmed by two peaks at 234.6 and 231.6 eV [12, 16]. In addition, the ratio of peak area between Mo^{6+} and Mo^{5+} (3.65) could estimate that the percentage of Mo^{6+} and Mo^{5+} are 78.5% and 21.5%, respectively. That means that most of Mo exists in samples is Mo^{6+}. The presence of Mo^{5+} was an explanation for the aforementioned comment about the significant increase of lattice parameters *a* and *c*, in which most of the previous literatures recommend that due to larger radius of Mo^{5+} [22, 26]. Additionally, the formation of Mo^{5+} could be clarified due to the state of oxygen insufficiency in anatase lattice [22]. The inadequacy of oxygen could be explained via the difference of O1s spectra between TiO_2 and 10MT500. The O1s core level spectroscopy, as shown in Fig. 4C, is the combination of a peak at 530.1 eV, ascribed to BE of anion O^{2-} in TiO_2 lattice, and a slight shoulder at 531.7 eV, related to the form of absorbed oxygen. By contrast, the intensity increase of shoulder could be observed in the O1s spectrum of 10MT500. The increase of absorbed oxygen in modified sample could be clarified due to the deviation in oxygen coordination number of Ti^{4+} and Mo^{6+} [16].

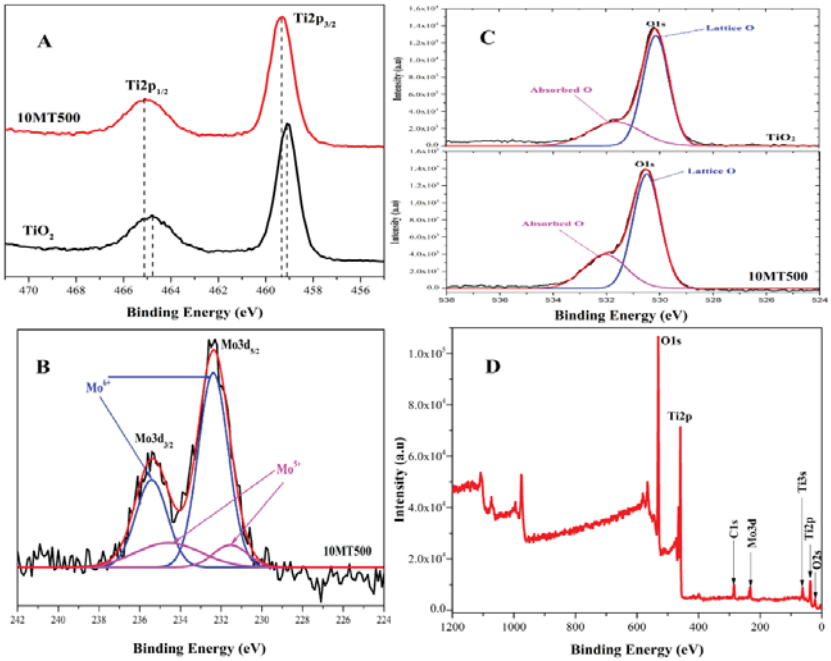


Fig. 4. XPS analysis of TiO_2 and 10MT500

Photo-catalytic activity

Photo-degradation of RhB under illumination of the visible light source was presented in Fig 5. According to the results, all of the modified samples perform higher photodegradation efficiency of RhB than TiO_2 in which 10MT500 exhibits the highest decomposition percentage up to 86.7% after 5-hour visible light irradiation. The enhanced photocatalytic activity of nMT500 compared to TiO_2 could be clarified by parallel effects. Firstly, the insertion of Mo-atom into TiO_2 lattice causes the forming more defects which act as trapping sites to decrease recombination of photogenerated charge carriers. This mechanism was discussed in another previous report of Osmín Avilés-García et al. [17]. Accordingly, after being excited to jump through band gap to the conduction band (CB), the photo-induced electron could be trapped by Mo^{+6} to reduce it to Mo^{+5} then extent lifetime of active species. In the next step, electrons could be donated to or trapped by absorbed oxygen or dye molecules to perform its reactivity. The content of Mo-precursors, however, reach an optimal ratio at 10MT500 then the photo-catalytic activity decrease with 15MT500 which could be explained by the fact that the over-increase of defects could lead to forming more recombination sites preventing the performance of active species [22, 27, 28]. Secondly, the Mo-doping introduce an impurity level in the band gap which is close to the bottom of CB due to the similarity of orbital energy of Mo3d and Ti3d [29] leading to the narrowing its band gap as illustrating by aforementioned UV-Vis DRS analysis. Lastly, the formation of the second semiconductor of MoO_3 could construct a hierarchy energy band structure due to the appropriate CB and VB position of both components. Although pure TiO_2 only activated in the UV region due to its wide band gap [30], band gap between VB of TiO_2 and CB of MoO_3 estimated as 2.6 eV [31, 32] is confirmed that located in the visible region. Therefore, the photo-induced electron could be transferred directly from VB of TiO_2 to CB of MoO_3 though newly-formed Ti-O-Mo bonds [33]. In addition, the Mo-doped TiO_2 with narrower band gap could be activated by photons of onset visible light region to form photo-induced electrons and holes. Hence, the photo-induced electrons could transfer from CB of TiO_2 (-0.25 eV [34]) to more positive CB of MoO_3 (0.52 eV [35]) causing reduction of recombination of photo-induced charge carriers which is beneficial for photocatalysis

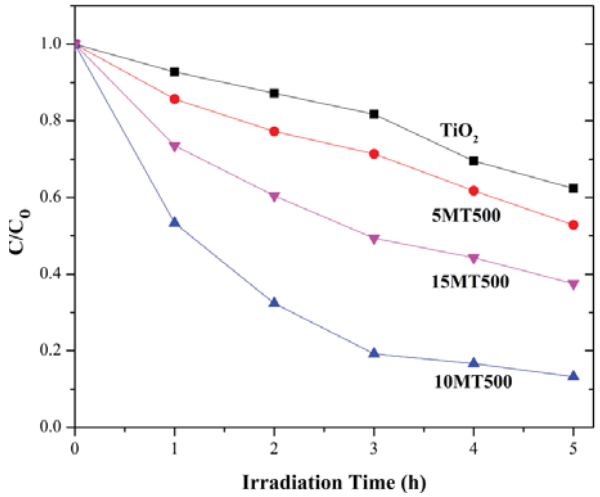


Fig 5. Photo-degradation efficiency of all samples under 5-hour visible illumination

Conclusion

In this work, we report the enhancement in photocatalytic activity of TiO_2 via modification by $(NH_4)_6Mo_7O_{24}$ with facile impregnation synthesis combining heating treatment. All of the characteristic evidences illustrate the role of Mo as hetero-atom inserting in to anatase lattice in the main form of Mo^{6+} beside the small amount of MoO_3 to create heterojunction structure. The results of photo-degradation testing with RhB of all samples

demonstrate improvement in photocatalytic activity of modified samples in which the 10MT500 shows the highest efficiency. The mechanism of this enhancement within a few parallel effects had been discussed.

Acknowledgements: The authors sincerely thank the partial support from Team of VLIR – UOS project with code ZEIN 2016 PR431.

Reference

[1] M. Adachi, Y. Murata, M. Harada, Formation of Titania Nanotubes with High Photo-Catalytic Activity, Chem. Lett., (2000), 8, 942–943.
[2] T. Ali, P. Tripathi, Ameer Azam, Waseem Raza, Arham S. Ahmed, Ateeq Ahmed and M. Muneer, Photocatalytic performance of Fe-doped TiO_2 nanoparticles under visible-light irradiation, Materials Research Express, (2017), 4(1), 015022.
[3] O. Teruhisa, M. Takahiro, M. Michio, Photocatalytic Activity of S-doped TiO_2 Photocatalyst under Visible Light, Chemistry Letters, (2003), 32(4), 364-365.
[4] J. Wang, D. N. Tafen, J. P. Lewis, Z. Hong, A. Manivannan, M. Zhi, M. Li and N. Wu, Origin of Photocatalytic Activity of Nitrogen-Doped TiO_2 Nanobelts, J. Am. Chem. Soc., (2009), 131 (34), 12290–12297.
[5] K.Vinodgopal, I. Bedja, and P. V. Kamat, Nanostructured Semiconductor Films for Photocatalysis. Photoelectrochemical Behavior of SnO_2/TiO_2 Composite Systems and Its Role in Photocatalytic Degradation of a Textile Azo Dye, Chem. Mater., (1996), 8 (8), 2180–2187.
[6] K. Woan, G. Pyrgiotakis, W. Sigmund, Photocatalytic Carbon nanotube – TiO_2 Composites, Advanced Materials, (2009), 21(21), 2233-2239.
[7] J. SukJang, H. Kim, P. H. Borse, J. SungLee, Simultaneous hydrogen production and decomposition of H_2S dissolved in alkaline water over CdS–TiO_2 composite photocatalysts under visible light irradiation, International Journal of Hydrogen Energy (2007), 32(18), 4786-4791.
[8] Q. Xiang, J. Yu and M. Jaroniec, Synergetic Effect of MoS_2 and Graphene as Cocatalysts for Enhanced Photocatalytic H_2 Production Activity of TiO_2 Nanoparticles, J. Am. Chem. Soc., (2012), 134(15), 6575–6578.
[9] Q. Liu, J. Hu, Y. Liang, Z. C. Guan, H. Zhang, H. P. Wang, and R. G. Du, Preparation of MoO3/TiO2 Composite Films and Their Application in Photoelectrochemical Anticorrosion, Journal of The Electrochemical Society, (2016), 163(9), C539-C544.
[10] A. Chithambararaj, N. S. Sanjini, S. Velmathi and A. C. Bose, Preparation of h-MoO_3 and α-MoO_3 nanocrystals: comparative study on photocatalytic degradation of methylene blue under visible light irradiation, Phys. Chem. Chem. Phys., (2013), 15, 14761-14769.
[11] Z. Li, Z. Wang, G. Li, Preparation of nano-titanium dioxide from ilmenite using sulfuric acid-decomposition by liquid phase method, Powder Technology, (2016), 287, 256–263.
[12] N. Boonprakob, N. Wetchakun, S. Phanichphant, D. Waxler, P. Sherrell, A. Nattestad, Jun Chen, Burapat Inceesungvorn, Enhanced visible-light photocatalytic activity of g-C_3N_4/TiO_2films, J. Colloid Interface Sci., (2014), 417, 402-409.
[13] R.A. Senthil, J. Theerthagiri, A. Selvi, J. Madhavan, Synthesis and characterization of low-cost g-C_3N_4/TiO_2 composite with enhanced photocatalytic performance under visible-light irradiation, Optical Materials, (2017), 64, 533-539.
[14] I. Shakir, J. H. Choi, M. Shahid, Z. Ali and D. J. Kang, MoO_3-MWCNT nanocomposite photocatalyst with control of light-harvesting under visible light and natural sunlight irradiation, J. Mater. Chem., (2012), 22, 20549.
[15] J. Huang et. al., Synthesis and Photocatalytic Activity of Mo-Doped TiO_2 Nanoparticles, Hindawi Publishing Corporation Journal of Spectroscopy, (2015), 2015, ID 681850, 8 pages.
[16] S. Wang, L.N. Bai, H.M. Sun, Q. Jiang, J.S. Lian, Structure and photocatalytic property of Mo-doped TiO_2 nanoparticles, Powder Technology, (2013), 244, 9–15.

[17] Osmín Avilés-García, Jaime Espino-Valencia, Rubí Romero, José Luis Rico-Cerda, Manuel Arroyo-Albiter, Reyna Natividad, W and Mo doped TiO_2: Synthesis, characterization and photocatalytic activity, Fuel, 2017, 198, 31-41.
[18] V.D. Mote et. al., Williamson-Hall analysis in estimation of lattice strain in nanometer-sized ZnO particles, Journal of Theoretical and Applied Physics, (2012), 6(6).
[19] L. Gomathi Devi, B. Narasimha Murthy, S. Girish Kumar, Photocatalytic activity of V^{5+}, Mo^{6+} and Th^{4+} doped polycrystalline TiO_2 for the degradation of chlorpyrifos under UV/solar light, Journal of Molecular Catalysis A: Chemical, (2009), 308, 174–181.
[20] Fei Kong, Li Huang, Leilei Luo, Sheng Chu, Ying Wang and Zhigang Zou, Synthesis and Characterization of Visible Light Driven Mesoporous Nano-Photocatalyst MoO_3/TiO_2, Journal of Nanoscience and Nanotechnology, (2012), 12, 1931–1937.
[21] Fattima Al-Zahra, G. Gassim, Ahmed N. Alkhateeb, Photocatalytic oxidation of benzyl alcohol using pure and sensitized anatase, Desalination, (2007), 209, 342–349.
[22] Matiullah Khan, Junna Xu, Wenbin Cao and Zi-Kui Liu, Mo-Doped TiO_2 with Enhanced Visible Light Photocatalytic Activity: A Combined Experimental and Theoretical Study, Journal of Nanoscience and Nanotechnology, (2014), 14, 6865-6871.
[23] W. K. Jo, T. Adinaveen, J. J. Vijaya and N. C. S. Selvam, Synthesis of MoS2 nanosheets supported Z-scheme TiO_2/g-C_3N_4 photocatalysts for the enhanced photocatalytic degradation of organic water pollutants, RSC Adv., (2016), 6, 10487-10497.
[24] L.E. Firment, A. Faretti, Stoichiometric and oxygen deficient MoO_3 (010) surfaces, Surface Science, (1983), 129, 155-176.
[25] T. H. Fleisch, G. J. Mains, An XPS study of the UV reduction and photochromism of MoO_3 and WO_3, Journal of Chemical Physics, (1982), 76, 780-788.
[26] V. Štengl and S. Bakardjieva, Molybdenum-Doped Anatase and Its Extra-ordinary Photocatalytic Activity in the Degradation of Orange II in the UV and vis Regions, J. Phys. Chem. C, (2010), 114(45), 19308–19317.
[27] Batzill M, Morales EH, Diebold U, Influence of nitrogen doping on the defect formation and surface properties of TiO_2 rutile and anatase, Phys. Rev. Lett., (2006), 96, 026103.
[28] H. E. Cheng, Y. R. Chen, W. T. Wu, and C. M. Hsu, Nitrogen-doped titanium dioxide (N-doped TiO_2) for visible light photocatalysis, Mater. Sci. Eng. B , (2011), 176, 596.
[29] Yanqin Gai, Jingbo Li, Shu-Shen Li, Jian-Bai Xia, and Su-Huai Wei, Design of Narrow-Gap TiO_2: A Passivated Codoping Approach for Enhanced Photoelectrochemical Activity, Phys. Rev. Lett., (2009), 102, 036402.
[30] H. Mahmood, A. Habib, M. Mujahid, M. Tanveer, S. Javed, A. Jamil, Band Gap Reduction of Titania Thin films using Graphene Nanosheets, Mater. Sci. Semicond. Process., (2014), 24, 193–199.
[31] S. H. Elder et. al., The Discovery and Study of Nanocrystalline TiO_2-(MoO_3) Core-Shell Materials, J. Am. Chem. Soc., (2000), 122, 5138-5146.
[32] A. Q. Khan, S. Yuan, S. Niu, L. Zheng, W. Li and H. Zeng, Synthesis of molybdenum oxide-titanium dioxide nanocomposites with ultrashort laser ablation in water, Optics Express, (2017), 25(12), A539-A546.
[33] H. Liu, T. Lu, C. Zhu, Z. Zhu, Direct bandgap narrowing of TiO_2/MoO_3 heterostructure composites for enhanced solar-driven photocatalytic activity, Solar Energy Materials & Solar Cells, (2016), 153, 1–8.
[34] Shelly Burnside, Jacques-E. Moser, Keith Brooks, and Michael Grätzel, Nanocrystalline Mesoporous Strontium Titanate as Photoelectrode Material for Photosensitized Solar Devices: Increasing Photovoltage through Flatband Potential Engineering, J. Phys. Chem. B, (1999), 103 (43), 9328–9332.
[35] Wen Li, Jinfen Chen, Rongting Guo, Jiaming Wu, Xiaosong Zhou and Jin Luo, Facile fabrication of a direct Z-scheme MoO_3/Ag_2CrO_4 composite photocatalyst with improved visible light photocatalytic performance, Journal of Materials Science: Materials in Electronics, (2017), 28(21), 15967–15979.

A technical solution providing fuel mixed for high power engines using only biogas

TRAN Thanh Phong[1,a*], NGUYEN Quang Minh[2,b] and TRAN Quoc Cuong[2,c]

[1] Office of Scientific Research & Technology and International Cooperation, Tien Giang University,
[2] Faculty of Industrial Engineering, Tien Giang University,

119 Ap Bac, Ward 5, My Tho City, Tien Giang Province, Vietnam.

{[a] tranthanhphong, [b] nguyenquangminh, [c] tranquoccuong}@tgu.edu.vn

*Corresponding author. Tel: (+84) 938780209;

Keywords: biogas, engine, fuel mixer, Venturi, electronic control

Abstract. Nowadays, the original source of mineral fuel for engines was depleting increasingly while combustion products make the environment to be polluted, CO_2 emission which caused many greenhouse gases; this also makes crude oil prices fluctuate and rise. They tend to use biogas as a fuel for internal combustion engines which have been interested in the powerful countries. Supply of biogas from the waste of farms, flour production, fish processing, landfills, etc., with hundreds or thousands of cube meter of biomass daily leads demand on high-power generators using biogas in order to make good use of produced gas. This article introduces a technology solution for fuel engines using purely large-capacity biogas and operating under compression type fire. Accordingly, the tubular biogas Venturi mixer with electronic controller has been used to supply the mixture of fuel to engine. The CDI-DC ignition circuit provides a high voltage of 28kV for forced combustion of the mixture. Experimental results show that the mixer operates stably, well controlled and allows adjusting the ratio of air/fuel, as well as easily changing its speed when it is used as a hybrid engine for the generator. Some results of performance evaluation of biogas mixer will be presented in this article.

1. INTRODUCTION

In Vietnam, biogas is a common source of energy in the countryside. Up to now, biogas has been mainly used for cooking purposes. Millions of cubic meters of biogas per year (equivalent to hundreds of thousands of liters of diesel) are wasted. In order to make good use of this abundant resource, several biogas engine designs have been proposed and implemented. In particular, there are four typical designs based on improving gasoline engines and diesel engines. The strengths are simple, low-cost, reduced CO and HC emission, easy to start up and reliable. However, they still have weaknesses. In detail, the weaknesses of each design are as follow: *(i)* - The first design was based on gasoline engines. This design tapered by using valve with variable section was simple because of low cost and reduction of HC and CO emission. It is applicable only for the engines with a capacity of less than 5HP and its performance is low; *(ii)* - The second design was also based on gasoline engines by using an existing carburetor, using petrol or biogas fuel. With low cost and simple design, it can apply on motor less than 5HP and it consumes petrol fuel for burning prey. In addition, their performance is low too; *(iii)* - The third design was based on diesel engines by using petrol or biogas fuel in the condition of unchanged compression ratio. It couldn't only reduce emission of HC and CO, but also startup more easily and perform more reliably. However, it has still some disadvantages such as low performance, exploded probability, unadjustable oil spray angle. In addition, it emits NOx gas, soot and consumes more diesels to start; *(iv)* - The fourth design was also based on diesel engines by using only biogas, forced ignition, compression ratio reduction. It can adjust AFR manually and use fan to pump biogas into engine. A strong point of this proposition is low cost. However, it's complicated and its engine functions unstably due to improper AFR. Moreover, it has a high emission of HC and CO due to incomplete combustion and it is difficult to start up *(Nguyen Quang Minh, 2011)*.

The engines using biogas ignition and working at a high compression ratios (converted from diesel engines) will deal with their defects. However, this conversion technique should solve the ignition in a high-pressure condition; adjust the early angle of ignition and the A/F ratio to optimize the power, the fuel consumption and anti-explosion; reduce NOx emission; control engine speed easily for sudden changes of load (especially when it is applied for large-capacity generators) *(Jam I. Walsh et al., 1988; Mitzlaff & Klaus Von, 1988)*. For research and development of renewable energy, a complete model built on a 70kW Kunming Yunnei diesel engine, four cylinders in a straight line, a single combustion chamber is proposed based on Stamford 50kVA generator of 220/380V ~ 50Hz and 4 phases 4 wires. It uses an automatic Venturi biogas mixer that is enable to adjust easily the A/F ratio at the desired value and a direct ignition system as a CDI-DC type allowing to adjust the early angle of ignition separately for each cylinder. It also uses a central control system for collecting data and monitoring engine parameters (such as temperature, pressure, air flow, biogas flow, speed, generator voltages...). This model is suitable to research solutions of techniques and technologies related to biogas engines, to develop complete biogas generators for research and training in the field of heat, power and automatic control.

This article introduces the techniques and technologies applied in the model generator by converting diesel engines into biogas ignition engines which can perform at high compression ratios and tested results on the model for assessing the effectiveness of the controller. It is organized as follow. The second section will briefly describe the studying method, the electronic mixer system and the electronic control unit. To discuss the proposed method relevance, experimental numerical results will be presented in the third section. Concluding remarks are proposed in the last section.

2. METHODOLOGY

2.1. Studying method

In this paper, we introduce our research on design and experimentation of biogas mixer which is mounted on a large-capacity engine. It consists of: (a)- Biogas mixer based on Venturi tube; (b)- Electronic system for controlling Air Fuel Ratio (AFR); (c)- Electronic Control Unit (ECU) with functions of AFR control, feedback control from oxygen content in exhausted gas.

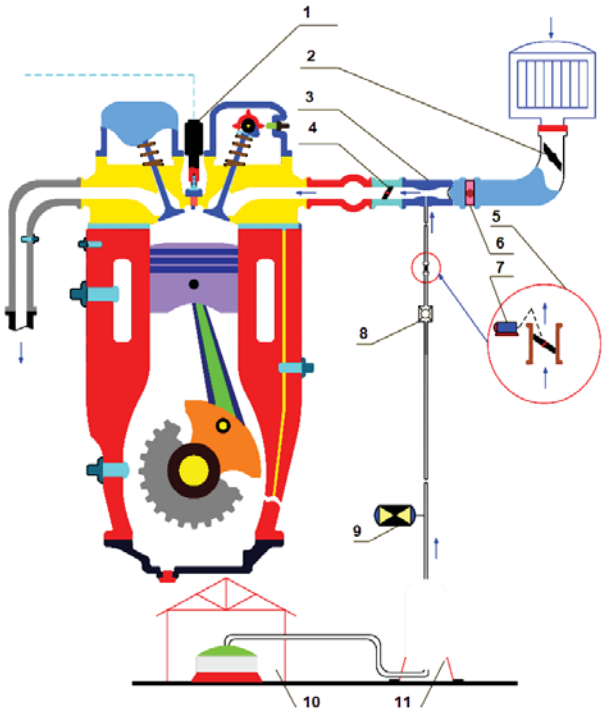
Based on the requirements of the experimental engine (input air volume, engine speed, etc.), as well as the requirements of the procedure of complete combustion of the fuel in the engine, the technical parameters of the design of fuel system are calculated based on the Venturi mixer. Then, a simulation of fluid flow in the mixer is implemented by using Ansys Fluent and Fluent CFD software to determine the appropriated parameters. Simultaneously, the simulation will check the flow, the flow velocity of the mixture to ensure the mixing time and the air homogeneous level.

The study was carried out on a four-cylinder diesel engine Kunming Yunnei 4102QB with a power of 70 kW using only biogas. The oil injectors of engine are removed and replaced by the spark plugs which are modified to adapt the available bushings. The biogas mixer Venturi is automatically controlled to mix the fuel and to control AFR. High pressure diesel pumps are no longer used, but they are equipped with an encoders and a camshaft position sensor. Stamford generators with a power of 30 kVA, 220/380 V, 50 Hz are used for tests with loads.

2.2. Electronic mixer system of biogas

Electronic mixer system for controlling biogas mixer which helps to determinate the desired A/F ratio is a very important in the prototype to ensure accurate biogas supply. This system uses a Venturi to reduce the pressure on the feed pipe, allowing biogas to be fed into the engine easily. The throat diameter and outlet angle of the Venturi tube, the number and size of the biogas supply holes are designed with the aid of Fluent CFD software to determine suitable parameters of size, to check the turbulence and the velocity of the air mixture after passing through the Venturi to ensure the mixing time and homogenous level of the air *(ASME Standard MFC-3M-1989, 1995)*.

In fig.1, biogas from the biomass tank (10) was pumped into the filter and stored at reservoir (11) and the air is flowed through the butterfly valve throttle (5) into the Venturi mixer (3)(fig.2). Here, the biogas and air are mixed, then into the engine. Airflow and biogas flow are determined by the gauges (6) and (8). A solenoid valve (9) disables the fuel line when the engine is idle; Vacuum valves (2) are used to adjust the AFR at starting time and when the pressure of the biogas decreases. The biogas butterfly throttle-valve (5) regulates the amount of biogas supplied to produce the desired AFR. The throttle valve (4) adjusts the air level entering the engine when the external load changes. Valves play an important role in controlling the engine speed when used with a generator.



1. Direct ignition bobine
2. Vacuum valve
3. Venturi throat
4. Throttle valve
5. Biogas butterfly throttle-valve
6. Inlet air flow sensor
7. Stepper for controlling biogas valve
8. Biogas flow sensor
9. Biogas solenoid valve ON/OFF
10. Biomass boiler
11. Filter & reservoir

Fig 1. *Diagram of biogas fuel supply system*

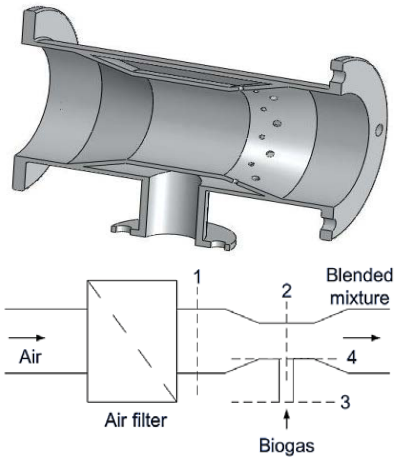


Fig 2. *3D section of mixer and Diagram of biogas mixer (Venturi)*

2.3. Electronic Control Unit (ECU)

The ECU is based on ATMEL microprocessor AT89S53 and Microchip's dsPIC30F4011 processor because of low cost and commonality (fig.4). The central control system for collecting data and monitoring operating parameters (referred to as a Central Control Unit) is built with their working functions as Table 1 and input/output specifications shown in Table 2, Table 3 respectively. The control system is equipped with multiple sensors to collect data and determine the state of the engine. The output power will provide control signals to actuators (valves, warning light relay, etc).

Table 1. *Description of ECU functions*

Data collection and calculation		Process and control	
№	***Data***	**№**	***Description***
1	Inlet air flow, m_a	**1**	Mixing ratio of air/fuel, *AFR (*)*
2	Inlet biogas flow, m_f	**2**	Ignition
3	Engine speed, N_e	**3**	Early ignition angle
4	Position of above dead point, *TDC*	**4**	Speed controlling
5	Cooling water temperature, *THW*	**5**	Emergency stop in case of problem
6	Inlet air temperature, T_a	**6**	Warning of sliding the transmission belt
7	Biogas temperature, T_f	**7**	Warnings system errors
8	Battery voltage, *BATT*	**8**	Communication with computer, *PC*
9	Position of throttle valve, *TPS*; Biogas valve, *BPS*; Vacuum valve, *APS*	**9**	Warning of engine operating status
10	Lubricating oil pressure, *OIL*	**10**	Diagnostics of system errors

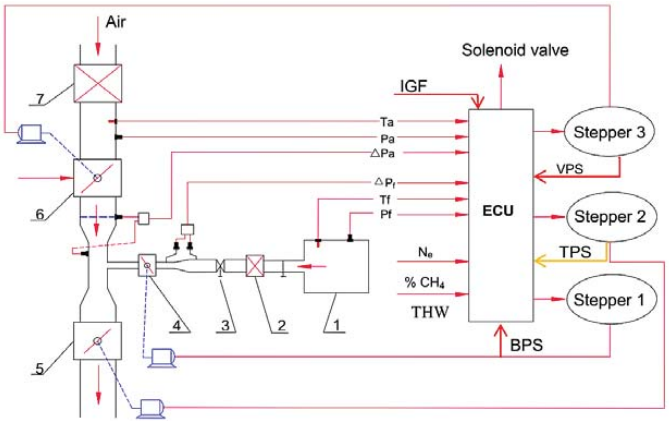
Table 2. *Description of ECU inputs*

№	Inputs	Sensor	Purpose of use
1	Venturi air pressure difference, ΔP_a	Sensor MAP x 2 pieces	Calculate inlet air flow, m_a
2	Inlet air temperature, T_a	Negative temperature coefficient, NTC	
3	Air pressure, P_a	Sensor MAP	
4	Orifice plate differential pressure, ΔP_f	Sensor MAP x 2 pieces	Calculate biogas flow, m_f
5	Biogas temperature, T_f	Negative temperature coefficient, NTC	
6	Biogas source pressure, P_f	Sensor MAP	
7	Number of engine revolutions, N_e	Electromagnetic sensors	Fuel correction
8	Aperture gas throttle valve, *TPS*	Potentiometer	Fuel correction with variation
9	Aperture vacuum valve, *VPS*	Potentiometer	Control *AFR*
10	Aperture biogas valve, *BPS*	Potentiometer	Control *AFR*
11	Cooling water temperature, *THW*	Negative temperature coefficient, NTC	Correction *AFR*
12	Start signal, *STA*	ECU direct recording	
13	Methane ratios in biogas, $\%CH_4$	Hand adjustable resistor	
14	Oxygen content in exhaust gas, $\%O_2$	Oxygen sensor	
15	Exhaust temperature, T_e	Thermocouple	
16	Ignition signal, *IGF*	ECU direct recording	Supervision

Table 3. *Description of ECU outputs*

№	Outputs	Object of control	Purpose of control
7	Position of throttle valve	Motor to control throttle valve	Engine speed control
8	Position of biogas valve	Motor to control biogas valve	Control *AFR*
9	Position of vacuum valve	Motor to control vacuum valve	Control *AFR*
10	Signal of biogas valve ON/OFF	Solenoid valve	Open/lock pipes biogas

In fig.3, the signals provided by the inlet air temperature T_a, the inlet air pressure P_a and the pressure difference ΔP_a in the Venturi tube are used to calculate the inlet biogas mass m_a. Similarly, the signals provided by T_f, P_f and differential pressure ΔP_f are used to calculate biogas mass m_f before and after the orifice plate. The ECU also receives additional signals namely Cooling Water Temperature (THW) and Start signal (STA) to correct the fuel base. Generally, it provides a rich mixture for the engine to explode when the engine cools and starts. The signal from the CH_4 changeover ($\%CH_4$) in the biogas is calculated (e.g. computed value CH_4=65%). The rotation signal (Ne) of engine is used to calculate the optimal AFR for each actual motor speed *(Bhavin Kanalyalal Kapadia, 2006).*



Remarks:
1. Biogas source
2. Biogas filters
3. Biogas pressure reducing valve
4. Biogas throttle valve
5. Biogas butterfly throttle-valve
6. Vacuum valve
7. Air filter

P_a: Inlet air pressure
T_a: Inlet air temperature
P_f: Inlet biogas pressure
T_f: Inlet biogas temperature
Ne: Revolutions per minute, rpm
ΔP_a: Venturi air pressure difference
ΔP_f: Biogas air pressure difference
IGF: Inlet gas flow

Fig 3. *Diagram of the fuel mixer controller*

In the case of absence of an IGF feedback signal, the ignition engine cannot ignite the mixture. Then, the ECU locks the solenoid valve to shut-off the supply of biogas to ensure safety and also to stop the program. The feedback signals from the oxygen content and temperature of exhausted gas to correct the fuel ratio in order to limit the pollution caused by combustion products. Moreover, the ECU calculates the variation of the load to calibrate the content of air mixture to help the engine

respond quickly when loading or unloading. An algorithm of fuel mixing control is represented step by step as follow.

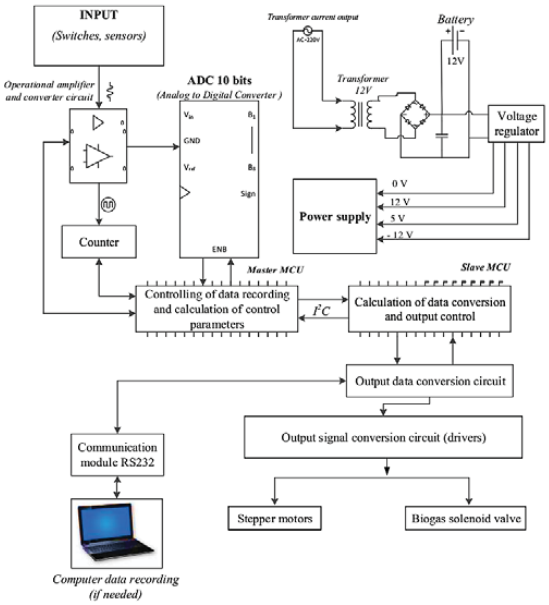


Fig 4. Principle diagram of the central controller

Algorithm of fuel mixing control

Step 1: ***Initialization of parameter***
Step 2:
WHILE (period) *//for waiting timer*
Determine values: ΔV_a, T_a, P_a, ΔV_f, T_f, P_f, TPS, BPS, VPS, THW, STA, $\%CH_4$, IGF, $\%O_2$, T_e
IF(control cycle)
Calculate :
- *inlet air flow* $m_a=f(\Delta V_a, P_a, T_a)$
- *biogas flow* $m_f=f(\Delta V_f, P_f, T_f)$
- $AFR_{ref} = \frac{m_a}{m_f}$
- *adjusted coef. by motor temperature,* K_{THW}
- *correction factor at startup,* K_{STA}
- *correction coef. according to variation load speed,* K_{load}
- *factor correction by component* CH_4 *of biogas,* $K_{methane}$
- *correction factor when the engine is full load,* K_{power}
- *correction factor by %O2 and t0 exhaust gas, Ke*

Adjust $AFR_{adj} = K_{THW}.K_{STA}.K_{load}.K_{methane}.K_{power}.K_e.AFR_{ref}$
Calculate $eAFR = AFR - AFR_{adj}$
IF (eAFR>0)
IF (BPS<100%) *Open biogas valve; BPS=100%*
Close vacuum valve
ELSE IF (APS <100%) *Open vacuum valve; APS=100%*
Close biogas valve
END IF
Switch ouput
END IF
END IF
Step 3: ***Go to step 2***

3. RESULTS AND DISCUSSION

3.1. Simulation of biogas mixer design

The aim of this approach is to calculate all technical parameters and tocreate a design of Venturi tube mixer by using inlet air flow and velocity of the experimental engine. Therefore, a technical design of the Venturi tube mixer is represented by Fig 5 and its characteristic graph is shown in Fig 6.

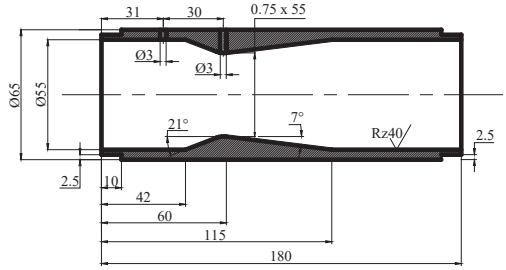


Fig 5. Technical design of the Venturi tube mixer

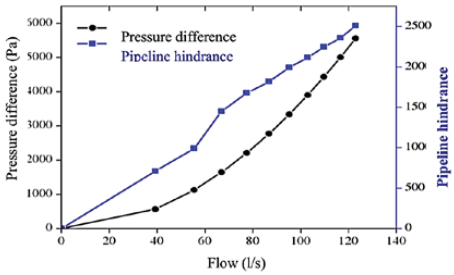


Fig 6. Characteristic graph of Venturi tube

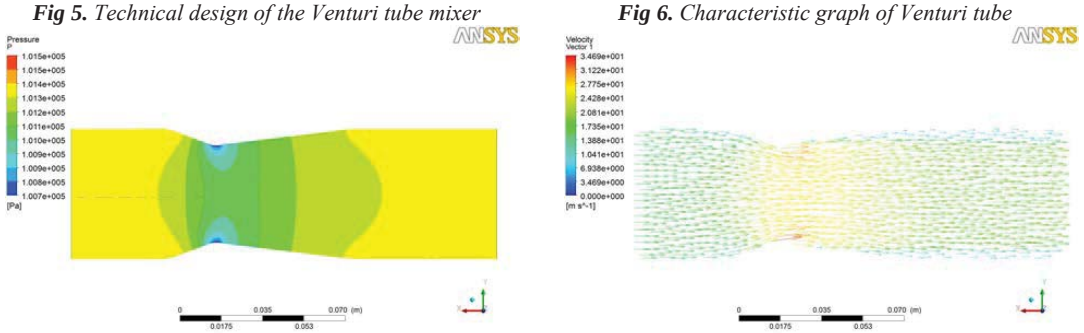


Fig 7. Simulation results of Venturi tube at pressure difference 200 (Pa)

Simulation results of biogas mixer design are shown in Fig 7. Accordingly, the figure shows the velocity of fluid flow in the pipe is about 62 *l/s* (corresponding to the maximum load of the

experimental motor of 225 m^3/h). When the resistance coefficient is 1250, the pressure difference at the throat is 1553 *Pa*, the flow velocity is 21 *m/s*. This result is only acceptable when the biogas mixer is designed to supply the mixture to the engine *(N. Mustafi, et al., 2006)*.

3.2. Experimental results of mixers in laboratory

3.2.1. Experimental model configurations

To simulate suction power of engine, the four-cylinder diesel engine Kunming Yunnei 4102QB with a capacity of 70kW was used as experimental engine. As the roller rotates, the engine will suck fuel/air through the mixer. The data describing the behavior of the system is recorded by the computer from the RS232 circuit integrated in the ECU. Each biogas throttle valve position (equivalent to load variation) will help build AFR corresponding with vacuum valve position.

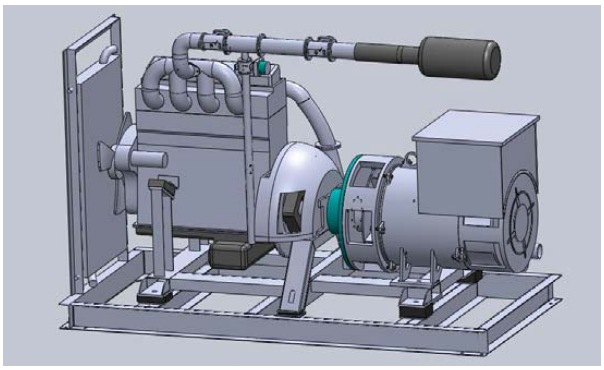


Fig 8. *Simulation prototype design*



Fig 9. *Real experimental prototype*

3.2.2. Experimental model results

In Fig. 10, a representation of the working zone of the biogas mixer illustrates:

- The controllable AFR mixer is in the range of 9.4 ÷ 12.5 in according to variation of the inlet air flow. It satisfies completely the mixed supply biogas 55% of methane to diesel engines with poor fire type.

- The mixer allows changing the AFR from 6 to 15. This means the mixture can be supplied to the engine when the methane content in the biogas is changed up to 70%.

This simulation shows also the results of vacuum valve aperture (Fig 11) and throttle valve aperture (Fig 12) according to m_a and *AFR*.

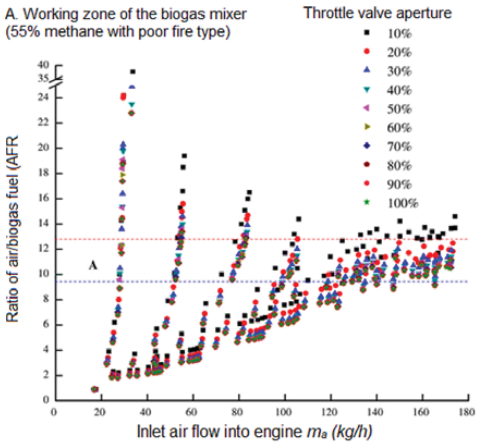


Fig 10. The working zone of the biogas mixer

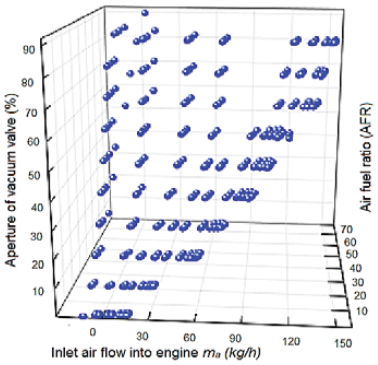


Fig 11. Vacuum valve aperture m_a and AFR

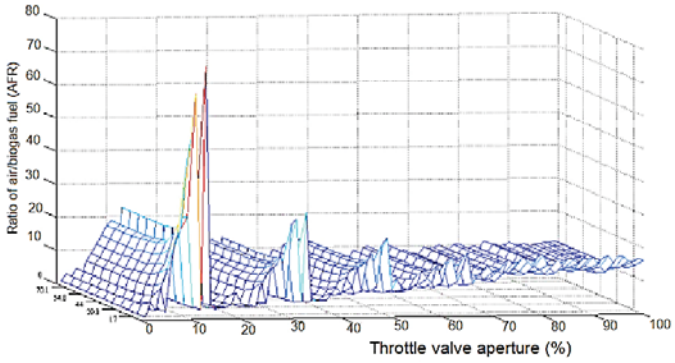


Fig 12. Throttle valve aperture according to ma and AFR

From the working specifications of the mixer, it shows that the ECU can calculate the aperture of the biogas throttle and the aperture of vacuum valve to control the gas mixture with the AFR_{actual} corresponding to each value m and the $AFR_{desired}$

3.3. Experimental results of mixers on real engine

From the parameters of the newly designed mixer provided by simulation, the control procedure is programmed and set. The results are shown in Fig 13.

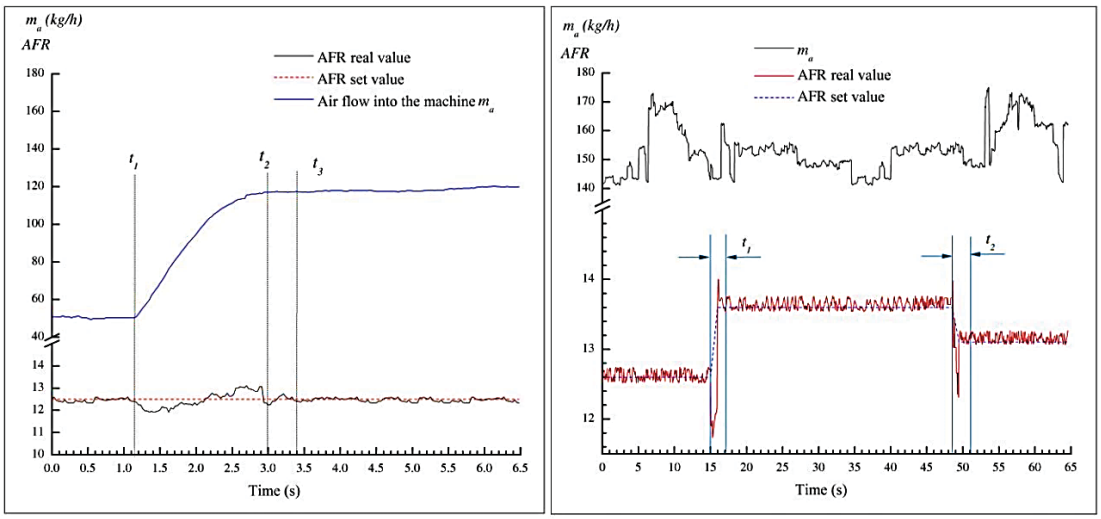


Fig 13. Some results of our research - ability of the mixer with variation of (a) ma (b) AFR

When the inlet air m_a is changed:

$m_{a\text{-}max}$=120,25 *(kg/h)*

$m_{a\text{-}min}$= 49,28 *(kg/h)*

- Amplitude fluctuations $m_{a\text{-}amp}$=70,97 *(kg/h)*
- Actual time with changing airflow:

$$\Delta t_a = t_2 - t_1 = 1,82\,(s)$$

When the inlet air m_a is changed:

$m_{a\text{-}max}$=172,9 *(kg/h)*

$m_{a\text{-}min}$=141,1 *(kg/h)*

Ability to respond AFR of the mixer:

- Amplitude fluctuations AFR_{amp}=1,288
- Steady-state error: 4.48 %
- Setting time: $\Delta t_{AFR} = t_3 - t_1 = 2,22(s)$
- Setting error $e_{xl} \approx 0$
- Control error AFR_{error}=$12,5^{+0,606}_{-0,682}$
- Time control error: $t_{error} = \Delta t_a - \Delta t_{AFR} = 0,4\,(s)$

Ability to respond AFR of the mixer:

- Steady-state error average 2.94 %
- Setting time average:

- Average value: $m_{a\text{-}ave}$= 153,9 *(kg/h)*
- Amplitude fluctuations: $m_{a\text{-}amp}$= 31,8 *(kg/h)*
- The average time with change of the control command $AFR_{desired}$=1,39 *(s)*

$$t_{ave} = (t_1 + t_2)/2 = 2{,}17 \ (s).$$

- Setting error $e_{xl} \approx 0$
- Time control error: $t_{error} = 0{,}81$ *(s)*.

4. SUMMARY

In this paper, a design for measuring air and fuel flow consumed on biogas engines was proposed by using Venturi and Orifice effects. Experimental results show that maximum flow can measure 225 kg (inlet air) and 40 kg (biogas) per hour. It is possible to mount this on any engine when the threshold of inlet air flow is in the measured range for using in the fuel gauge or in the study. The automatically controlled Venturi fuel mixer incorporating a methane control system which has been appropriately programmed, it can: *(a)*- Allow to change the AFR from 6 to 15, meaning that the mixture can be supplied to the engine when the methane content in the biogas is changed from 55-70%; *(b)*- Control AFR very well in the range of 9.0 ÷ 12.5; *(c)*- Improve stability and control error and AFR response time; *(d)*- Supply completely fuel mixture for any biogas engine with air flow lower than 225 kg/h. When the AFR = 12.1 (biogas with CH_4 content= 65%) was supplied, the study shows that the engine was operating at a high compression ratio (ε=17) with an early ignition angle of 42^0 before upper dead point. This approach will also be a reference for research and technology transfer related to build a model of biogas mixers.

REFERENCES

[1]. ASME Standard MFC-3M-1989, Measurement of Fluid Flow in Pipes Using Orifice, Nozzle and Venturi, American Society of Mechanical Engineers (1995) pp. 178-185.

[2]. Bhavin Kanalyalal Kapadia, Development of a single cylinder for 100% biogas operation, A thesis submited for the degree of Master of Science, Indian Institude of Science, Bangalore, India (2006) pp. 4-5.

[3]. James I. Walsh, Jr., P.E. and Charles C. Ross, and Michael S. Smith, Handbook on biogas utilization. U.S. Department of energy – Southeastern regional biomass energy program, U.S (1988) pp. 315-319.

[4]. Nguyen Quang Minh, Conversion of a diesel engines to entirely biogas, A thesis submited for the degree of Master of Science, Ho Chi Minh City University of Technology and Education HCMUTE, Vietnam (2011) 1-5, 20-25, pp. 67-70.

[5]. Mitzlaff, Klaus Von, Engine for biogas, Deutsche Gesellschaft für Technische Zusammenarbeit (GTZ) GmbH (1988) 78-82.

[6]. N. Mustafi, R. R. Raine and P. K. Bansal, Biogas Fuel for Internal Combustion Engines, Department of Mechanical Engineering, The University of Auckland (2006) pp. 5-8.

Investigation of BTEX adsorption on Carbon Nanotubes cartridges from air samples

Le Huu Quynh Anh*, Phan Đinh Tuan

Hochiminh University of Natural Resources and Environment, 236 Le Van Sy Street, Tan Binh District, HoChiMinh City, VietNam

E-mail: quynhanh.lehuu@gmail.com

Keywords: VOCs, carbon nanotubes, air pollution, BTEX, adsorption capacity

Abstract. The volatile organic compounds (VOCs) contribute to serious air pollution problems in Viet Nam. Many studies have investigated in air quality monitoring and treatment, in order to determine the average concentrations of Benzene, Toluene, Ethylbenzene and Xylene (BTEX). Carbon nanotubes (CNTs) have been widely used as adsorbent in environmental treatment, especially for VOCs. This paper aims to determine the adsorption capacity of multiwalled carbon nanotubes for removal of BTEX from air samples. In preliminary study, the effects of various parameters during adsorption experiments were monitored such as flow rate, temperature and BTEX concentrations in air samples. The equipment for BTEX removal was developed by our research team consisting of filter columns, air sample bags, adsorption cartridge. The air samples containing BTEX were conducted directly through a cartridge packed with adsorbent. The adsorption experiments were carried out under various operating conditions such as temperature (30 - 40ºC), gas concentration (0,57 - 4,77 mg/L) and the gas flow rate (10 - 90 mL/min). In addition, isotherm studies of CNTs for BTEX removal were achieved by using Langmuir and Freundlich models. The results showed that the experimental parameters were optimized at a flow rate of 30 mL/min and an ambient temperature at 30°C. The adsorption capacity of CNTs increased proportionally with BTEX concentrations. The specific affinity of CNTs for BTEX from air samples was in order of X > E > T > B. The experimental isotherm data were well-fit with the Langmuir model for Benzene and Xylene removal, and the Freundlich model for Toluene and Ethylbenzene adsorption. The CNTs presented highly potential application for BTEX adsorption thanks to their microporous structure and high surface area.

1. Introduction

Carbon nanotubes (CNTs) have attracted considerable attention because of their significant properties such as the unique structure, exceptional mechanical and electronic properties. Hence, this material have been applied in many areas such as biomedical devices, catalyst supports and especially in the environmental remediation in recent years. In the literature, the CNTs exhibited excellent selective adsorption for aromatic compounds compared to conventional activated carbon. Most of these studies focused on the removal of organic pollutants, metal and nucleotide in aqueous media. Peng et al. [1] examined the adsorption of 1,2-dichlorobenzene from water by carbon nanotubes used as adsorbents. Gotovac et al. [2] studied the influences of different functional groups and diameters of CNTs on the adsorption of poly-aromatic hydrocarbons and found that acid functionalized CNTs had higher absorbability for the poly-aromatic molecules. Long et al. [3] have used CNTs as an adsorbent for the removal of dioxin from model air samples.

Currently, the volatile organic compounds (VOCs) are used in common industrial processes, especially in the paint, dyes, polymer and varnishing industries. Benzene and its derivative Toluene, EthylBenzene, Xylene (BTEX) were the principal solvent components involved in these industries which have a significant impact on the quality of ground water and the public health. For the removal of BTEX vapors, various adsorbents were exanimated such as zeolite, activated carbon fiber, compost and the promising CNTs…However, research studied on adsorption of BTEX in air samples from CNTs and on their adsorption isotherms are very limited so far.

The aim of this paper was to investigate the adsorption performance of pristine CNTs for BTEX removal in air samples. In preliminary study, adsorption capacities of four VOCs (Benzene, Toluene, EthylBenzene, Xylene) on CNTs cartridge were investigated in using the local equipment for air samples. The influence of some parameters (e.g., flow rate, temperature and gas concentration) on the adsorption mechanism with CNTs was studied. Finally, the equilibrium adsorption isotherms were carried out, using different isotherm models fitted to the experimental data.

2. Materials and methods

2.1.Materials

All chemicals, such as Benzene, Toluene, EthylBenzene, Xylene, Carbon disulfide (CS_2) were purchased from Sigma Aldrich with > 99% purity. Multiwalled Carbon Nanotubes (CNTs) was synthesized by the Institute of Materials Science of Vietnam, with the fundamental physical properties as follows: diameter 20-100nm, length 1-10 µm, purity > 95%.

2.2.Methods

2.2.1. Experimental set-up :

A lab scale system for BTEX adsorption on CNTs was shown in Fig. 1. This proposed equipment was designed to obtain two targets: a preparation of a standard air sample and adsorption experiments.

The air sampling bag was carried out by conducting fresh air through a silica gel column and an activated carbon column in order to remove moisture and impurity such as dust, CO_2. The flow rate of the air was monitored by a float flow meter. The BTEX compounds were evaporated and transferred into the carrier gas for preparing the air sampling bag with a total volume of 1.5L.

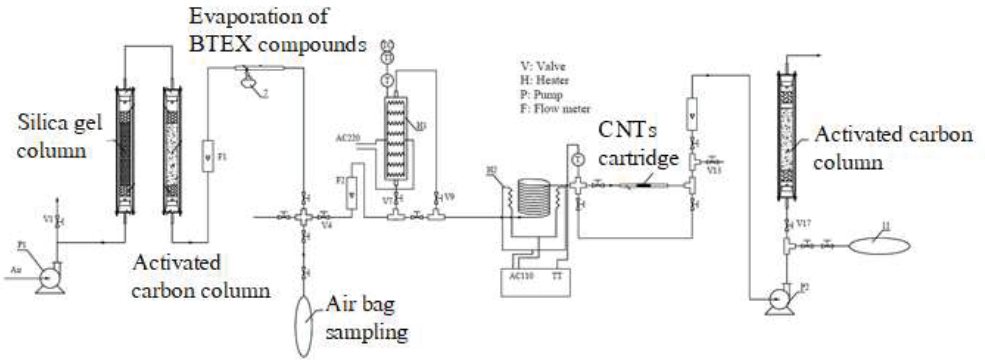


Fig. 1. Schematic diagram of the experimental set-up for the BTEX adsorption

2.2.2. Preparation of Carbon nanotube cartridges :

The commercial CNTs was dried in an oven until reaching constant weight in order to eliminate the moisture. The sample CNT cartridge was prepared by adding 50mg of dried CNTs into a glass tube (7mm in inner diameter and 10cm in length) and packed with a cotton wool plug.

2.2.3. Adsorption experiments :

The air sample bag containing BTEX vapors was passed through the CNTs cartridge at a controlled flow rate and under vacuum pressure. The bed temperature was controlled by a thermo-sensor installed at the center of the system. At the end of each experiment, the CNTs was directly taken out of the glass tube and extracted with 7mL of CS_2 solvent overnight in order to desorb the trapped BTEX. The CS_2 solvent is a low boiling point liquid; therefore, desorption process must be performed in closed bottle and then stored in refrigerator at 4ºC. The concentration of BTEX adsorbed by the CNT cartridge was analyzed by a Gas Chromatography (GC-FID). All the experiments were duplicated and the mean values were reported.

The stock sample flow was set up in various levels (from 10 to 90 mL/min) for kinetic investigation of BTEX adsorption on CNTs. To determine the effects of temperature on the adsorption of VOCs, the experiments were performed at different bed temperatures (30, 35 and 40ºC). To perform the adsorption isotherm study, the air samples were prepared by mixing 1,5L of carrier gas and different concentrations of BTEX in range of 0,57 - 4,77 mg/L.

2.2.4. Adsorption isotherms :

The adsorbed amount on adsorbents (q, $mg.g^{-1}$) was calculated in the following the equation (1):

$$q = (Co - Ct) \times \frac{V}{m} \quad (1)$$

where Co and Ct ($mg.L^{-1}$) are the concentration of BTEX at initial time and at equilibrium state, respectively. V (L) is the volume of the air sample and m (g) is the adsorbent weight.

The adsorption experiment data were fitted using two basic types of adsorption isotherms models : Langmuir and Freundlich.

The linearized Langmuir isotherms is represented [4] by equation :

$$\frac{C_e}{q_e} = \frac{1}{q_{\max} b} + \frac{1}{q_{\max}} C_e \quad (2)$$

where, Ce is equilibrium concentration of adsorbate ($mg.L^{-1}$), qe is the adsorption capacity in equilibrium ($mg.g^{-1}$), qm ($mg.g^{-1}$), and b ($L.mg^{-1}$) are empirical constants, can be evaluated from the slope and intercept of the linear plot of Ce /qe against Ce.

The second fitting equation using Freundlich model is presented as below :

$$\ln q_e = n \ln C_e + \ln k \quad (3)$$

where, K is the Freundlich characteristic constant [$(mg.g^{-1})(L.g^{-1})1/n$] and 1/n is the heterogeneity factor of sorption, obtained from intercept and slope of ln qe versus ln Ce linear plot respectively [5].

2.2.5. Characterization and analytical methods :

The Brunauer, Emmett and Teller specific surface area (BET) of CNTs was performed from the adsorption-desorption isotherms of N_2 at 77 K using a NOVA 3200e-Quantachrome USA instrument. The concentration of BTEX were quantified by a Gas Chromatography equipped with flame ionization detector (GC-FID) (Shimazu, QP2010ULTRA). The GC-FID was operated at injection temperature of 200°C. The following procedure was used: 60°C for 5min and increased at a rate of 10°C/min to 200°C with 5min of holdtime. The total operation time was 24 min.

3. Results and Discussion :

3.1. Physical properties of CNTs :

The physical properties of adsorbent such as tube diameter, surface functionnalization, amorphous carbon impurities are important contributors to vary surface area and adsorption capacity. In this study, the surface area, pore volume and pore size distribution on CNTs were provided in Table 1. The obtained surface area of CNTs is in accordance with other studies [6]. The pore size distribution of CNTs has been determined in the range of mesopore (2-50 nm) with pore volume of 0,409 cm^3/g. The CNTs pore diameter (6,06 nm) could be play a key role for selective adsorption of BTEX with molecular sizes lower than 1 nm.

Table 1. Physical properties of pristine CNTs

Adsorbents	Surface area [m^2/g]	Pore volume [cm^3/g] [mesopore 5-100 nm]	Average pore diameter [nm]
CNTs	150,660	0,409	6,06

3.2. Effects of flow rate on the BTEX adsorption :

The effect of flow rate on adsorption experiment was perfomed in the range of 10 to 90 mL/min for BTEX and the adsorptive capacity for each compound was determined (Fig. 2). It can be clearly seen that the relative rate of adsorption decreases with increasing flow rate for BTEX which is an

influential parameter. There is not sufficient time for BTEX vapors adsorbed on CNTs due to the high flow rate (90 min/mL), which could disturb the adsorption and led to reducing the adsorptive capacity. When the flow rate was 30 min/mL, the optimum adsorption performance could be obtained.

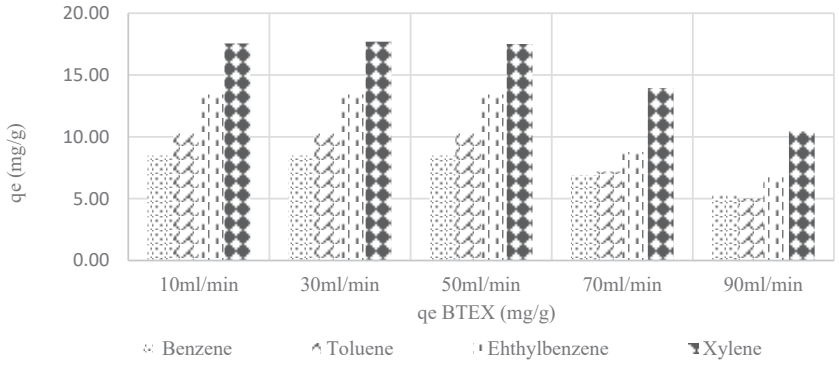


Fig. 2. Effects of flow rate on the adsorptive capacity of the CNTs for BTEX

3.3. Adsorption temperature studies on the BTEX adsorption :

The correlation of temperature and adsorption uptake for BTEX of CNTs was shown in Fig. 3. Different temperatures were set at 30-35-40 ºC during adsorption of BTEX by CNTs. It may be observed in Fig. 3 that the adsorption capacities of CNTs for BTEX decreased significantly at higher temperatures due to the gas diffusion between BTEX molecules and CNTs layer. Similar results were observed in other studies. Das et al. proved that the reduced adsorption due to possible loss of active sites for adsorption at relatively higher temperatures [7]. Therefore, all experiments were done at maximum adsorption temperature of 30 ºC.

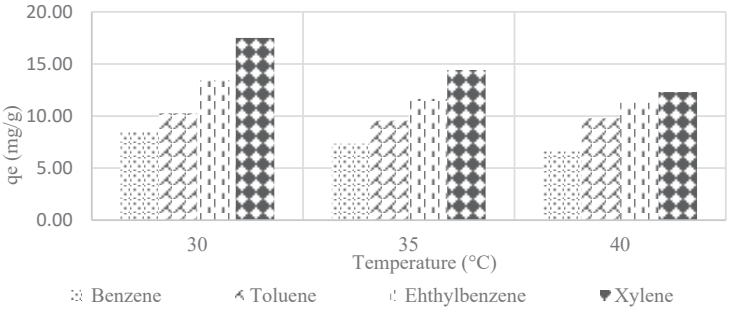


Fig. 3. Effects of temperature on the adsorptive capacity of the CNTs for BTEX

3.4.Adsorption performance studies :

Various initial concentrations of BTEX in range of 0,57 mg/L - 4,77 mg/L were evaluated in order to investigate the interest of adsorption performance of CNTs. The adsorption capacity of these

VOCs increased proportionally with initial adsorbate concentrations, as shown in Fig. 4. The adsorption efficiencies of the CNTs for BTEX were 10,71 mg/g, 13,38 mg/g, 18,19 mg/g, 37,40 mg/g, respectively, with an average inlet concentration of 4,77 mg/L. These values are in the same order of magnitude with previous report. Sone et al. [8] determined for Xylene, Toluene, and Benzene, adsorption capacities were 740.3, 274.1 and 178.6 µg/g, respectively.

Furthermore, the CNTs cartridge display high activity to aromatic compounds with an affinity order Xylene > EthylBenzene > Toluene > Benzene. In fact, this could be attributed to the rich electronic structure of Xylene due to the electron donating methyl groups, which enhance the π- π coupling interaction. Daifullah et al. [9] indicated that the adsorption of Benzene and Toluene on activated carbon proceeds in the order of Toluene > Benzene.

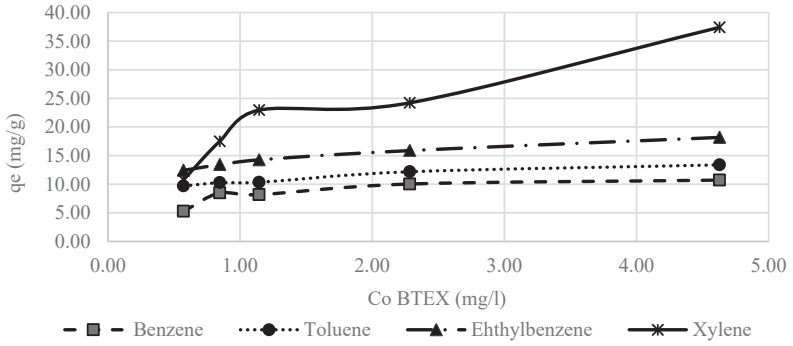


Fig. 4. Concentration effects of BTEX on the adsorptive capacity of CNTs

3.5. Adsorption isotherms :

The Langmuir and Freundlich model were used in this study in order to characterize the correlation between interaction equilibrium of CNTs and BTEX compounds. The linear form of these models was fitted based on experimental data and fitted plots were presented in Fig. 5.

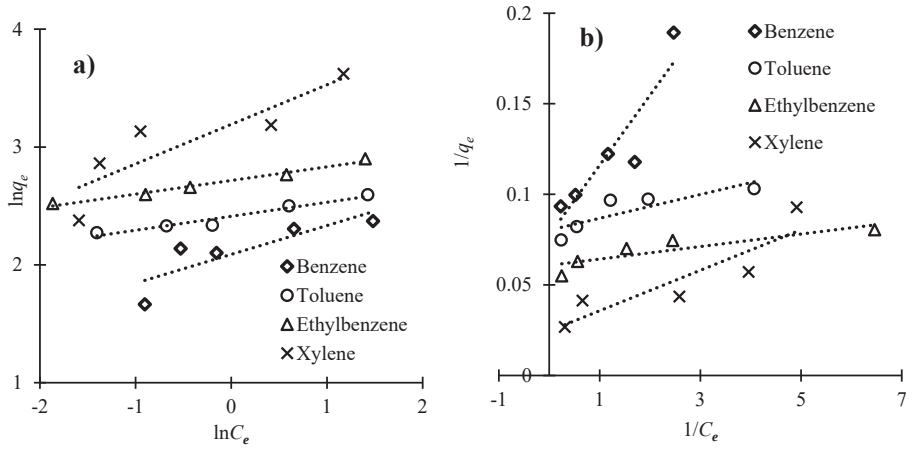


Fig. 5. Linear fitted plot with (a) Freundlich isotherm model, (b) Langmuir isotherm model

The best fitting model was selected based on the highest correlation coefficient R^2. Respective fitting parameters were determined from the fitted linear plots and given in Table 2. Good fits of Freundlich model were obtained for Toluene and EthylBenzene adsorption, while, Benzene and Xylene adsorption equilibrium data fitted to the Langmuir model. According to Freundlich model, the adsorption mechanism of Toluene and EthylBenzene tend to form a multilayer adsorption on a heterogeneous CNTs surface.

Table 2. The calculated parameters in the Langmuir and Freundlich models for BTEX adsorption on CNTs

Adsorbents	Langmuir			Freundlich		
	q_{max} [mg.g^{-1}]	b [L.mg^{-1}]	R^2	n [L.mg^{-1}]	K [mg.g^{-1}] [mg/L]$^{1/n}$	R^2
Benzene	16.45	17.88	0.759	4.09	8.08	0.721
Toluene	12.47	12.15	0.720	8.42	11.16	0.946
EthylBenzene	12.90	2.01	0.836	8.63	15.13	0.983
Xylene	40.65	2.20	0.801	2.98	24.35	0.779

From the Table 2, the magnitude of Freundlich isotherm constants k and n, suggest that the adsorption capacities of TEX on CNTs were considered more meaningful than that of Benzene. These observations were in accordance with the results of prior studies [7,9]. The influence of functional groups in organic pollutant on their adsorption depends on the type, number, and position of functional groups in organic molecules. In fact, it can be observed in this study that substituted groups alter the adsorption affinity of BTEX on CNTs [10]. The value of heterogeneity factor of sorption 1/n for BTEX varies between 0 and 1 and indicated that the adsorption process was favorable.

4. Conclusion

In summary, the adsorption capacities of CNTs for BTEX in air sample were investigated in this study. There factors, including the flow rate, temperature and VOCs concentration, were evaluated for their effects on the adsorption performance of CNTs. The results showed that these parameters play important roles in the adsorption process. The optimal parameters were determined at a flow rate of 30 min/mL and a temperature of 30ºC. The significant adsorption capacity of CNTs for BTEX has proved, due to the π- π interactions between the graphene sheet of CNTs and the benzene ring of aromatic compounds. The affinity order for BTEX of CNTs was X > E > T > B. The experimental isotherm parameters for BTEX removal on CNTs were determined and the data fit well as using the Langmuir model for Benzene and Xylene removal, and the Freundlich model for Toluene and Ethylbenzene adsorption. The results suggested that the removal of BTEX from air samples of CNTs could be enhanced by adding functional groups on CNTs surface and applied for other environmental pollutants.

Acknowledgments. The authors acknowledge financial support through the project TNMT.2016.04.15 of the Ministry of Natural Resources and Environment

5. References

[1] X. Peng, Y. Li, Z. Luan, Adsorption of 1,2-dichlorobenzene from water to carbon nanotubes, Chem. Phys. Lett. 376 (2003) 154-158.

[2] S. Gotovac, C.M. Yang, Y. Hattori, K. Takahashi, H. Kanoh, K. Kaneko, Adsorption of polyaromatic hydrocarbons on single wall carbon nanotubes of different functionalities and diameters. J. Colloid Interface Sci. 314 (2007) 18–24.

[3] R.Q. Long and R.T. Yang, Carbon nanotubes as superior sorbent for dioxin removal, J. Am. Chem. Soc. 123 (2001) 2058.

[4] Irving Langmuir, The adsorption of gases on plane surfaces of glass, mica and platinum. J. Am. Chem. Soc. 40 (9) (1918) 1361–1403.

[5] H. Freundlich, Adsorption in solution, Physical Chemistry 57 (1906) 384–410.

[6] M. Jahangiri and S. J. Shahtaheri, The adsorption of Benzene, Toluene and Xylenes (BTX) on the carbon nanostructures: the study of different parameters, Fresenius Environmental Bulletin 20 (4a) (2011)

[7] D. Das and V.Gaur, Removal of volatile organic compound by activated carbon fiber, Carbon 42 (2004) 2949–2962.

[8] H. Sone and B. Fugetsu, Affinity-based elimination of aromatic VOCs by highly crystalline multi-walled carbon nanotubes Talanta 74 (2008) 1265–1270.

[9] A.M. Daifullah, B.S. Girgis, Impact of surface characteristics of activated carbon on adsorption of BTEX, Colloids and Surfaces Journal A: Physicochemical and Engineering Aspects 214 (1−3) (2003) 181−193.

[10] X. Ren, C. Chen, M. Nagatsu -Carbon nanotubes as adsorbents in environmental pollution management: A review, Chemical Engineering Journal 170 (2–3) (2011) 395-410.

Investigation and optimization of power based smart home module integrated with automatic solar tracking system and MPPT technique

Dang Thai-Viet[1,a*]; Dinh Si-Thong[1,b] and Bui Xuan-Toi[1,c]

[1]Hanoi University of Science and Technology, Vietnam

[a]viet.dangthai@hust.edu.vn, [b]dinhsythong@gmail.com, [c] xuantoi.bk@gmail.com

Keywords: Radiation, tracking control, performance, smart home, wireless network, solar.

Abstract. Currently, the world has a lot of research and practical application of smart building systems integrated with smart power systems. Because Vietnam is a country with potential for solar energy, the integrator of solar energy is being strongly developed. However, the research result of the optimization of electrical energy used by the intelligent type solar integration is rare. This paper presents the design and structure of the module of intelligent control and monitoring via wireless network integrated with the automatic solar concentration system. The system allows easy connection and operation of all electrical power sources including the dispersal solar power to ensure the efficient and lower power consumption. In addition, the solar cell system is applied the Maximum Power Point Tracking technique (MPPT), which helps to stabilize and improve the power generation efficiency of the PV panels. The test results on the module showed absorption performance of automatic solar-cell flat plate systems is raised by 20-30% and power consumption in small households reduced approximately 30%.

1. Introduction

In Vietnam, fossil energy resources are declining because of the limitation of available energy and the huge demand of use. Furthermore, the consumption of these energy causes serious environmental pollution. Meanwhile, the potential for renewable energy development is huge. Power generation from renewable energy sources is considered to supply to power shortages. Moreover, renewable energy has diversified energy sources, diverted the risks, enhanced and guaranteed national energy security. Vietnam has a potential for solar energy, stretching from 8" North to 23" North latitude, located in areas with relatively high solar radiation intensity. The abundant solar energy with average solar radiation is 5 kWh/m^2/day so the use of solar energy in our country will bring great economic effect. [1,7].

Recently, solar energy has been strongly investigated. The photovoltaic panels (PV) convert radiation into electrical energy by the photovoltaic effect [2]. The production of electricity is the photovoltaic effect based on the conversion of sunlight. The direct sunlight is extremely important for the generation. The problem of remaining the maximum of light angle to panel has been approached. Therefore, the panels should be able to capture the maximum amount of solar radiation during the day. There are some methods used for increasing energy production, such as solar trackers, which provide a performance better than those with fixed angle due to the amount of direct radiation on the panels [3,4].

However, the PV modules working with insufficient load have still had low efficiency of electricity conversation. Therefore, Maximum Power Point Tracking (MPPT) technique of Photovoltaic is very necessary. Furthermore, the advancements in sensor technology it is a very viable option to connect the solar energy systems to the cloud (internet) with the help of Internet of Things. IoT has also support to manage effectively all electrical equipment and to observer the

situation by wifi or 3G/4G network. The researches about managing electricity consumption with the module of smart home in Vietnam integrated with solar energy is missing and incomplete [5,6].

This article presents the design of smart home module which is controlled and monitored by wireless network. The system integrates with PV system that automatically tracks to the sun to enhance the efficiency of solar panels. The MPPT technique integrates with the power converter to guarantee the stable power generation. The system allows to connect easily and to operate all power sources such as distributed power and solar power. The controller will make the system more efficient and economical. Experimental module presents that the absorption efficient increases more 1.57 times than the traditional fixed solar arrays. At the same time, the measuring process has also shown that smart home integrated with solar energy saved energy about 30% of energy consumption at least.

2. Problem Formulation

2.1. Photovoltaic System

Solar radiation suffers the influence of atmospheric air, clouds and pollution before reaching the ground. Hence, it is necessary that the photovoltaic panels are properly installed for capturing as much solar energy as possible.

The off-grid generators are those with no connection to the national electrical distribution network. These systems are usually installed in mountains, islands and remote areas. They must require a battery bank to store the generated energy and to provide it when no light. They are mainly composed of photovoltaic panels, charge controller, batteries and inverters.

The Grid-tie generators are effectively connected to the national power grid. They are directly injected into the power grid, without the battery bank. They are basically composed of the photovoltaic panels and the inverters. The systems will supplement the components of control, protection and monitoring of the energy generation.

2.2. Automatic solar tracking system

The experimental module consists of a smart home module and a PV system using MPPT as follows

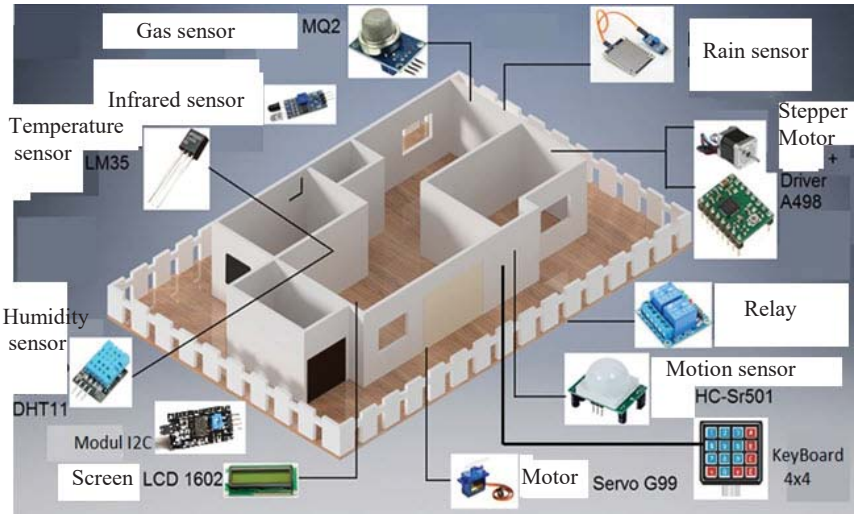


Figure 1. The structure of Smart home module

The smart home module is connected to a PV system which supplies the electrical energy for simple equipment such as televisions, fans, water pump and lights in Table 1. The automatic solar tracking system use the PV panel of 30 WP. The power converter of the solar panels is applied the Maximum Power Point Tracking technique (MPPT)



Equipment	Number	Power (w/h)	Used time/day (h)
Television	1	70	4
Speaker	1	70	4
Light	4	36	8
Fridge	1	130	24
Fan	2	67	12
Ventilators	1	600	1
Auxiliary		30	5
Total(w/day)			5618

Figure 2. The automatic solar tracking system **Table 1.** The number of equipment in the experiment

Based on the smart home module, the electrical equipment will be connected to the electricity from the national grid and from the solar battery system. The automatic solar tracking system uses the power converter equipped with the MPPT. Based on the experiment model, the study will demonstrate the optimal process of using energy in the home. The experiment results also show an improvement in the efficiency of solar system's power generation as well as the stability of voltage and current efficiency when applying MPPT.

2.3. Control algorithm

2.3.1 Automatic solar tracking technology

The two-axis panel with the main axis of rotation is perpendicular to the ground. This axis allows to track the change of the sun's position. The second axis allows the system to follow the height of the sun.

To determine the sun's position, we use a combination of 4 light sensors. The error of the combination will be used as the inputs of controller in Fig. 4. The controller will rotate the solar panels in the azimuth and the height so that the obtained energy is maximized

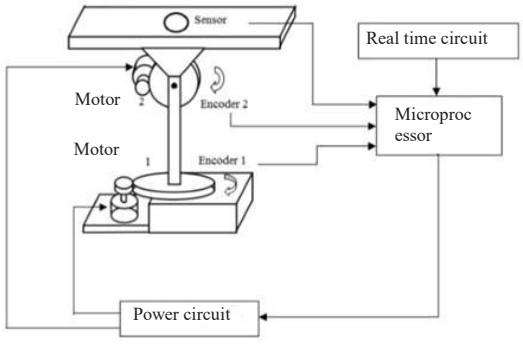


Figure 3. The structure of solar system

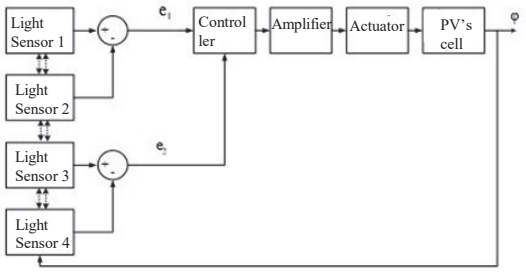


Figure 4. The blog diagram of the auto solar system

The power capacity of the PV is determined by the multiplication of the two values the current I_{PV} and the voltage V_{PV}. The MPPT sets the voltage V_{ref} (or the width of pulse) to control the DC-DC power converter so that the DC voltage is set on the load which will be changed the power consumption to match the power of PV.

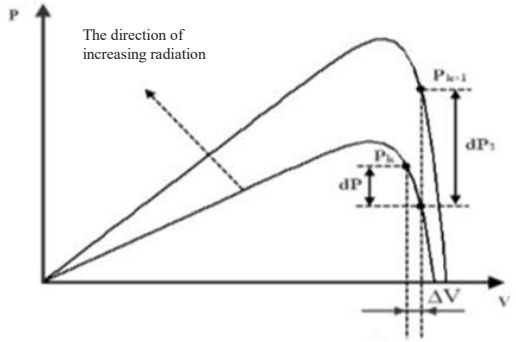


Figure 5. The finding technique of MPP's point

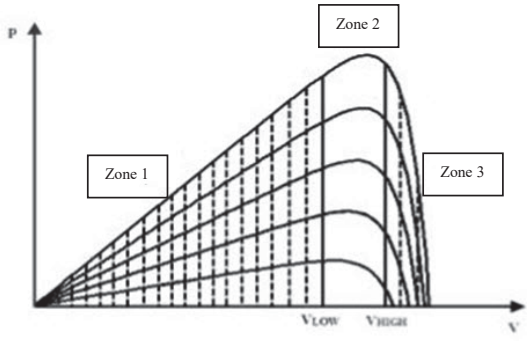


Figure 6. PV's working characteristic

where: $V_{LOW} \leq 0.75V_{OV}.ref$ and $V_{HIGH} \geq 0.85V_{OV}.ref$ Trong đó: $V_{OV.ref}$ is open voltage at the standard of temperature. The blog diagram of PV's system applying MPPT in Matlab-Simulink in Fig. 10.

The system consists of a fixed server at an address on the Internet. The sensing network node is connected to the internet via the http protocol in the client server model in which the client is an internet sensing network node connected to the server using the GET method. The user or administrator performs the management through a web interface with the domain name connected to the database in the server. With this connection, anywhere the internet can manage and control the devices. The program for controlling and distributing solar power will be programmed based on the PV's accumulated energy and mesh power, provided for equipment including televisions, fans and lights corresponding to the assumed power consumption.

The system will be controlled via a set of four light sensors and will receive control signals through the Arduino Uno to the DC motor on two rotating axes. The solar energy will be converted to DC current by DC/DC converter.

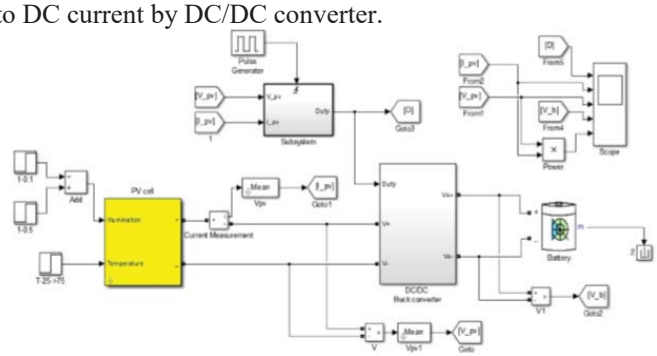


Figure 7. The blog diagram of PV's system applying MPPT

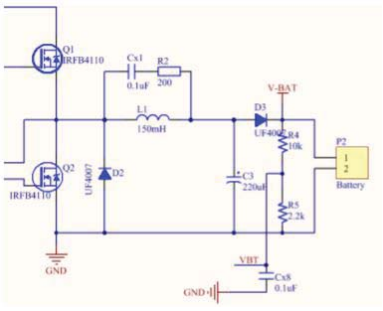


Figure 8. The DC/DC converter

3. Experiment result

Change of solar radiation I=700÷1000 W/m^2 after t = 0.25 seconds; Temperature T=25°C (constant) The simulation results are shown in Figs.9 to 14 with an execution cycle. At t=0(s), the solar radiation is 700W/m^2, the algorithm will find MPP. By adjusting the execution cycle, it also changes the voltage of the PV panels and compares the energy at different cycles to obtain the new MPP. At t = 0.25(s), the increase in solar radiation is 1000 W/m^2, because the characteristics of the

PV cell, MPP will be changed so that the obtained MPP is not the maximum points. Therefore, the execution cycle continues to change and compare the strength to find the new MPP. The new MPP is V = 25V, I = 3A, P_{max} = 75W, which is precisely matched to the characteristics of PV cells at 25ºC. The experiment illustrates the results of controlling PV's system with T=25÷75 ºC and I=700÷1000 W/m^2 which is applied MPPT.

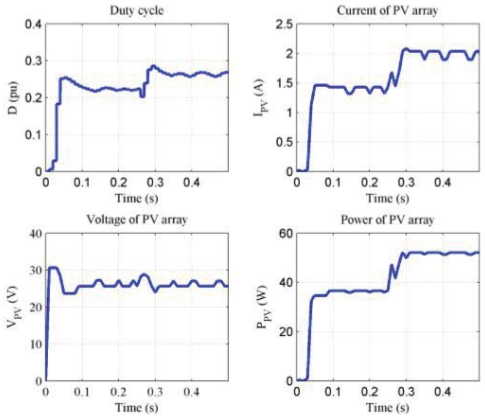


Figure 9. The completed cycle, voltage, current and power of system at T=25°C, I=1000 W/m^2

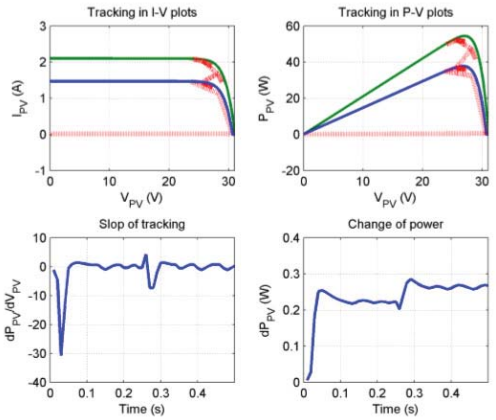


Figure 10. The plots of I-V, P-V point and the change of power at T=25°C, I=1000 W/m^2

The experiment results in Figs. 10, 12 and 14 show the new MPP points are found to be close to the maximum power at the PV areas. Fig. 15 shows the stability of the system when surveyed and tested in practical example.

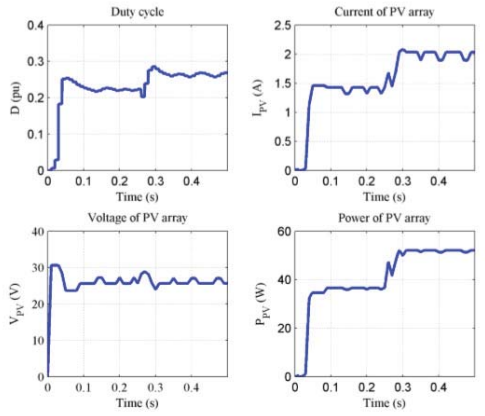


Figure 11. The completed cycle, voltage, current and power of system at T=25°C, I=700 W/m^2

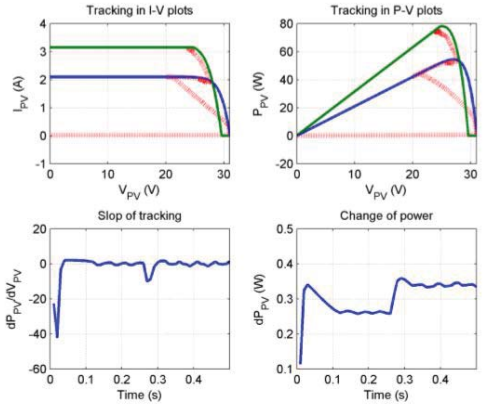


Figure 12. The plots of I-V, P-V point and the change of power at T=25°C, I=700 W/m^2

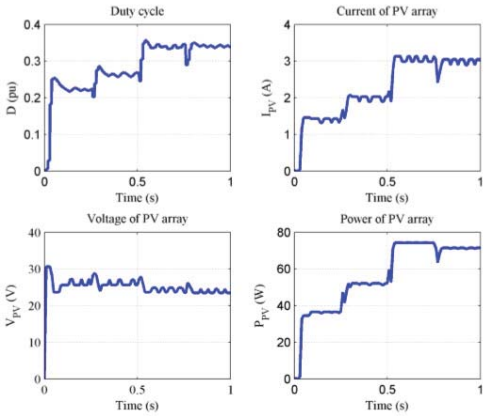


Figure 13. The completed cycle, voltage, current and power of system at T=75°C, I=1000 W/m^2

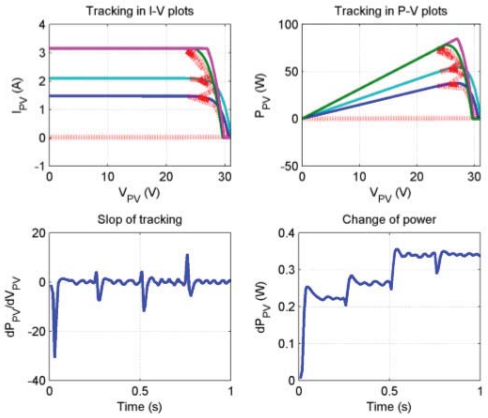


Figure 14. The plots of I-V, P-V point and the change of power at T=75°C, I=1000 W/m^2

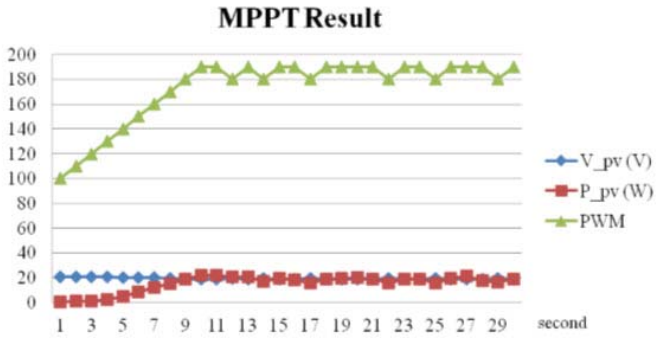


Figure 15. The practical results of PV system in the operation

4. Conclusion

This paper presents the design of smart controlling and monitoring via wireless network integrated with the automatic solar concentration system in smart home module. The system allows easy connection and operation of all electrical power sources including the dispersal solar power. The control software program improves the efficient and lower power consumption. In addition, the solar cell system is applied the Maximum Power Point Tracking technique (MPPT), which helps to stabilize and improve the power generation efficiency of the PV panels. The test results on the module showed absorption performance of automatic solar-cell flat plate systems is raised by 20-30% and power consumption in small households reduced approximately 30%.

5. Acknowledgement

This research was funded by the Vietnam National Foundation for Science and Technology Development (NAFOSTED) under the project number 107.03-2013.15.

References

[1] Muhammad Asif and Tariq Muneer, Energy supply, its demand and security issues for developed and emerging economies. Renewable and Sustainable Energy Reviews, 11,7 (2007)1388–1413.

[2] T. P. Chang, The suns apparent position and the optimal tilt angle of a solar collector in the northern hemisphere. Solar energy, 83, 8(2009):1274–1284.
[3] C. Y. Lee, P. C. Chou, C. M. Chiang and C. F. Lin, Review Sun Tracking Systems, Sensors. (2009) 3875-3890,
[4] J. M. Wang and C.L. Lu, Design and Implementation of a Sun Tracker with a Dual-Axis Single Motor for an Optical Sensor-Based Photovoltaic System (2013) 3157-3168.
[5] J. Ahmad, and H.J. Kim, A Voltage Based Maximum Power Point Tracker for Low Power and Low Cost Photovoltaic Applications, World Academy of Science, Engineering and Technology (2009) 60.
[6] M. Farhat, L. Sbita, Advanced Fuzzy MPPT Control Algorithm for Photovoltaic Systems, Science Academy Transactions on Renewable Energy Systems Engineering and Technology, 1, 1, (2011).
[7] Ly Cong-Thang, Research and Design of Automatic Solar Tracking System to Improve the Effect of Equipment using Solar Energy, Report of I203 Project, Vietnam Ministry of Industry and Trade.

Iron (III)-based Metal-Organic Frameworks as potential visible light – driven catalysts for the removal of NOx: A solution for urban air purification

Hoang Phuc Nguyen[1], Tae Ho Kim, Soo Wohn Lee[2,*]

[1]Research Center for Eco Multi-Functional Nano Materials, SunMoon University, Asan, Republic of Korea

[2]Department of Environmental & Bio-Chemical Engineering, Sun Moon University, Asan, Republic of Korea

*Corresponding author. Tel: (+82) 41 530 2882; E-mail: swlee@sunmoon.ac.kr

Keywords: Metal-organic Framework, Fe–based MOFs, gaseous pollutant, de-NOx, photocatalyst.

Abstract. Due to the rapid industrializations, the urban environment is confronting with serious problems related to air pollution. Among various exhaust gases, oxides of nitrogen (NOx) gases have been considered as one of the most fatal pollutants for environment and living organisms. Photocatalysis, which is based on advance oxidation processes, is thought to be the best alternative for removal of NOx in ppb level. The most typical photocatalyst is TiO2. However, TiO2 is only activated by UV irradiation which comprises about 4-5% of the total solar spectrum, thereby limiting its application under natural condition [1]. Metal-organic frameworks might be a promising candidate as an alternate solution. MOFs are crystalline porous materials composed of metal ions, as clusters, and organic ligands, or linkers. The versatility in the composition of the organic linkers and metal clusters, the possibility of post-synthetic modification, together with the large surface area and high porosity that facilitate the incorporation of guests molecules into the framework are some characteristics of MOF which makes it a potential material in the field of energy and environment [2]. In this work, three different structures of Fe-based MOFs with the same organic linker Benzene-1,4-dicarboxylic acid (H2BDC); MIL-53, MIL-88B, and MIL-101; have been synthesized successfully by microwave-assisted solvothermal method, which is confirmed by XRD, SEM, FT-IR results. The thermal properties of as-synthesized samples have been characterized TGA, whilst their porosity and surface area was obtained by nitrogen gas absorption-desorption method. The interaction between the samples and photon was investigated by DRS and PL measurements.The samples were examined for photocatalytic de-NOx reaction under solar irradiation. This is the first time that Fe-based MOFs' photocatalytic ability for de-NOx performance is investigated. The work demonstrates the potential of Fe-based MOFs, particularly MIL-101 photocatalyst, in de-NOx photooxidation performance. MIL-101's rigid, porous network allows gases molecules easily penetrate and contact with CUSs dispersed in catalyst's network. The large specific surface area of MIL-101 can provide more active sites for de-NOx reaction, and nano-sized clusters in the network inhibited the recombination of light-driven charges, thus improved the efficiency of de-NOx performance. This work has opened up a new solution for NOx photo-abatement and air pollution treatment as well.

Acknowledgements. This research was supported by Global Research Laboratory Program of the National Research Foundation of Korea (NRF) funded by the Ministry of Education, Science and Technology (MEST) of Korea (Grant No.: 2010-00339) and Basic Science Research Program through the National Research Foundation of Korea (NRF) funded by the Ministry of Science, ICT and Future Planning (NRF-2015R1C1A1A01052893).

References

1. J. Ângelo, L. Andrade, L.M. Madeira, A. Mendes, Jornal of Environmental Manage, 2013, 129, 552.
2. A. Dhakshinamoorthy, A.M. Asiri, H. Garcia, Angewantdte Chemie International Edition, 2016, 55, 5414.

Fabrication of Sn doped blue and black TiO_2 for NO_X removal

Adriana Martinez Oviedo, Huy Hao Nguyen, Schindra Kumar Ray, Soo Wohn Lee*

Research Center for Eco-multifunctional Nano Materials, Sun Moon University, Asan, Republic of Korea

*Tel: (+82) 10 41-530-2882; E-mail: swlee@sunmoon.ac.kr

Keywords: Surface Structure; Reduced TiO2; Sn Doping.

Abstract. The surface science studies of the semiconductor TiO2 are essential in understanding the optical and electrochemical functionality properties, which are paramount in the development of photocatalytic technology. The TiO2 exists in different polymorphs; anatase, rutile, and brookite. Generally, anatase and rutile are widely studied due to their high photocatalytic performance. In this paper, two types of defects were introduced in the TiO2 surfaces' structure. Interstitial and substitutional defects were generated in the structure with the aim to understand the different effects that are produced in the material properties. At first, a reductive treatment using lithium in ethylenediamine was performed to form Ti3+ species and oxygen vacancies at the surface of TiO2. Secondly, the defect was generated by the doping of the Sn metal ions. The physical and chemical properties were studied by X-Ray diffraction (XRD), Transmittance electron microscopy (TEM), Raman spectroscopy, Ultraviolet–Visible diffuse reflection spectrum (UV–vis), Photoluminescence spectrum (PL), and X-ray photoelectron spectroscopy (XPS). The photocatalytic activity was evaluated by the reduction of NO and NO2 species. Here, the relationship between the Sn and Ti3+ impurities and the different effects that these generate in both the anatase and rutile TiO2 phases was studied and compared. It is shown that the new configuration of the TiO2 surface enhances the optical properties of the material. Moreover, it is observed that the addition of defects Ti3+ and Sn contributes to the reduction of electron-hole recombination and contraction of the band gap, respectively. The particles reported have a narrow bandgap of 2.7 nm attributed to the Sn doping. To the oxygen vacancies we attribute the low intensity of PL spectra. However, the bulk structure contributes to the transport of excitons to the surface of the material. Therefore, the study reports the contribution of modified properties, physical and chemical, of the TiO2 in the photocatalytic activity for the reduction of NOx species.

Acknowledgements. This research was supported by the Global Research Laboratory program of the National Research Foundation of Korea (NRF) funded by the Ministry of Education , Science and Technology (MEST) of Korea (Grant Number: 2010-00339).

References

1. Zhu, Q.; Peng, Y.; Lin, L.; Fan, C.-M.; Gao, G.-Q.; Wang, R.-X.; Xu, A.-W. Stable Blue TiO2−x Nanoparticles for Efficient Visible Light Photocatalysts. J. Mater. Chem. A 2014, 2 (12), 4429.
2. Duan, Y.; Fu, N.; Liu, Q.; Fang, Y.; Zhou, X.; Zhang, J.; Lin, Y. Sn-Doped TiO 2 Photoanode for Dye-Sensitized Solar Cells. J. Phys. Chem. C 2012, 116 (16), 8888–8893.
3. Cao, Y.; Zhang, X.; Yang, W.; Du, H.; Bai, Y.; Li, T.; Yao, J. A Bicomponent TiO 2 /SnO 2 Particulate Film for Photocatalysis. Chem. Mater. 2000, 12 (11), 3445–3448.
4. Liqiang, J.; Honggang, F.; Baiqi, W.; Dejun, W.; Baifu, X.; Shudan, L.; Jiazhong, S. Effects of Sn Dopant on the Photoinduced Charge Property and Photocatalytic Activity of TiO2 Nanoparticles. Appl. Catal. B Environ. 2006, 62 (3–4), 282–291.

5. Liqiang, J.; Honggang, F.; Baiqi, W.; Dejun, W.; Baifu, X.; Shudan, L.; Jiazhong, S. Effects of Sn Dopant on the Photoinduced Charge Property and Photocatalytic Activity of TiO2 Nanoparticles. Appl. Catal. B Environ. 2006, 62 (3–4), 282–291.

Investigation of geometric properties of melt-electrospun microfibers for precision deposition

Tung Nguyen Nhat[1], Jeong Hwa Kim[1], Young Hun Jeong[2,*],Gyu Man Kim[2], Cheol-Woo Park[2], Moon Kyu Kwak[2]

[1]Department of Mechanical Engineering, Graduate School, Kyungpook National University, Daegu, Korea

[2]School of Mechanical Engineering, Kyungpook National University, Daegu, Korea

*Corresponding author. Tel: (+82) 950-5577; E-mail: yhjeong@knu.ac.kr

Keywords: Melt-electrospinning, Direct writing, 3D printing, Fibers, Bioengineering.

Abstract. Melt-electrospinning is a cost-effective and flexible process to fabricate nano- and micro-scale fibrous structures of thermoplastic polymers, and it is a strong candidate for miniaturized and precision printing. Moreover, this process can introduce high porosity and unique fibrous morphology to two or three-dimensional structures. In this regard, the melt-electrospun microfibers can provide numerous advantages in various fields. However, there are various issues in introduction of melt-electrospinning to precision printing; the randomly oriented deposition, heterogeneous pore size caused by the whipping motion and buckling of microfibers. Here, we presented an experimental method to identify deposition and thermal deflection behavior of microfibers fabricated using direct-write melt-electrospinning. Using the proposed experimental procedure, the optimal condition for geometric features of structure and geometric quality could be identified. Consequently, with a range of electrospun fiber diameters from s, we demonstrated that the three-dimensional microfibrous lattice structures of 10-to-15-micrometer fibers could be fabricated with regular pore shape, high porosity and great geometric fidelity. Furthermore, 14-days in-vitro cell test were performed using mouse embryonic fibroblast cell line to assess biocompatibility of the fabricated structures. Also, cell attachment and spreading were investigated using scanning electron microscopy and F-actin/DAPI staining.

Acknowledgements. This research was supported by Basic Science Research Program through the National Research Foundation of Korea(NRF) funded by the Ministry of Science, ICT and future Planning, Republic of Korea (No. NRF-2015R1A2A2A01005515).

References

1. Brown, T. D., Dalton, P. D., Hutmacher, D. W., Advanced Materials, 2011, 23 (47), 5651-5657.
2. Brown, T. D., Dalton, P. D., Hutmacher, D. W., Progress in Polymer Science, 2016, 56, 116-166.
3. Hochleitner, G., Jungst, T., Brown, T. D., Hahn, K., Moseke, C., Jakob, F., Groll, J., Biofabrication, 2015, 7(3), 035002.

Calculating Cutting Force in Grinding

Do Duc Trung[1,a]*, Nguyen Van Thien[2,b], Hoang Tien Dung[3,c], Phung Xuan Son[4,d]

[1,2,3,4]*Faculty of Mechanical Engineering, Hanoi University of Industry, Ha Noi, Vietnam*

[a]Email: dotrung.th@gmail.com

[b]Email: thiendhcn2@gmail.com

[c]Email: tiendunghaui@gmail.com

[d]Email: phungxuanson@gmail.com

Keywords: calculating, cutting force, grinding, undeformed chip thickness

Abstract

The ability to calculating grinding force is important to many aspects of grinding process optimization, monitoring, and control. In this paper, based on the theory of grinding process, the relationship between cutting force, undeformed chip thickness and cutting parametres (grinding wheel velocity, workpiece velocity, depth of cut); grinding wheel parameters (diameter, the mesh number used in the grading sieve, volume fraction) and other factors is developed. These relationship used to calculate cutting force of grinding process, its value is good agreement experiment value. So, results of this paper can be used for calculating the cutting force in practical cases.

Introduction

The ability to caculated grinding force is important to many aspects of grinding process optimization, monitoring, and control. There are some authors researched on cutting force in grinding: Salje [1] developed the initial grinding force model considering the shear strength as a specific parameter for the workpiece material and the model parameters are taken from a characteristic diagram that considers the influences of the respective combination of the material and the grinding wheel. Brach et al. [2] took the grinding wheel topography into consideration in twodimensional forms. Ono [3] considered the average grain distance and took the distance between the cutting edges into consideration for the modelling of the grinding forces. Lindsay [4] developed two grinding models for specific normal force, one for the materials that are easy to grind and the other for the materials that are difficult to grind. Werner [5] developed a grinding force model taking into account the combined effects of friction and chip formation. His model predicts the effect of workpiece properties on grinding. Lichun and Jizai [6] developed a grinding force model from the Werner model that takes friction and chip formation into account; here they separated out the effects of frictional and chip formation forces. Younis et al. [7] extended Werner's work taking the combined effect of ploughing, friction and chip formation forces for cylindrical grinding, where the loaded area is found out using a fiber optic system….

In this paper, based on the theory of grinding process, the relationship between cutting force, undeformed chip thickness and parameters of grind process is developed. These relationship used to calculate cutting force of grinding process, its value is good agreement experiment value.

Normal and tangential force

The normal and tangential force per grit was modelled by Hecker et al. [8] based on the similarity between the grain indentation and Brinell hardness test proposed by Shaw [9]. The tangential and normal forces per grain are calculated from:

$$F_t^{''} = F''(sin\alpha + f cos\alpha) \quad (1)$$

$$F_n^{''} = F''(cos\alpha - f sin\alpha) \quad (2)$$

Where:

f is the friction coefficient between the grain and the workpiece material;

α is the effective attack angle;

The force F'', calculated directly from Brinell test definition, is [10]:

$$F'' = d_f \frac{HB.\pi.D_g}{2}(D_g - \sqrt{D_g^2 - b^2}) \quad (3)$$

Where:

d_f is an empirical constant to be adjusted with experimental data. This factor lumps together the unmodeled phenomena such as thermal effects, imperfect spherical grain geometry, and the difference between Brinell harness number and dynamic harness test [11].

D_g is the grain diameter.

b is the diameter of the impression given by $b = D_g sin(\alpha)$;

The effective attack angle α is unknown. This angle can be calculated from geometry relation in Figure 1, for which we have $\alpha = arcos(1 - 2h_m/D_g)$, with h is undeformed chip thickness or depth of grain engagement.

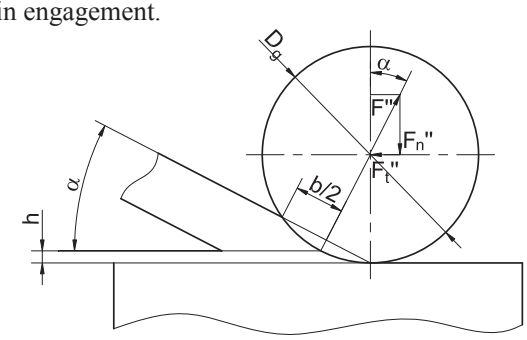


Fig 1. Force model per grain representation

The tangential and normal forces per unit width of cut can be expressed as:

$$F_t' = F_t'' N_d' \quad (4)$$

$$F_n' = F_n'' N_d' \quad (5)$$

Where:

N_d' is the number of active grain per width of cut.

$$N_d' = C_d l_c = w C_{d(z')} l_c \quad (6)$$

Where:

C_d is dynamic grain density;

l_c is real wheel – workpiece contact length;

w is wheel width of cut;

$C_{d(z')}$ is cumulative dynamic cutting edge density, as [12].

$$C_{d(z')} = \frac{C_{s(z')}}{1 + \frac{2}{3}\frac{C_{s(z')}}{z}\frac{tg(\theta)}{tg(\varepsilon)}E(h^3)} \quad (7)$$

In which the modified static grain distribution due to local grain deflection δ is given by

$$C_{s(z')} = A(z + \delta)^k \quad (8)$$

Where:

A is constant for the static grain distribution, it is difficult to determine.

The local grit deflection is calculated from $\delta = F'' K_g$, with K_g being the equivalent grit spring constant, it is difficult to determine and F'' the expected value of the normal force per grit.

The radial distance into the wheel that participates in cutting during grinding, z, is equal to the maximum value of the chip thickness. This maximum value can be approximated by $z = E(h) + 3\sigma(h)$; where $E(h)$ and $\sigma(h)$ are the expected value and the standard deviation, respectively, for the undeformed chip thickness; the chip triangular assumed cone grain geometry

with an internal angle of 2θ. This internal cone angle also determines the relationship between the chip thickness (h) and the chip width (b) given by $tg(\theta) = b/2h$ (Figure 2) [13].

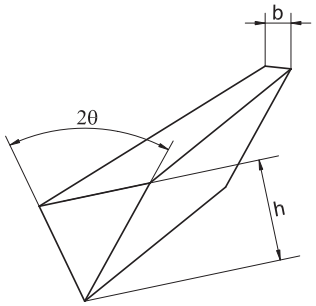


Fig 2. Chip produced

Another factor included in the formulation of Eq. 7 is the kinematic shadow generated by an active grain that reduces the chances for some grains to find material to cut and become active. The geometry of this shadow is given by the factor $tg(\varepsilon) = 2v_w t/v_s d_e$; where t is the depth of cut, v_w and v_s are the workpiece and wheel tangential velocity. The equivalent diameter is defined as $d_e = d_G/(1 \mp d_G/d_w)$ where d_G is the wheel diameter, d_w is the workpiece diameter, the minus sign is for internal grinding, and the plus sign is for external grinding.

From equations (1) to (8) see that cutting force depends on many factors, such as HB, d_f, D_g, v_w, $E(h)$,…

Expected value of undeformed chip thickness

The existing chip thickness model proposed by Anne Venu Gopal et al. [14]. The equation is as follows:

$$\mathrm{E(h)} = 2\sqrt{\frac{1}{Nr}\frac{v_w}{v_G}\sqrt{\frac{t}{d_e}}} \tag{9}$$

Where:

v_w – workpiece velocity;

v_s – grinding wheel velocity;

t – depth of cut;

r - is the chip width to thickness ratio. The value of 'r' is difficult to determine and is assumed in the range of 10-20 [15, 16].

N - The number of active grits per unit area 'N' derived by Xu. Hockin et al [17] is as follows:

$$N = 4f_d \frac{1}{d_g^2}\frac{1}{\sqrt[3]{\left(\frac{4\pi}{3\vartheta}\right)^2}} \tag{10}$$

In which:

f_d – the fraction of diamond particles involved in active grinding. The value of f_d is difficult to determine.

d_g – The equivalent spherical diameter of diamond grit, is given [18] as:

$$d_g = 15.2/M \tag{11}$$

Where:

M is the mesh number used in the grading sieve.

ϑ- volume fraction of diamond in grinding wheel.

Substituting the eq (10), (11) in (9) and after mathematical simplification, the value of expected value of undeformed chip thickness will be:

$$E(h) = 6.8254\left(\frac{1}{f_d.r}\right)^{1/2}\left(\frac{v_w}{v_G}\right)^{1/2}\left(\frac{4\pi}{3\vartheta}\right)^{1/3}\left(\frac{t}{d_e}\right)^{1/4} \quad (12)$$

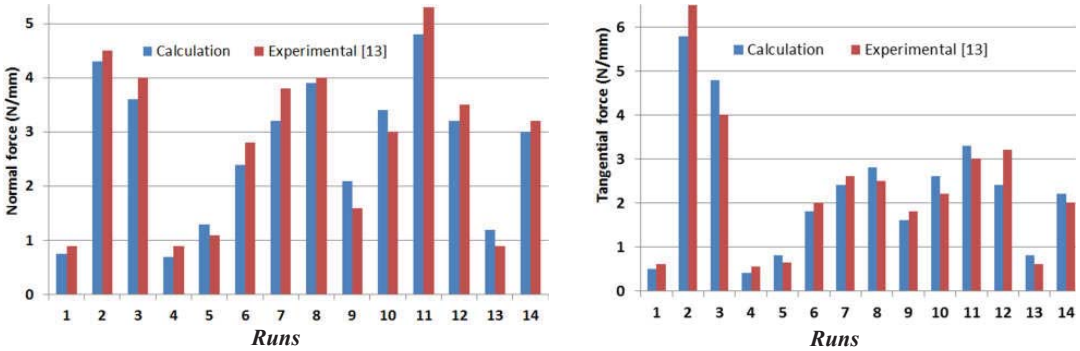
These above equations so that, value of cutting force will be increased if value of mesh number used in the grading sieve, HB, depth of cut and are increased. Beside, if value of the equivalent diameter is increased, these make cutting force will be reduced.

Comparasion cutting force value with experiment

For comparasion value of cutting force between calculation process and its of experiment. In this work, cutting force of calculation had comparased cutting force of experiment by L. Hecker et at. [13].

Tab 1. Parameters for calculation and experiment

Factor	Value	Unit	Notes	Ref
d_f	0.5			[10]
k	1.2			[10]
A	0.96			[10]
K_g	3710.10^{-5}	mm/N		[12]
r	10			[15, 16]
d_G	200	mm	grinding condition	[13]
$q = v_G/v_w$	92 - 363	m/min	grinding condition	[13]
a	1 - 8	μm	grinding condition	[13]
w	10	mm	grinding condition	[13]
θ	37.5	degree	dressed before every experiment with a sharp (cone angle of 75^0)	[13]
HB	65400	N/mm^2	grinding condition	[13]
D	0.08	mm	grinding condition	[13]
f	0.25		grinding condition	[13]
α	75	degree	dressing condition	[13]
M	80		grinding condition	[13]
f_d	0.5		grinding condition	[13]
ϑ	0.2		grinding condition	[13]



a) Normal force *b) Tangential force*

Fig 3. Comparasion between calculation and experimental

Parameters of grinding process were use in Table 1. In which, some factors were the same in both calculation and experiment, other factors were choice following in final grinding condition. The results of cutting force calculation (using all of above equations) and its of experiment process are show in Figure 3. From these so that there is a good agreement between cutting force value of calculation process and its of experiment.

Conclusions

Cutting force depends on many factors, such as cutting parameters, grinding wheel parameters, and other factors. In this paper, a simple equation is proposed for caculating the cutting force in grinding. From above equations so that, value of cutting force will be increased if value of mesh number used in the grading sieve, HB, depth of cut and are increased. Beside, if value of the equivalent diameter is increased, these make cutting force will be reduced. Cutting force of caculating is good agreement with experiment value. These result of this work can be used for predictive the cutting force in practical cases.

Acknowledgements

To obtain the results of this research, the authors would like to thank to Dr. Rogelio L. Hecker (Facultad the Ingenieria, Universidad Nacional de La Pampa, General Pico, LP, 6360, Argentina) helped during the research process.

References

[1] E. Salje, Grundlagen des schleifvorganges, Werkstatt und Betrieb 86 (1953) 177–182.
[2] K. Brach, D.M. Pai, E. Ratterson, M.C. Shaw, Grinding forces and energy, Transactions of ASME, Journal of Engineering for Industry 110 (1988) 25–31.

[3] K. Ono, Analysis of the grinding force, Bulletin of the Japan Society of Grinding Engineers 1 (1961) 19–22.

[4] Lindsay, R.P.: On the metal removal and wheel removal parameters—surface finish, geometry and thermal damage in precision grinding, Ph.D. Thesis, Worcester Polytechnic Institute, 1971.

[5] G. Werner, Influence of work material on grinding forces, Annals of CIRP 27 (1978) 243–248.
[6] Li Lichun, Fu Jizai, A study of grinding force mathematical model, Annals of CIRP 29 (1980) 245–249.

[7] M. Younis, M.M. Sadek, T. El Wardani, A new approach to development of a grinding force model, Transactions of ASME 109 (1987) 306–313.

[8]. Hecker RL, Ramoneda I, Liang SY (2003) Static and dynamic wheel microstructure characterization. Trans North Am Manuf Res Inst Soc Manuf Eng.

[9] Shaw M (1972) Fundamentals of grinding. Proceeding of the international grinding conference: new developments in grinding. Pittsburgh, PA, pp 221–258.

[10] Rogelio Lorenzo Hecker, Part surface roughness modeling and process optimal control of grinding, PhD Thesis, Georgia Institute of Technology November (2002).

[11] Subhash, G., Koeppel, B., Chandra, A., Dynamic Indentation Hardness and Rate Sensitivity in Metals, *Journal of Engineering Materials and Technology*, Vol. 121, pp. 257-263, (1999).

[12] Shaw, M., Principles of Abrasive Processing, Oxford University Press, New York, (1996).

[13] Rogelio L. Hecker , Steven Y. Liang , Xiao Jian Wu , Pin Xia , David Guo Wei Jin Grinding force and power modeling based on chip thickness analysis, Int J Adv Manuf Technol (2007) 33: 449–459.

[14] Anne Venu Gopal, P. Venkateswara Rao. A new chip-thickness model for performance assessment of silicon carbide grinding. Int J Adv Manuf Technol (2004) 24: 816–820.

[15] J. E. Mayer. G. P. Fang, Effect of grit depth of cut on strength of ground ceramics. Annals CIRP (1994). 43. 309-312.

[16] S. Somasundaram1. C. Thiagarajan, Experimental Evaluation of a Chip Thickness Model Based on the Fracture Toughness of Abrasive and Work Material in Grinding of Alumina Ceramics. International Journal of Modern Engineering Research (2013). Vol. 3. Issue. 6. Nov – Dec. pp-3825-3829.

[17] Xu. Hockin, S. Jahanmir, L. K. Ives, Effect of grinding on strength of tetragonal zirconia and zirconia-toughned alumina'. Journal of Machining Science Technology. 1. 1997. 49-66

[18] Malkin S, Grinding technology. theory and applications of machining with abrasives. Ellis Horwood. Chichester (1989).

Investigation of particles separation efficiency of a dielectrophoresis microfluidic device

Jae Heon Lee[1], Haider Ali[1], Kyung Won Kim[1], Cheol Woo Park[1,*]

[1]Kyungpook National University, Daegu, South Korea

*Corresponding author. Tel: (+82) 539507569; E-mail: chwoopark@knu.ac.kr

Keywords: Dielectrophoresis; Particle Separation; Microfluidic Device.

Abstract. Dielectrophoresis is a primarily used technique in microfluidic devices to separate particles or biological cells for their applications in the medical field. A microfluidic device based on dielectrophoresis separates the particles based on their size and dielectric properties. The performance of the microfluidic device mainly depends on the size and dielectric properties of the particle, the applied voltage, and the electrical properties of the fluid. In this study, a microfluidic channel based on dielectrophoresis field-flow fractionation was developed for separating particles of different sizes. A low voltage (6V) was applied to electrodes to separate the particles of three different sizes (i.e., 2 μm, 7μm, and 15 μm). The microfluidic channel of PDMS material was fabricated using the bio-MEMS technology (photolithography). Dielectrophoresis force was generated in the microfluidic device using seven liquid electrodes with equal electric voltage. The left side of the microfluidic device is called the injection section with the sample fluid and buffer fluid inlets. The right side of the device is called collection section with three different outlets for particles. The electric voltage was supplied using a source meter, and a syringe pump was used to inject sample fluid in the microfluidic channel. An inverted-type microscope connected with the CCD camera was used to visualize the separation process and count the number of successfully separated particles at their respective outlets. The separation efficiency of the microfluidic device was examined considering the effects of different particle sizes, buffer flow rates, and electric voltages. The results show that the separation efficiency of the device was significantly reduced with the use of particles of large size (15 μm). High buffer flow rates increased the movement of the particles in the device, which in turn reduced the separation efficiency because of less experience of dielectrophoresis process. An electric voltage of 6V is suitable for efficiently separating the particles and increasing or decreasing the voltage from 6V reduced the separation efficiency of the microfluidic device.

Acknowledgements. This study was supported by a National Research Foundation of Korea (NRF) grant funded by the Korea government (MSIP) (No. 2017R1A2B2005515), and a grant from the Priority Research Centers Program through the NRF, as funded by the MEST (No. 2010-0020089).

References

1. Braschler, T., N. Demierre, E. Nascimento, T. Silva, A.G. Oliva, P. Renaud, Continuous separation of cells by balanced dielectrophoretic forces at multiple frequencies, Lab Chip, 2008, 8, 280-286.
2. Piacentini, N., G. Mernier, R. Tornay, P. Renaud, Separation of platelets from other blood cells in continuous-flow by dielectrophoresis field-flow-fractionation, Biomicrofluidics, 2011, 5, 1-8.
3. Cetin, B., D. Li, P. Renaud, Dielectrophoresis in microfluidics technology, Electrophoresis, 2011, 32, 2410-2427.
4. Tatsumi, K., K. Kawano, H. Okui, H. Shintani, K. Nakabe, Analysis and measurement of dielectrophoretic manipulation of particles and lymphocytes using rail-type electrodes, Medical Engineering Physics, 2016, 38, 24-32.

5. Mernier, G., N. Piacentini, R. Tornay, N. Buffi, P. Renaud, Cell viability assessment by flow cytometry using yeast as cell model, Sensors and Actuators B-Chem, 2011, 154, 160-163.

The Micro-holes Array in Thin Ag-film as a Chemosensor and Biosensor

Nguyen Thi Huyen Trang [2,4,6,a*], Baikova Tatyana Valeryevna[1,b], Danilov Pavel Alexandrovich[2,3,c], Gonchukov Sergey Alexandrovich[1,d], Yermachenko Valery Mikhailovich[1,e], Ionin Andrey Alekseevich[2,f], Khmelnitsky Roman Abramovich[2,g], Kudryashov Sergey Ivanovich [2,3,h], Rudenko Andrey Andreevich[2,i], Saraeva Irina Nikolaevna [2,3,j], Svistunova Tatyana Stepanovna [5,k], Zayarny Dmitry Albertovich[2,l].

[1]National Research Nuclear University MEPhI (Moscow Engineering Physics Institute), Kashirskoeshosse 31, 115409 Moscow, Russia

[2]Lebedev Physical Institute, Leninskiy prospect 53, 119991 Moscow, Russia; email: sikudr@sci.lebedev.ru

[3]ITMO University, Kronverkskiy prospect 49, 197101 St. Peterburg, Russia, Russia

[4]Moscow Institute of Physics and Technology, Institutskiypereulok 9, 141701 Dolgoprudny, Moscow Region, Russia

[5]Infectious Clinical Hospital No 2, 8-thSokolinaya Gora street 15, 105275 Moscow, Russia

[6]Ha Tinh University, No 447, street 26/3, precinct Dai Nai, city Ha Tinh, province Ha Tinh, Viet Nam.

[a]trang.nguyenthihuyen@htu.edu.vn, [b]info@mephi.ru, [c]pavel-danilov2009@yandex.ru, [d]gonchukov@mephi.ru, [e]info@mephi.ru, [f]aion@sci.lebedev.ru,[g]roma@sci.lebedev.ru, [h]sikudr@sci.lebedev.ru, [i]aa_rudenko@mail.ru, [j]insar@lebedev.ru, [k]gonchukov@mephi.ru, [l]dzayarny@sci.lebedev.ru

* corresponding author: Tel: +7(967)132-83-39; E-mail: trang.nguyenthihuyen@htu.edu.vn

Keywords: arrays of microholes; surface-enhanced IR absoprtion; rhodamine 6G; Staphylococcus aureus.

Abstract. Selective IR absorption at 1261 cm^{-1} enhanced by 455 times, was demonstrated for rhodamine 6G molecules, covering a 2D-photonic crystal, represented by a regular array of 4-micron wide holes in a 30 nm thick silver film on a CaF_2 substrate. The reference absorption lines were taken near 2900 cm^{-1}, where the IR radiation is freely channeling through the microholes, indicating the reference substrate coverage by the dye molecules for its relative internal calibration. The limit of background-free detection for the analyte was determined at the level ~10^{-2} monolayer. Using a micro-hole grating in a supported silver film as a laser-fabricated novel optical platform for surface-enhanced IR absoprtion spectroscopy, characteristic absorption bands of Staphylococcus aureus, in particular, its buried carotenoid fragments, were detected in FT-IR spectra with 10-fold analytical enhancement, paving the way for the spectral express-identification of pathogenic microorganisms.

Introduction

Ultrasensitive detection of critical chemical or biological agents is demanding nowadays for counterfeiting and medical applications. This nonlinear-optical method relying upon nanoscale near-field enhancement of intense electromagnetic (EM) fields of localized plasmons in the UV–near-IR range [1], in general, has its intrinsic draw-backs, such as critical nanocontamination (poisoning) of sensing nanostructured surfaces, luminescence background, degradation of sensing nanoelements under elevated thermal loads in CW laser fields. As a result, alternative sensing principles – surface-enhanced IR absoprtion (SEIRA) – were previously developed [2, 3], invoking nano-scale

enhancement of IR-range fields by localized surface plasmons in metallic surface nanoislands and nanoshells [2–6], or their micro-scale enhancement by delocalized surface plasmon-polaritons (SPP) in diverse regular micropatterns [7]. These micro-structured sensing platforms provide an opportunity for luminescence background-free, broad-band or spectrally selective IR-range sensing of functional groups –fingerprints of explosives, narcotics. Comparing to elaborate, multi-step nanofabrication processes, diverse miscroscale surface patterns – e.g. arrays of microholes or microbumps in thin films of plasmonic metals – can be readily directly printed with a high throughput by focused single nano- or femtosecond laser pulses [8, 9].

These micro-structured sensing platforms provide an opportunity for luminescence background-free, broad-band or spectrally selective IR-range sensing of various functional groups – fingerprints of explosives, narcotics and poisoneous substances [10]. Moreover, such micro-structured sensing platforms become especially important in supramolecular biosensing of micro-scale pathogens with their rather buried fingerprint functional groups [11–13]. For example, Au-nanoparticle enhanced SERS of Staphylococcus aureus (SA) samples demonstrated broadband plasmonic enhancement of IR absoprtion for molecular vibrations of extracorporal functional groups, related to amide, proteins and DNA, while characteristic intracorporal vibrations of carotenoid fragments were not significanly affected by the nanoscale plasmonic EM near-fields due to their micron-scale spacings [14]. In contrast, micron-scale evanescent EM fields from micro-structured biophotonic sensors can provide efficient SERS or SEIRA excitation owing, apparently, to lightning-guide [15] or diffraction-resonance [7, 16] effects, respectively, in corresponding sharpened micro-columnar or diffraction grating-like structures.

In this work we report high-rate femtosecond laser fabrication of a number of SEIRA sensors on a thin silver film deposited on an IR-transparent fluorite substrate and FT-IR characterization of their sensing capabilities, using rhodamine 6G dye and Staphylococcus aureus (SA) as a model analyte.

Materials and Methods

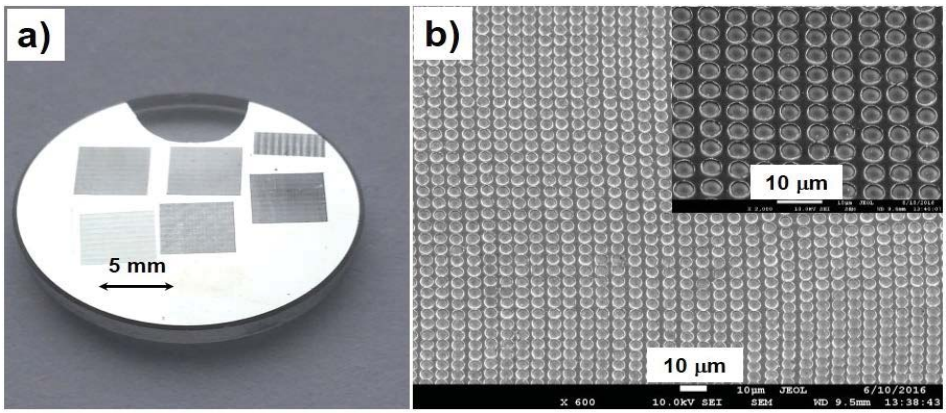


Fig.1. (a) Optical image of the 11-mm wide CaF_2 substrate with the top 30-nm thick Ag-film and a number of micro-hole arrays (typical square – 4×4 mm^2). b) Top-view SEM image of the array with diameter D = 4 μm and period P = 6 μm (inset: its magnified view).

We used a silver (Ag) film with thickness 30 nm, deposited onto a 1-mm thick CaF_2 substrate by magnetron sputtering in argon. Laser radiation was focused 515 nm, 220 fs TEM_{00}-mode with an energy of 85 nJ on the surface of the sample in air through the objective of an optical microscope with the numerical aperture 0.25. Holes in the film located on a three-dimensional motorized holder with computer control and linearly scanned at the scan speeds of 750 $\mu m.s^{-1}$ in a number of lines with a shot-to-shot shift of 6 μm and interline spacing of 6 μm to produce on its frontal surface 4 mm × 4 mm wide large regular arrays of millions microholes with a 4 μm large diameter (Fig. 1). We used Rhodamine 6G and bacteria-Staphylococcus aureus for research surface enhanced IR

absorption of sensors. The arrays of microholes characterized by means of scanning electron microscopy (SEM, JEOL 7001F). IR unpolarized transmittance of the arrays was measured in vacuum in the near-mid IR range of spectral wavenumbers υ = 400-5000 cm^{-1}, using a FT-IR spectrometer V-70 (Bruker).

Results and Discussion

The large-hole sensor with monolayer R6G demonstrates a few much stronger absorption lines for ν = 900 – 1300 cm^{-1} (the strongest one at 1261 cm^{-1}) (Fig.2a). In comparison with this sensor, similar surface density of R6G molecules on the bare CaF_2 substrate indicates much stronger absorption in the range of 2800 – 3000 cm^{-1}, while, surprisingly, much less absorption in the mid-IR range of 900 – 1300 cm^{-1}. Comparison of the mid-IR absorbance for the sensor- and CaF_2-supported R6G molecules demonstrates the analytical SEIRA enhancement – 40 ± 11, 47 ± 19 and 455 ± 230 times for the mid-IR spectral bands at 1024, 1097 and 1261 cm^{-1}, respectively (Fig.2a). However, being normalized to the six-fold enhancement of the absorption in the near-IR range (see above), the spectrally sensitive physical SEIRA enhancement appears to be more moderate –7 ± 2, 8 ± 3 and 76 ± 38 times at 1024, 1097 and 1261 cm^{-1}, respectively. Furthermore, the limit of R6G detection for the sensor, taken for the most SEIRA-enhanced band at 1261 cm^{-1}, at the 3σ-level is equal to LOD = $\Delta/A_{1261} \approx 10^{-2}$ monolayer.

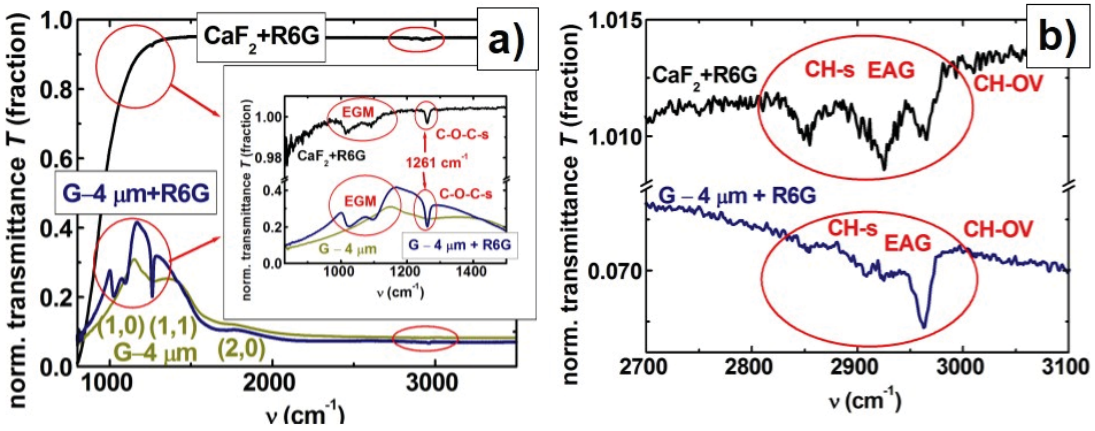


Fig.2. (a) Normalized FT-IR transmission spectra of the CaF_2 substrate with the R6G monolayer, of the clean array and of the array with the R6G monolayer. Inset: the magnified view of their normalized low-ν transmittance with the assignment of the R6G absorption bands on the CaF_2 substrate and the array. b) Magnified view of their normalized high-ν transmittance in the overtone region with the assignment of the composition R6G absorption bands.

Such internal calibration was performed, considering the waveguide-like transmission through the array in the mid-IR range of 2800-3000 cm^{-1} at the transmittance level ≈0.08 (8%) in the clean array and ≈0.069 (6.9%) in the array with the R6G monolayer. The corresponding transmittance dips of R6G bands are 0.11% (≈2850 cm^{-1}), 0.35% (≈2920 cm^{-1}) and 0.2% (≈2960 cm^{-1}) on the CaF_2 substrate, representing combination CH-stretching modes of the main xanthene ring (XR), phenyl, ethyl and methyl groups with the lower-wavenumber external group modes (EGM), but with the overall wave-numbers less than those of C-H stretching overtones (Fig. 2b). On the array, these R6G absorption bands demonstrated, on average, much – almost 7-fold – lower signals of 0.04% (≈2850 cm^{-1}), 0.03% (≈2920 cm^{-1}), while the R6G absorbance at 2960 cm^{-1} unexpectedly appears even two-fold higher (0.4%). Comparing to the 13-fold stronger IR-transmission through the CaF_2 substrate – 92% vs 7% (this array), such 7-fold lower R6G absorbance on the array effectively means its 2-fold, on average, enhancement of R6G absorbance,

with the corresponding 26-fold enhancement of the absorption band at 2960 cm^{-1}. Generally, such enhancement could occur due to plasmonic (spectrally homogeneous over the narrow range of 2800-3000 cm^{-1}) or chemical (R6G-Ag-comlexing, spectrally-selective for the different R6G bonds) factors, which will be discussed below during the analysis of the characteristic absorption bands. Meanwhile, taking the minimal enhancement conditions at ≈2920 cm^{-1}, 13-fold difference in the R6G absorbance on the CaF_2 and the grating could be expected over the entire IR spectrum at the absence of the relevant plasmonic and chemical enhancement factors.

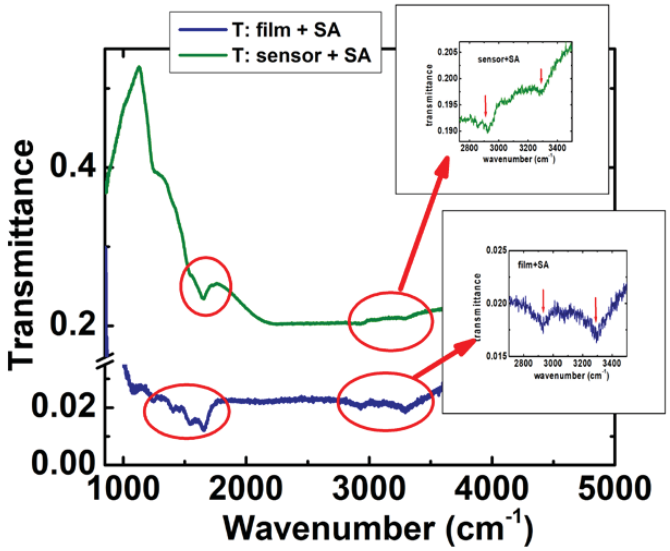


Fig. 3. IR transmission (T) spectra of the film (bottom curve) and the sensor (upper curve) with the SA-layer. Inset: Magnified view of their normalized high-ν transmittance in the overtone region with the assignment of the composition SA absorption bands.

Comparison of the SA-absorption bands observed in the transmission mode for the non-structured film and the sensor indicates that such characteristic absorption of the bacteria is present in the spectral regions of 1300 – 1500 cm^{-1} and 1500 – 1700 cm^{-1} of the sensor, respectively (see the corresponding SA-absorption in figure 2b over the range 1100 – 1700 cm^{-1} for the SA-layer on the film). Likewise, SA-absorption bands appear also as overtones in the region of 2800 – 3700 cm^{-1} with almost equal amplitudes both for the film and sensor (see the insets in figure 2b), indicating, that the order of magnitude higher transmittance of the sensor in the mid-IR range does not result in stronger SA-absorbance, and thus providing the internal calibration of the analyte distribution for evaluating the sensor response [16]. In fact, the evenly deposited SA-layer yields in the almost equal absorbance amplitudes for SA overtones in figure 2b. Hence, the amplitudes of the main characteristic SA-absorption bands – $A_{T,max} \approx 0.007$ for the film and $A_{T,max} \approx 0.025 – 0.03$ for the sensor – can be directly compared, exhibiting the 3 – 4 fold sensor enhancement regarding the non-structured Ag-film, similarly to the previous tests for rhodamine 6G analyte [16]. Effectively, this may mean 10-fold analytical enhancement of the sensor regarding inert – e.g. bare CaF_2 substrates, as was demonstrated previously for this dye [16].

Summary

Our research has demonstrated high mid-IR sensitivity and ultralow limit of background-free detection of the easy-to-fabricate microhole-array SEIRA sensor on the 30 nm thick silver film, as well as, for the first time, the important opportunity for its relative internal calibration in the near-IR spectral range. A novel optical platform for surface-enhanced IR absoprtion spectroscopy, based on

a micro-hole grating in a supported silver film, was tested, demonstrating 10-fold analytical enhancement of the characteristic absorption bands of SA, while the buried carotenoid fragments, as the fingerprints of such bacteria, were also detected in the IR-spectra, paving the way for spectral express-identification of this and potentially other pathogenic microorganisms. Importantly, the sensing grating with a few hundred thousands of microholes was rapidly fabricated by high-throughput laser ablation (single shot per microhole), using a femtosecond fiber laser with MHz-repetition rates and a fast electromechnical positioning system.

Acknowledgments

This work was supported by the grant of the RAS Presidium program, the Russian Foundation for Basic Research (grant nos. 15-02-08400, 16-32-00880), and by the Government of the Russian Federation (Grant 074-U01) through ITMO Visiting Professorship Program for S. I. Kudryashov.

References

[1] V.V. Klimov, Nanoplasmonics, CRC Press., 2014.
[2] A. Hartstein, J. R. Kirtley, and J. C. Tsang, Enhancement of the Infrared Absorption from Molecular Monolayers with Thin Metal Overlayers, Phys. Rev. Lett, V. 45, (1980) p. 201.
[3] T. V. Baikova, P. A. Danilov, S. A. Gonchukov, V. M. Yermachenko, A. A. Ionin, R. A. Khmelnitskii, S. I. Kudryashov, T. T. H. Nguyen, A. A. Rudenko, I. N. Saraeva, T. S. Svistunova, and D. A. Zayarny, Microstructures as IR-sensors with Staphylococcus aureus bacteria, AIP Conference Proceedings 1874, (2017) 040052.
[4] Masatoshi Osawa, Masahiko Ikeda, Surface-enhanced infrared absorption of p-nitrobenzoic acid deposited on silver island films: contributions of electromagnetic and chemical mechanisms, J. Phys. Chem., V.95 (24), (1991) pp 9914 – 9919.
[5] M. Osawa et al, Surface-enhanced infrared spectroscopy: the origin of the absorption enhancement and band selection rule in the infrared spectra of molecules adsorbed on fine metal particles, Applied spectroscopy, T. 47, № 9, (1993) p 1497 – 1502.
[6] J. Kundu et al, Surface enhanced infrared absorption (SEIRA) spectroscopy on nanoshell aggregate substrates, Chemical Physics Letters, T. 452, № 1, (2008) p. 115 – 119.
[7] D. A. Zayarny, A. A. Ionin, I. V. Kiseleva, S. I. Kudryashov, S. V. Makarov, A. A. Rudenko, I. A. Timkin, R. A. Khmel'nitskii and T. H. T. Nguyen , Surface Enhanced Infrared Absorption of a Dye on a Metallic Diffraction Grating, JETP Lett., 100, (2014) p. 295.
[8] Y. N. Kulchin, O. B. Vitrik, A. A. Kuchmizhak, A. V. Nepomnyashchii, A. G. Savchuk, A. A. Ionin, S. I. Kudryashov, and S. V. Makarov, Through nanohole formation in thin metallic film by single nanosecond laser pulses using optical dielectric apertureless probe, Optics Letters., Vol. 38, Issue 9, (2013) p 1452 – 1454.
[9] P. A. Danilov, D. A. Zayarnyi, A A Ionin, S. I. Kudryashov, S. V. Makarov, A. A. Rudenko, V. I. Yurovskikh, Yu N. Kulchin, O. B. Vitrik, A. A. Kuchmizhak, Mechanisms of formation of sub- and micrometre-scale holes in thin metal films by single nano- and femtosecond laser pulses, Quantum Electronics, Volume 44, Number 6, (2014).
[10] C. D'Andrea et. al, Optical Nanoantennas for Multiband Surface-Enhanced Infrared and Raman Spectroscopy, ACS Nano, 7 (4), (2013) p 3522–3531.
[11] M. Darvin, I. Gersonde, S. Ey, N. Brandt, H. Albrecht, S. Gonchukov, W. Sterry and J. Lademann, Noninvasive detection of beta-carotene and lycopene in human skin using Raman spectroscopy, Laser Phys., 14, (2004) p 231.
[12] S. Gonchukov, T. Baikova, M. Alushin, T. Svistunova, S. Minaeva, A. Ionin, S. Kudryashov, I. Saraeva. and D. Zayarny, Single Bacterium Detection Using Sers, J. Phys.: Conf. Series, 691, (2016) 012010.
[13] T. V. Baikova, P. A. Danilov, S. A. Gonchukov, V. M. Yermachenko, A. A. Ionin, R. A. Khmelnitskii, S. I. Kudryashov, T. T. H. Nguyen, A. A. Rudenko, I. N. Saraeva, T. S. Svistunova

and D. A. Zayarny, Diffraction micrograting as a novel optical biosensing platform," Laser Phys. Lett., V.13, (2016) p 075602 (4pp).
[14] Z. Movasaghi, S. Rehman and I. Rehman, Raman spectroscopy of biological tissues, Appl. Spectrosc. Rev., 42, (2007) p 493.
[15] X. Wang , C. Bhadra, T. Hoang, Y. Dang, R. Buividas, J. Wang, R. Crawford, E. Ivanova and S. Juodkazis, A bactericidal microfluidic device constructed using nano-textured black silicon, RSC Adv., 6, (2016) p 26300.
[16] P. A. Danilov, S. A. Gonchukov, A. A. Ionin, R. A. Khmelnitskii, S. I. Kudryashov, T. T. H. Nguyen, A. A. Rudenko, I. N. Saraeva and D. A. Zayarny, Background-free, highly sensitive surface-enhanced IR absorption of rhodamine 6G molecules deposited onto an array of microholes in thin silver film, Laser Phys. Lett., V.13, (2016) p 055602.

Effect of Ethylene Vinyl Axetate (EVA) on the Mechanical Properties of Low-Density Polyethylene/ EVA Blends

Le Thi My Hoa[1,a], Pham Thi Hong Nga[1,b]

[1]University of Technology and Education Ho Chi Minh City, Vietnam

[a] myhoa263@gmail.com, [b]hongnga@hcmute.edu.vn

Key words: LDPE/ EVA; Ethylene Vinyl Acetate; Tensile strength; Elongation; Blend

Abstract. The extensive range of fillers used nowadays indicated the major significance of filler in the plastic industry. Although their original purpose was to lower the cost of the molding compounds; prime importance is now attached to selective modification of the properties of a specific plastic. In this study, the examples of LDPE/EVA blends, were put into 0, 3, 6, 9, 12 and 15 wt.% of EVA. The tensile strength, bending strength and impact strength of samples were determined according to ASTM D638, ISO 178 and ISO 179. Results showed that when increasing ratio of EVA in LDPE/ EVA blends, tensile strength decreased from 10.9 MPa to 8.6 MPa. Bending strength decreased linearly from 9.63 MPa to 5.46 MPa. Charpy impact strength decreased from 47.5 kJ/m^2 to 6.3 kJ/m^2. On the contrary, elongation in 100% LDPE is 78.3%; with the appearance of EVA, elongation of the LDPE/ EVA blends increased upto 109.1%. In addition, SEM micrographs indicated that, it was more crystal-clear when the EVA content is less; in the highest EVA content with 15%, it can be seen that the specimen after pressing is slightly opaque and darker than the orthers. From that showed the addition of EVA to the polymer leads the tensile strength, bending strength were not affect much, impact strength decreased but elongation experienced an increase.

Introduction

Low-Density Polyethylene (LDPE) is thermoplastic with the basic features of LDPE such as low density, toughness, impact resistance at low temperature, good insulation, durable chemicals and good anti-worn [1]. EVA (Ethylene Vinyl Acetate Copolymer) is one kind of plastic which is a compound between Ethylene and Acetate, produced by high pressure stage with pressure above 2,500 atm [2]. Among the types of PE, LDPE has many properties that can match with EVA better such as low-density branching, melting points are close to EVA... So choosing LDPE blends with EVA can overcome the limitations of each component polymer, contributing to increased mechanical properties, increased flexibility, elasticity, toughness and resistance to cracking under the impact of the environment [3, 4].

According to the study of H. Azizi the mechanical properties of XLPE/ EVA blends improve by increasing the EVA content by up to 15% by weight, in addition, the tensile strength of XLPE/ EVA blends is slightly reduced [5]. The study of Bistra Borisova with the wt.% of EVA in LDPE/ EVA blends were 1.8, 3.6, 5.4, 7.1, and 8.9, it has been shown that EVA particles are capable of blocking cracks propagation, increasing the toughness of the material and reduce the elongation [6]. The study of S. M. A. Salehi, LDPE and mixtures of LDPE with 5, 10, 20, and 30% EVA, in all cases, it has been found that the gel-content variations increased with increasing absorbed dose [7]. M. A. Rodri´guez-pe´rez studied about the effect of EVA addition on the technical characteristics of LPDE/ EVA foam, with LDPE/ EVA blend containing 10, 30, 90% EVA; and 25% EPR, EVA 75% [8]. The study of Siqin Dalai shown that, when the percentage of EVA in the LDPE/ EVA blends was 0, 20, 25, 30, 50 and 100%, the tensile strength of the LDPE/EVA blend increased with increasing gel percentage on the LDPE / EVA blends [9]. According to G. Takidis, tensile strength and elongation at break of LDPE/ EVA blend increased almost linearly by increasing EVA content [2].

In LDPE/EVA blends, the mechanical properties of the blends will increase linearly as the EVA increases the same amount of radiation or time and temperature of mixing increase. However, there are some studies that indicate that LDPE/EVA and PE/EVA blends will reduce the mechanical, namely tensile strength when increasing the EVA in the mixture. To clarify the effect of EVA on the LDPE/ EVA blends, the mechanical properties of LDPE/ EVA blends were tested such as tensile strength, bending strength and impact strength of the mixture with EVA content in the LDPE/ EVA blends are 0, 3, 6, 9, 12, 15 wt.%.

Experiment

Materials and chemicals was used in this study: Polyethylene (LDPE): SABIC - LDPE 4024 origin Saudi Arabia, provided by Thuan Thang Plastics Co., Ltd; Ethylene vinyl acetate (EVA) is supplied by Dong Nhat Phat Company. The test specimen consisted of LDPE and EVA was mixed and pressed in the proportions given in Table 1.

Table 1: Proportion of LDPE and EVA in the test specimens

Sample / Component	M1	M2	M3	M4	M5	M6
EVA (%)	0	3	6	9	12	15
LDPE (%)	100	97	94	91	88	85

The ASTM D638 was used to measure plastic tensile strength. Samples were processed according to the size shown in Figure 1. The experiment was carried out at a speed of 50 mm / min at room temperature and mounted on the test machine. The experiment was carried out on a Shimadzu Autograph AG-X Plus 20 kN (Japan) with longitudinal extension, a high resolution (1.8 µm) camera with no contact with the specimen and basic specifications. as follows: The maximum test power was 20 kN, speed range 0.001 - 1600 mm/ min, speed accuracy: ± 0.1% test speed, operating temperature at 5 – 50^{0}C, data acquisition speed 1000 Hz. The sample size was shown in Figure 1.

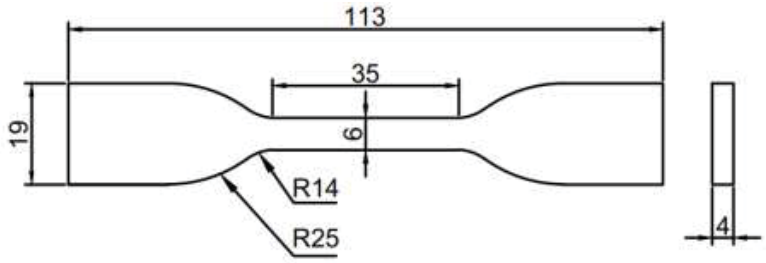


Figure 1: Sample size of the tensile test [10]

The analogous test to determine bending strength of materials in the ISO system is ISO 178. Test specimens for bending strength and impact strength was mixed and pressed using a Shine Well SW-120B injection machine. The size of the sample tested in this experiment was processed according to the parameters: 125 × 12 × 3.2 mm (Figure 2). The device was used in this method is the Instron 5566 machine with load capacity is 10 kN (2250 lbf); maximum power is 200 VA; weight of load frame is 136 kg (300 lb).

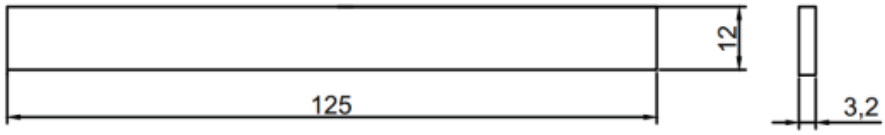


Figure 2: Sample size for bending strength testing [11]

Impact strength was determined according to ISO 179-1. Size of the samples in this experiment were calculated by the following parameters: 125 × 12 × 3.2 mm (Figure 3). The device was used to test the impact velocity is impact tester machine model IT504 -Tinius Olsen-England.

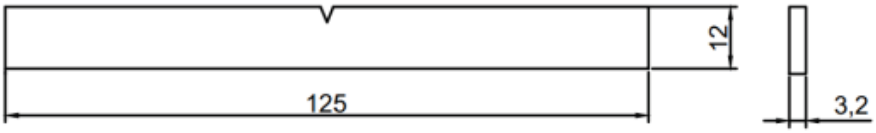


Figure 3: Sample size for Charpy impact strength [12]

Results

The tensile strength' results of each sample group were showed in Figure 4. The tensile strength of the LDPE/EVA blends decreased as EVA content in the mixture increased. The tensile strength of the sample containing 100% LDPE was 10.9 MPa, however, when adding 3% EVA to the LDPE/EVA blend the tensile strength was reduced to 10.3 MPa. When the EVA content of the mixture was increased to 6%, the tensile strength of the mixture was 9.8 MPa, ie 0.5 MPa lower than that of the LDPE/EVA containing 3% EVA. EVA content increased to 9% in the mixture, the tensile strength decreased to 9.3 MPa. With an EVA content of 12% LDPE / EVA, the tensile strength was reduced by 0.3 MPa compared to the EVA by 9%, which means that the tensile strength was only 9.0 MPa. With the highest EVA of 15%, the tensile strength was reduced by 0.4 MPa to 8.6 MPa.

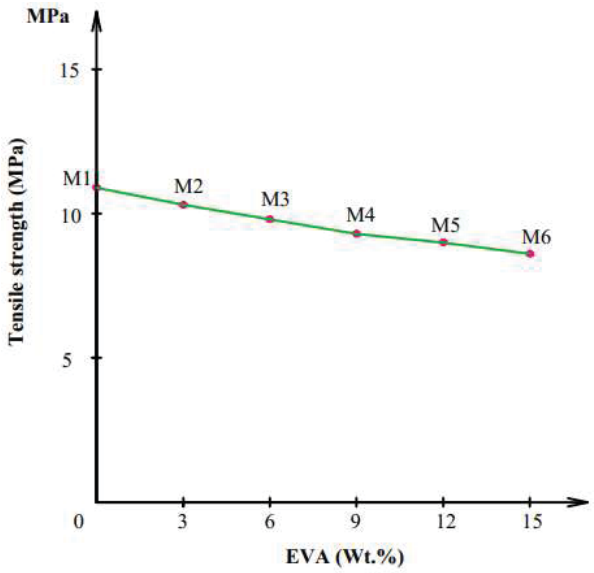


Figure 4: The average tensile strength of test samples

The elongation' results were shown in Figure 5. The elongation of samples containing 100% LDPE was the lowest (78.3%). The elongation increased when the EVA was added into the LDPE/EVA blends. Specifically, when adding 3% EVA, the elongation increased to 95%, 6% EVA

increased slightly (95.8%), then dropped to 93.4% for samples containing 9% EVA. As the EVA content increased to 12%, the deformation increased sharply, up to 109.1% and dropped to 87.5% when the blends contained 15% EVA.

:

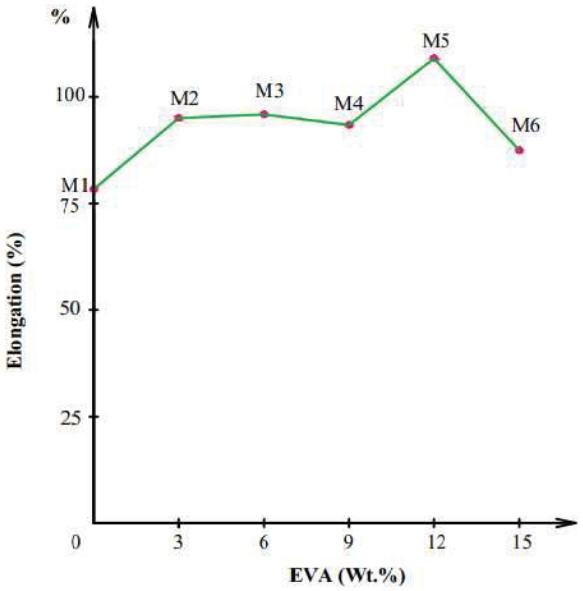


Figure 5: The average elongation of test samples

Figure 6 summarized the bending strength' results of samples M1, M2, M3, M4, M5, M6. The average reduction in pressure from M1 (9.63 MPa) to M2 (6.88 MPa) continued to decrease to M3 (6.51 MPa) and slightly increased in M4 (6.56 MPa), followed by reduction in B6 (6.08 MPa) and sample M6 (5.46 MPa). This results shown that when the EVA content in the blends increased, the bending strength decreased.

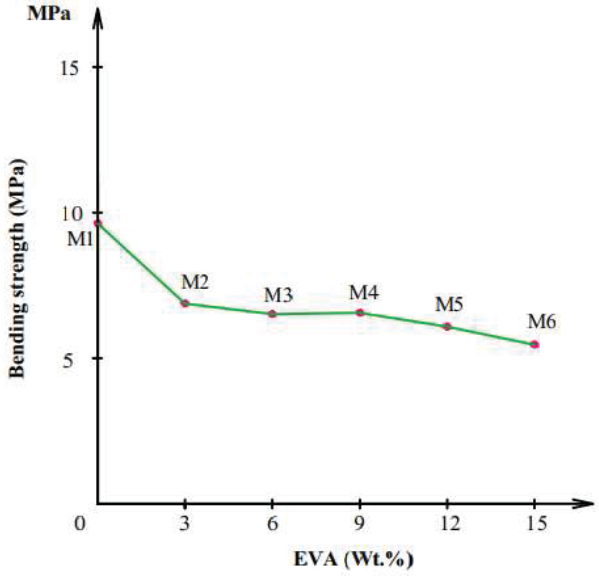


Figure 6: The average bending strength of test samples

The results of Charpy Impact strength was shown in Figure 7. The maximum impact velocity of the sample was 100% LDPE, when EVA was added into LDPE / EVA blends, the impact strength decreased very strong. For the EVA ratios in the LDPE / EVA blend, 3% EVA had the highest impact strength of 8.3 kJ/m^2, then it decreased slightly by increasing wt % of EVA to 6% and 9%. At 12% of EVA, the impact strength was increased to 7.1 kJ/m^2, and then decreased to 6.3 kJ/m^2 by increasing the wt % of EVA upto 15%.

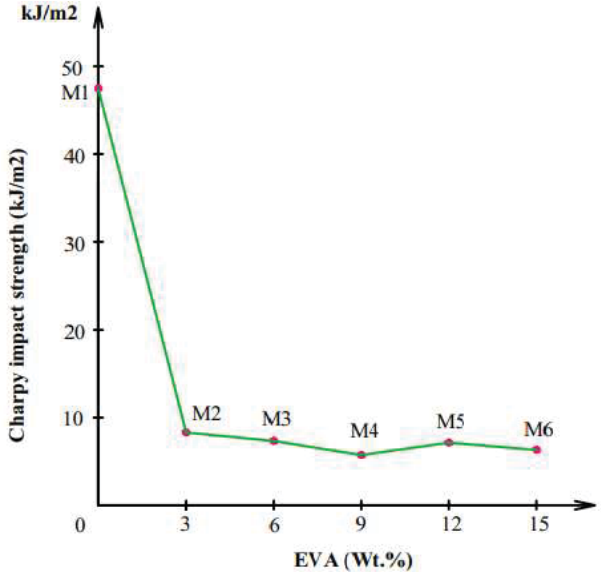
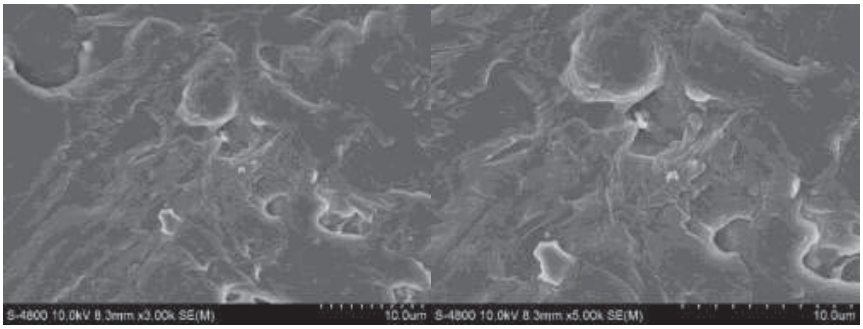
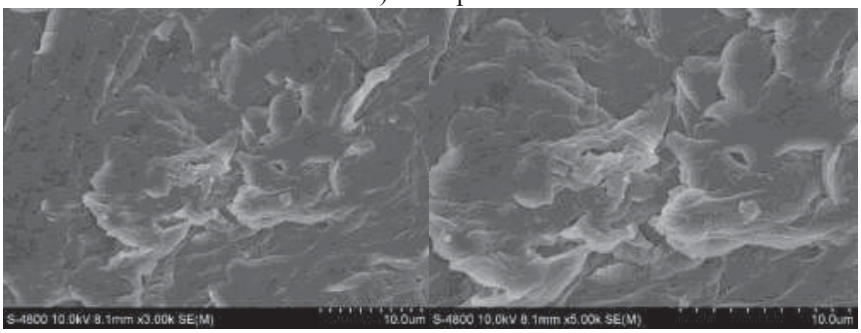


Figure 7: The average Charpy impact strength of test samples

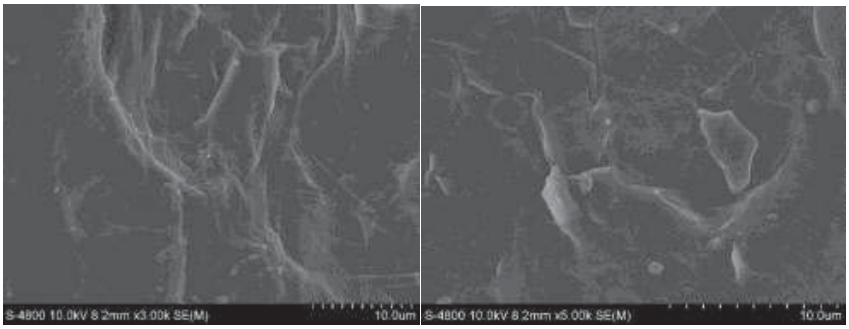
To better analyze the mechanical properties of the LDPE / EVA mixture. SEM micrographs for the LDPE/EVA blends was conducted. The results was shown in Figure 9 (a-b-c-d-e-f).



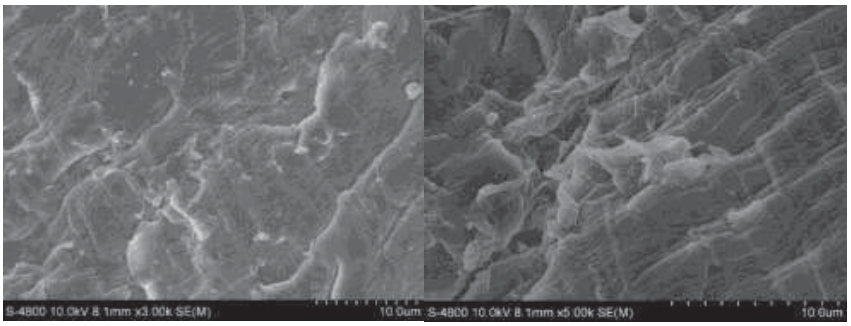
a) Sample M1



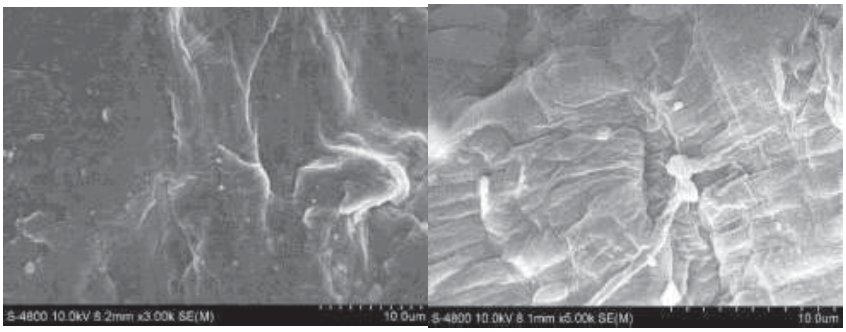
b) Sample M2



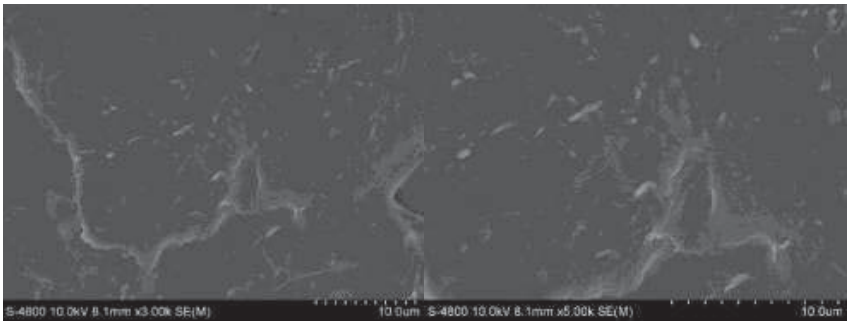
c) Sample M3



d) Sample M4



e) Sample M5



f) Sample M6

Figure 9: SEM micrographs for the LDPE/EVA blend with different weight percent of EVA

Discussion

About the tensile strength and elongation of LDPE/EVA blends, the reaction between the radicals of PE and EVA to form copolymers and block copolymers (PE-g-EVA and PE-b-EVA) acting as a compatibilizer for these two polymers is unlikely. As for LDPE, low density polymers and during fabrication, the mixing process is merely a labyrinthine hybridization of LDPE and EVA under mechanical impact. LDPE and EVA are different with their chemical nature, chemical structure, polarization, surface energy interaction… compatibility of the two polymers is low. Therefore, the material obtained does not enhance the outstanding properties of the component polymers [2, 9]. In studies about the tensile strength of the LDPE/ EVA blends, when irradiated with radiation to alter the chemical structure of the mixture, the same absorbed dose, the mechanical properties of the LDPE/ EVA blend will increase linearly when increasing wt % of EVA. Based on empirical data, it was found that when EVA was increased in the mixture of LDPE/ EVA blends, the tensile strength of the LDPE/EVA blends material decreased linearly as the wt % of EVA in the blends increased.

To explain the result of Charpy impact strength, enhanced compatibility of LDPE and EVA had been explained by the occurrence of chemical reactions during the melting process. Because the large molecule EVA is capable of generating free radicals easily, so EVA-free radicals may react with the vinylylene group or the free radicals of LDPE at high temperatures. The cross-link between LDPE and EVA polymers is made to increase adhesion between polymers in the blend. For the samples to be prepared the mixing process is a mix and macromolecules of LDPE and EVA under mechanical impact. Therefore, the increase in the EVA ratio in the LDPE/ EVA blends does not increase the impact strength of the mixture [4, 9].

The results of the SEM images, from the sample M2, there were EVA spherical particles dispersed on the LDPE substrate, in the sample with the highest EVA content of 15% (M6), the number of these particles appears was quite high. The number of EVA particles increased from the M2 to M6 dispersed fairly evenly across the surface. The size of EVA particles decreased and the number of particles increased as the EVA content in the blend increased. Clear bipartite boundaries and relatively poor adhesion.

Conclusion

Based on the above results, when increasing 0, 3, 6, 9, 12 and 15 wt.% of EVA into LDPE/ EVA blends, the tensile strength decreased. Bending strength of samples decreased when the EVA content in the blends increased. When adding EVA to LDPE/ EVA blends, the impact strength decreased strongly. Elongnation increased with the appearance of EVA, compared to samples containing 100% LDPE.

References

[1] Yang Chen, Investigations of Environmental Stress Cracking Resistance of HDPE/EVA and LDPE/EVA Blends, Wiley Periodicals, Inc. J. Appl. Polym. Sci., 131 (2014) 3988

[2] G. Takidis, D. N. Bikiaris, G. Z. Papageorgiou, at al. Compatibility of Low-Density Polyethylene/Poly (ethyleneco-vinyl acetate) Binary Blends Prepared by Melt Mixing, Journal of Applied Polymer Science, 90 (2003) 841-852

[3] A. Noori, F. Ziaie, The Infuence of morphology on the electrical properties of 10MeV electron beam irradiated polyethylene/ethylene-vinyl-acetate blend (PE/EVA), Journal of Applied Chemical Research, 14 (2010) 37-44

[4] I. Ray, D. Khastgir, Correlation between morphology with dynamic mechanical, thermal, physic, mechanical properties and electrical conductivity for EVA-LDPE blends, Polymer, 34 (10), (1993) 2030-2037

[5] H. Azizi, J. Barzin, J. Morshedian, Silane crosslinking of polyethylene: the effects of EVA, ATH and Sb_2O_3 on properties of the production in continuous grafting of LDPE, EXPRESS Polymer Letters, 1, No.6 (2007) 378-384

[6] Bistra Borisova, Jo¨rg Kressler, Environmental Stress-Cracking Resistance of LDPE/EVA Blends, Macromol. Mater. Eng. 288 (2003) 509-515

[7] S. M. A. Salehi, G. Mirjalili, J. Amrollahi, Effects of High-Energy Electron Beam on Low-Density Polyethylene Materials Containing EVA, Journal of Applied Polymer Science, 92 (2004) 1049-1052

[8] M. A. Rodri´guez-pe´rez, A. Duijsens, j. A. De saja, Effect of Addition of EVA on the Technical Properties of Extruded Foam Profiles of Low-Density Polyethylene/EVA Blends, Journal of Applied Polymer Science, 68 (1998) 1237-1244

[9] Siqin Dalai, Chen Wenxju, An Investigation on Radiation Crosslinked Foam of LDPE/EVA Blends, JAERI-Conf, 03 (1995)

[10] ASTM D638 Standard test method for tensile properties of Plastic

[11] ISO 178:2010 Plastics - Determination of flexural properties

[12] ISO 179-1:2010 Plastics - Determination of Charpy impact properties

Utilization of functionalized Graphene in based-epoxy paint coatings for anti- corrosive protection of steel surfaces

Nguyen Dinh Lam[1], Phan Thi Thuy Hang[1,2]*

[1] The University of Danang – University of Science and Technology, Danang-Vietnam

[2] The University of Da Nang - University of Education, Danang-Vietnam

* Tel: (+84) 935606756; E-mail: thuyhang@dut.udn.vn

Keywords: nanocarbon materials, functionalized graphene, anti-corrosion property, epoxy paint coatings.

Abstract. Steel materials are selected because of their mechanical properties and machine-ability at a low price but they are not resistant in the corrosion medium. The coatings of anti-corrosion paint always play essential role in this area [1]. By applying an appropriate coating, steel with good mechanical properties can be utilized in many applications, also for decorative purposes. Epoxy resins are known thank to their excellent properties of anti-corrosion and of chemical resistance. Also epoxy resins will form a durable protective coating [2]. The addition in polymer binders as a pigment or a filler in order to improve physico-mechanical performances and corrosion protection for paint coatings is crucial in the paint coating technology. Therefore, this work presents the use of nanocarbon materials to fill in epoxy binder for application as anti-corrosion coatings for steel surfaces. The main results of the nanocarbon materials addition in epoxy resin for this purpose were investigated and presented in this paper. Chemically functionalized graphene material (GO), obtained from oxidative reaction by the mixture of H_2SO_4, H_3PO_4 and $KMnO_4$ mixture of natural graphite, was selected as filling nanocarbon materials. Playing a very important role as a good interfacial bonding between matrixes and graphene sheets, the uses of functionalized graphene evidenced that the performance of GO-based epoxy nanopaint have been enhanced about 5.75 times more than that of neat epoxy coating. In addition physico-machenical properties of this type of GO- based epoxy nanopaint also were improved significantly.

Introduction

Corrosion is a natural process. Just like water flows to the lowest level, all natural processes tend toward the lowest possible energy states [2]. Metallic corrosion is inspected by the chemical reactions between the metal surface and the environment, leading to an irreversible disintegration of the material under formation of oxides, hydroxides and salts [1]. The corrosion resistance is fastly weakened when metallic materials are subjected to a medium containing chloride or moisture environment, with a tendency to suffer localized corrosion [1,2]. This may lead to the modification of aesthetic appearance and original structure, and can be accompanied by the release of potentially toxic ions. The effects of corrosion in our daily lives are both direct, in that corrosion affects the useful service lives of our possessions, and indirect, in that producers and suppliers of goods and services incur corrosion costs, which they pass on to consumers [3]. At home, corrosion is readily recognized on automobile body panels, charcoal grills, outdoor furniture, and metal tools... Corrosion protection is applied for all major household appliances such as water heaters, furnaces, ranges, washers, and dryers [2]. The coatings of anti-corrosion paint always play essential role in this area. By applying an appropriate coating, a base metal with good mechanical properties can be utilized for many different applications. Organic coatings provide protection either by a barrier action from the layer or by active corrosion inhibition from pigments in the coating [4]. Hence, graphene, which

is a nanostructural carbon material was used as a pigment or filler for epoxy paint coating in this work. As known, in paint technology, the pigment is the second important component after binder. Graphene is a two dimensional material made entirely of carbon atoms and it is only a single atom thick. Graphene is mechanically very strong it is also lightweight and flexible [5]. Due to the excellent properties of graphene, it is believed that it could be used to enhance significantly the performance of coating. In addition, it can be used with nanoparticles to form graphene nanoparticles composites coating and as a high quality coating materials [5]. However, graphene nanosheets are hard to be incorporated and distributed homogeneously into various matrices for applications [5,6]. Recently, research into graphene-based materials, which includes graphene, graphene oxide (GO), reduced graphene oxide (rGO), and graphene embedded polymers, has demonstrated potential for applications in anti-corrosion coatings [6]. For nanofiller or nanopigment based coating, the functionalization of graphene rends this latter to achieve good interfacial bonding between matrices and graphene nanosheets. The functionalization of graphene can be performed via physical or chemical approaches. The graphene nanosheets are tightly attached to each other making them directly insoluble in any solvent while GO shows desirable dispersion behavior [6,7]. The reactive oxygenic groups, present on the edges (carbonyl and carboxyl groups) and planes (hydroxyl and epoxide groups) of GO sheets, can stabilize the dispersion of GO in aqueous media, enhance the interfacial bonding with molecules of the dispersant, and facilitate the stress transfer in the composites, theses behaviors render GO as attractive and promising nanoscale reinforcement fillers in polymer composites [6,7]. In 1958 year, Hummers introduced a method for oxidation of graphite using $KMnO_4$, H_2SO_4 and HNO_3 to synthesis GO [8]. The report of an improved Hummers method [8] for the preparation of GO which was studied by authos group of James M.Tour comes from Rice University (Texas, USA) was published on ACS Nano journal in 2010 year [9]. This improved Hummers method provides a greater amount of hydrophilic oxidized graphene materials when compared to that from Hummers method. With additional $KMnO_4$ and excluding $NaNO_3$, the reactions taking place in improved Hummers method are kept away from toxic gases formation [8,9] therefore this method is considered as an environment-friendly approach. In this work we adopted improved Tour method [9] to synthesis graphene oxide from natural graphite powder and investigated the effects of graphite, Graphene and Graphene oxide on physico-mechanical and anticorrosion properties of epoxy primer paints.

Experiental

Materials

Graphite powder was supplied by General Pencil company (USA); for facilitating handling, Epotec YD 011 disolved in xylene was used as a binder for the paint coatings. Epotec TH 7515 is a high viscosity reactive polyamide used as a curing agent for epoxy resins; aceton, etanol, n-butanol, xylene are used as a solvent. They are produced by Xilong Chemical Factory and Guangdong Guanghua Sci-Tech Co. The substrate material of test samples is Q-Panel standard steel. Graphene was purchased from Amstrongmaterials company (USA) and used for this study without any further treatment.

Preparation of Graphene oxide from graphite

The modified Tour's method [9] was reported for chemical modification of natural graphite materials in this paper. The modification of this method is that only HCl acid was used to remove oxidative agent ($KMnO_4$) without using hydroperoxide (H_2O_2), which was used by Tour's method. The detailed synthesis procedure is shown as follow:

The oxidation reaction was carried out in a system of a glass three-necked reactor, a welding tube, a thermometer and a heating magnetic stirrer. At first, both H_2SO_4 acid and H_3PO_4 acid (volume ratio of acids is 9:1) were mixed together in the reactor. The reactor was

putted in an ice bath to refrigerate down below 5 °C for about 30 minutes and kept on stirring the slurry at the same time. The next step, graphite materials were incorporated into the acid mixture and stirred for about 30 minutes. After that, oxidizing agent ($KMnO_4$) was divided into three parts and loaded into the reactor three times for 45 minutes and $KMnO_4$: Graphite wt.% ratio of 6: 1 was used. The reaction slurry was followed stirring for 15 minutes more, then the ice bath was removed from the reaction system. Heating upto 35 °C temperature for the slurry and kept for 30 minutes. Follow that, the reaction was increased until 60 ºC and maintained for 3 hours. After that, HCl acid was added to the reactor and stirred with a higher speed for 5 minutes and finished reaction. Then the slurry was carried out steps such as filter, wash and dry. The product was packed in plastic bag for using in further experiments. The product was graphene oxide or can be called as functionalized graphene and symbolized of GO in this paper. This was demonstrate by characterization methods such as FTIR and XRD was presented in the results and discussion section.

Sample preparation

Preparation of nanofiller (nanopigment)/epoxy resin paint: The nanofillers were added in the paint with a content of 0,1wt% of epoxy resin, that was graphene oxide or graphene respectively [3]. At first, the nanofiller was putted in n-butanol solvent with 10 mg/10 ml ratio by a sonication rod for 1h until creating an uniform dispersion. This mixture was incorporated into the epoxy binder by a stirrer bar until becoming a homogeneous mixture.

Preparation of the substrates: The adhesion of the coating and the anti-corrosion property of the product depend on the preparation of the surface. Before a coating is applied to the substrate, the contaminants on the surface has to be removed. The preparation is often referred to as pretreatment. Hence, in this work the substrate pretreatment was done according to three–stages procedure as follows:

Stage 1 – Abrading by mechanical method as a sanding to remove dirt, rust, oxides...

Stage 2 – Cleaning by hand wiping with a special liquid detergent for 15 minutes at ambient temperature to remove abrasion dust.

Stage 3 – Drying in the vacuum dryer for 10 minutes at 50 ^oC and putting into plastic bags for preservation before coating paint on the surface.

Paint film deposition: Before applying paint on the surface, the curing agent (calculated weight ratio of 10:1 on the epoxy binder weight) was mixed together with solution of Epotec YD 011 disolved in xylene . The film deposition on the pretreated substrate surfaces was done by a spray gun. Then the samples were kept at room temperature until the paint films were cured fully. The samples were then subject to physico-mechanical and anti-corrosion properties tests. Dry the film thickness was about 20-30 µm.

Characterization methods

In this work, Fourier Transform Infrared spectroscopy (FTIR) was employed to evaluate results of synthesis of GO from graphite material. A Thermo Nicolet 6700 spectrometer was used to collect the FTIR data for chemical structure analysis of the fillers. The crystal structure characterization of them were analyzed by X-ray diffraction (XRD) and performed using a Siemens D5005 X-ray diffractometer.

Results and discussions

The result of synthesis GO

The results of chemical structure characterization by FTIR

The FTIR analysis was used to approve presence of chemical group containing oxygen of obtained product from the reaction. The FTIR spectrum data was analysed and listed in table 1.

The presence of these functional groups demonstrated that GO product was formed by modified Tour's method from graphite material successfully.

Table 1. Summary of FTIR spectra on presence of the functional groups of GO

Wavenumber (cm^{-1})	Peak assignment
1050	C-C stretching vibration of graphite structure (both two Fig. 1A and 1B
1150	Peak of C-O-C bond of epoxide group (only Fig. 1B)
1650	C=C stretching vibration of graphite structure (both two Fig. 1A and 1B)
1730	Peak of C=O bond of carboxyl group (only Fig. 1B)
3475	Peak of OH bond (only Fig. 1B)

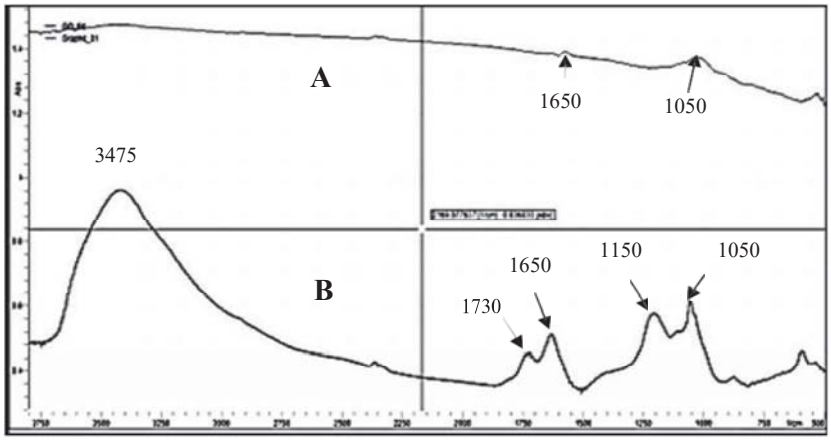


Fig. 1. FTIR spectrum of Graphite (A) and GO (B).

The results of XRD analysis

The XRD spectrum was conducted in order to clarify the change in the crystal structure of graphite material and GO product.

The XRD pattern of natural Graphite material is indicated in Fig. 2A. Can see a strong di raction peak at $2\theta = 26.5^{o}$ is the specifics peak of crystal structure of graphite. This result sames reports indicated in publications [10-13]. In Fig. 2B also showed the peak at $2\theta = 26.5^{o}$ still exists but the height is considerably decreased and without apperiance of a new strong di raction peak at $2\theta=10^{o}$ of the crystal structure of graphite oxide. This result is the same as results reported in the papers of Hummer's group and Tour's group [8-10]. XRD spectrum of the product in Fig. 2B is similar to one of graphene nanosheets reported in references [11-14]. This expected that the formed product in this work was exfoliated to graphene oxide fewer-nanoplates without using methods such as sonication, microwave or chemical agents etc. reported in references [11,12].

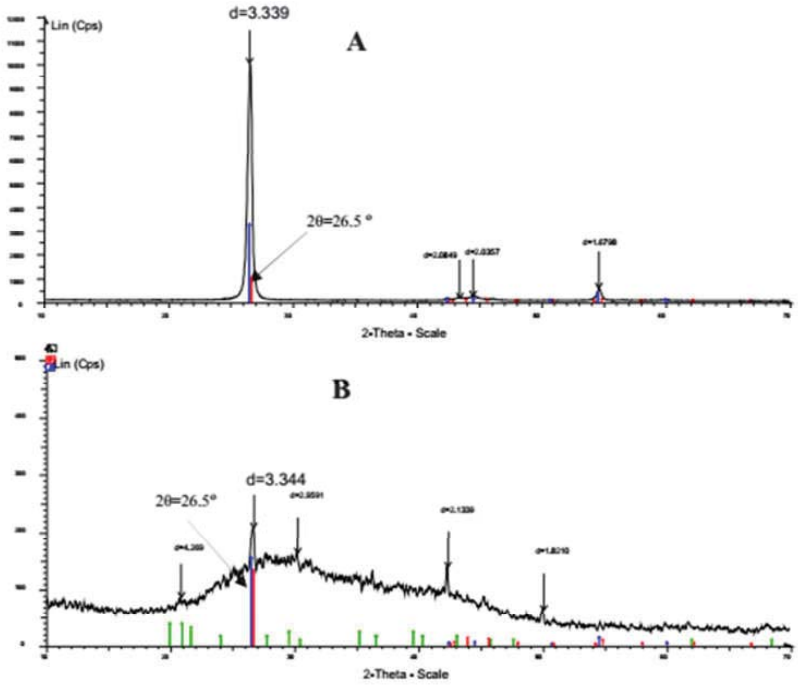


Fig. 2. XRD spectrum of Graphite (A) and chemically functionalized Graphene- GO (B)

The result of physico-mechanical properties tests of samples

Physico-mechanical properties tests is an important part of the operation of a paint system. Test is performed to monitor the system and to con rm that the paint coatings meets quality standards and the expectations of the customer. The used particular tests depend on the properties that the coating has to provide and to respect the established quality standards [2,5]. The results of physico- mechanical properties test of the samples are showed in table 2.

The reported data in table 2 showed that with the concentration of filler as low as 0,1wt%, the performances of epoxy paint system have been significantly improved. In fact, the hardness of the paint coatings with nanofiller (~1H) is higher than that of original epoxy without filler or pigment and microfiller-graphite/epoxy paint (~HB). The adhesion strength of GO nanofiller/epoxy sample is the highest in all. In there the bending strength of GO/epoxy sample increased upto ~200 % compared to one of neat epoxy and graphite/epoxy samples, and ~100 % to graphene/epoxy sample. Also the impact resistance increased 120 %, 57 % and 22% compared to epoxy, graphite/epoxy and graphene/epoxy samples, respectively. These results verified that the incorporation of fillers into epoxy binder enhanced significantly mechanical properties of epoxy binder. It can be considerd that the fillers play a role as a pigment or reinforcement for the paint coatings [16-20]. However the effeciency of the fillers on epoxy film performance is different from one to other. This can be explained that structural performance of pigments or fillers is one of important factors that could be impact to reinforcement for paint [1-3]. Moreover it is known pigments or fillers are particulate solids that are dispersed in paints to provide certain characteristics to them, including color, opacity, durability, mechanical strength, and corrosion protection for metallic substrates [2]. In order to achieve the desired results, pigments have to possess certain properties. Pigments or fillers must be uniformly dispersed in the binder to provide a consistent appearance [3,4]. Therefore, these results could be explained that the presence of the oxygen containing functional groups of GO nanosheets may form covalent boding with epoxy resin and leaded to create strong interfacial bonding between the filler and epoxy resin so that further great distribution and dispersion of GO compared to graphene and graphite [10,17]. Hence,

the effect of GO nanofiller on physico-mechanical properties and anticorrosion of epoxy paint coatings is higher than those of graphene and graphite.

Table 2. Physico-mechanical and anticorrosion properties of the paint samples

Physico-Mechanical properties	Epoxy	Graphite Epoxy	Graphene Epoxy	GO Epoxy	Standard method	Unit
Hardness	HB	HB	1H	1H	ASTM D3363	6B-6H
Adhesion	2	2	2	1	ASTM D3359	mark
Bending strength	3	3	2	1	ASTM D522	mm
Impact resistance	50	70	90	110	ASTM D2794	kG.cm
Salt spray test	96	144	336	552	ASTM B117	hours

The results of anticorrosion properties test

The paint coatings samples were examined for their applications in anti-corrosion by salt spray method. The results are presented in table 2. The time of rust appearance at the cross cut of GO/epoxy samples is longer: 5.75 times, 3.5 times and approximately 1.5 times compared to the original epoxy, graphite/epoxy and graphene/epoxy samples, respectively. It means the salt spray resistance of GO/epoxy samples was the greatest in all. The results demonstrate that the addition of fillers such as graphite, graphene and GO enhanced anti-corrosion property of epoxy paint coatings. Likewise, GO offered efficiency better than that of graphene and graphite. That could be explained by the attachment of O-containing functional groups to GO nanosheets aiding the dispersion in a hydrophilic media, as well as in the polar organic polymer. Hence, an efficient approach to the production of surface-functionalized graphene nanosheets may form covalent boding with epoxy binder so that could promote stronger interfacial bonding between GO sheets and epoxy resin and leading to the fully curing paint films that become tighter and stronger than graphene/epoxy films, graphite/epoxy and original epoxy films [17,18]. Therefore barrier ability and corrosion protection of GO/epoxy coatings for the metal surfaces are the greatest in all.

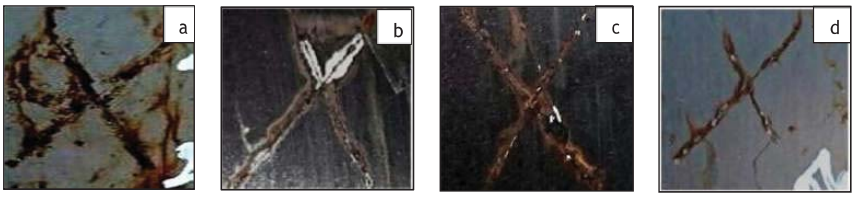


Fig. 3. Performance of salt spray resistance test samples: epoxy (a), graphite/epoxy (b), graphene/epoxy (c), GO/epoxy (d)

Conclusions

The results obtained from this study allow us draw the following conclusions:

- The chemically functionalized graphene was carried out successfully via modified Tour's method from natural graphite material.
- The physico-mechanical properties of the epoxy paint coatings have been significantly improved by addition of 0,1 weight% of nanofiller only in the epoxy binder.
- The anti-corrosion ability for the metal surfaces is greatly enhanced. Regarding to this application, the anti-corrosion performance of GO/epoxy nanofiller paint is 5.75 times and 1.5 times higher than the original epoxy paint and graphite/epoxymicro-filler paint respectively.
- The chemically functionalized graphene is greatly promised candidate in primer paints application for metal surfaces anti-corrosion.

Acknowledgements

This work was supported by The Foudation for Science and Technology Development - University of Danang, code number of protect : B2016 – ĐN02 – 05.

References

[1] Philip A.Schweitzer, Paint and coatings: Applications and corrosion resistance, ISBN 987-1-57444-703-3, 2008.

[2] Rodger T., Paint technology handbook, ISBN 987-1-57444-703-3 9, 2008.

[3] F. N. Jones, S. P. Pappas, D. A. Wicks, Organic Coatings: Science and Technology, Hoboken, N.J: Wiley-Interscience, 2007.

[4] J. Van der Geer, J.A.J. Hanraads, R.A. Lupton, Corrosion: Understanding the Basics, ASM International. 163 (2000), 1-21.

[5] Mayne.J. E. O., Paints for the protection of steel - A review of research into their modes of action, Br. Corros. J., (1970), 106.

[6] T. Yao, B. Siva, M. Song, Review on Graphene based materials and their composites as coatings, Austin Journal of Nanomedi. & Nanotech., (2013)

[7] Jianchang Li, Xiangqiong Z., Tianhui R., Emile H., Review The Preparation Graphene Oxide and Its Derivatives and Their Application in Bio-Tribological Systems, Lubricants, vol 2 (2014), 137-161

[8] William S.Hummers, Jr. Richard, E.Offeman, Preparation of graphitic oxide, Journal of American Chemical Society, 80 vol.6 (1958), 1339-1339.

[9] Daniela C.M., Dmitry V.K., Jocob.M.B., Tous Jame M., Improved synthesis of Graphene Oxide, ACS Nano, vol.4 (2010), 4806-4814

[10] Ayrat M, Dimiev, Lawrence B. Alemany, James M. Tour, Graphene Oxide. Origin of Acidity, Its Instability in Water, and a New Dynamic Structural Model, ACS Nano, 7 (1) (2013), 576–588

[11] Yanwu Zhu, Shanthi Murali, Meryl D. Stoller, Aruna Velamakanni, Richard, D. Piner, Rodney S. Ruoff, Microwave assisted exfoliation and reduction of graphite oxide for ultracapacitors, Carbon, 48 (7) (2010), 2118-2122.

[12] Artur Ciesielski and Paolo Samori, Graphene via sonication assisted liquid phase exfoliation, Chem Soc Rev., 43 (2014), 381-398.

[13] Paulchamy B., Arthi G., LignesD., A Simple Approach to Stepwise Synthesis of Graphene Oxide, Journal Nanomedicine Nanotechnology, vol 6:1 (2015).

[14] Shivangi Kosta, Prerna Bansal, N. K. Sahu, Improved Oxidation of Graphite by Optimizing the Oxidation Time and Concentration of Oxidizing Agent for Cellular Sensing, World Journal of Research and Review (WJRR) ISSN:2455-3956, Volume-3, Issue-1 (2016), Pages 56-58.

[15] Kevin A. W., Billy A. Smith & Julie L. Bitter D. Howard Fairbrothe, Review of Chemical and structural characterization of carbon nanotube surfaces, Anal Bioanal Chem DOI 10.1007/s00216-009-3332-5, 2010.

[16] Karthikeyan K., JeyasubramanianK., Premanathan.M., HubbiahG., Suk ShinH., KimS., Graphene oxide nanopaint, Carbon Journal, vol. 72 (2014), 328-337

[17] Yu Ma, Haihui Di, Zongxue Yu, Ling Liang, Liang Lv, Yang Pan, Yangyong Zhang, Di Yin, Fabrication of silica-decorated graphene oxide nanohybrids and the properties of composite epoxy coatings research, Applied Surface Science, Vol.360, Part B (2016), Pages 936-945.

[18] H. Zheng, Y. Shao, Y. Wang, G. Meng, B. Liu, Reinforcing the corrosion protection property of epoxy coating by using graphene oxide–poly(urea–formaldehyde) composites, Corrosion Science, vol.123 (2017), 267-277.

[19] Zhiyi Zhang, Wenhui Zhang, Diansen Li, Youyi Sun, Zhuo Wang, Chunling Hou, Lu Chen, Yang Cao, Yaqing Liu, Mechanical and anticorrosive properties of Graphene/Epoxy resin composites coating prepared by in-situ method, International Journal of Molecular Sciences, vol. 16 (2015), 2239-2251.

[20] B. Ramezanzadeh, M.H. Moghadam, N. Shohani, M. Mahdavian, Effects of highly crystalline and conductive polyaniline/graphene oxide composites on the corrosion protection performance of a zinc-rich epoxy coating, Chemical Engineering Journal, Vol.320 (2017), Pages 363-375.

Fabrication of glucose/oxygen biofuel cell controlling limiting factors in microfluidic channel

Haroon Khan[1], Chul Min Kim[1], Sung Yeol Kim[1], Sanket Goel[2], Prabhat K. Dwivedi[3], Ashutosh Sharma[3], Gyu Man Kim[1,*]

[1]School of Mechanical Engineering, Kyungpook National University, Daegu 41566, South Korea.

[2]Birla Institute of Technology and Science, Pilani, Rajasthan 333031, India.

[3]Department of Chemical Engineering, Indian Institute of Technology, Kanpur 208016, India.

*Corresponding author. Tel: +82-(53)-950-7570 E-mail address: gyuman.kim@knu.ac.kr

Keywords: Biofuel cell; MWCNT; membraneless; oxygen depletion layer.

Abstract. Enzymatic biofuel cells (EBFCs) have gained great interest by researchers due to its possible application in medical implants. In this study, we present a glucose/oxygen biofuel cell with new design of electrodes to overcome main issues related to microfluidic channel i.e. oxygen depletion layer and cross diffusional mixing of fuel and oxidant at the end of microchannel. Both of these limitations are functions of the distance from the inlet of microchannel [1]. Therefore, the microchannel length was reduced to half keeping the same area of multiwalled carbon nanotubes (MWCNT) electrodes. It was accomplished by placing just half of the anode and cathode at the top of microchannel. The electrodes were fabricated by Polydimethylsiloxane (PDMS) stencil using multiwalled carbon nanotubes (MWCNT) patterned on etched Indium Tin Oxide (ITO) glass. The microchannel was produced by PDMS casting. The electrodes were modified with glucose oxidase and laccase via direct covalent bonding [2]. The performance of both devices at different microchannel heights was studied, ranging from 450 μm to 1 mm, at a constant electrolyte flow velocity of 5.14 mm•s-1. The device with a 450-μm-high microchannel showed the highest power density owing to a diminished effect of the depletion layer at the electrode surface. The device was also studied at different flow rates ranging from 5 to 45 mL•h-1, obtaining a maximum power and current density of 76.5 μW•cm-2 and 225 μA•cm-2, respectively, at a flow rate of 25 mL•h-1. The double-layer EBFC shows a 23% improvement in the performance compared to a single-layer EBFC.

Acknowledgements. This work was supported by “Project of Advanced Technology Center (10077414, 2017)” funded by the Korean Government (MOTIE), and the National Research Foundation of Korea Grant (NRF-2017R1A2B4004966) funded by the Korean Government (KMEST).

References

1. Zebda, A., et al. "Enzyme-Based Microfluidic Biofuel Cell to Generate Micropower." Biofuel's Engineering Process Technology. InTech, 2011.
2. Beneyton, T., et al. "Membraneless glucose/O 2 microfluidic biofuel cells using covalently bound enzymes." Chemical Communications, Vol. 49, No. 11, pp. 1094-1096, 2013.

Effect of angle of attack of the buoyant shell on the aerodynamic performance of the airborne wind turbine in shell configuration

Arslan Saleem[1], Man-Hoe Kim[2,*]

[1]Kyungpook National University, Daegu, South Korea

[2]Kyungpook National University, Daegu, South Korea

*Corresponding author. Tel: (+82) 539505576; E-mail: manhoe.kim@knu.ac.kr

Keywords: airborne wind turbine; angle of attack; shell aerodynamics.

Abstract. In the crucial ongoing world energy crisis, wind energy is one of the most intensively investigated intermittent renewable energy source. Researchers in the recent years have conducted several studies in order to maximize the energy harvested from the wind. Airborne wind turbines have a huge edge over the conventional ground based and offshore wind turbine since they can operate at several times higher altitudes compared to their counterparts, moreover they are far less dependent on the geographical topography. Operation at higher altitudes means higher wind speeds that results in higher wind turbine performance since wind power is a function of third exponent of wind velocity. The buoyant shell encloses the turbine and generator assembly and acts in a similar manner as a duct does in case of a conventional wind turbine. The design of this buoyant shell thus is highly important in the aerodynamic performance of the airborne wind turbine since the total generated thrust force is a sum of thrust generated by the rotor and thrust generated by the buoyant shell. In this study the effect of angle of attack of the buoyant shell on the aerodynamic performance of the airborne wind turbine is numerically investigated. An axis-symmetric geometry of buoyant shell based on aerofoil cross-section NACA5415 was modelled. The simulations were performed for wind speeds ranging from 10m/s - 25m/s at eight different angle of attack while actuator disc method was used for the rotor. The buoyant shell was assumed at 300m altitude from the sea level and the variation in the properties of air were also considered. All the cases for the study were solved using two equation k-ω shear stress transport (SST) model. The aerodynamic performance of the airborne wind turbine with the shell was calculated in terms of buoyant shell thrust coefficient and power coefficient and its maximum values were found between 22°-26°.

References

1. M. Saeed, M.H. Kim, Energy Conversion and Management, 2016, 120.
2. M. Saeed, M.H. Kim, Energy Conversion and Management, 2017, 134.
3. A. Saleem, M.H. Kim, Energy Conversion and Management, 2017, 151.

Shaft Torsional Vibration Reduction Using Tuned-Mass-Damper (TMD)

CHINH Duy Nguyen

Faculty of Mechanical Engineering, Hungyen University of Technology and Education,

Hungyen, Vietnam

* Corresponding author. Tel:(+84)979795539; Email: duychinhdhspkthy@gmail.com

Keywords: *TMD , torsional vibration, optimal parameters.*

Abstract: *The paper presents a torsional vibration reduction method for shaft by using a symmetric tuned-mass-damper (TMD). The research consists of two components: formulation of shaft dynamic equations is provided via Lagrange's equations of the second kind, and then determination of optimal parameters of the TMD is derived by using the principle of minimum kinetic energy. Analytical and numerical studies are implemented to verify the reliability of the proposed research.*

1. Introduction

Nowadays, rapid development of industries leads to a variety of industrial machines. Many deteriorated vibrations of machine shafts occur during different working conditions. Thus, research on eliminating degraded oscillations plays an important role in improving the safety and stability of machines or structures in the presence of external factors. Work in [3] presents the method to reduce the vibration by using the TMD-D and DVA (dynamic vibration absorber). The research results are applied successfully to reduce the vibration for the articulated tower. Researches in [4], [5], [6] present methods for reducing the shaft torsional vibration in the presence of external forces. Work in [4] presents the method to reduce shaft vibration by minimizing the effects of unwanted vibrations to ability to work of shaft and then the Runge-Kutta- Nystrom algorithm is used to determine the optimal parameters of the vibration absorber. Results can be applied to reduce vibration for shaft of machines to improve the working life of the machines. However, those proposals are approached numerically for optimal parameters, and then some properties of the system such as performances and stability are not able to predict due to the external actions. The question arises whether there is a way to present analytically optimal parameters through system parameters or not. The answer for the question can be found in [7], [8]. In this paper, the principle of minimum kinetic energy is used for formulating analytically optimal parameters of the symmetric TMD in terms of system parameters to shaft torsional vibration. Numerical simulation studies are implemented in different operating conditions to verify the feasibility and validation of the proposed research.

2. Mathematical Bacground

2.1 Lagrange's Equations Of The Second Kind

The Lagrange's equations of the second kind is used for formulating the differential equation of motions of dynamic systems with respect to independently generalized coordinates in References [2], [3], and [4]. A generalized Lagrange's equations of the second kind is written as follows

$$\frac{d}{dt}\left(\frac{\partial T}{\partial \dot{q}_i}\right)-\frac{\partial T}{\partial q_i}=Q_i^{\Pi}+Q_i^{*}+Q_i^{\Phi};\quad i=1..f \tag{1}$$

where *f is* the number of degrees of freedom; *T* is kinetic energy; q_i is the ith generalized coordinate; $\dot{q}_i$ is the ith generalized velocity; Q_i^{Π} is the generalized force w.r.t. the ith generalized coordinate; Q_i^* is the generalized force without potential energy w.r.t. the ith generalized coordinate; Q_i^{Φ} is the non-conservative generalized force w.r.t. the ith generalized coordinate.

2.2. Derivation of Motion of Equations

Consider rotational motion of a machine shaft with angular velocit $\Omega = \frac{\pi n}{30} \text{s}^{-1}$, where *n* is the number of rotations per minute. A mass disc, with radius ρ, mass M, and a symmetry-typed TMD, is installed in machine shaft, as shown in Figure 1.

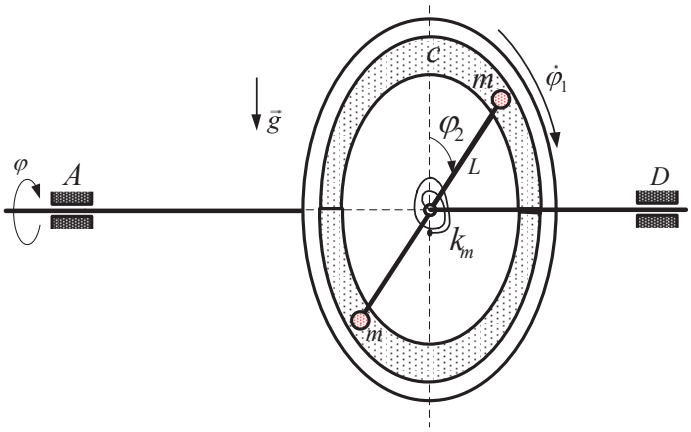


Figure 1. Shaft Model with Installed TMD

By considering the whole system, one can conclude that the system is completely determinated if two coordinates φ_1 and φ_2 are given. Thus, independent generalized coordinates are absolute angle of rotation of disc φ_1 and relatively angel of rotation of the TMD to the disc φ_2. By using Eq. (1), one gets

$$\frac{d}{dt}\left(\frac{\partial T}{\partial \dot{\varphi}_1}\right) - \frac{\partial T}{\partial \varphi_1} = -\frac{\partial \Pi}{\partial \varphi_1} - \frac{\partial \Phi}{\partial \dot{\varphi}_1} + Q_{\varphi 1}^* \tag{2}$$

$$\frac{d}{dt}\left(\frac{\partial T}{\partial \dot{\varphi}_2}\right) - \frac{\partial T}{\partial \varphi_2} = -\frac{\partial \Pi}{\partial \varphi_2} - \frac{\partial \Phi}{\partial \dot{\varphi}_2} + Q_{\varphi 2}^* \tag{3}$$

The kinetic energy of the system is written as

$$T = T_d + T_L + T_m \tag{4}$$

The kinetic energies of the disc, link L, and mass m are respectively given as

$$T_d = \frac{1}{2} J_d \dot{\varphi}_1^2 = \frac{1}{2} M \rho^2 \dot{\varphi}_1^2 \tag{5}$$

$$T_L = 2\left(\frac{1}{2} J_L (\dot{\varphi}_1 + \dot{\varphi}_2)^2\right) = 2\left(\frac{1}{2}\left(\frac{1}{3} m_t l^2\right)(\dot{\varphi}_1 + \dot{\varphi}_2)^2\right) = \frac{1}{3} m_t l^2 (\dot{\varphi}_1 + \dot{\varphi}_2)^2 \tag{6}$$

$$T_m = 2\left[\frac{1}{2} m L^2 (\dot{\varphi}_1 + \dot{\varphi}_2)^2\right] \tag{7}$$

Substituting Eqs. (5) - (7) into Eq. (4) results in the total energy of the system as

$$T = \frac{1}{2} M \rho^2 \dot{\varphi}_1^2 + \frac{1}{3} m_t L^2 (\dot{\varphi}_1 + \dot{\varphi}_2)^2 + mL^2 (\dot{\varphi}_1 + \dot{\varphi}_2)^2 \tag{8}$$

The total potential energy of the system is

$$\Pi = \frac{1}{2} k_m (\varphi_2)^2 + \frac{1}{2} k_t (\varphi_1 - \varphi)^2 + \text{const} \tag{9}$$

The non-conservative generalized forces of the system are written as

$$Q^*_{\varphi_1} = M(t);\ Q^*_{\varphi_2} = 0 \tag{10}$$

The dissipation function of the system is

$$\Phi = 2\left[\frac{1}{2} c \left(L\dot{\varphi}_2\right)^2\right] \tag{11}$$

By substituting Eqs. (8) – (11) into Eqs. (2) – (3), the motion equations of the system is written as

$$M\rho^2 \ddot{\varphi}_1 + 2(\frac{1}{3} m_t L^2 + mL^2)(\ddot{\varphi}_1 + \ddot{\varphi}_2) = M(t) - k_t(\varphi_1 - \varphi) \tag{12}$$

$$2(\frac{1}{3} m_t L^2 + mL^2)(\ddot{\varphi}_1 + \ddot{\varphi}_2) = -k_m \varphi_2 - 2cL^2 \dot{\varphi}_2 \tag{13}$$

3. Determination of Optimal Parameters of TMD

Consider the case of constant angular velocity or $\Omega = \text{const}$, one gets:

$$\varphi_1 - \varphi = \theta \rightarrow \varphi_1 = \theta + \Omega t;\ \dot{\varphi}_1 = \dot{\theta} + \Omega;\ \ddot{\varphi}_1 = \ddot{\theta} \tag{14}$$

Substituting Eq. (14) into Eqs. (12) – (13) achieves as

$$(M\rho^2 + \frac{2}{3} m_t L^2 + 2mL^2)\ddot{\theta} + 2(\frac{1}{3} m_t L^2 + mL^2)\ddot{\varphi}_2 = M(t) - k_t \theta \tag{15}$$

$$2(\frac{1}{3} m_t L^2 + mL^2)\ddot{\theta} + 2(\frac{1}{3} m_t L^2 + mL^2)\ddot{\varphi}_2 = -k_m \varphi_2 - 2cL^2 \dot{\varphi}_2 \tag{16}$$

For simplicity, following variables are introduced as

$$\mu = \frac{m + m_t/3}{M}, \omega_D = \sqrt{\frac{k_t}{M\rho^2}}, \omega_d = \sqrt{\frac{k_m}{2(m + m_t/3)L^2}}, \xi = \frac{c}{2(m + \frac{m_t}{3})\omega_d}, \alpha = \frac{\omega_d}{\omega_D},\ \gamma = \frac{L}{\rho} \tag{17}$$

Variables in Eq. (17) are defined as follows:

μ is the mass ratio between TMD and shaft.
γ is an extended coefficient of length of the TMD;
ω_d is natural frequency of vibration of the TMD;
ω_D is natural frequency of vibration of the shaft;
ξ is damping ration of the TMD.

Combining Eqs. (15) - (16) and Eq. (17) results in the following equations

$$\mathbf{M}\ddot{\mathbf{x}} + \mathbf{C}\dot{\mathbf{x}} + \mathbf{K}\mathbf{x} = \mathbf{F} \tag{18}$$

where

$$\mathbf{M} = \begin{bmatrix} 1 + 2\mu\gamma^2 & 2\mu\gamma^2 \\ 1 & 1 \end{bmatrix}; \mathbf{C} = \begin{bmatrix} 0 & 0 \\ 0 & 2\xi\alpha\omega_D \end{bmatrix};\ \mathbf{K} = \begin{bmatrix} \omega_D^2 & 0 \\ 0 & \omega_D^2\alpha^2 \end{bmatrix};\ \mathbf{x} = \begin{bmatrix} \theta \\ \varphi_2 \end{bmatrix} \tag{19}$$

By introducing coordinate transformations as

$$y_1 = x_1, \quad y_2 = x_2, \quad y_3 = \dot{y}_1 = \dot{x}_1, \quad y_4 = \dot{y}_2 = \dot{x}_2 \tag{20}$$

The Equations (18) – (19) is transformed into a new form as

$$\dot{\mathbf{x}} = \mathbf{A}\mathbf{y} + \mathbf{F} \tag{21}$$

where **A** is defined as

$$\mathbf{A} = \begin{bmatrix} 0 & 0 & 1 & 0 \\ 0 & 0 & 0 & 1 \\ -\omega_D^2 & 2\mu\gamma^2\alpha^2\omega_D^2 & 0 & 4\mu\gamma^2\xi\alpha\omega_D \\ \omega_D^2 & -(1+2\mu\gamma^2)\alpha^2\omega_D^2 & 0 & -2(1+2\mu\gamma^2)\xi\alpha\omega_D \end{bmatrix} \tag{22}$$

There are many different methods for determining optimal parameters of the system such as force-balance method and quadratic minimum torque method. In this paper, the minimum kinetic energy method in References [5], [6] is used for determining optimal parameters of the TMD. The problem is to find the parameters of the TMD so that the functionals in Eq. (23) reaches the minimum values

$$L = \frac{1}{2}\mathbf{y}_o^T\mathbf{B}\mathbf{y}_o \tag{23}$$

where $\mathbf{y}_0$ is a vector of initial conditions and matrix **P** is a solution of Lyapunov algebraic equation in Eq. (24).

$$\mathbf{A}^T\mathbf{B} + \mathbf{B}\mathbf{A} + \mathbf{Q} = 0 \tag{24}$$

where **Q** is a weighted function. The goal of the method is minimize the potential energy of the whole system through the use of kinetic energy. Thus, the weighted matrix **Q** is selected as follows

$$\mathbf{Q} = \begin{bmatrix} 0 & 0 & 0 & 0 \\ 0 & 0 & 0 & 0 \\ 0 & 0 & Q_{33} & 0 \\ 0 & 0 & 0 & 0 \end{bmatrix} \tag{25}$$

Necessary minimum conditions for the objective function L are represented as

$$\left.\frac{\partial L}{\partial \alpha}\right|_{\alpha=\alpha^*} = 0, \quad \left.\frac{\partial L}{\partial \zeta}\right|_{\xi=\xi^*} = 0 \tag{26}$$

Solving the system of equations (22) – (26) results in optimal solutions of the TMD, as shown in Eq. (27) and Eq. (28).

$$\alpha = \frac{\sqrt{1-\mu\gamma^2}}{1+2\mu\gamma^2} \tag{27}$$

$$\xi = \frac{\gamma\sqrt{\mu(2+3\mu\gamma^2-2\mu^2\gamma^4)}}{2\sqrt{1-\mu\gamma^2}(1+2\mu\gamma^2)} \tag{28}$$

4. Numerical Simulation Study

In this section, numerical simulation is employed for the system by using the achieved optimal parameters of the TMD, as shown in Eq. (27) and Eq. (28).

4.1. System Parameters

The parameter k_t is denoted as stiffness of shaft with length L and is defined as

$$k_t = \frac{GJ_P}{L} \ (Nm)$$

where G is shear young module of shaft (N/m^2), J_P is a polar inertia moment of cross-section of shaft (m^4), L is length of shaft measured from right head of shaft to the cross-section of the disc. Consider a machine shaft of radius $\Phi 50$, length *L=500 mm*, and C45 shaft materials of shear young module $G = 8.10^{10} \ \frac{N}{m^2}$. Thus, stiffness of shaft is determined by Eq. (29).

$$k_t = \frac{GJ_P}{L} = \frac{G.0,1.d^4}{L} = 10^5 \ (Nm) \tag{29}$$

For disc of mass M = 500 kg and inertia radius of ρ =1m, the parameters of the TMD is calculated in Eq. (30) as

$$\mu = 0.03, \quad \gamma = 0.9 \tag{30}$$

From Eq. (17), non-dimensional parameters is determined as follows

$$\omega_D = \sqrt{\frac{k_t}{M\rho^2}} = \sqrt{\frac{10^5}{500(1.0)^2}} = 14,142 rad/s \tag{31}$$

Combining Eqs. (27) – (28) and Eq. (30) results in optimal parameters as

$$\alpha = \frac{\sqrt{1-\mu\gamma^2}}{1+2\mu\gamma^2} = \frac{\sqrt{1-(0.03)(0.9)^2}}{1+2(0.03)(0.9)^2} = 0.942 \tag{32}$$

$$\xi = \frac{\gamma\sqrt{\mu(2+3\mu\gamma^2-2\mu^2\gamma^4)}}{2\sqrt{1-\mu\gamma^2}(1+2\mu\gamma^2)} = \frac{(0.9)\sqrt{0.03(2+3(0.03)(0.9)^2-2(0.3)^2(0.9)^4)}}{2\sqrt{1-(0.03)(0.9)^2}(1+2(0.03)(0.9)^2)} = 0.0188 \tag{33}$$

From the Eq. (17), the optimal parameters of the TMD are determined as Eqs. (34) and (35), or

$$k_m = 2\mu M\alpha_{opt}^2\omega_D^2L^2 = 2(0.03)(500)(0.942)^2(14.142)^2(0.9)^2 = 4312,5(N/m) \tag{34}$$

$$c = 2\mu M\xi_{opt}\omega_D\alpha_{opt} = 2(0.03)(500)(0.11)(14.142)(0.942) = 43,94(Ns/m) \tag{35}$$

4.2. Simulation Results

Numerical simulations for torsional vibration of machine shaft using the Maple are implemented in different operating conditions. In the case 1, simulation is implemented with initial condition of φ_{10} = 0,03 (rad). Secondly, simulation results of initial deflection φ_{10} = 0 (rad) and initial angular velocity of $\dot{\varphi}_1 = 0,6$ (rad/s) is shown. Finally, simulation study presents the simulation with initial deflection φ_{10} = 0.03 (rad) and initial angular velocity of $\dot{\varphi}_1 = 0,6$ (rad/s).

Case 1: Initial Deflection of φ_{10} = 0,03 (rad)

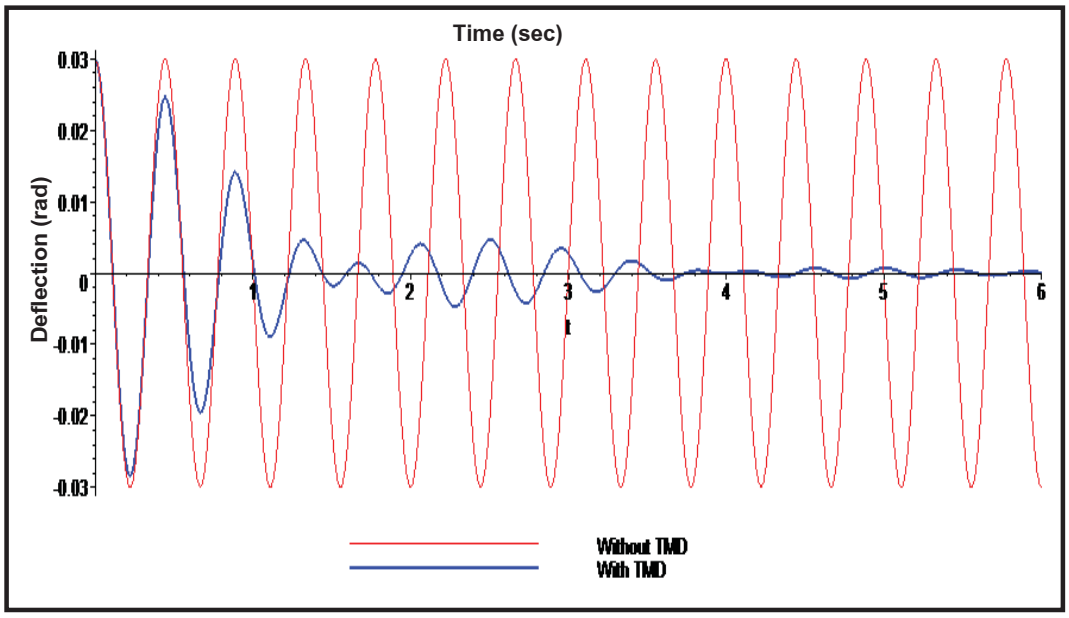


Figure 3. Vibration Amplitude of Angular Angle with Initial Deflection φ_{10} = 0.03 (rad)

Case 2: Initial Deflection φ_{10} = 0 (rad) and Initial Angular Velocity of $\dot{\varphi}_1 = 0,6$ (rad/s)

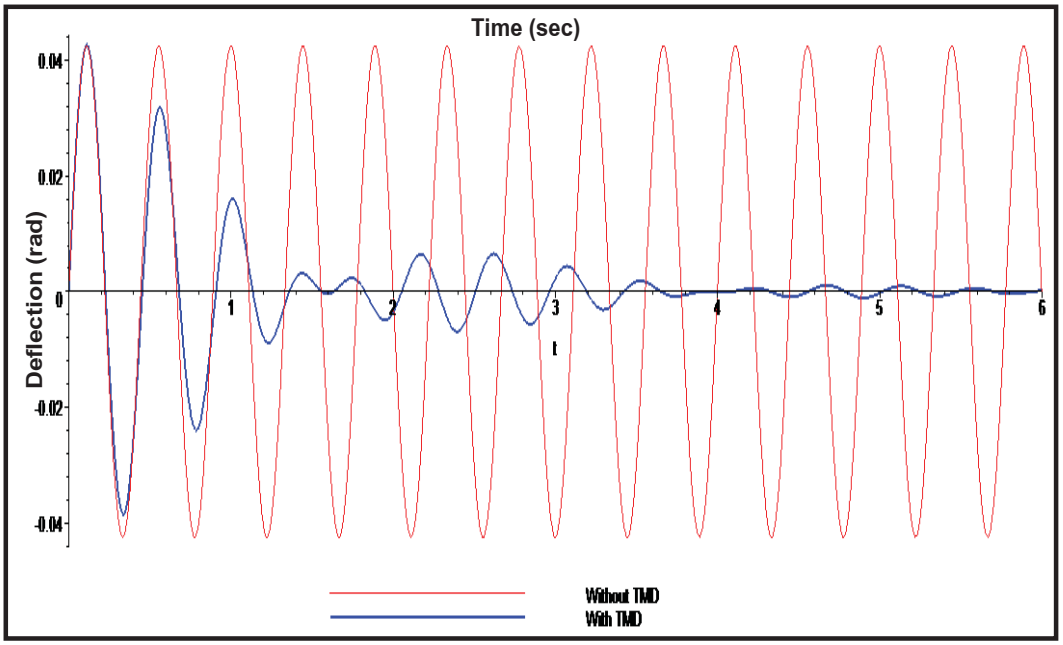


Figure 4. Vibration Amplitude of Angle with Initial Angular Angle $\dot{\varphi}_1 = 0,6$ (rad/s)

Case 3: Initial Condition of φ_{10} = 0,03 (rad) and Initial Angular Velocity of $\dot{\varphi}_1 = 0,6$ (rad/s)

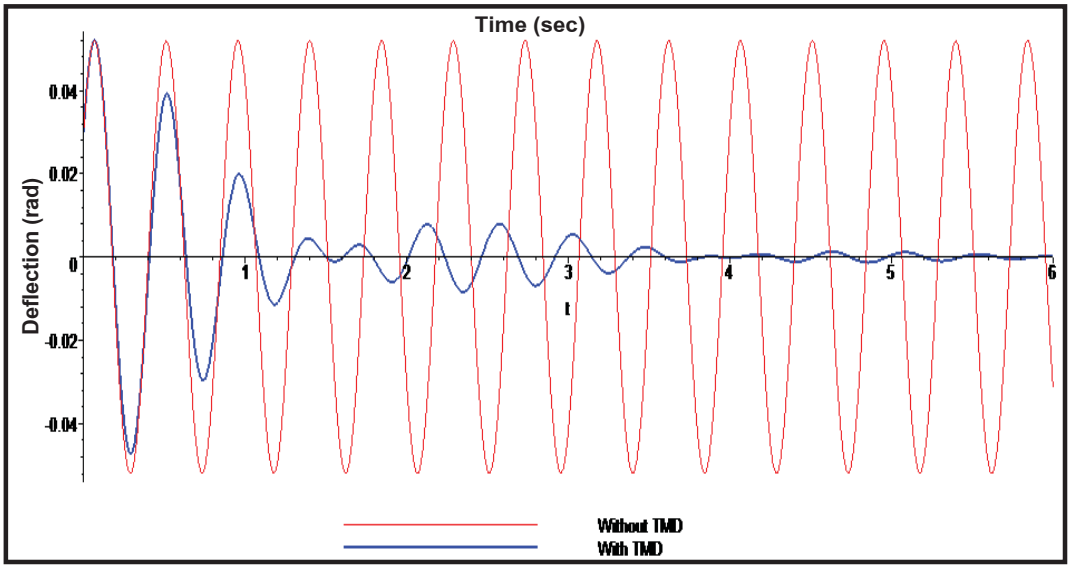


Figure 5. Vibration Amplitude of Angular Angle with Initial Deflection φ_{10} = 0,03 (rad) and Initial Angular Velocity of $\dot{\varphi}_1 = 0,6$ (rad/s)

5. Conclusions

Torsional vibration plays an important role in degrading the safety and stability of structures under the effects of torsional torque such as machine shafts, turbine shafts, etc. In reality, shaft torsional vibration occurs in the presence of machinery shaft deformation. This process affects on working conditions of components of structures. In this paper, a method is proposed for reducing the shaft torsional vibration by using a symmetric tuned-mass-damper (TMD) and then optimal parameters of the TMD are determined through the principle of minimum kinetic energy. Some conclusions are made as follows:

- Differential equations of motion are formulated for the machine shaft system installed with the TMD. This is an important step in optimal design of system parameters to shaft torsional vibration problems.
- With the achieved dynamic equations, minimum kinetic energy method is used for determining the optimal parameters of the TMD, as shown in the following equations.

$$\alpha = \frac{\sqrt{1-\mu\gamma^2}}{1+2\mu\gamma^2} \;;\; \xi = \frac{\gamma\sqrt{\mu(2+3\mu\gamma^2-2\mu^2\gamma^4)}}{2\sqrt{1-\mu\gamma^2}(1+2\mu\gamma^2)}$$

- Numerical simulation studies are implemented by using the Maple software. Simulation results are shown to validate the reliability and feasibility of the proposed method.

This research was supported by Center for Research and Applications in Science and Technology, Hung Yen University of Technology and Education, under grant number UTEHY.T034.P1819.01.

Reference

[1] Nguyen Thuc An, Nguyen Dinh Chieu, and Khong Doan Dien, Theory of Vibration, Agricultural Publisher, Hanoi, 2004.
[2] Khong Doan Dien, Nguyen Duy Chinh and Vu Xuan Truong, Numerical Method in Mechanical Engineering, Science and Technics Publishing House, Hanoi, 2014.

[3] Khong Doan Dien, Nguyen Duy Chinh, *Optimal parameters of vibration reduction system TMD-D and DVA for an inverted pendulum type structure*, Vietnam Journal of Mechanis, VAST, Vol. 32, No 1 (2010), pp.59-69.

[4] Khong Doan Dien, Nguyen Duy Chinh, Vu Xuan Truong, *Research to reduce vibration for shaft of machine using the reduced vibration TMD*, Proceedings Of The Regional Conference on Mechanical and Manufacturing Engineering 2014 (RCMME2014).

[5] Truhar Ninoslav, Veselic Kresimir (2004), ‘‘*On some properties of the Lyapunov equation for* damper *systems* ”, Mathematical Communications, pp. 189-197.

[6] Truhar Ninoslav (2004), ‘‘ *An efficient algorithm for damper optimization for linear vibrating systems using Lyapunov equation*”, J.Comput. Appl. Math 172(2004), 169 -182.

[7] Khong Doan Dien, Nguyen Duy Chinh, Vu Xuan Truong, and Doan Van Mien, “Optimal parameters of the circle slide TMD for reducing torsional vibration of machine’s shaft by using Euler method”, Journal of Science and Technology, No. 6 (2015), 9-14.

[8] Khong Doan Dien, Nguyen Duy Chinh, Vu Xuan Truong, and Dao Cong Luat, “Research on specific iptimal parameters of eccentric pendulum TMD for reducing torsional vibrations of machine’s shaft”, Journal of Science and Technology, No. 7 (2015), 9-14.

DETERMINATION OF OPTIMAL PARAMETERS FOR REDUCING THE VIBRATION TO AN INVERTED PENDULUM TYPE STRUCTURE WITH THE TUNED MASS DAMPER USING THE MAXIMUM METHOD OF EQUIVALENT RESISTANCE

CHINH Duy Nguyen

Faculty of Mechanical Engineering, Hung Yen University of Technology and Education, Hung Yen, Vietnam

* Corresponding author. Tel:(+84)979795539; Email: duychinhdhspkthy@gmail.com

Keywords: *tuned mass damper, inverted pendulum, optimal parameters.*

Abstract: *There are many rotational mechanisms in form of the inverse pendulum structures subjected to the adversely external forces, which generate dangerous vibrations to the structure and are necessary to eliminate or reduce. In this paper, the author proposes a new approach, in which a tuned mass damper (TMD) is installed in an inverted pendulum type structure with one degree of freedom. The used TMD consists of the mass, spring and damping. Then, the equations of motion of system are formulated for analyzing and selecting the optimal parameters of the TMD to reduce the unprofitable oscillations. Numerical simulation results are made to validate the proposed method.*

1. Introduction

A tuned-mass damper (TMD) is proposed to reduce the vibration for an inverted pendulum [1]. Since the mass ratio of TMD to the primary structure is usually not greater than 5%, therefore the stiffness and the damping ratio can be determined in TMD design by balancing the two fixed points in the frequency response, in the case of harmonic excitation. A mass–spring inverted-pendulum-type DVA is proposed to reduce the vibration for a stable inverted pendulum [2]. In their approach, the analytical solutions of the DVA are determined by maximizing the damping characteristics of the combined system. With the achieved parameters from the proposed method, the only specific oscillations are reduced in this case. Also, the actual structures are usually subjected to many type of complex forces in which the optimal parameters corresponding to each force can be determined by a corresponding method. In order to develop and extend the research results in [1, 2], In this paper, the author proposes an approach to reduce the oscillation using a tuned mass damper (TMD), optimal parameters are selected by using the maximum method of equivalent resistance. Numerical simulation results are made to validate the proposed method [3].

2. Inverted pendulum-TMD system

As shown in Fig.1, the inverted pendulum structures have a concentrated mass M at the top and one degree of freedom φ about z-axis. The concentrated mass is supported by a beam. We consider the case where the beam bending stiffness is large enough so that the beam can be modeled as a rigid rod. The mass and length of the supported rod are M_o and L, respectively. The damping of the pendulum is neglected. To keep the structure have a stable upright position, a restoring moment is produced by a torsion spring with the spring constant of k_2. The dynamic absorber has mass-spring type with the mass of m, the spring constant of k_1, and the damping constant of c. Denoting the

displacement of the dynamic absorber with respect to the main structure is u.

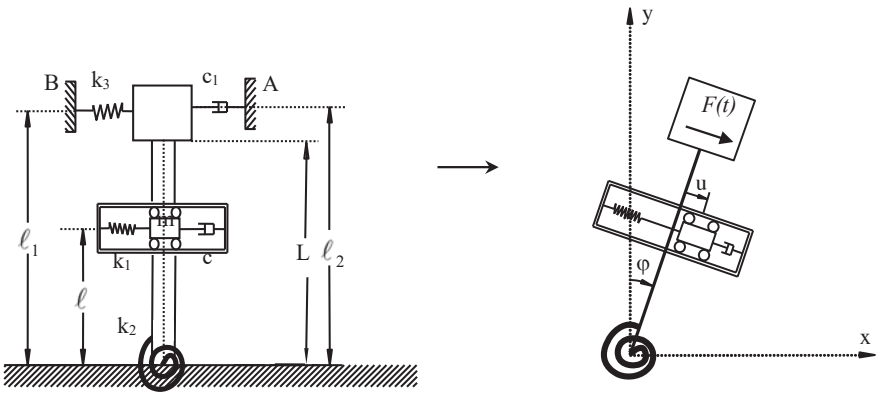


Fig. 1. Dynamic model of pendulum with a dynamic absorber

From [1], we have

$$(J+m\ell^2)\ddot{\varphi}+m\ell\ddot{u}+\left[k_2-g(ML+\frac{1}{2}M_oL+m\ell)\right]\varphi-mgu=LF(t),$$
$$m\ell\ddot{\varphi}+m\ddot{u}-mg\varphi+k_1u+c\dot{u}=0. \quad (1)$$

Here: $J=ML^2+\frac{1}{3}M_oL^2$ (2)

Equations (1) can be used in the design of TMD

3. Optimal adjusting

Introducing the normalized symbols,

$$\mu=\frac{m}{M+\frac{1}{3}M_o};\ \gamma=\frac{\ell}{L};\ \omega_a^2=\frac{k_1}{m};\ \zeta=\frac{c}{2m\omega_a};\ u_s=L\varphi;\quad (3)$$

$$\omega_s^2=\frac{6k_2-(6M+3M_o)Lg}{2(3M+M_o)L^2};\ \alpha=\frac{\omega_a}{\omega_s};\ \eta=\frac{g}{\omega_s^2L};\ a=1+\mu\gamma^2;\ b=(1-\mu\gamma\eta)$$

where μ is the mass ratio, γ specifies the position of the dynamic absorber, ω_s is natural frequency of the structure, ω_d and ξ are atural frequency and damping ratio of TMD, respectively, α is natural frequency ratio, η specifies the distribution of mass of the structure, and further defining

Therefore, Eqs. (1), (2) and (3) can be expressed by

$$a\ddot{u}_s+\mu\gamma\ddot{u}+b\omega_s^2u_s-\mu\eta\omega_s^2u=\frac{3F(t)}{3M+M_0} \quad (4)$$

$$\mu\gamma\ddot{u}_s+\mu\ddot{u}+2\xi\alpha\mu\omega_s\dot{u}-\mu\eta\omega_s^2u_s+\mu\alpha^2\omega_s^2u=0 \quad (5)$$

The matrix form of Eqs.(4) and (5) are expressed as

$$\mathbf{M\ddot{q}+C\dot{q}+Kq=F} \quad (6)$$

where

$$\mathbf{q} = \{u_s \quad u\}^T \tag{7}$$

$$\mathbf{F} = \left\{ \frac{3F(t)}{3M + M_0} \quad 0 \right\}^T \tag{8}$$

The mass matrix, viscous matrix, stiffness matrix can be derived as

$$\mathbf{M} = \begin{bmatrix} a & \mu\gamma \\ \mu\gamma & \mu \end{bmatrix} \quad \mathbf{C} = \omega_s \begin{bmatrix} 0 & 0 \\ 0 & 2\xi\alpha\mu \end{bmatrix} \qquad \omega_s^2 \begin{bmatrix} b & -\mu\eta \\ -\mu\eta & \mu\alpha^2 \end{bmatrix} \tag{9}$$

The state equations of Eqs. (6, 7, 8, 9) are expressed as [5]:

$$\dot{\mathbf{y}}(t) = \mathbf{B}\mathbf{y}(t) + \mathbf{H}_f F(t) \tag{10}$$

where

$$\mathbf{y} = \{u_s \quad u \quad \dot{u}_s \quad \dot{u}\}^T \tag{11}$$

Matrix of excitation force is obtained as [4, 5]

$$\mathbf{H}_f = \frac{1}{F(t)} \begin{bmatrix} \mathbf{0} & \mathbf{M}^{-1}\mathbf{F} \end{bmatrix}^T \rightarrow \mathbf{H}_f = \frac{1}{M + \frac{1}{3}M_0} \begin{bmatrix} 0 & 0 & 1 & -\gamma \end{bmatrix}^T \tag{12}$$

The system matrix **B** is derived in [4] and has the form

$$\mathbf{B} = \begin{bmatrix} \mathbf{0} & \mathbf{E} \\ \mathbf{-M^{-1}K} & \mathbf{-M^{-1}C} \end{bmatrix} \tag{13}$$

where $\mathbf{E} \in \mathbb{R}^2$ is matrix unit.

Hence the **B** matrix can be obtained as

$$\mathbf{B} = \begin{bmatrix} 0 & 0 & 1 & 0 \\ 0 & 0 & 0 & 1 \\ -\omega_s^2 & \omega_s^2\mu(\gamma\alpha^2 - \eta) & 0 & 2\gamma\xi\alpha\omega_s\mu \\ \omega_s^2(\gamma - \eta) & \omega_s^2(1 - b - \alpha^2 - \mu\gamma^2\alpha^2) & 0 & -2a\xi\alpha\omega_s \end{bmatrix} \tag{14}$$

The quadratic torque matrix **P** is solution of the Lyapunov equation [6]

$$\mathbf{BP} + \mathbf{PB}^T + S_f \mathbf{H}_\mathrm{f} \mathbf{H}_\mathrm{f}^T = \mathbf{0} \tag{15}$$

where S_f is the white noise spectrum of the excitation torque.

The first step of this method is to specify these quadratic torques. Substituting Eqs.(12-14) into Eq.(15) and solving this equation, these quadratic torques for vibration response of shaft were obtained as

$$P_{32} = \frac{9S_f(\alpha^2 - 1)}{4\omega_s\alpha\xi\mu(3M + M_0)^2(\gamma - \eta)} \tag{16}$$

$$P_{33} = -\frac{9}{2\mu\omega_s^2} \frac{S_f}{(3M + M_0)^2(\gamma - \eta)} \tag{17}$$

$$P_{34} = \frac{9S_f}{4\xi\mu\alpha\omega_s} \frac{(\mu\gamma^2 + 1)\alpha^4 + 2(2\xi^2 - 1)(\gamma\eta\mu + 1)\alpha^2 + \mu\eta^2 + 1}{(\gamma - \eta)^2(M + M_0)^2} \tag{18}$$

After short caculation the Eqs.(4, 5) we obtained

$$(M+\frac{1}{3}M_0)\ddot{u}_s+(M+\frac{1}{3}M_0)\omega_s^2u_s=2(M+\frac{1}{3}M_0)\xi\alpha\mu\gamma\omega_s\dot{u}+ \\ +(M+\frac{1}{3}M_0)\mu\omega_s^2(\gamma^2\alpha^2-\eta)u+F(t) \tag{19}$$

Hence the torque equivalent effect on the primary structure which was obtained as

$$F=2(M+\frac{1}{3}M_0)\xi\alpha\mu\gamma\omega_s\dot{u}+(M+\frac{1}{3}M_0)\mu\omega_s^2(\gamma^2\alpha^2-\eta)u \tag{20}$$

Thus the equivalent resistance coefficient of the TMD on the primary structure was obtained as

$$c_{td}=-\frac{\langle F\dot{u}_s\rangle}{\langle\dot{u}_s^2\rangle}=-\frac{2(M+\frac{1}{3}M_0)\xi\alpha\mu\gamma\omega_s\langle\dot{u}\dot{u}_s\rangle+(M+\frac{1}{3}M_0)\mu\omega_s^2(\gamma^2\alpha^2-\eta)\langle u\dot{u}_s\rangle}{\langle\dot{u}_s^2\rangle} \tag{21}$$

If the primary system is excited by random moment with a white noise spectrum S_f, then the average value of Eq.(21) are the components of the matrix **P** in Eq.(15), Lyapunov equation, this means

$$c_{td}=-\frac{2(M+\frac{1}{3}M_0)\xi\alpha\mu\gamma\omega_sP_{34}+(M+\frac{1}{3}M_0)\mu\omega_s^2(\gamma^2\alpha^2-\eta)P_{32}}{P_{33}} \tag{22}$$

Maximum condition are expressed as

$$\left.\frac{\partial c_{td}}{\partial\alpha}\right|_{\alpha=\alpha^*}=0 \tag{23}$$

$$\left.\frac{\partial c_{td}}{\partial\xi}\right|_{\xi=\xi^*}=0 \tag{24}$$

Optimal parameters of the TMD was determined by solving the equation Eqs.(22-24)

$$\alpha_{opt}=\alpha^*=\sqrt{\frac{1+\gamma\eta\mu}{1+\mu\gamma^2}} \tag{25}$$

$$\xi_{opt}=\xi^*=\frac{(\gamma-\eta)\sqrt{\mu}}{2(1+\gamma\eta\mu)} \tag{26}$$

4. Applying the study result of fluctuation receiver and reducing fluctuation to running water tower.

In fact, the running waters are made of steel rod concrete with great height, great pulling pressing particularity and small anti curling particularity, so we do not need to mention its vertical fluctuation but horizontal shaking moves. Therefore, we only need to use fluctuation receiver TMD to damper horizontal fluctuation

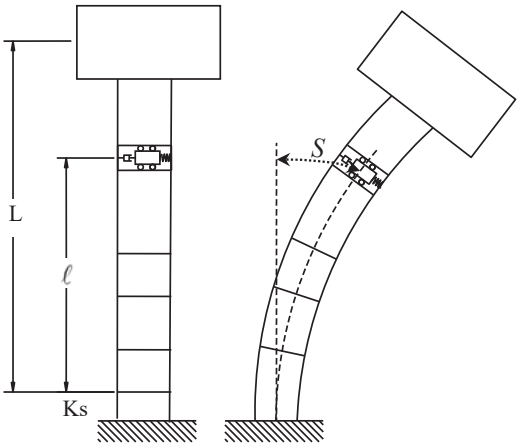


Fig. 2. Consider running water tower as an elastic oar connected to the foundation

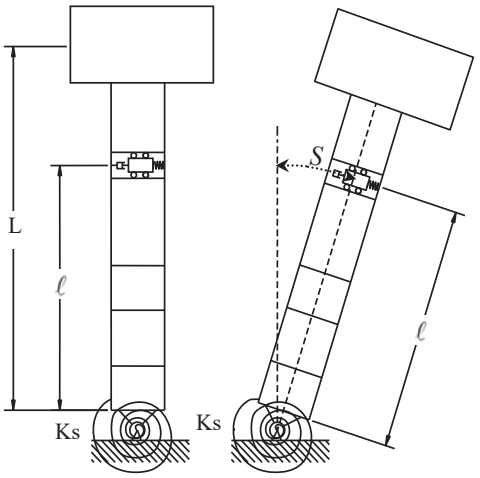


Fig. 3. Calculation of deviation S through spring coefficient K3 of running water tower

Consider a tower with the following parameters:

- tower length L = 250 m,
- tower diameter: inside diameter d = 14 m, outside diameter D = 15 m,
- end mass $M = 10 \times 10^5$ kg,
- Material is steel rod concrete with the parameters: E =3,1.10^{10} N/m^2, ρ = 2400kg/m^3.

Defining the spring coefficient through the particularity of the materials of the running water tower:

* For running water tower, we consider it as an elastic oar connected to the foundation. The deviation S at the assigning position of the fluctuation receiver is defined as followed [7,8] (Fig *2*), we have:

$$S = \frac{P(t)L_2^3}{3EJ} \tag{27}$$

Here:
$$J = \frac{\pi D^4}{64}(1-\varepsilon);\ \varepsilon = \frac{d}{D}$$

Among them:
P (t): Power effects on the assigning position of the fluctuation receiver.
EJ : The tower stiffness

Calculate *S* through spring K_S:

$$S = \frac{P(t)L_2^2}{K_S} \tag{28}$$

The spring constant of K_S is calculated from (27, 28):

$$K_S = \frac{EJ}{L_2} \tag{29}$$

The mass of tower is determined by:

$$M_0 = \pi\rho\left(\frac{D^2}{4} - \frac{d^2}{4}\right)L_4 = 13{,}7.10^6\ kg \tag{30}$$

We design the mass of TMD as m = $11{,}1\times10^4$ kg, up from the earth's surface a distance of $\ell = 250m$. (31)

The spring constant of K_S is calculated from (29):

$$K_s = 2{,}23.10^{11}\ Nm \tag{32}$$

The natural frequency of the tower is calculated from (3):

$$\omega_S = 0{,}765(rad/s) \tag{33}$$

From (25) and (26), one obtains two dimensionless parameters of the absorber:

$$\alpha_{opt} = \ 0.99;\ \xi_{opt} = \ 0.066 \tag{34}$$

The physical parameters of TMD are obtained from (3). We have

$$k_1 = m\alpha_{opt}^2\omega_S^2 = 63776.79(N/m) \tag{35}$$

$$c_1 = 2\xi_{opt}m\omega_S\alpha_{opt} = 11053.97(Ns/m) \tag{36}$$

The motion of inverted pendulum determined in the *Fig under* is established by using the Maple 18 software of the following initial conditions other.

Case one: Figs. 4 show the time response of the tower's displacement induced by initial deviation $\varphi_1 = 0.05$ rad.

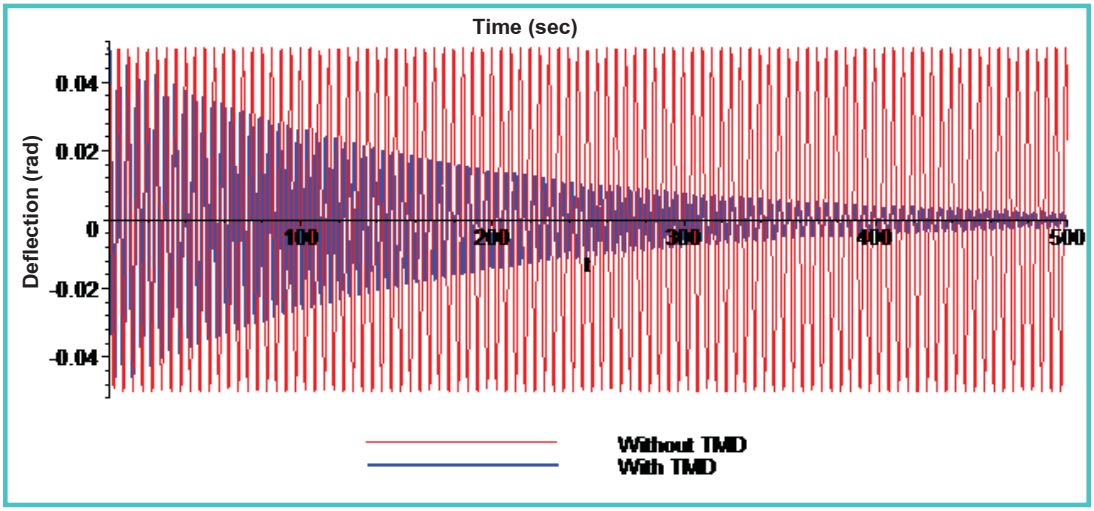


Fig. 4. Time response of the running water tower with initial deviation $\varphi_1 = 0.05$ (rad)

Case two: Figs. 5 show the time response of the tower's displacement induced by initial deviation $\varphi_1 = 0.05$(rad) and initial velocity $\dot{\varphi}_1 = 0.01$(rad/s)

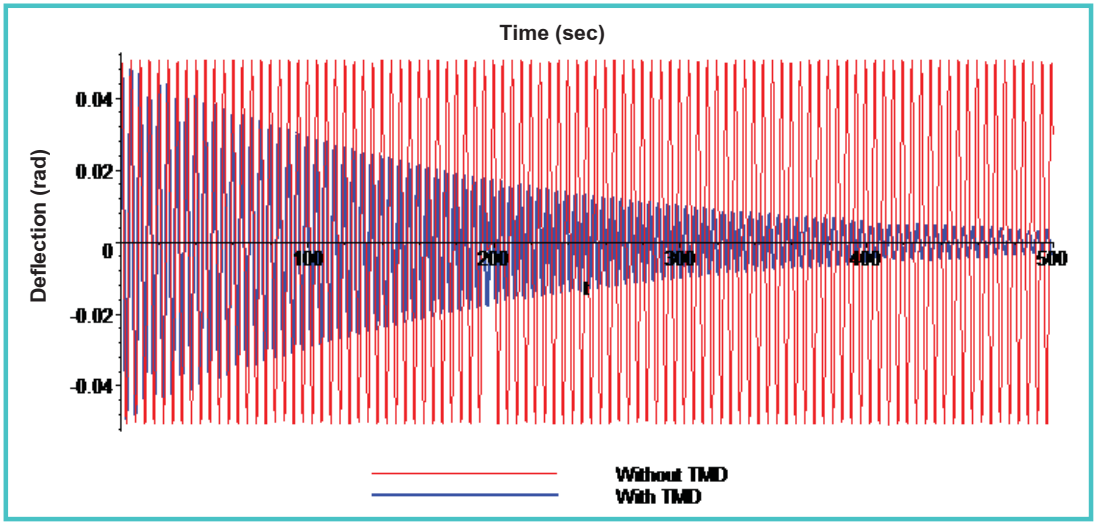


Fig. 5. Time response of the running water tower with initial deviation $\varphi_1 = 0.05$(rad) and initial velocity $\dot{\varphi}_1 = 0.01$(rad/s)

From the diagrams Figs. 4 and 5 we realized that the vibration of the inverted pendulum installed the TMD has the good efficiency for damping the oscillation of system. It can be seen that the mass-spring-inverted pendulum type TMD has good effect in two cases.

5. Conclusion

The goal for designing the absorbers is to reduce the vibration optimally of inverted pendulum system in order to meet the technical demands. The above aforementioned results assumed that the absorbers designed under the theory of optimal control make a good effect in reducing the oscillatory amplitude of system, that is, the oscillatory amplitude of inverted pendulum structure of installed TMD is much smaller than that of no TMD. Moreover, the resonant peak of oscillatory amplitude, or the most dangerously oscillatory position, of inverted pendulum structure of installed TMD is very much smaller than that of no TMD. The aim of designing fluctuation vibration is to damper the fluctuation of the inverted pendulum structure at most as to meet the technical requirement. The results show that: when applying the study results, assigning TMD in fitting the water tower can reduce the fluctuation much more and longer than without it. That can meet the technical standards required.

This research was supported by Center for Research and Applications in Science and Technology, Hung Yen University of Technology and Education, under grant number UTEHY.T034.P1819.02.

References

[1] Nguyen Duy Chinh, Study of oscillator absorber for an inverted pendulum, Master thesis, Institute of Mechanical Engineering – Vietnam Academy of science and Technology (2005).

[2] N. D. Anh, H. Matsuhisa, L. D. Viet, M. Yasuda, Vibration control of an inverted pendulum type structure by passive mass-spring-pendulum dynamic vibration absorber, Journal of Sound and Vibration 307 (2007) 187–201.

[3] Luft, R. W, Optimal Tuned Mass Damper for building, J. Struct. Div., ASCE, (1979), 105(12), 2766-2772.

[4] Khang N.V, Engineering Mechanics, Viet Nam Education Publishing House (2009).

[5] Nagashima I. (2001), Optimal displacement feedback control law for active tuned mass damper, Earthquake engineering and structural dynamic, 30, 1221-1242.

[6] Warburton G.B. (1982), Optimum absorber parameters for various combinations of response and excitation parameters, Earthquake Engineering and Structural Dynamics 10, 381-401.

[7] Nguyen Duy Chinh, Studying and applying optimal parameters of the TMD-N absorber for an inverted pendulum type to the damping of the water tower oscillation, Building science and technology journal 143 (2008), 12-20.

[8] Singiresu S. Rao, Mechanical Vibrations, University of Miami, ISBN-10: 013436130X • ISBN-13: 9780134361307 (2016).

[9] Nguyen Duy Chinh, Optimal parameters of vibration reduction system TMD-D for an inverted pendulum type structure by using the energy minimization method, Building science and technology journal 151 (2016), 26-31.

Determination of the expedient motion trajectory of the bucket on the side dump bucket loader MVC E500-1 during the digging and filling materials.

VAN HUY Ta[1,a*], VAN DAT Chu[1]

[1)]Military Technical Academy, Ha Noi, Viet Nam
[a)]Email: quanghuycb1971@gmail.com; Phone: 0985 187 589

Keywords: Side Dump Bucket Loader, working equipment, trajectory motion.

Abstract. This article presents the method determining the motion trajectory of the bucket on the side dump bucket loader MVC E500-1 during the materials digging through the combinative method. The kinematic equations of the working equipment are established in order to determine the location of the special points on the bucket at different times, from that the necessary space for the machine to safely and effectively operate in the tunnel can be determined. The preliminary obtained results of the present work can be used for reference in the design and application of the Side Dump Bucket Loader MVC E500-1 in tunnel construction by the exploding-drilling method.

Introduction

The material filling process on the front loader by a combinative method is operated when all the main components of the machine are working: The forward movement of the excavator to push the bucket into the pile of material, which is carried out by the shifting mechanism of the vehicle; The jib lift and bucket rotation by hydraulic cylinders; The motion trajectory of the bucket, depending on the forward velocity of the vehicle, the lifting velocity and the bucket rotation speed. To obtain the proper trajectory of the bucket teeth and bucket in the material pile; First of all, it is necessary to analyze the dynamics of the loader working equipment, to give the geometric relation equations between the length of the hydraulic cylinders and the angles of the jib and the bucket. Thereby the ratio of the speed of movement of the piston rods of the hydraulic cylinders lifting and rotating the buckets and the movement speed of the loader is determined to capture the most efficient bucket trajectory. In previous researches, the theory of machinery kinematics (Wilson and Sadler, 1991) was used to establish the kinematic models of the mining machinery. The dynamic models of Load-Haul-Dump loader (Hemami, 1994; Takahashi et al., 2004) and backhoes excavator (Koivo, 1992) were built in three-dimensional (3D) space based on the robot kinematics (Ho and Sriwattanathmma, 1989). In this paper, the mathematical and physical models for the side dump bucket loader MVC E500-1, which has been made in Viet Nam, are developed. Section 2 contains the kinematic modeling of the machine, determination of the resistance and trajectory of the bucket. The experimental results are carried out in Section 3. And the conclusions, which is one of the preliminary research directions on this equipment, are given in Section 4.

Building the kinetic model and determining the motion trajectory of the bucket

The dynamic model of the bucket. Scheme general layout of operating equipment on a side dump bucket loader, *Fig. 1*, is the basis for building a calculation scheme to give kinematic equations of the bucket, *Fig. 2*.

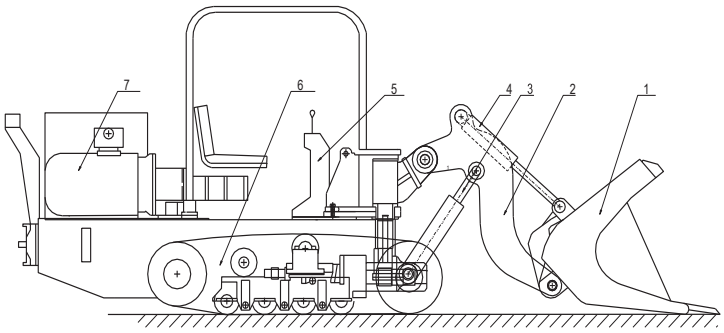


Fig. 1. Scheme of the Side Dump Bucket Loader MVC E500-1: 1,2,3,4. The details of working equipment; 5. Control unit; 6. The moving section; 7. Power source.

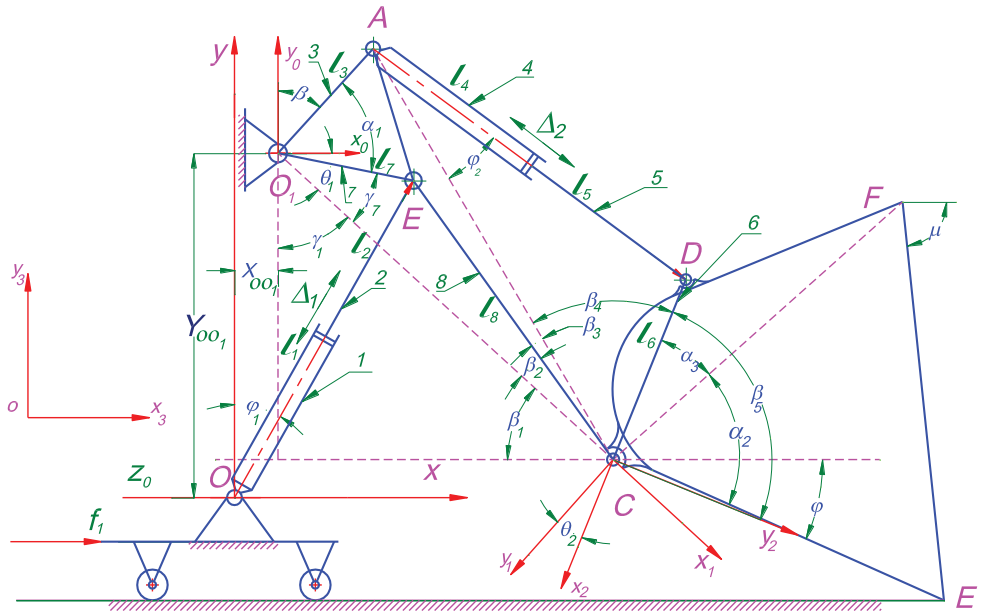


Fig. 2. Calculating scheme to give the kinematic equations of bucket movement and determine the trajectory of the jib and bucket when the machine is working.

Research purpose: Determining the angle of the bucket vertically and horizontally, which is the angle between CE and the axis Oy, Ox. This angle depends on the stroke of the hydraulic cylinder (link 1- 2, 4-5), rotating the bucket, and simultaneously determine the trajectory of the bucket through the points on the boom and ladle from which you can calculate a reasonable height when the machine is working in the tunnel.

To achieve the research purpose, we proceed to determine the coordinates of points B, A, D, C, E in two degrees of freedom, when the cylinder, lifting jib, and the cylinder, rotating the bucket, move with Δ_1, Δ_2, which are two strokes of the corresponding hydraulic cylinders.

Calculating scheme, Fig. 2: the fixed coordinate system Oxy is selected, with the corresponding coordinate and length parameters, defined on the figure, giving the kinematic equations of the bucket movement.

Calculating the angle φ_1: Suppose at the survey time, the cylinders were moving away with the distance x_1, x_2; Select the fixed coordinate system Oxy as shown in fig. 2, the origin O goes through the point O, the angle φ_1 is determined by:

$$\varphi_1 = \angle O_1OB + \angle O_1OY$$

$$\cos\angle O_1OB = \frac{O_1O^2 + OB^2 - O_1B^2}{2O_1O.OB} = \cos\angle O_1OB = \frac{x_{O_1O}^2 + y_{O_1O}^2 + l_7^2 - (l_1 + l_2 + x_1 - \Delta_1)^2}{2\left[\sqrt{x_{O_1O}^2 + y_{O_1O}^2}.(l_1 + l_2 + x_1 - \Delta_1)\right]} = a$$

Angle O_1OY is determined as follows: $\cos\angle O_1OY = \frac{Y_{OO_1}}{OO_1} = \frac{Y_{OO_1}}{\sqrt{x_{OO_1}^2 + Y_{OO_1}^2}}$

In this case, x_{O_1O}, y_{O_1O} is constant then $O_1OY = \text{const}; \Rightarrow \cos\angle O_1OY = \text{const} = b$

$\Rightarrow \varphi_1 = \arccos(a) + \arccos(b)$

Determining the point B coordinates, which is cylinder linkage point between the cylinder, lifting jib and jib; Use the projection formula in coordinates system Oxy.

$f(t)$: Law of motion of the vehicle.

$$\begin{cases} x_B = f(t) + OB.\sin\varphi_1 = f(t) + (l_1 + l_2 + x_1 - \Delta_1)\sin\varphi_1 \\ y_B = OB.\cos\varphi_1 = (l_1 + l_2 + x_1 - \Delta_1)\cos\varphi_1 \end{cases}. \quad (1)$$

Determining the coordinates of point A, which is the fixed linkage point of the cylinder, rotating the bucket on the bucket rod. α_1 is the angle formed by O_1A and O_1B, which are on the same jib, then the angle α_1 is constant.

$$\alpha_1 = \angle AO_1B = \text{const}$$

β is the angle formed by O_1A and axis Oy; this angle is determined as follows:

$$\tan(\alpha_1 + \beta) = \frac{x_{O_1B}}{y_{O_1B}} = \frac{x_B - x_{O_1}}{y_B - y_{O_1}} = \frac{O_1B.\sin\varphi_1 - x_{OO_1}}{O_1B.\cos\varphi_1 - y_{OO_1}} = d;\ \alpha_1 + \beta = \arctan(d);\ \beta = \arctan(d) - \alpha_1$$

The system of equations determines the coordinates of point A:

$$\begin{cases} x_A = f(t) + x_{OO_1} + O_1B.\sin\beta \\ x_B = y_{OO_1} + O_1B.\cos\beta \end{cases} \Leftrightarrow \begin{cases} x_A = f(t) + x_{OO_1} + l_3.\sin\beta \\ x_B = y_{OO_1} + l_3.\cos\beta \end{cases}. \quad (2)$$

Determining the coordinates of point C, which is the link point of the jib and the bucket. To determine the coordinates of point C, we need to determine the angle between O_1C and Ox or O_1C and Oy. In this model, following the logic of the problem, we define the angle between O_1C and Oy; $(\angle O_1C, OY) = \gamma_1$)

γ_7 is the angle formed by O_1C and O_1B. Because of the points O_1, B, C are on the same link then γ_7 is constant. γ_7 is determined as following:

We will look at the triangle O_1BC, using the cosine function theorem in the triangle we have:

$$\cos\gamma_7 = \frac{O_1B + O_1C - BC^2}{2.O_1B.O_1C} = \frac{l_7^2 + l_{O_1C}^2 - l_8^2}{2.l_7.l_{O_1C}} = e;\quad \gamma_7 = \arccos(e);$$

Finally, the angle γ_1 is completely determined

$$\gamma_1 + \gamma_7 + \alpha_1 + \beta = \pi \Rightarrow \gamma_1 = \pi - \gamma_7 - \alpha_1 - \beta\ (*)$$

The system of equations, determining coordinates of point C:

$$\begin{cases} x_c = f(t) + O_1C.\sin\gamma_1 \\ y_c = O_1C.\cos\gamma_1 \end{cases} \Leftrightarrow \begin{cases} x_c = f(t) + l_{O_1C}.\sin\gamma_1 \\ y_c = l_{O_1C}.\cos\gamma_1 \end{cases}. \quad (3)$$

Determining the coordinates of point D, which is the link point of the cylinder, rotating bucket and the bucket. To determine the coordinates of point D, we need to determine the angle between CD and horizontal. In order to determine β_5:

We will call $\beta_1 = (\angle O_1B, Ox);\ \beta_2 = \angle O_1CB;\ \beta_3 = \angle BCA;\ \beta_4 = \angle ACD$

$$\Rightarrow \beta_5 = \pi - \beta_1 - \beta_2 - \beta_3 - \beta_4$$

In which: $\beta_1 = \frac{\pi}{2} - \gamma_1$; ($\gamma_1$ is defined above); $\beta_2 = \text{const}, \beta_3 = \text{const}$ because of O_1BA and C are on the same link.

With $\cos\beta_2 = \frac{BC^2 + O_1C^2 - O_1B^2}{2.BC.AC} = \frac{l_8^2 + l_{AC}^2 - l_{AB}^2}{2.l_8.l_{O_1C}}$; $\cos\beta_3 = \frac{BC^2 + AC^2 - AB^2}{2.BC.AC} = \frac{l_8^2 + l_{AC}^2 - l_{AB}^2}{2.l_8.l_{O_1C}}$

To determine β_4: $\cos\beta_4 = \frac{AC^2 + CD^2 - AD^2}{2.AC.CD} = \frac{l_6^2 + l_{AC}^2 - AD^2}{2.l_6.l_{AC}}$

AD is a variable-length link => β_4 is variable, $AD = l_4 + l_5 + x_2 - \Delta_2$; x_2 is a move of the cylinder 2; Δ_2 is a stroke of the cylinder 2 (in this time, we will suppose that the cylinder 2 is initially closed $\Delta_2 = 0$); v_2 is the velocity of the piston of the cylinder 2.

$$\Rightarrow \cos\beta_4 = \frac{l_{AC}^2 + l_6^2 - (l_4 + l_5 + \int_0^{t_2} v_2.dt - \Delta_2)^2}{2.l_{AC}.l_6}$$

$\beta_5 = \pi - \beta_1 - \beta_2 - \beta_3 - \beta_4 =>$ The system of equations determines the coordinates of point D

$$\begin{cases} x_D = x_C - DC.\sin\beta_5 \\ y_D = y_C + DC.\cos\beta_5 \end{cases}. \quad (4)$$

Determining the point E, which is contact point of bucket tooth and material:

α_2 will be an angle formed by CD và CE; $=> \alpha_2 = \text{const}$.

φ will be the angle formed by CE và Ox $=> \varphi = \alpha_2 - \beta_5$. (5)

$$=> \begin{cases} x_E = x_C + CE.\cos\varphi \\ y_E = y_C - CE.\sin\varphi \end{cases}. \quad (6)$$

Determining the point coordinates F, which in on the edge of the bucket, through point C as defined above:

$$\begin{cases} x_F = x_C + l_{CF}\cos(\alpha_2 - \beta_5 - 9\pi/180) \\ y_F = y_C + l_{CF}\sin(\alpha_2 - \beta_5 - 9\pi/180) \end{cases}. \quad (7)$$

In summary, the system is defined by the following equations: Equations (1), (2), (3), (4), (6), (7) is the system of equations, determining the trajectory of the jib and bucket through points A, B, C, D; Equation (5) determines the digging angle relative to the horizontal Ox.

Resistance forces acting on the bucket when the material is filled into the bucket. During the filling of the material, the forces continuously change from the beginning moment to the end of digging process, at each point in the digging process, the resistance forces will be the combinative forces of component forces r1, r2, r3, r4, r5; as shown in *Fig. 3*:

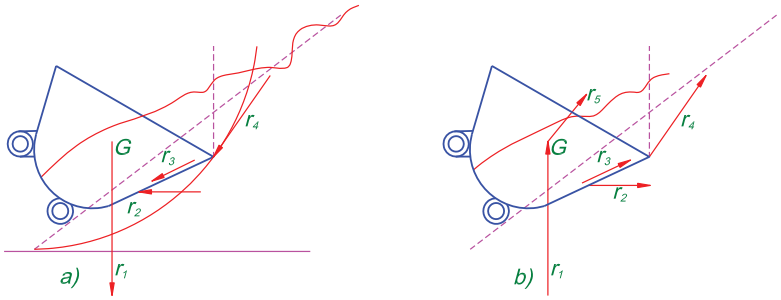


Fig. 3. The forces acting on the bucket: a - the resistance forces; b - the lifting forces

In this, r_1 is the mass of the loaded material in the bucket. This force acts on the center of gravity of the bucket, and changes during the digging, so that both the magnitude and the set point of the force change continuously; r_2 is the resistance force, acting on the surface under the bucket during digging; r_3 is the friction force between the bucket and the material; r_4 is the resistance force of the material to the cutting edges of the bucket; r_5 force needed to transfer material into the bucket. The change in magnitude, set point and direction of the forces is investigated to incorporate these forces into the digging movement control process of the bucket. Among the forces mentioned above, the forces r_1, r_4, r_5 are more important, because the force r_2 can be zero, the value of r_3 is not big and can be determined by experiment [1].

The trajectory of the bucket

Velocity problem. The trajectory of the bucket cutting edge depends on the velocity of the piston rods of the hydraulic cylinder, which lifts jib and rotates the bucket, as well as the velocity of the forward motion of the machine. The values of the resistance force, generated during material digging, as well as the performance of the whole working process, are dependent on the trajectory of the cutting edge of the bucket in the material pile during the material filling. In order to have the correct trajectory of the bucket, it is necessary to determine the trajectory of the edge of the bucket during the filling of the material by a combinative method, which must coincide with the line of material displacement or close to it (Fig. 3). This can be achieved by determining the speed of the hydraulic pistons of the lifting cylinder, lifting buckets and the speed of the loader. The calculation scheme for determining the ratio of the speed is shown in Fig. 4, in the scheme use the following conventional symbols: $\vec{v}_{pk}; \vec{v}_{Ey}; \vec{v}_{Ex}$ - the vector of the absolute velocity of the point E, in which $\vec{v}_{Ex}$ - the speed of the translational movement of the loader; the value of the angles ρ created by the links of working equipment with the height of the material pile, H_{min} - the minimum height of the material pile, φ - the friction angle of the material $30^o < \varphi < 44^o$, depending on the material [2].

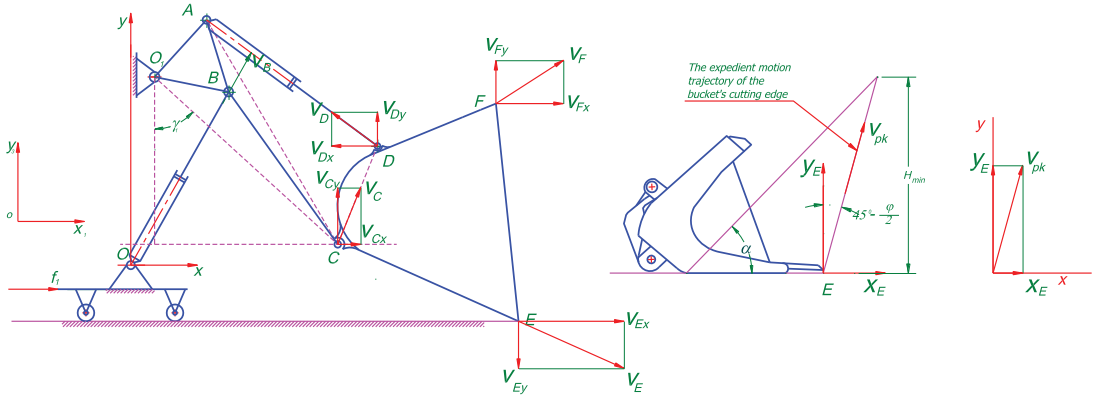


Fig. 4. Calculation scheme, defining the velocity parameters of the material digging process

We determine the long velocity of points A, B, D, E, F and determine the angular velocity of the links 1-2; 3-7-8; link 4-5 and link 6; Here we know in advance that the velocity of the two cylinders 5, 2 is v_1, to find the velocity of the point D, E and the angular velocity of the bucket when the machine operates, we apply the analytical method for calculation, because the equation (4) is known. Here we denote: $(\ ')$ - the first derivative of time t, f (t) is the function of the law of motion of the vehicle.

$$=> \quad \dot{v}_D^2 = \dot{x}_D^2 + \dot{y}_D^2 . \tag{7}$$

$$\dot{x}_D = \dot{x}_C - DC\dot{\beta}_5 \cos\beta_5 = f'(t) + l_{O_1C}\dot{\gamma}_1 \cos\gamma_1 - DC\dot{\beta}_5 \cos\beta_5$$

$$\dot{y}_D = \dot{y}_C - DC\dot{\beta}_5 \sin\beta_5 = -\left[l_{O_1C}\dot{\gamma}_1 \sin\gamma_1 + DC\dot{\beta}_5 \sin\beta_5 \right]$$

$$\Rightarrow v_D = \sqrt{\dot{x}_D^2 + \dot{y}_D^2} . \tag{8}$$

Determining V_D according to Ox and Oy:

$$\begin{cases} \cos(\vec{v}_D, Ox) = \dfrac{\dot{x}_D}{v_D} \\ \cos(\vec{v}_D, Ox) = \dfrac{\dot{y}_D}{v_D} \end{cases}$$

Determine the absolute velocity of the point F.

$$\begin{cases} x_F = x_C + l_{CF}\cos(\alpha_2 - \beta_5 - 9\pi/180) \\ y_F = y_C + l_{CF}\sin(\alpha_2 - \beta_5 - 9\pi/180) \end{cases} \Rightarrow v_F = \sqrt{\dot{x}_F^2 + \dot{y}_F^2} \ . \quad (9)$$

The directions are determined by the cosine angle as follows: $\cos(\vec{v}_F, Ox) = \frac{\dot{x}_F}{v_F}; \cos(\vec{v}_F, Oy) = \frac{\dot{y}_F}{v_F}$

Calculating the absolute velocity of the point E by

$$\begin{cases} x_E = f(t) + l_{O_1C}\sin\gamma_1 + CE\cos(\alpha_2 - \beta_5) \\ y_E = l_{O_1C}\cos\gamma_1 - CE\sin(\alpha_2 - \beta_5) \end{cases} \Rightarrow v_E = \sqrt{\dot{x}_E^2 + \dot{y}_E^2} \ ; \quad \alpha_2 = \text{const}. \quad (10)$$

$$\dot{x}_E = l_{O_1C}\dot{\gamma}_1\cos\gamma_1 - CE(\dot{\alpha}_5 - \dot{\beta}_5)\cos(\alpha_5 - \beta_5) + f'(t) = l_{O_1C}\dot{\gamma}_1\cos\gamma_1 + CE\dot{\beta}_5\sin(\alpha_5 - \beta_5) + f'(t)$$

$$\dot{y}_E = l_{OC} - \dot{\gamma}_1\sin\gamma_1 - CE(\dot{\alpha}_5 - \dot{\beta}_5)\cos(\alpha_5 - \beta_5) + f'(t) = -l_{O_1C}\dot{\gamma}_1\sin\gamma_1 + CE\dot{\beta}_5\cos(\alpha_5 - \beta_5) + f'(t)$$

$\dot{\gamma}_1$ and $\dot{\beta}_5$ were defined above $\Rightarrow v_E = \sqrt{\dot{x}_E^2 + \dot{y}_E^2}$ the directions is determined by the cosine angle as follows: $\cos(\vec{v}_E, O_X) = \frac{\dot{x}_E}{v_E}; \cos(\vec{v}_E, Oy) = \frac{\dot{y}_E}{v_E}$

The algorithm, analyzed above, allows studying the velocity characteristics of the material digging process for the purpose of selecting the optimal parameters of the digging process on Side Dump Bucket Loader by a combinative method with a reasonable trajectory of motion.

Experimental results

Some survey data: the size of the Side Dump Bucket Loader MVC E500-1: long x wide x high (4.910 x 1.530 x 2.810) m; height of the jib boom relative to the bearing surface y_{O1} = 0.25 m; length of the boom, l_7 = 1.280 m; The bucket has a length x width (1.53 x 1.25) m; Working stroke of cylinder, lifting jib: 0.366 m, Working stroke of the cylinder rotating bucket: 0.425 m, Working stroke of the cylinder turning over bucket: 0.390 m. Survey with some process of filling the material for the working equipment: the process of filling materials into the bucket can be carried out in different ways, separately or simultaneous movement. In *Fig. 5*, describes the trajectory of the bucket in the digging process by a combinative method by MATLAB software.

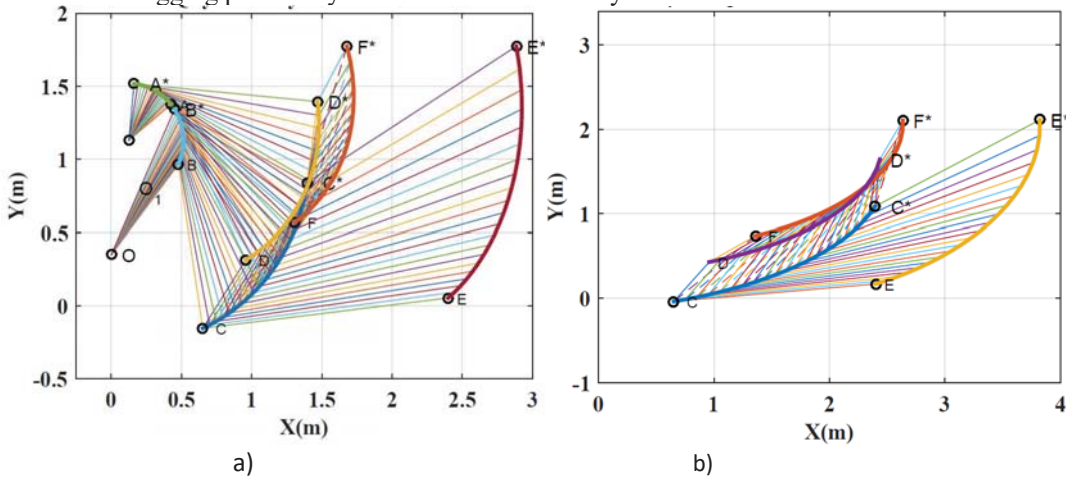


Fig. 5. The trajectory of the bucket in case the bucket is shedding the material by the method of coordination. a) Combination of bucket lift and rotation. b) Combination of bucket lift and rotation, and translational movement of the vehicle

In *Fig. 5* show that when changing the working stroke of cylinders, lifting and turning the bucket, making changes of the distances OB and AD and translational movement of the loader, the trajectory of the bucket will be changed. Through the special points on the bucket: F point on the top edge of the bucket, point E on the bucket tooth and two points on the back of bucket, the changes of C, D, E, and F in the material filling process will draw the CC *, DD *, EE *, FF * curve. This is the trajectory of the bucket when filling the material by the combinative method.

Conclusion

The working equipment of Side Dump Bucket Loader works as a robotic arm with three degrees of freedom, linked by a sliding joint and two rotary joints. The paper presents the kinematical investigation of the material filling process into the MVC E500-1 bucket and gives the method for determining the proper trajectory of the bucket when filling material by the combinative method, with the purpose of filling materials into the bucket with the lowest energy costs. In order to have a proper trajectory, the trajectory of the cutting edge of the bucket during the material filling process must coincide with the moving line of the material or be close to this line (shown in Fig. 3). The ratio of the speed of movement of the piston rods of the hydraulic cylinders lifting and rotating the buckets and the movement speed of the loader is determined in Fig. 4. Results of calculations and surveys of the article by the MATLAB software, shown in Fig. 5, shows that the motion curve of point E roughly coincides with the desired curve in Fig. 3, which demonstrates the need of the relationship between the jib lifting, bucket rotation and displacement of the machine , to ensure the most efficient filling of the bucket and keep the material in the bucket not to drop out during lifting bucket to discharge position. The results of the study can be used to choose to machine operation options and to automate the process of material loading under specific conditions.

References

[1] Ahmad Hemami， Modelling, analysis and preliminary studies for automatic scooping/loading in a mechanical loader, International Journal of Surface Mining and Reclamation 6 (1992) 151-159.
[2] Профессор СВ. Абрамов, Диссертация на соискание ученой степени кандидата технических наук, 2002, pp.37-38.
[3] I.V. Boyarkina, Технологическая механика одноковшовых фронтальных, погрузчиков, Монография, 2011.
[4] Chu Văn Đạt, Lê Văn Dưỡng, Tạ Văn Huy, Nghiên cứu xác định lực cản tổng quát trong quá trình tích vật liệu vào gầu của máy xúc lật, Tạp chí Nghiên cứu khoa học và công nghệ quân sự, 4, 2016, pp. 166-172.
[5] Y. Li and W. Liu, Spatial kinematics modeling and simulation of wheel loader, J Model Simul Identify Control, vol. 1, 2013, pp. 78-88.

CONTROLLED SYNTHESIS OF TiO_2/GRAPHENE PHOTOCATALYSTS BY HYDROTHERMAL METHOD

Lieu ThiThanh Le[1,2], HiepThiThanh Le[2], Ngoc Thi My Duong[2], Truong Giang Le[3], Vien Vo[2,4]

[1]*Graduate university of Science and Technology, Vietnam Academy of Science and Technology*
[2]*Department of Chemistry, QuyNhon University*
[3]*Institute of Chemistry, Vietnam Academy of Science and Technology*
[4]*Applied research Institute for science and technology, QuyNhon University*
18 Hoang Quoc Viet, HaNoi capital, Vietnam
170 An Duong Vuong, QuyNhon city, Vietnam
[*]*Tel. (084)0978844549. E – mail: lethithanhlieu@qnu.edu.vn*

Keywords: Synthesis of TiO_2/Graphene, hydrothermal method, $TiCl_4$, Rhodamine B.

Abstract

Owing to its high photocatalytic activity, highly chemical and structural stabilities, nontoxicity, low environmental impact and abundance, TiO_2 is one of the most popularly used photocatalysts in many environmental and energy-related applications such as air and water treatment, hydrogen energy, and other energy conversion and storage applications. However, due to its large band gap (i.e., ~3.2 eV), which absorbs photons with wavelengths in the UV range, TiO_2 does not harvest efficiently sunlight that provides highest photon flux in the visible and infrared regions. In addition, the rapid recombination of photogenerated charge carriers, electrons and holes, is a limiting factor to achieve high photocatalytic efficiency of TiO_2. The coupling of TiO_2 with graphene has recently demonstrated as an efficient photocatalyst that can overcome the disadvantages of TiO_2. Accordingly, the combination of TiO_2 and graphene not only enables the visible light absorption, but also reduces the charge recombination, which consequently increases the photocatalytic efficiency. This work presents the synthesis and photocatalytic properties of TiO_2/graphene nanocomposites prepared by hydrothermal method using $TiCl_4$ as a precursor. The morphology and crystalline structures of the as-synthesized TiO_2/graphene were investigated by transmission electron microscopy and X-ray diffraction,diffuse reflectance ultraviolet-visible spectroscopy, respectively. The results show that by varying the concentration of the $TiCl_4$ precursor, reaction time, and the subsequent thermal annealing, highly uniform TiO_2 nanoparticles with tunable size on the graphene can be achieved. The photocatalytic performance of the TiO_2/graphene was evaluated by the photodegradation of Rhodamine B under visible light irradiation, showing higher photocatalytic activity than uncoated graphene and bare TiO_2.

Introduction

Titanium dioxide (TiO_2) is one of the most widely investigated semiconducting metal oxides that exhibits photocatalytic activity and is used in a wide range of applications [1−5]. When TiO_2 is irradiated with UV light, electrons are excited from the valence band (VB) to the conduction band (CB), creating electron−hole pairs, which are mainly responsible for the photocatalytic activity. However, the photogenerated electron−hole pairs have faster recombination rates than the rate of chemical interaction between TiO_2 and adsorbed pollutants, reducing the photocatalytic efficiency. Therefore, the challenge is to prevent electron−hole pair recombination and improve the photocatalytic activity of TiO_2.

Graphene sheet is the amazing monolayer of sp^2 - bonded carbon atoms arranged in honeycomb structure, whichhas attracted extensive interest in recent years and emerged as the most intensively studied material [6]. Graphene is a gapless semiconductor with unique electronic properties and its electron mobility can reach 10,000 cm^2/V.s at room temperature and has a micrometer-sized 2D plane with large π–π conjugation [7]. The bandgap within graphene sheet can be opened by reducing the dimensions of the graphene sheets to the nanolevel [8] or by introducing dopants [9]. Due to the unique structure and physicochemical properties, graphene has attracted attention of numerous researchers and has been extensively investigated [10-15]. Among the applications of graphene, integrating graphene with other inorganic materials to fabricate composites or hybrids is the focus. Assembling metal or metal oxide nanoparticles on graphene sheets has been reported [16-18].

Recently, various kinds of nanopaticles have been synthesized and decorated on graphene, including SnO_2 [19], TiO_2 [20], and Al_2O_3[21]. But, TiO_2 maybe one of the most "popular" and widely used photocatalyst and making a composite with graphene. The advantages of TiO_2 over other metal oxide such as innocuous, nature, cheap and chemically stable makes it superior. Coupling of TiO_2 with graphene has been shown to enhance the photocatalytic performance of the composite and synthesizing TiO_2 on graphene sheets may favor the dispersion of nanoparticles, thus facilitates the photodegradation of the pollutant. In several reports, the photoactivity of TiO_2/reduced graphene composites also depends on synthesis conditions. Nevertheless, few studies have reported on them. In this paper, we present a simple method to prepare modified graphene–TiO_2 composites. Particularly, we report on the synthesis of TiO_2 nanoparticles on modified graphene sheets via hydrothermal method under basis conditions and focus on their photocatalytic activities under visible light irradiation.

Experimental

Modification of graphene

The modified Hummers method was used to modify graphene surface of graphene. In a typical procedure, 15mL of H_2SO_4 was added into a 500 mL flask containing 0.6 gam graphene and 0.3 g of $NaNO_3$ at room temperature. The suspension was stirring consecutively during 22 hours. Then the flask was cooled down to 0-5°C in an ice bath in 1 hour. In the next step, taking the flask out of ice bath, while stirring them continously, 1.8 g of potassium permanganate ($KMnO_4$) was added slowly into the above mixture, which was allowed to warm to room temperature. The suspension was continuously stirred for 5 hours at room temperature, then heating up to 98°C, adding by 30 mL of distilled water and keepingat this temperature during 30 minutes. After that, it was cooled down to 40°C and subsequently diluted by 90 mL of water. Then 7.5 mL H_2O_2 (30%) was added to reduce residual permanganate. Finally, the resulting suspension was washed with HCl (5%) three times and ethanol till removing all Cl^-, and dried at 80 °C for 24 h to obtain graphene oxide (denoted as G).

Hydrothermal synthesis of TiO_2-G nanocomposites

210 mL of ethanol (99%) was added into a beaker 250 mL containing 0.12g G modified above, which was then stirring for 1 hour and cooling down to 0-5°C. After that, V mL (V = 0.1; 0.5; 1.0; 1.5; 2.0) of $TiCl_4$ was slowly added to the mixture with stirring for 2 hours. Then, the mixture was transferred to a Teflon-lined autoclave and then heated at 180°C under static condition for t hours (with t=2.5; 4.0; 8.0). The resulting grey gel was washed 3 times with distilled water and 2 times with ethanol. The solid was isolated by centrifugation. The obtained products were dried at 80°C for 12 hours and annealed at T^{o}C (with T=200; 300; 400) for 2 hours, and denoted as TiO_2/G-V-t-T, where V, t and T are volume (mL) of $TiCl_4$, time (h) and temperature (^{o}C) of hydrothermal treatment, respectively.

Photocatalytic study

The photocatalytic activity of the TiO_2/G-V-t-Tcomposites was evaluated by the degradation of Rhodamine B. 50 mg of the catalyst was added to 80 mL of 30 mg/L Rhodamine B in a 250 mL flask and placed inside a dark box. The mixture was stirred in the dark for 2.5 h to reach the adsorption–desorption equilibrium.The photocatalytic reaction was started by turning on the 220V-60W lightbulb. 10 mL of the mixed suspensionwas extracted at various irradiation times and centrifugated remove the photocatalyst. The concentration of residual RhB was determined by recording the maximum absorbance of RhB at 553 nm ona UV-visspectrophotometer.

Characterization

For characterization of the samples, Powder X-ray diffraction (XRD) was conducted on an X-ray diffractometer (Brucker D8 Avandce) using Cu Kα irradiation (λ = 0.1540 nm), accelerating voltage 30kV and applied current 0.01A. Transmission electron microscope (TEM) images were taken at several locations on the grids using a JEOL JEM1400 transmission electron microscope operating at a voltage of 120kV and a current density of 50pAcm^{-2}. Infrared spectra were recorded using IRAffinity-IS (Shimadzu) spectrometer. UV-VIS absorption spectra were obtained by UV-VIS spectrocope (UV-1800, Shimadzu).

Results and discussion

Preparation of photocatalysts

Effect of hydrothermal times

The crystalline phase of TiO_2/G-V-t-Tcomposites in the various hydrothermal times was characterized by XRD measurements (Figure 1) and the XRD of G was also showed to compare (Figure 2). As can be seen clearly, the modified graphene has a characteristic diffraction at 26.3°. When the time was raised from 2.5 hours to 4.0 and 8.0 hours, the results showed that composites mostly existed in the pure anatase phase, with six characteristic diffractions at 25.3° (101), 37.9° (004), 48° (200), 54.1° (105), 55.1° (211), and 62.7° (204) ([JCPDS] 21-1272) [22]. The average crystallite size of TiO_2 of anatase phase is 3.97; 4.26; and 3.43 nm for the sample TiO_2/G-0.1-2.5-300; TiO_2-4.0-300 and TiO_2-8.0-300, respectively, indicating that average crystallite size of the samples with the hydrothermal time of 8.0 hours is the smallest. Comparing to the pure TiO_2, it is much smaller (11.03 nm for the pure TiO_2). Another point shown in the XRD patterns of TiO_2/G composites that no diffraction peak for G located at ~26.3° could not be distinguished. This can be explained that this peak can be overlapped by the (101) peak of TiO_2 at 25.3°.

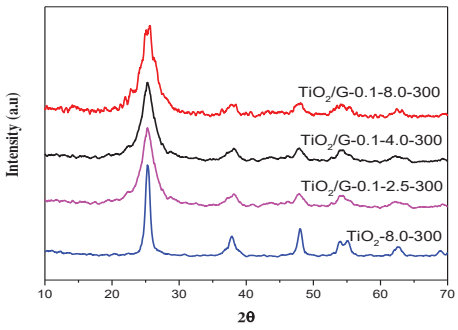


Figure 1. *XRD patterns of TiO_2-8.0-300 and TiO_2/G-0.1-y-300 (y=2.5, 4.0, 8.0)*

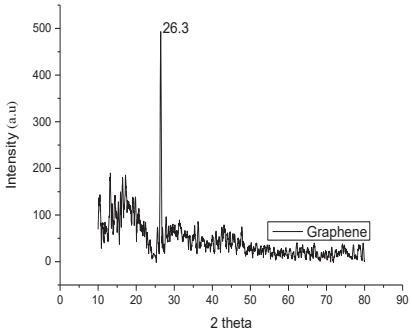


***Figure 2**. XRD parttern of G*

Figure 3 shows the TEM images of samples with different hydrothermal times at 300°C for 2 hours. It can be seen clearly that in the three samples, the structures of the composites present the graphene sheets decorated with TiO_2 particles densely. The fringe of graphene can be explicitly identified, convincing the presence of TiO_2.

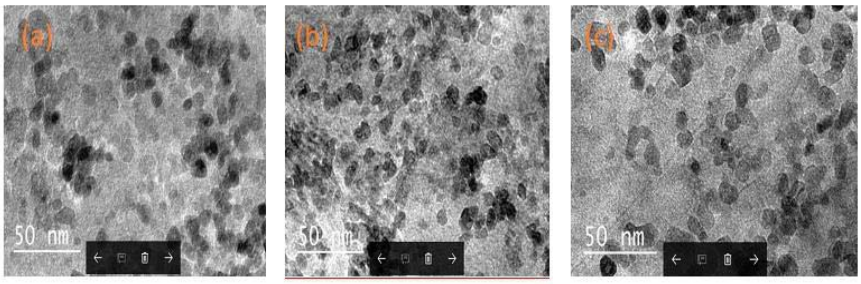


***Figure 3.** TEM images of TiO_2/G-0.1-2.5-300 (a) ;TiO_2/G-0.1-4.0-300(b) và TiO_2-0.1-8.0-300 (c)*

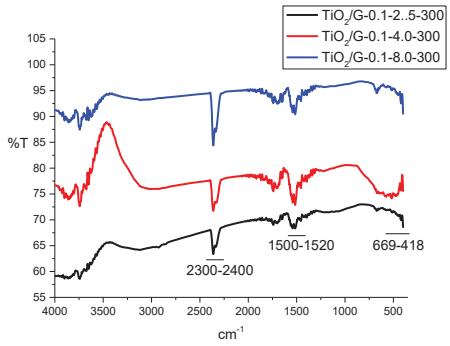


***Figure 4**. IR spectra of TiO_2/G-0.1-y-300 (y=2.5, 4.0, 8.0)*

To provide information on the structure, IR spectroscopy was also be used for charactering TiO_2/G composites. Figure 4 shows the IR spectra of composites prepared with different hydrothermal times. It can be seen from figure 4 that, in the three samples, there are characteristic peaks of Ti-O bond at special region (669 - 418 cm^{-1}) and Ti−O−Ti bonds show low frequency bands around 670 cm^{-1}. At the same time, there are graphene-specific peaks with ranges of 2300-2400 $cm^{-1}$and 1500-1520 cm^{-1} [23]. From the results of XRD patterns, TEM and

IR spectra, it can be concluded that TiO_2/G composites have been successfully synthesized at different hydrothermal times, and the appropriate time for synthesis of TiO_2 was between 4 and 8 hours. To investigate effect of temperature, $TiCl_4$ volume of 0.1 mL and hydrothermal time of 8 hours were selected.

Effect of calcination temperature

To investigate effect of hydrothermal temperature on synthesis, we kept a fixed volume of $TiCl_4$ as 0.1 mL and a hydrothermal time of 8 hours and changed the calcination temperatures at 200 °C, 300 °C and 400 °C. Figure 5 illustrates XRD patterns of three samples, TiO_2/G-0.1-8.0-200, TiO_2/G-0.1-8.0-300, TiO_2/G-0.1-8.0-400. According to Figure 5, we could clearly see that the phase formation of TiO_2 on the G substrate when changing the temperatures from 200 °C to 400 °C as follows: at 200°C, the nanocrystals formation of TiO_2 nanoparticles was not formed clearly. Especially, when the temperature was raised from 200°C to 300°C and 400°C, the phase formation of TiO_2 nanoparticles existed in pure anatase phase with six characteristic diffractions at 25.3° (101), 37.8° (004), 48.1° (200), 54.1° (105), 55.1° (211), and 62.6° (204). The characteristic diffraction at 25.3° (with TiO_2 101 plane) appeared moreintensively and is clear with increasing temperature, indicating crystallinity increasing with annealing temperatures. The XRD showed only a slight increase in the average particle size with increasing annealing temperatures.

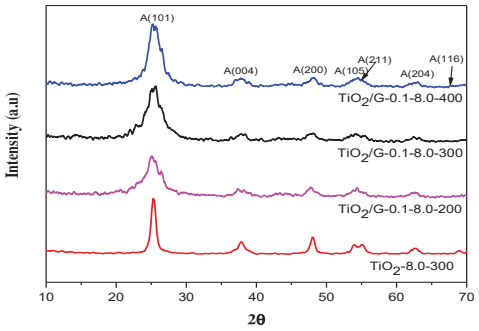


Figure 5. *XRD patterns of TiO_2/G-0.1-8.0-T (T=200, 300, 400)*

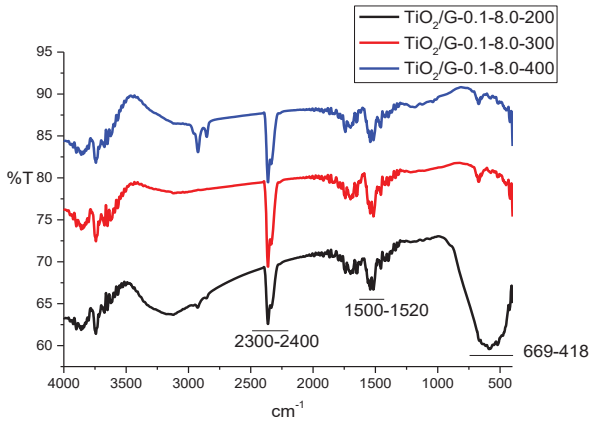


Figure 6. *IR spectra of TiO_2/G-0.1-8.0-T (T=200, 300, 400)*

Figure 6 shows IR spectra of the products obtained with various temperatures. The strong absorption in the region 669-418 $cm^{-1}$is attributed to the vibration of Ti-O bond in TiO_2. Besides, characteristic peaks for graphene in the range of 2300-2400 cm^{-1}, 1500-1520 cm^{-1} were obtained. As a result, within a calcination temperature range of 200-400 °C, not change of the structure of graphene can be observed.

Effect of concentration of $TiCl_4$ precursor

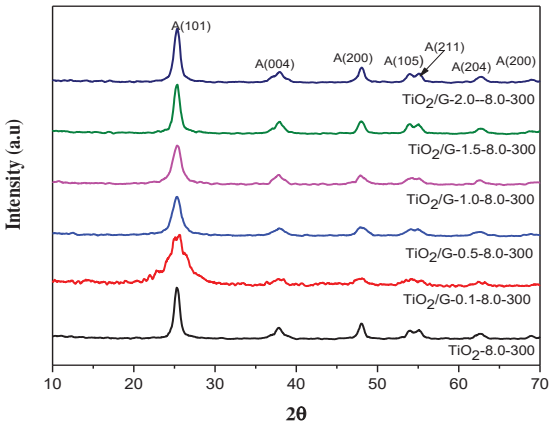


***Figure 7**. XRD pattern of TiO_2-8.0-300 and TiO_2/G-x-8.0-300 (x=0.1, 0.5, 1.0, 1.5, 2.0)*

The crystalline phase of TiO_2/G composites with different concentrations of $TiCl_4$ precursor was characterized by XRD (**Figure 7**). All the diffraction peaks belong to the anatase phase of TiO_2 (JCPDS 21-1272). Furthermore, the XRD results seem revealed that crystalline extent of the samples increases with concentration of $TiCl_4$ precursor.

Photocatalytic activities

In order to study effect of the hydrothermal time on photocatalytic activity, three samples, TiO_2/G-0.1-2.5-300; TiO_2/G-0.1-4.0-300 and TiO_2/G-0.1-8.0-300, were investigated via decomposition ability of Rhodamine B (RhB) under visible light. From the photocatalytic results of those samples (Figure 8), it can be seen that the catalytic performance under the visible region of TiO_2/G composites is much significantly higher than that of either TiO_2 or graphene. For photocatalysts, band gap and absorption range of light could strongly affect photocatalytic activity. Hence, TiO_2 particles were dispersed on graphene substrates, which helped to narrow the band gap of single particles of TiO_2 and enhanced the photocatalytic activity. Consequently, compared to the pure TiO_2 and graphene, the photocatalytic activity of TiO_2/G composites in the different hydrothermal times was much more higher.

RhB decomposition increased rapidly over hydrothermal time and the highest photocatalytic performance belonged to TiO_2/G-0.1-8.0-300 sample (70.57%). This can be explained by the average size of TiO_2 nanoparticles.

Figure 9 illustrates the variation in RhB concentration over time on TiO_2/G composites with different calcination temperatures. Generally, in comparison with the pure TiO_2 and graphene, it can be clearly seen that TiO_2/G composites exhibit a photocatalytic performance intensively much higher.

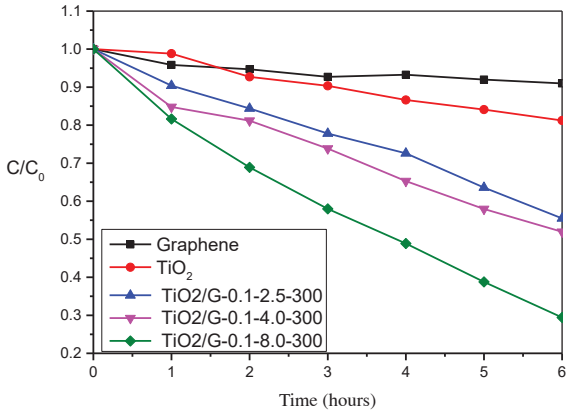


Figure 8 *.The degradation of RhB over the TiO_2/G-0.1-y-300 composites (y=2.5, 4.0, 8.0)*

When raising calcination temperature from 200°C to 300°C, the photocatalytic activity increases. However, if the temperature is continuously increased, the rate of photodegradation decreases. According to Figure 10, approximately 70% of Rhodamine B was degraded by TiO_2/G-0.1-8.0-300 catalyst over the period of 6 hours, concluding that the TiO_2/G-0.1-8.0-300 exhibits the highest synergistic effect among those samples. Two control samples at 200°C and 400°C exhibits much lower photocatalytic activity than that of the TiO/G-0.1-8.0-300 sample. This strongly suggests that the improved photocatalytic activity requires effective charge transfer between TiO_2 and graphene. Therefore, a close interfacial contact between TiO_2 and graphene is an essential factor. Moreover, one more important factor which influences directly to the photocatalytic performance is formation of TiO_2 particles. In the sample TiO_2-0.1-8.0-200, the formation of TiO_2 crystal was not obviously (according to Figure 5,the characteristic peak at $2\theta=25.3^{\circ}$ is weak). For the TiO_2-0.1-8.0-400 sample, there is a cluster formation of TiO_2. However, in the sample TiO_2-0.1-8.0-300, the formation of TiO_2 crystal on the graphene substrate was highly uniform TiO_2 nanoparticles with tunable size.

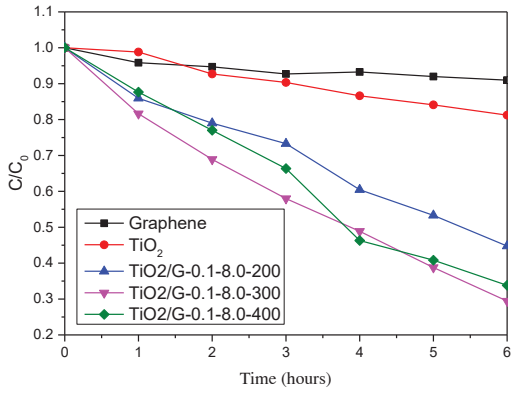


Figure 9*.The degradation of RhB over theTiO2/G-0.1-8.0-T composites (T=200, 300, 400)*

The figure 9 shows that by varying the concentration of the $TiCl_4$ precursor, TiO_2/G-0.1-8.0-300 is the best material in photocatalytic degradation of RhodamineB. This result shows that the nanoparticle size influences a lot on the degradation of RhB.

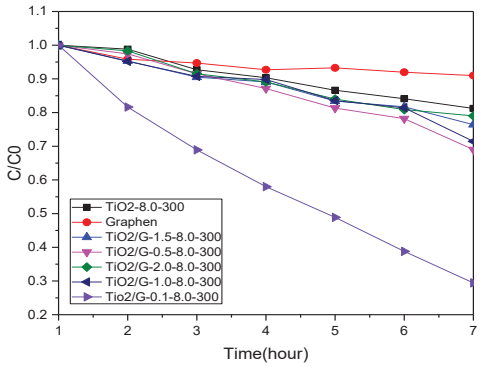


Figure 10. *The degradation of RhB of TiO_2/G-x-8.0-300 composistes (x=0.1, 0.5, 1.0, 1.5, 2.0)*

Conclusion

In this study, TiO_2 nanoparticles-graphene composite we successful prepared via a hydrothermal method in the different hydrothermal time, calcination temperatures and precursor volume. Most of the composite materials were obtained in small size and fairly uniform. There was no rutile phase, only anatas phase in the samples with increasing calcination temperature to 400°C. As-prepared TiO_2-graphene composites exhibit much higher photocatalytic activity toward degradation of RhB than TiO_2 or graphene itself. It was found that TiO_2 nanoparticle size in the TiO_2 nanoparticles-graphene composite affects photocatalytic performance, and the sample TiO_2/G-0.1-8.0-300 had the best photocatalytic performance.

Acknowledgements

This work was supported by The World Academy of Sciences (Grant 16-496 RG/CHE/AS_G – FR3240293298).

References

[1] B. A. Bhanvase, T. P. Shende & S. H, A review on graphene–TiO_2 and doped graphene–TiO_2 nanocomposite photocatalyst for water and wastewater treatment, Environmental Technology Reviews. 6 (2016) 1-14.

[7] Zhang, Y.; Tang, Z. R.; Fu, X.; Xu, Y. J, TiO_2 - graphene nanocomposites for gas-phase photocatalytic degradation of volatile aromatic pollutant: is TiO_2-graphene truly different from other TiO_2-carbon composite materials, ACS Nano. 4 (2010) 7303 – 7314.

[3] Huitong Wu, Jun Fan, Yuhao Yang, Enzhou Liu, Xiaoyun Hu, Yongning Ma, Xiao Fan, Chunni Tang, Hydrothermal synthesis of Graphene-TiO_2 nanowire with an enhanced photocatalytic activity, Russian Journal of Physical Chemistry A. 89 (2015) 1189-1194.

[4] Wang, G.; Wang, H.; Ling, Y.; Tang, Y.; Yang, X.; Fitzmorris, R.; Wang, C.; Zhang, J.; Li, Hydrogen-treated TiO_2 nanowire arrays for photoelectrochemical water splitting, Y. Nano Lett. 11 (2011) 3026-3033.

[5] Wang, D.; Choi, D.; Li, J.; Yang, Z.; Nie, Z.; Kou, R.; Hu, D.; Wang, C.; Saraf, L.; Zhang, J.; Aksay, I.; Liu, J, Self-Assembled TiO_2–Graphene Hybrid Nanostructures for Enhanced Li-Ion Insertion, ACS Nano. 3 (2009) 907.

[6] Geim K et al., The rise of graphene, Nat Mater. 6 (2007) 183-191.

[7] Novoselov KS, Geim AK, Morozov SV, Jiang D, Zhang Y, Dubonos SV et al, Electric Field Effect in Atomically Thin Carbon Films, Science. 306 (2004) 666-669.

[8] Barone V, Hod O, Scuseria GE, Electronic structure and stability of semiconducting graphenenanoribbons, Nano Lett. 6 (2006) 2748-2754.

[9] Wei DC, Liu YQ, Wang Y, Zhang HL, Huang LP, Yu G, Synthesis of N-Doped Graphene by Chemical Vapor Deposition and Its Electrical Properties, Nano Lett. 9 (2009) 1752-1758.

[10] K. S. Novoselov et ak., Electric field effect in atomically thin carbon films, A. Firsov Science. 306 (2004) 666.

[11] C. Niyogi, E. Bekyarova, M. E. Itkis, J. L. McWilliams, M. A. Hamon and R. C. Haddon, J. Am, Solution Properties of Graphite and Graphene, Chem. Soc. 128 (2006) 7720.

[12] Ng, Y. H.; Lightcap, I. V.; Goodwin, K.; Matsumura, M.; Kamat, P. V. J., To What Extent Do Graphene Scaffolds Improve the Photovoltaic and Photocatalytic Response of TiO_2 Nanostructured Films, Phys. Chem. Lett. 1 (2010) 2222−2227.

[13] A. K. Geim, Graphene: status and prospects, Science. 324 (2009) 1530.

[14] S. Park and R. S. Ruoff, Nat, Chemical methods for the production of graphenes, Nanotechnol. 4 (2009) 217.

[15] C. Go´ mez-Navarro, J. C. Meyer, R. S. Sundaram, A. Chuvilin, S. Kurasch, M, Atomic structure of reduced graphene oxide, Nano left. 10 (2010) 1144-1148.

[16] E. Yoo, T. Okata, T. Akita, M. Kohyama, J. Nakamura and I. Honma, Enhanced electrocatalytic activity of Pt subnanoclusters on graphenenano sheet surface, Nano Lett., 9 (2009) 2255.

[17] B. S. Kong et al,, Layer-by-layer assembly of graphene and gold nanoparticles by vacuum filtration and spontaneous reduction of gold ions, Chem. Commun. 16 (2009) 2174-2176.

[18] Z. Yin et al., Electrochemical deposition of ZnO nanorods on transparent reduced graphene oxide electrodes for hybrid solar cells, Small, 6 (2010) 306-12.

[19] Waghuley SA. Synthesis, Charecterization and CO_2 gas sensing response of SnO_2/Al_2O_3 double layer sensor, Indian J. Pure Appl. Phys. 49 (2011) 816-819.

[20] Telipan G, Ignat M, Tablet C, Parvulescu V. Synthesis, characterization and gas sensing properties of rutile TiO_2 doped with Pt obtained by sol-gel method, J Opto. Adv. Mater. 10 (2008) 2138-2141.

[21] Nemade KR, Waghuley SA, Highly responsive carbon dioxide sensing by graphene/Al_2O_3 quantum dots composites at low operable temperature, Indian J Phys. 88 (2014) 577-583.

[22] ShivaSalem, AminSalem, MostafaRezaei, Facile decoration of TiO_2 nanoparticles on graphene for solar degradation of organic dye, Solid State Sciences. 61 (2016) 131-135.

[23] YongfangYang, LidongXu, HefangWang, WenjieWang, LixinZhang, TiO_2/graphene porous composite and its photocatalytic degradation of methylene blue, Materials and Design. 108 (2016) 632-639.

OPTIMIZATING SPRAY PARAMETERS OF HIGH VELOCITY OXY FUEL (HVOF) FOR Cr_3C_2 - NiCr COATING

Dinh Van Chien[1,a*], Nguyen Thanh Phu[2,3,b] , Doan Thanh Hoa[2,c] and Bui Van Khoan[2,d]

[1]Hanoi University of Mining and Geology, Ha Noi, Viet Nam

[2]Hung Yen University of Technology and Education, Hung Yen, Viet Nam

[3]National Research Institute of Mechanical Engineering, No. 4, Pham Van Dong, Cau Giay, Hanoi, Vietnam

[a]vanchien.dinh@gmail.com, [b]thanhphuhk3@gmail.com, [c]hoaspkthy@gmail.com, [d]buikhoan.utehy@gmail.com

* Corresponding author. Tell: (+84)913214028; E-mail: vanchien.dinh@gmail.com

Keywords: HVOF; Taguchi method; Optimization; Cr_3C_2-20(80Ni20Cr).

Abstract. Porosity, hardness, and adhesion mainly affect the performance of thermal spray coating and significantly depend on spray parameters. Therefore, determining value of the spray parameters and their effects on the coating properties are always taken into consideration. This paper studies optimization as well as evaluates influences of HVOF spray parameters which include powder feed rate (M), rotational speed of the details per minute (N) and step movement of the nozzle per revolution (S) to the adhesion, porosity, micro-hardness of Cr_3C_2-20(80Ni20Cr) coating on 40Cr steel shaft substrate. Taguchi experimental design L9 combined with analysis of variance (ANOVA) was used to determine optimum spray parameters and percentage of effect of each spray parameter on properties of the coating. From obtained results, the optimal spray parameters are m = 35 $g.min^{-1}$, n = 130 rpm, S = 6 mm for the highest hardness coating of 658.2 HV; with m = 45 $g.min^{-1}$, n = 130 rpm, S = 3 mm for the smallest porosity of 1.27 %; with m = 35 $g.min^{-1}$, n = 130 rpm, S = 3 mm for the coating with a maximum adhesion of 44.07 MPa. The percent effects of the parameters m, n, S to adhesion, porosity and hardness were (2.8 %, 33.6 %, 63.6 %), (0.1 %, 1.3 %, 98.6 %), (32.7 %, 43.3 %, 24 %), respectively. The percent effects of spray parameters on corresponding coating property allows adjustment of spray parameters to obtain the desired coating. Verified experiment results shows that the results are reliable. Taguchi method and ANOVA can find optimal parameters of the HVOF spray to acquire high-performance coating.

Introduction

Cr_3C_2-NiCr coating has good wear resistance at room temperatures and high temperatures [1]. Compared to some other popular carbide coatings such as WC-Co or WC-Ni then Cr_3C_2-NiCr coatings have the same wear resistance under room temperatures [2]. However, at high temperatures Cr_3C_2-NiCr coating with wear resistance is better than WC-Co and WC-Ni coating because Cr_3C_2-NiCr coating has a lower frictional coefficient [3]. Thermal spray coating is an effective solution in hardfacing technology because of cheaper spray coating cost of replacement detail, especially with the case of high volume details or noble material details. Currently, piston rods were necessary to recover very popular, they shouldn't be replaced because they have large volume and high cost. The piston rods can recover by thermal spray coating or chromium plating. Picas et.al proved coating Cr_3C_2-NiCr were perfected replacement for the chromium plating [4]. Although WC-Co, WC-Ni coatings resistance wear revealed well at room temperature, but it was good in dry conditions. Therefore, the Cr_3C_2-20(80Ni20Cr) coating with good wear resistance on the 40Cr [5] steel substrate of the worn piston rod is perfectly suited [4]. However, the wear resistance of Cr_3C_2-NiCr coating depends on spraying method. HVOF is used in this study because its sprayed coating is better than other common spray methods under normal conditions such as

Plasma spray (low porosity, adhesion and hardness) [6]. Purpose of this paper is to determine the optimal spray parameters. Taguchi method [7,8] has some advantaged properties such as reduced sample size, low investment cost, easy to calculate, fast and reliable results. Then Taguchi method combined with ANOVA has become a powerful mean for solving optimal problems for multiple factors to each response and widely used [10]. In addition, MINITAB is an application software that helps the experimental design and analysis of Taguchi methodology rapidly. An analysis of some studies on the optimization of HVOF spray parameters to Cr_3C_2-20(80Ni20Cr) coating indicated that: research on the optimal rotational speed of the details per minute (N) and the movement of the nozzle on each revolution (S) isn't published so far [11-17]. Spray parameters including fuel flow, oxy Flow, air flow, spraying distance, particle velocity, oxygen pressure, fuel pressure, air pressure are basic studied parameters. Therefore, this study optimizes three spray parameters: N, S and powder feed rate (M). The spray was applied to the axial detail that N and S changed, powder feed rate (M) would be a factor that could be significantly affected by the change in density; thus, M was chosen in this study. The other spray parameters are selected by the reference to previous studies [11-17] and recommendations on the manufacturer's equipment given will be kept fixed. The experimental design of Taguchi L9 was used to arrange number of experiments. An analysis of variance based on S/N ratio was used based on experimental results. Optimal spray parameters and corresponding optimum values of the coating were found. Verification is performed after obtaining the optimal level to verify the result of the problem.

Experimental procedure

Materials of coating and substrate

The spray powder used in this study was Cr_3C_2-20(20Ni80Cr) powder supplied by Oerlikon Metco Company with particle size from 15 μm to 45 μm and component are 80 % Cr_3C_2, 1.6 % Ni, 4 % Cr. The morphology of powders are shown in Fig. 1.

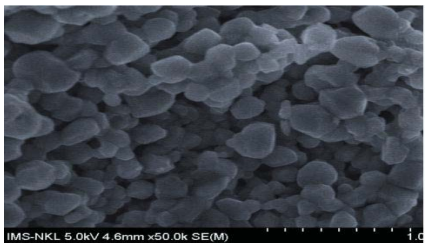


Fig. 1. SEM of Cr_3C_2-20(20Ni80Cr) powder

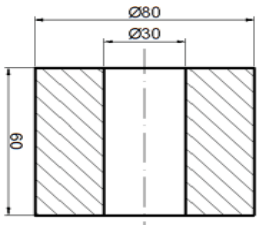


Fig. 2. Size of samples

Material of substrate is steel shaft 40Cr with component chemistry shown in Table 1. The samples size is prepared as shown in Fig. 2. The samples are cleaned of the surface from dirt, and chemicals. They are sand-blasted to increase the surface roughness with the purpose of increasing the coating's adhesion. Sand blasting process was performed on TSA-206-Viet Nam with corundum particles size of 150 μm to 300 μm. The surface roughness of the prepared sample is in the range of 8 μm to 10 μm.

Table 1. Chemical composition of steel shaft 40Cr (%)

Chemical composition	C	Si (max)	Mn (max)	Cr	Ni (max)
Percentage of chemical elements	0.37~0.44	0.17~0.37	0.8	0.8~1.1	0.3

HVOF thermal spraying procedure

Experimental spray was performed on HVOF General Metal Alloys-Beglgum includes: Control panel MP-2100; HP-2700M spray gun; Powder feeders PF-3350. The studied spray parameters M, N, S are presented in Table 2. Other spray parameters are kept constant as shown in Table 3. Table 4 indicates the orthogonal L9 experiments. To facilitate the adhesion test, the thickness of the coating to be kept constant is 400 ± 20 μm for all coatings.

Table 2. Set of factors and levels used in this study

Parameter	Symbol	Level 1	Level 2	Level 3
Powder feed rate (g.min^{-1})	M	25	35	45
Revolutions per minute(rpm)	N	57	130	170
Movement step-S(mm)	S	3	6	9

Table3. Process parameters set for the depositions

Parameters	Oxygen pressure (MPa)	Oxygen flow (l.min^{-1})	Propylen pressure (MPa)	Propylen flow (l.min^{-1})	Air Pressure (MPa)	Air flow (l.min^{-1})	Nitrogen Pressure (MPa)	Nitrogen Flow (l.min^{-1})
Values	0.981	300	0.686	60	0.686	550	0.49	20

The samples was cut into small samples for SEM and measured for the adhesion, porosity, hardness of the coatings. The S/N ratios and analysis of variance was calculated on statistical software Minitab version 17 by the Taguchi method.

Table 4. Orthogonal array Taguchi L9 for parameter validation study

Expriment	Powder feed rate-M (g.min^{-1})	Revolutions per minute-N (rpm)	Movement step-S (mm)
1	25	57	3
2	25	130	6
3	25	170	9
4	35	57	6
5	35	130	9
6	35	170	3
7	45	57	9
8	45	130	3
9	45	170	6

Test method

Olympus corporation GX51F Optical Microscope-Japan with 100, 200, 500 and 2500 magnifications were used to observe microstructure of coatings, the boundary between the coating and substrate. The sample size was 15 x 20 x 5 (mm) and polished surface. GX51F optical microscope was used to measure the porosity of the coating based on the method of metallography according to JIS-H-8664-1997- Japan standard [18]. The porosity was the percentage of the area of voids in the total area measured by each sample.

The adhesion strength of coating was determined by Shearing Strength method according to JIS-H-8666-1994 standard (Shearing Strength method) [19] for all samples. The sample for the adhesion test is designed as shown in Fig. 3. TUTM machine were used together with computer systems and specialized software that connects computer systems to devices for testing microhardness of coating is determined by measurements taken at five different positions on a sample. The measured hardness of the sample is the mean of the five measured values. The measurement process were performed on the Indenta Met 1106 (USA) machine according to ASTM E384-17-2011 standard with microforce of 100÷300 gram [20].

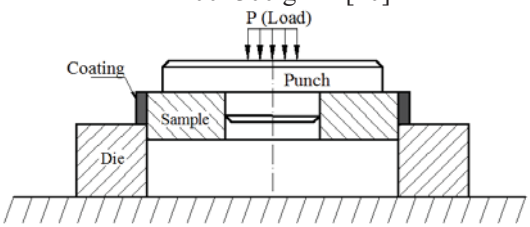


Fig. 3. Standard shear bond strength system (JIS-H-8666-1994 standard)

Results and Discussion

Experimental results



Fig. 4. Sample image before and after spraying

Fig. 4. is a photograph of 9 samples before and after experimental spraying in the same order as in Taguchi's orthogonal L9 table (Table 4). The coating measurements for adhesion, porosity and hardness of the coating were obtained shown in Table 5. The results in Table 5 indicated that spraying parameters for: the best adhesion was A2B3C1 with 43.5 MPa; the lowest porosity was A3B2C1 with 1.28 %; the highest hardness was A2B2C3 with 543 HV. Modification of the spray parameters changed the test results which proved that the study parameters affected the coating properties.

Based on the results in Table 5, calculate the S/N [19] value for each coating property with different characteristics according to Taguchi: Larger is better with adhesion and hardness; Smaller is better with porosity. The measured values of each coating property and the corresponding S/N ratio were calculated [19] with different quality characteristics presented in Table 3.

Table 5. Experimental results of HVOF sprayed Cr_3C_2-20(20Ni80Cr) coatings and S/N ratios.

Run	Spray Parameter			Adhesion		Porosity		Microhardness	
	M	N	S	Test Value (MPa)	S/N Ratio	Test Value (%)	S/N Ratio	Test Value ($HV_{0.3}$)	S/N Ratio
1	25	57	3	41.8	32.6086	1.55	-3.8066	586.4	55.3639
2	25	130	6	41.5	32.3695	2.37	-7.4950	635.0	56.0555
3	25	170	9	40.4	32.1354	3.10	-9.8272	503.2	54.0348
4	35	57	6	39.9	32.0175	2.59	-8.2660	616.1	55.7930
5	35	130	9	41.0	32.2474	3.01	-9.5713	643.6	56.1723
6	35	170	3	43.5	32.7688	1.36	-2.6708	571.5	55.1403
7	45	57	9	38.0	31.6039	3.11	-9.8552	564.2	55.0287
8	45	130	3	43.1	32.6895	1.28	-2.1442	541.6	54.6736
9	45	170	6	41.3	32.3280	2.49	-7.9240	566.0	55.0563

Coating morphology

From the microstructure image on Experiment No.01 (refer to Fig.5), it were possible to determine the thickness of Cr_3C_2-20(20Ni80Cr) coating and showed that there were fewer impurities and not cracks exist in boundary between coating and substrate. It was observed that the microstructure was quite similar across the length of the sample and the coating had good adhesion.

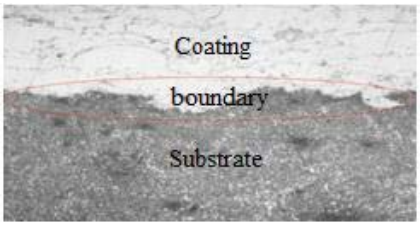


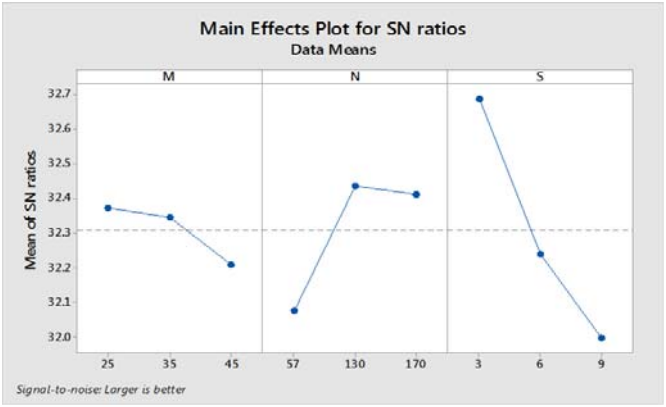
Fig. 5. Optical micrograph of Cr_3C_2-20(20Ni80Cr) coatings

Optimizing for adhesion of coatings

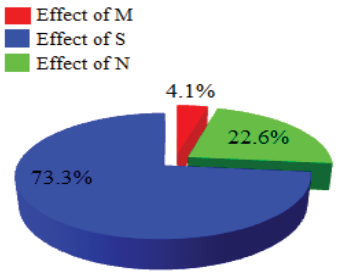
The influence of the parameters was determined and shown in the Table 6 and Fig. 6.a. The results showed that the A1B2C1 (M = 25 g.min^{-1}, N = 130 rpm, S = 3 mm) parameters provided the highest adhesion and the predicted value was 43.97 MPa. The optimum adhesion was found to be greater than the values measured on the samples showed that the optimum result is reliable. The analysis of variance pointed that the percentage influence of spray parameters (m, n, S) on the adhesion of the coating in descending order was: N (73.3 %) > S (22.6 %) > M (4.1 %) (Table 7) (Fig. 6. b)

Table 6. S/N response table for adhesion

Level	M	N	S
1	32.37	32.08	32.69
2	32.34	32.44	32.24
3	32.21	32.41	32.00
Delta	0.16	0.36	0.69
Rank	3	2	1



a. Main effects plot for adhesion



b. Percentage contributions by process parameterson adhesion

Fig. 6. Optimal level and percentage of effects of spray parameters to adhesion

Table 7. Result of ANOVA analysis for S/N ratios of adhesion

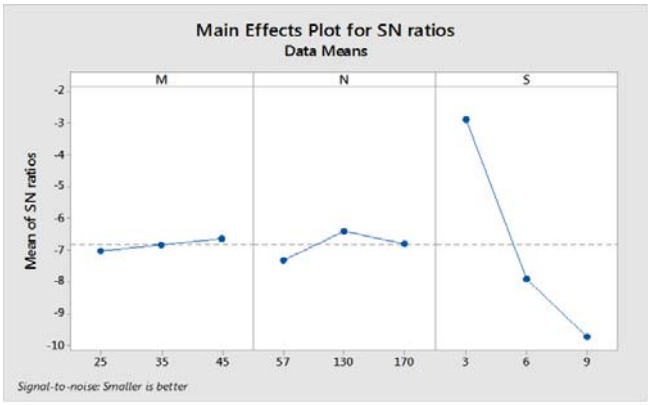
Source	DF	AdjSS	AdjMS	F-Value	P-Value	Predicted optimal value
M	2	0.9366	0.4683	1.33	0.429	
N	2	5.1614	2.5807	7.32	0.120	43.97 MPa
S	2	16.7709	8.3855	23.79	0.040	
Error	2	0.7051	0.3525			
Total	8	23.5740				

Optimizing for porosity of coatings

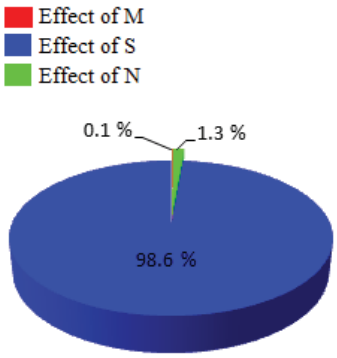
The influence of the parameters was determined and shown in the Table 8 and Fig. 7. a .The results showed that the A3B2C1 (M = 45 g.min^{-1}, N = 130 rpm, S = 3 mm) parameters provided the lowest porosity and the predicted value was 1.27 %. The optimum porosity was found to be less than the values measured on the samples showed that the optimum result is reliable. The analysis of variance showed that the percentage influence of spray parameters (m, n, S) on the porosity of the coating in descending order was: N (73.3 %) > S (22.6 %) > M (4.1 %) (Table 9) (Fig. 7. b).

Table 8. S/N response table for porosity

Level	M	N	S
1	-7.043	-7.309	-2.874
2	-6.836	-6.403	-7.895
3	-6.641	-6.807	-9.751
Delta	0.402	0.906	6.877
Rank	3	2	1



a. Main effects plot for porosity



b. Percentage contributions by process parameterson porosity

Fig. 7. Flow chart showing the optimal level and percentage of effects of spray parameters to porosity

Table 9. Result of ANOVA analysis for S/N ratios of porosity

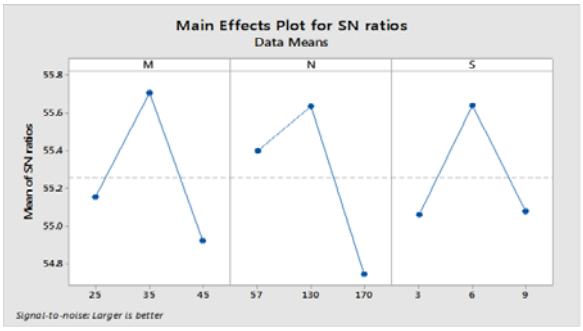
Source	DF	AdjSS	AdjMS	F-Value	P-Value	Predicted optimal value
M	2	0.00329	0.00164	0.44	0.695	
N	2	0.05802	0.02901	7.75	0.114	1.27%
S	2	4.34016	2.17008	579.55	0.002	
Error	2	0.00749	0.00374			
Total	8	4.40896				

Optimizing for microhardness of coatings

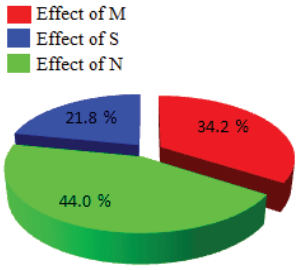
The influence of the parameters was determined and shown in the Table 10 and Fig. 8.a. The results indicates that using the A2B2C2 (M = 30 g.min^{-1}, N =130 rpm, S = 6 mm) parameters will acquired the highest microhardness (661.1 HV). The optimum microhardness was found to be greater than the values measured on the samples showed that the optimum result is reliable. Hence, it demonstrates that the present optimal method is reliable. The analysis of variance reveals that the percentage influence of spray parameters of m, n, S on the adhesion of the coating are 4.1 %, 73.3 % and 22.6% (Refer to Table 11 and Fig. 8. b), respectively.

Table 10. S/N response table for microhardness

Level	M	N	S
1	55.15	55.40	55.06
2	55.70	55.63	55.63
3	54.92	54.74	55.08
Delta	0.78	0.89	0.58
Rank	2	1	3



a. Main effects plot for microhardness



b. Percentage contributions of process parameters on microhardness

Fig. 8. The optimal level and percentage of spray parameters affected on microhardness

Table 11. ANOVA analysis resuts for S/N ratios of microhardness

Source	DF	AdjSS	AdjMS	F-Value	P-Value	Predicted optimal value
M	2	4396	2198	1.28	0.439	
N	2	5662	2831	1.65	0.378	661.1 HV
S	2	2802	1401	0.81	0.551	
Error	2	3439	1719			
Total	8	16298				

Verified experiments

In order to verify the optimal spray parameters, verified experiments were performed. The predicted and measured results are given in Table 12. The difference between them is smaller than 2 % (1.4 % for adhesion; 0.8 % for porosity; 1.5 % for hardness) for all factors. These results also exhibits that there is an improvement on the properties of coating (porosity, oxide content, tensile adhesion). When the porosity is reduced and the adhesion and microhardness are increased, the improvement of the coating quality can be reached with the optimal parameter. Therefore, it can be said properties of the Cr_3C_2-20(20Ni80Cr) coating on 40Cr steel substrate has been successfully obtained.

Table 12. Comparison of the confirm experiment and prediction results

Measurement value	Optimal level	Predicted value	Verified experiments	Variation
Adhesion (MPa)	M1N2S1	43.97 MPa	44.6 MPa	1.4 %
Porosity (%)	M3N2S1	1.27 %	1.28 %	0.8 %
Microhardness (HV)	M2N2S2	661.1 HV	657.0 HV	-1.5 %

Conclusion

In this study, spray parameters including powder flow rates, the rotational speed of the components and the movement of the spray guns are simultaneously estimated to improve the coating properties (adhesion, porosity, and hardness). The Taguchi method combined with the analysis of variance is employed to find optimal spray parameters. Results show that with M = 25 g.min-1, N = 130 rpm, S = 3 mm, the received coating has the highest adhesion; M = 45 $g.min^{-1}$, N = 130 rpm, S = 3 mm received coating has the lowest porosity; and M = 30 $g.min^{-1}$, N = 130 rpm, S = 6 mm received coating has the highest microhardness. The percent influence of spray parameters to adhesion, porosity, microhardness are N (73.3 %) > S (22.6 %) > M (4.1 %); N (98.6 %) > S (1.3 %) > N (0.1 %); S (44%) > M (34.2 %) > N (21.8 %). The results of verified experiments quite closes to the predicted results. Hence, it demonstrates that the present optimization method were reliable. The Taguchi method has been provided a simple and effective solution to find the best output based on the input parameters.

References

[1] Sarjas, H. Kulu, P. Juhani, K. Viljus, M. Matikainen, Vuoristo, Wear resistance of HVOF sprayed coatings from mechanically activated thermally synthesized Cr_3C_2-Ni spray powder. Proceedings of the Estonian Academy of Sciences, 65 (2016) 101-106.
[2] N. Vashishtha, S.G. Sapate, Abrasive wear maps for High Velocity Oxy Fuel (HVOF) sprayed WC-12Co and Cr_3C_2-25NiCr coatings, Tribology International, 2017.
[3] N. Vashishtha, S.G. Sapate, P. Bagde, A.B. Rathod, Effect of heat treatment on friction and abrasive wear behavior of WC-12Co and Cr_3C_2-25NiCr coatings, Tribology International, 2017.
[4] J.A. Picas, G. Matthaus, HVOF coatings as an alternative to hard chrome for pistons and valves, Wear, 261 (2006) 477-484.
[5] JIS G4053-2003, Low-Alloyed Steels for Machine Structural Use, 2003.
[6] L. Pawlowski, The Science and Engineering of Thermal Spray Coatings, Wiley and Sons, UK, ISBN No 0471952532, (1995).
[7] G. Taguchi, Designing Quality into Products and Processes, 1986.
[8] G. Taguchi, S. Konishi, Taguchi Methods, orthogonal arrays and linear graphs, tools for quality, American supplier institute, (1987) 8-35.
[9] Yujiao Qin, Yuping Wu, Jianfeng Zhang, Sheng Hong, Wenmin Guo, Liyan Chen, Hao Liu, Optimization of the HOVF Spray Parameters by Taguchi Method for High Corrosion-Resistant Fe-Based Coatings, Journal of Materials Engineering and Performance, 24 (2015) 2637-2644.
[10] Wahyudin, Angel Kharisma, Richard Dimas Julian Murphiyanto, Muhammad, Kevin Perdana, Tota Pirdo Kasih, Application of Taguchi method and ANOVA in the optimization of dyeing process on cotton knit fabric to reduce re-dyeing process, The International Conference on Eco Engineering Development ICEED 2017, 2017.
[11] J. C. Tan, Optimisation of the HVOF Thermal Spray Process for Coating, Forming and Repair of Components, Ph.D. Thesis, Dublin City University, Ireland, 1997.
[12] A.B. Adnan, Evaluating the Effects of High Velocity Oxy-Fuel (HVOF) Process, Jordan Journal of Mechanical and Industrial Engineering, 3 (2009) 157-160.
[13] Josep A. Picas, Elisa Rupérez, Miquel Punset, Antonio Forn, Influence of HVOF spraying parameters on the corrosion resistance of WC-CoCr coatings in strong acidic environment, Surface & Coatings Technology, 225 (2013) 47-57.
[14] T. Varis, T. Suhonen, O. Calonius, J. Čuban, M. Pietola, Optimization of HVOF Cr_3C_2-NiCr coating for increased fatigue performance, Surface & Coatings Technology, 305 (2016) 123-131.
[15] Gustavo Bavaresco Sucharski1, Anderson Geraldo Marenda Pukasiewicz, Rodolpho Fernando Váz, Ramón Sigifredo Cortés Paredes, Optimization of the Deposition Parameters of HVOF FeMnCrSi+Ni+B Thermally Sprayed Coatings, Technical Papers, 2015.
[16] H. Voggenreiter, H. Huber, H-J. S, Pies, and H. Baum, "HVOF-Sprayed Alloy IN718-The Influence of Process Parameters on the Microstructure and Mechanical Properties, A United Forum for Scienttific and Technological Advances, ed. C.C. Berndt, ASM International, Materials Park, (1997) 895-900.
[17] O. Maranhoa, D. Rodrigues, M. Boccalini, A. Sinatora, Influence of parameters of the HVOF thermal spray process on the properties of multicomponent white cast iron coatings, Surface & Coatings Technology, 202 (2008) 3494-3500.
[18] JIS H 8664 - Test methods for build-up thermal spraying, 2004.
[19] JSA - JIS H 8666, Test methods for ceramic sprayed coatings, 1994.
[20] ASTM E384-17, Standard Test Method for Microindentation Hardness of Materials, 2011.

Investigation of the Effects of Technological Parameters on Surface Roughness in Extrusion Bars of Aluminum Allloy

Nguyen Trong Mai [1,a], Tran Đuc Quy[1,b], Pham Van Nghe[2,c], Nguyen Van Canh[1,d]

[1]Hanoi University of Industry, Hanoi, Vietnam.

[2]Hanoi University of Science and Technology, Hanoi, Vietnam.

[a] Email: trongmai85@gmail.com

[b] Email: tdquy@haui.edu.vn

[c]Email: nghe.phamvan@hust.edu.vn

[d]Email: 3041982@gmail.com

Keywords: Surface roughnes, ram speed, billet temperature, aluminum extrusion.

Abstract

In this research work, the result of the effects of technological parameters (ram speed, billet temperature) on surface roughness in extrusion bars of aluminum alloy were pesented. The results of this study may be used for choosing optimal parameters of extrusion process so that surface quality of extruded bar was improved.

Introduction

The aluminum extrusion is a hot process used for producing rod, bar and tube profiles and has a wide application in construction industry, automotive, railway, aerospace engineering…[1,2].

Surface roughness, which influences not only on workability but also on aesthetics of the aluminum extruded bar, is important criteria for evaluating the quality of the aluminum extruded bar.

Principally, there are many factors that effect on the surface roughness extruded product such as: direct or indirect extrusion, material types, billet temperature, ram speed, extrusion ratio, friction, die geometry…[1].

In order to obtain better finished surfaces with the available machine, the technological parameters (ram speed, billet temperature) were chosen suitably [3].

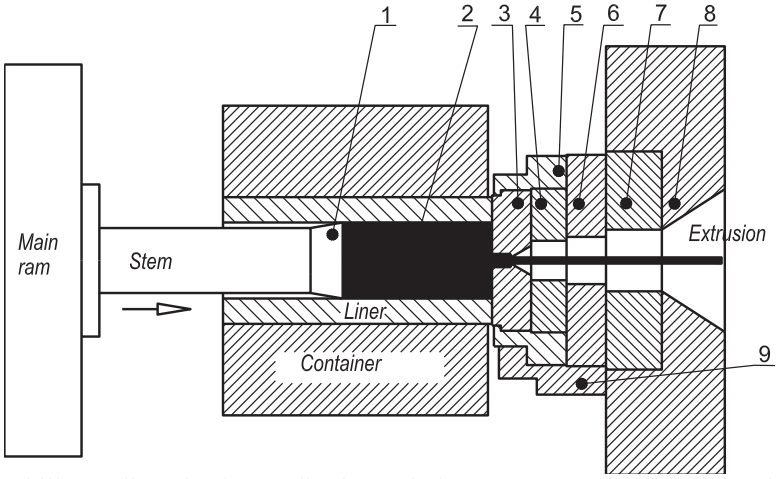
Therefore, it is necessary for to study, which was performed by an experiment, to build the relationship between the ram speed and the billet temperature to the surface roughness of the extruded product. This will help the technologist choose the right extrusion depending on the requirements of surface roughness.

Experiment

Extrusion is a plastic deformation process in which a block of metal (billet) is forced to flow by compression through the die opening of a smaller cross-sectional area than that of the original billet [1,2,4].

In aluminum extrusion, the billet is preheated to facilitate plastic deformation.

Figure 1 shows the die and tooling configurations for conventional direct extrusion processes. Experiment of the paper is done on this system.



1.Dummy Block; 2.billet; 3.die; 4.backer; 5.die ring; 6.bolster; 7.pressure pad; 8.press platen; 9.die slide

Figure 1. Tooling configuration in direct extrusion processing with a solid die

Experiment conditions

The profile aluminum extrusion products of experiments is shown in figure 2.

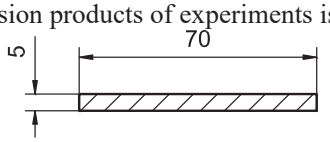
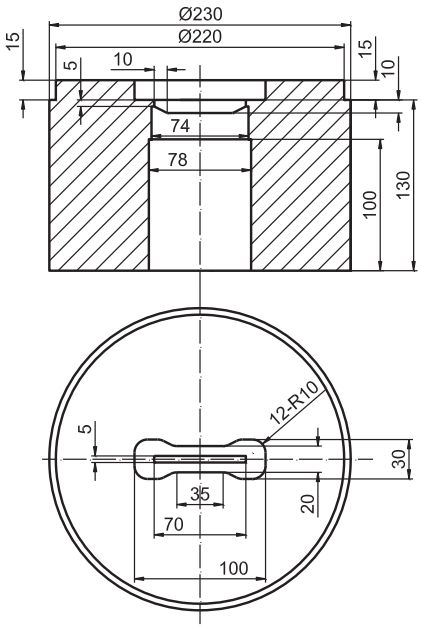


Figure 2. Profile of aluminum bar for experiment

Extrusion ratio K = $\frac{S_{container}}{S_{profile}.N}$ = (3,14*90*90)/(3,14*70*5*1) = 23 (1) [1]

Where: K is the extrusion ratio, $S_{container}$ is the area of container (the diameter of the container is Ø180 mm), $S_{profile}$ is the area of product section, N is the number of symmetrical holes (N=1) .

The extrusion die of the experiment is shown in figure 3.





a) Die drawing b) Real die

Figure 3. Die for experiment

Billet of the experiment: the diameter is Ø180 mm, the length is 500 mm, the material is Al-6061 with chemical composition is mentioned in table 1.

Table 1. Chemical composition of billet [2]

Billet	Chemical composition							
	Si	Fe	Cu	Mn	Mg	Cr	Zn	Other
Al-6061	0,4÷0,8	0,7	0,15÷0,4	0,15	0,8÷1,2	0,04÷0,35	0,25	

Direct extrusion press of the experiment: SAMWOO-1800 in Huyndai Aluminum Vina Factory, Hung Yen, Vietnam is shown in figure 4.



Figure 4. Direct extrusion press SAMWOO-1800

The surface roughness of the aluminum bar product was measured on the Mitutoyo Surftest SJ-400 machine, specification: Evaluation criteria ISO, standard lenght 0,8 mm, stylus type diamond, contact measurement, press: 0,75 N, speed: 0,05 mm/s (figure 5).



Figure 5. Mitutoyo Surftest SJ-400 machine

Experimental method

Surface roughness is related to extrusion technical parameters by equation:

$$R_a = f(V_{ep}, T_p).$$

Where: R_a is surface roughness, V_{ep} is ram speed, T_p is billet temperature.

Asuming that this relationship is nonlinear and can be written as follows [3]:

$$R_a = C.V_{ep}^{\ a}.T_p^{\ b} \quad (2)$$

Where: C is a constant, a and b is defined by experiments.

To define R_a expressing in Eq. (2), the experiments have been carried out with different technical parameters. The experiment results have been analized by the least squares method in oder to find out relationship between surface roughness and ram speed, billet temperature. The relationship can be written as [5].

$$y = a_0 + a_1.x_1 + a_2.x_2 + \ldots + a_n.x_n \quad (3)$$

The number of experiments was determined by the formula:

$$n = 2^k = 2^2 = 4. \quad (4)$$

With the input variant k=2, the number of experiments is n = 4. To improve the accuracy of experiment model, we add two experiments in the middle. So, the number is real experiments is n = 4 + 2 = 6.

Based on the specifications of the machine, the allowable range of press process as ram speed and billet temperature [5]. The pressing parameters are selected as follows:

Ram speed: $4 \le V_{ep} \le 6$ mm/s, billet temperature: $420\ ^0C \le T_p \le 470\ ^0C$.

The parameters of pressing mode is mentioned in table 2.

The experimental elements are: The max level is $x_i^{(t)} = \ln x_{imax}$, the min level $x_i^{(d)} = \ln x_{imin}$, the fundamental level is $x_i^{(0)} = 1/2.(\ln x_{imax} + \ln x_{imin})$, the variation is $\rho_i = 1/2.(\ln x_{imax} - \ln x_{imin})$.

Result of experiment

Firstly, transform the nature variant into coding dimensionless variant. After press, perform surface roughness test on an Mitutoyo surftest SJ-400 machine. The result is mentioned in table 2, the real workpieces of experiment are shown in figure 6.

Table 2. Result of experiment

No.	Coding variant		Varient		Roughness
	X_1	X_2	V_{ep} (mm/s)	T_p(^{o}C)	R_a (μm)
1	-1	-1	4	420	3,48
2	1	-1	6	420	3,16
3	-1	1	4	470	2,37
4	1	1	6	470	3,51
5	0	0	5	445	2,95
6	0	0	5	445	2,94



Figure 6. Workpieces of experiments

Analyze the results

From Eq. (2): $R_a = C.V_{ep}^{\ a}.T_p^{\ b}$

Taking the logarithm to the base e find that:

$$\ln(R_a)=\ln(C)+a.\ln(V_{ep})+b.\ln(T_p) \quad (5)$$

Besides, the variables can be changed as: $y = \ln(R_a)$, $a_0 = \ln(C)$, $a_1 = a$, $a_2 = b$, $x_1 = \ln(V_{ep})$, $x_2 = \ln(T_p)$.

Thus, the equation can be written:

$$y = a_0 + a_1.x_1 + a_2.x_2 \quad (6)$$

Using Matlab software to analys experiment data obtain [4]:

$$R_a = 3{,}54.V_{ep}^{\ 0{,}35}.T_p^{\ -1{,}25}\ (\mu m) \quad (7)$$

The relationship between input ram speed and billet temperature to the surface roughness R_a of aluminum alloy bar is based on the Matlab software [6]. The relationship diagram is shown in Figure 7.

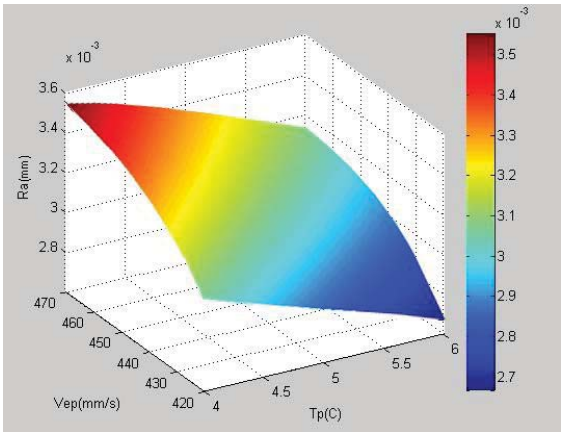


Figure 7. Relationship diagram between R_a and V_{ep}, T_{ph}

Evaluate the reliability of the experimental regression model

The reliability of the experimental regression [5]:

$$r = \frac{\sigma_y^2 - \hat{\sigma}_y^2}{\sigma_y^2} \quad (8)$$

Where: $\sigma_y^2 = \frac{1}{n-1}.\sum_{i=1}^{n}(Y_i - \bar{Y})$, $\hat{\sigma}_y^2 = \frac{1}{n-1}.\sum_{i=1}^{n}(Y_i - \hat{Y}_i)^2$, r is reliability of the experimental regression, n is number of experiments, Y_i is measurement value, $\hat{Y}_i$ is value of the empirical regression function, $\overline{Y}$ is average measurement value.

So:

$$r = \frac{\sum_{i=1}^{n}(Y_i - \bar{Y})^2 - \sum_{i=1}^{n}(Y_i - \hat{Y}_i)^2}{\sum_{i=1}^{n}(Y_i - \bar{Y})^2} \quad (9)$$

The values of the regression of formula (7) is mentioned in table 3.

Table 3. The value of the regression of formula (7)

TT	V_{ep} (mm/s)	T_p (^{O}C)	R_{ai} (µm)	$(R_{ai}- R_{ai}\hat{})^2$	$(R_{ai}- \bar{R}_{ai})^2$
1	4	420	3,48	0,002	0,168
2	6	420	3,16	0,001	0,008
3	4	470	2,37	0,001	0,490
4	6	470	3,51	0,003	0,194
5	5	445	2,95	0,013	0,014
6	5	445	2,94	0,015	0,017
Sum			18,41	0,035	0,891
Average			3,07		

Replace the value into the formula (9):

r = [(0,891-0,035)/0,891].100% = 96%

So, the reliability of function is more than 96%

Summary

Experimental results have pointed out the relationship between surface roughness of the extruded product (R_a) and technical extrusion parameters (ram speed: V_{ep}, billet temperature: T_p) for aluminum alloy 6061:

$$R_a = 3{,}54.V_{ep}^{0,35}.T_p^{-1,25}\ (\mu m)$$

Figure 7 shows that the surface roughness of the extruded product reduces when increasing the ram speed and reducing the billet temperature. Besides, the influence of billet temperature on the surface roughness of the extruded product is much larger on that of the ram speed.

This result could help technician to calculate and select the suitable extrusion parameters in order to increasing surface quality of the extruded product.

Acknowledgements

The author thanks the help of Hyundai Aluminum Vina factory Alumium during experiments of this paper.

References

[1] Pradip K. Saha, Aluminum Extrusion Technology, ASM International, 2000.
[2] Bauser, Extrusion Second Edition, ASM International, 2006.
[3] Nguyen Trong Binh, Optimization the Cutting Process, Vietnam Education Publishing House, 2003.
[4] Pham Van Nghe, Nguyen Đac Trung, Le Trung Kien, Metal Forming Technology, Bach Khoa Publishing House, 2016.
[5] Tran Van Đich, Research Machining Accuracy by Experiment, Science and Technics Publishing House, 2003
[6] Hoang Phuong, Matlab Graphics Solutions, Tre Publishing House, 2000.

A RESEACH ON MANUFACTURING TECHNOLOGY BODY SHELL OF ANTI-TANK ROCKET

Bui Khac Khanh[1,3,a*], Nguyen Ha Tuan[2,b], Vu Trung Tuyen[3,c] and Nguyen Truong Huy[2,d]

[1]Faculty of Defence, Mechanical Engineering, Hungyen University of Technology and Education, Dan Tien Commune, Khoai Chau District, Hungyen Province, Vietnam

[2]Institute of technology - Ministry of National, No.3 Cau Vong, Duc Thang Ward, Bac Tu Liem District, Hanoi City, Vietnam

[3]National Research Institute of Mechanical Engineering (NARIME), No.4 Pham Van Dong Street, Cau Giay District, Hanoi City, Vietnam

[a]khanhutehy@gmail.com, [b]hatuan262@yahoo.com.vn, [c]tuyen.narime@gmail.com, [d]truonghuy9978@gmail.com.

*Corresponding author. Tel: (+84)2213713519; E-mail: khanhutehy@gmail.com

Key works: Body shell of anti-tank rocket; Steel 30X3MΦ; Backward extrusion; Heat treatment.

Abstract: Body shell of anti-tank rocket which is a pipe part working under extreme conditions of high pressure and temperature, is manufactured from low-alloyed high quality steel 30X3MΦ. Steel 30X3MΦ made in Vietnam appropriate of standard to produce body shell anti-tank rocket, the shell ensure technical requirements of composition, with very low rate of P, S good mechanical properties. After casting, steel billets were backward extrusion, includes 3 steps of thinned stamp, heat treatment and drawing processes, body shell fabrication is satisfied technique anti-tank rocket shell. Results of fire testing of the body shells are in agreement with that of Russian ammunition. The body shells of anti-tank rocket which were manufactured in Vietnam conditions, satisfied desired technical requirement.

Introduction

Pressure processing is a method of manufacturing details that not only achieve desired shape and size but also improve mechanical properties of the material through deformation method. Therefore, products of noncutting shaping technology are diversified and widely applied in industries, especially for manufacturing of cartridges, body shell of anti-tank rocket [1].

Body shell of anti-tank rocket is made from high-grade steel 30X3MΦ, according to ГОСТ 4543-71. The content P, S are required at minimum level P ≤ 0.015 %, S ≤ 0.012 %. Normally, the body shell is made by thinned stamping from steel sheet. However, in our country, production of steel billet with necessary mechanical properties to serve the production of body shell of anti-tank rocket faces many difficulties. Therefore, it is essential to study a different method of manufacturing the body shell. Applying backward extrusion technology from casting billet is an effective solution for manufacture of body shell of anti-tank rocket. In Vietnam, steel fabrication research and manufacturing technology for anti-tank guided reference gear [1] includes the following steps: smelting-refining, forging, backward extrusion, thinned stamping tubing, stamping to create details. This article focuses on deformation and shaping to produce body shell of anti-tank rocket, including backward extrusion, thinned stamping and tapering.

Experiment

Research material and equipment

Conducting a survey of materials taken on foreign body shell samples with chemical composition as table 1, mechanical properties as table 2, this component conforms to standard and serves as a basis for steel processing.

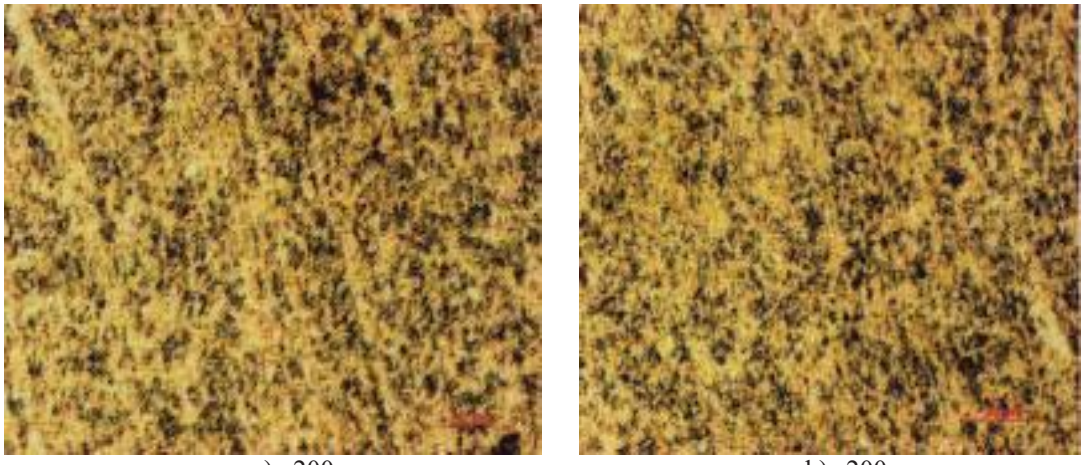
Table 1. Component of material chemical reserched from body shell (foreign rocket)

Chemical composition (% volume)								
C	Si	Mn	Cr	Ni	Mo	V	P	S
0.33	0.22	0.396	2.66	0.14	0.285	0.062	0.01	0.008

Table 2. Requirement on steel mechanical properties to produce body shell of anti-tank rocket

Limited durability σ_b, (MPa)	Elastic limit σ_c, (MPa)	Average Hardness, (HRC)	Elongation (%)
>1500	>1200	$42^{\pm 1}$	>28

The microstructure of the Russian-made body shell of anti-tank rocket is very fine in which steel has fine particles in both axial (vertical) and perpendicular (horizontal) directions. Microscopic organization is observed in the same two perpendicular directions, comprising pearlite (P) and ferrite (F) background in which pearlite is dark-colored particles (in the form of dark-colored lines combined with light colored bands), ferrite phase is bright color particles (bright color) as shown in figure 1.



a) 200x b) 200x

Figure 1. Microstructures of Russian-made body shell of anti-tank rocket
a. In axial direction; b. In perpendicular direction

Some of main equipment are used to form products as follow:

- 2 KHz medium-frequency heating equipment (MAG-M-300KW) to heat billets.
- Sonel DIT-500 measuring instrument, tester with range of (50 ÷ 1600) ^{0}C of Sonel brand.
- CTP250 vertical hydraulic press with capacity of 250 tons (ZDAZ RD1 - Czech Republic) and CRU400 hydraulic press with capacity of 400 tons (Russia).
- Horizontal hydraulic press CTQ250 with capacity of 250 tons (ZDAZ-Czech).

Steel billets processing aims to shape products and is carried out on following equipments: medium-frequency induction furnace 500 kg and refining on electro-slag equipment ĐX – 725, capacity of 725kW.

Backward extrusion

Backward extrusion in manufacturing of tube embryo is much researched because of unstable technology, difficult test conditions. In the past, backward extrusion mainly based on theoretical calculations. Main technological parameters for backward extrusion can be calculated according to following formula:

Technical parameter calculation

Deformation level φ_p [2]:

$$\varphi_P = \ln\frac{A_0}{A_1} \quad . \tag{1}$$

In which:
A_0 – Horizontal cross section of detail before deformation – mm^2;
A_1 – Horizontal cross section of detail after deformation – mm^2;
Deformation force required for backward extrusion [2]:

$$F = \frac{A_0.k_{fm}}{\eta_F}(2 + 0{,}25.\frac{h_0}{S}) \; . \tag{2}$$

In which:
S: thickness of details after backward extrusion;
h_0 - initial steel billets height;
$\eta_F = (0.5 \div 0.7)$ - deformation performance, depending on the detailed shape;
k_{fm} - average flow rate of material - N/mm^2.

However, results of theoretical calculations in equation (1) and (2) do not usually reach desired level because the model for theoretical problems is much different from reality and boundary conditions directly affect on backward extrusion process such as: Contact conditions, friction, lubrication, etc are not mentioned in calculation process. Therefore, a new method is being applied to study pressure processing technology in general and backward extrusion in particular is to use digital simulation combining with experiment.

Numerical simulation of backward extrusion

Perform a digital simulation of backward extrusion by Abaqus software with the geometry parameters of steel billets and tools as follows: pestle diameter d = 86 mm, mortar diameter D = 106 mm, billets size Φ106x120 mm, processing the hole R50 mm as shown in figure 2.

Material model was chosen according to material DIN-30CrMoNi5 is equivalent to the material 30Х3МФ (according to ГОС 4543-71), density γ = 7.860 kg/cm^3, relationship curve between stress and deformation as shown in figure 3, mortar and pestle are considered as absolute hard materials [3].

Mesh element model: In this problem, the author selects C3D8R element [3]. This is a block element with 8 nodes that allow calculation of stresses, strianes, displacements, etc. of each node to meet the purpose of simulation problem. Two sliding contact surfaces use Penalty function with presence of contact friction [3]. Lubricant is graphite powder and oil [4], elastic modulus E, sliding elastic module G, the coefficient Poatxon υ, etc is taken according to material properties at backward blowing temperature (1200 ^{0}C), coefficient of friction between steel billets and the pressing tool is μ = 0.5 [4].

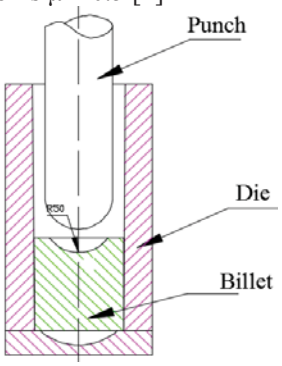


Figure 2. The geometry of backward extrusion

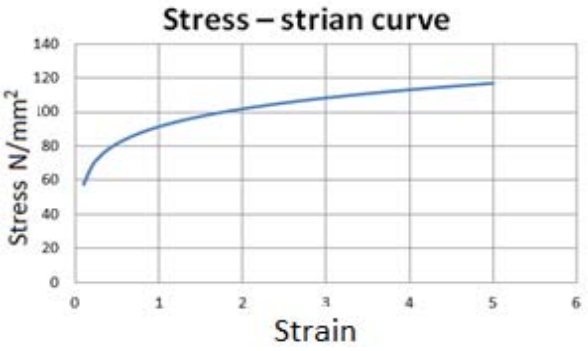


Figure 3. Relationship curse between stress and deformation of 30CrMoNi5 material

Simulation result and calculation result is basis to carry out experiment

Experiment on backward extrusion

After simulation, the experiment of backward extrusion of 30X3MΦ steel with aforementioned technical parameters and technology was conducted. Backward extrusion procedures is implemented as follows: The steel billets was heated to 1250 ^{0}C on a medium-frequency heater as shown in figure 4 with a time of 10 minutes, followed by backward extrusion on CTP250 vertical hydraulic press in 3 seconds (figure 5), the maximum force measured is 220 tons. Then remove the billet out to cool it atmosphere (figure 6) and product after backward extrusion has the size (Φ117x275 mm) as shown in figure 7. This product is used as an input for subsequent thinned stamp manufacture body shell of anti-tank rocket.



Figure 4. Image of billet heating before backward extrusion



Figure 5. The process of hot rolling of billet



Figure 6. The process of removing steel billets and cooling in the air



Figure 7. Post-process products of backward extrusion (Φ117x275 mm)

Details after the backward extrusion is checked and lather internal and external. The purpose of lathering is to remove metal oxide at the surface and detect cracking defects of the component. After finishing the process, cutting excess metal residue at the mouth of details before thinned stamping.

Thinned stamping

Thinned stamping is carried out at 1250 ^{0}C through three steps on CTQ250 horizontal thinned stamping machine as shown in figure 8.

Step 1: Heat the billet to 1250 ^{0}C on induction heater, the heating time is 6 minutes and then put the billet into horizontal hydraulic press for stamping with a force of 80 tons and thickness of details $\Delta S = 2$ mm.

Step 2: The details are fired in 5 minutes, then put to stamping with force of 70 tons. This step is proceeded with stamping with an excess of workpiece diameter ΔS = 2 mm.

Step 3: Continue to heat the detail in 4 minute, then put into thinned stamping to adjust the dimension and boundary deviation of the detail. Remove billet out of the mold and cool in static air (figure 9).



Figure 8. Image of thinned stamping process

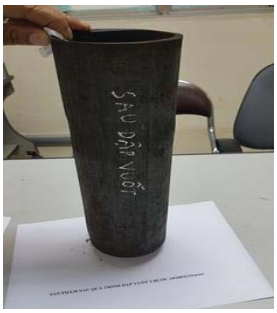


Figure 9. Product after thinned stamping of 3 steps (Φ102x330 mm)

Drawing processes

After 3 steps of backward extrusion, the detail was quenched and mechanically processed (figure 10), then put into drawing processes. The drawing process is carried out in 2 steps on a CRU400 vertical hydraulic press with a force of 170 tons on drawing mold (figure 11), details received desied shape (figure 12). After drawing, the details are machined and finished as product in figure 13.



Figure 10. Image of billets after mechanical processing



Figure 11. Mold used in drawing process



Figure 12. Billet after drawing process



Figure 13. Body shell of anti-tank rocket

Research result and discussion

Material research result

After refining, the steel has required components under standard of steel 30X3MΦ as table 3. That content of phosphorus (P) and sulfur (S) is very low, is apropriates with standard of weapon manufacturing steel [1], consistent requirement of anti-tank rocket body shell.

Table 3: Chemical composition of steel 30X3MΦ made by Vietnam

Mechanical components (% volume)									
C	Si	Mn	Cr	Ni	Mo	Al	V	P	S
0.3301	0.2756	0.3731	2.4897	0.0895	0.2466	-	0.0972	0,0145	0.0044

Carry out mechanical test of two samples which are perpendicular to each other, axial direction of billets and perpendicular to the axis. Results of mechanical tests with steel billets after being fabricated as table 4:

Table 4. Material properties of 30X3MΦ produced by Vietnam in two perpendicular directions

Samples's name	Elastic limit σ_c, (MPa)	Strength σ_b, (MPa)	Elongation, A (%)
M5A-1 Perpendicular direction	351	570	26.0
M 5A-2 Perpendicular direction	338	579	22.0
M 5B-1 Axial direction	338	563	22.0
M 5B-2 Axial direction	333	563	24.0

Tensile test results in table 4 show that durability limits strength of the samples in the axial and the perpendicular directions are approximately equal.

Samples analyzed as material structure (microscopic metallorgaphy) is carried out in two perpendicular directions, namely: Figure 14a is image of metallorgaphy of steel in axial direction, figure 14b is an image of microscopic in axis direction.



a) 100x b) 100x

Figure 14. Microscopic organism
a. In axial direction; b. In perpendicular direction to the axis

In two direction, the steel has peclit and ferrite background organization, particles with spherical and multi-sided shapes and bits are evenly distributed equations on the background and on the boundary of the nucleus. In the microorganism, there is no longer a fibrous, longitudinal band, which indicates that the cast-forged alloy material is clear isotropic, which overcomes some limitations. Anisotropic materials cause the product.

Numerical simulation result

Stress: Due to the shifting of the metal in the gap between the pestle and the mortar, the metallurgical melting of the part is divided into different regions [5]. Stress is distributed in areas as shown in figure 15 with a maximum value of 152.015 MPa distributed over a wide area, the largest value at the bottom of the part due to direct pressure of the plywood, transition of the embryo and reduce it to a value of at least 93.758 MPa on the mouth of the part because this region is only affected by the frictional force between the embryo and the embryo.

Strian: The level of distortion equivalent to the maximum value is ε_{max} = 3.408 at the transitional region and the smallest value in the detail region as shown in figure 16.

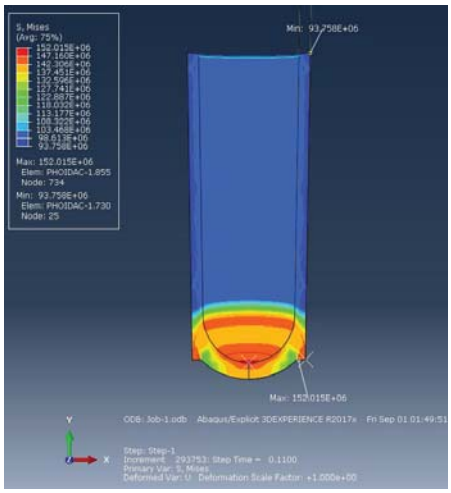


Figure 15. Stress distribution

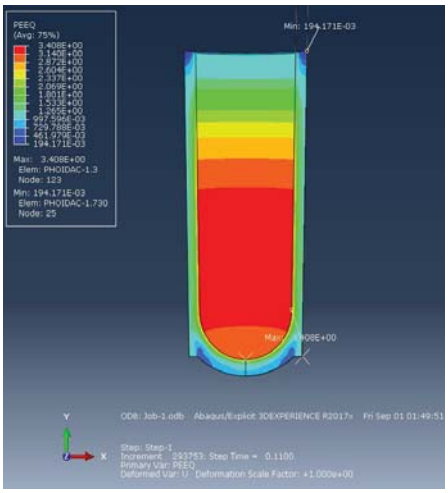


Figure 16. Equivalent distortion distribution

Force distribution chart: Figure 17 shows the distribution of force, the force of distribution in accordance with the law of compression process: initial pressure increased, embryos are deformed filling the heart. As the material starts to flow through the drainage hole, the deformation force reaches its maximum value and is maintained in the pressing process [5], the maximum pressure value reaching Pmax = 207 tons.

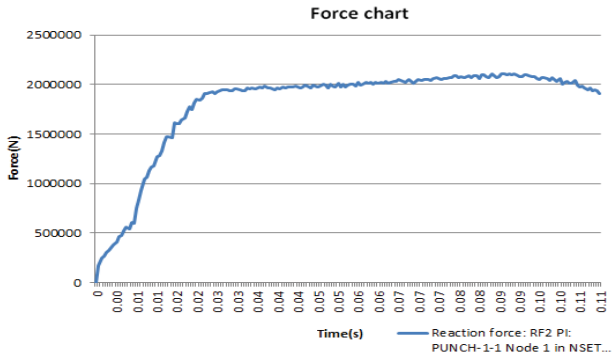
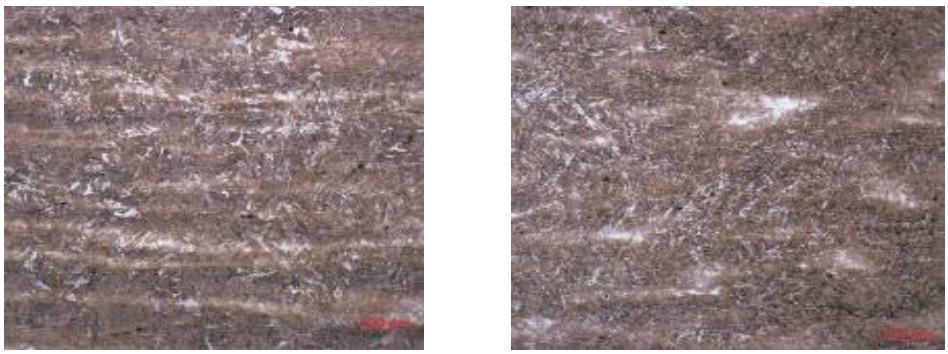


Figure 17. Force distribution diagram

Manufacturing results on body shell of anti-tank rocket

Details after mechanical processing to meet the technical requirements and then tested for durability. Test results show that the engine shell steel has a strength of 1535 MPa to meet the requirements. The metallography of the steel shell of the anti-tank shell is very good, the fine particles smooth in both axial direction and in the direction of perpendicular to the axis as (figure 18). After checking the structure, the mechanical shell of the engine was put to test pressure 650 kG/cm^2 to ensure the new bridge to assembly.



a) 100x b) 100x

Figure 18. Microstructures of body shell of anti-tank rocket
a. In axial direction; b. In perpendicular direction

To test the working ability, the body shell is assembled and tested fire. Results meet technical requirements [6].

Conclusion

- High-grade 30X3MΦ steel made by Vietnam ensures chemical composition, very low P, S content, good metallorgaphy organization and mechanical properties to meet the requirements of producing anti-tank engine shell.
- The simulation of backward extrusion on Abaqus software for reliable results is the basis for the experimental development of the anti-tank engine shell.
- Vietnam is fully able to manufacture of body shell of anti-tank rocket reachs to ensure technical requirements.

References

[1] R.O.Davidson, Research and development of materiel, Headquarters United States Army Materiel Command Washington, D.C 20315, 31 July 1964.

[2] Le Trung Kien, Le Gia Bao, Pressing mold design and manufacturing, Publishing house of Hanoi University of Science & Technology, 2016.

[3] K.Abrinia and S.Orangi, Numerical study of backward extrusion process using finite element method, School of Mechanical Engineering, College of Engineering, University of Tehran, I.R.Iran, 2010.

[4] Taylan Altan, ERC/NSM, Ohio State University Gracious Ngaile, North Carolina State University, Gangshu Shen, Ladish Company, Cold and Hot forging Fundamentals and Applications, ASM International@ Materials Park, OH 44073-0002, 2005.

[5] W.H.Sillekens, Backward Can Extrusion and Meterials Behavior, 5 June 1992.

[6] A research on manufacturing technology steel and body shell of anti-tank rocket, Summary report of Scientific and Technical report, General Department of Defense Industry, Hanoi 2016.

Research on relative wear and roughness follow the current density in EDM die sinking

Tran Quang Huy[1,a*], Hoang Vinh Sinh[2,b] and Tran Van Khiem [3,c]

[1]Hanoi university of science and technology, Vietnam

[2]Namdinh university of technology education, Vietnam

[a]quanghuy511@gmail.com, [b]hvsinh03@yahoo.com, [c]tranvankhiemspkt@gmail.com

Keyword: EDM die sinking, relative wear in EDM, roughness in EDM, current density in EDM

Abtract. EDM die sinking is using in mold and die making. The prediction of electrode wear will help engineer to estimate the processing to make electrode. This article shows the relation between relative wear, roughness and current density during EDM die sinking of Cooper and SKD11 steel. Those results will be very useful to apply in mold manufacturers for optimaled process.

Introduction

EDM die sinking (called shortly EDM) is a non-traditional machining. This method is applied in concave area which cannot machining by traditional method such as deep concave, thin wall which is smaller than normal cutting tool, and especial the steel after heat treatment.

The big problem in EDM is the electrode wear. The workpiece could be NG if the form and dimension of electrode is changed during EDM machining. There's many research results show the relation between electrode wear and other factors such as: wear of weight[1], wear of form[2, 3, 4], wear of dimension[5, 6]. Almost results use technical parameters such as EDMing current, initial voltage, ON time, OFF time,… to do regimes and find the relation between above parameters and electrode wear. Nowadays, Japanese and other makers apply AI to change the parameters automatically in order to improve productivity and surface quality of workpiece. The first problem for all of them is how to predict electrode wear!

Exprimental

Experimental conditions: Copper electrode with diameter is Ø10, Ø12, Ø14, Ø15, Ø18, Ø20 mm; workpiece is SKD11 with height -circle square 20mm and heat treatment as in 58HRC.

Table 1: SKD11 alloy

Steel alloy	**C**	**Si**	**Mn**	**Cr**	Mo	**V**
SKD11	1,5	0,25	0,45	12,0	1,0	0,35

Table 2: Copper and component

Copper	**Cu**	**P**	**Component**
C12200	99,90	0,015 – 0,040	-

Experimental conditions:

- Electrode material: Copper
- Electrode dimension: Diameter of 10, 12, 15 and 20 mm
- Workpiece material: SKD11 alloy
- EDMing current: I_e = 6A … 10A
- Time ON: t_{on} = 10 µs
- Time OFF: t_{off} = 50 µs

- Di-electric oil: Shell EDM Fluid
- Working time: 180 minutes



Figure 1: EDM EXPRESS machine (Taiwan), electronic balances and SURFTEST SJ-210 (Japan)



Figure 2: Electrode and workpiece before machining



Figure 3: Electrode and workpiece after machining

Experimental results

Table 3: Weight of electrode and workpiece

No.	$D_{electrode}$ (mm)	I_e (A)	$m_{elec.before\ EDM}$ (gram)	$m_{elec.\ after\ EDM}$ (gram)	$m_{workpiece\ before\ EDM}$ (gram)	$m_{workpiece\ after\ EDM}$ (gram)
1	10	6	18,58	18,57	47,68	39,38
2	12	6	24,34	24,31	47,09	24,70
3	14	7	32,72	32,69	46,57	26,55
4	15	7	35,80	35,77	46,11	28,40
5	18	10	47,35	47,33	110,72	101,65
6	20	10	57,88	57,86	111,31	104,02

Table 4: Relative wear and current density

No.	$D_{electrode}$ (mm)	I_e (A)	Wear of electrode (gram)	Wear of Workpiece (gram)	Area of electrode (cm^2)	Current density	Relative wear
1	10	6	0,01	8,30	0,79	7,64	0,120482
2	12	6	0,03	22,39	1,13	5,31	0,133988
3	14	7	0,03	20,02	1,54	4,55	0,149820
4	15	7	0,03	17,71	1,77	3,96	0,169396
5	18	10	0,02	9,07	2,54	3,93	0,220460
6	20	10	0,02	7,29	3,14	3,18	0,274348

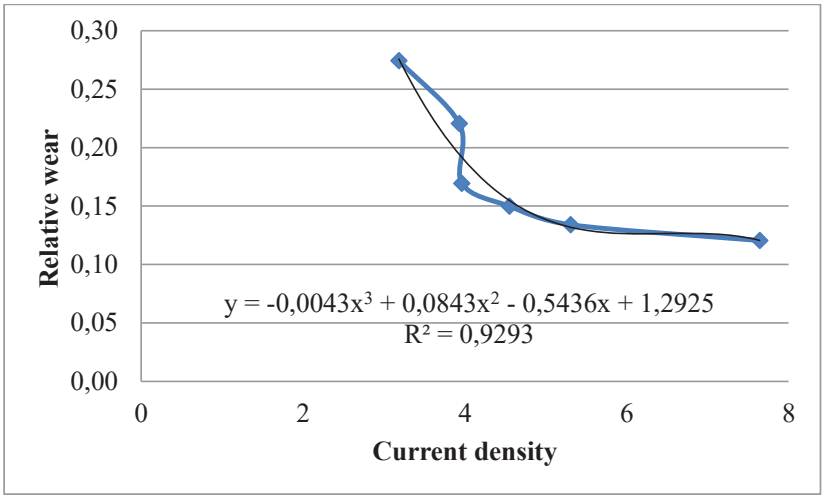


Figure 4. Chart of relation between realative wear and current density

Apply the method of least square approximation with relative wear (shown as y in chart) and current density (shown as x in chart), the formula could be shown as following:

$$y = -0{,}0043x^3 + 0{,}0843x^2 - 0{,}5436x + 1{,}2925 \quad (1)$$

with R-squared value $R^2 = 0{,}9293$

It is easily to find that the relative wear will be reduced if current density increases. It means that the rough EDM machining will cause the electrode wear is smaller than workpiece wear. This point is suitable to the other research result: relative wear is small while rough machining.

Engineer could use this equation to estimate the current which is suitable to workpiece area and also estimate the amount of electode for finished machining.

Table 5: Roughness and current density

No	$D_{electrode}$ (mm)	I_e (A)	Elec.area (cm^2)	Current density	Workpiece roughness R_a
1	10	6	0,79	7,64	6,991
2	12	6	1,13	5,31	6,715
3	14	7	1,54	4,55	5,534
4	15	7	1,77	3,96	5,469
5	18	10	2,54	3,93	4,167
6	20	10	3,14	3,18	2,865

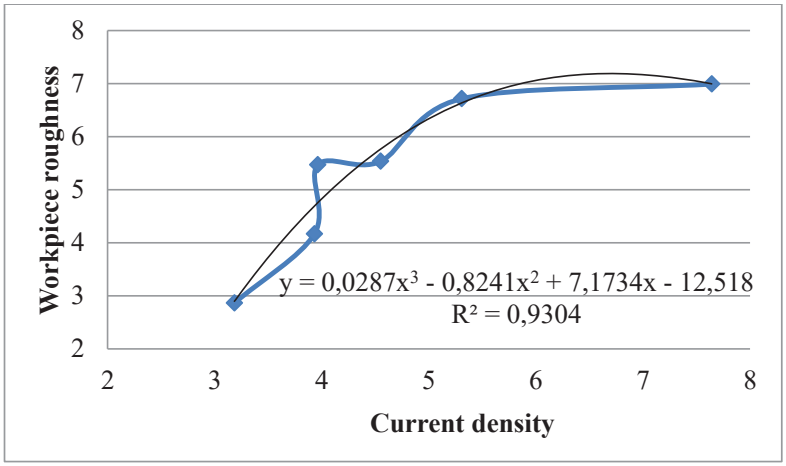


Figure 5. Surface roughness follow the current density

Apply the method of least square approximation with the surface roughness (shown as y in chart) and current density (shown as x in chart), the formula could be shown as following:

$$y = 0{,}0287x^3 - 0{,}8241x^2 + 7{,}1734x - 12{,}518 \quad (2)$$

with R-squared value $R^2 = 0{,}9304$.

The surface roughness will be increased if current density is increased. It means the surface will be so bad while rough machining. In another way, the current should be selected based on the electrode surface area.

Conclusion

Current density is a parameter which represent to technical parameter (current) and dimension of electrode.

Relative wear and surface roughness are according to current density differently: relative wear is reduced and roughness is increased while current density increases.

Base on equation (1) and (2), engineer could estimate the amount of electrode and current to be suitable to technical requirement of workpiece.

References

[1] Hoang Vinh Sinh, PhD thesis, Optimized metal processing on the spark pulse machine, 2003.

[2] Allen, P and Chen, X Process simulation of micro electro-discharge machining on molybdenum, Journal of Processing Technology. 186 (2007) 346 - 355.

[3] H.C Tsai, B.H Yan; EDM performance of Cr/Cu-based composite electrodes, International Journal of Machine Tools and Manufacture. 43 (2003) 245 - 252.

[4] A. A. Khan, Electrode wear and material removal rate during EDM of aluminum and mild steel using copper and brass electrodes, The International Journal of Advanced Manufacturing Technology. 39 (2008) 482 - 487.

[5] Yan Cherng Lin, Surface modification of Al-Zn-Mg aluminum alloy using the combined process of EDM with USM. J Mater Process Technol, Journal of Materials Processing Technology. 115 (2001) 359 - 366.

[6] P. Bleys, J.-P. Kruth,Real-time Tool Wear Compensation in Milling EDM, CIRP Annals - Manufacturing Technology. 51 (2002) 157 - 160.

The influence of part geometry on changes of the dynamic geometric parameters of cutting tools and cutting conditions when contour turning on CNC lathes

Bui Ngoc Tuyen [1], Nguyen Chi Cong[2]

[1] Ha Noi University of Science and Technology, Ha Noi, Viet Nam,
[2] The 21 Chemical One Member Limited Liability Company - Phu Tho town, Phu Tho province

** Tel: (+84) 904 180 428;* E-mail: tuyen.buingoc@hust.edu.vn
Congncz4@gmail.com

Key words: Contour turning, CAM, Dynamic geometric parameter, CNC lathe

Abstract

Contour turning is a specific process of the machining on CNC lathes. In the finishing operation to create the part profile, the turning tool must be moved in a trajectory of a complex flat curve (a toolpath) based on the part profile . The variation of feed vector on the toolpath according to the part profile in the machining process will results in changing dynamic geometric parameters of the cutting tool, which affects cutting conditions and machined part quality. This article presents the results of theoretical studies on the influence of part geometry on rake angle, clearance angle, approach angle and end cutting-edge angle of the turning tool. Based on the theoretical development, the authors also set up mathematical expressions that allow to define gouge-free cutting condition and the limit of feedtate for contour turning. An empirical model to define the influence of part geometry on the roughness of the part when countour turning on CNC lathe is also presented in this report.

I. Introduction

Profile-Turning is the one of the important features to distinguish CNC lathes and normal multi-purpose lathes. The profile line of the part are understood as the profile on the section passing through the axis of the part, that including a set of curves, straight lines and in special cases the profile may be a straight line or arc. On each section plane, through the center of the part, there are two profile lines located on two sides of the center line. Ideally, these two profile lines are perfectly symmetrical with the shaping tool.

Theoretically, to shape the part profile in the turning process, the tool must move in the orbit which is parallel with the part profile. Actually not all cutting tools can machine the part with a certain profile. Manufacturers need to chose tools with the shape and geometry which are suitable to profile turning as required to ensure gouge-free cutting condition, delicate roughness, physico-mechanical properties of part surface, the rigidity of the technology system and the tool-life. Profile-turning can be carried out by the forming tool. However, the type of this cutter has some limits. It is difficult to manufacture, its cost is high, the cutting edge is unevenly worn

when cutting and each forming tool is only specialized for one profile. Nowaday, the use of cutter with carbide insert for profile turning on CNC lathe has become popular. This overcomes the disadvantages of the forming tool and bring high effects. For each of the different profiles, a number of suitable cutters are required.

Here are some studies, which have concerned with this issue:

According to [2], Nguyen Van Cuong has constructed theorical formulas to define the roughness which depends on the tool geometry, part geometry and feed in cases of CNC turning cylindrical, conical surfaces and surfaces with complex profile. In this study, the author used cutter insert M02L012520M08 of Sandvik and the machined material was 40X steel. According to [7] Yoshitaka Morimoto and his colleagues have studied on forming of part 3D surface with an asymmetric axis, which was performed on special lathes. However, the results of the study suggested a new shaping method on nonmetallic specimens, which has not yet been announced specifically for metallic materials.

According to [3], M.Kaladhar studied the multi-goal optimization by Taguchi method using AISI 202 on CNC lathes. The author used carbide insert CNMG 120408, CNMG 120404 (SECO) with a nose radius of 0.8 mm and 0.4 mm. The research result showed that with a nose radius 0.8 mm, results are best with lower roughness and greater removal volume. However, the object used for the study was a cylindrical shaft Φ25x70 mm.

According to [10], Virender Singh studied on the influence and the optimization of cutting mode parameters and tool geometry (nose radius 0.4mm, 0.8mm, 1.2mm alternately). When turning AISI steel 1045 on a CNC lathes, using the carbide insert of WNMG331RP, WNMG332RP and WNMG333RP, the assessment criteria was surface roughness and the speed of material removal. The results indicated that the optimal value of the nose radius of the insert is 0.4 mm. However, the part used for this experiment were cylindrical shaft Φ20x50 mm.

According to [1] L. B. Abhang and his colleagues have studied the influence of cutting mode and nose radius (0.4 mm, 0.8 mm, 1.0 mm) to surface roughness and cutting force during turning on EN31 steel. The study has shown that nose radius 0.4 mm is the optimum result to ensure the surface roughness and minimum cutting force.

II. Solve the problem

2.1. Set up gouge-free cutting condition when profile turning

A studying the general case when turning the part with any profile is shown in Fig. 1. Assume that the nominal tool cutting edge angle and tool minor cutting edge angle at point A when turning cylinder are φ, φ_1, in turn. The dynamic tool cutting edge angle and dynamic tool minor cutting edge angle during turning the profile at that point are φ^*, φ_1^*. The amount of variation of the angles due to the influence of the part profile is τ. τ is formed by the tangent line to the part profile at the considered point and the line that parallel to the part axis. The relationship formular between these angles are as follows:

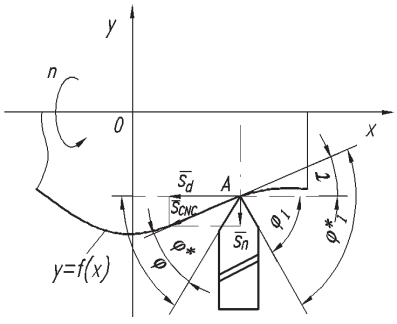


Figure 1 *Influence of the profiles to Plane angles*

$$\begin{cases} \varphi^* = \varphi - \tau \\ \varphi_1^* = \varphi_1 + \tau \end{cases} \quad (1)$$

Angle τ is calculated according to the formula:

$tg\tau = f'(x) \Rightarrow \tau = arctg\left[f'(x)\right]$ and replace it into (1),

we have :

$$\begin{cases} \varphi^* = \varphi - arctg\left[f'(x)\right] \\ \varphi_1^* = \varphi_1 + arctg\left[f'(x)\right] \end{cases} \quad (1)'$$

To ensure gouge-free cutting condition when profile turning, the dynamic angles should be always positive:

$$\begin{cases} \varphi^*_{\min} = \varphi - \tau_{max} > 0 \\ \varphi^*_{1\min} = \varphi_1 + \tau_{\min} > 0 \end{cases} \quad (2)$$

$$\text{With} \begin{cases} \tau_{max} = \text{arc}ctg\left[f'(x)_{max}\right] \\ \tau_{\min} = \text{arc}ctg\left[f'(x)_{\min}\right] \end{cases} \Rightarrow$$

$$\begin{cases} \varphi^*_{\min} = \varphi - \text{arc}ctg\left[f'(x)_{max}\right] > 0 \\ \varphi^*_{1\min} = \varphi_1 + \text{arc}ctg\left[f'(x)_{\min}\right] > 0 \end{cases} \quad (3)$$

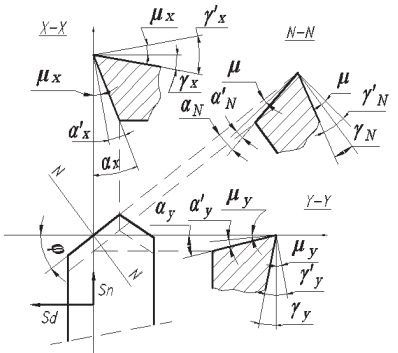


Figure 2 *Geometric parameters of cutting tools during turning*

From formula (3), we can see that the magnitude of dynamic angles φ^*, φ_1^* at the shaping point depends on the nominal angles φ, φ_1 and the variation of the bevel angle τ at the considered point. The nominal angles depend on the cutting tool's structure and the positioning of the tool on the machine. They are standardized and constant, commonly. The angle τ depends on the slope of the part profile. The larger is the slope, the smaller is the dynamic tool cutting edge angle φ^* and when φ^*<0 the gouge cutting phenomena occurs by the main edge. As the slope in the opposite direction is larger, the angle τ < 0. When φ_1^*< 0, the gouge cutting phenomena occurs by the minor edge.

2.2. Variation of dynamic clearance angle when profile turning

According to [5], when designing lathe tool, it is necessary to define appropriate parameters of the clearance angle α, the rake angle γ. The main factor that directly influences on the cutting process is the clearance angle α_N measured in the normal section of the edge. At any point on the edge, the clearance angle in the normal section N-N, α_N must be greater than the allowed minimum value $[\alpha]_{\min} = 3^o \div 5^o$. During the cutting process, the dynamic clearance angle α'_N in the normal cross section N-N is defined by the follow formula:

$$\alpha'_N = \alpha_N - \mu \quad (4)$$

Where μ is the change of flank angle due to the influences of the feed-movement in the longitudinal direction s_d and the feed-movement in the horizontal s_n. The angle μ has an important influence on the surface quality, especially on the accuracy of the dimension and the roughness of the surface. In the cutting process, if $\mu < \alpha_N$ then there is a gap between the tool and

the processed workpiece surface and the tool does not directly contact on the workpiece surface This avoids friction, abrasion, so it should reduce the cutting force, cutting heat and therefore does not adversely affect to the surface quality. If $\mu > \alpha_N$ this means $\alpha'_N < 0$ at this time a part of the flank of the tool will be directly ground into the machined surface and the cutting process may be stopped . The phenomenon is called as notched cutting condition.

The dynamic clearance angle in the Y-Y cross section is defined as following:

$\alpha'_y = \alpha_y - \mu_y$

As [5]: $tg\mu_y = \dfrac{s_n}{\pi D} \rightarrow \mu_y = arc\tan\dfrac{s_n}{\pi D}$ (5)

$\rightarrow \alpha'_y = \alpha_y - arc\tan\dfrac{s_n}{\pi D}$ (6)

The dynamic clearance angle in the Y-Y cross section is calculated as following: $\alpha'_x = \alpha_x - \mu_x$

With: $\mu_x = arc\tan\dfrac{s_d}{\pi D} \rightarrow \alpha'_x = \alpha_x - arc\tan\dfrac{s_d}{\pi D}$ (7)

As [5]: $\begin{cases} s_d = s_{CNC}.\cos\tau \\ s_n = s_{CNC}.\sin\tau \\ D = 2|y| = 2|f(x)| \end{cases} \Rightarrow \begin{cases} \alpha'_x = \alpha_x - arctg\dfrac{s_{CNC}.\cos\tau}{2|f(x)|\pi} \\ \alpha'_y = \alpha_y - arctg\dfrac{s_{CNC}.\sin\tau}{2|f(x)|\pi} \end{cases}$ (8)

- **Determine the maximum feed according to the condition of the permitted dynamic clearance angle:**

Considering $[\alpha_x]$ and $[\alpha_y]$ are the permitted clearance angles in two cross sections XX and YY, alternately. The limit conditions of the permitted maximum feed:

$$\begin{cases} s_1 = \dfrac{2\pi|f(x)|tg(\alpha_x - [\alpha_x])}{\cos\tau} \\ s_2 = \dfrac{2\pi|f(x)|tg(\alpha_y - [\alpha_y])}{\sin\tau} \end{cases} \quad (9)$$

$\Rightarrow$ The maximum feed must satisfy the non-notched cutting condition in both X-X and Y-Y sections: $s_{max} = \min(s_1, s_2)$

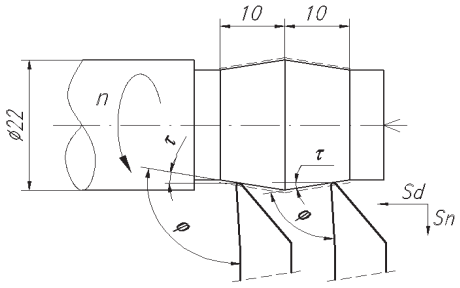


Figure 3 *Experiment of cone turning*

2.3. Experiment

*** *Purpose:*** studying the influence of part geometry on the surface roughness when CNC profile turning conical surface.

*** *Experimental conditions.***

- Equipment: The experiment was done on CNC lathe, symbol PLG-42 (Taiwan); Mitsubishi operating system: the power of main shaft is 10KVA; Spindle diameter 55mm, speed 100 ÷ 6000 r.p.m, accuracy 0.001mm.

- Roughness measuring instrument: POCKETSURF (USA), measuring range: R_a = 0,03µm ÷ 6,35µm, assessment length: 0.8mm; 2.4mm; 4.0mm, accuracy according to ASME B46.1, DIN standard

- Cutting tools: carbide insert of TT10K8 (according to ГОСТ 3882-74 standard). It is manufactured by 13 mechanic and chemicals one member Limited liability Company, 21 chemicals one Member Limited liability Company-Vietnam. Tool cutting edge angle in the static status: $\varphi = 93^o$, tool minor cutting edge angle $\varphi_1 = 52^o$, rake angle $\gamma = -7^o$, inclination angle $\lambda = 0^o$, clearance angle $\alpha = 12^o$, nose radius $r = 0,4mm$ as shown in Figure 3.

- Materials: SUS304 steel has chemical composition, mechanical properties according to JIS G-4303-91 standard.

- Sample: The sample after processing meets the requirements as shown in Figure 3.

Processing conditions: Each test is carried out at a temperature of 25 ° C, a moisture content of 60%, by unique carbide insert, with the assumption that the vibration of the system is constant. During cutting process, the carbide insert is insignificant worn. Do not use cool lubricating liquid .

*** *Experimental results***

The experiment is conducted with 13 different tests, in which 03 parameters of cutting regime are constant with cutting speed v = 50m/min, feed s= 0.08mm/round, depth of cutting t = 0,1mm (This is the optimal set of parameters, which was found by the authors when researched CNC finishing turning stainless steel SUS304 with conical surface by the carbide insert TT10K8 made in Vietnam). Figure 3 shows that when τ is $10^o/15^o/20^o/25^o/30^o/35^o$ respectively, tool cutting edge angle φ, tool minor cutting edge angle φ1 are changed when turning the left cone: φ = $103^o/108^o/113^o/118^o/123^o$, φ1 = $42^o/37^o/32^o/27^o/22^o/17^o$; when turning the right cone: φ = 58° / 63° / 68° / 73° / 78° / 83°;. $\varphi_1=62^o/67^o/72^o/77^o/82^o/87^o$. One test is conducted by CNC turning a shaft Φ16 that is corresponding to $\tau = 0^o$ with tool cutting edge angle $\varphi=93^o$, tool minor cutting edge angle $\varphi_1=52^o$

*** *Check the*** gouge-free cutting condition

The equations for the profile of cone surfaces are presented in Table 1. Calculating the dynamic tool cutting edge angle φ^*_{min} and dynamic tool minor cutting edge angle $\varphi^*_{1_{min}}$ according to formula (3), we obtain the results in Table 1. The values of φ^*_{min} and $\varphi^*_{1_{min}}$ are positive. It means that gouge-free cutting condition is satisfied.

Table 1 Calculation results of φ^*_{min} **and** $\varphi^*_{1_{min}}$ **angles**

No	Left cone turning				Right cone turning			
	τ, (^{o})	**y**	φ^*_{min}	$\varphi^*_{1_{min}}$	**τ,** (^{o})	**y**	φ^*_{min}	$\varphi^*_{1_{min}}$
1	-10	-0,18x - 11	103	42	10	0,18x - 11	83	62
2	-15	-0,27x - 11	108	37	15	0,27x - 11	78	67
3	-20	-0,36x - 11	113	32	20	0,36x - 11	73	72
4	-25	-0,47x - 11	118	27	25	0,47x - 11	68	77
5	-30	-0,58x - 11	123	22	30	0,58x - 11	63	82
6	-35	-0,7x - 11	128	17	35	0,7x - 11	58	87

**** Experiment on roughness***

Each experiment was tested for 3 times and then the mean value of roughness was taken at the same diameter position Φ16. Experiment results of roughness are presented in Table 2. From the experimental results table, using the Minitab software, we have the roughness Ra versus angle **τ** plot, that is shown in Figure 4.

From the results of Table 2 and the plot in Figure 4, it is shown that in the case of left cone turning, when the angle τ increases from -35° to -10°, corresponding to the tool cutting edge angle φ decreases from 128° to 103°, the surface roughness decreases from 1,23μm to 0,67μm. In the case of right cone turning, when τ increases from 10° to 35°, corresponding to the tool cutting edge angle φ decreases from 83° to 58°, the surface roughness increases from 0,58μm to 1,19μm.

The relationship expression between roughness R_a and angle τ in the form of quadratic function also has been found by Minitab:

$$R_a = 0,5802 - 0,001705\tau + 0,000520\tau^2$$

The decision coefficient (R-sq = 98.2%) and the adjusted decision coefficient (R-sq (adj) = 97.9%) are greater than 90%. That indicates that the experimental obtained data is quite good for building a quadratic regression model.

Table 2 *Experiment result of roughness test*

TT	τ, (°)	φ, (°)	φ1, (°)	Ra, (μm)
I	**Left cone turning**			
1	-35	128	17	1,23
2	-30	123	22	1,12
3	-25	118	27	0,95
4	-20	113	32	0,82
5	-15	108	37	0,77
6	-10	103	42	0,67
Average roughness:				***0.92***
II	**Smoothing turning**			
7	0	93	52	0,61
III	**Right cone turning**			
8	10	83	62	0,58
9	15	78	67	0,63
10	20	73	72	0.76
11	25	68	77	0,87
12	30	63	82	0,99
13	35	58	87	1,19
Average roughness:				***0.83***

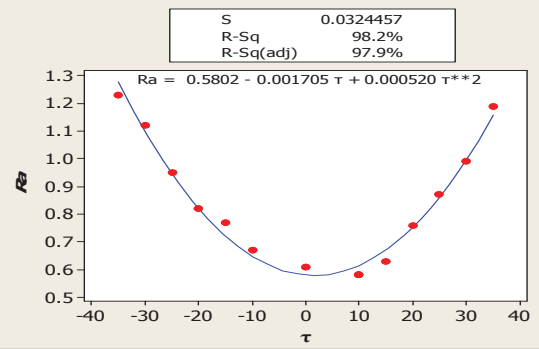


Figure 4 *Fitted line plot between R_a- τ*

3. Conclusion

Nowaday, profiles turning is not a new issue, however, there are very few published works on it about machining conditions and surface quality of the machined part. In this study, the relationship formula between dynamic tool cutting edge angle and dynamic tool minor cutting edge angle with the part profile geometry has been developed. From that, the gouge-free cutting condition in the general case has been established

The study has found out the relationship expression between the dynamic clearance angle with the static clearance angle, feed and part profile geometry when contour turning. This is the base for constructing the mathematical expression to define maximum feed when turning profiles.

The experiments which has been conducted for turning left cone surfaces, right cone surfaces on CNC lathe show that:

1)With the experimental conical surfaces in this study, when the minimum dynamic tool cutting edge angle $\varphi^*_{\min}$ and minimum dynamic tool minor cutting edge angle $\varphi^*_{1\min}$ are positive, gouge-free cutting condition meets fully. The result is consistent with the theory.

2) The processing surface roughness is significantly affected by the part profile. As the absolute value of profile angle (the derivative of profile equation) increases, the roughness increases, too. The study has also established the regression expression between roughness R_a and the variation of the profile angle τ in the form of quadratic equations

The results of this study enrich the theory of turning profiles, which is the base for calculating and selecting geometric parameters of cutting tool and cutting regime when turning profile on CNC lathe. They are also used as reference material for teaching and research.

References

1. L. B. Abhang* and M. Hameedullah (2010), *Power Prediction Model for Turning EN-31 Steel Using Response Surface Methodology*, Journal of Engineering Science and Technology Review 3 (1) (2010) 116-122.
2. Nguyen Van Cuong (2014), *Improved efficiency in shaping details,* Ph.D. thesis, Tula University, Russian Federation.
3. M. Kaladhar, K. Venkata Subbaiah, Ch. Srinivasa Rao and K. Narayana Rao (2011), *Application of Taguchi approach and Utility Concept in solving the Multi-objective Problem when turning AISI 202 Austenitic Stainless Steel*, Journal of Engineering Science and Technology Review 4 (1) (2011) 55-61, ISSN: 1791-2377 © 2011 Kavala Institute of Technology. All rights reserved. www.jestr.org.
4. Robert I. King, *Handbook of high speed machining technology*, TJ1185.H16 1985 671.3'5 85-4113, ISBN-13:978-1-4684-6423-8; D01: 10.1007/978-1-4684-6421-4.
5. Banh Tien Long, Tran The Luc, Tran Sy Tuy (2011), *principle of material cutting*, Hanoi Technic and Science Publishing House.
6. Banh Tien Long, Bui Ngoc Tuyen (2013), *Theory of surface shaping and application in mechanical engineering*, Vietnam education Science and Technics Publishing House, Hanoi.
7. Yoshitaka Morimoto, Souichiro Emoto, Takayuki Moriyama, Hideharu Kato, Katsuhiro Nakagaki, Naohiko Suzuki, Yoshiyuki Kaneko and Minoru Isobe (2012), *Creation of Curved Surface by Lathe Turning Development of CAM system using original tool layout*, 2212-8271 © 2012 The Authors. Published by Elsevier B.V. Selection and/or peer-review under responsibility of Professor Konrad Wegener, Open access under CC BY-NC-ND license, http://dx.doi.org/ 10.1016/j.procir.2012.04.018. Procedia CIRP 1 (2012) 114 - 119.
8. David A. Stephenson, John S. Agapiou, *Metal Cutting Theory and Practice*, Taylor & Francis Group, 2016.
9. Graham T. Smith (2008), *Cutting Tool Technology Industrial Handbook*, ISBN-13: 9781848002043, Library of Congress Control Number: 2008930567, Springer-Verlag London Limited 2008.
10. Virender Singh, Tasmeem Ahmad Khan (2013), *Comparative Performance Analysis of Insert Geometry for Turning Operation on CNC Turning Centre*, International Journal of Scientific Engineering and Technology (ISSN : 2277-1581), Volume No.2, Issue No.7, pp : 626-630. 1 July 2013.

Biological hydroxyapatite nanomaterial extracted from fish bones

Pham Viet Nam[1,*], Van Hoa Nguyen[2], Trang Si Trung[2]

[1]Ho Chi Minh University of Food Industry, 140 Le Trong Tan, Tan Phu District, HCM city, Vietnam

[2]Nha Trang University, 2 Nguyen Dinh Chieu, Nha Trang, Vietnam

*Corresponding author. Tel: (+84) 975557749; E-mail: pvnam@cntp.edu.vn

Keywords: Hydroxyapatite; Thermal treatment; Impurities; Fish bones.

Abstract. Hydroxyapatite (Ca10(PO4)6(OH)2, HA) is a well-known biomaterial which is widely used for biomedical applications such as bone implants, bone cements and dental pastes due to its chemical properties similar to the mineral component of bones and hard tissues in mammals. Generally, HA could be obtained by two ways including: (i) a synthetic method using calcium and phosphate sources, (ii) an extraction method using biological resources such as animal bones, fish scales and bones, egg shells and cuttle bones.

Biological HA obtained from fish bones can be used for biomedical applications including bone and dental engineering. However, HA has different crystallinities and purities due to various fish species, which much affect on the further applications. In this study, HA was produced from several popular fish bones by a heat treat method and characterized by elemental analysis, X-ray diffraction (XRD), scanning electron microscopy (SEM), transmission electron microscopy (TEM) and X-ray photoelectron spectroscopy (XPS). The prepared HA exhibited different crystallinities and impurity contents according to the sources of fish bones. This finding is practically useful to consider for any further applications of prepared HA from fish bones.

Researching on bearing ability of canopy of 2ANSHA powered roof support by finite element method

Nguyen Chan Phuong[1,a], Dr. Dinh Van Chien[2,b]

[1] Vinacomin - Institute of Energy and Mining Mechanical Engineering, No 565 Nguyen Trai Street, Thanh Xuan District, Hanoi City, Vietnam.
[2] Hanoi University of Mining and Geology, Hanoi, Vietnam, No 18, Pho Vien Street, Duc Thang Sub-district, Bac Tu Liem District, Hanoi City, Vietnam.
[a]chanphuongiemm@gmail.com
[b]vanchien.dinh@gmail.com

Keywords: Canopy of 2ANSHA, powered roof support.

Abstract

The content of this article presents distribution rule of ground stress on canopy of 2ANSHA powered roof support. Autodesk Inventor software is used to model 3D model and ANSYS Workbench software is utilized to calculated bearing ability of canopy. Therefore, results of stress, deflections and high stress points in powered roof supports in those cases will be generated.

1 Introduction

Vietnam National Coal and Mineral Industries Holding Corporation Limited (Vinacomin) always focuses on researching on domestically manufactured products in order to proactive supply chains. The 2ANSHA powered roof support is manufactured by Ukraine, has been used in Vinacomin since 2008 that proves the efficiency of this equipment and powered roof supports is needed to study and applied universally. In working process, powered roof supports bears pressure of ground roof directly. Finally, results of stress, deflections and high stress points in powered roof supports in those cases will be generated. These results will be applied in designing and innovating 2ANSHA powered roof supports and could be applied in other powered roof supports.

2 Research content

The combine of 2ANSHA powered roof support is manufactured by Ukraine and was used in 2008 in Mao Khe and Hong Thai Mines. This combine of powered roof support contains 2ANSHA powered roof support and 1ASHM Shearer which are used for 35^0 to 90^0 coal seam with the thickness from 1,1m to 2,2m. The roof of 2ANSHA is welded and assembled by steel planes and Q345R steel with U200x82x5.4 in dimensions and Technical Property of Q345R steel is shown in the Table 1 below. The dimensions of roof are 2450 mm in length, 800 mm in wide and 117 mm in height. There are two spherical supports under the canopy and fixed to two hydraulic legs which are set 1.3 m to each other. The roof bears 240 kN/m^2 pressure which is distributed in the Figure 2 [1;2].

Table 1: Technical Property of Q345R steel

Parameter	Young's Modulus (GPa)	Density ρ (kg / m^3)	Poisson's ratio μ	Yield Strength σ_{ch} (MPa)	Tensile Strength σ_k (MPa)
Value	206	7860	0.3	345	510

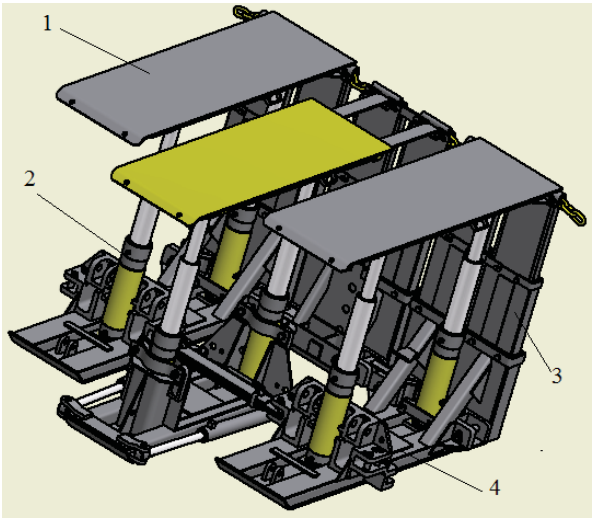


Figure 1: 2ANSHA powered roof support

1- Sliding canopy; 2-Hydraulic Leg; 3- Goaf shield; 4- Footplate

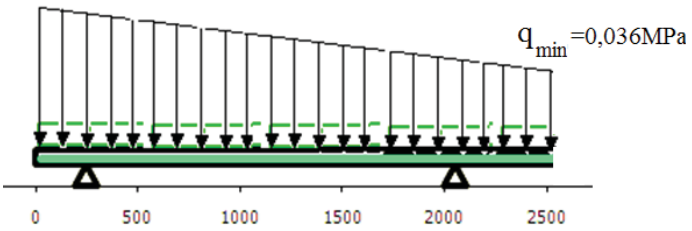


Figure 2: Pressure distribution on Sliding canopy

Static Structural Module of ANSYS Workbench software is used to calculate bearing ability of sliding canopy by finite element method. There are three steps to calculate bearing ability of sliding canopy, which are modeling 3D model, setting up material properties and meshing. Autodesk Inventor is utilized to model 3D model of sliding canopy *(Figure 3)*. Then 3D model is imported into ANSYS Workbench software. Material property of Q345R steel is set specifically E = 206 GPa, Density ρ = 7860 kg / m^3 and Poisson's ratio μ = 0.3. The 3D model is meshed into 426,223 quadrilateral finite elements and 112783 Hexahedron finite elements (Figure 4).

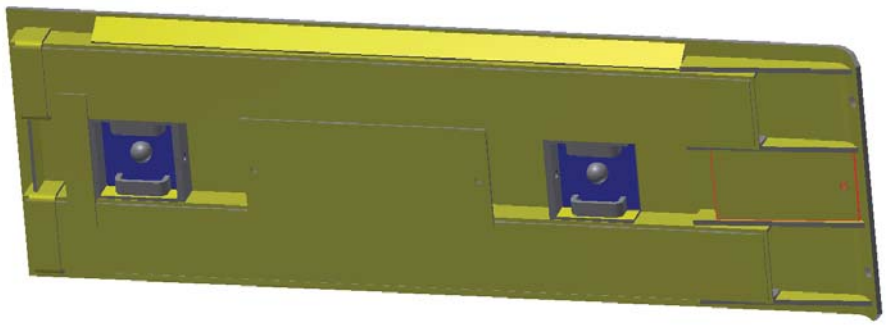


Figure 3: 3D Model of 2ANSHA sliding canopy

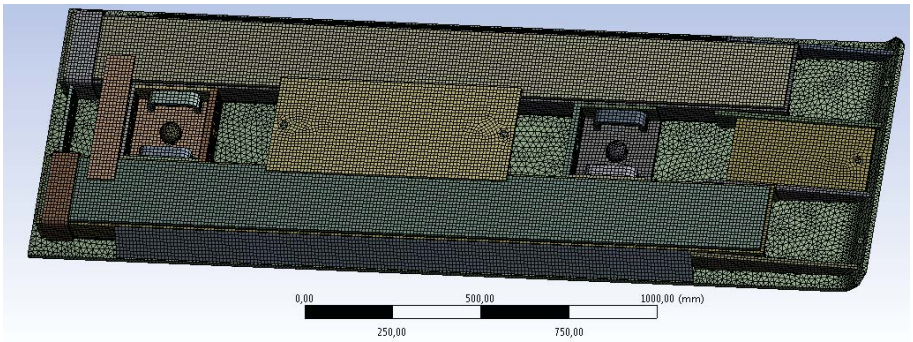


Figure 4: Meshing 2ANSHA sliding canopy finite element

After finishing the above step, pressure and constrains are set up specifically q_{max} = 0.268 MPa and q_{min} = 0.036 MPa on the top side of canopy *(Figure 5)*, two spherical supports are fixed completely *(Figure 6)* [6].

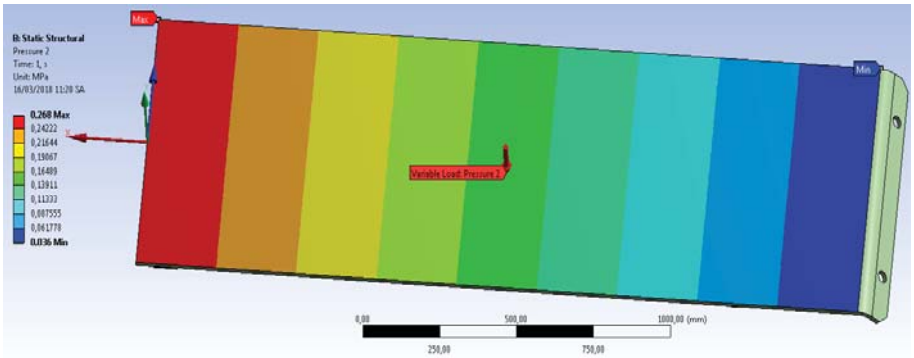


Figure 5: Pressure distribution on the canopy

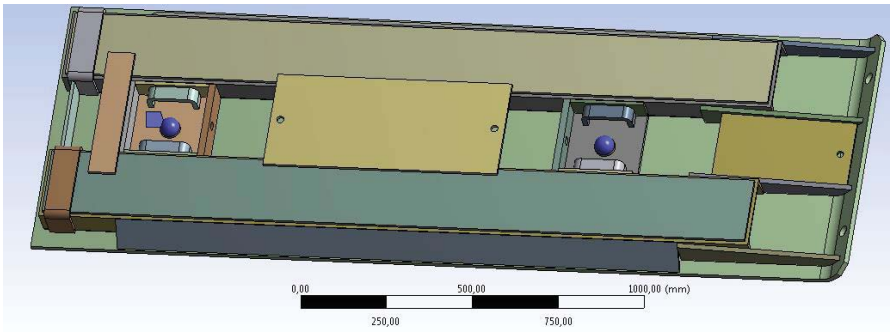


Figure 6: Two fixed supports

The calculation results show that the maximum stress is 266.2 MPa (Figure 7). The high stress areas are located at two supports and in the middle of canopy. However, the highest stress value is lower than the yield strength. Hence, the structure of canopy meets the working bearing need. The maximum deflection is 0.78 mm and the distribution are shown in the Figure 8 and located in the middle of the outer edges. However, the highest deflection values are not high; therefore, this deflection does not have an effect on working ability of canopy and other equipment.

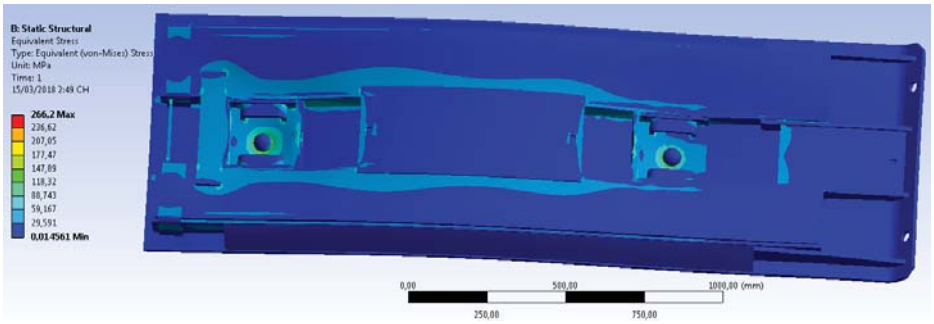


Figure 7: Pressure distribution of model

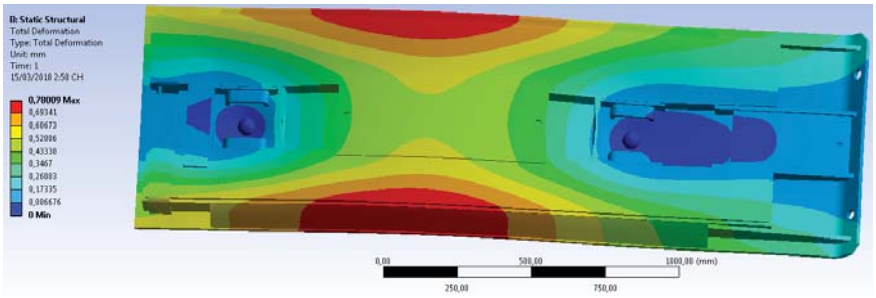


Figure 8: Deflection distribution of model

3. Conclusion

The canopy of 2ANSHA powered roof support could bear the maximum pressure, which is 266.2 MPa and is located at two supports and in the middle of canopy. the highest stress values is lower than the yield strength. Hence, the structure of canopy meets the working bearing need. The maximum deflection is 0.78 mm, and the distribution is shown in the Figure 8 and located in the middle of outer edges. However, the highest deflection values are not high; therefore, this deflection does not have an effect on working ability of canopy and other equipment in the combine.

References

[1] Nguyen H T, Researching on designing mining combine for angled seam (Type 2ANSHA). Summary report of Vinacomin's research, Hanoi, 2014.
[2] Vu C C, Designing and manufacturing powered roof support for coal seam with angled from 350 to 900 (type 2ANSHA) in underground mining. Summary report of Ministry of Industry and Trade's research, Hanoi, 2018.
[3] Truong T H, Ho N H, Khang S D. ANSYS 14.0 Tutorial. Mechanical Industry publisher, Beijing, 2012.
[4] Hua T P, ANSYS Workbench 15.0 self-learning. Electronic Industry publisher, Beijing, 2016.
[5] Ly P X, ANSYS Workbench designing model and simulation, Electronic Industry publisher, Beijing, 2011.
[6] Ton T N, Designing and Optimizing structure of powered roof support by ANSYS. Technical Postgraduate thesis, Shandong Science and Technology University, China, 2008.

Prediction of Combustion Behavior in a Boiler fired by Mixture of Vietnamese Anthracite and Coal Gas Using CFD

GIA MY TRAN[1,a*], DUC DUNG LE[2,b]

Hanoi University of Science and Technology,

Hanoi, Vietnam

[a] my.trangia@hust.edu.vn

[b] dung.leduc@hust.edu.vn

Keywords: anthracite-coal gas, composition, unburned carbon, CFD simulation

Abstract. The domestic anthracite is the most important fuel for Vietnamese thermal power plants. Due to high carbon percentage and low volatile matter it is difficult to ignite and to burn out the domestic anthracite. The rest carbon in ash is very high, in some cases approximately 40 %. To solve this problem some methods have been tested. In this research a mixture of anthracite and coal gas is considered. The purpose of the research is to describe a combustion behavior in a boiler, namely temperature, carbon and volatile matter distributions using CFD. The mixture consists of 4.3 % coal gas and 95.7% anthracite in mass. The boiler is divided into two combustion zones, the main zone 1 and the zone 2, to extend combustion area and through it to improve burning conditions for anthracite particles and to reduce NOx formation. All the anthracite mass and 1/3 coal gas volume are delivered into the zone 1, the rest of coal gas is into the zone 2. The CFD simulation is used for the zone 1. The simulation findings show that anthracite particles are ignited earlier, the mixture combustion develops in a larger space with higher temperatures, the carbon burning rate is remarkably improved due to coal gas. That means the domestic anthracite can be used better in boilers if some coal gas, 4 or 5 %, is mixed and the obtained ash can have lower unburned carbon, below 10%, and be more friendly for the environment.

Introduction

According to the master power plan VII, in the period 2015 – 2030 the electrical energy from coal power plants increases and takes the biggest percentage, from 34.4% in 2015 to 53.2 % in 2030. The thermal power plants are fired mostly with domestic anthracite or mixtures of domestic anthracite and imported bituminous coal. The shortage of coal used to generate power will be 48 million tons by 2020 [1]

The domestic anthracite has high carbon rate, approximately 60%, but low volatile matter, ≤7%. That is why the domestic anthracite is difficult to ignite and to burn out in boilers. The unburned carbon rate in ash from old plants is very high, 15-40%, from the new ones is not low, ≥12% [13].

To reduce unburned carbon rate the domestic anthracite can be mixed with imported bituminous coal, that makes a volatile matter of the anthracite higher [13].

Pulverized coal combustion is a complicated phenomenon of chemical reactions and depended highly on various factors such as fuel properties, primary air, secondary air and phasing of air supply, particle diameter [3]. Blending coal enables a better control the coal quality and improves combustion efficiency [11].

Many CFD studies undertaken of coal combustion relating to coal fired furnace, for example [6-10] have shown that CFD provides an accurate tool for predict the behavior of coal combustion and the results obtained from these studies are relatively reasonable comparing with the experiment.

To be independent of imported coals we would like to provide a new solution, namely to mixing domestic anthracite with coal gas produced from anthracite itself on the spot.

The objective of this study is to predict the combustion behavior of single coal and mixing domestic anthracite with coal gas when fired in a downshot furnace operated in Vietnam by using

CFD numerical simulation. The firstly, the results are emphasized on Vietnamese single coal. Then the influence of mixing coal gas combustion to the combustion process will be assessed in the terms of conversation rate, volatile matter distribution, and burning rate of volatile and char.

Input data conditions

The composition of the fuels delivered into a boiler is shown in the table 1 and the table 2.

Table 1: Domestic anthracite composition, (mass %)

C	H	O	N	S	A	W	V	HHV
57.3	2.0	2.5	0.7	0.6	28.7	8.2	7.5	21788(kJ/kg)

Table 2: Coal gas composition

	CO	H_2	CO_2	CH_4	O_2	N_2	
Vol. %	38.0	50.0	6.0	0.5	0.5	5	100
Mass %	66.8	6.3	16.6	0.5	1.0	8.8	100

To make the volatile matter of the anthracite approximately 15% [13], the coal gas mass ratio in the mixture must be

$$M_{cg}: M_{anth} = 0.045 \text{ (kg/kg)} [14]$$

After the conversion of the anthracite and the coal gas, the mixture has the composition shown in the table 3.

Table 3. The mixture composition, (mass %)

C	H	O	N	S	A	W
56.36	2.24	4.84	0.74	0.55	27.45	7.83

To guarantee a 600 MW power the mass input must be 224 600 (kg/h) for the anthracite and 10145 (kg/h) for the coal gas. The excess air ratio $\alpha = 1.2$.

To extend the combustion area and through it to improve burning conditions for anthracite particles and to reduce NOx formation. The mixture of anthracite coal and coal gas was introduced to primary burners. It can be enhanced rich fuel zone and reduced period of coal ignition time. Rich fuel zone (zone 1) is reforming condition zone, therefore NOx could be reduced [8,12]. The combustion furnace can be assumed as two zones as showing in Fig 1. The main combustion and reduction NOx, zone 1 and the complete combustion, zone 2.

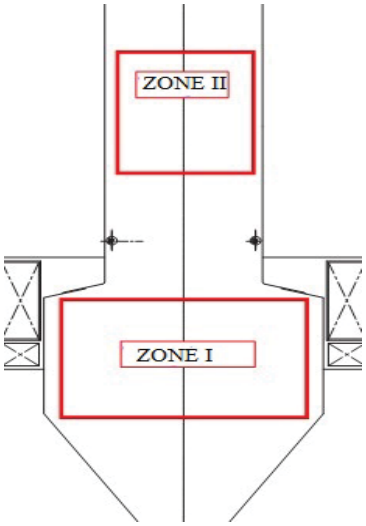


Fig.1. The calculation zones in the boiler

A 3D model of boiler according to ANSYS is shown in the Fig.2

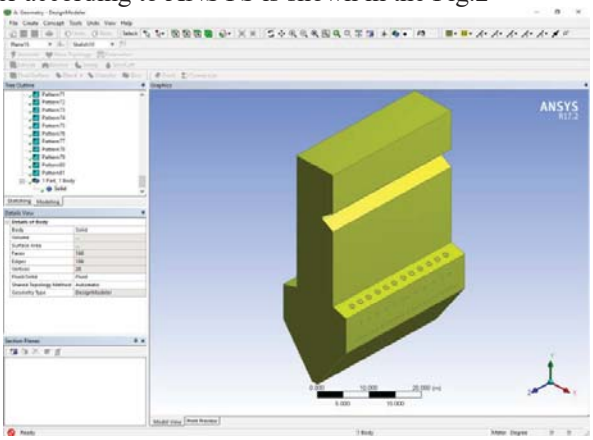


Fig.2. The 3D model of boiler according ANSYS

Numerical simulation

The model is solved using ANSYS-Fluent 17.2. In Fluent, the governing equations including the mass, momentum, chemical species and energy equations are discretized by using the finite Volume method. The continuity and momentum equations were solved using the coupled algorithm. The grid-independent study is done for all cases. All simulations are run K-ε reliable model for turbulent gas phase. The motion of the representative coal particles was calculated by Lagrangian formulation. The radiative heat transfer among the gas, particles and wall were simulated by DO model. Boundary conditions used are mass flow rate and temperature. Meshing is done in ANSYS meshing. The inlet surface and volume meshing were done with approx. 700.000 tetrahedral element.

The coal combustion process is modelled by the following two step reaction mechanism:

$$\text{Coal} + aO_2 \rightarrow bCO + cH_2O \qquad \text{(Eq. 1)}$$

$$CO + \tfrac{1}{2}\,O_2 \rightarrow CO_2 \qquad \text{(Eq. 2)}$$

Here, a, b, c are determined by the coal constituent. A general model of pulverized coal devolatilization and a general model of char combustion were incorporated into the comprehensive model in Fluent. Further details regarding the fluid flow, turbulence models, radiation models, and coal combustion models can be found in [6] [8] [9] [11].

The results and discussion

Flow field and particle trajectories

The velocity distribution and vectors in cross sections along the furnace height are shown in Fig.3. The speed velocity vectors are mostly similar. It is well distribution of particles in the furnace in both cases.

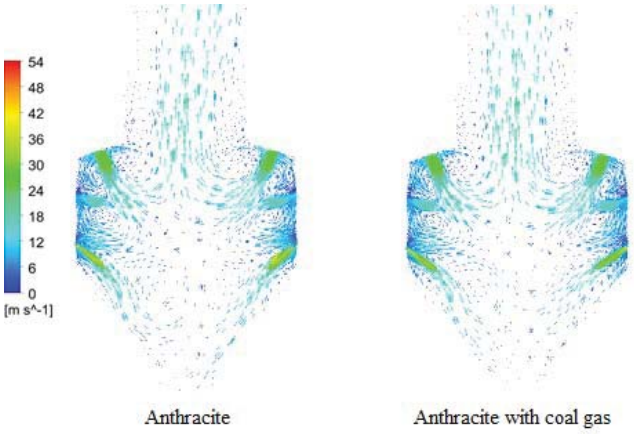


Fig.3. Velocity vectors in different fuels

Temperature distribution

Temperature distributions for two kind of fuels are shown in the Fig.4, the left for the anthracite and the right for the mixture. The anthracite has 100% input, the mixture has less, about 97%, nonetheless the combustion area of the mixture is remarkably larger and the temperatures are higher, Fig.5.

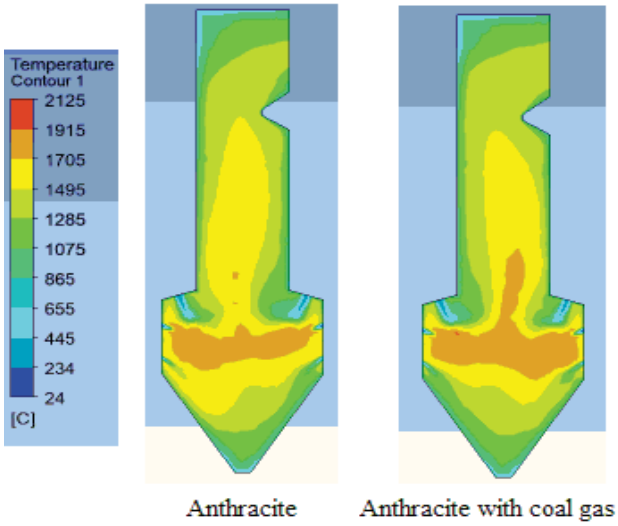


Fig.4. Temperature distribution in the boiler

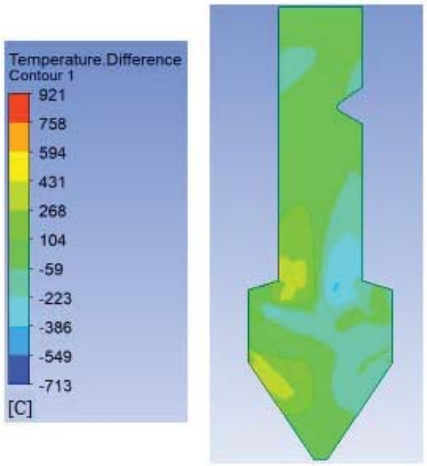


Fig.5. Temperature difference

The carbon burning rate is shown in the Fig.6. It is clearly that a single anthracite has more unburned carbon than the mixture.

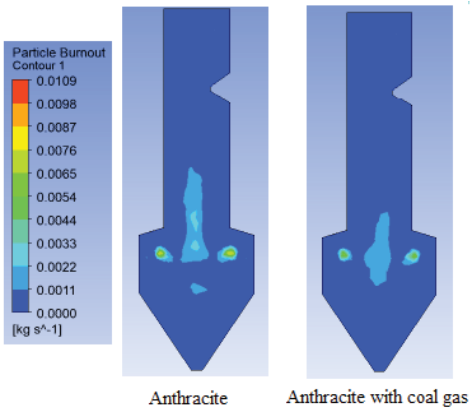


Fig.6. The carbon burning rate

The volatile matter distributions are shown in the fig.7. The volatile matter in the mixture is distributed in a larger area with higher concentrations that makes anthracite particles easier to ignite and to burn out.

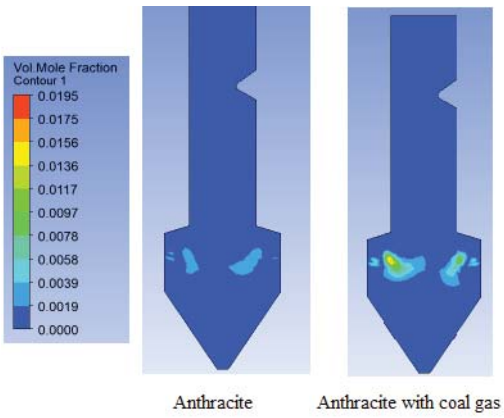


Fig.7. Volatile matter distribution

Conclusion

The combustion simulation of mixture of Vietnamese anthracite and coal gas show positive results. Mixture of anthracite coal and coal gas and stage combustion can be a solution for increasing carbon burning rate.

References

1. Vietnam Government, *Power Planning VII*, Hanoi, 18.03.2016.
2. Philip J. Stopford, *Recent Applications of CFD Modelling in the Power Generation and Combustion industries*, Applied Mathematical Modelling 26 (2002) 351 – 374.
3. Rajesh Holkar, Dr. Omprakash. D. Hebbal, *CFD Analysis of Pulverized-Coal Combustion of Burner Used In Furnace with Different Radiation Models*, Journal of Mechanical and Civil Engineering, Vol 5 (2013) 25-34.
4. Ryoichi Kurose, *Numerical Simulations of Pulverized Coal Combustion*, KONA (Review) in press.
5. Efim Korytnyi, Roman Saveliev, Miron Perelman, Boris Chudnovsky, Ezra Bar-Ziv, *Computational Fluid Dynamic Simulation of Coal-Fired Utility Boilers: An Engineering Tool*, Fuel 88 (2009) 9-18.
6. T. Asotani, T. Yamashita, H. Tominaga, Y. Uesugi, Y. Itaya, S.Mori, *Prediction of Ignition Behavior in a Tangentially Fired Pulverized Coal Boiler Using CFD*, Fuel 87 (2008)482-490.
7. Z.Q. Li, F.Wei, Y. Jin, *Numerical Simulation of Pulverized Coal Combustion and NO Formation*, Chemical Engineering Science 58 (2003) 5161-5171.
8. Choeng Ryul Choi, Chang Nyung Kim, *Numerical Investigation on the Flow, Combustion and NOx Emission Characteristics in 500 MWe Tangentially Fuel Pulverized Coal Boiler*, Fuel 88 (2009) 1720-1731.
9. Cristiano V. da Silva, Maria Luiza S. Indrusiak, Arthur B. Beskow, *CFD Analysis of the Pulverized Coal Combustion Processes in a 160 MWe Tangentially-Fired-Boiler of a Thermal Power Plant*, J. of the Braz. Soc. of Mech. Sci. & Eng. Vol XXXII, No.4, 2010.
10. Minghou Xu, Jianwei Yuan, Shifa Ding, Handing Cao, *Simulation of the Gas Temperature Deviation in Large-Scale Tangential Coal Fired Utility Boilers*, Comp. Methods Appl. Mech. Engineering 155 (1998) 369-380.
11. Y.S. Shen, B.Y. Guo, P.Zulli, D. Maldonado, A.B. Yu, *A Three- Dimensional CFD Model for Coal Blends Combustion: Model Formation and Validation*, Fifth International Conference on CFD in the Process Industries, 2006.
12. R.I. Backreedy, J.M. Jones, L.Ma, M. Pourkashanian, A. Williams, A. Arenillas, B. Arias, F. Rubiera, *Prediction of Unburned Carbon and NOx in a Tangentially Fired Power Station Using Single Coals and Blends*, Fuel 84 (2005) 2196-2203.
13. C.T. Nguyen, *Investigating Solution Improving Vietnamese Anthracite Burning Efficiency for Thermal Power Plants*, 2017.
14. Q.M. Vu, *Investigating Combustion of Domestic Anthracite Mixed with Coal Gas*, 2017.

A STUDY ON THE RECOVERY OF PRECIOUS METALS FROM GOLD MINE TAILING

Jei-Pil Wang

Department of Metallurgical Engineering, Pukyong National University, Busan, South Korea

Tel: (+82) 516296341; E-mail: jpwang@pknu.ac.kr

Keywords: Gold tailing 1; Viscosity 2; Basicity 3.

Abstract. Gold production produces much gold mine tailing and 100 tons of them are generated daily in the Republic of Korea. The gold mine tailing for the current studies contains 0.11g/t Au and 3.38g/t Ag, which shows the possibility of recovering gold and silver through dissolve smelting the slag and separating the gold and silver from the molten copper by mass. Better slag fluidity provides to better dissolve process of gold and silver. Slag fluidity and viscosity depend on the temperature and slag composition. As melting temperature increases, the slag viscosity decreases. The studied gold mine tailing consists mostly from SiO2, FeO and Fe2O3 oxides and by adding CaO it will create a melting composed of CaO•SiO2, 2FeO•SiO2, CaO•FeO•SiO2 and 2CaO•Fe2O3 complex molecules. Reduction of slag viscosity is directly related to its basicity. In other words, when CaO/SiO2 at optimal ratio, viscosity reaches its minimum value.

Improving the efficiency of Dye sensitized solar cells by usingCr-doped TiO2 material

Nguyen HuyHao[1], Soo Wohn Lee[1,a*]

[1]Research Center for Eco-multifunctional Nano Materials,

Sun Moon University, Asan, Republic of Korea

[a]email: swlee@sunmoon.ac.kr

Keywords: TiO2; solar cell; microwave;efficiency; photoelectrons

Abstract. In recent years, the depletion of fossil fuels has become one of the big problems that people are currently facing. Dye sensitized solar cells (DSSCs) which converts solar light into electric energy, are expected to be a potential solution for energy problems due to possessing a number of potential applications such as low-cost technology and simple fabrication procedure. A typical DSSC is composed of a mesoporous TiO2film, Ruthenium(II) based photosensitizer, an electrolyte containing I3−/I− redox couple, and a Pt counter electrode. Its principle working is based on photoelectric effect. In this work, Cr-doped TiO2 was synthesized by microwave hydrothermal method. This material was then applied to prepared dye sensitized solar cell. By using microwave, the reaction time was decreased from several days in sol-gel traditional way to 4 h. The dye sensitized solar cell based on the (TiO2-P25+ Cr-TiO2)/TiO2-P25 hetero-structure was fabricated. We showed through our analyses thatthis hetero-structure hasformed amultiple conduction band system, leading to a significant improvement in the photoelectron lifetime. Also, the results indicated that inserting Cr atoms in TiO2 crystal lattice structure has created Ti3+ which can prevent the movement of holes and cause photoelectron more mobile to transport forward the anode. These effects of hetero-structure increase the power conversion efficiency of dye sensitized solar cells. The X-ray diffraction was used to analyze the crystal structure of all samples. The microstructure of material was observed by transmission electron microscopy. Photoluminescence spectra (PL) were measured to analysis the recombination of electron-hole pairs. The X-ray photoelectron Spectroscopy (XPS) was performed with an X-ray monochromator XR5 Gun-500 um from Thermo scientific. The band gap energy was determined by UV-vis diffuse reflectance spectroscopy. The conversion efficiency of the fabricated DSSCs was measured under a simulated solar light source (Portable solar simulator PEC-L01, Pecell 200 W) (Am 1.5G). Electrochemical Impedance (EIS) and Incident Photon Conversion Efficiency (IPCE) were measured by IVIUMSTAT (electrochemical interface, Netherlands).

Reference

[1] M. Adachi, Y. Murata, J. Takao, J. Jiu, M. Sakamoto, and F. Wang J. Am. Chem. Soc, 2004, 126, 14943–14949.

[2] B. O'Regan, M. Gratzel, Nature, 1991, 353, 737–740.

[3] N. H. Hao, G. Gyawali, S. W. Lee, J. Ceram. Process. Res, 2016, 17, 409–413.

[4] N. H. Hao, G. Gyawali, T. Sekino, S. W. Lee, Prog. Nat. Sci. Mater. Int, 2016, 26, 375–379.

[5] Z. He, Z. Hou, Y. Xing, X. Liu, X. Yin, M. Que, J. Shao, W. Que, P.J. Stang, Sci. Rep, 2016, 6, 6–13.

Dissimilar metals joining between AA5083 and high strength steel sheets

Kwangjin Lee[1,a*],Euipyo Kwon[1], Hyunkyung Park[2], Jiwon Jeong[2]

[1]Korea Institute of Technology, Jeonju, South Korea

[2]Donghae Metal, Pyeongtaek, South Korea

[a]email: kjleei@kitech.re.kr

Keywords: Self Piercing Rivet; Friction Stir Spot Welding; Mechanical property; Al Alloy; High Strength Steel

Abstract. Weight reduction of various transportation components is strongly required now for environmental protection and energy savings. Production of all-aluminum auto body is one of the answers satisfying this requirement. However, several problems, such as the cost increase, insufficient formability and poor fracture resistance of aluminium products still remain unsolved. Another probable measure for weight reduction is the so-called "multi-componentization of structural parts." This is the attempt to achieve weight reduction of the vehicle by choosing the most adequate materials for each usage with minimum cost increase. The development of new joining method for dissimilar metals is an indispensable technique for multi-componentization. The most popular combination of metals is aluminium and steel. Several joining method, such as diffusion bonding,1) explosive welding,2) rolling,3) and friction welding4) have been attempt so far in order to obtain sound joint. However, sound joints with acceptable strength have not yet been attained since the formation of a brittle Fe-Al intermetallic compound layer at the welding interface has been inevitable.5) In this study, lap joining of automotive 5083 aluminum alloy and high strength dual phase steel sheets was performed using both self-piercing rivet(SPR) and friction stir spot welding(FSSW) method. In SPR process, geometry of die, punch and rivet was varied to select optimised condition. In FSSW process, tool geometry, tool rotational speed and plunge depth was controlled. The authors also used adhesive bonding material to avoid galvanic corrosion at the welding interface between aluminium and steel. Tensile test and fatigue test were performed to evaluate the mechanical properties of the joints. Optical microscopy (OM), Scanning electron microscopy (SEM) and Electron probe micro analyser (EPMA) were applied to investigate welding region. Maximum tensile shear strength of 11KN was obtained in both SPR and FSSW joints. Fatigue limit of the joints was over 1.7KN. As the results, it was revealed that both SPR and FSSW processes with adhesive are promising joining process to get sound dissimilar metal joints.

Reference

[1] N. Iwamoto, M. Yoshida, T. Takeuchi, M. Makino, *Trans. JWRI*, **1975**, 4, 67.

[2] M. Kikuchi, H. Takeda, S. Morozumi, *J. Jpn. Inst. Light Metals,* **1984**, 34, 165.

[3] H. Oikawa, T. Saitoh, T. Nagase, T. Kiriyama, *Iron & Steel,* **1997**, 83, 614.

[4] T. Shinoda, M. Ogawa, S. Endo, K. Miyahara, *J. Jpn. Weld Soc.,* **2000,** 18, 365.

[5] E. Schubert, M. Klassen, I. Zerner, C. Walz, G. Sepold, *J. Mater. Pro. Tech.,* **2001**, 115, 2

PROCEEDINGS

THE FIRST INTERNATIONAL CONFERENCE ON MATERIAL, MACHINES AND METHODS FOR SUSTAINABLE DEVELOPMENT

Bach Khoa Publishing House, Hanoi

1 – Dai Co Viet – Hanoi

Tel. (84.24) 3868 4569; Fax. (84.24) 3868 4570

http://nxbbk.hust.edu.vn

-----***-----

Responsible for Publication

Director and Editor-in-Chief: Dr. Bui Duc Hung

Editor: Nguy Thi Lieu

Book designer: Nguyen Thi Hong Minh

Cover designer: Kim Chi

Printed at: Tandaiviet Printing and Office Services Joint Stock Company, 16 Chua Lang Street, Dong Da District, Hanoi, Vietnam.

Quantity: 150 copies. Size: (21 x 29,7) cm.

Registration No.: 1455-2018/CXBIPH/01-36/BKHN; ISBN: 978-604-95-0502-7

Decision publish No.: 41/QĐ-ĐHBK-BKHN, 8/5/2018

Archived: II/2018.

MMMS 2018

PROCEEDINGS

THE FIRST INTERNATIONAL CONFERENCE
ON MATERIAL, MACHINES AND METHODS
FOR SUSTAINABLE DEVELOPMENT

Research Development in Industrial Material, Machining and Methods towards Sustainability

EDITORS
Banh Tien Long
Hyungsun Kim
Kozo Ishizaki
Nguyen Duc Toan
Nguyen Thi Hong Minh

ISBN: 978-604-95-0502-7



SÁCH KHÔNG BÁN